Measurement of Spin Correlations in $t\bar{t}$ Systems in the muon+jets Channel using a Matrix Element Method with the CMS Detector at the LHC.

Kelly Beernaert

Promotors: Prof. Dr. Martin Grünewald, Prof. Dr. Dirk Ryckbosch and Dr. Efe Yazgan

Proefschrift ingediend tot het behalen van de academische graad van
Doctor in de Wetenschappen: Fysica

Universiteit Gent
Faculteit Wetenschappen
Vakgroep Fysica en Sterrenkunde
2011 - 2015

She soon found the door the alethiometer had told her about. The sign on it said DARK MATTER RESEARCH UNIT, and under it someone had scribbled R.I.P. Another hand had added in pencil DIRECTOR: LAZARUS. Lyra made nothing of that. She knocked, and a woman's voice said, "Come in."
- Phillip Pullman, His Dark Materials [1]

Acknowledgements

First and foremost I would like to thank both Prof. Dr. Dirk Ryckbosch and Prof. Dr. Martin Grünewald for giving me the opportunity to do a PhD at the University of Ghent. Dirk, thank you for the support and advice you gave me when I, once again, walked through the open door of your office with an unanswerable question. Martin, your guidance was invaluable during this PhD. You provided the necessary insight when I was stuck and the skills I learned will undoubtedly serve me a lifetime.

Efe, I can safely say this thesis would not be here without you. I think most people who will read this know that I'm not always the most easy person to work with, but it truly has been a pleasure working with you. Nobody could ask for a better supervisor than you have been. You've guided me through technical and conceptual difficulties with the analysis. You've always had a listening ear (I do not dare to count the hours I've spent in your office talking, discussing, ...) and a helping hand. I wish nothing but the best for you, Yasemin and Ege.

This measurement was only made possible by the theoretical work of Prof. Werner Bernreuther. In addition, I am very grateful for the help and explanation he provided during this measurement. In the CMS Top quark group, there are many people who have provided support and experience to ensure the quality of this measurement, which was greatly appreciated.

Benjamin, Sinead, thank you for helping me take my first steps in the Ghent Top group. Volker, your opinion and expertise were always appreciated. Anna, you've been more than a colleague. Thanks to the many colleagues at the INW for the help, advice and talks. Thank you to The Dudes: John, Daniel, Anna and Andrea, for many enjoyable Monday-evenings and weekends in Geneva. Thank you to my office mates and lunch group, too many to mention, for many hours of lunchtime conversation at CERN. I owe a big thank you to the administrators of the computing resources at the IIHE, their quick response to all sorts of technical problems has been greatly appreciated.

Een welgemeende dank u aan mijn vrienden voor de steun door de jaren heen: Joyce, Maaike, Elodie, Yasmien, Sofie, Maxime, Sebastian en de vrienden van de fysica van de tweede rij. En als laatste, maar zeker niet de minste, bedank ik mijn familie voor de steun en goede zorgen.

Contents

Abstract

In this work, the consistency of the spin correlation strength in top quark pair events with the Standard Model (SM) prediction is tested in the muon+jets final state. The events are obtained from pp collisions at a centre-of-mass energy of $\sqrt{s} = 8$ TeV, corresponding to an integrated luminosity of 19.7 fb^{-1}. Using a Matrix Element Method, event likelihoods are calculated under two different top quark pair hypotheses: the SM hypothesis and a hypothesis which predicts zero spin correlation. Using the event likelihoods, a variable sensitive to the spin correlation strength is constructed. In a hypothesis testing procedure, the data are found to favour the SM hypothesis. Using a template fit method, the fraction of events that show SM spin correlations is measured to be $f = 0.72 \pm 0.08\,(\text{stat})^{+0.15}_{-0.13}\,(\text{syst})$, representing the most precise measurement of this quantity in the lepton+jets channel to date.

Introduction

For over two thousand years, mankind has been contemplating the fundamental constituents of nature. Already in ancient Greece, the concept of an indivisible particle or building block of matter was introduced as an atom. In the twentieth century, experimental evidence for ever smaller particles was found: atoms consist of an atomic nucleus with an electron cloud, the atomic nucleus consists of protons and neutrons and in their turn protons and neutrons consist of quarks. Large progress in the search for the fundaments of reality was made with the advent of Quantum Physics and elementary particle physics. Particle physics tries to describe the fundamental constituents of matter and the interactions between them. The Standard Model is the theoretical framework describing our current knowledge of particle physics. At present day, the Standard Model does not include a description of gravity. In the Standard Model, all matter is built up of twelve fundamental particles: six leptons and six quarks. The heaviest particle discovered is the top quark with a mass of $173.21 \pm 0.51\,(\text{stat.}) \pm 0.71\,(\text{syst.})\,\text{GeV}/c^2$ [2]. Due to its high mass, the top quark plays an important role in higher order corrections of the Standard Model and New Physics model predictions.

In March 2010, the Large Hadron Collider (LHC) at the European Organisation for Nuclear Research (CERN) started producing high energy proton-proton collisions at a centre-of-mass energy of 7 TeV. At this energy, the top quark production rate is over 20 times higher than any other collider achieved. The data events are recorded by detectors such as the Compact Muon Solenoid (CMS), which collected the data used in this work. With the large set of top quark events, it is possible to perform measurements of the top quark properties with a high precision.

Top quarks are mainly produced in pairs at the LHC. Although there are no restrictions on the direction of the top quark spin itself, there is a high degree of correlation between the spins in a top quark pair. This spin correlation strength is predicted by the Standard Model and its measurement is the object of this thesis. Any deviations from this Standard Model value can point to New Physics.

This thesis is organised in four parts. The first part describes the theoretical background and the experimental set up for this analysis. In chapter one, the Standard Model of particle physics is introduced with details on top quark physics and a particular emphasis on the spin correlation strength. Chapter two describes briefly the LHC and the CERN accelerator complex with a particular focus on the CMS detector and some aspects of the data-taking process. The second part of this thesis focusses on the simulation and other software tools necessary to perform this analysis, described in chapter three. In chapter four, more information is given on the reconstruction of physics objects based on the signature in the CMS detector. And in addition, an introduction to the reconstruction of top quark pairs is given. Part three is dedicated to event selection. In chapter five, the event selection performed to select the data used for this measurement is detailed. Chapter six describes the monitoring of some trigger paths which are responsible for selecting and storing top quark events during data-taking. The fourth and final part of this thesis describes the spin correlation measurement. Chapter seven goes into a description of the Matrix Element Method which is used to calculate event likelihoods. Chapter eight describes how these event likelihoods can be used for the extraction of the spin correlation strength and a hypothesis testing of the data. Initial tests to check the feasibility of this method are detailed in this chapter, in addition to further tests at reconstruction level simulation. Chapter nine deals with the results and the systematic uncertainty sources influencing this measurement. We finish in chapter ten with a critical assessment of the analysis method and an outlook. In chapter eleven, a Dutch summary is given. There are several appendices, describing some technical de-

tails needed to reproduce this work: names of the simulation samples used, code for the matrix element calculation, settings of the likelihood calculations, ...

Part I

Theory and Experimental Set-up

Chapter 1

Theoretical Overview

In this chapter the Standard Model (SM) of elementary particle physics will briefly be described. The SM describes the fundamental particles which are the building blocks of matter and the interactions between them. After a general overview of the SM, more details will be provided on one of the fundamental particles: the top quark. The top quark has a unique position in the SM, making it an interesting field of research, which will be highlighted in section 1.2. In the final section of this chapter, section 1.3, a short theoretical introduction on spin correlations in the $t\bar{t}$ system will be presented. The measurement of spin correlations in $t\bar{t}$ systems is the main topic of this thesis, so a motivation for this measurement from the theory perspective will be given in the final section of this chapter.

1.1 Standard Model of Physics

The Standard Model (SM) of elementary particle physics is a quantum field theory that comprises our current knowledge of the fundamental constituents of matter and the interactions between them. There is a multitude of physics textbooks describing the SM, here I refer to [3]. All matter can be built up from a collection of 12 particles called fermions and their corresponding anti-particles. All fermions have spin 1/2. The identity of a fermion is also referred to as the flavour of the particle. The fermions can be categorised in two groups: six leptons and six quarks. The leptons consist of three charged particles: the electron, the muon and the tau. In addition there are three neutral leptons: the neutrinos. There are six quarks which all carry fractional electric charges: up, down, charm, strange, top and bottom. The particles and their characteristics are listed in table 1.1. As can be seen from the table, both the leptons and quarks can be grouped together in families or generations. Between each generation, all the particles have the exact same quantum numbers, but the particles in each generation are heavier than their corresponding particles in the lower generation. For neutrinos, this is not established, as the masses are very small and have not been precisely measured yet. As for quarks, it was found that neutrino flavour-eigenstates are superpositions of different neutrino mass-eigenstates [2]. The particles of the second and third generation are unstable and decay to (eventually) first generation particles. All matter around us is made up of first generation particles: up- and down-quarks make up the proton (uud) and neutron (udd) to form the atomic nucleus and together with an electron cloud atoms are formed. It is still unknown why there are three generations.

Currently we know of four interactions working on the fermions: the Strong interaction, the Weak interaction, the Electromagnetic interaction and gravity. Of these four interactions, only gravity is not described in the SM, since no renormalisable theory of gravity has been developed yet. The forces are carried by the exchange of particles called bosons which are listed in table 1.2. The electromagnetic force is carried by the photon which is massless and interacts with particles carrying an electric charge. The photon itself carries no electric charge. The interaction between photons and charged particles is described in Quantum electrodynamics (QED). Quantum chromodynamics (QCD) describes the interaction between gluons and coloured objects. The gluons are the carriers of the strong interaction and work on particles with a colour charge. There are three colour charges: red, green and blue (and the corresponding anti-colours). There are in total eight gluons which are massless and carry colour charge themselves. As a consequence, gluons

can interact with themselves. The size of the strong coupling constant $\alpha_s(M_Z) = 0.12$ is very large at low energies meaning the strong interaction cannot usually be described perturbatively, unlike the electromagnetic interaction with a coupling constant $\alpha \approx 1/137$. A consequence of the large α_s at low energies, is the phenomenon of colour-confinement i.e. coloured objects can never be observed as free particles. Instead we can only observe colourless or "white" objects by the combination of colour-anticolour or the combination of red, blue and green together. At high energies, where α_s is smaller, quarks become asymptotically free ($\alpha_s \to 0$).

Table 1.1: Fundamental matter particles in the SM and their quantum numbers.

Fermions	Generations			Electric	Colour	Isospin T_3
0	1	2	3	Charge	Charge	(3^{rd} comp.)
units				$[e]$	$[r, g, b]$	$[-]$
Leptons	$\begin{pmatrix}\nu_e \\ e\end{pmatrix}_L$	$\begin{pmatrix}\nu_\mu \\ \mu\end{pmatrix}_L$	$\begin{pmatrix}\nu_\tau \\ \tau\end{pmatrix}_L$	0	-	1/2
				-1	-	-1/2
	e_R	μ_R	τ_R	-1	-	0
Quarks	$\begin{pmatrix}u \\ d\end{pmatrix}_L$	$\begin{pmatrix}c \\ s\end{pmatrix}_L$	$\begin{pmatrix}t \\ b\end{pmatrix}_L$	+2/3	r,g,b	1/2
				-1/3	r,g,b	-1/2
	u_R	c_R	b_R	+2/3	r,g,b	0
	d_R	s_R	t_R	-1/3	r,g,b	0

The weak interaction is carried by three intermediate vector bosons: the W^+, W^- and Z^0. The intermediate vector bosons have the precisely measured masses of $91.1876 \pm 0.0021\,\mathrm{GeV}/c^2$ for the Z and $80.385 \pm 0.015\,\mathrm{GeV}/c^2$ for the W [2]. All particles, apart from the gluons and photons, carry the weak charge. The theory of the electromagnetic and weak interaction can be described in a unified theory: electroweak theory (EWK) [4–6].

Table 1.2: Gauge bosons of the SM and their quantum numbers.

particle	interaction	J^P	Electric Charge	Isospin T_3 (3^{rd} comp.)
photon (γ)	electromagnetic	1^-	0	0
8 gluons (g)	strong	1^-	0	-
Z^0	weak	1	0	0
$W^\pm$	weak	1	$\pm e$	± 1

There are two types of electroweak interactions: neutral current and charged current. The neutral current interaction is mediated by the Z boson or by the photon. The neutral current interaction conserves the colour, charge and flavour of the fermion. The charged current interaction is mediated by the W bosons. In the charged current interaction, the flavour of the fermion is changed, and the charge of the initial and final state fermion differs by one unit. In the weak interaction, the mass eigenstates do not correspond to the flavour eigenstates of the quarks. The coupling of the weak interaction to the up-type quarks and down-type quarks is described by the Cabibbo-Kobayashi-Maskawa (CKM) matrix [2] given by 1.1. Here, the ($|d\rangle$, $|s\rangle$, $|b\rangle$) are the mass eigenstates, while ($|d'\rangle$, $|s'\rangle$, $|b'\rangle$) are the flavour eigenstates. The CKM matrix is given with respect to the down-type quarks, but since the matrix is unitary, we would obtain the same for the up-type quarks. The probability of a quark i decaying to a quark j is

proportional to $|V_{ij}|^2$.

$$\begin{pmatrix} |d'\rangle \\ |s'\rangle \\ |b'\rangle \end{pmatrix} = \begin{pmatrix} V_{ud} & V_{us} & V_{ub} \\ V_{cd} & V_{cs} & V_{cb} \\ V_{td} & V_{ts} & V_{tb} \end{pmatrix} \begin{pmatrix} |d\rangle \\ |s\rangle \\ |b\rangle \end{pmatrix} \tag{1.1}$$

The quantum field theory description of the SM describes all gauge bosons as massless fields. However, we know that the W and Z bosons are not massless. There is no renormalisable Lagrangian which includes mass terms. The Higgs mechanism describes the generation of the boson masses by spontaneous symmetry breaking. In the Higgs mechanism, a complex doublet of scalar fields is introduced: the Higgs doublet. When the vacuum expectation value of the neutral component of the Higgs doublet is non-zero, EWK symmetry breaking occurs. During the process of symmetry breaking massless Goldstone bosons are produced which are absorbed by the W and Z boson, giving them mass. The remaining component of the Higgs doublet remains free (else also the photon would be massive) and is referred to as the Higgs boson. The masses for the fermions are generated by coupling to the Higgs field by Yukawa couplings. The Higgs (or Brout-Englert-Higgs) mechanism was independently postulated by Higgs [7] and Brout and Englert [8]. In July 2012, both the ATLAS and CMS collaboration at CERN presented the observation of a new particle with mass around 125 GeV/c^2 [9,10]. Later, it became apparent that the observed particle is consistent with the SM Higgs boson, after which Francois Englert and Peter Higgs were awarded the Nobel Prize in Physics in 2013. The discovery of the Higgs boson confirms the EWK unification theory. The generated masses of the fermions and intermediate vector bosons are free parameters of the SM, along with the electromagnetic and strong coupling constants and the parameters of the CKM matrix.

1.2 Top Quark Physics

In 1977 at Fermilab, the Upsilon was discovered as a bound state of a bottom and anti-bottom quark [11]. The discovery of a third generation quark, led to the expectation of a third generation partner for this quark: the top. The top quark was discovered at the Tevatron in 1995 by the CDF and DØ collaborations [12, 13]. The top quark mass is a free parameter in the SM and is measured to be 173.21 $\pm$ 0.51 (stat.) $\pm$ 0.71 (syst.) GeV/c^2 (PDG world average) [2]. The top quark is the heaviest particle known today and because the top quark is so massive, it offers an interesting field of study. The lifetime of the top quark, given by

$$\tau_t = \frac{1}{\Gamma_t} \sim 0.5 \times 10^{-24}\, s < \frac{1}{\Lambda_{QCD}} < \frac{m_t}{\Lambda^2_{QCD}} \sim 3 \times 10^{-21} s \tag{1.2}$$

is smaller than the hadronisation time-scale ($\frac{1}{\Lambda_{QCD}}$) and spin decorrelation time-scale ($\frac{m_t}{\Lambda^2_{QCD}}$). This means that the top quarks do not form hadrons or bound states and that all the information concerning the properties of the top quark is directly transferred onto its decay products. By measuring these decay products and reconstructing the quark, we can observe a quark largely unaffected by colour-confinement and can therefore, to a certain extent, test the SM predictions for the behaviour of a free quark. In addition, due to its large mass, the top quark has a significant contribution in loop corrections to the propagators of for example the Higgs and W/Z bosons. Top quarks and top quark pairs are also a background to many beyond the Standard Model (BSM) processes. An accurate measurement of the top quark mass, production cross-section and properties is still of particular interest, even 20 years after the discovery.

1.2.1 Top Quark Production

Top quarks can be produced either as individual quarks through weak processes or as quark-anti-quark pairs by strong processes. The top quark decay happens through weak processes. At

the LHC, top quark pairs ($t\bar{t}$) are produced in abundance as can be seen from fig. 1.1. In this figure, the theoretical production cross sections in pp or $p\bar{p}$ collisions of various processes as a function of the centre-of-mass energy are displayed. The top quark pair production cross section at the Tevatron is measured to be 7.60 ± 0.41 pb at a centre-of-mass energy of 1.96 TeV [14] whereas at the LHC the cross section is measured to be 241.4 ± 8.5 pb at 8 TeV [15]. The Tevatron has delivered a total of 12 fb^{-1} of integrated luminosity at a centre-of-mass energy of 1.96 TeV, while the LHC has already collected more data with 5.0 fb^{-1} at 7 TeV and about 20 fb^{-1} at 8 TeV.

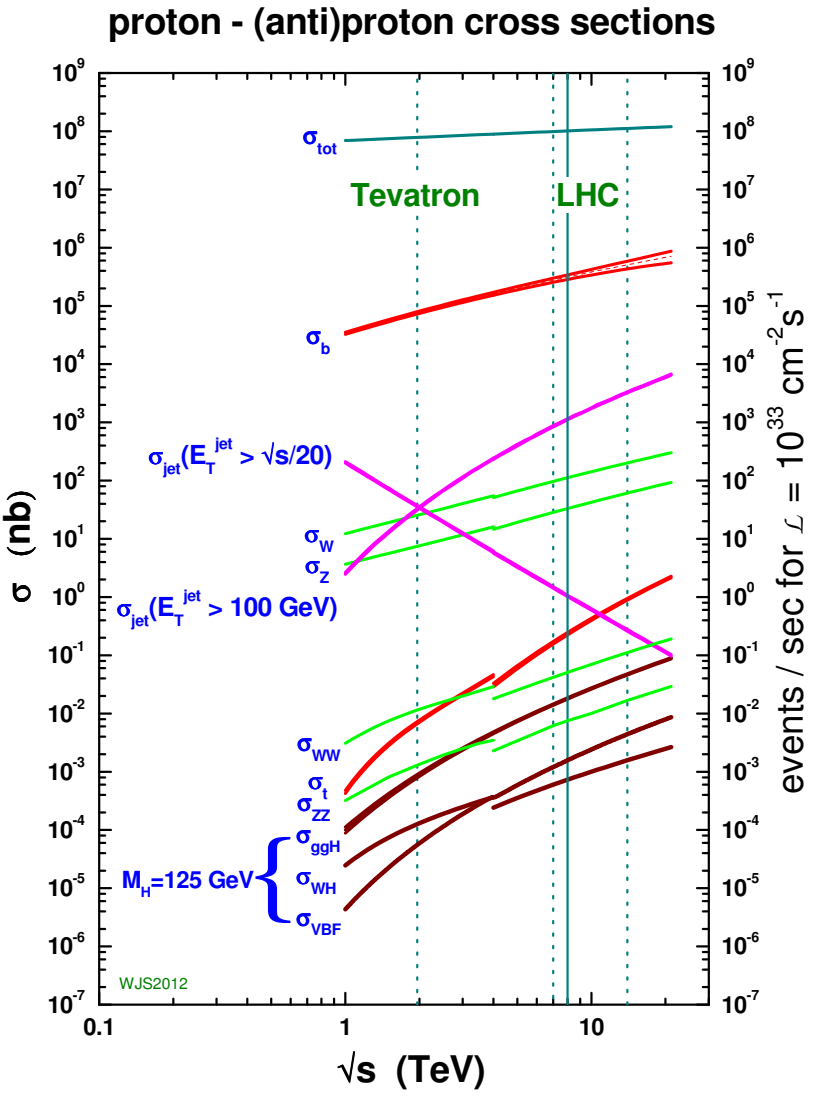

Figure 1.1: Theoretical production cross sections as a function of centre-of-mass energy. The vertical lines indicate the centre-of-mass energy at the Tevatron and during the different data-taking periods at the LHC. Figure taken from [16].

Protons have three valence quarks (two ups and a down) which carry the largest fraction of the proton momentum. In addition, protons contain sea quarks and gluons which can also significantly contribute to the proton momentum. The probabilistic distribution of the fractional

momentum of the proton carried by the partons is referred to as the parton distribution function (PDF). At the LHC, $t\bar{t}$ pairs can be produced, at leading order, by both gluon-gluon fusion or quark-anti-quark annihilation. The Feynman diagrams connected to leading order $t\bar{t}$ production are shown in fig. 1.2.

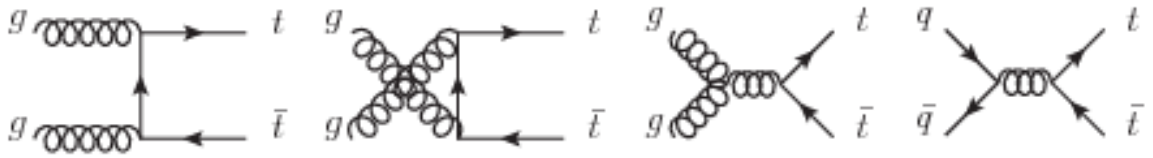

Figure 1.2: Feynman diagrams of leading order $t\bar{t}$ production.

The top quark pair production cross section in hard scattering processes in pp collisions is given by

$$\sigma(pp \to t\bar{t}X) = \sum_{i,j=q,\bar{q},g} \int dx_i dx_j f_i(x_1,\mu^2) f_j(x_2,\mu^2) \hat{\sigma}_{ij}(ij \to t\bar{t}X, Q^2, \mu^2) \qquad (1.3)$$

where $Q^2 = x_1 x_2 s$ is the effective centre-of-mass energy which is the characteristic scale of the hard scattering, x is the fractional proton momentum carried by the parton, $f_i(x)$ is the PDF for parton flavour i (shown in fig. 1.3 in the MSTW parametrisation) and $\hat{\sigma}(ij \to t\bar{t}X)$ is the partonic cross section. Here, we have denoted the inclusive cross section with the X being particles which are produced in addition to the $t\bar{t}$ pair such as radiated gluons. The partonic cross section is calculated in perturbative QCD up to a certain order. The factorisation scale μ_F [17] makes the distinction between short distance effects like the partonic cross section and long distance effects like the PDFs. Effects dominated by short distance (and high energy scales) can be described in perturbative QCD, while long distance effects are non-perturbative. The renormalisation scale μ_R [18] deals with the divergent terms in the higher order calculations in the partonic cross section since the coupling constant α_s is dependent on μ_R. In equation 1.3, $\mu_R = \mu_F = \mu$.

At the Tevatron, a proton-anti-proton collider, the quark-anti-quark annihilation was dominant, whereas at the LHC, a proton-proton collider, the gluon-gluon fusion process dominates being responsible for about 85-90 % of production depending on the centre-of-mass energy.

Single top production is governed by weak processes with much smaller cross sections. Single top production is a non-negligible background for top quark pair production, despite the low cross sections. At leading order, the single top production diagrams are shown in fig. 1.4.

1.2.2 Top Quark Decay

As the mass of the top quark is much heavier than the mass of the W boson, the top quark decay is dominated by $t \to Wq$ producing a real W. Due to the large value of the CKM matrix element V_{tb}, the top quark decays almost exclusively to a W boson and a b quark, making the decay of the top quark characterised by the decay modes of the W boson which are shown in table 1.3.
Depending on the decay modes of the W boson, we can categorise the decay of top quark pairs ($t\bar{t} \to W^+bW^-\bar{b}$) in three groups where either zero, one or two W bosons decay leptonically. The possible $t\bar{t}$ decay modes (at leading order) are listed in table 1.4.

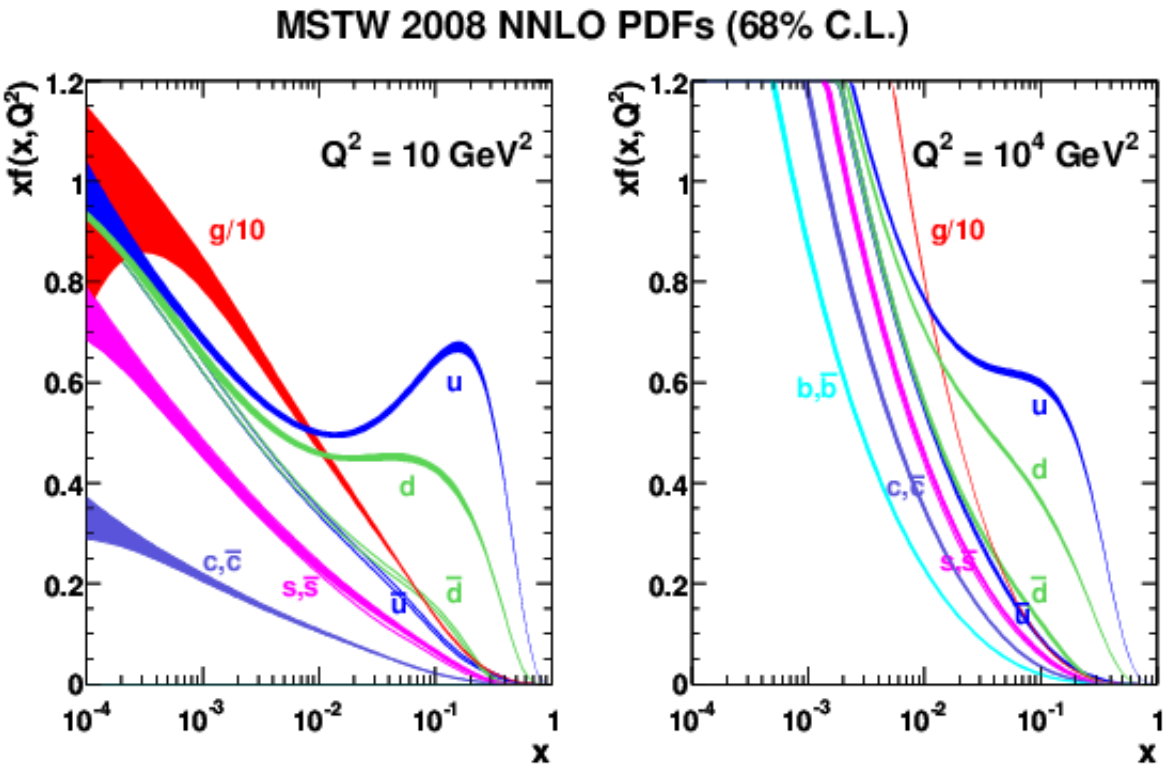

Figure 1.3: Probabilistic distribution of the fractional proton momentum x carried by the partons for a given proton energy scale Q. Figure taken from [16].

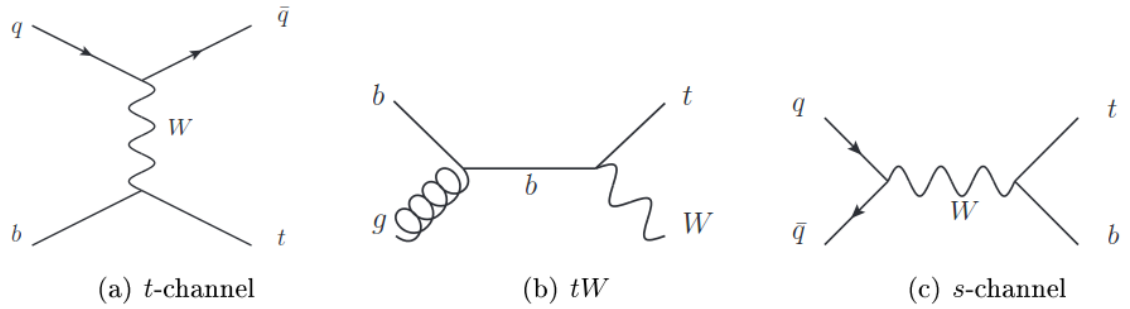

(a) t-channel (b) tW (c) s-channel

Figure 1.4: Feynman diagrams of leading order single top production.

In the final state, the quarks will be identified in the event as jets and the neutrinos will show as missing energy. The all-hadronic final state has the highest branching fraction and will therefore yield more statistics, but it also suffers from a large background due to QCD multijet events. The dileptonic final state is the cleanest final state to look for, since it is characterised by two isolated leptons with high transverse momentum and a significant amount of missing energy due to the two neutrinos. However, the dileptonic channel also has the lowest branching fraction. The semi-leptonic final state is a compromise between the all-hadronic and dileptonic final states as it has a large branching fraction, but also one isolated, high transverse momentum lepton. The semi-leptonic final state has at least four jets, two of which are b-quark jets. Jets arising from b-quarks are identified using a b-tagging algorithm as will be described in section 4.1. In

Table 1.3: Decay modes and branching ratios for the W^+ boson [2]. The W^- decay modes are charge conjugates to the W^+ decay modes. Here l denotes any lepton type.

W^+ decay mode	Branching fraction (%)
$e^+\nu$	10.71 ± 0.16
$\mu^+\nu$	10.63 ± 0.15
$\tau^+\nu$	11.38 ± 0.21
$l^+\nu$	32.72 ± 0.30
hadrons	67.41 ± 0.27

Table 1.4: Leading order $t\bar{t}$ decay modes.

Channel name	Final state	Branching fraction (%)
all-hadronic	$q\overline{q'}bq''\overline{q'''}\overline{b}$	45.44
semi-leptonic	$q\overline{q'}bl^-\overline{\nu}_l\overline{b}$ or $l^+\nu_l bq''\overline{q'''}\overline{b}$	43.85
dileptonic	$l^+\nu_l bl'^-\overline{\nu}_{l'}\overline{b}$	10.71

this analysis, the semi-leptonic $t\bar{t}$ channel was chosen, and more specifically the case where the lepton is a muon. The muon semi-leptonic channel is also referred to as the muon+jets channel and is considered our signal. Events coming from $t\bar{t}$ events, but in the other decay channels are considered as background. These $t\bar{t}$ background events can still pass the event selection designed to look for muon+jets events when for example additional jets are reconstructed in dileptonic events, or when an inclusive muon in a jet due to heavy hadron decay is reconstructed in an all-hadronic event.

1.2.3 Top Quark Properties

The unique position that the top quark has, because it decays before hadronisation takes place, has often been interpreted as the possibility of observing a "free" quark. Top quark physics offers the possibility to test SM predictions in the quark sector and to access many new physics models. A few examples of such analyses are given below

- top quark mass
- measurement of $|V_{tb}|$ matrix element
- measurement of top quark and anti-top quark mass difference
- top quark charge measurement
- search for Flavour Changing Neutral Currents (FCNC)
- spin correlations in $t\bar{t}$ pairs

The theoretical considerations on spin correlation in $t\bar{t}$ pairs will be discussed extensively in section 1.3.

One of the most interesting discussions in top quark physics is the definition of the top quark mass. The top quark mass is a free parameter of the SM but the top quark is not directly observable. The top quark pole mass is based on the unphysical concept of a free quark, but due to

self-energy corrections the pole mass is ambiguously defined up to ~ 200 MeV. The running top quark mass as defined in the $\overline{MS}$ renormalisation scheme has a scale-dependent top quark mass definition. The transition between the pole mass and $\overline{MS}$ mass can be done in perturbative QCD. For more details on the discussion, I refer to [19]. The particular interest in the top quark mass is due to its effects on electroweak theory. Before the discovery of the Higgs boson, the top quark and W boson mass values were used to place constraints on the Higgs boson mass. With the discovery of the Higgs boson, and therefore the validation of electroweak theory, one can extrapolate the model up to the highest energy scales and set a requirement on the Higgs boson mass needed to allow for stability of the electroweak vacuum at high energy scales. The limit on the Higgs mass needed for stability, is dependent on the top quark mass, creating the necessity for top quark mass measurements with increasing precision. The dependence of the universe stability on the Higgs and top pole mass is shown in fig. 1.5.

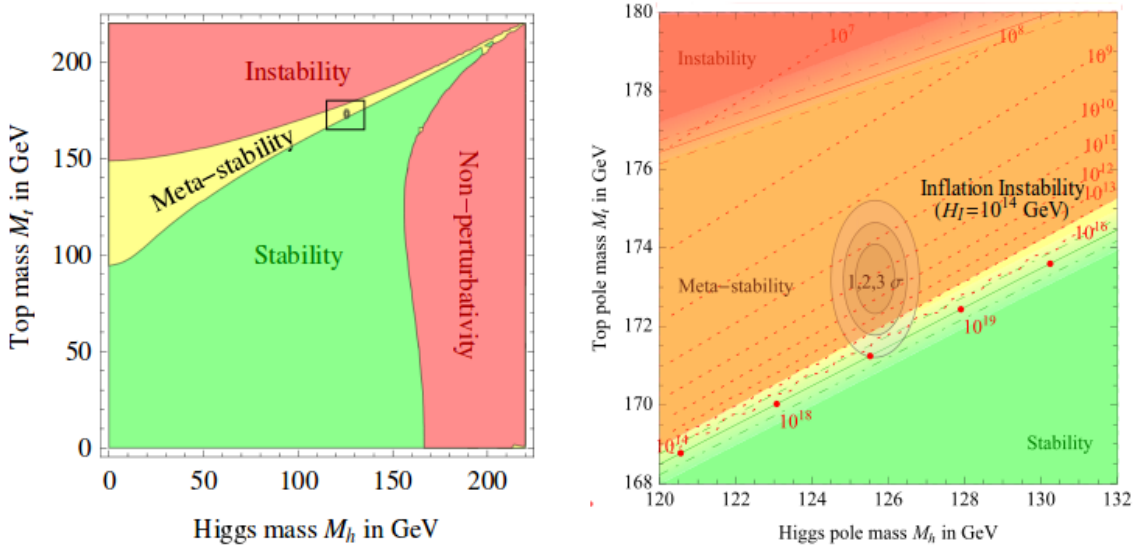

Figure 1.5: The 2σ-ellipses in the (m_{Higgs}, m_t^{pole})-plane obtained from the top quark and Higgs mass measurements at the Tevatron and the LHC, compared to areas where the SM vacuum is stable, meta-stable or unstable. Figure taken from [19].

1.3 Spin Correlations in Top Quark Pair Systems

The top quark has a spin 1/2, as all fermions do. For the other quarks, direct measurements of their spin is highly non-trivial due to the dilution coming from hadronisation which effectively destroys the spin information. However for the top quark, the spin information gets transferred to its decay products as the top quark decays before hadronisation takes place.

1.3.1 Standard Model Spin Correlations

Spin polarisation refers to the quantity describing the preference of a particle with a spin to have its spin in a particular direction. In single top production, which is an electroweak process, the top quark spin is fully polarised. Production of $t\bar{t}$ pairs is a strong process, which due to parity invariance, leads to zero polarisation at leading order and very small polarisation at higher orders. So even though in top quark pair production the spins do not take a preferential direction, there is correlation between the spins of the top and anti-top quark in the SM. The spin

Table 1.5: Spin analyser quality α for the decay products of the top quark. For the decay products of the anti-top quark $\overline{\alpha}$, the signs are flipped. Values are obtained from [20].

particle	LO value	NLO value
b	-0.40553	-0.39256
$\overline{d}$,$\overline{s}$	1	0.96647
u,s,$\overline{\nu}$	-0.31964	-0.31676
l^+	1	0.99850
j	0.50708	0.47367

correlation strength is not a free parameter of the SM, its value is rather determined by several aspects. The spin correlation is different depending on the $t\bar{t}$ production mode: gg fusion or $q\overline{q}$ annihilation. Therefore the spin correlation strength depends on the relative contributions of the production modes and the collision energy. A measurement of the spin correlation strength offers a stringent test of the SM.

Spin correlations can be accessed through the angular correlations of the decay products. Each decay product in the top quark decay carries only a fraction of the parent spin information, this fraction is called the spin analyser quality or sometimes spin analysing power (α) which depends on the flavour of the decay product. Values for the spin analyser qualities for the top quark decay products are given in table 1.5. The correlation between the top quark spin and the direction of the daughters can generally be given by a double differential distribution:

$$\frac{1}{N}\frac{d^2N}{d\cos\theta_1\cos\theta_2} = \frac{1}{4}(1 + P_1\alpha_1\cos\theta_1 + P_2\alpha_2\cos\theta_2 - C\cos\theta_1\cos\theta_2) \tag{1.4}$$

with $\theta_{1,2}$ the angle between the direction of the decay product and its parent in a particular basis, $P_{1,2}$ the polarisation of the top and anti-top and $\alpha_{1,2}$ the spin analyser qualities of the decay products. There is a constant term, two terms depending on the top polarisation which we know to be approximately zero and a term depending on the spin correlation between the top quarks. The angles $\theta_{1,2}$ are chosen with respect to a spin quantisation axis, which can for example be the beam axis. In the beam axis basis, $C_{beam} = 0.370$ in the lepton+jets channel, while for dilepton channels the correlation strength is higher. At the LHC, usually the helicity frame is used in which the angles are defined with respect to the top parent direction in the $t\bar{t}$ rest frame. The spin correlation strength A can be obtained from $C = \alpha_1\alpha_2 A = -\alpha_1\overline{\alpha}_2 A$ and can also be expressed in the form of

$$A = \frac{N(\uparrow\uparrow) + N(\downarrow\downarrow) - N(\uparrow\downarrow) - N(\downarrow\uparrow)}{N(\uparrow\uparrow) + N(\downarrow\downarrow) + N(\uparrow\downarrow) + N(\downarrow\uparrow)} \tag{1.5}$$

which is the asymmetry of the amount of aligned and anti-aligned top quark pairs, with the arrows representing the spin of the (anti-)top quark with respect to a spin quantisation axis.

At the Tevatron the beam axis was a convenient choice that gave $C_{beam} = 0.370$. The basis in which the spin vector is defined is presented in fig. 1.6 where the angle ξ defines the direction of the spin vector. The beam axis basis is defined by $\cos\xi = \cos\theta$. The beam axis basis relates the particle spins with respect to the beam direction. Since the Tevatron was a proton-anti-proton collider and the dominant $t\bar{t}$ production channel is $q\overline{q}$ annihilation, the direction of the incoming quark is well defined. At the LHC, being a proton-proton collider, this is not true, in addition the dominant production channel is gluon-gluon fusion. At the LHC, the helicity basis is used where the spins are relative to the direction of the top quark itself, defined as

$\cos\xi = \pm 1$. Spin correlations are well described in this basis at relatively low top-antitop quark invariant mass, giving rise to $C_{hel} = 0.158$ [21]. Both of the quoted C values are calculated at NLO in the lepton+jets channel. The uncertainty on the theoretical prediction is less than 10 %.

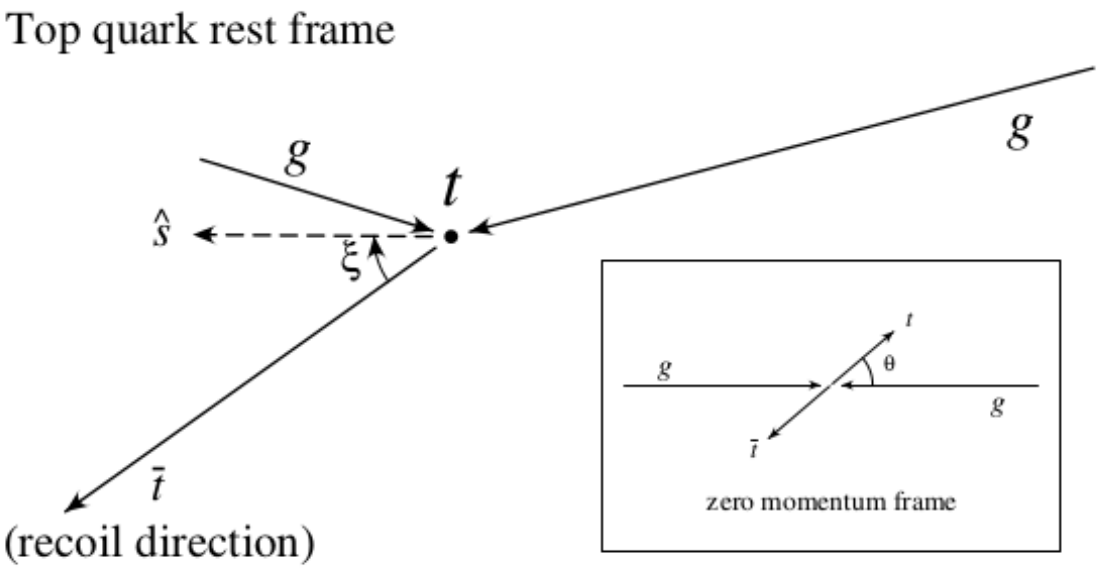

Figure 1.6: Spin vector for top quark pair production. The direction of the top quark spin vector s is given by the angle ξ. In the smaller figure the zero-momentum frame is shown with the angle θ defined with respect to the incoming beam direction.

There are various observables which access $t\bar{t}$ spin correlations or top polarisation, most of which require reconstruction of the top and anti-top quark. A few of these observables are listed below.

- Top-quark polarisation P is given by $P = 2A_P$ in the helicity basis in the dilepton channel with A_P

$$A_P = \frac{N(\cos\theta_l > 0) - N(\cos\theta_l < 0)}{N(\cos\theta_l) + N(\cos\theta_l)} \tag{1.6}$$

  where the θ-angle of the leptons is defined with respect to the helicity frame.

- A direct measure of the spin correlation strength C in the dilepton channel is possible through $A_{c_1c_2}$

$$A_{c_1c_2} = \frac{N(c_1c_2 > 0) - N(c_1c_2 < 0)}{N(c_1c_2 > 0) + N(c_1c_2 < 0)} \tag{1.7}$$

  where $c_{1,2} = cos(\theta_{l_1,l_2})$ with the θ-angle defined with respect to the helicity frame. Here we have $C_{hel} = -4A_{c_1c_2}$.

- The opening angle distributions:

$$\frac{1}{\sigma}\frac{d\sigma}{d\cos\delta\phi_{ij}} = \frac{1}{2}(1 - D_{ij}\cos\delta\phi_{ij}) \tag{1.8}$$

  where $\delta\phi_{ij} = \phi_i - \phi_j$ is the angle between the direction of daughter i of the top quark and daughter j of the anti-top quark, both defined in their respective top parent rest frames. This D_{ij} parameter depends on the decay products used in its definition and is related to

the spin correlation strength A in a non-trivial way. It is the sum of three double spin asymmetries multiplied by the corresponding spin analysing powers [21].

A commonly followed strategy is to not directly measure the spin correlation strength, but rather to measure the fraction of events f which exhibit SM spin correlation. In this way, one can infer the value of A in the selected basis using

$$A_{basis}^{measured} = A_{basis}^{SM} f \tag{1.9}$$

where

$$f = \frac{N_{t\bar{t}}^{SM}}{N_{t\bar{t}}^{SM} + N_{t\bar{t}}^{uncor}} \tag{1.10}$$

In the SM $f = 1$. This relies on the assumption that there are only SM-correlated or uncorrelated $t\bar{t}$ pairs.

Tevatron experiments made measurements of the SM fraction f using template fits to the angular distributions of the top decay products. CDF extracted the SM fraction using the lepton+jets final state [22] and DØ using the dilepton final states [23,24]. DØ also made the first spin correlation measurement using the Matrix Element Method (MEM) [25] again in the dilepton channel and found the first direct evidence of $t\bar{t}$ spin correlation by combining the measurements using MEM in the dilepton and lepton+jets channels [26]. The combined DØ MEM measurement yielded $f^{SM} = 0.85 \pm 0.29\,(\text{stat} + \text{syst})$.

At the LHC, ATLAS and CMS measured the spin correlation using template fits to the azimuthal angle difference between the two oppositely charged leptons in the dilepton channel. The ATLAS collaboration obtained $f^{SM} = 1.30 \pm 0.14\,(\text{stat.})\,^{+0.27}_{-0.22}\,(\text{syst.})$ [27] and CMS measured $f^{SM} = 0.74 \pm 0.08\,(\text{stat.}) \pm 0.24(\text{syst.})$ [28]. In the lepton+jets channel at the LHC, a measurement is made by ATLAS using the $\Delta\phi(l,j)$-distributions [29]. The CMS lepton+jets analysis is discussed in this work in part IV and found in [30].

1.3.2 New Physics Contributions to Spin Correlations

There are various physics effects beyond the Standard Model which could influence the spin correlation strength in $t\bar{t}$ pairs. One of the assumptions made in SM spin correlation measurements is that the top quark lifetime is shorter than the spin decorrelation time and the hadronisation time-scale and that the top quark can be observed as a quasi-free quark. As such, a measurement of the $t\bar{t}$ spin correlation strength can be used to set limits on the top quark lifetime and therefore also on the relevant CKM matrix elements.

Non-SM effects in the production of $t\bar{t}$ pairs can affect the spin correlation strength, such as new heavy resonances in the production via a scalar or pseudoscalar or anomalous couplings connected to technicolour [31]. New physics effects can also modify the top quark decay, for example the top quark decaying to a charged Higgs ($t \to H^+ b$) would affect the spin correlation strength if the branching fraction is large enough [32]. Flavour changing neutral currents (FCNC), allowing for a decay of $t \to cZ$ would also have an influence on the top quark lifetime and therefore on the top quark spin correlations.

An effective model describing new physics effects in hadronic $t\bar{t}$ production by means of a new heavy particle exchange has been discussed by Bernreuther and Si in [33]. An effective

Lagrangian, describing the new physics effects at energies lower than the new heavy particle mass scale, while respecting the SM gauge symmetries, is given by:

$$L_{eff} = L_{SM} - \frac{\tilde{\mu}_t}{2}\bar{t}\sigma^{\mu\nu}T^a t G^a_{\mu\nu} - \frac{\tilde{d}_t}{2}\bar{t}i\sigma^{\mu\nu}\gamma_5 T^a t G^a_{\mu\nu} \tag{1.11}$$

The L_{eff} can be interpreted in terms of chromo dipole couplings of the top quark to the gluon. In L_{eff}, $\tilde{\mu}_t$ and $\tilde{d}_t$ are the chromo-magnetic (CMDM) and chromo-electric (CEDM) dipole moments of the top quark respectively. $G^a_{\mu\nu}$ is the gluon field strength tensor, T^a are the generators of SU(3) colour, t is the top quark field, $\sigma^{\mu\nu} = (i/2)(\gamma^\mu\gamma^\nu - \gamma^\nu\gamma^\mu)$ where γ^μ, γ^ν and γ^5 the Dirac matrices. The dimensionless chromo-moments $\hat{\mu}_t$ and $\hat{d}_t$ are defined by

$$\tilde{\mu}_t = \frac{g_s}{m_t}\hat{\mu}_t, \quad \tilde{d}_t = \frac{g_s}{m_t}\hat{d}_t \tag{1.12}$$

where m_t is the top quark mass and g_s the strong coupling constant. A large CEDM would mean a new type of CP-violating interaction. In the most general expressions the chromo-moments are complex. Limits on the modulus of the CMDM and CEDM have been set using constraints based on the experimental $t\bar{t}$ production cross section [34].

One of the most sought-after physics models beyond the SM is Supersymmetry. For the Higgs boson to be the correct mechanism in electroweak symmetry breaking, there are constraints to its mass. Loop corrections with SM particles (in particular the top quark) give rise to divergent corrections in the Higgs boson mass. One of the frameworks which offers a solution to these divergent corrections is Supersymmetry. Supersymmetry is a new symmetry interchanging bosons and fermions which postulates the existence of a Supersymmetric twin for each particle in the SM. The quantum loop corrections to the Higgs mass from a bosonic loop and a fermionic loop cancel exactly if the boson and fermion have the same couplings and mass. Since the supersymmetric partners for the SM particles have not been observed yet, this symmetry must have been broken. As long as the breaking only occurs in the masses and not in the couplings, Supersymmetry can still cancel the divergences in the Higgs mass. An additional attractive feature of the Supersymmetric model is gauge coupling unification at high energies. Supersymmetry consistent with baryon number conservation results in a stable lightest supersymmetric particle which can be a dark matter candidate. An elaborate discussion of Supersymmetry can be found in [35].

In Supersymmetry, as in the SM, the masses of the particles are free parameters. Depending on the supersymmetric particle (or sparticle) masses there are different decay chains possible. In the scenario with a stop squark mass of the order of the top quark mass and a nearly massless lightest supersymmetric particle, it is very difficult to disentangle stop squark pair production to top quark pair production. The stop squarks are scalars and do not preserve spin information, hence the top quark pair produced in the stop quark pair decay does not have spin correlation. A precision measurement of top quark spin correlations can lead to an exclusion of this Supersymmetric scenario. In fig. 1.7 the effect of stop squark production in the $\Delta\phi(\ell^+, \ell^-)$ distribution is shown. A description of this Supersymmetric scenario and predictions for spin-sensitive top quark pair distributions is given in [36].

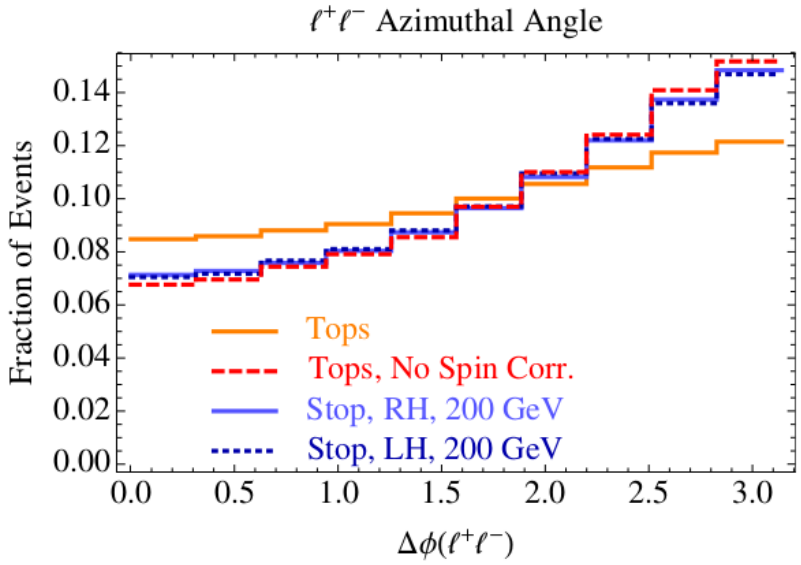

Figure 1.7: $\Delta\phi(\ell^+, \ell^-)$ distribution for SM $t\bar{t}$ production, uncorrelated SM $t\bar{t}$ production and $\tilde{t}\tilde{t}^*$ (stop) production. Figure taken from [36]

Chapter 2

Experimental Set-up

The Large Hadron Collider (LHC) is a proton collider located underground near Geneva, Switzerland. Protons are accelerated in two beams traveling in opposite directions in circular beam-pipes of 26.7 km circumference. The beams collide in four interaction points, one of them being the location of the Compact Muon Solenoid (CMS). In this chapter both the structure of the LHC will be introduced and the CMS detector used to analyse the proton collisions.

2.1 The Large Hadron Collider

2.1.1 The Accelerator

The LHC [37] was installed in the tunnel of the Large Electron Positron (LEP) collider. Unlike LEP, which collided electrons and positrons which are fundamental particles, the LHC collides composite particles such as protons and ions. The constituent quarks and gluons in the proton carry only a fraction of the total proton energy. The centre-of-mass energy of the proton constituents which actually engage in the collision is therefore unknown, which causes its limitations for high-precision measurements. The advantage of a hadron collider is that protons can be accelerated to higher energies than leptons, since protons are much heavier than eg. electrons and as such lose less energy when accelerated on a curved trajectory. This gives hadron colliders a larger potential for discovering unknown particles. High intensity beams ensure large collision rates. The proton beams are not continuous, but packed together to obtain bunches which are separated by 25 ns.

The requirements on the magnet strength in the LHC are set by the desired beam energy and the scale of the existing tunnel that holds the LHC. 1232 dipole magnets keep both beams on their circular trajectory in opposite directions. With the design energy of 7 TeV per beam, the magnetic field needs to be 8.4 T. A cross-section of a dipole magnet is shown in fig. 2.1. One can clearly distinguish the two beam-pipes, each of which is surrounded by superconducting coils made of NbTi cables. The coils are cooled to 1.9 K using liquid helium, inducing a superconducting state in which electricity can flow without resistance. The design is very cost-effective as it allows both beam-pipes to be contained within the same cooled dipole magnet. In addition to dipole magnets to keep the beam on a circular orbit, quadrupole magnets are used to focus the beam. The main operation mode of the LHC is to collide proton on proton, but heavy ion collisions or proton-ion collisions are provided in dedicated runs. For these collisions, lead ions (Pb) are used.
The number of collisions N that the LHC provides to the experiments is proportional to the cross section σ of the interaction (which is a measure for the probability that the interaction occurs in a collision) and to the integrated luminosity $\int \mathcal{L}dt$.

$$N = \sigma \times \int \mathcal{L}dt \tag{2.1}$$

The instantaneous luminosity $\mathcal{L}$ depends solely on the beam parameters, with

$$\mathcal{L} = \frac{N_b^2 n_b f_{rev}}{A} \tag{2.2}$$

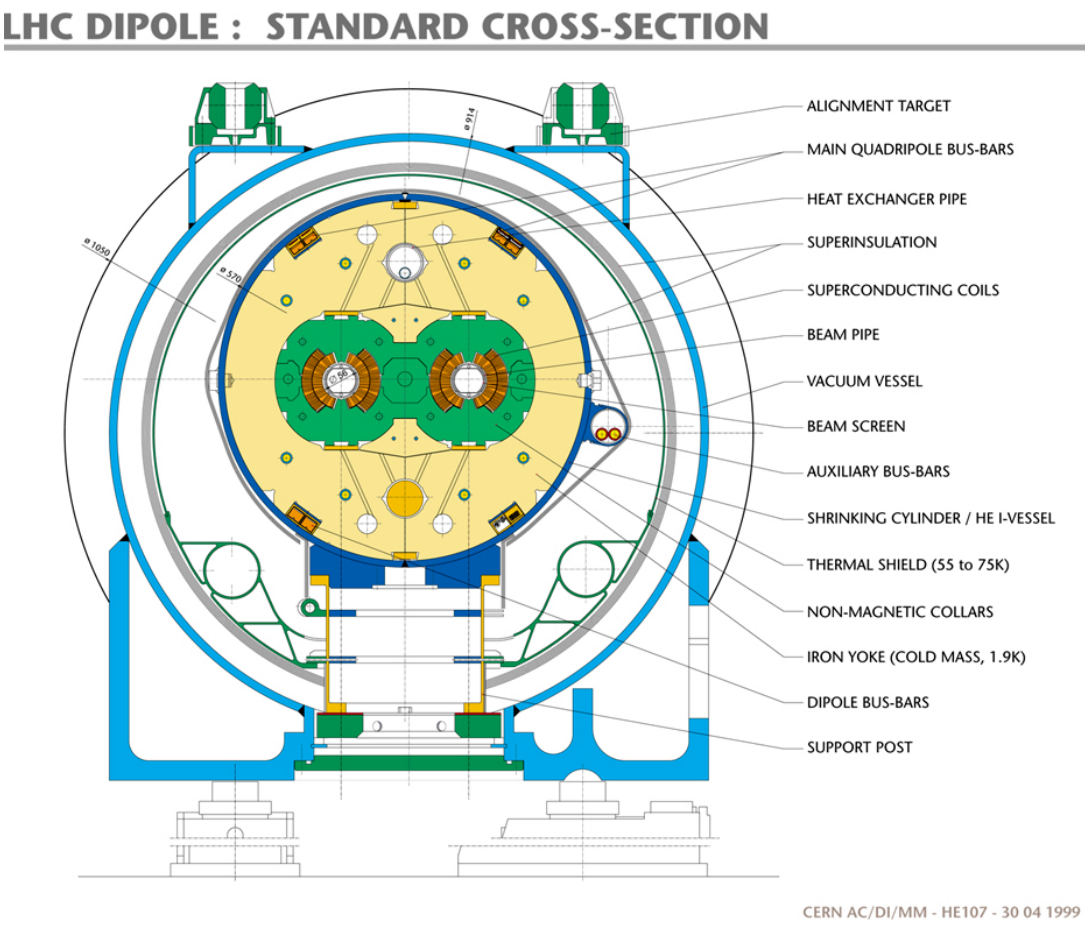

Figure 2.1: Cross-section of a LHC dipole magnet. Figure taken from [38].

Here, N_b is the number of particles per bunch, n_b is the number of bunches, f_{rev} is the revolution frequency of the beams in the machine and A is the overlap area of the beams at the interaction point. When the beams collide head on, the overlap area A is given by

$$A = 4\pi\sigma_x\sigma_y \tag{2.3}$$

with σ_x and σ_y the horizontal and vertical width of the beams respectively, assuming a Gaussian beam distribution. The importance of the beam focusing at the interaction point is evident from this relation. The beam intensity decreases steadily as the LHC runs in collision mode. Particles are lost in the collisions at the experiments, due to beam-gas interactions or in the beam scraping process due to the collimation system [39]. When the instantaneous luminosity drops below a certain threshold, the beam is dumped and the machine is prepared for a new fill of proton beams. Taking all effects into account, the estimated lifetime of the luminosity is of the order of $\tau = 15$ hours [37]. The time-dependence of the instantaneous luminosity is described by

$$\mathcal{L} = \mathcal{L}_0 e^{-\frac{t}{\tau}} \tag{2.4}$$

with $\mathcal{L}_0$ the luminosity at the start of the fill. The integrated luminosity delivered during the various data-taking periods is depicted in fig. 2.2. During the 2012 data-taking period, a total integrated luminosity of 23.3 fb^{-1} was delivered to the CMS detector.

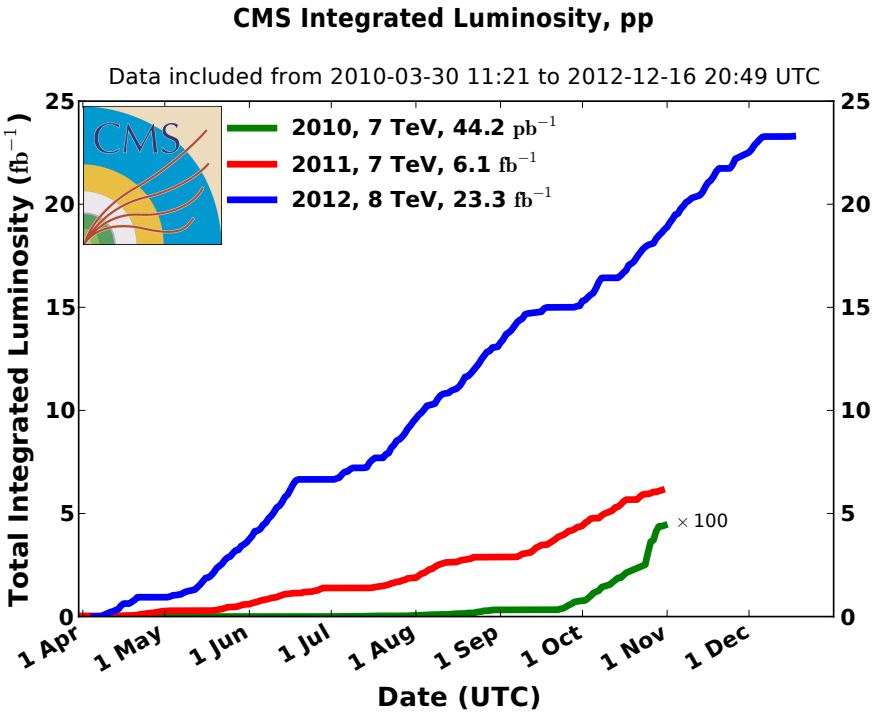

Figure 2.2: Cumulative luminosity versus day delivered to CMS during stable beams and for p-p collisions. This is shown for 2010 (green), 2011 (red) and 2012 (blue) data-taking. Figure taken from [40].

2.1.2 CERN accelerator complex

At the CERN accelerator complex, the proton bunches are accelerated in several steps before being inserted to the LHC as is shown in fig. 2.3. The initial acceleration step consists of a 50 MeV linear accelerator, Linac 2. The proton beams are then injected to a synchrotron, the Booster. In the Proton Synchrotron (PS), the beams are accelerated up to 26 GeV and there the protons are bunched together in the pattern required for the LHC. The final stage, pre-LHC, is the Super Proton Synchrotron (SPS) where the beam is accelerated up to 450 GeV. After the LHC ring has been filled in both directions, the beams can be accelerated to varying energies in stages, from 3.5 TeV per beam as in 2010 to the design energy of 7 TeV.

2.1.3 LHC Experiments

At four points along the LHC ring, detectors are located. There are two large multi-purpose experiments, ATLAS (A Toroidal LHC ApparatuS) and CMS. ALICE (A Large Ion Collider Experiment) is a heavy-ion detector, designed to study the quark-gluon plasma and the strong interaction at extremely high energy density. LHCb (LHC bottom) is designed to study CP violation and rare decays of mainly B and B_s mesons. LHCf (LHC forward) is a smaller scale experiment, located in the very forward region of ATLAS at both sides. LHCf is designed to measure the cascade of particles at very small angles with respect to the beamline, and so tries to study physics similar to cosmic ray showers in laboratory conditions. TOTEM (TOTal cross section, Elastic scattering and diffraction dissociation Measurement at the LHC) is another smaller scale experiment but in the forward region of CMS. TOTEM is designed to accurately measure the proton-proton interaction cross section and to shed further light on the structure of the proton.

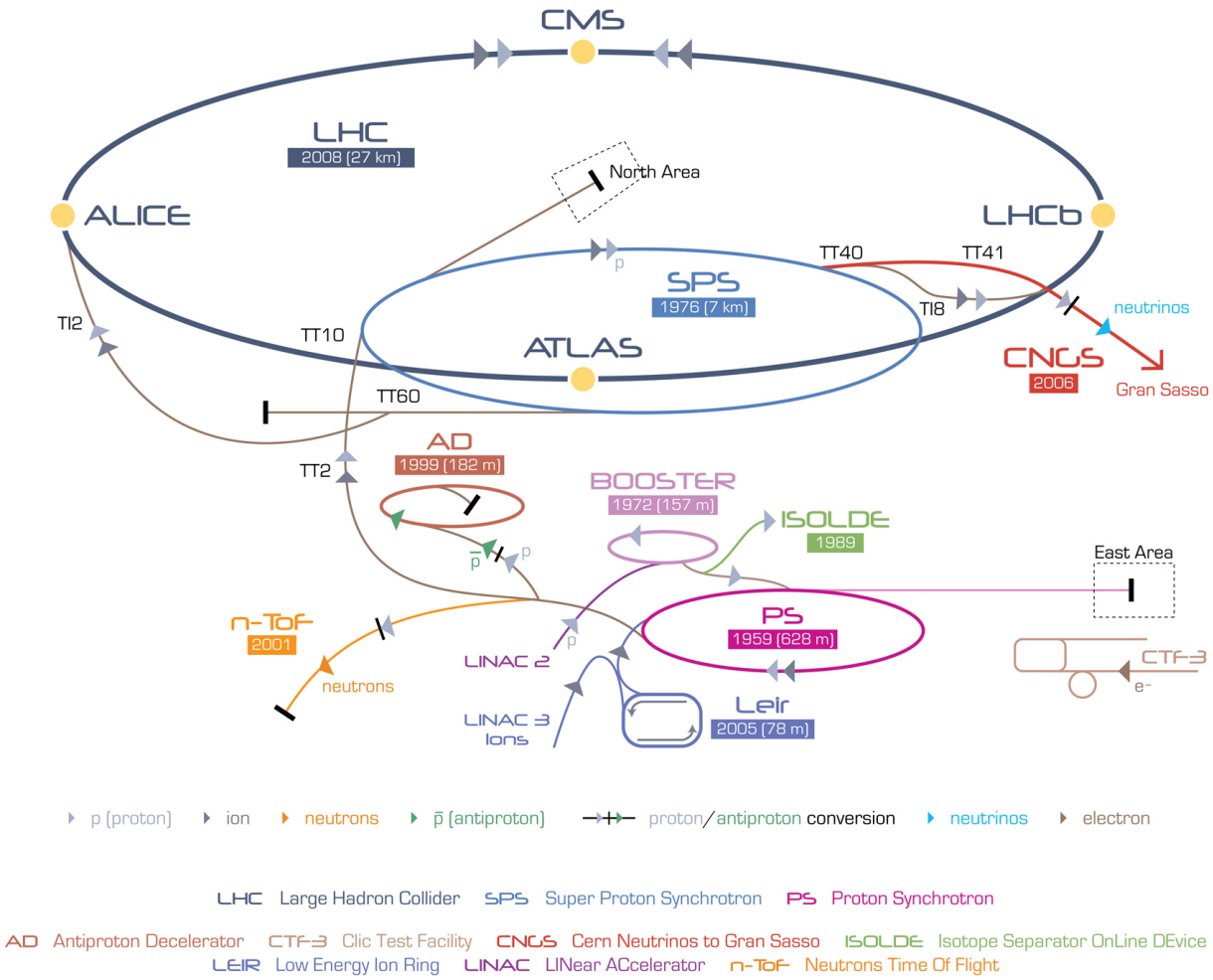

Figure 2.3: Schematic overview of the acceleration chain for the LHC at CERN. Figure taken from [41].

2.2 The Compact Muon Solenoid

The CMS detector is a general-purpose detector which has been described in [42]. A schematic view of the detector is shown in fig. 2.4. The detector has a length of 21.6 m, a diameter of 14.6 m and a weight of 12500 tons. CMS is cylindrical in shape, consisting of the central part which is called the barrel and is closed at the ends by the endcaps and the Hadron Forward (HF) calorimeter. CMS was mostly constructed above ground in large pieces, eg. the barrel consists of 5 pieces called wheels and the endcaps consist of three rings each, which were lowered through the shaft to be assembled in the cavern.

One of the main design goals of CMS was to have a good resolution on muon momenta of up to 1 TeV. A good momentum resolution is obtained by using a high solenoidal magnetic field. The CMS detector has a layered structure around the interaction point where the collisions occur. The interaction point is the centre of the CMS coordinate system. The y-direction is the vertical axis towards the top of the detector. The horizontal axis of the detector pointing towards the centre of the LHC ring is the x-axis. The z-axis is then counter-clockwise along the beam direction, giving us a right-handed coordinate system. In the xy-plane, we define the azimuthal angle ϕ with respect to the x-axis. The polar angle θ is measured from the z-axis. The pseudo-rapidity η is defined as $-\ln[tan(\theta/2)]$.

CMS was designed to cover almost the complete spatial angle of 4π with calorimeters to allow for missing transverse energy measurements. The CMS calorimeters in the forward region go up to $|\eta| < 5$ [43].

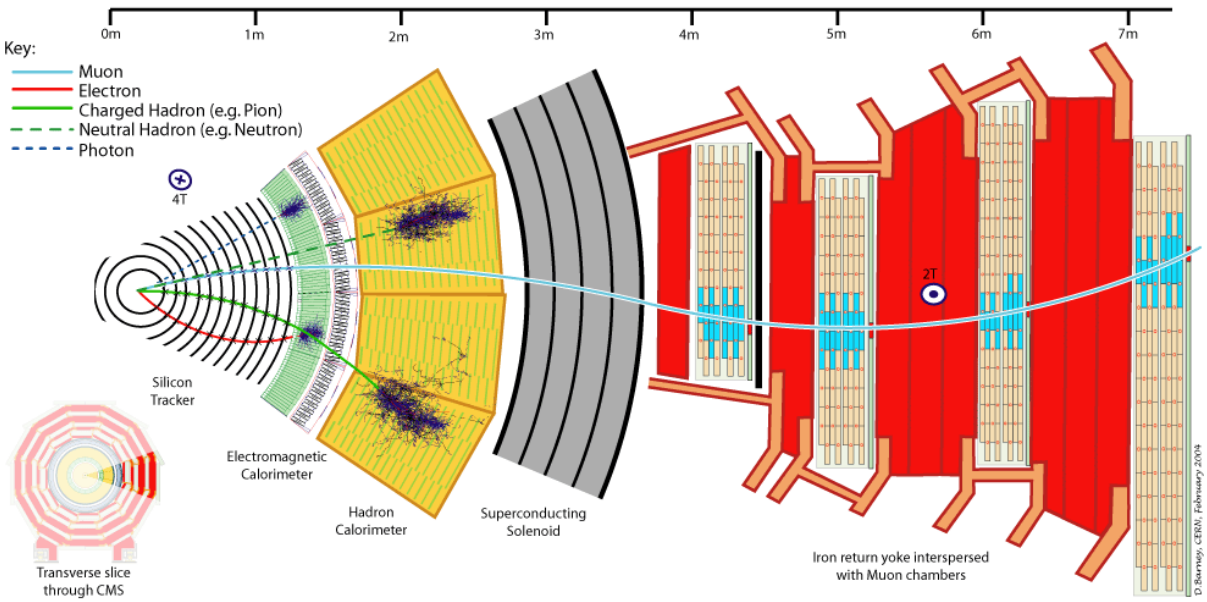

Figure 2.4: Schematic overview of a slice of the CMS detector. Figure taken from [44].

2.2.1 The Superconducting Solenoid Magnet

The most prominent feature of CMS is the superconducting magnet, designed to reach a magnetic field of 4 T, with a diameter of 6 m and a length of 12.5 m. Up to now, the running conditions of CMS have been to keep the magnetic field at a value of 3.8 T. The magnet consists of a superconducting coil of NbTi. The magnetic field is returned through a 10000 ton iron yoke. The tracker and the calorimeters are located within the coil as can be seen in fig. 2.4, while dedicated muon detectors are located within the iron return yoke. As such the iron yoke also acts as a support structure.

2.2.2 The Inner Tracker

The tracker is the detector layer closest to the beam pipe around the interaction point. It consists of a cylinder of length 5.8 m and diameter 2.4 m. A schematic view of the tracker is shown in fig. 2.5. The first layer of the tracker is a silicon pixel detector, located within a radial distance of 20 cm, and designed to provide two to three points of a three-dimensional particle trajectory with high precision. There are three layers to the pixel detector in the barrel and two layers in the endcap incorporating in total 66 million pixels. The pixels have an active size of $100 \times 150\,\mu m^2$. The next layer of the tracker consists of the silicon strip detector. The silicon strip detector consists of several modules: the Tracker Inner Barrel and Disks (TIB/TID), the Tracker Outer Barrel (TOB) and Tracker EndCaps (TEC). The TIB/TID consists of four layers in the barrel and three in the endcap, each $320\,\mu m$ thick and length varying between $80-120\,\mu m$ in the TIB and $100-141\,\mu m$ in the TID. The TOB encloses the TIB/TID and consists of six layers with strips of $500\,\mu m \times 122-183\,\mu m$. The last module is the TEC consisting of nine disks of four to seven rings. The inner tracker provides precision measurements of particle trajectories which enables transverse momentum determination for charged particles, impact

parameter measurements and reconstruction of secondary vertices. An extensive overview of the tracker can be found in [45].

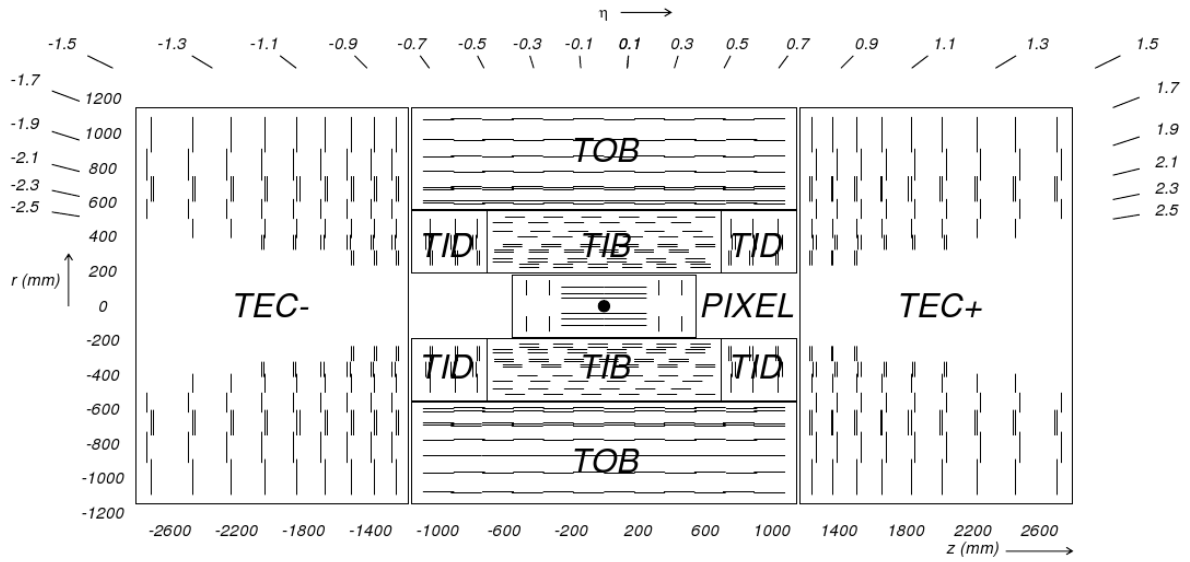

Figure 2.5: Schematic view of the CMS tracker. Each module in the detector is represented by a line. Figure taken from [46].

2.2.3 The Electromagnetic Calorimeter

The next layer in CMS's concentric structure is the Electromagnetic Calorimeter (ECAL) [47]. A calorimeter is designed to measure energy depositions. In the case of the ECAL, this is the energy deposited by electromagnetically interacting particles. The ECAL is mainly used to reconstruct electrons and photons which lose their energy predominantly by radiative processes. The ECAL is constructed out of lead tungstate crystals ($PbWO_4$) arranged in two regions: the barrel (EB) and endcaps (EE). A schematic view of the ECAL is shown in fig. 2.6 where the transition region between the barrel and endcap is clearly marked. The barrel covers a region of $|\eta| < 1.479$ and the endcap is restricted to $1.479 < |\eta| < 3.0$. Even though the barrel and endcap region nicely match in η, at the edges there is a region where a clustering of readout cables is present leading to unreliable reconstruction in the gap region of $1.4442 < |\eta| < 1.566$. The absorbed energy in the calorimeter is converted to scintillation light which is detected by avalanche photodiodes (APDs) in the barrel and vacuum phototriodes (VPTs) in the endcap [48]. The $PbWO_4$ crystals have a short radiation length X_0 of 0.89 cm, which is defined as the mean free path for radiative processes. It takes a crystal of about 20 X_0 thick to stop most electrons and photons with an energy of 100 GeV so a crystal length of 25.8 X_0 in the barrel and 24.7 X_0 in the endcap was chosen. The crystals have a high density (8.3 g/cm^3) and have a fast timing. About 80 % of the scintillation light is emitted in 25 ns. In the barrel the crystals are aligned according to rings of constant η and in the endcap as a disk. The crystals are slightly slanted with respect to lines of constant η, to prevent particles slipping through the cracks between crystals. In the barrel each crystal has a surface size of 22 $\times$ 22 mm^2 and in the endcap a size of 28.62 $\times$ 28.62 mm^2.
In front of the endcaps there is a preshower detector (ES) covering the region of $1.653 < |\eta| < 2.6$, with main aim to identify neutral pions. The ES has two layers: incoming photons and electrons produce showers in lead radiators while the silicon strip detectors placed after the radatior measures the energy deposited and the transverse shower profile. The lead radiator has a length of 2 X_0 in the first layer and 1 X_0 in the second layer. The preshower can separate two closely

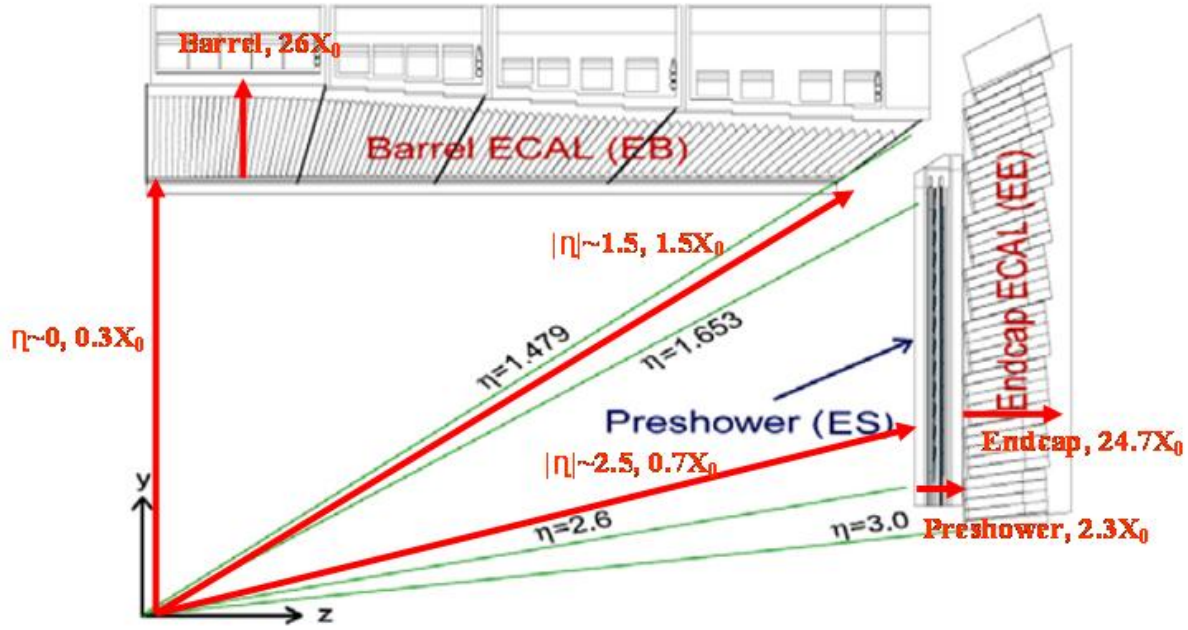

Figure 2.6: Schematic view of the CMS electromagnetic calorimeter and preshower detector. Figure taken from [47].

spaced photons eg. coming from the neutral pion decay, whereas the crystals in the endcap cannot. In the barrel, the granularity is better so there is no need for a preshower detector.

The energy resolution $\sigma(E)/E$ was measured to be $\sigma(E)/E = 0.39 \pm 0.01\%$ in a 3×3 cluster in test beams [48] for electron beams with momenta of 120 GeV. At an energy of 500 GeV, the showers are no longer fully contained in the ECAL. The calorimeter energy resolution has three contributions:

$$(\frac{\sigma(E)}{E})^2 = (\frac{R}{\sqrt{E}})^2 + (\frac{N}{E})^2 + C^2 \tag{2.5}$$

The first term is the resolution term coming from among others fluctuations in shower size and the collection of photoelectrons. The second term is the noise term coming from noise in electronic components and as last a constant term with various contributions eg. the leakage of energy through the end of the crystal.

2.2.4 The Hadronic Calorimeter

Around the ECAL there is the hadronic calorimeter (HCAL) consisting of a brass/scintillator sampling calorimeter. An extensive overview of the HCAL system can be found in [49]. The HCAL is designed to measure the energy deposited by hadrons by nuclear interactions. The HCAL provides coverage up to $|\eta| < 5.0$ and consists of four parts: the barrel (HB) covers up to $|\eta| < 1.4$, the endcaps (HE) cover $1.3 < |\eta| < 3.0$, the outer calorimeter (HO) is placed after the barrel section, outside the magnetic field, to attain shower containment and the forward part (HF) covers up to $2.9 < |\eta| < 5.0$ [43].

The HCAL consists of flat brass absorber plates, interspersed with active plastic scintillator tiles, in total 17 active layers in the barrel and 19 active layers in the endcap. The scintillator tiles have a dimension of $\Delta\eta \times \Delta\phi = 0.087 \times 0.087$ in the central region and are equipped with a single wave-length shifting fibre, each of which is read out by hybrid photodiodes (HPD),

leading to the construction of towers in η and ϕ, as shown in fig. 2.7. The HCAL has an energy resolution of $\Delta E/E = \frac{a}{\sqrt{E(GeV)}} + b$ with $a = 84.7 \pm 1.6\,\%$ and $b = 7.4 \pm 0.8\,\%$ [50].

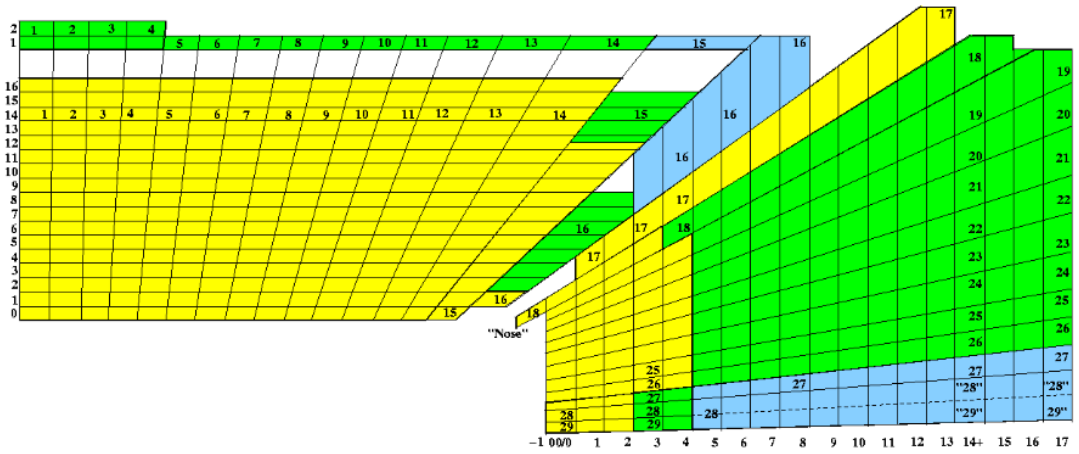

Figure 2.7: Schematic view of the tower mapping in the r-z plane of the HCAL barrel and endcap regions. Figure taken from [48]. Each colour represents the depth of the segmentation of an HCAL tower layer. The HB only has one layer in yellow, the HO (located around the HB) has one layer in green and the HE has up to three layers.

2.2.5 The Muon System

CMS has a very extensive muon system consisting of three distinct detector systems: drift tubes (DT), cathode strip chambers (CSC) and resistive plate chambers (RPC). An extensive overview of the muon system can be found in [51]. Up to $|\eta| < 1.2$, the neutron-induced background and the muon rate is low, that is where the drift tubes are used. The dimension of the drift tubes varies from $1990 \times 290 \times 2536$ mm to $5966 \times 290 \times 2536$ mm. In the endcap region, up to $|\eta| < 2.4$ with a high neutron background rate, the CSCs are used. In both the barrel and endcap region, there are RPCs installed.

In the barrel region, there are four concentric layers called "stations" in each of the five wheels as can be seen in fig. 2.8. Each wheel consists of twelve sectors, each covering 30 degrees in azimuthal angle. The two inner stations, called MB1 and MB2, consist of a DT chamber in between two RPC layers, while MB3 and MB4 consist of one DT chamber attached to a layer of one to four RPCs. In most stations, the DT chamber comes in 12 layers of drift tubes, grouped in three layers, two of which measure the r-ϕ coordinate and the third measures the z-coordinate. Each drift tube consists of a gas tube with a positively charged wire inside, allowing for a resolution of 200 μm. Each RPC chamber has a double-gap bakelite chamber, with a gap width of 2 mm, operating in avalanche mode. RPCs have a time resolution of 3 ns, making them very suitable for prompt muon triggering.

The endcap consists of four "stations" or disks, ME1 to ME4. Each disk consists of two to three concentric rings of CSCs. CSCs have a high radiation resistance and a fast response, making them suitable for the endcap which encounters high rates. Each CSC consists of 6 gas gaps, with each gap having a plane of radial cathode strips and a plane of anode wires perpendicular to the strips. Each CSC provides a (r,ϕ,z)-measurement in each layer with a spatial resolution of about 200 μm. In the endcap there is also a layer of RPCs in each disk.

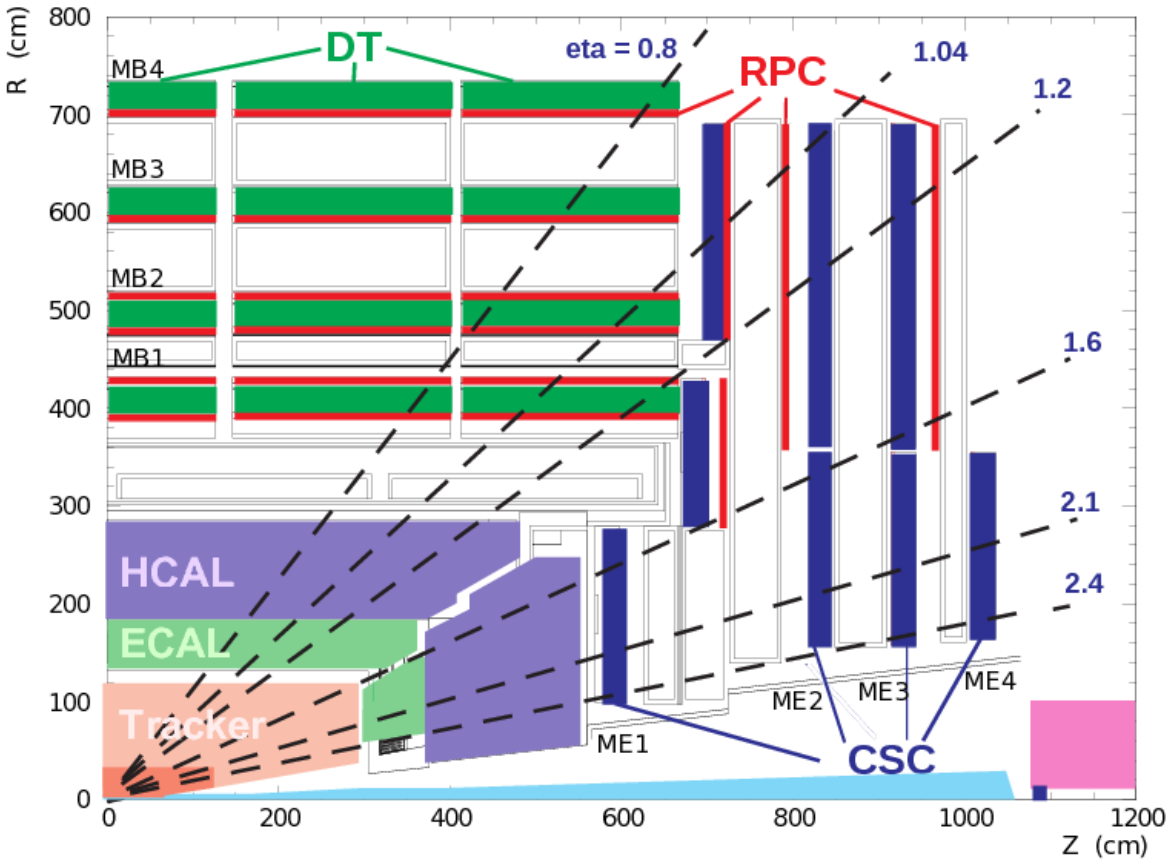

Figure 2.8: Schematic view of the CMS Muon system. Image taken from [52].

2.2.6 Luminosity Determination

A precise measurement of the amount of data the CMS detector has recorded, is very important for cross-section determinations or normalisations. During the 2012 data-taking period, the luminosity has been measured using the pixel cluster counting method [53]. The luminosity delivered by the LHC as a function of time in 2012 and the comparison with the luminosity recorded by the CMS detector is shown in fig. 2.9.
We have described the CMS pixel detector already in sec. 2.2.2. Due to the high amount of pixels in the detector, the occupancy is very low. As a consequence, the probability that a pixel hit is part of more than one track is very low, causing the number of pixel cluster hits to be linear as a function of the number of interactions per bunch crossing. This linearity holds up to very high number of pile-up interactions. Due to this linear relation with the number of proton-proton interactions, the pixel detector provides an excellent measure of the instantaneous luminosity in a given time interval. For this time interval, the length of one luminosity section is chosen, which corresponds to 23.3 seconds.

The instantaneous luminosity $\mathcal{L}$ is measured based on

$$\langle N_{cluster} \rangle = \frac{\sigma_{cluster}}{f} \mathcal{L} \tag{2.6}$$

where $\langle N_{cluster} \rangle$ is the mean number of pixel cluster hits per trigger, f is the LHC revolution frequency $f = 11{,}243$ Hz, and $\sigma_{cluster}$ is the effective pixel cross section. The trigger selected for the luminosity determination is a zero-bias trigger, which has as only requirement that the proton bunches cross. The $\sigma_{cluster}$ is measured in van der Meer scans. Eq. 2.6 can then be

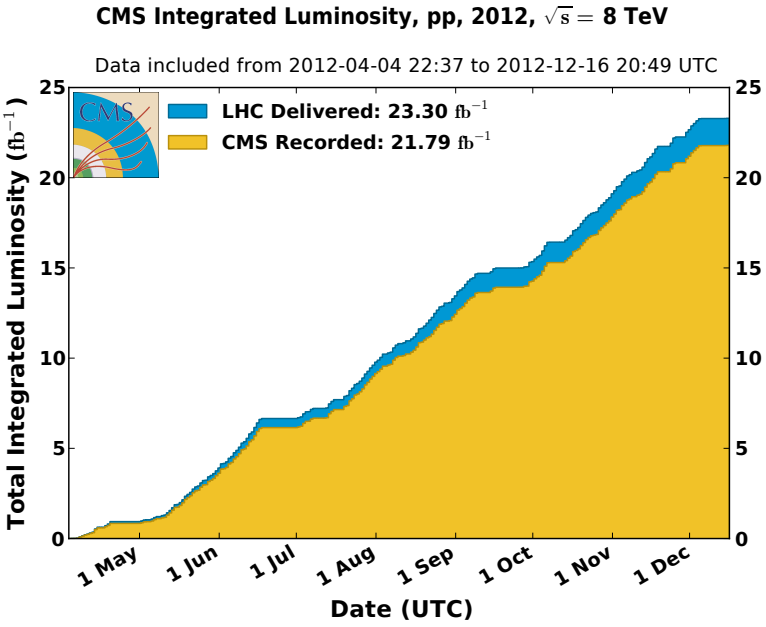

Figure 2.9: Amount of recorded data as a function of time for the year 2012. [40]

solved to obtain the instantaneous luminosity and from that the integrated luminosity.
The pixel cluster counting method has a bias due to out-of-time response or afterglow, coming from a tail in the electronic pulse shape of the pixel cluster readout and a tail coming from the activation of the detector. For 2012 fills with 1380 bunches per beam, this results in a subtraction of 2.5 % of the integrated luminosity per luminosity section with an uncertainty of 0.4 %. The total uncertainty on the integrated luminosity is 2.5 % (syst.) + 0.5 % (stat.) [53]. The largest systematic uncertainty is due to the determination of the $\sigma_{cluster}$: the variation of the fit model of the bunch shapes has a non-negligible effect. Also the integration of the luminosity assumes a stable pixel detector over time, which is also accounted for in the systematic uncertainty.

2.3 Online Object Reconstruction and Trigger System

At nominal operating conditions, using a bunch spacing of 25 ns, the LHC provides collisions with a rate of 40 MHz at the design luminosity. However, with the current resources, it is not possible to write out and store the information of every single collision produced in the CMS detector. To store all the information, we need a rate which is of the order of 100 Hz. To solve this problem, CMS only reads out and stores a subset of the produced events using the trigger system. The concept behind the trigger system is to make a rough scan of the detector read-outs for each event and decide, based on that information, whether the event is interesting enough to be stored and processed further. This strategy allows to not waste computing resources on events which will teach us nothing new. To design the selection criteria for the triggers, it is imperative to have a good understanding of how the physics we are looking for will look like in the CMS detector. We need to make sure that the physics we are interested in, will be selected with a very high efficiency and we need to be careful not to miss physics effects we were not expecting to see. Events which are not stored by the trigger system cannot be recovered afterwards.

The trigger system is implemented in two stages as is shown in a schematic view of the flow of information in CMS in fig. 2.10. The first stage, the Level-1 (L1) Trigger is hardware based and reduces the rate from 20 MHz in 2012 to roughly 100 kHz. The second stage is called the

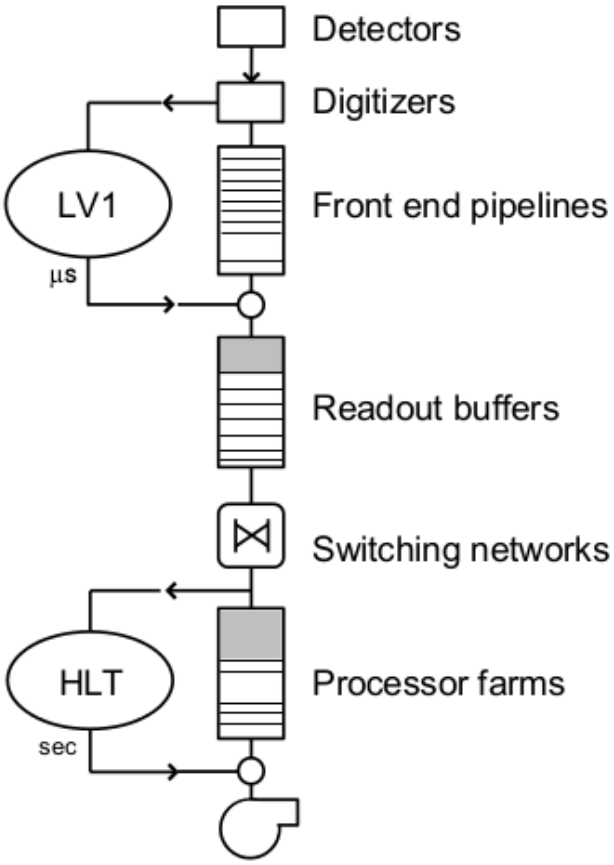

Figure 2.10: Information flow in the trigger system with two stages: L1 and HLT. Figure taken from [54].

High-Level Trigger (HLT) and uses a software based analysis of the events to determine whether the event will be stored or not.

2.3.1 Level-1

The L1 trigger system is designed to reduce the rate of events to 100 kHz before being passed to the HLT. The event data is read by the front-end electronics and stored in pipelined memories. The pipelines provide memory during 128 bunch crossings (3.2 μs). Most of this 3.2 μs window is occupied by the time of the signal propagation from the front-end boards to the control room where the L1 is run. As a result the actual L1 calculations should only take about 1 μs. When the L1 makes the decision to accept/reject the event, the decision is propagated back to the front-end boards and the event is either discarded or propagated to the HLT, allowing the next event to enter the pipeline. The L1 system uses local detector information only and cannot make use of the preshower nor the tracker data, since these systems take too long to read out. The L1 trigger can only perform very simple calculations.

The L1 system consists of three subsystems: the calorimeter, the muon and the global trigger. A schematic view of the flow of information in the L1 system is shown in fig. 2.11. The information available to the L1 system does not have the full granularity available to the HLT system. Due to the lower resolution available to the L1 system, the transverse momentum thresholds on the trigger objects are kept low at L1. When an object is found that passes a trigger, we call it the L1 seed and the event readout data is transmitted to the HLT system through the Trigger

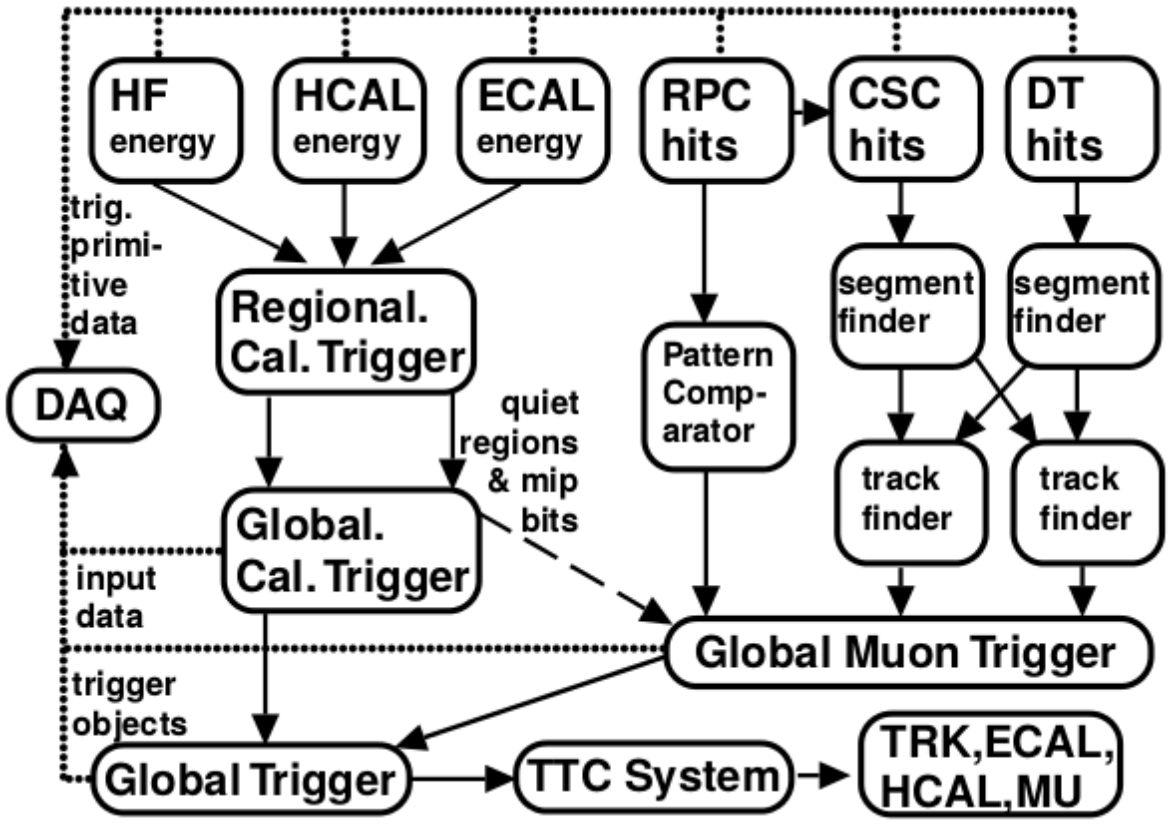

Figure 2.11: Schematic view of the CMS Level-1 trigger system. Figure taken from [55].

Timing and Control (TTC) system, along with any trigger objects found. More information on the L1 trigger system can be found in [55].

2.3.2 High-Level Trigger

The maximum input rate of 100 kHz of the HLT system comes from the average time to read in the information and to complete the algorithms used to make the trigger decision. The selected events are then further propagated to mass storage and offline computing systems, restricting the output rate to no more than 100 Hz. The HLT system works with consecutive filters combined into a path, reducing the rate at each step to allow for more complex, time-consuming filters at the end of the path. The HLT system uses the trigger objects from the L1 as a starting point for the calculations which require a higher granularity of the information. The objects reconstructed at the HLT level are designed to be as close as possible to the offline reconstructed events, using the full CMS reconstruction software, so that the offline selection criteria can be kept close to the thresholds used in the trigger. Each group of physics analyses has its own trigger paths, tailored to the process they want to observe. In addition there are some trigger paths used to measure the efficiency of the physics trigger paths or to monitor the performance of the detector. The thresholds for these control triggers are usually kept low, which would result in high trigger rates. To reduce the rate, the control paths are pre-scaled, meaning only a certain fraction of the events passing the trigger are actually stored. The HLT system is fully software based allowing for an update of the trigger paths during the data-taking.

Several trigger paths are grouped together according to the physics object content and the data is then written out in separate data streams called primary datasets. This makes it easier

for the end user to determine which data set is useful for her or his physics analysis and reduces the processing time by removing the need to run over the full dataset. For example the Single Electron primary dataset contains only events triggered by single electron triggers. More information on the HLT system can be found in [54].

2.3.3 Online Object Reconstruction

Electron and jet reconstruction at L1 are based on calorimetric information. In the electromagnetic calorimeter, a 5 × 5 cell of crystals constitutes a trigger tower. The size and location of the electromagnetic trigger towers match the size and location of the hadronic calorimeter trigger towers. At HLT, tracker information is added to the electron and jet reconstruction.

Electron Reconstruction

An overview of the electron/photon reconstruction algorithm at L1 is given in [56]. For the electron reconstruction a sliding window technique is used (depicted in fig. 2.12) which consists in looking for an electron candidate in a central hit trigger tower, using the information in the eight neighbouring cells. In a next iteration, the neighbouring cell is used as central hit trigger tower and the algorithm is repeated, thus eventually covering the entire η-ϕ plane. The E_T of the electron/photon candidate is determined as the sum of the E_T in the hit tower and the maximum E_T tower of its four broad side neighbours. Apart from a programmed E_T threshold, an electron/photon candidate must pass some extra reconstruction cuts to trigger. There are two paths of reconstruction: isolated and non-isolated electron/photon candidates. Both the isolated and non-isolated electron/photon candidates must pass the fine-grain veto and HAC veto, which are vetos on the shower profile. The fine-grain veto compares, within the 5×5 crystal hit tower, the E_T of the maximum E_T η-strip pair to the total E_T in the hit tower and rejects the candidate if e.g. less than 90% of the E_T is in the maximum pair (see fig. 2.12). The HAC veto rejects the candidate if the ratio of the HCAL E_T over the ECAL E_T is above a pre-defined value e.g. 5 %, this ensure the shower is contained in the ECAL. In addition to this, an isolated candidate must pass two extra vetos: first all eight of the hit tower neighbours must pass the fine-grain and HAC veto and second at least one corner of the neighbouring towers must be quiet, i.e. each crystal in the tower must be below a certain threshold, e.g. 1.5 GeV. The isolated and non-isolated candidate collections are mutually exclusive. These collections are then sorted according to E_T in each calorimeter region, of which the four highest isolated and four highest non-isolated candidates are sent as L1 seeds to the HLT.
At HLT, as in offline reconstruction, the Island algorithm [48] is used to reconstruct clusters and superclusters, which are then geometrically matched to a L1 electron candidate [57]. The Island algorithm starts by looking for crystals above a certain energy threshold which are called seeds. Starting from the seed position, crystals are added to the cluster, scanning first in ϕ then in η. Crystals are added as long as there is a positive energy deposit in the crystal, which is lower than the energy deposit in the previous crystal and the crystal does not already belong to a different cluster. The clusters found in this way are then grouped together in superclusters to reconstruct the electrons together with the brehmstrahlung photon contributions. The distinction between electrons and photons is made by requiring a hit in the pixel tracker for electrons, matched to the electron supercluster. In addition several isolation and identification requirements, very similar to the offline reconstruction, are posed on the electron, see section 5.4.

Jet Reconstruction

At L1, jet reconstruction uses a similar sliding window technique as in the electron case [48], shown in fig. 2.13. The transverse energy E_T used in the jet trigger is the summed E_T of the ECAL and HCAL energy depositions in a calorimeter region, defined as 4 × 4 trigger towers. The window consisting of 3 × 3 of these calorimeter regions is then moved over the entire η-ϕ

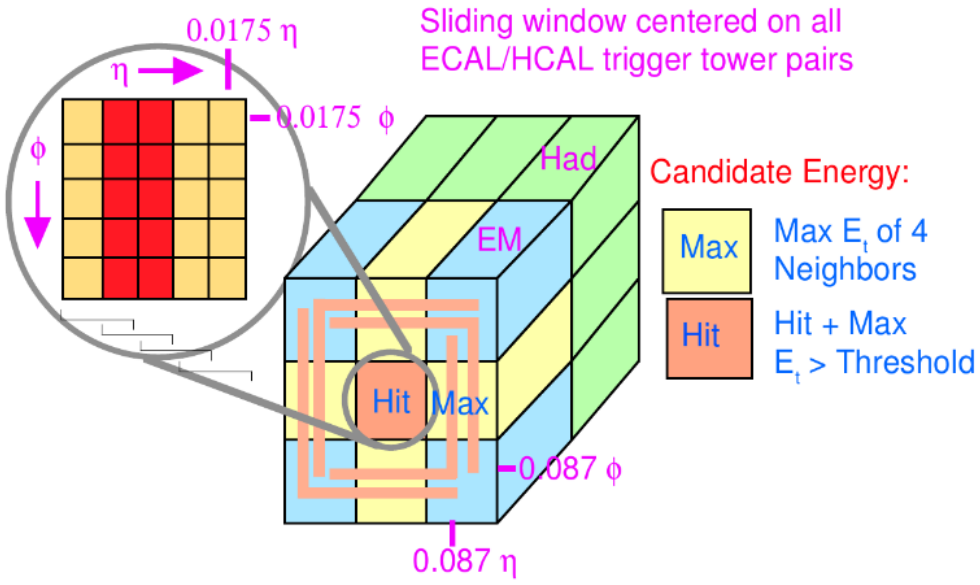

Figure 2.12: Sliding window technique for electron reconstruction at L1 [56].

plane. The E_T of the central region has to be higher than the E_T of the neighbouring calorimeter regions. The four highest E_T jets in the central region ($|\eta| < 2.6$) and the four highest E_T jets in the forward region ($|\eta| > 2.6$) are passed on to the HLT. The calorimeter system extends up to $|\eta| < 5$, so calorimeter jets can be reconstructed in the forward region, however due to the lack of tracker information in this region these high forward objects are not used in physics analyses.

At HLT, jets are reconstructed with the anti-k_T algorithm [58], which will be described in section 4.1.5. In 2012, the algorithm was run online on both calorimeter towers and particle flow objects, depending on the trigger path. Particle flow will be described in section 4.1.2.

Muon Reconstruction

The L1 muon trigger system makes use of all three muon systems: the DT trigger in the barrel region, the CSC trigger for the endcap and the RPC trigger covering both. RPCs offer superior time resolution and can unambiguously match a muon to a bunch crossing. In a first step, both the DT and the CSC process the information locally to reconstruct track segments giving us positional information. The track segments are then further processed by the regional trigger to be combined in a muon candidate. The curvature of the muon track in the muon system gives an estimate of the transverse momentum of the candidate. The regional trigger also assesses the quality of the muon candidate by considering among others the number of hits in coincidence and the matching between different chambers. The regional triggers store up to four muon candidates in both the barrel and endcap detectors. The hits from the RPC system are sent to the Pattern Comparator Trigger (PACT) which is based on the time and spatial coincidence of hits in four RPC stations. The PACT returns a transverse momentum estimate of the muon candidate, in addition to spatial and quality information. Up to four muon candidates from the PACT are stored. The muon candidates from all three subsystems are passed to the Global Muon Trigger. The Global Muon Trigger receives the four best barrel DT and the four best endcap CSC muons and tries to match them to the muons passed by the RPC PACT based on spatial information. If the muons from both systems can be matched, the information of both systems is combined to provide better precision. If the muons cannot be matched, the

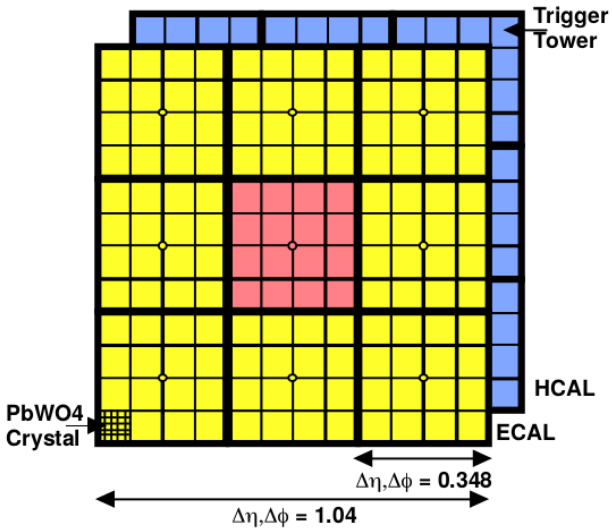

Figure 2.13: Sliding window technique for jet reconstruction at L1 [48].

candidate is only kept if the quality of the candidate in one of the systems is very high. The Global Muon Trigger in addition receives calorimeter information to determine whether the candidate track extrapolates back to the calorimeter to an isolated, minimum ionizing particle. In total, up to four muon candidates are put out by the L1 muon trigger. A schematic view of the data flow in the L1 Muon system is shown in fig. 2.14. More information can be found in [55].

At HLT, muons are selected in two steps. In the first step called L2, muons are reconstructed using only information from the muon system based on the L1 seeds, called the standalone reconstruction. The p_T threshold at this step reduces the rate to allow for a more time-consuming reconstruction algorithm using the full tracker information. The L3 reconstruction extrapolates the L2 muon tracks to the tracker to look for hits compatible with the candidate track. The combination of the muon system and tracker information allows for a more precise p_T determination. After L2, calorimeter information is applied. The energy deposited in the calorimeter in a hollow cone around the muon candidate is summed up to determine whether the muon candidate is isolated or not. Isolation requirements can also be based on tracker information. This requires reconstructing full tracks in the vicinity of the muon candidate, making this a very time intensive computation.

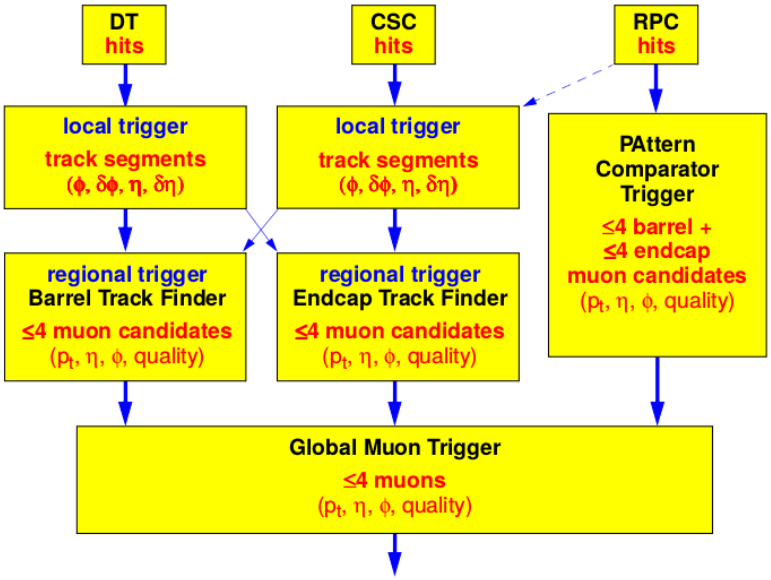

Figure 2.14: Muon Trigger data flow [55].

Part II

Simulation and Reconstruction

Chapter 3

Simulation and Software Tools

Through Monte Carlo (MC) event generation, we are able to simulate the physics processes we are interested in to verify the compatibility of the collected data to our current theory understanding and to tune the MC simulation using well-known processes from data. Varying event generators are available by the theory community in high energy physics, but only two of them will be described in this chapter: MadGraph [59] and MC@NLO [60]. Event generators allow us to produce simulated events in proton-proton collisions (or another collision of choice) in a specific physics process of interest combining all the theoretical knowledge of the SM or another hypothetical model. The physics process under investigation (also called the hard process) is then passed on to a showering program to hadronise the produced partons in the process. The final state particles are then passed on to detector simulation software to mimic the raw data output from the detector. By comparing this simulated detector output to the detector output from the LHC collisions, we can obtain a deeper understanding of the detector which in turn helps to understand the data better. The raw output is processed by the reconstruction framework of the collaboration to reconstruct physics objects for the analysts to work with. The volume of data to be processed requires a considerate amount of computing resources. The software framework of CMS is highly modular. Modular frameworks offer the advantage that not every user needs to be familiar with the details of all of the code. It is also much more flexible to updates and extensions of the existing modules and addition of new modules. Each user needs to be able to track the relevant data and code and access it when necessary.

3.1 Monte Carlo Event Generation

A Monte Carlo (MC) Event generator simulates how physical processes, either known physical processes in the SM or hypothetical processes, are visible in the detector by simulating the decay chains and the proper kinematic ranges the process will appear in. This event generation happens in several steps. Firstly the user defines the colliding particles, which in the case of the LHC are protons. The protons as a whole do not enter in the physical process to be generated, but rather the partons that make up the proton. A schematic view of a proton-proton interaction with the various stages depicted is shown in fig. 3.1. Parton Distribution Functions (PDFs) describe the fractional momentum distribution of a certain parton type within the proton probabilistically. For each of the colliding protons, the decision is made to generate a quark, anti-quark or gluon with a certain momentum based on these PDFs. These partons are then called the initial state partons. With the set of initial state partons, all possible Feynman diagrams for the chosen physical process are calculated, leading to the final state particles, either at leading order (LO) or next-to-leading order (NLO) depending on the generator. This is called the hard process. Examples of generators are MadGraph and MC@NLO. After the hard process, parton shower (PS) models come into play to simulate higher order effects by radiating gluons off the final state partons, these are called the soft processes. PS is performed on both the initial state and final state particles called Initial State Radiation (ISR) and Final State Radation (FSR) respectively. The partons in the final state are subject to colour confinement which gives rise to a stream of colourless hadrons, which in their turn can decay. Examples of PS generators are Pythia [61] and Herwig [62].

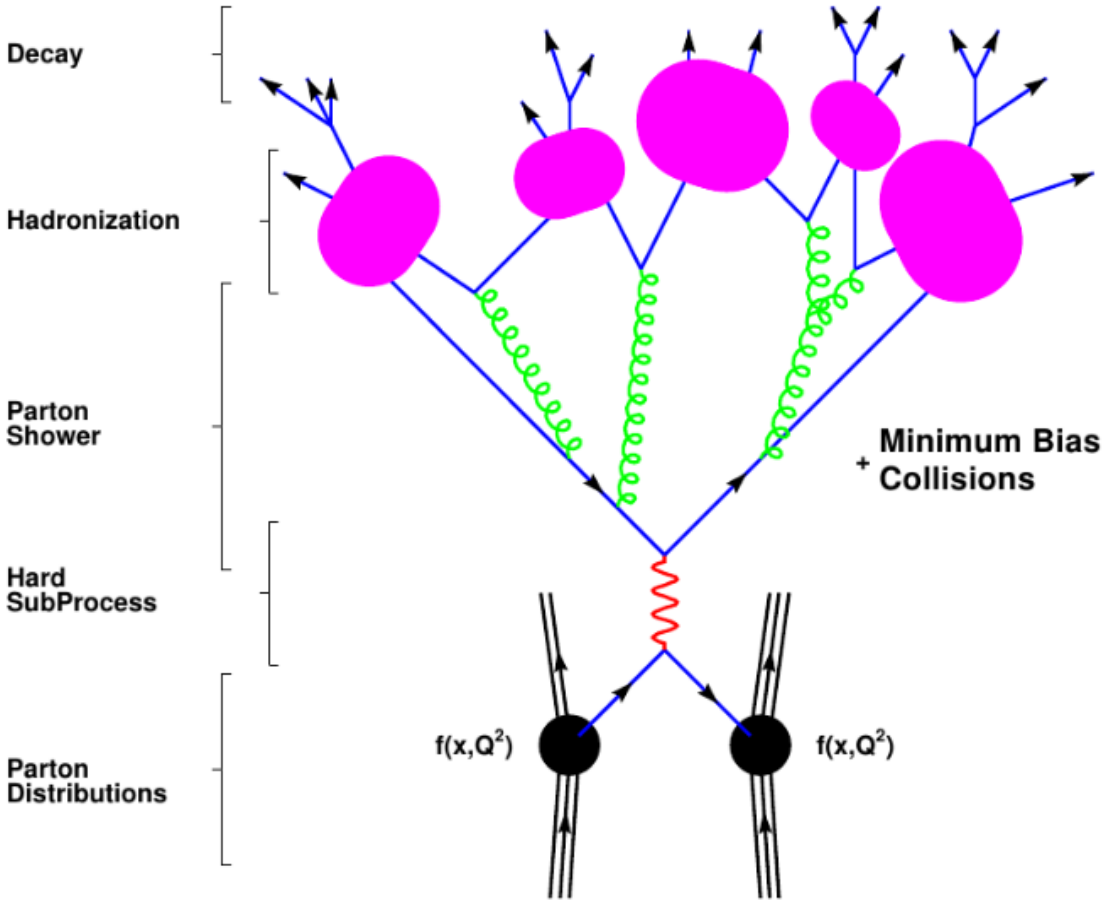

Figure 3.1: Schematic view of a proton-proton collision. Two partons inside the proton interact in the hard process. The produced partons in the interaction can radiate gluons in the parton shower. The partons hadronise and finally decay.

3.1.1 MadGraph

MadGraph 5 [59] is a LO matrix element generator for any particle physics process in a Lagrangian-based model. MadGraph generates all tree-level Feynman diagrams for processes such as decays and $2 \longrightarrow n$ scatterings and provides the code to evaluate the matrix element of the process in a given phase space point. The MadGraph code can be used for cross section calculations or to generate events for a specific process. In this work, we used W + jets and Z + jets samples produced as CMS official samples with MadGraph. In addition we used MadGraph to simulate $t\bar{t}$ production in the lepton + jets channel in a private event sample at the generator level. The various samples used will be discussed in section 5.1.

3.1.2 MC@NLO

MC@NLO is a Fortran package implemented to combine NLO calculations to a parton shower MC simulation [60]. Hard emissions are treated in the NLO computations. Soft emissions are handled in the parton shower MC simulation. Another interesting feature of the MC@NLO event generator, is the conservation of spin correlations in decays. In most event generators, the resonant production and subsequent decay of particles with non-zero spin is treated separately. First the resonance is generated and then replaced by its decay products, which are then distributed isotropically in the resonance rest frame. Any spin correlations in the system are

then destroyed. In MC@NLO, the decay is considered as part of the Born process and as such the angular distribution of the decay products is weighted according to the tree-level matrix element [63]. NLO effects are fully propagated to the production of resonances in MC@NLO but not fully to the decay process, so spin correlations obtained from MC@NLO are not exactly the same but very close to the NLO theory calculations. In this analysis, where we want to study the spin correlations in the $t\bar{t}$ system, we use MC@NLO for the production of the signal samples.

3.1.3 Pythia, Herwig

PYTHIA 6.4 [61] is an example of a showering and hadronisation event generator. The shower simulation part is based on the JetSet package [64] which was developed by the Lund group. The Lund string model [65] connects divergent partons by colour flux tubes. When partons diverge the potential energy between them increases until it becomes energetically more favourable to produce a new parton pair which then pair up with the original partons to produce a colourless hadron. PYTHIA can be matched to the output of a different event generator to perform the hadronisation.

Similar to Pythia, Herwig [62] is a showering and hadronisation event generator but it makes use of the cluster fragmentation model. The most notable difference is that Herwig conserves spin correlations between the particles of the hard interaction process while these are destroyed in Pythia. For this analysis the $t\bar{t}$ processes simulated with MC@NLO are interfaced with Herwig.

3.2 Detector Simulation

The CMS detector simulation largely relies on the Geant 4 [66] package. Geant 4 is a tool-kit that simulates the passage of particles through matter. Geant 4 is an object-oriented framework written in C++. Users can insert the detector geometry and material specifications in the framework, choose the primary particles in the interaction, the physics interactions of the particles (electromagnetic, hadronic or optical), and the energy range of the initial particles, in order to obtain the particle trajectories and energy losses through the detector medium. Various magnetic field models and strengths can be added to the simulation. After the simulation of the particle hits, these can be propagated to a simulated read-out system of the detector. The particle hits are digitised, taking into account energy losses, electronic noise, cross talk between channels, etc.

The CMS detector simulation [67] covers all CMS subdetectors and creates hit collections stored as products in the event information. The settings of the simulation are stored in the event to allow for reproducibility. The detector simulation has been tuned and improved using test beam data.

3.3 Tools and Computing Clusters

There are various other tools and resources which have contributed to the completion of this and many other analyses in the high-energy physics community. The most significant will be described in this section.

3.3.1 MadWeight

MadWeight [59] is a part of the MadGraph 5 framework described in section 3.1.1. MadWeight is used to perform a matrix element method in this analysis which will be described in detail

in section 7.1. In short, unlike an event generator which starts from the matrix element of a certain process and gives as output event kinematics produced by this process, MadWeight takes as input event kinematics produced through experiment or an event generator and calculates the compatibility of these event kinematics to the matrix element of a hypothetical process. The event kinematics are passed to MadWeight in a format called an LHC Olympics file or LHCO file [68]. The LHCO file contains the identification number of the event, and a set of information on the reconstructed or generated physics objects in the event. For each physics object, the type (muon, electron, photon, jet or missing transverse energy) is specified. The four-vector of the object is stored in the (η, ϕ, p_T, invariant mass) format. The number of tracks associated to the object is also stored, which is multiplied by the charge of the object. In the case of a jet, it is tagged as coming from a b-quark or not. Some additional dummy variables are available, to be filled according to the needs of the analysts. MadWeight receives this information and checks whether the particle types and their charge is compatible with the final state of the process under study and if so, the likelihood of the event for this process is calculated.

3.3.2 ROOT

ROOT is an object-oriented data analysis framework, developed in 1995 by Rene Brun and Fons Rademaker at the NA49 experiment at CERN [69]. With the advent of object-oriented programming languages and significant improvements in computer science, it was possible to organise large amounts of data. ROOT is now officially adopted by the CERN experiments and beyond, making it one of the leading frameworks used in high-energy physics. ROOT offers a variety of features useful in a physics analysis. ROOT offers efficient input and output of mass storage and data-compressing techniques. ROOT can handle multi-dimensional histograms, fitting procedures, statistical methods, function evaluation and many other features. An additional feature of ROOT is the RooFit library [70]. RooFit offers additional advanced tools for statistical modelling, likelihood fits, event generation based on probability density functions and more. In this analysis, RooFit is used to perform a maximum-likelihood, template fit where the templates are probability density functions based on histograms.

3.3.3 CMSSW

The overall collection of official software for the CMS Collaboration is referred to as the CMS Software (CMSSW) [71], [48]. It is a modular framework written in an object-oriented programming language C++ and configuration files written in Python which allows for an efficient development and deployment of reconstruction and analysis code. CMSSW only has one executable called cmsRun which is configured at runtime by a user-specific configuration file, and can be run on both detector and simulation data. In the configuration file, the user can specify which modules should be run with which parameters, on which data the modules should be performed, the sequence of the modules and what information to return as output.

The framework is built around an event data model (EDM) which works with the concept of events. An event is a C++ container for all the data (unprocessed RAW data as well as reconstructed RECO data) related to a particular collision. The events are stored in ROOT file format. An event contains all information related to a certain collision since the data acquisition step when the event passed the trigger. All reconstruction and calibration performed on the event is stored in addition, leading to collections of reconstructed physics objects like jets. In addition all information to trace the source and conditions of data-taking of the event are also stored as the meta-data of the event.

There are several types of modules available in CMSSW. A large collection of modules is made available to the collaboration for analysis steps almost every user has to deal with, but users

can very easily develop their own modules and plug these into the processing sequence. A list of the types of modules is given next:

- **Source**
  The source module reads in the simulation or data events from ROOT files, so that these can be used in further modules.
- **EDProducer**
  EDProducer modules add extra content to the event, for example reconstructed objects
- **EDFilter**
  Filters read in data from the event and return a boolean decision for that event based on some criteria. If the event passes these criteria, it is then passed on for further processing to other modules.
- **EDAnalyzer**
  An EDAnalyzer is used to study the properties of the event. EDAnalyzers do not add to the event content, nor do they influence the rest of the executed path. Typically, some quantities are calculated in the EDAnalyzers and stored as output in for example histograms in a ROOT file.
- **EDLooper**
  A Looper module is used to pass multiple times over the same event, for example in the track based alignment procedure.
- **OutputModule**
  The OutputModule reads in the event data produced and stores all the necessary output after the full path has been processed.

3.3.4 Computing Resources

The computing resources needed for the processing and storage of the recorded or simulated data cannot be provided by a central computing centre. The LHC Computing Grid (LCG or the Grid) has been designed as a hierarchical structure of computing centres to meet with demand of computing resources.

The computing centres in the Grid are arranged in Tiers and allow for real-time data access. The system allows for multiple copies of the data to be stored in different locations and across time-zones, thus ensuring continuous availability and support. In total there are four Tiers, ranked from 0 to 3. Each Tier consists of several sites and has a specific purpose. A schematic view of the hierarchical structure of the Grid is shown in fig. 3.2.

The central computing centre is the Tier-0 which is located at the CERN site. The CERN Tier-0 stores the raw data coming from the experiments and a first reconstruction is performed. The Tier-0 distributes the raw data to the Tier-1 centres. 13 Tier-1 centres each store a portion of the raw data, ensuring a back up of the data at the Tier-0. The Tier-1 also provides the resources to do a reprocessing of the data and store the output. Connection of the Tier-0 to the Tier-1 is ensured by optical-fibre links allowing for downloading speeds of 10 Gb/s. Tier-2 centres are smaller scale, but more abundant. There are about 150 Tier-2 centres all around the world, mainly consisting of the computing capacities of universities and other scientific institutes. The Tier-2 mainly offer computing power for the production and reconstruction of simulated events and user activity. The Belgian Tier-2 has been used extensively during the making of this thesis, offering CPU resources, storage for personal code and data and storage for the official CMS Top group data collection. The Tier-3 are small scale, local resources such as clusters at universities or individual computers dedicated to user activity and analyser tasks.

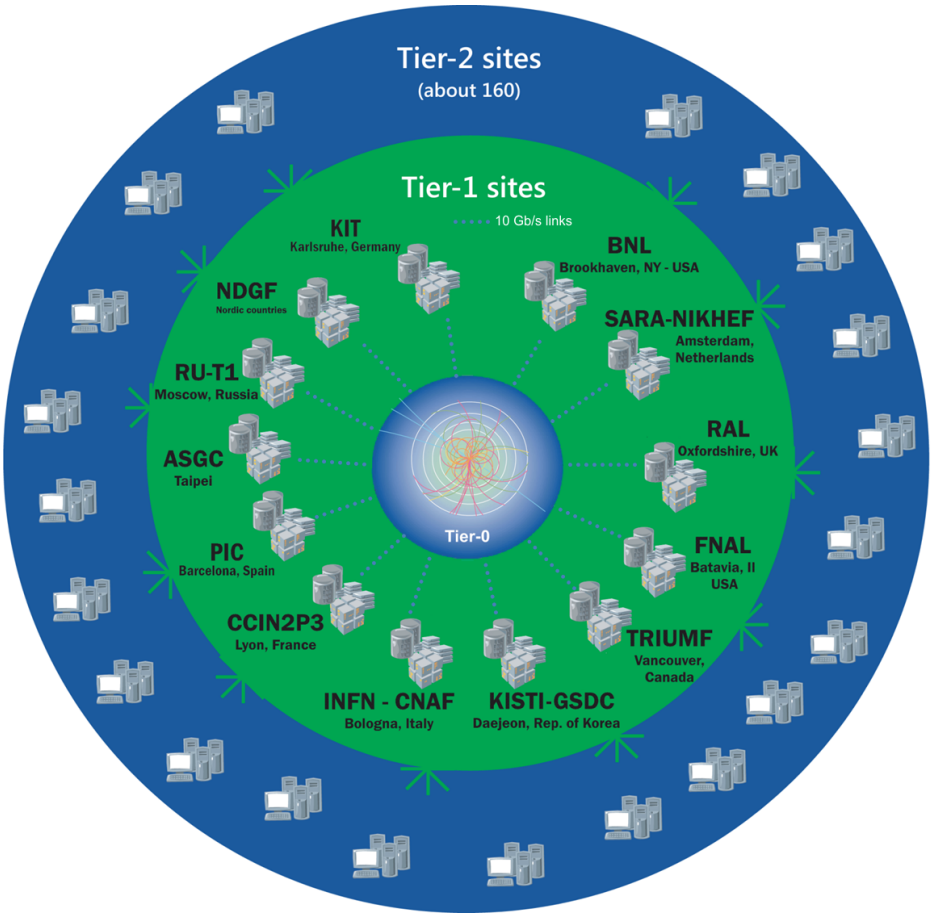

Figure 3.2: Schematic view of the tiered structure of the LCG.

Chapter 4

Reconstruction

In this chapter we will discuss the (offline) reconstruction from detector signals to physical objects such as electrons or muons. In most physics analyses the reconstruction stops at this level: the physical objects and their properties are selected in certain combinations to obtain a relatively pure sample of events produced by a certain physics process. With this sample of events, one can perform counting experiments for cross section determinations, or look for certain properties of the process or produced particle. However in top quark pair production, we do not directly observe the top quarks but rather the decay products. In the reconstruction of the events for this analysis, we go a step further and try to reconstruct the top quark pair using a kinematic fitting procedure which will be described in the second section of this chapter.

4.1 Physics Object Reconstruction

4.1.1 Vertex Reconstruction

Vertices identify interaction points in pp collisions. At the LHC multiple collisions occur per bunch-crossing, making an accurate vertex reconstruction necessary to be able to assign particles to the individual collisions. Vertex reconstruction uses only silicon tracker information to first find possible candidates for vertices and then use a fit to obtain the best estimate for the vertex parameters associated to a group of tracks. Here, we describe primary vertex reconstruction. Secondary vertices can arise when a long-lived particle decays. Secondary vertices have much lower track multiplicity and therefore a different reconstruction algorithm which we will not describe here.

First, a sample of fully reconstructed tracks is selected based on their distance of closest approach to the beam, their p_T and the track fit quality. Tracks are clustered together in vertex candidates based on the z-coordinate of their point of closest approach to the beam line using the Deterministic Algorithm [72].

A vertex candidate is fitted using the Adaptive Vertex Fitter [73]. In this iterative fit, tracks associated to the vertex are down-weighted according to their χ^2 distance to the vertex. This makes the algorithm robust against outlier tracks. The number of degrees of freedom is defined as ndof = 2Σ w_i - 2 where w_i is the weight of track i and calculated as

$$w_i(\chi_i^2) = \frac{exp(-\chi_i^2/2T)}{exp(-\chi_i^2/2T) + exp(-\chi_c^2/2T)} \tag{4.1}$$

with χ_i^2 the compatibility of the track i with the vertex, χ_c^2 is the threshold where the weight equals 1/2 and T is a shape parameter. The collection of primary vertices is sorted according to the sum of the p_T^2 of the tracks in that vertex.

4.1.2 The Particle Flow Algorithm

The Particle Flow or PF algorithm (PFA) is the preferred reconstruction technique in CMS at the moment. The PFA combines the information from all the subdetectors to follow all the particles produced into the event along the CMS subdetectors. Particles are identified by their

combination of signatures in the subdetectors, in this way it offers a consistent picture of the event, by not allowing for overlap between particle collections. In this section, we will give a brief overview of the main algorithms used in PF, while in the next sections the usage of PF to reconstruct various physics object collections will be described. PF event reconstruction requires a highly efficient tracking algorithm and a good clustering algorithm, taking advantage of the high granularity of the ECAL. The reconstructed tracks and calorimeter clusters are linked together. The links are then used to reconstruct and identify physical objects. For a full description of the Particle Flow reconstruction, we refer to [74].

Iterative Tracking

The tracker has superior momentum resolution with respect to the CMS calorimeters for transverse momenta up to several hundreds of GeV/c. The direction of a charged particle is most accurately determined in the tracker close to the interaction vertex, where the particle hasn't had time to deflect in the magnetic field. Therefore the success and accuracy of the PF method relies to a large extent on the tracker reconstruction. We need high efficiency so that we can benefit of the better resolution the tracker offers for each charged particle produced in the event. At the same time, we also need a low tracker fake rate, since fake tracks can give rise to large energy excesses.

Reconstruction is performed with an iterative-tracking strategy [75, 76]. In the first iteration, very tight criteria are placed on the seeds and the reconstruction of tracks. Hits in three pixel layers are needed to produce a seed at this step. This leads to a modest reconstruction efficiency, but a negligible fake rate. In the next iteration, the hits making up the tracks found in the first iteration are removed, and the selection criteria are loosened, only needing hits in two layers to make a seed. Loosening the criteria allows for a larger efficiency, and due to the reduced combinatorics of the remaining hits, the fake rate is still low. This is repeated for the next iteration, leading to a reconstruction efficiency larger than 90% for charged hadrons and even higher for muons in the first three iterations.

In the fourth and fifth iteration the constraint that the track should originate in the collision vertex is released. This allows for reconstruction of tracks coming from secondary vertices due to photon conversions or decays of long-lived particles. Using the iterative-tracking technique, charged particles can be reconstructed with p_T down to 150 MeV/c, only three hits and associated with a vertex up to 50 cm away from the beam line with a fake rate at the percent-level.

Calorimeter Clustering

The calorimeter is highly important to detect and measure the energy of stable neutral particles like photons and neutral hadrons. With an accurate clustering mechanism, these neutral particles need to be resolved from charged hadrons. The calorimeters also help in the identification of electrons by reconstructing the pattern of bremsstrahlung photons accompanying electrons. Sometimes the calorimeter can also improve the momentum resolution of charged hadrons, when these have low quality tracks or very high momentum.

Just as with the track reconstruction, we want a high detection efficiency in the calorimeter and a granularity fine enough to separate closely spaced energy deposits. The clustering algorithm is performed separately in the ECAL barrel, ECAL endcap, HCAL barrel, HCAL endcap, and separately in the two layers of the pre-shower.

Clustering is performed in three steps. In the first step, cluster seeds are reconstructed by

selecting calorimeter cells with an energy above the threshold, higher than the energy of their direct neighbours. In a second step, the cluster seed grows by adding neighbour cells which have an energy above a certain threshold. This threshold consists of two standard deviations away from the electronic noise (note that this threshold is different for barrel vs. endcap and ECAL vs. HCAL). This step is performed until no neighbouring cells with adequate energy are found. These clusters are called topological clusters. In a third step, PF clusters are formed from the topological clusters. A topological cluster can contain as many PF clusters as there are seeds and a calorimeter cell can be part of several PF clusters. This is a difference with respect to the standard calorimeter clustering where each cell can only be associated to one cluster. In the PF clustering algorithm, the energy of each cell is shared between several clusters based on the distance between the cell and the cluster centre. The cluster position and energy is determined iteratively until the list of cells associated to the cluster no longer varies.

Topological Linking

Usually a particle will be detected in several subdetectors and therefore give rise to more than one PF element. The linking algorithm puts all these elements together in a consistent way to follow the particle through the several subdetectors. It ensures that no particle is double-counted. The link algorithm is performed on PF elements of each subdetector pair. PF elements can therefore be linked directly or indirectly with one another into blocks. The quality of each link is expressed as the distance in the (η-ϕ)-plane between the two elements.

A link between a track and a calorimeter cluster is made by extrapolating the track from the last hit in the tracker to the calorimeter. The position in the calorimeter chosen to extrapolate the track to is either the two separate layers of the PS, the depth in the ECAL where one expects the maximum of the longitudinal shower profile of an electron or one interaction length in case of the HCAL. The track is then linked to the cluster if the extrapolation falls within the cluster boundaries. The link distance is defined as the distance between the extrapolated track position and the calorimeter cluster in the (η,ϕ)-plane. In order to collect the energy of the brehmsstrahlung photons, the tangent of the track at each tracker layer is extrapolated to the ECAL. If the extrapolated tangent is within the cluster boundaries, the cluster is linked.

Two calorimeter clusters can be linked, for example an ECAL and HCAL cluster or PS and ECAL cluster, when the cluster position of the finer grained calorimeter is within the boundaries of the coarser grained calorimeter. The link distance is again the distance in the (η,ϕ)-plane.

A tracker-track will be linked to a muon track to form a global muon when the fit between the two tracks has a low χ^2. The link distance is defined by the χ^2. An example of how the linking procedure works is shown in fig. 4.1.

4.1.3 Muon Reconstruction

There are three categories of reconstructed muons: standalone, tracker and global muons. Standalone muons are reconstructed using only the muon subdetectors very similar as described in section 2.3.3. First track segments are constructed by a linear fit to the hits in each DT or CSC chamber separately. Second the track segments are used, in combination with the RPC information, to construct muon trajectories using a Kalman filter technique [77]. Tracker muons only use the tracker information. All tracks with a $p_T > 0.5$ GeV/c and $p > 2.5$ GeV/c are considered muon candidates when their extrapolation to the muon system matches at least one hit. Global muons make use of both the tracker and muon systems by extrapolating the tracks in both systems.

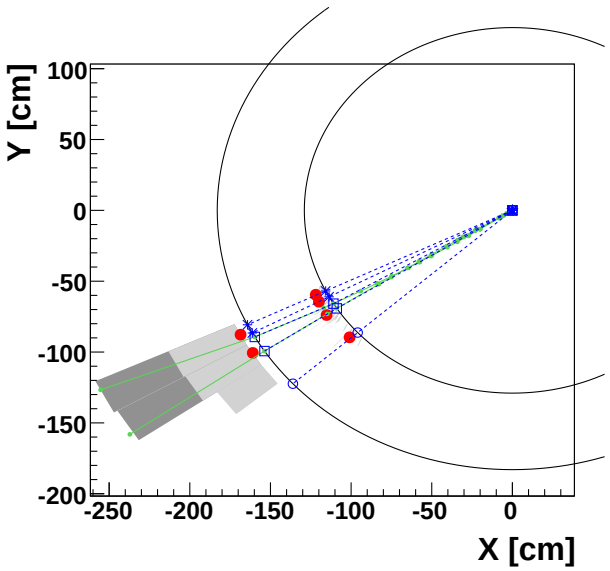

(a) view in the (x,y)-plane

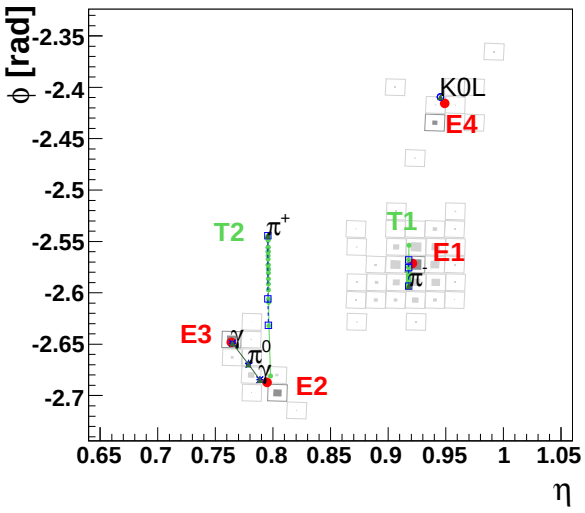

(b) (η,ϕ)-view on the ECAL

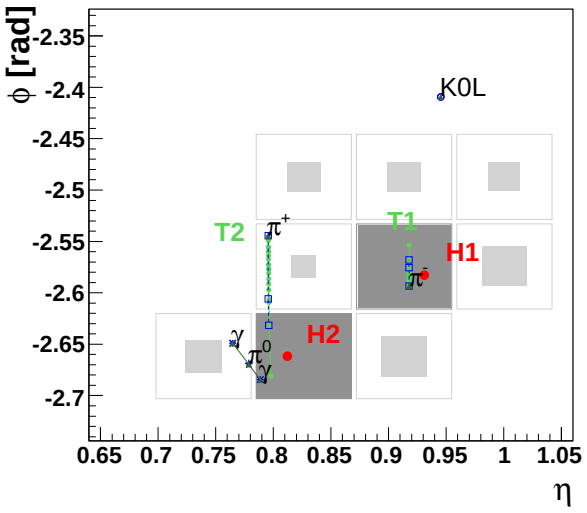

(c) (η,ϕ)-view on the HCAL

Figure 4.1: Schematic view of the event display of a simplified jet from three different viewpoints. In the jet there are four particles: a K_L^0, a π^+, a π^- and a π^0 decaying to two photons. Four separate clusters are reconstructed in the ECAL, coming from the K_L^0, two photons and the π^-. The π^+ doesn't show as a cluster in the ECAL. There are two clusters in the HCAL coming from the π^+ and the π^-. The tracks left by these charged particles points to these HCAL clusters. Figure taken from [74]

The reconstructed muon collection contains a significant amount of misidentified charged hadrons. In PF muon reconstruction [78] extra selection criteria are placed on the reconstructed muons. There are three categories of PF muons: isolated, PF-tight and PF-loose. A muon is isolated when the summed p_T of the tracks and transverse energy in the calorimeter in a cone of size $R = 0.4$ around the muon is less than 10 % of the muon p_T. The PF-tight and PF-loose criteria are tested on the remaining non-isolated muon candidates. The PF-tight and PF-loose categories are designed to identify muons within jets. The PF-tight selection requires a minimum number of hits in the muon system. In addition the energy deposited in the calorimeter needs to be consistent with that of a minimum ionizing particle. The PF-loose selection is applied on the muon collection which passes neither the isolated, nor the PF-tight category. The number of hits required is lowered and the requirement on the energy deposit is replaced by a matching requirement between the tracker track and the muon system track. The PF links from the PF muons are removed from the list in the next steps of the event reconstruction.

The resolution of muons is measured in $Z \rightarrow \mu\mu$ events in the range $20 < p_T < 100$GeV. The average bias in the muon momentum is consistent with zero and has been measured with a precision of 0.2 %. The relative p_T resolution is in the range of $1.3 - 2$ % in the barrel and better than 6 % in the endcaps, shown in fig. 4.2. The resolution on the p_T is better than 10 % for muons with p_T up to 1 TeV [79].

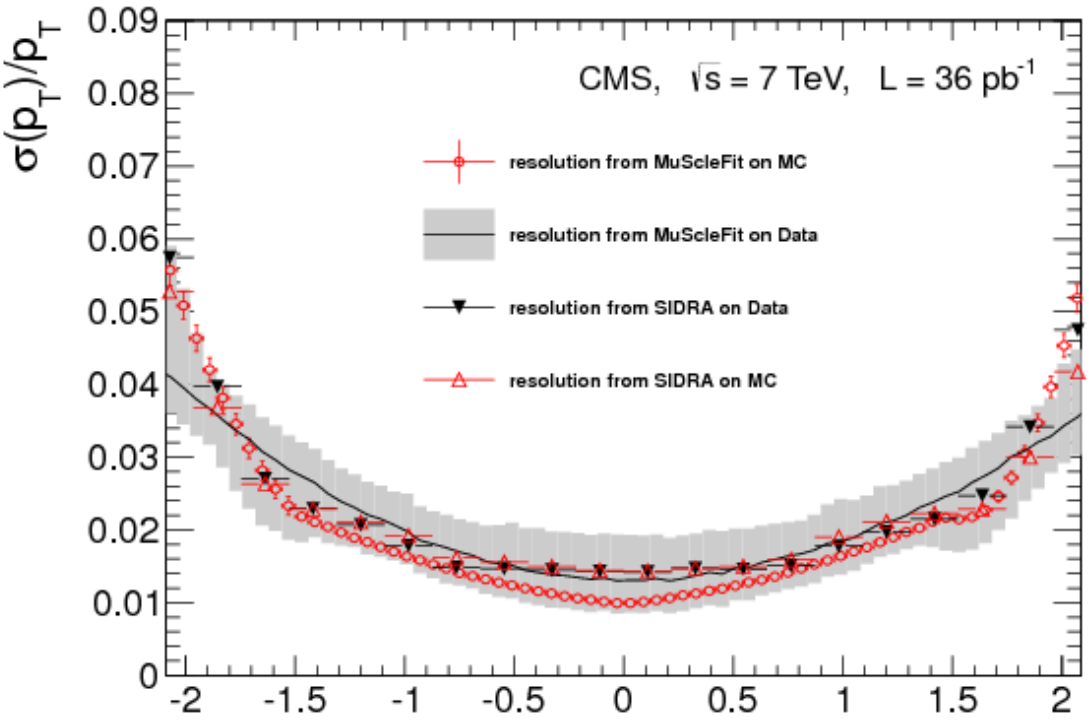

Figure 4.2: Relative transverse momentum resolution $\sigma(p_T)/p_T$ as a function of the muon pseudo-rapidity as measured in data and simulation with MuScleFit and SIDRA two calibration methods. Figure taken from [79].

4.1.4 Electron Reconstruction

Electrons are first reconstructed as Gaussian Sum Filter (GSF) electrons [80]. There are two procedures for electron reconstruction: tracker driven seeding and ECAL driven seeding. The

tracker driven seeding is used for low energy electrons or electrons within jets, while ECAL driven seeding works best for electrons with p_T larger than 5 GeV/c. Electron tracks require a more detailed reconstruction than other tracks since electrons suffer from non-Gaussian energy losses due to bremsstrahlung emission. The GSF is a non-linear generalisation of the Kalman Filter [77]. The benefit of using GSF tracks is that hits are collected along the full trajectory of the electron. This allows for a better extrapolation of the electron track to the ECAL and allows for an estimate of the momentum radiated off by bremsstrahlung photons by evaluating the momentum difference based on the inner and outer track parameters. The ECAL driven seeding reconstruction is based on the formation of superclusters very similar as in section 2.3.3. Based on the energy and position measurement of the supercluster, the electron is propagated back to the inner layers of the tracker where it is matched to track seeds.

The PF electron is reconstructed by extrapolating the electron track to the ECAL and matching it to the energy deposit. The tangents of the electron track need to be matched to the bremsstrahlung photons reconstructed by the PF clustering algorithm. The PF links associated to the electrons are removed from the list in the further steps of the event reconstruction.

The resolution of electrons is measured in $Z \rightarrow ee$ events with electrons of about $p_T \approx 45\,\text{GeV}$ and is shown in fig. 4.3. The resolution ranges from 1.7 % in the barrel region to 4.5 % in the endcap region [81].

4.1.5 Jet Reconstruction

When quarks and gluons are produced in an event, these fragment and hadronise due to colour confinement. What becomes visible in the detector is a spray of hadrons, leptons and photons, which is referred to as a jet. Even though jets leave a very distinct signature in the detector, the reconstruction of jets is highly non-trivial since they are composed of both charged and neutral particles, isolated and non-isolated objects, making the properties of a jet very different on an event-to-event basis. Because of the complexity of jets, there is no single perfect jet reconstruction method and different clustering algorithms will give rise to different jet definitions. Even with a perfect jet reconstruction, there is no one-to-one correspondence between a jet and the produced parton, since partons can radiate off gluons and be reconstructed as two jets or merge together.

Jet Clustering

A jet reconstruction algorithm has two parts: the jet algorithm with its specific parameters and a recombination scheme. The jet algorithm clusters the particles together in a jet with some parameters on the maximal distance between particles in one jet. The recombination scheme deals with the total momentum of the combined particles. In most of the analyses in CMS the anti-k_T clustering algorithm is used [82]. The four-momenta of PF objects are used as input for the anti-k_T algorithm. Two distance parameters are defined as

$$d_{ij} = min(k_{ti}^{2p}, k_{tj}^{2p}) \frac{\Delta_{ij}^2}{R^2} \tag{4.2}$$

$$d_{iB} = k_{ti}^{2p} \tag{4.3}$$

where d_{ij} is the distance between particle i and j and d_{iB} is the distance between particle i and the beam. In these expressions, we have $\Delta_{ij}^2 = (y_i + y_j)^2 + (\phi_i + \phi_j)^2$, and k_{ti}, y_i and ϕ_i are the transverse momentum, rapidity and azimuthal angle of particle i. R is the radius parameter of the algorithm. In CMS one usually sets R to 0.5 for analyses performed on LHC Run I data, however occasionally an R of 0.7 is used. The parameter p is the power of the jet

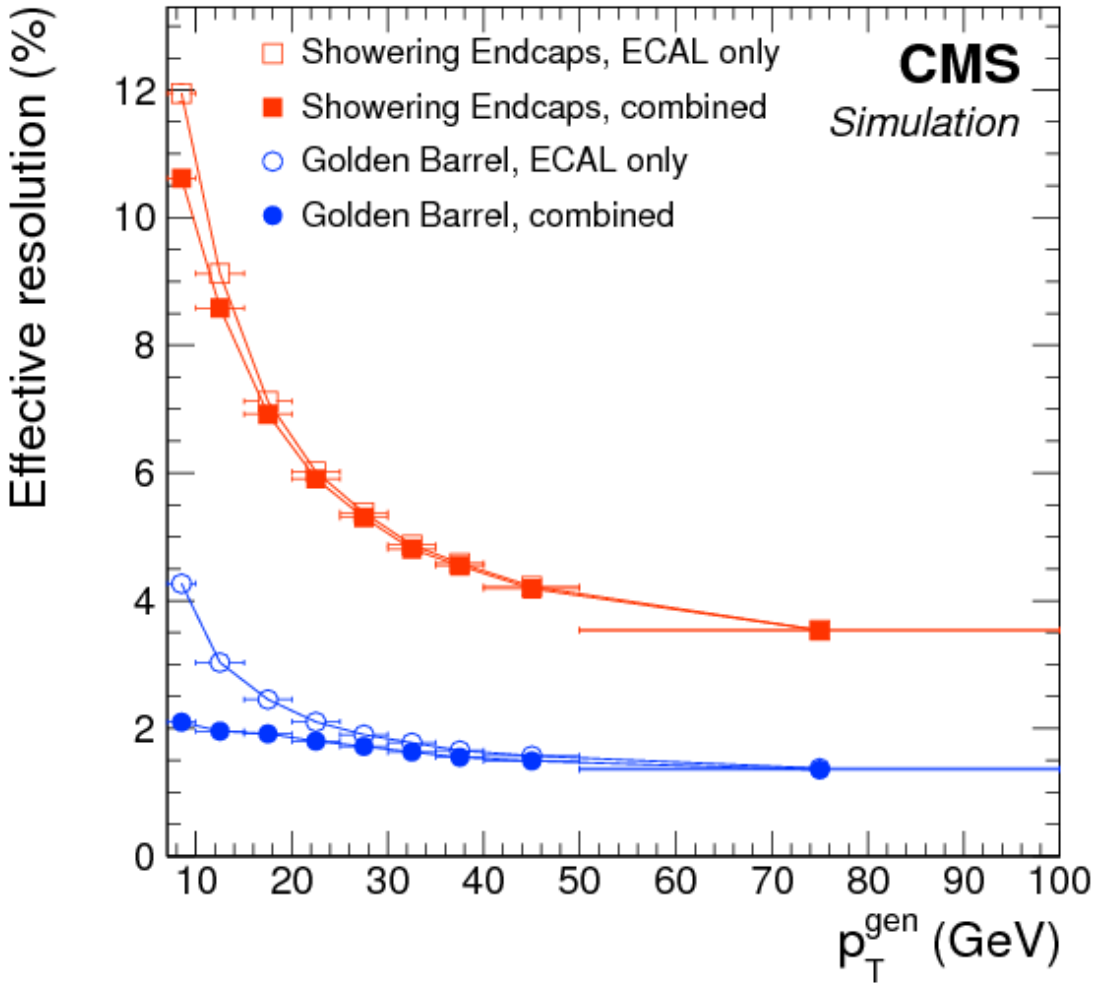

Figure 4.3: Relative electron resolution as a function of the electron transverse momentum measured in simulation. Figure taken from [81].

clustering algorithm. In the anti-k_T algorithm $p = -1$, in the Cambridge/Aachen algorithm [83] $p = 0$ and in the k_T algorithm [84] $p = 1$. In the clustering, the distance parameters d_{ij} and d_{iB} are calculated for each particle pair (i, j). If the smallest distance is between the particles i and j, these are merged together in a new particle k with kinematics $E_{T,k} = E_{T,i} + E_{T,j}$, $\eta_k = [E_{T,i}\eta_i + E_{T,j}\eta_j]/E_{T,k}$ and $\phi_k = [E_{T,i}\phi_i + E_{T,j}\phi_j]/E_{T,k}$. The assumption is that the particle masses are small compared to the transverse momenta. If the smallest distance is between particle i and the beam, particle i is considered as a jet and it is removed from the particle list. The clustering continues until there are no more particles left. The definition of a jet in this algorithm depends on the value of R: if a particle i has no other particles within a distance R, then d_{iB} will be smallest and particle i will be considered a jet. The anti-k_T algorithm results in circular jets, as can be seen in fig. 4.4. Circular jets are very intuitive to work with, since it is very easy to assess whether the jet is contained within the fiducial volume of the detector. One of the other big advantages of the anti-k_T algorithm is that it is infrared and collinear (IRC) safe. An IRC safe clustering algorithm will result in the same set of hard jets when one modifies the event adding a soft gluon emission to one of the jets or do a collinear splitting of a particle. In essence, IRC safety shows that the algorithm is insensitive to

the clustering seed. This is the case for sequential recombination schemes of which the anti-k_T algorithm is an example. Algorithms such as the iterative cone algorithm [85], which perform the clustering by starting off with a particle direction i and keep adding particles in a cone around that particle direction, are not IRC safe.

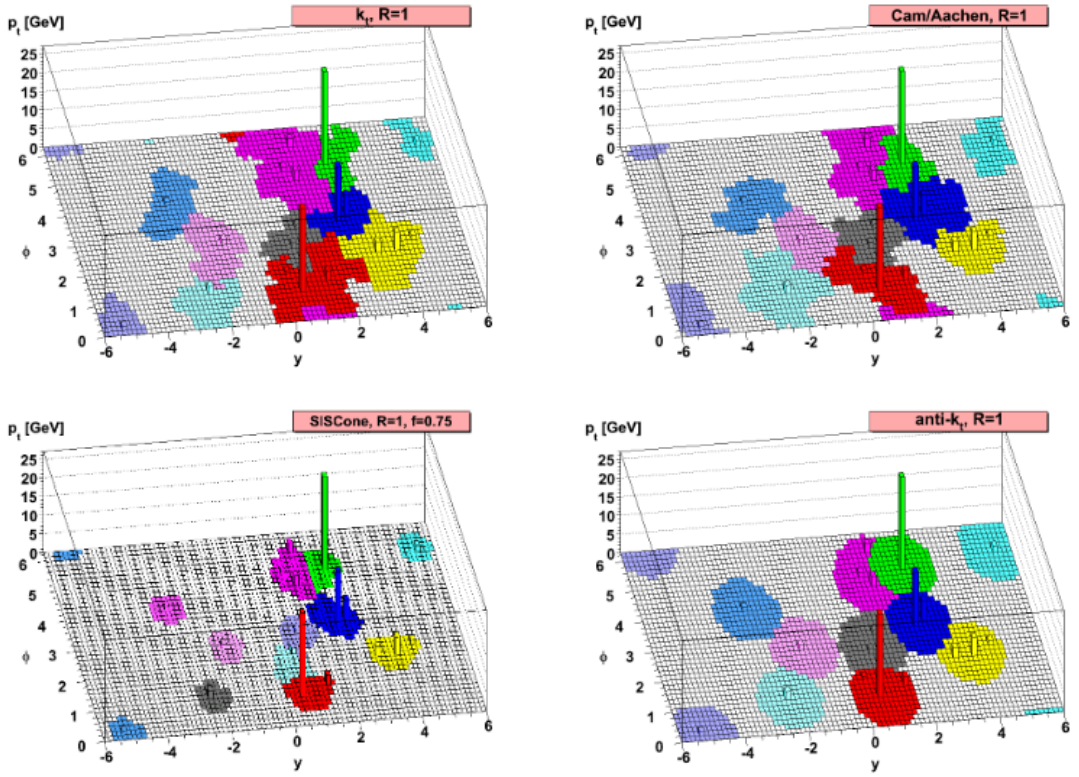

Figure 4.4: A parton-level event with soft radiation. The result of four different clustering algorithms are displayed. Figure taken from [82].

As mentioned earlier, the anti-k_T algorithm can use the list of PF particles as input. PF muons and electrons which have been reconstructed as isolated particles are not included in the jets. Also charged hadrons can be excluded from a jet when these are originating from pile-up interactions. Particles from pile-up interactions are identified by their association to a different vertex.

Jet Energy Corrections

There can be large discrepancies between the energy of the jet measured in the detector and the energy of the produced particle jet. The energy of the true particle jet can be obtained from simulation by clustering the particles produced in the hard process and the hadronisation. The correction of the measured jet momentum to the particle level jet is done in multiple steps called the Jet Energy Scale corrections (JES or JEC). The corrections are applied in the form of scale factors and are applied both to data and simulation, but with an extra correction on the data to account for data-simulation discrepancies. The methodology to obtain the JES corrections is described in [86]. There are four corrections applied: an offset correction (L1), relative (η) correction (L2), an absolute (p_T) correction (L3) and a residual correction on the data (L2L3Residual).

The corrections are applied from right to left in equation 4.4. The L2 and L3 corrections

are applied simultaneously in the C_{MC} step and two residual factors (C_{abs} and C_{rel}) are applied on data.

$$p_T^{cor} = C_{abs}(p_T^{''}) \cdot C_{rel}(\eta) \cdot C_{MC}(p_T^{'}, \eta) \cdot C_{offset}(p_T^{raw}) \cdot p_T^{raw} \tag{4.4}$$

with $p_T^{'} = C_{offset}(p_T^{raw}) \cdot p_T^{raw}$ and $p_T^{''} = C_{rel}(\eta) \cdot C_{MC}(p_T^{'}, \eta) \cdot p_T^{'}$.

- Offset correction (L1): The offset correction is designed to remove all energy not coming from the hard process but due to pile-up and electronic noise.

- Monte-Carlo correction (L2L3): The MC calibration corrects the energy of reconstructed jets back to the average of the simulated particle jets. The MC calibration is the largest correction factor and is p_T,η-dependent. The η-dependence corrects for the non-uniform detector response while the p_T dependence corrects for the non-linearity of the detector response with p_T. The MC correction depends on the type of reconstructed jets: jets reconstructed using only calorimeter information need very large corrections. PF jets combine calorimeter and tracker information for the momentum determination which is more accurate and therefore requires smaller correction factors. Large correction factors are applied to jets in the transition region between the barrel and the endcap where accurate momentum determination is more difficult.

- Relative residual correction (L2 Residual): The relative residual correction is applied to data to correct for remaining non-uniform detector response. Using γ+jets or Z+jets events, a calibration factor is set up which corrects jets with any η back to the response seen in the central detector region ($|\eta| < 1.3$). The central detector region has a uniform response after the L2L3 correction.

- Absolute residual correction (L3 Residual): The absolute residual correction is applied to data and measured with jet in the central detector region. Using γ+jets or Z+jets events, the momentum of the balanced jet can accurately be measured.

There are several other correction factors available to calibrate the reconstructed jet energy back to the parton level and not just the particle jet level, but these are not the default corrections for each physics analysis. The L4 correction ensures that the jet response is uniform with respect to the fraction of electromagnetic energy in the jet. The L4 correction gives a small improvement to the jet resolution. The L5 correction is used to unify the response of different jet flavours. B-quark and gluon jets have a higher energy response than light jets. L5 corrections are determined relative to the default flavour-mixing and are therefore dependent on the sample e.g. QCD jets or top quark pair events. The various contributions to the Jet Energy Scale corrections are shown in fig. 4.5.

Jet Energy Resolution

After the jet energy, also the jet energy resolution is calibrated. The width of the corrected jet p_T distribution is slightly different in data and simulation. The simulation is corrected using a η-dependent scale factor to scale the transverse momentum of the jets in the simulation to obtain a jet energy resolution in agreement with the data.

The energy resolution for jets is around 15% at 10 GeV, 8% at 100 GeV, and 4% at 1 TeV, to be compared to about 40%, 12%, and 5% obtained when the calorimeters alone are used for jet clustering [88].

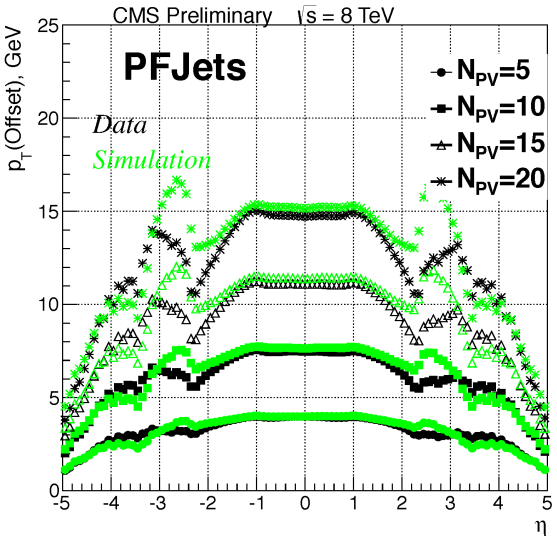

(a) L1 Offset correction

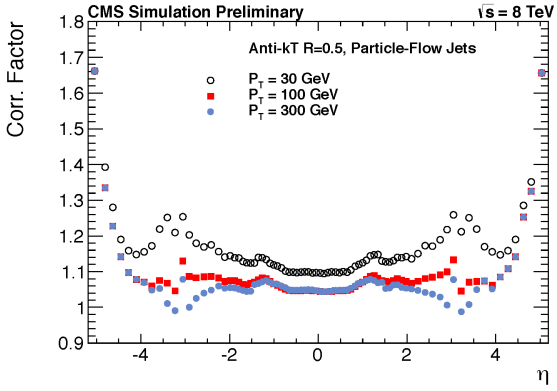

(b) L2L3 Monte Carlo Truth correction

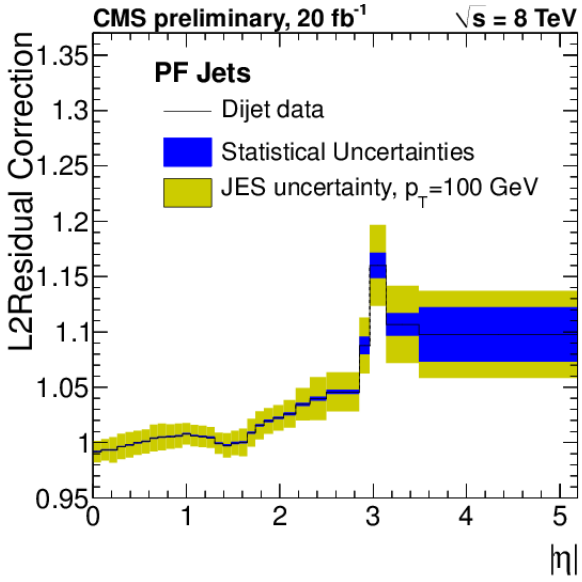

(c) L2 residual correction

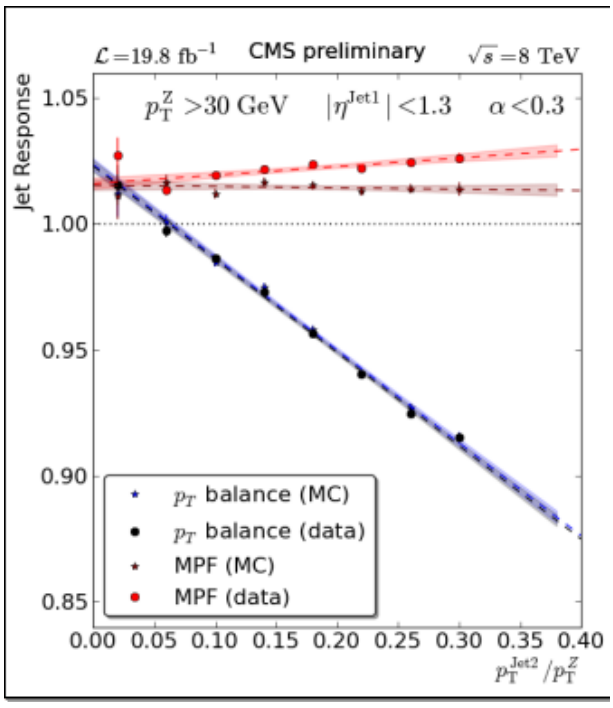

(d) L3 residual correction

Figure 4.5: JEC factors in the 2012 data-taking period split up in the different components. Figures taken from [87].

4.1.6 Missing Transverse Energy Reconstruction

Neutral weakly-interacting particles, such as neutrinos, will leave the detector unnoticed since these do not interact with any of the detector components. Using conservation of energy, we can deduce the presence of these particles. In a proton-proton collider, the centre-of-mass energy of the colliding partons is only known probabilistically. In addition, the CMS detector is not completely hermetic and particles such as the proton-remnants may escape through the beam-pipe. This means that we can only use conservation of transverse momentum. If we assume there was only one neutral weakly-interacting particle produced in the event, the transverse momentum imbalance will give us the transverse momentum vector of the unseen particle and is referred to as missing transverse momentum ($\not\!\!E_T$ or MET) [89].

Missing transverse energy can be calculated in various ways: using the PF information, using only calorimeter information or using in addition tracker information. The PF-$\not\!\!E_T$ is calculated as the negative vectorial sum of the transverse momenta of the PF-particles in the event. The $\not\!\!E_T$ reconstruction is only as good as the reconstruction of the other particles in the event. Noisy calorimeter cells can give rise to large artificial $\not\!\!E_T$. The noisy calorimeter cells are masked at reconstruction. Cracks between calorimeter cells and the gap between the barrel and endcap calorimeter, can cause particles to be reconstructed with degraded resolution. The calorimeter crystals and the barrel-endcap gap are slightly slanted with respect to lines of constant η, so that particles coming from the interaction point travelling on straight lines in η, will not be completely missed in the reconstruction.

The resolution of the PF $\not\!\!E_T$ is shown in fig. 4.6. This resolution is entirely dependent on the resolution obtained on the other objects in the event.

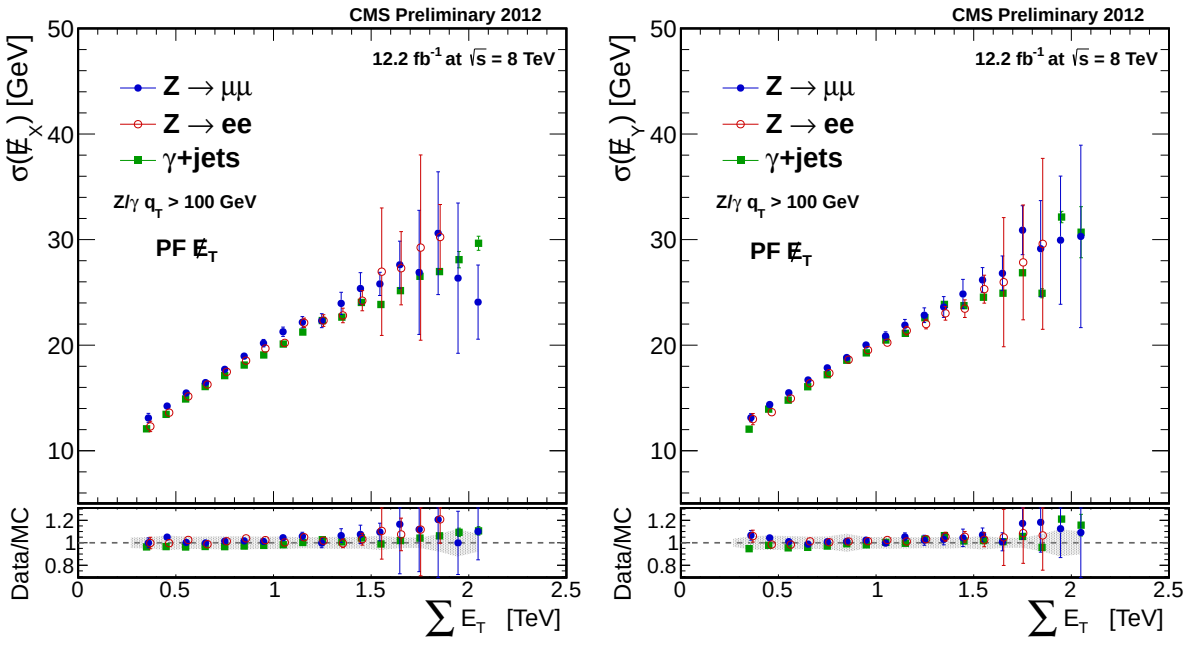

Figure 4.6: Resolution of the PF $\not\!\!E_T$ projected along the x- and y-axis in the left and right plot respectively as a function of the summed transverse energy in the event. Figure taken from [89].

4.1.7 B-jet reconstruction

In many physics processes of interest, for example the decay of the top quark or Higgs boson, b-quarks are produced. The ability to identify jets originating from a b-quark offers reject-

ing power against background coming from QCD processes. Based on the specifics of b-quark hadronisation and decay, tracks, vertices and leptons can be used to discriminate between b-jets and jets coming from lighter quark flavours. There are several algorithms available which yield a discriminator value for a jet. When the discriminator value of a jet is above a certain threshold, the jet is marked as a b-jet. There are usually three different values for the threshold (loose, medium or tight), called the working point of the algorithm. The algorithm itself is referred to as a tagger. For each tagger, a tighter working point corresponds to a lower b-tagging efficiency, but also a reduced probability of mistakenly tagging a light jet as a b-jet, called the mistag rate. A full description of the several b-tagging algorithms can be found in [90].

A b-tagging algorithm can be run on jets from various reconstruction algorithms, but by default it is applied on PF-jets. Each algorithm makes use of the trajectory of the charged particles in the jet. In addition to the default quality criteria placed on tracks at reconstruction, additional requirements are placed on the tracks to be used for b-tagging. The additional criteria vary from algorithm to algorithm, but usually require a transverse momentum of the track of over 1 GeV/c, at least eight hits in the track, two of which should be pixel hits. The χ^2/ndof of the track fit should be below 5. Some loose requirements are placed on the impact parameters. The tracks considered for b-tagging are also required to be within a certain cone around the jet axis.

Below, we give an overview of the available algorithms and a short explanation of their working principle.

- **Track Counting**
  B-hadrons have a long lifetime and will therefore decay in a secondary vertex, away from the primary vertex. The impact parameter of a track with respect to the primary vertex can be used to distinguish between a track coming from a secondary vertex and a track originating at the primary vertex as tracks originating from a decay along the jet axis tend to have positive impact parameters, whereas tracks from the primary vertex can have a positive or negative value. For each track in the jet, the impact parameter with respect to its uncertainty (the impact parameter significance) is calculated. The tracks in a jet are then sorted by decreasing impact parameter significance. The impact parameter significance of the second or third track is then used as discriminator value, since the first track is biased to high positive values. Using the value of the second track gives a highly efficient algorithm called the Track Counting High Efficiency (TCHE), whereas using the third track gives a very pure algorithm called Track Counting High Purity (TCHP).

- **Jet Probability**
  The Jet Probability algorithm is an extension of the Track Counting algorithm. It uses the calculated impact parameter significances of all the tracks in a jet to estimate the likelihood that all tracks associated to the jet come from the primary vertex. There are two version of the algorithm: the Jet Probability (JP) uses the information from all the tracks, whereas the Jet B Probability (JBP) uses only the four highest impact parameter significance tracks (which is average multiplicity of tracks in a b-hadron decay).

- **Soft muon/electron Algorithm**
  This algorithm looks for the lepton coming from a leptonic B-hadron decay. This lepton usually has a large transverse momentum with respect to the jet. In a simple version of the algorithm just the presence of this lepton and a transverse momentum threshold is required, but a more complex version is available where a neural net is used based on the lepton and jet properties.

- **Simple Secondary Vertex**
  The Simple Secondary Vertex (SSV) looks for the displaced vertex coming from the B-hadron decay. The adaptive vertex finder is used to reconstruct the secondary vertex. The

distance between the primary and secondary vertex divided by its uncertainty is called the decay length significance and is used as the discriminator for this algorithm. Several quality criteria are imposed on the secondary vertex to improve the purity of the algorithm.

- **Combined Secondary Vertex**
  This algorithm is the most sophisticated as it combines the impact parameter significances, the secondary vertex and the jet properties (lepton information is not included). The likelihood ratio of the jet being compatible with either a b-jet or a c-jet is constructed, in addition with the likelihood ratio of the b-jet versus light jet hypothesis. Even if no secondary vertex is reconstructed for a jet, a pseudo-vertex is constructed with the large impact parameter tracks. As a consequence, the Combined Secondary Vertex (CSV) algorithm has a higher efficiency than the SSV.

The loose working points of the algorithms are chosen to have an efficiency of $\approx 80-85\,\%$ and a mistag rate of 10 %. A medium working point has a mistag rate of 1 %, whereas a tight working point has a mistag rate of only 0.1 % allowing for high purity, but at the cost of an efficiency of $\approx 45-55\,\%$. In the case of CSV, the discriminators for the working points are 0.244, 0.679 and 0.898 for the loose, medium and tight working point respectively. The tagging efficiency as a function of the discriminator value is shown in fig. 4.7 for b-jets, c-jets as well as light flavour jets and gluons.

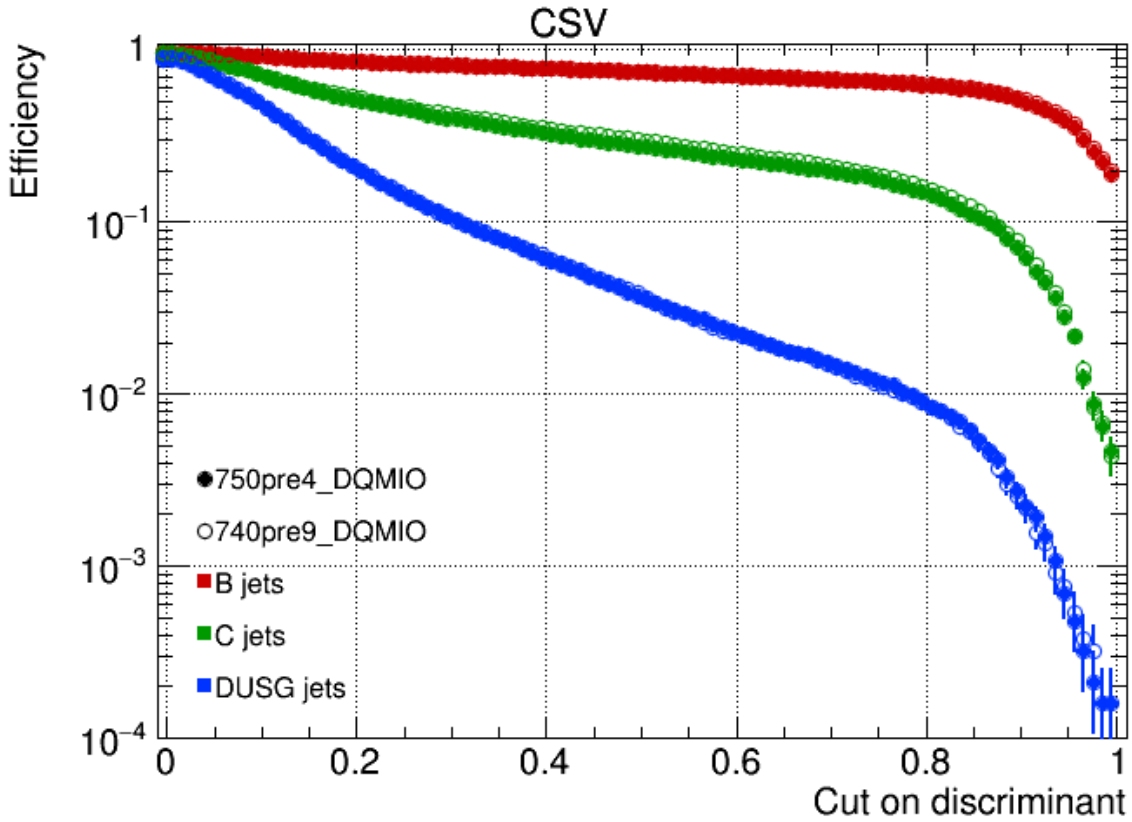

Figure 4.7: Efficiency of the CSV algorithm for b-jets, c-jets and light flavour jets and gluons as a function of the discriminator value. Figure taken from [91].

4.2 Kinematic Fitting and HitFit

Kinematic fitting is the procedure to reconstruct a physical process (like $t\bar{t}$ production and decay) by estimating the proper combination of final state reconstructed objects while simultaneously improving the resolution of the final state kinematics. In the example of a $t\bar{t}$ pair decaying semi-leptonically (see section 1.2), there are four partons which need to be matched to reconstructed jets. For more technical details on kinematic fitting, we refer to [92]. In this analysis we have chosen to use the HitFit package to perform the kinematic fitting.

HitFit is a kinematic fitting package developed by S. Snyder [93] at the DØ collaboration for the reconstruction of $t\bar{t}$ pairs in the semi-leptonic decay channel. HitFit is based on the SQUAW algorithm [94]. HitFit has been translated to C++ by S. Sumowidagdo [95] and added to our Gent analysis framework.

In a kinematic fit, a χ^2 function is built for each event based on the four-vectors of the reconstructed objects and their resolution functions (based on [92]). Various constraints are posed on the system originating from the event hypothesis. The χ^2 is minimised by varying the object kinematics within their resolutions to obtain improved kinematics which correspond best to the chosen hypothesis. Suppose we have a system with n measured objects with kinematics $\vec{y}$, p unmeasured objects with kinematics $\vec{a}$ and m constraints $\vec{f}$. The constraints will be fulfilled for the true object kinematics noted as $\overline{a}$ and $\overline{y}$.

$$f_1(\overline{a}_1, \overline{a}_2, \ldots, \overline{a}_p, \overline{y}_1, \overline{y}_2, \ldots, \overline{y}_n) = 0 \tag{4.5}$$
$$f_2(\overline{a}_1, \overline{a}_2, \ldots, \overline{a}_p, \overline{y}_1, \overline{y}_2, \ldots, \overline{y}_n) = 0 \tag{4.6}$$
$$\vdots \tag{4.7}$$
$$f_m(\overline{a}_1, \overline{a}_2, \ldots, \overline{a}_p, \overline{y}_1, \overline{y}_2, \ldots, \overline{y}_n) = 0 \tag{4.8}$$

The measured kinematics $\vec{y}$ will usually not fulfil the constraints so that these have to be corrected by $\Delta\vec{y}$. The sum $\vec{y'} = \vec{y} + \Delta\vec{y}$ will agree with the constraints. The weighted sum

$$S(\vec{y}) = \Delta\vec{y}^T V^{-1} \Delta\vec{y} \tag{4.9}$$

should be minimal with V being the covariance matrix of the $\vec{y}$. The covariance matrix is diagonal containing the object resolutions which have been determined from simulation. By introducing Lagrangian multipliers, we can construct the likelihood as follows

$$L(\vec{y}, \vec{a}, \vec{\lambda}) = S(\vec{y}) + 2\Sigma_{k=1}^{m} \lambda_k f_k(\vec{y}, \vec{a}) \tag{4.10}$$

with $\vec{\lambda}$ the Lagrangian multipliers. A local minimum then corresponds to a minimum of $S(\vec{y})$ when $f_k(\vec{y}, \vec{a}) = 0$. The minimum is usually found iteratively.

If we apply the kinematic fitting technique to the case of a semi-leptonic $t\bar{t}$ decay with HitFit, we have (at leading order) four jets, two of which are coming from a b-quark, one lepton and missing transverse energy (MET) coming from the undetected neutrino. This gives us 4! possible jet-parton permutations and an unknown longitudinal momentum component for the neutrino. To fully constrain the system, we need the four-vector of each particle in the final state. In this case, this means we need 24 measured variables. If we assume the particle masses to be known and fixed (zero mass for all particles except for the b-quark, for which we take the value 4.7 GeV/c^2), we can bring this down to 18. HitFit uses the (η, ϕ) coordinate system, so for each particle we need the (η, ϕ, E_T) coordinates of the particle. Since the neutrino goes undetected, we rely on the measurement of missing transverse energy $\not\!\!E_T$ which leaves us with

an unknown longitudinal component for the neutrino.

On the semi-leptonic $t\bar{t}$ system, there are several constraints possible. We can use the precisely known value of the W boson (80.4 GeV/c^2) to constrain the invariant mass of the lepton-neutrino pair and the pair of light jets. We can require that the reconstruction mass of the top quark is equal to the mass of the anti-top. If the analysis is not sensitive to this variable, we can in addition constrain the top quark mass. This gives us:

$$m_{l\nu_l} = m_W \tag{4.11}$$
$$m_{q\bar{q}} = m_W \tag{4.12}$$
$$m_{bq\bar{q}} = m_{bl\nu_l} \tag{4.13}$$

The transverse momentum of the neutrino is set equal to the transverse momentum imbalance of the $t\bar{t}$ pair, which is valid when we assume that the top quarks are not boosted perpendicular to the beam axis. The longitudinal momentum of the neutrino can be obtained from the first or the third constraint. When there are two real solutions for the longitudinal neutrino momentum, both are considered and the option which gives the lowest χ^2 is used for the rest of the fit. When there are two complex solutions, the discriminant of the system is artificially set to zero to obtain one real solution. At each iteration the kinematics of the particles are varied within the resolution to obtain the χ^2 and the sum of the constraints of the system. If both the χ^2 and the sum of constraints converge with a user-defined convergence limit, within a predefined number of iterations, we consider the fit of that particular jet-parton permutation successful and we obtain a set of updated kinematics. For each event, each of the 24 jet-parton permutations (4 jets at LO) is tried. If more than one jet-parton permutation returns a result, the permutation which has the lowest χ^2 is chosen as the solution for the event.

In addition to the measured three-momenta of the jets, HitFit also accepts information from b-tagging algorithms. The user can choose to let HitFit reject all solutions which do not agree with the b-tagging information. HitFit was designed to look for solutions of a LO semi-leptonic $t\bar{t}$ decay. However, at the LHC in general, we can not expect to work at LO. A large fraction of semi-leptonic $t\bar{t}$ events will have more than four jets in the final state. When we try to match this to the LO final state, we will obtain more than 24 permutations. Even at LO, due to mis-reconstruction or jet splitting, there can be more than four jets available in the final state. In this case, any solution which HitFit returns will not be a fully correct reconstruction of the $t\bar{t}$ pair.

There are various ways to use the HitFit output: use the jet-parton permutation and updated kinematics, use the jet-parton permutation but keep the original kinematics, use the χ^2 as selection cut on the event sample. In this analysis, as will be described in chapter 5 we use HitFit mainly as a selection criterium. We use the χ^2 to reduce the background contamination in our sample, to increase the quality of the selected $t\bar{t}$ events and to select which four jets to use for the $t\bar{t}$ reconstruction when there are more jets in the event. In section 8.1.4 more information will be given on the performance of HitFit and the various ways HitFit information can be incorporated in particular in this analysis.

Part III

Selection

Chapter 5

Event Selection

Selection criteria are applied to the recorded data to select a sample of top quark pairs decaying in the muon+jets channel, referred to as the signal. The selection is designed to obtain a very pure sample while trying to maintain a large enough signal efficiency. The $t\bar{t}$ muon+jets channel is characterised by one isolated muon and at least four jets in the final state, two of which coming from b-flavoured quarks.

In a first step the events are selected online by the trigger system which has been described in section 2.3. In the offline selection, there are selection criteria pertaining to physical objects which define the quality of the reconstructed objects in the event. Finally, there are criteria on the presence of certain physical objects in the event. The same selection criteria (both on- and offline) are applied to simulated events which offers the possibility to verify the purity and composition of the selected data sample.

In section 5.1, some details are given on the used dataset and simulation samples. In the following sections, the selection criteria of physical objects are discussed. Several corrections are applied to the simulation to cover small deviations between data and simulation reconstruction. These corrections are described in section 5.6. The full event selection is given in section 5.7.

5.1 Monte Carlo and Data Samples

The data used for this analysis was collected with the CMS detector during the 2012 data-taking period at a centre-of-mass energy of 8 TeV. All the run periods in 2012 combined add up to an integrated luminosity of $19.7 \pm 0.4\,\mathrm{fb}^{-1}$. The latest event reconstruction of early 2013 was used (Jan22ReReco), corresponding to the 5_3_7_patch5 CMSSW version. Rereconstruction of the data and simulation is done to include the latest alignement and calibration procedures. The list of data samples used, is shown in table 5.1. The data is recorded with the HLT_IsoMu24_eta2p1 trigger path. This particular trigger path will store events when in the online event reconstruction there is at least one isolated muon with a transverse momentum of at least 24 GeV and a pseudo-rapidity of $|\eta| < 2.1$. The data stored by this trigger path is part of the SingleMuon primary dataset, which comprises the events selected by any trigger path which requires at least one muon.

Table 5.1: 8 TeV data samples used and the integrated luminosity in the trigger path. Sample names are /SingleMuon/Run2012X-Jan22ReReco/AOD with X the run period of 2012.

run period	run range	int. lumi. (fb^{-1})
A	190645-193621	0.87
B	193834-196531	4.43
C	198049-203002	7.14
D	203894-208357	7.30
total	190645-208357	19.74

In the simulation both signal and background processes are considered. There are two signal samples produced, both using a NLO Monte Carlo event generator MC@NLO: one with SM correlated top quark pairs and one where the top quark decays have been performed spherically destroying the spin correlation. In table 5.2, the list of used simulation samples is given. The explicit names of the simulation samples are given in Appendix A.1 in tables A.1-A.2.

Table 5.2: Summer12 8 TeV Monte Carlo samples used for the estimation of the backgrounds along with their cross-sections. Cross sections taken from theory.

Sample	cross section [pb]
$t\bar{t}$ SM	245.8
$t\bar{t}$ uncorrelated	245.8
W + 1 parton	6662.8
W + 2 partons	2159.2
W + 3 partons	640.4
W + 4 partons	264.0
Z + jets	3503.71
single top, s-channel	3.79
single anti-top, s-channel	1.76
single top, t-channel	56.4
single anti-top, t-channel	30.7
single top, tW-channel	11.1
single top, $\bar{t}$W-channel	11.1
multijet	10.4×10^7

5.2 Vertices

Selected events are required to have at least one good primary vertex. A good vertex is required to have more than four degrees of freedom associated to it, which means that the vertex contains more than four particle tracks in the vertex fit. The cut on the z and radial (ρ) coordinates of the primary vertex ensures that it is within the fiducial volume. The vertex is flagged as a fake when the vertex was not successfully reconstructed but is based on the beam spot position. The vertex selection criteria are summarised in table 5.3.

Table 5.3: Selection criteria applied to the reconstructed vertex collection.

Parameter	Value
ndof	≥ 4
$\|z\|$	< 24 cm
ρ	< 2 cm
is fake	false

5.3 Muons

Selection criteria are applied to particle flow muons to obtain tight isolated muons. The selection is designed to retain muons coming from the decay of the W boson, and to reject muons

produced in jets coming from the decay of heavy flavour particles or decays in flight of light flavour hadrons like pions. A second collection of muons is constructed in the event based on looser criteria used to veto any additional muons in the event.

Tight Isolated Muons
Tight muons are required to have a p_T larger than 26 GeV. This p_T value is chosen to be sufficiently above the threshold of the HLT_IsoMu24_eta2p1 trigger, ensuring the trigger is in the efficiency plateau. The muon $|\eta|$ is restricted to 2.1 as this is the range the trigger is restricted to. The identification and isolation criteria, summarised in table 5.4, are designed to select muons produced in the collisions, outside of jets. The χ^2 requirement on the fit of the global muon track and the number of hits in the muon chambers reject background from hadron showers which are not fully contained in the calorimeters, called punch-through. The number of matched muon stations should be two or more to discriminate against punch-through or incorrect matches between a track and a muon chamber. The impact parameter cuts d_{xy} and d_z are efficient in rejecting cosmic muons which pass through the detector, but have a low probability of passing near the primary vertex. The requirement on the number of pixel hits and hits in the inner tracker help in addition to select muons produced at the primary vertex in contrast to muons from decays in flight. Muons are required to be isolated to reject muons produced within jets. A relative isolation requirement checks the amount of transverse momentum in a cone around the particle under study, in this case in a cone of $\Delta R < 0.4$ around the muon, where $\Delta R = \sqrt{(\Delta\eta)^2 + (\Delta\phi)^2}$. The relative isolation of the muon is defined in equation 5.1.

$$\text{relative iso}(\mu) = \frac{\Sigma p_T(CH) + max(0., \Sigma p_T(NH) + \Sigma p_T(\gamma) - 0.5\,\Sigma p_T(CP))}{p_T^{\mu}} \tag{5.1}$$

In equation 5.1 CH, NH and γ are charged hadrons, neutral hadrons and photons respectively. The summation runs over all CH, NH and γ contained within the cone around the muon. The transverse momentum sum is corrected from contributions of neutral particles contained within the muon isolation cone, but originating from pile-up vertices. The ratio of neutral to charged particles within a jet corresponds to 0.5. Therefore, the factor $0.5\Sigma p_T(CP)$, which considers the charged particles CP within the cone around the muon but associated to pile-up vertices, is a good estimate of the neutral particle contribution from pile-up [96]. Charged particles originating in pile-up events are removed by only summing over charged particles associated to the primary vertex. This correction ensures that the efficiency of the isolation criterium is largely independent as a function of number of pile-up vertices.

Loose Muons
A second muon collection is set up using looser identification and isolation criteria, applied to the PFmuon collection. The loose muon collection is used to identify additional muons coming from the dimuon $t\bar{t}$ channel, or muons from a Z-boson decay. The p_T must be larger than 10 GeV. The $|\eta|$ must be smaller than 2.5. The PFmuon candidates can either be global muons or tracker muons. The relative isolation requirement is loosened to be < 0.2, with the same cone size and pile up corrections as in the case of the tight muon collection. The selection criteria for loose muons are summarised in table 5.5.

5.4 Electrons

On the particle flow electron collection in the event, a set of loose criteria is applied to select isolated electrons. A loose selection is applied because we do not want to use the selected electrons, but rather veto events with electrons passing the selection. The p_T is required to be larger than 20 GeV. The $|\eta|$ should be smaller than 2.5. Information on the shape of the calorimeter cluster deposited by the electron candidate is fed into a multi-variate analysis (MVA) which combines

Table 5.4: Selection criteria applied to particle flow muons to obtain tight isolated muons.

Parameter	Value
p_T	> 26 GeV
$\|\eta\|$	< 2.1
global muon	true
χ^2/ndof	< 10
nr. muon hits	≥ 1
nr. matched stations	≥ 2
d_{xy}	< 0.2 cm
d_z	< 0.5 cm
nr. pixel hits	≥ 1
nr tracker layers	≥ 5
$\Delta R(\mu, \text{jet})$	> 0.3
relative iso(μ)	< 0.12

Table 5.5: Selection criteria applied to particle flow muons to obtain loose muons.

Parameter	Value
p_T	> 10 GeV
$\|\eta\|$	< 2.5
global or tracker muon	true
relative iso(μ)	< 0.2

all the information to calculate a discriminator value for the electron candidate. The discriminator value (called the MVA ID) is required to be larger than 0 to make a positive electron ID. In the MVA, the shape of the ECAL cluster is taken into account, the width of the cluster in ϕ allows to discriminate between electrons which undergo brehmsstrahlung and photons which do not. The ratio in energy deposited in the HCAL and ECAL is considered as well as the ratio of energy over momentum and many other variables. More information on the performance of the electron reconstruction and selection can be found in [97]. The relative isolation of the electron is defined differently than in the muon case, as shown in equation 5.2. In the case of electrons the cone size is chosen to be $\Delta R = 0.3$. In the relative isolation, the term $\rho \cdot EA$ corrects for the energy due to pile up. Here, ρ is the average energy density in the event due to pile up and EA stands for the Effective Area of the isolation cone. The Effective Area for the neutral hadron and photon components is defined as $(\Delta R)^2$, scaled by the ratio of the slope of ρ as a function of the number of primary vertices and the slope of the energy density for the neutral hadron and photon components only. The pile up correction to the relative isolation ensures that the isolation efficiency is quite constant with respect to pile up. The selection criteria for loose electrons are summarised in table 5.6.

$$\text{relative iso}(e) = \frac{\Sigma p_T(CH) + max(0., \Sigma p_T(NH) + \Sigma p_T(\gamma) - \rho \cdot EA)}{p_T^e} \tag{5.2}$$

The selection criteria for tight electrons are listed in table 5.7. These tight electrons are not used in the analysis but are shown here for completeness and in addition these are used in the trigger efficiency determination in chapter 6. The p_T threshold is raised to 30 GeV. The MVA ID selection cut is tightened to larger than 0.5. The relative isolation is required to be smaller

Table 5.6: Selection criteria applied to particle flow electrons to obtain loose electrons.

Parameter	Value
p_T	> 20 GeV
$\|\eta\|$	< 2.5
MVA ID	> 0
relative iso(e)	< 0.15

than 0.1. In addition it is required that the electron does not come from the conversion of a photon into a lepton pair and that the impact parameter d_{xy} with respect to the primary vertex is below 0.02 cm.

Table 5.7: Selection criteria applied to particle flow electrons to obtain tight electrons.

Parameter	Value
p_T	> 30 GeV
$\|\eta\|$	< 2.5
MVA ID	> 0.5
relative iso(e)	< 0.1
conversion rejection	true
d_{xy}	< 0.02 cm

5.5 Jets

Jets coming from the $t\bar{t}$ decay process are usually higher in p_T than jets coming from QCD radiation. There are no requirements on the p_T coming from the trigger side, since a single muon trigger was chosen. Some quality and identification criteria are applied to the particle flow jet collection, these are summarised in table 5.8. Jets are required to have more than one constituent particle. This helps to reduce the fraction of misidentified muons or electrons which would be reconstructed as a single hadron. There should be at least one charged hadron in the jet, which removes jets that have been reconstructed due to calorimeter noise. The fraction of energy deposited by charged hadrons should be larger than zero. The fraction of electromagnetic energy deposited by the charged constituents should be less than 0.99 to reject electrons. The neutral hadronic and electromagnetic energy fraction should both be smaller than 0.99. This also helps to reject jets solely reconstructed due to calorimeter noise.

In this analysis we wish to consider events with four or five jets only. Therefore it is vital to keep the p_T threshold on jets as low as possible, as to not neglect jets in the event. A staggered p_T threshold was implemented for this purpose: the three highest p_T jets in the event must have $p_T > 30$ GeV, the fourth leading p_T jet must have a p_T of at least 25 GeV and the fifth leading jet of at least 20 GeV. The pseudo-rapidity is limited to $|\eta| < 2.4$ by the coverage of the strip tracker. To ensure that the jets in the range $|\eta| < 2.4$ describe the full event, we reject events with additional jets in the region $2.4 < |\eta| < 4.7$ with $p_T > 50$ GeV.

In this analysis, it is necessary to reconstruct the full $t\bar{t}$ muon+jets final state. Of the $t\bar{t}$ decay products, there should be two jets originating from the hadronisation of b-quarks which, as is described in section 4.1.7, can be distinguished from jets arising from light flavour quarks. We

require at least two b-tagged jets, reconstructed with the Combined Secondary Vertex algorithm with medium working point (CSVM). Requiring two b-tags drastically reduces the background arising from a W-boson with associated jet production.

Table 5.8: Selection criteria applied to particle flow jets to obtain the tight jet collection.

Parameter	Value
nr. constituents	> 1
charged hadron fraction	> 0
neutral hadron fraction	< 0.99
charged EM fraction	< 0.99
neutral EM fraction	< 0.99
nr. charged hadrons	> 0
p_T	$> 30, 30, 30, 25, 20$ GeV
$\|\eta\|$	< 2.4

5.6 Event-by-Event Corrections to Simulation

All the selection criteria described in the previous sections have an efficiency associated to them. The efficiency of a reconstruction, identification or isolation algorithm is usually dependent on the p_T of the physical objects involved and the detector region (making it dependent on η). The efficiencies are not identical in simulation and data, making a correction to the simulation necessary in order to describe the data more correctly.

The simulation samples are produced before and during data-taking and take a significant amount of time to produce and process. The simulation samples contain the detector simulation based on the state of the detector at the time of production. During data-taking, the set-up of the detector can vary due to technical problems, different running conditions or ageing effects of several detector components. Also the pile-up conditions or the trigger menu changes during data-taking. These changes are not included in the simulation that the data is compared with. The simulation is also limited by the precision of theoretical calculations of the physical processes involved. Perturbative effects are only taken into account up to a certain order.

In the analysis, events get a weight associated to them to correct for these differences in physics modelling and detector behaviour to correct the distributions in simulation to those observed in data. The event weights are usually provided in the form of scale factors which is the ratio of the efficiency observed in data and the efficiency observed in simulation, as a function of p_T and η. The uncertainties on these event weights are taken into account as sources of systematic uncertainty on the measurement. More details are given in section 9.2.

5.6.1 Trigger and Lepton Identification Event Weights

The scale factors for the HLT_IsoMu24_eta2p1 trigger path, the muon identification, isolation and tracking are centrally provided by the Muon POG [98] as a function of the muon pseudo-rapidity. The trigger efficiencies are determined with a "Tag and Probe" method very similarly as is described in chapter 6. The corresponding scale factors for the trigger are shown in table 5.9. The range and uncertainties of the muon scale factors is given in table 5.10.

Table 5.9: HLT_IsoMu24_eta2p1 trigger scale factors.

$\|\eta\|$	SF
$\|\eta\| < 0.9$	98.37 ± 0.02 (stat) ± 0.20 (syst) %
$0.9 < \|\eta\| < 1.2$	96.56 ± 0.07 (stat) ± 0.20 (syst) %
$1.2 < \|\eta\| < 2.1$	99.62 ± 0.05 (stat) ± 0.20 (syst) %

Table 5.10: Range and uncertainties of muon scale factors.

	SF range	uncer.
HLT	96.5-99.5 %	0.2 %
ID	99.25-99.60 %	0.5 %
Iso	98.5-106.5 %	0.2 %
Tracking	98-100 %	0.1 %

5.6.2 b-tag/mistag weights

The b-tagging algorithm used in the event selection has a certain efficiency and mistag rate associated to it. Algorithms for b-tagging were described in section 4.1.7. The event weight to correct the differences between the data efficiencies and simulation efficiencies makes use of the truth information. The event weight takes into account how many true b-jets were tagged or untagged in the event, how many light jets were correctly untagged or incorrectly tagged. Using this information, a probability is set up for the event once with data efficiencies and once with simulation efficiencies, using scale factors (SF) and the simulation efficiencies (ϵ) which depend on the jet flavour, p_T and pseudo-rapidity, as shown below. The ratio of these two probabilities then constitutes the event weight $w = P(\text{data})/P(\text{simulation})$.

$$P(\text{simulation}) = \prod_{i=\text{tagged}} \epsilon_i \prod_{j=\text{not tagged}} (1 - \epsilon_j) \tag{5.3}$$

$$P(\text{data}) = \prod_{i=\text{tagged}} SF_i\epsilon_i \prod_{j=\text{not tagged}} (1 - SF_j\epsilon_j) \tag{5.4}$$

For the CSVM working point, the scale factor is given by $0.938887 + 0.00017124p_T - 2.76366 \cdot 10^{-7}p_T^2$ for true b-jets and $1.07541 + 0.00231827p_T - 4.74249 \cdot 10^{-6}p_T^2 + 2.70862 \cdot 10^{-9}p_T^3$ for light flavour jets, where the p_T is expressed in GeV. These scale factors are provided centrally by the CMS btag POG. The uncertainty on the scale factors ranges from $1-8\,\%$, depending on the p_T. The simulation efficiencies are around 75% for true b-jets and around $1 - 5\,\%$ for light flavour jets, with uncertainties ranging from $0.5 - 2\,\%$ for b-jets and $0.5 - 1\,\%$ for light flavour jets.

5.6.3 Pile-up Interaction Weights

In the simulation a certain distribution for the pile-up is chosen. During data-taking the LHC is continually pushed towards higher instantaneous luminosity which results in an increase of pile-up. In the data, the average pile-up distribution tends to be shifted towards higher pile-up conditions. The normalised distribution of the number of pile-up interactions during the 2012 data-taking and simulation is shown in fig. 5.1. The simulation is reweighted to agree with the distribution observed in data by using the true number of pile-up interactions in the simulation. More details on the reweighting procedure are given in [99]. A 5 % uncertainty on the inelastic

pp cross section is taken into account which affects the distribution of the pile-up interactions as shown in fig. 5.1.

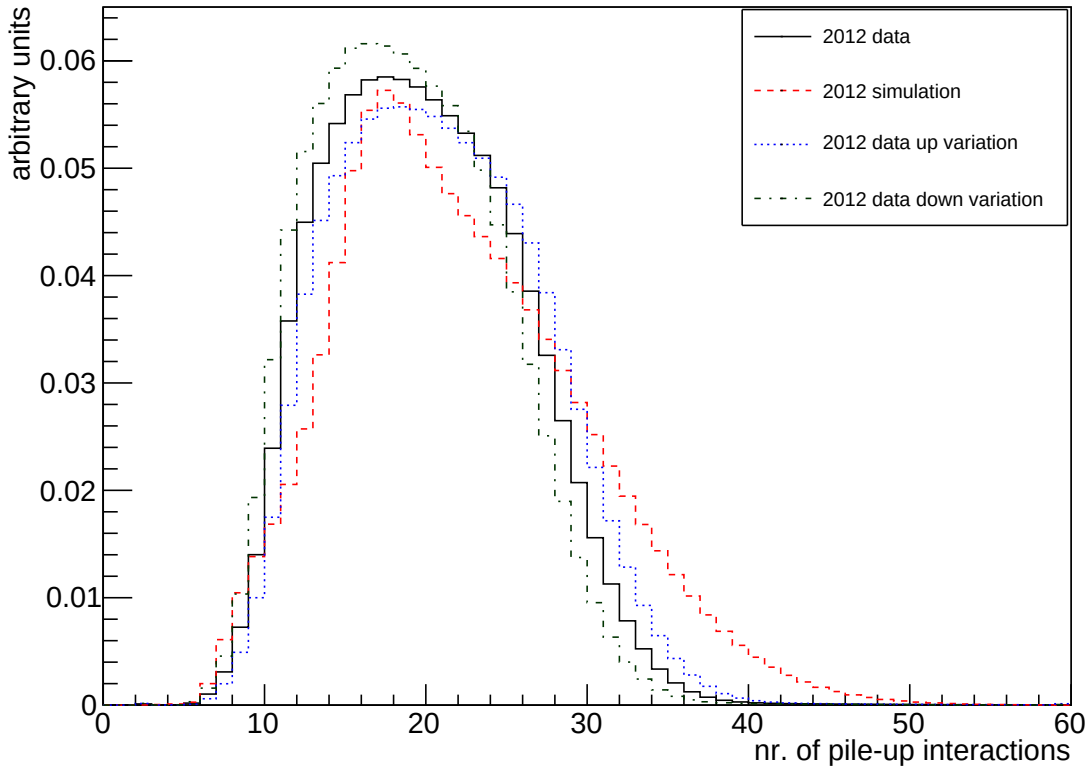

Figure 5.1: Normalised distribution of the number of pile-up interactions in the 2012 data-taking and simulation including the systematic variations.

5.6.4 Jet Energy Resolution and Scale

The jet energy resolution and scale corrections were described in section 4.1.5. On average, the jet resolution observed in data is 10% worse than the resolution seen in simulation. The jet resolution is therefore artificially decreased in the simulation. The jet resolution scale factors and their uncertainties are shown in table 5.11 and taken from [100]. The procedure to correct the simulated jet energy resolution is described in [101].
The jet energy scale has been corrected in both data and simulation using the tags Winter14_V5 and START53_V27 respectively. The uncertainties on the jet energy scale are taken into account in section 9.2 and are shown as a function of the jet transverse momentum in fig. 5.2. The derivation of the jet energy scale calibration and resolution and their corresponding uncertainties is described in [86].

5.7 Event Selection

Using the object selection criteria described in the previous sections, we can summarise the full event selection applied to both data and simulation in this analysis. We require:

- the event to be triggered by HLT_IsoMu24_eta2p1

Table 5.11: Scale factors (SF) of jet energy resolution in data/simulation as a function of the jet η with the statistical and systematic uncertainties.

jet $\lvert\eta\rvert$	SF (factor $\pm$ stat. $\pm$ syst.)
$0.0 - 0.5$	$1.079 \pm 0.005 \pm 0.026$
$0.5 - 1.1$	$1.099 \pm 0.005 \pm 0.028$
$1.1 - 1.7$	$1.121 \pm 0.005 \pm 0.029$
$1.7 - 2.3$	$1.208 \pm 0.013 \pm 0.045$
$2.3 - 2.8$	$1.254 \pm 0.026 \pm 0.056$
$2.8 - 3.2$	$1.395 \pm 0.036 \pm 0.051$
$3.2 - 5.0$	$1.056 \pm 0.048 \pm 0.185$

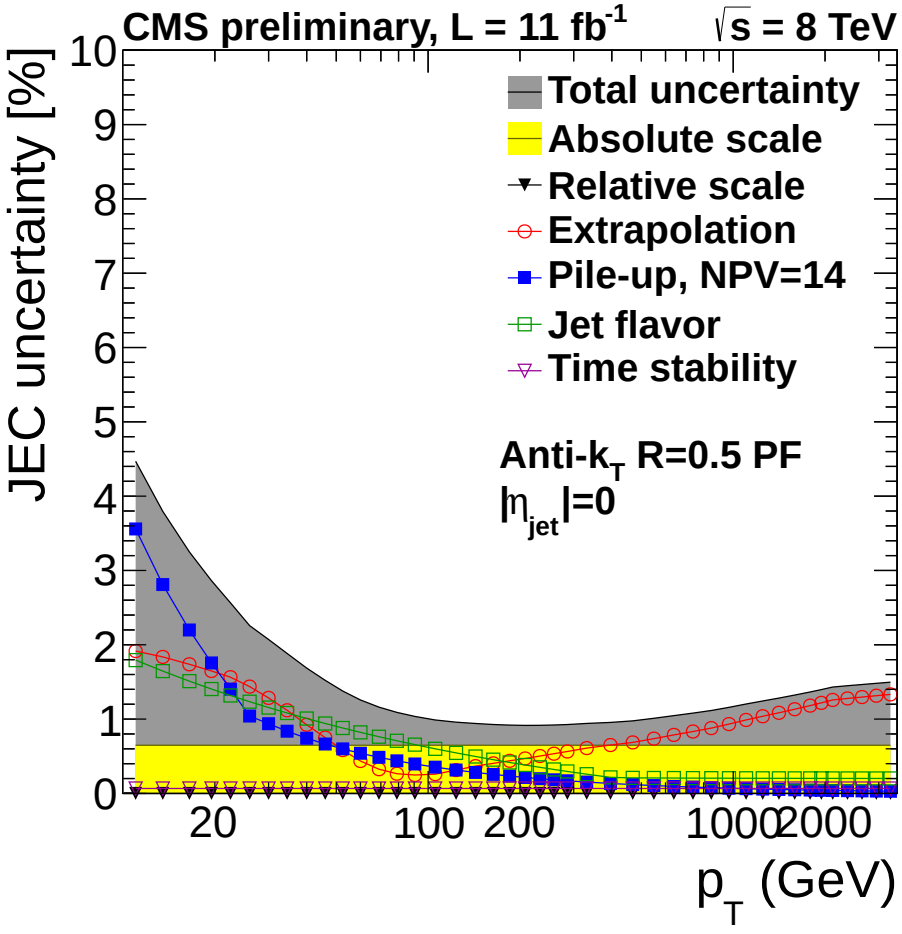

Figure 5.2: JEC uncertainties in the 2012 data-taking period with the various sources of uncertainties highlighted. Figure taken from [87].

- at least one good primary vertex
- exactly one tight isolated muon
- no loose electrons, no loose muons
- 4 or 5 tight jets
- no forward jets with $p_T > 50$ GeV

- 2 CSVM b-tags
- events must have a converging fit in HitFit
- $\chi^2/ndof < 5$ for selected HitFit solution
- Likelihood calculation must converge for both hypotheses (SM correlated and uncorrelated)
- Uncertainty on likelihood must be smaller than likelihood ($\ln(\delta L)/\ln(L) > 1.0$)

The importance and specific cut values of the HitFit and likelihood cuts will be discussed extensively in section 8.2.

The result of the full event selection is shown in table 5.12. In the table, the simulation processes are normalised using the theoretical cross sections of the processes given in table 5.2 at a centre-of-mass energy of 8 TeV and an integrated luminosity of 19.7 fb^{-1}. The uncertainties given are statistical only, based on the number of events generated in the simulation. In the third column from the right, the total event yield in the simulation is shown next to the data yield. There is a good data/simulation agreement in the event yield with a negligible overestimation of the simulation of about 0.7 %. For the W + jets sample, we have made use of exclusive samples, specifying the presence of 1, 2, 3 or 4 partons. The contribution from these individual W + jets samples is shown in table 5.13 and summed together in the last column. The dominant background contribution comes from $t\bar{t}$ pairs in other decay channels. In this background 68 % is due to dilepton events, 31 % due to semi-leptonic tau-decay and the remaining is a negligible contribution due to the semi-leptonic electron and hadronic channel. In the second column from the right of table 5.12, the signal selection efficiency is shown which is defined as

$$\epsilon_{sig.} = \frac{N_{sig.}^{sel.}}{N_{sig.}^{prod.}} \tag{5.5}$$

for $t\bar{t}$ events in the muon+jets channel with $N_{sig.}^{sel.}$ the number of selected signal events and $N_{sig.}^{prod.}$ the number of produced signal events. The purity of the event selection is given by

$$\pi = \frac{N_{sig.}^{sel.}}{N_{sig.}^{sel.} + N_{bkg.}^{sel.}} \tag{5.6}$$

with $N_{sig.}^{sel.}$ the number of selected signal events and $N_{bkg.}^{sel.}$ the number of selected background events. From the table, we can see that the first selection step (which includes trigger, one tight muon and lepton vetoes), drastically reduces the signal fraction. This is mainly due to the trigger requirement. During the 2012 data-taking period, the online and offline selection criteria for muons have been kept very close together so that the offline selection is very efficient with respect to the trigger selection. Also the requirement of two CSVM b-tagged jets reduces the signal efficiency significantly, but also increases the purity of the sample. Due to the high statistics for $t\bar{t}$ events at the LHC during the 2012 data-taking, it is possible to obtain a high purity sample with a background fraction of 15.9 %, retaining 4.5 % of the signal. This seems to be a very small signal efficiency, but as we will see, this analysis is not statistics limited, so a low signal efficiency is no reason for concern. The QCD Multijet contribution is maximally 1.4 % and will be neglected.

Next to data/simulation yield comparison, also the shape of various well-known kinematic quantities should be well described. This ensures that our simulation accurately describes the data and that we can use simulation predictions or distributions when necessary. A set of these control plots is shown in figures 5.3 to 5.15. In all these plots, the MC@NLO SM-correlated $t\bar{t}$ sample was used as signal unless stated otherwise. These plots show only a shape comparison between

the data and the simulation, meaning the simulation has been normalised to the observed data yield while the relative sample contributions in the simulation have been fixed by the theoretical cross sections. The uncertainty bars on the plots represent statistical uncertainties only, while the hatched bands show the statistical plus systematic uncertainties. In the bottom of each plot the ratio of data over simulation is shown. The uncertainty bars are again statistical only while the green band shows the statistical plus systematic uncertainties. The systematic uncertainty sources will be discussed in chapter 9. In figures 5.3 and 5.4, the transverse momentum of the muon and the jets in the event are displayed. From the plots it is clear that the transverse momentum spectra in the data are softer than what is predicted in the simulation. This is a known feature observed in all CMS $t\bar{t}$ simulation and is caused by a mismodelling of the transverse momentum distribution of the parent top quarks. The source of this feature (which was not present in the 2010 and 2011 simulations) has not yet been resolved. In CMS the $t\bar{t}$ simulations can be corrected for this by using an event weight (as will be described in chapter 9). In this analysis and the corresponding control plots shown here, this reweighting has not been applied for the nominal simulation distributions, but the effect is taken into account as a systematic uncertainty. We can conclude from the uncertainty bands in the ratio plots that the systematic uncertainties evaluated are sufficient to cover any data/simulation discrepancies. The angular distributions of η and ϕ are shown in fig. 5.5 and are well described. In fig. 5.6 and 5.7, the angular distributions of the jets are shown with overall good agreement between data and simulation. In fig. 5.8 the distribution of the number of primary vertices is shown in both data and simulation. In the right plot, the missing transverse energy distribution is shown with good agreement between data and simulation which indicates that we can neglect QCD multijet events. In fig. 5.9, we see that there are no discrepancies in either the jet or b-tag multiplicities. The following plots are made after reconstruction of the top quark pairs with HitFit. In fig. 5.10, the χ^2 of the selected HitFit permutations are shown, on which we have placed a selection criterium. An illustration on how HitFit improves the resolution of the reconstructed quantities is shown in fig. 5.11 where the reconstructed top quark mass is shown both using the original kinematics (which will be used in the analysis) and the updated kinematics by HitFit. We can clearly reconstruct the top quark mass peak. In fig. 5.12, the reconstructed transverse W boson mass (using original kinematics) is displayed both for the hadronically and leptonically decaying W boson. The hadronic W boson has a better resolution as the neutrino of the leptonically decaying W boson goes unmeasured. In fig. 5.13-5.15, some angular variables sensitive to spin correlations are shown with on the left using a SM correlated sample and on the right an uncorrelated sample. From these plots it is already clear that the data agrees better with the SM sample, but it is also clear that these distributions have little sensitivity in the lepton+jets channel. From this series of control plots, we can conclude that the simulation properly describes the data and that any deviations are covered by the systematic uncertainties. This allows us to trust the simulation and proceed with the analysis.

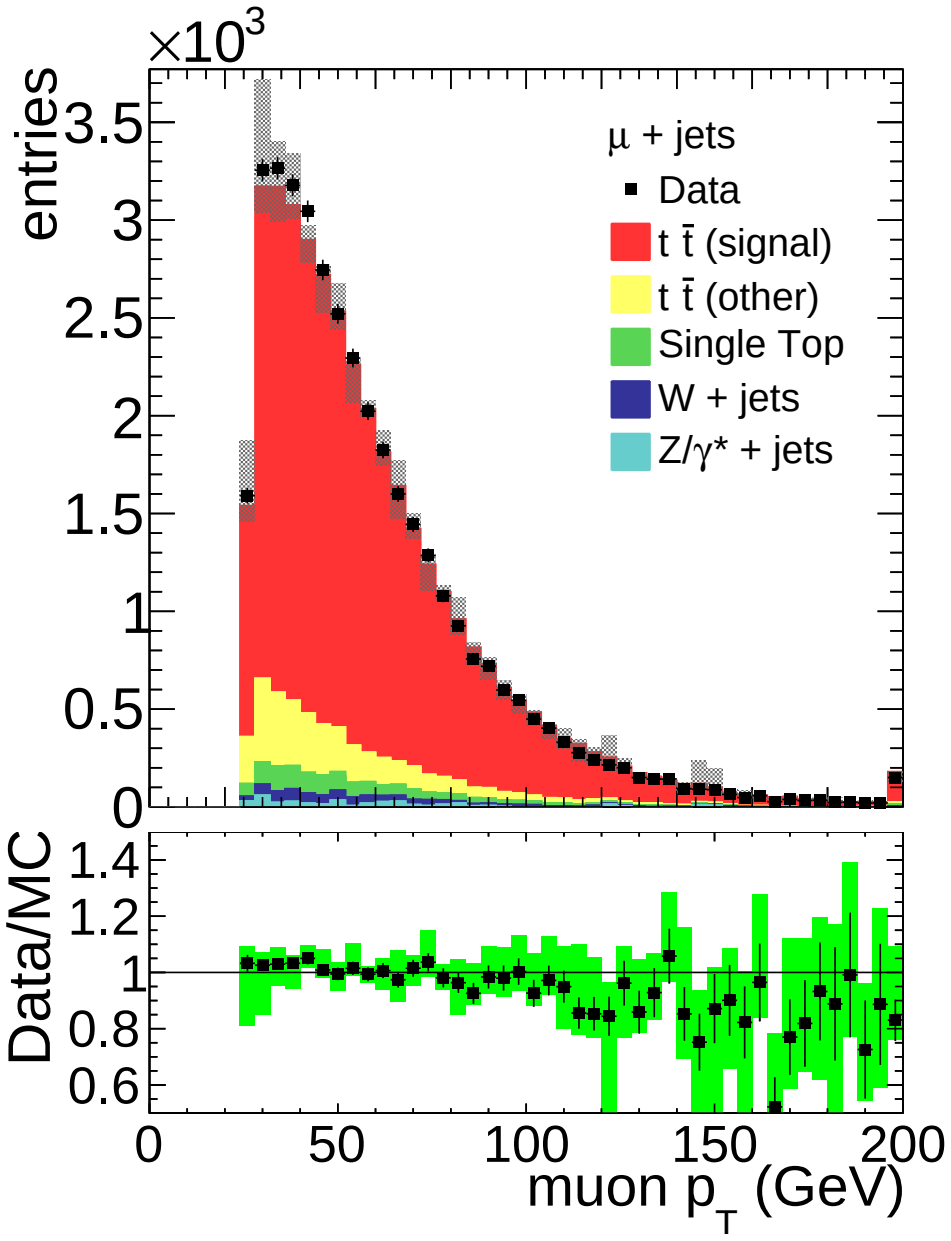

Figure 5.3: The muon transverse momentum distribution after selection cuts in the simulation and the data. Simulation has been normalised to data. The data/simulation agreement is shown in the bottom plot. Uncertainty bars are statistical only, hatched/green band show statistical and systematic uncertainties.

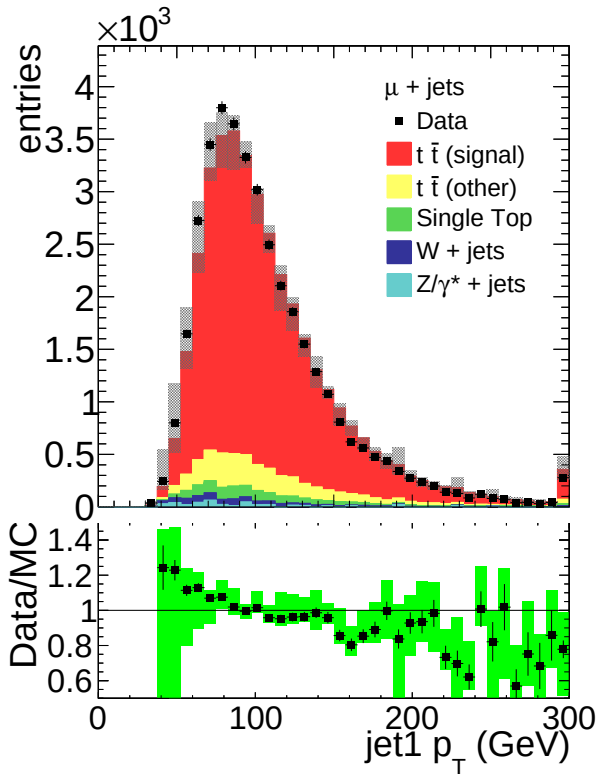

(a) leading jet

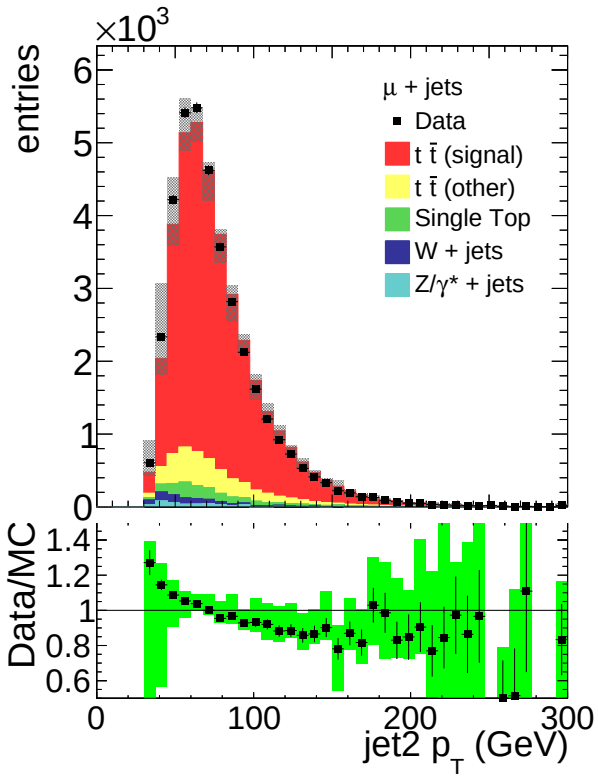

(b) second leading jet

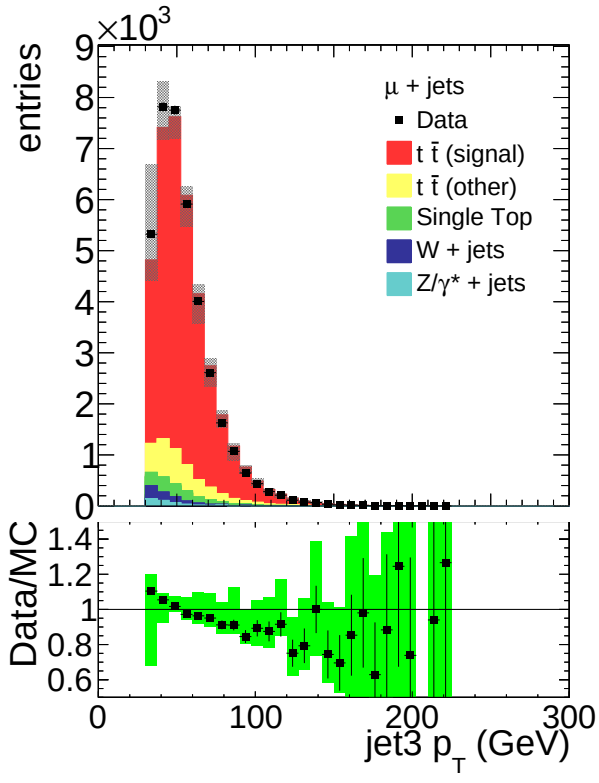

(c) third leading jet

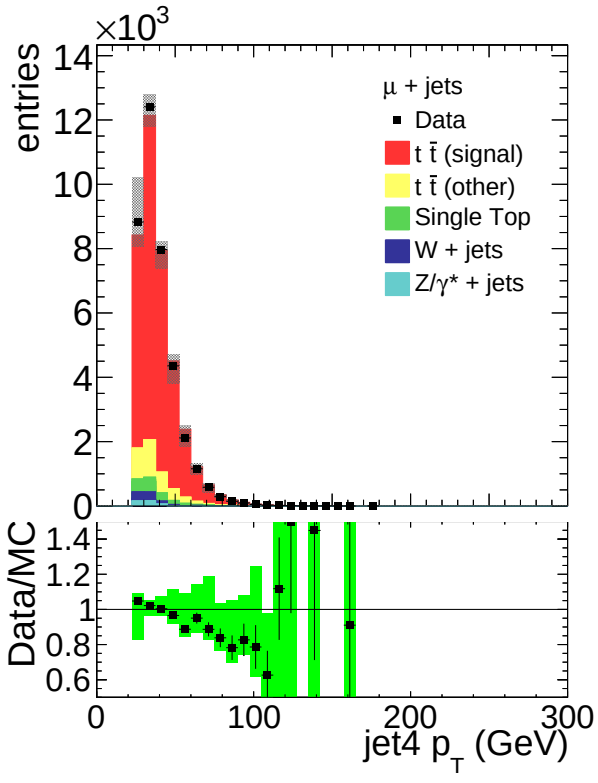

(d) fourth leading jet

Figure 5.4: The jet transverse momentum distribution after selection cuts in the simulation and the data. Simulation has been normalised to data. The data/simulation agreement is shown in the bottom plot. Uncertainty bars are statistical only, hatched/green band show statistical and systematic uncertainties.

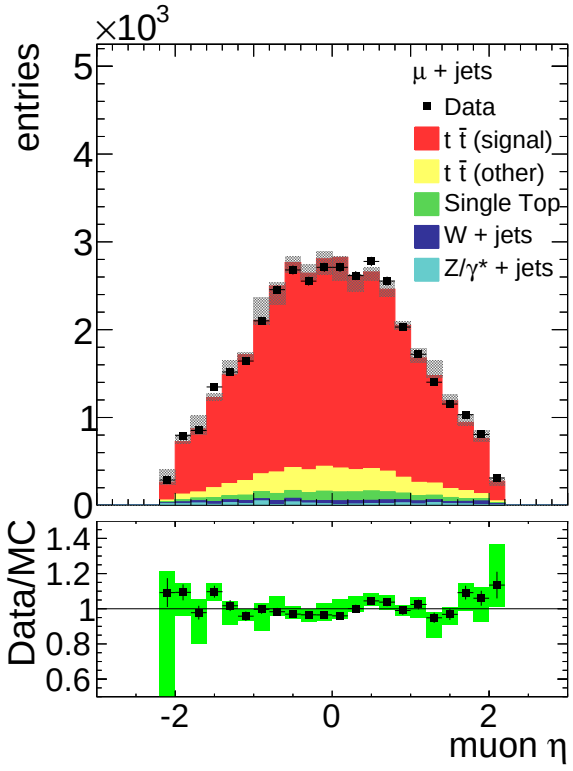

(a) muon η

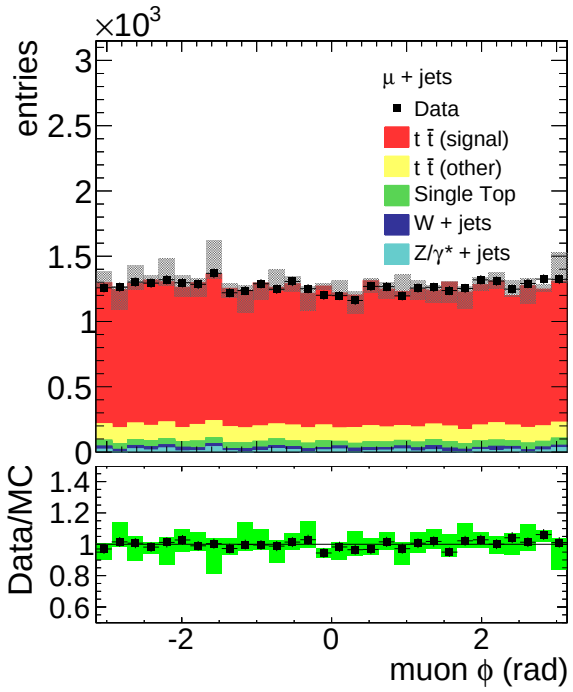

(b) muon ϕ

Figure 5.5: The muon pseudo-rapidity η distribution and azimuthal angle ϕ distribution after selection cuts in the simulation and the data. Simulation has been normalised to data. The data/simulation agreement is shown in the bottom plot. Uncertainty bars are statistical only, hatched/green band show statistical and systematic uncertainties.

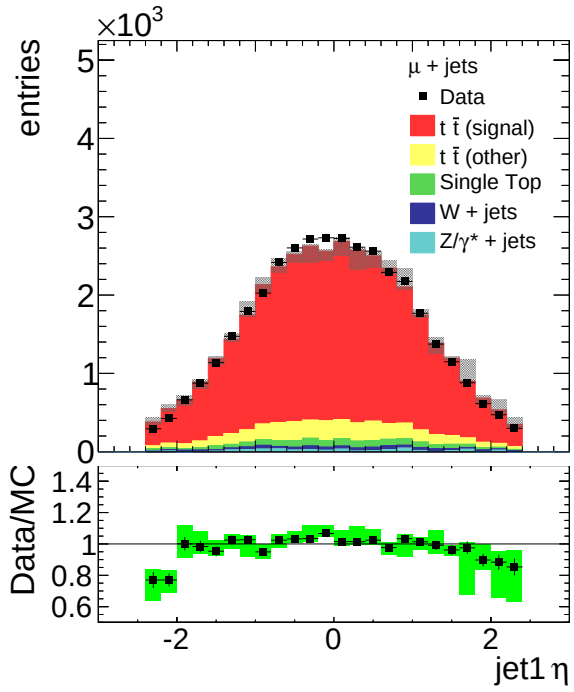

(a) leading jet

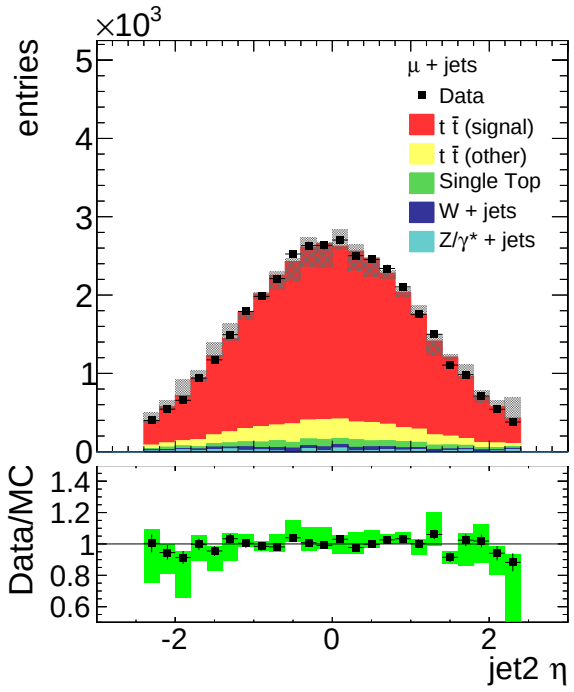

(b) second leading jet

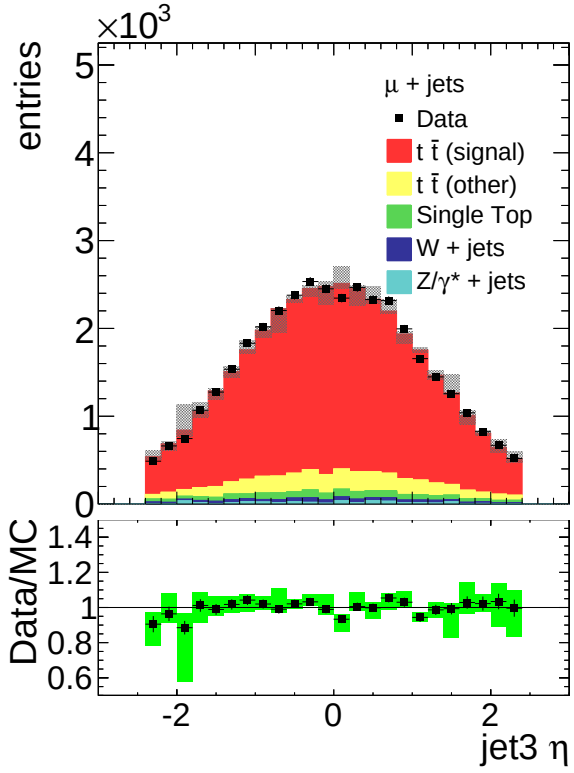

(c) third leading jet

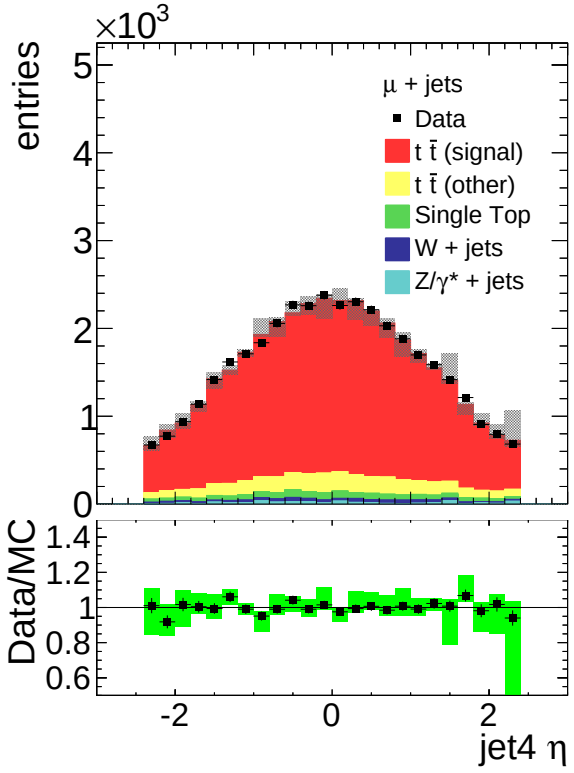

(d) fourth leading jet

Figure 5.6: The jet pseudo-rapidity distribution after selection cuts in the simulation and the data. Simulation has been normalised to data. The data/simulation agreement is shown in the bottom plot. Uncertainty bars are statistical only, hatched/green band show statistical and systematic uncertainties.

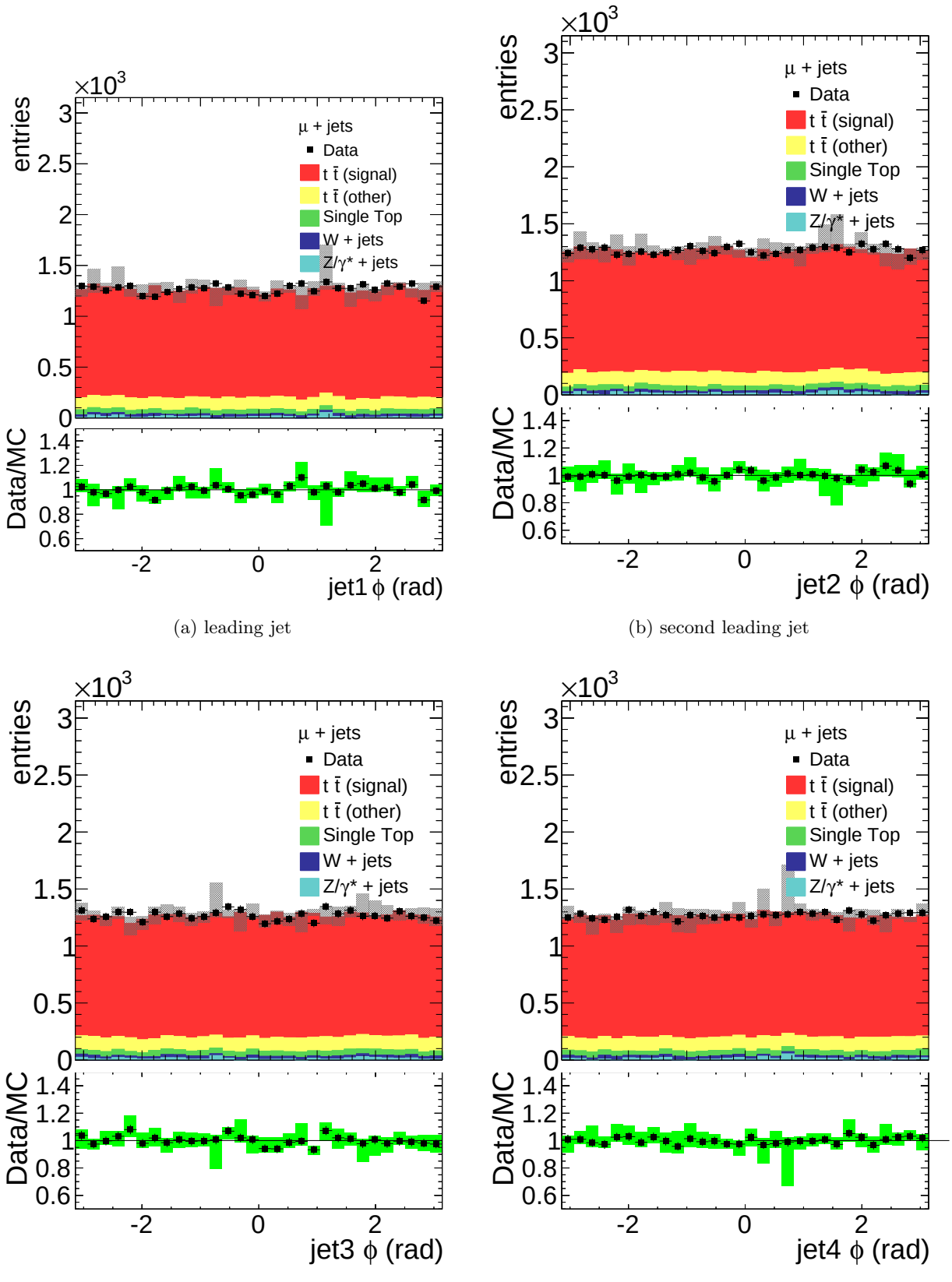

(a) leading jet

(b) second leading jet

(c) third leading jet

(d) fourth leading jet

Figure 5.7: The jet azimuthal angle distribution after selection cuts in the simulation and the data. Simulation has been normalised to data. The data/simulation agreement is shown in the bottom plot. Uncertainty bars are statistical only, hatched/green band show statistical and systematic uncertainties.

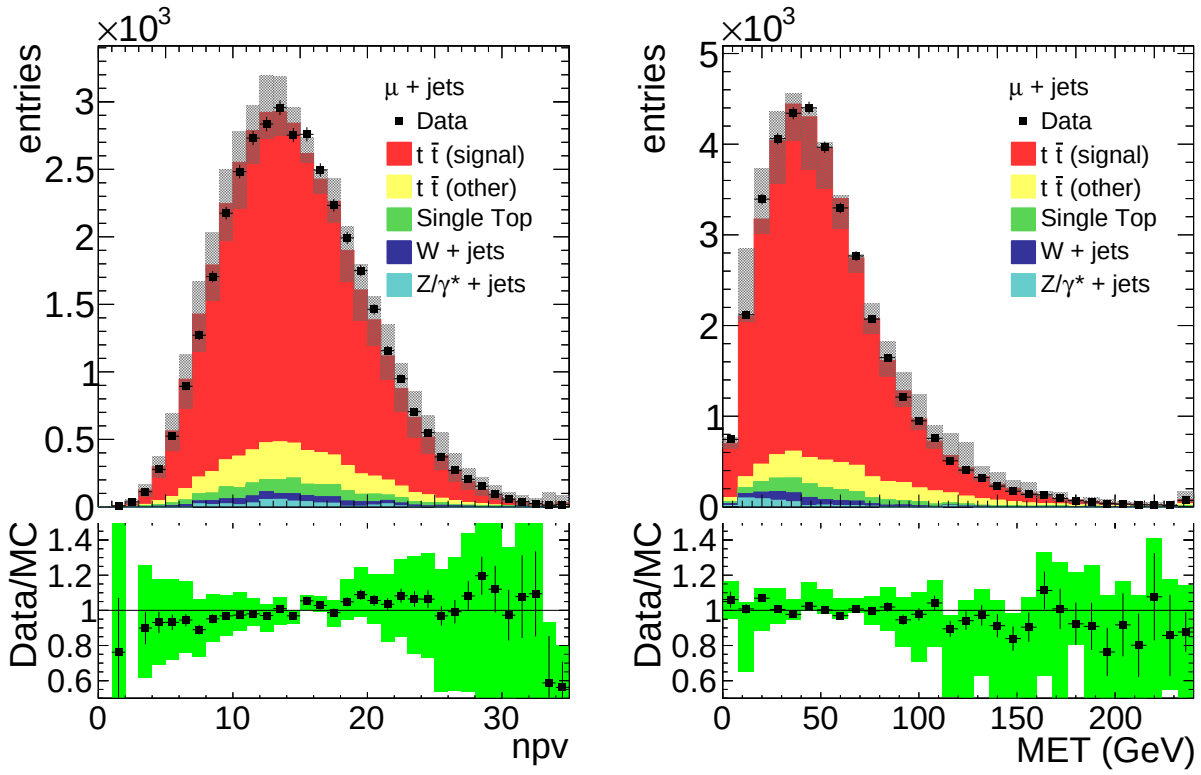

(a) primary vertex distribution

(b) missing transverse energy

Figure 5.8: Primary vertex distribution after selection cuts in the simulation and the data. Missing transverse energy distribution of the HitFit selected permutation. Simulation has been normalised to data. The data/simulation agreement is shown in the bottom plot. Uncertainty bars are statistical only, hatched/green band show statistical and systematic uncertainties.

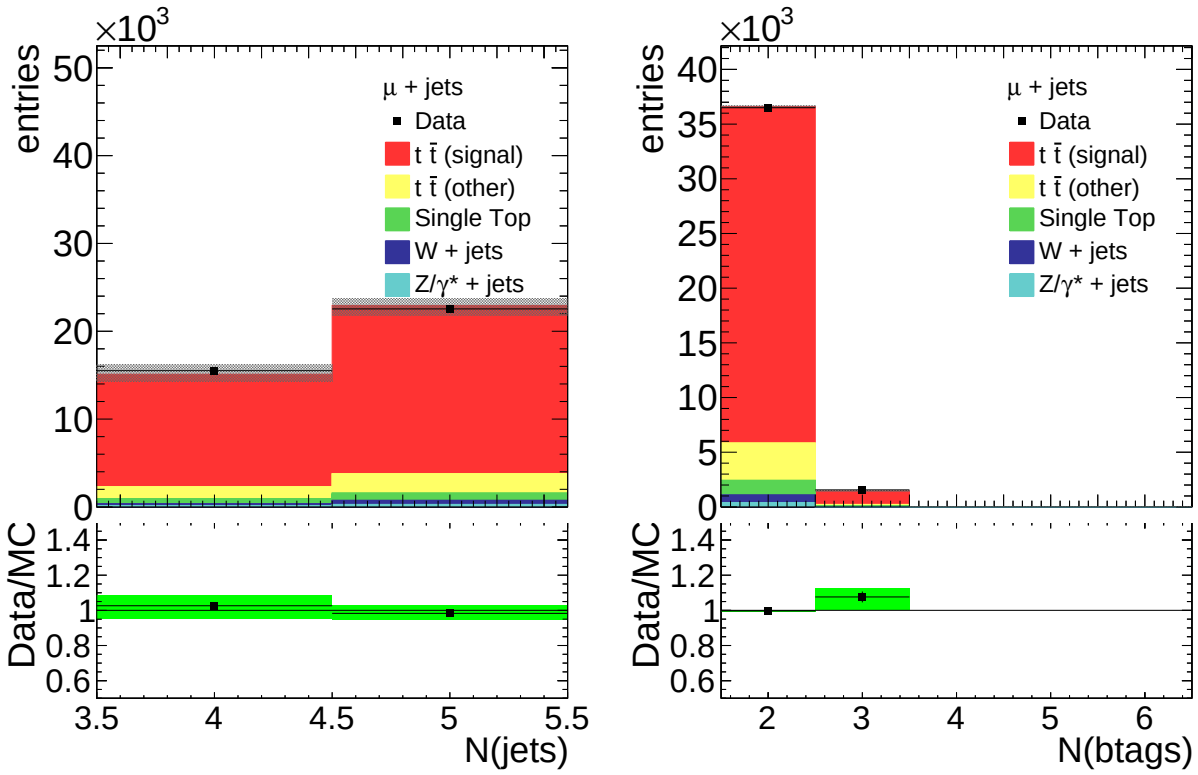

(a) jet multiplicity

(b) btag multiplicity

Figure 5.9: The number of jets and btags after selection cuts in the simulation and the data. Simulation has been normalised to data. The data/simulation agreement is shown in the bottom plot. Uncertainty bars are statistical only, hatched/green band show statistical and systematic uncertainties.

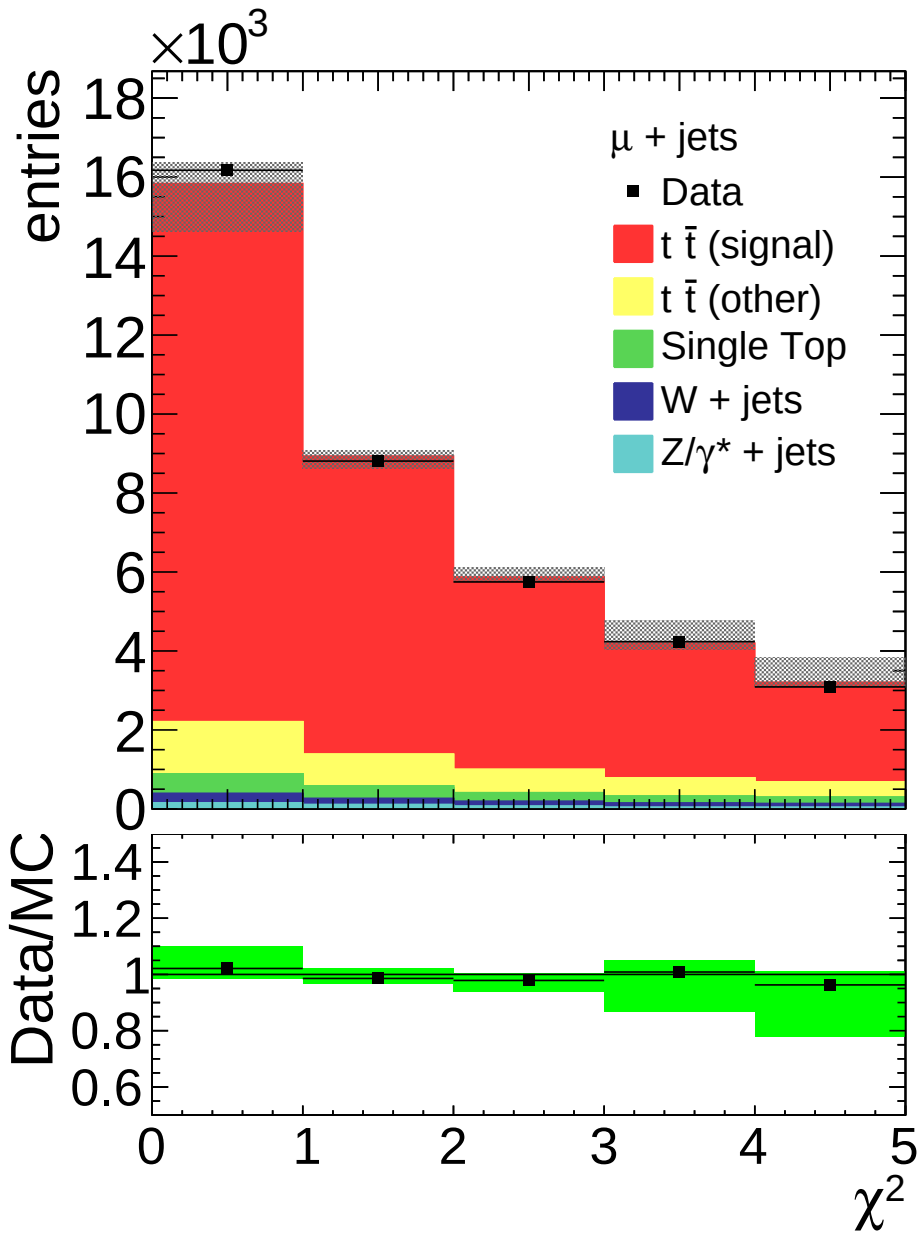

Figure 5.10: χ^2-distribution of the HitFit selected permutation. Simulation has been normalised to data. The data/simulation agreement is shown in the bottom plot. Uncertainty bars are statistical only, hatched/green band show statistical and systematic uncertainties.

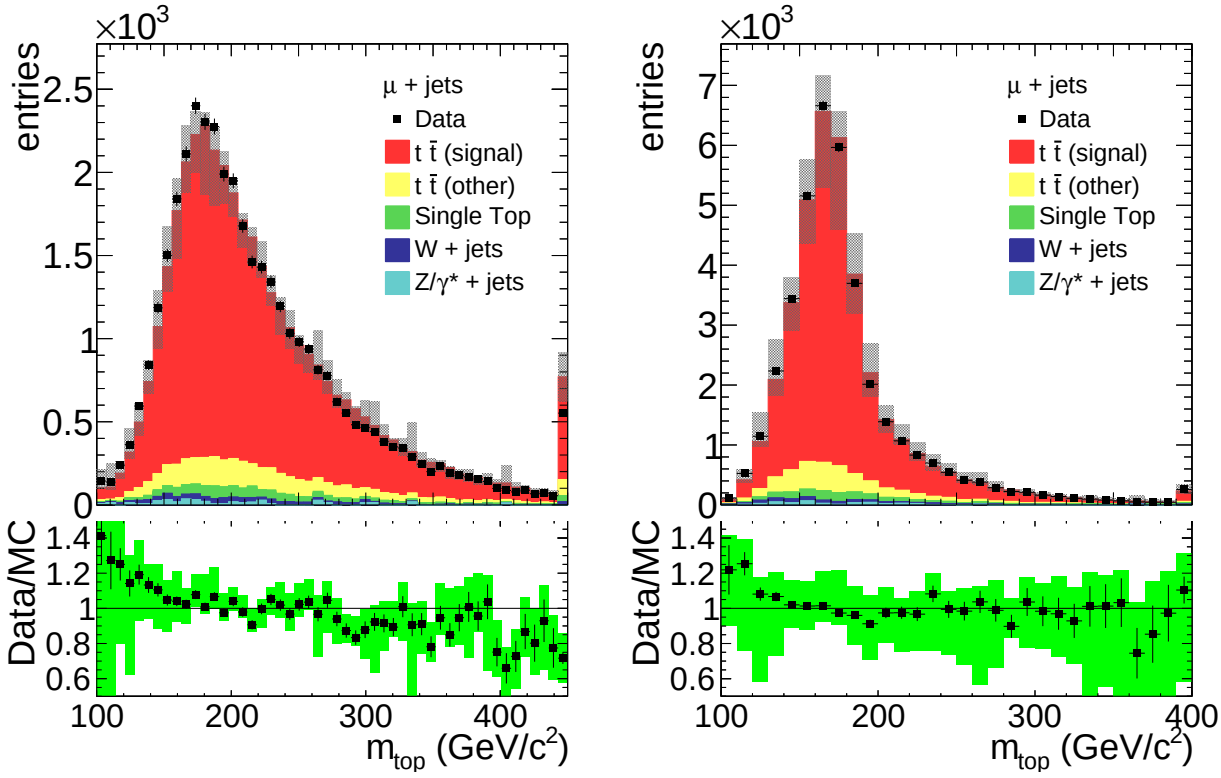

(a) original kinematics

(b) HitFit fitted kinematics

Figure 5.11: Top mass distribution of the HitFit selected permutation. The distribution is shown using the original kinematics of the MC@NLO correlated sample and the HitFit updated kinematics. Simulation has been normalised to data. The data/simulation agreement is shown in the bottom plot. Uncertainty bars are statistical only, hatched/green band show statistical and systematic uncertainties.

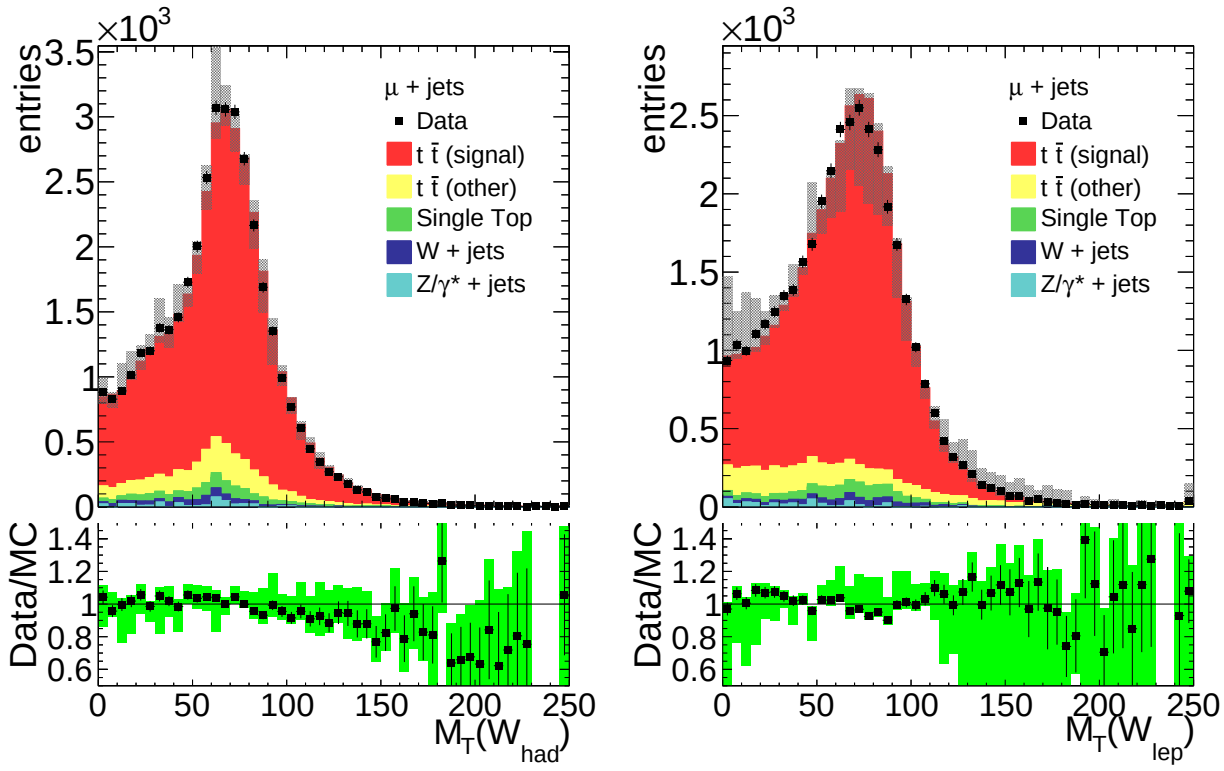

(a) $M_T(W_{had})$ (b) $M_T(W_{lep})$

Figure 5.12: Transverse mass distribution of the hadronically and leptonically decaying W boson of the HitFit selected permutation. Simulation has been normalised to data. The data/simulation agreement is shown in the bottom plot. Uncertainty bars are statistical only, hatched/green band show statistical and systematic uncertainties.

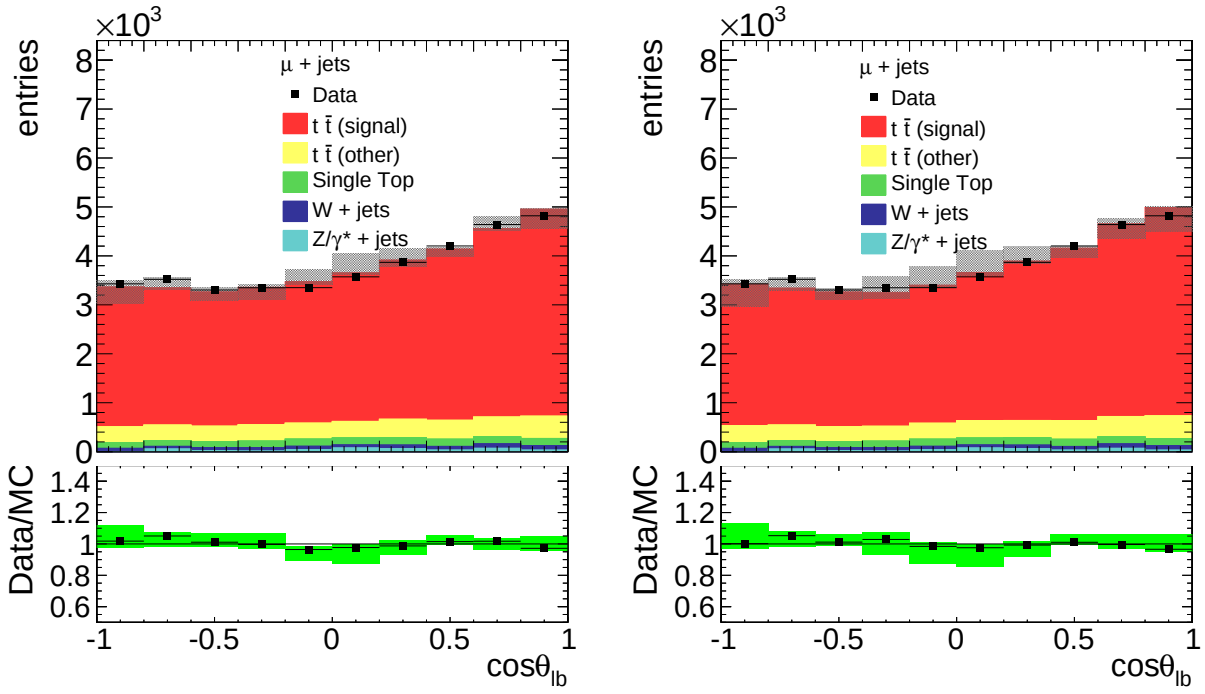

(a) SM correlated $t\bar{t}$

(b) uncorrelated $t\bar{t}$

Figure 5.13: $cos\theta_{lb}$ distribution between the direction of the lepton in its parent top restframe and the direction of the b-jet in the restframe of the hadronically decaying top quark. The distribution is shown using the original kinematics with once the SM correlated $t\bar{t}$ sample and once the uncorrelated $t\bar{t}$ sample. Simulation has been normalised to data. The data/simulation agreement is shown in the bottom plot. Uncertainty bars are statistical only, hatched/green band show statistical and systematic uncertainties.

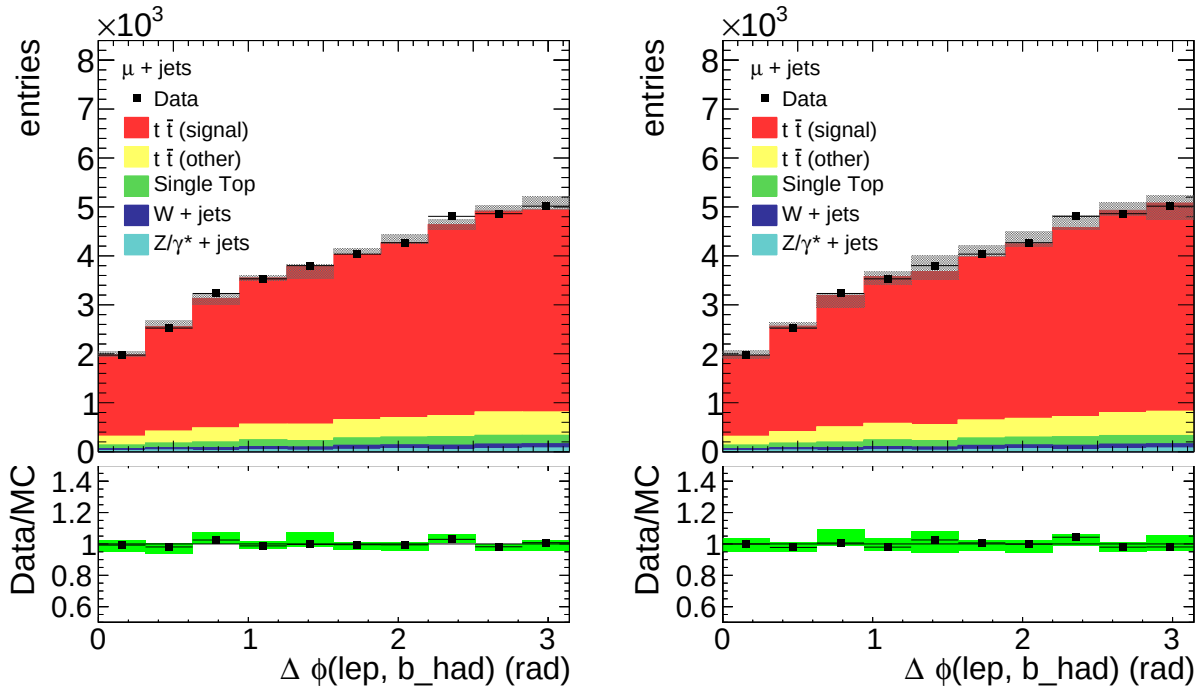

(a) SM correlated $t\bar{t}$

(b) uncorrelated $t\bar{t}$

Figure 5.14: Opening angle distribution ($\Delta\phi_{lb}$) between the direction of the lepton and the direction of the b-jet coming from the hadronically decaying top quark. The distribution is shown using the original kinematics with once the SM correlated $t\bar{t}$ sample and once the uncorrelated $t\bar{t}$ sample. Simulation has been normalised to data. The data/simulation agreement is shown in the bottom plot. Uncertainty bars are statistical only, hatched/green band show statistical and systematic uncertainties.

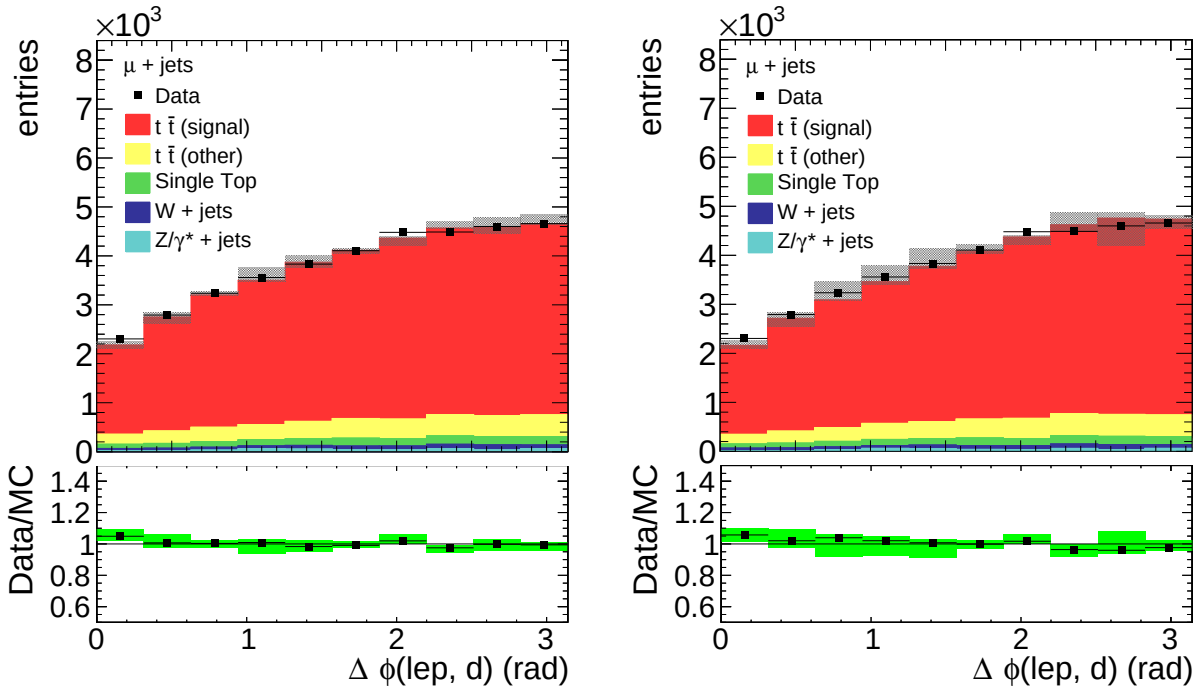

(a) SM correlated $t\bar{t}$

(b) uncorrelated $t\bar{t}$

Figure 5.15: Opening angle distribution ($\Delta\phi_{ld}$) between the direction of the lepton and the direction of the down-typ jet coming from the hadronically decaying top quark. The distribution is shown using the original kinematics with once the SM correlated $t\bar{t}$ sample and once the uncorrelated $t\bar{t}$ sample. Simulation has been normalised to data. The data/simulation agreement is shown in the bottom plot. Uncertainty bars are statistical only, hatched/green band show statistical and systematic uncertainties.

Table 5.12: Theory prediction of the data composition at each selection step. The comparison of the sum of the simulation and the data is shown. The uncertainties are statistical in nature.

Selection	$t\bar{t}$ (μ-signal)	$t\bar{t}$ (other)	W + jets	Z + jets	$t,\bar{t}$, s-chan	$t,\bar{t}$, t-chan	$t,\bar{t}$, tW-chan	Data	Simulation	$\epsilon_{\text{sig.}}$	π
Produced	713424	4144282	192221317	69243271	109684	1721343	438736				
lepton	419494 ±	125936 ±	10469916±	3566718±	4905 ± 39	73594 ±	45964 ±	87554619 ±	14706528 ±	0.588	0.029
selection	251	139	6697	4943		162	148	9357	8330.82		
≥ 4 jets,	239465 ±	36110 ±	198486 ±	72245 ±	541 ± 13	5817 ± 46	13649 ±	454754 ± 674	566312 ±	0.336	0.423
pt ≥	190	74	371	703			81		826.30		
30, 30, 30,											
25, 20 GeV											
4,5 jets	176002 ±	28586 ±	172261 ±	61918 ±	468 ± 12	5079 ± 43	10808 ±	362764 ± 602	455122.77 ±	0.247	0.387
	163	66	348	651			71		763.71		
≥ 2 btags,	58174 ±	9517 ± 38	2410 ±	1234 ± 92	151.7 ±	1394 ± 23	2137 ± 32	72060 ± 268	75016.88 ±	0.082	0.776
CVSM	94		38.4		6.9				147.39		
$\chi^2/ndof$ <	31992 ±	3896 ± 24	722 ± 20	139 ± 18	40.8 ± 3.3	314.2 ±	935 ± 20	37775 ± 194	38039.95 ±	0.045	0.841
5.0	69					9.8			81.02		

Table 5.13: Breakdown of the W+jets background of the various contributions at each selection step. In the last column, the sum of the exclusive samples is shown.

Selection	W + 1 parton	W + 2 partons	W + 3 partons	W + 4 partons	W + jets
Produced	131675870	42671931	12656125	5217391	192221317
lepton selection	5542869 ± 6124	2954788 ± 2426	1328330 ± 1096	643929 ± 506	10469916 ± 6697
≥ 4 jets, pt ≥ 30, 30, 30, 25, 20 GeV	4516 ± 175	10400 ± 144	26609 ± 155	156961 ± 250	198486 ± 371
4,5 jets	3958 ± 164	9461 ± 137	24658 ± 149	134184 ± 231	172261 ± 348
≥ 2 btags, CVSM	48 ± 18	87 ± 13	233 ± 14	2042 ± 28	2410 ± 38.4
$\chi^2/ndof$ < 5.0	7.5 ± 7.1	40.1 ± 7.4	78.2 ± 8.1	596 ± 15	722 ± 20

Chapter 6

Trigger Development and Monitoring

Already before data-taking starts, triggers are designed using simulation to select the events of interest, as was discussed in section 2.3. The trigger design decided upon is then used in the preparation of the CMS-wide simulation. Throughout data-taking, changes to the trigger menu are applied which are not reflected in the simulation. Because of this, scale factors are determined based on the observed efficiencies in data to correct for small differences in detector response in data and simulation, as was discussed in chapter 5. In this chapter, the efficiency corrections related to the 2012 trigger paths dedicated to the selection of top quark pair events in the lepton+jets channel are described. The trigger efficiencies described here were determined as service to the collaboration and have not been used in the described measurement.

6.1 Top Quark Trigger Paths

During the 2012 data-taking period all trigger paths have changed considerably throughout the year. There were two trigger paths dedicated to $t\bar{t}$ events in the lepton+jets channel: one for the electron and one for the muon channel. These dedicated triggers are so-called cross-triggers, requiring one lepton and several jets in the event. By adding requirements on the number of jets in an event, the rate of the trigger can be kept at a sufficiently low level, while keeping the transverse momentum threshold on the lepton as low as possible. The $t\bar{t}$ signal efficiency (defined as the fraction of $t\bar{t}$ pairs which is actually selected with the trigger) is highly dependent on the selection on the transverse momentum of the lepton. Therefore it is desirable to keep this threshold as low as possible. In addition there were some single lepton triggers available with slightly higher momentum thresholds without any requirement on jets.

The trigger paths under investigation are listed in table 6.1 with the corresponding run ranges where they were active. As can be inferred from the names, each trigger consists of a lepton which passes quite tight selection criteria and at least three jets in the central part of the detector. The transverse momentum thresholds on the jets were increased to maintain the trigger rate when the luminosity was increased. A staggered approach to the transverse momentum thresholds was adopted as the signal efficiency is more dependent on the momentum threshold of the third-leading jet than on the momentum of the leading or sub-leading jet. The trigger path used in the simulation is also given in table 6.1. During the design of the trigger, the online object reconstruction is kept as close as possible to the offline reconstruction. The offline event selection is designed to be tighter than the online trigger selection to ensure the trigger is fully efficient. By matching the online and offline object reconstruction, the thresholds in the offline selection can be kept as close as possible to the online threshold. During the data-taking jet energy corrections are applied online, while in the simulation the jet energy corrections were not fully taken into account in the trigger menu. The offline jet energy corrections are properly considered in the analysis of both data and simulation.

To assess the trigger efficiency of these paths, the latest reconstruction of the data was used with the latest version of the simulation. As a reminder, the different run periods in data were defined

in the previous chapter in table 5.1. The leptonic and hadronic part of the trigger are designed to be independent of each other, so the efficiencies can be factorised. In addition, the trigger decision of the leptonic leg (which comes first in the triggering sequence) is stored irrespective of the trigger decision of the full path. The efficiency of the leptonic leg is measured using a "Tag and Probe" method, while the hadronic leg is measured using a "Cut and Count" method.

Table 6.1: List of trigger paths in 2012 data-taking and in the CMSSW_5_3_X version of the simulation.

runrange	trigger name
electron path	
190645 - 191691	HLT_Ele25_CaloIdVT_CaloIsoT_TrkIdT_TrkIsoT _TriCentralPFJet30
191691 - 194225	HLT_Ele25_CaloIdVT_CaloIsoT_TrkIdT_TrkIsoT _TriCentralPFNoPUJet30
194225 - 199608	HLT_Ele25_CaloIdVT_CaloIsoT_TrkIdT_TrkIsoT _TriCentralPFNoPUJet30_30_20
199608 - 208357	HLT_Ele25_CaloIdVT_CaloIsoVL_TrkIdVL_TrkIsoT _TriCentralPFNoPUJet45_35_25
simulation	HLT_Ele25_CaloIdVT_CaloIsoT_TrkIdT_TrkIsoT _TriCentralPFNoPUJet50_40_30
muon path	
190645 - 193834	HLT_IsoMu17_eta2p1_TriCentralPFJet30
193834 - 194270	HLT_IsoMu17_eta2p1_TriCentralPFNoPUJet30
194270 - 199698	HLT_IsoMu17_eta2p1_TriCentralPFNoPUJet30_30_20
199698 - 208357	HLT_IsoMu17_eta2p1_TriCentralPFNoPUJet45_35_25
simulation	HLT_IsoMu17_eta2p1_TriCentralPFNoPUJet50_40_30

6.2 Tag and Probe Method

Lepton efficiencies, whether they are identification, isolation or trigger efficiencies, are measured using a "Tag and Probe" method. The "Tag and Probe" method relies on the reconstruction of $Z \rightarrow l^+l^-$ events. One of the leptons is identified using very tight selection criteria and is referred to as the tag. The other lepton of the pair is selected using looser criteria and is called the probe. The lepton pair is required to have opposite sign leptons and to have an invariant mass within the range of 60-120 GeV which is around the Z boson mass of 91.2 GeV. The probe collection obtained in this way is a sample of pure, isolated leptons on which the efficiency of selection criteria can be measured. The tag selection is usually tighter or equally tight as the probe selection. The efficiency ϵ of a certain selection criterium, is then given by

$$\epsilon = \frac{N_{TP,\text{pass}}}{N_{TP,\text{pass}} + N_{TP,\text{fail}}} \tag{6.1}$$

where $N_{TP,\text{pass}}$ is the number of tag and probe pairs where the probe passes the selection criterium under investigation and $N_{TP,\text{fail}}$ is the number of tag and probe pairs where the probe fails the selection criterium. If the tag selection is equally tight as the probe selection (or tighter as long as the selection criterium under study is not applied), the pair is counted twice with each of the leptons once fulfilling the role of the probe lepton. Note that the efficiency is obtained with respect to the probe lepton selection. A tighter or looser selection on the probe will change the efficiency of the criterium under study. The efficiency is often presented as a function of a

kinematic variable of the lepton, usually the transverse momentum or pseudo-rapidity.

There are various ways to obtain N_{TP}, the simplest being just counting the number of tag and probe pairs. This method is only valid when the selection of the tag (and probe) lepton is tight enough to remove any background coming from other processes. The background can also be estimated from simulation and subtracted from the selected sample.

A second way to obtain N_{TP} is to fit the invariant mass distribution of the opposite sign lepton pairs with a Breit-Wigner function which describes the decay shape of the Z boson with in addition a Crystal Ball function which describes the tails due to radiative losses. An example is shown in fig. 6.1 where the Z mass peak is clearly visible. A separate fit for the failing and the passing probes is performed. In the figure, no background contribution is visible, as tight identification and isolation criteria are applied in the determination of the trigger efficiencies. In case of the study of identification and isolation efficiencies this background is often not negligible and is described with an additional exponential distribution.

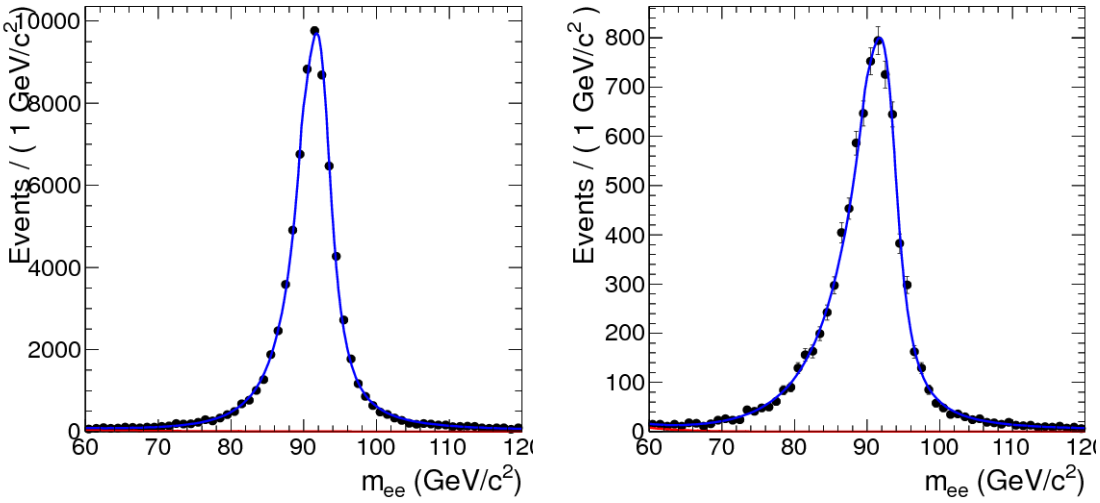

(a) passing probes (b) failing probes

Figure 6.1: Invariant mass distribution of reconstructed electron tag and probe pairs. Passing probes on the left and failing probes on the right.

One can calculate the overall efficiency or a binned efficiency as a function of some variable, using the obtained $N_{TP,\text{pass}}$ and $N_{TP,\text{fail}}$. The simulation is then corrected by applying the selection criterium on the simulation (with an efficiency $\epsilon_{\text{simulation}}$ associated to it) and weighting the simulation by a scale factor given by $SF = \epsilon_{\text{data}}/\epsilon_{\text{simulation}}$. Another option is to not apply the selection criterium in the simulation and apply the ϵ_{data} weight on the simulation. The former option is preferred as the efficiencies usually have a dependence on a multitude of variables, while the scale factor is usually quite stable. The scale factors have smaller uncertainties associated to them. If the scale factor is completely independent of any variable, an overall scale factor can be used. If there is some dependence on, for example the lepton transverse momentum, a binned scale factor is necessary. One could argue that an overall scale factor represents the average over all the bins and that using an overall scale factor will still be correct on average. This argument only holds if the scale factor is used to correct the Z+jets simulation sample. Leptons from for example top quark decays have a different kinematic distribution and will therefore populate different transverse momentum bins. A binned scale factor ensures that this different kinematic

behaviour is properly taken into account and the sample dependence is largely removed.

Electron channel
The electron leg of the trigger path is estimated by a "Tag and Probe" method where both the tag and the probe pass the tight electron selection described in chapter 5. A passing probe is matched to the trigger object of the electron leg of the triggers under study. The events are selected from the SingleElectron dataset and it is required that the tag electron must be matched to one of the trigger objects of the Ele27_WP80 trigger, so that the probe is not biased towards the electron trigger. The efficiencies in the data and simulation as a function of the transverse momentum, pseudo-rapidity, jet and vertex multiplicity are shown in figures 6.2-6.5 for each run period separately. In the bottom of each plot the scale factor is shown, which is the ratio of the data over simulation efficiency. As we can see, the efficiencies have a large dependence in the four variables displayed, but the scale factor is much more stable. In the scale factor plots, the horizontal line shows the average scale factor for this run period. This allows us to evaluate the spread of the binned values around the overall scale factor. From the plots, we can conclude that in the run periods A and B using the overall scale factor is feasible with an uncertainty of about 2% to cover the variation, while in run periods C and D, we see a larger deviation in the pseudo-rapidity variable, making it better to use a scale factor binned in this variable. The average scale factors for each run period are shown in table 6.2.

Table 6.2: Average HLT scale factor for the electron leg of the top trigger path per data run period. The statistical uncertainties are negligible. The given uncertainty covers the fluctuation in all variables if no parametrisation is needed.

run period	average SF	parametrisation
2012A	0.98 ± 0.02	no
2012B	0.98 ± 0.02	no
2012C	0.99	yes, in η
2012D	0.99	yes, in η

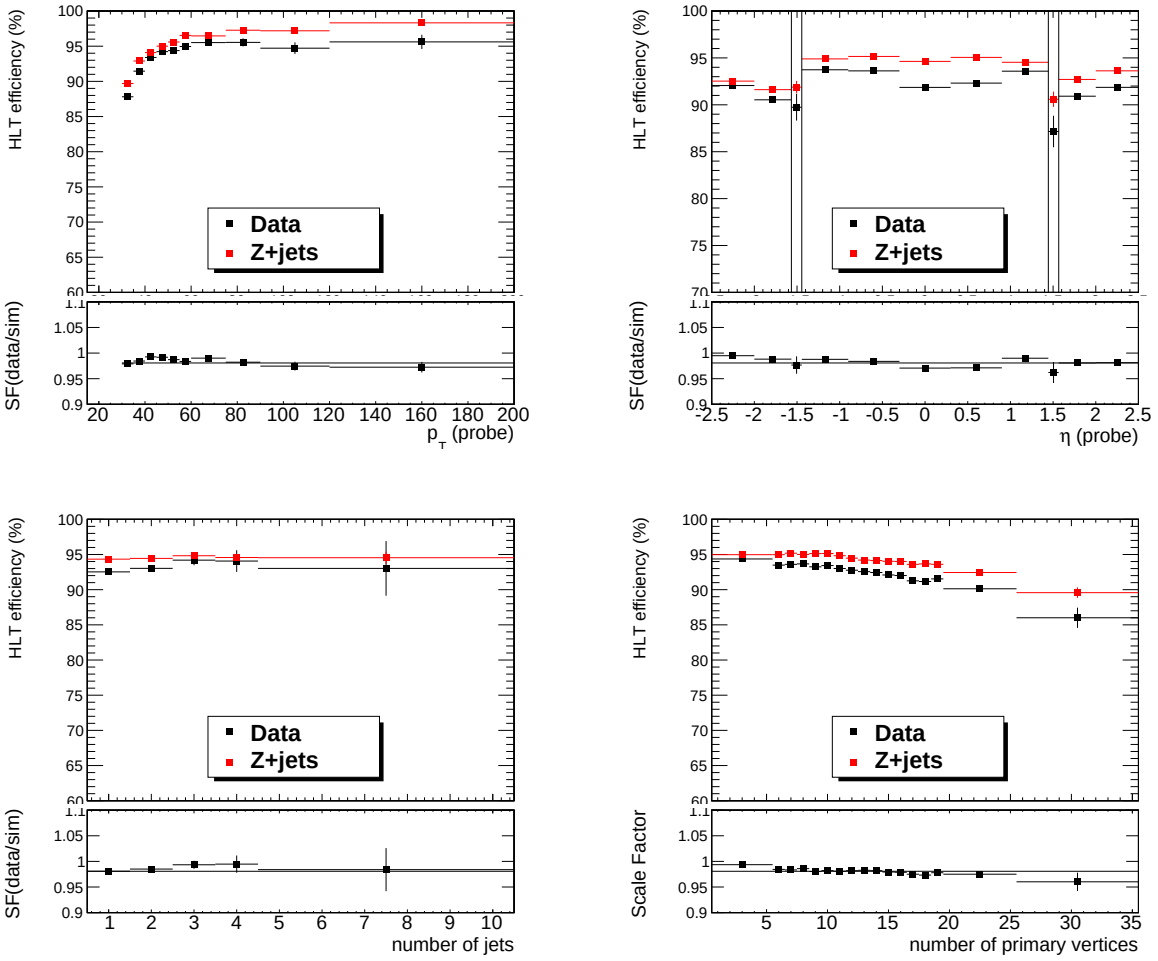

Figure 6.2: HLT efficiency for the electron leg of the top trigger path in the 2012A data run period as a function of the lepton transverse momentum, lepton pseudorapidity, jet multiplicity and vertex multiplicity. The scale factor (ratio of the data over simulation efficiency) is shown at the bottom where the horizontal line indicates the average scale factor for this data run period.

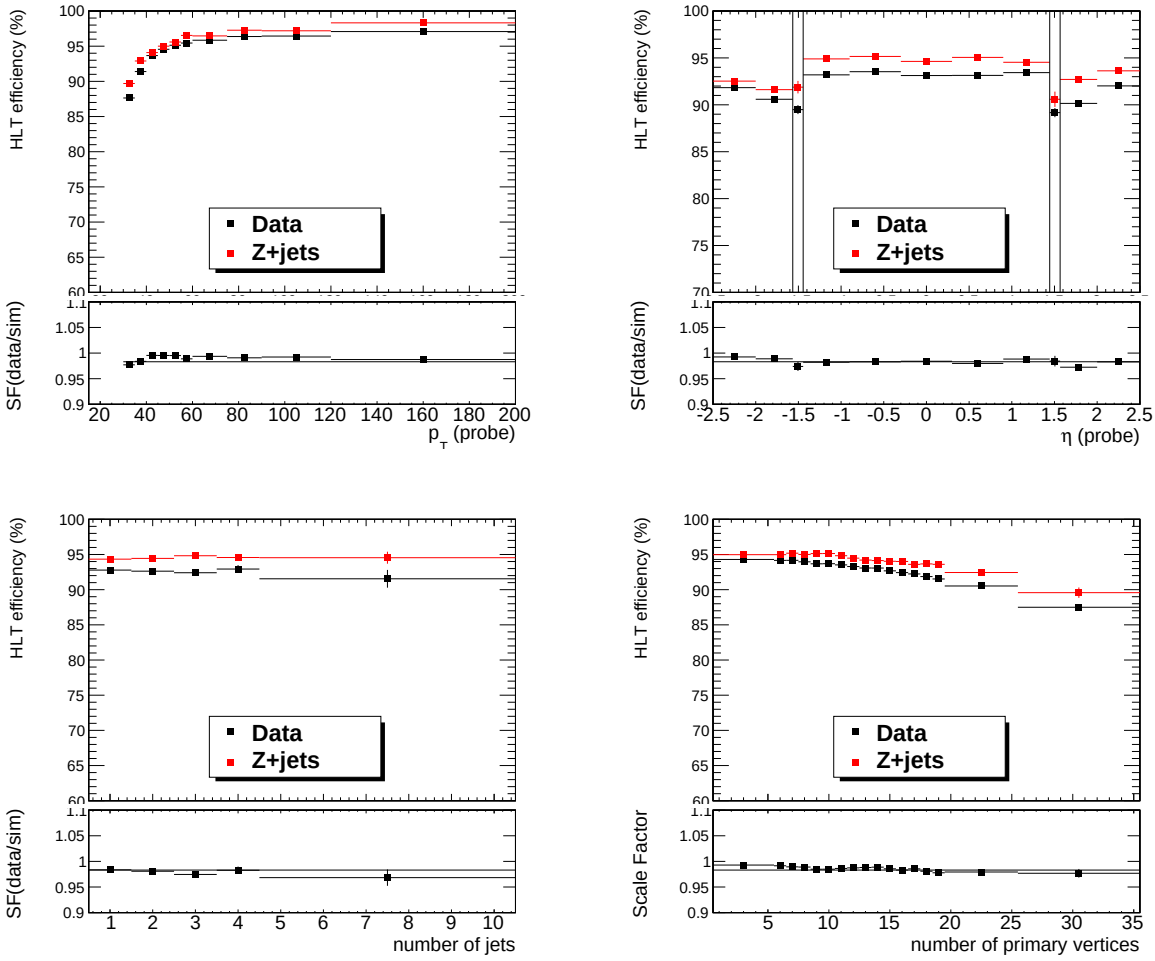

Figure 6.3: HLT efficiency for the electron leg of the top trigger path in the 2012B data run period as a function of the lepton transverse momentum, lepton pseudorapidity, jet multiplicity and vertex multiplicity. The scale factor (ratio of the data over simulation efficiency) is shown at the bottom where the horizontal line indicates the average scale factor for this data run period.

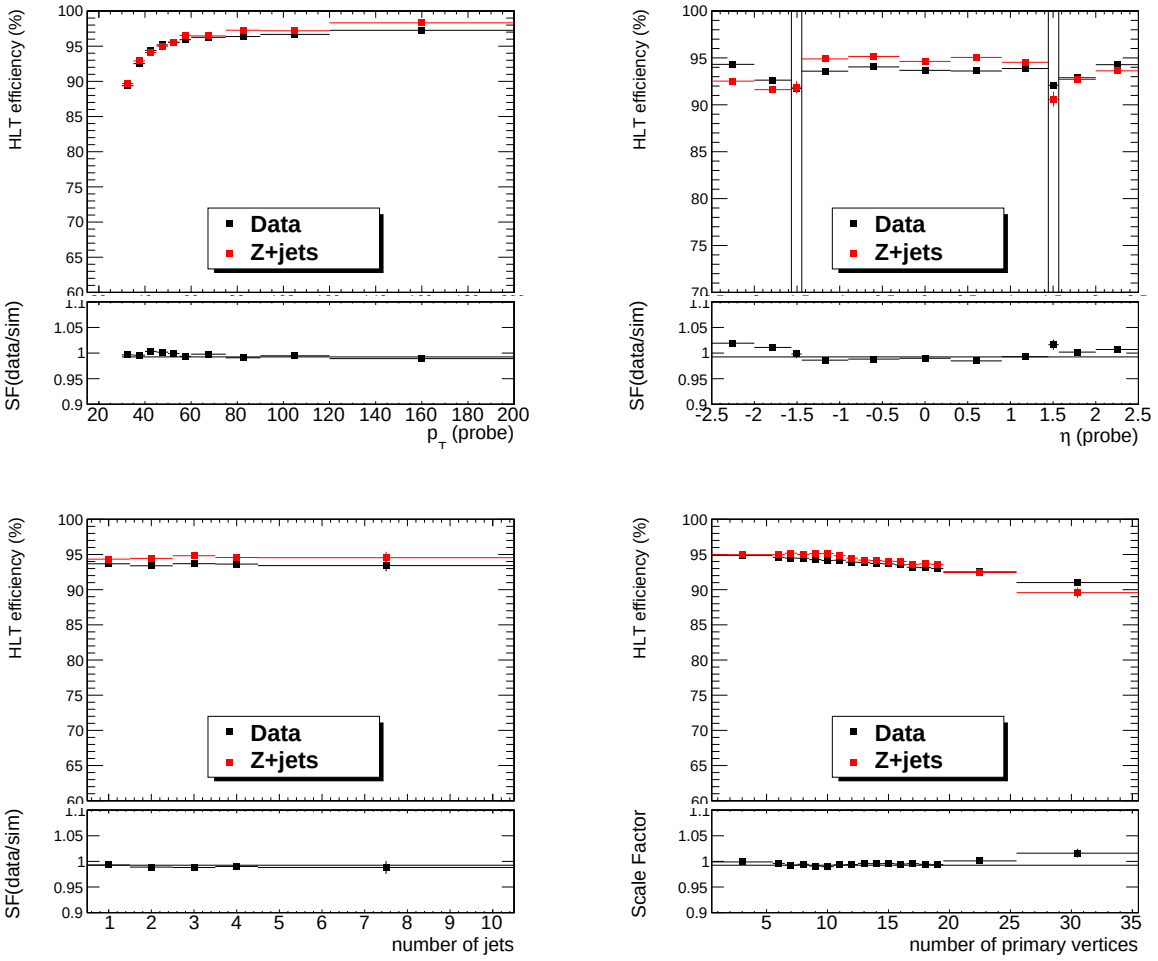

Figure 6.4: HLT efficiency for the electron leg of the top trigger path in the 2012C data run period as a function of the lepton transverse momentum, lepton pseudorapidity, jet multiplicity and vertex multiplicity. The scale factor (ratio of the data over simulation efficiency) is shown at the bottom where the horizontal line indicates the average scale factor for this data run period.

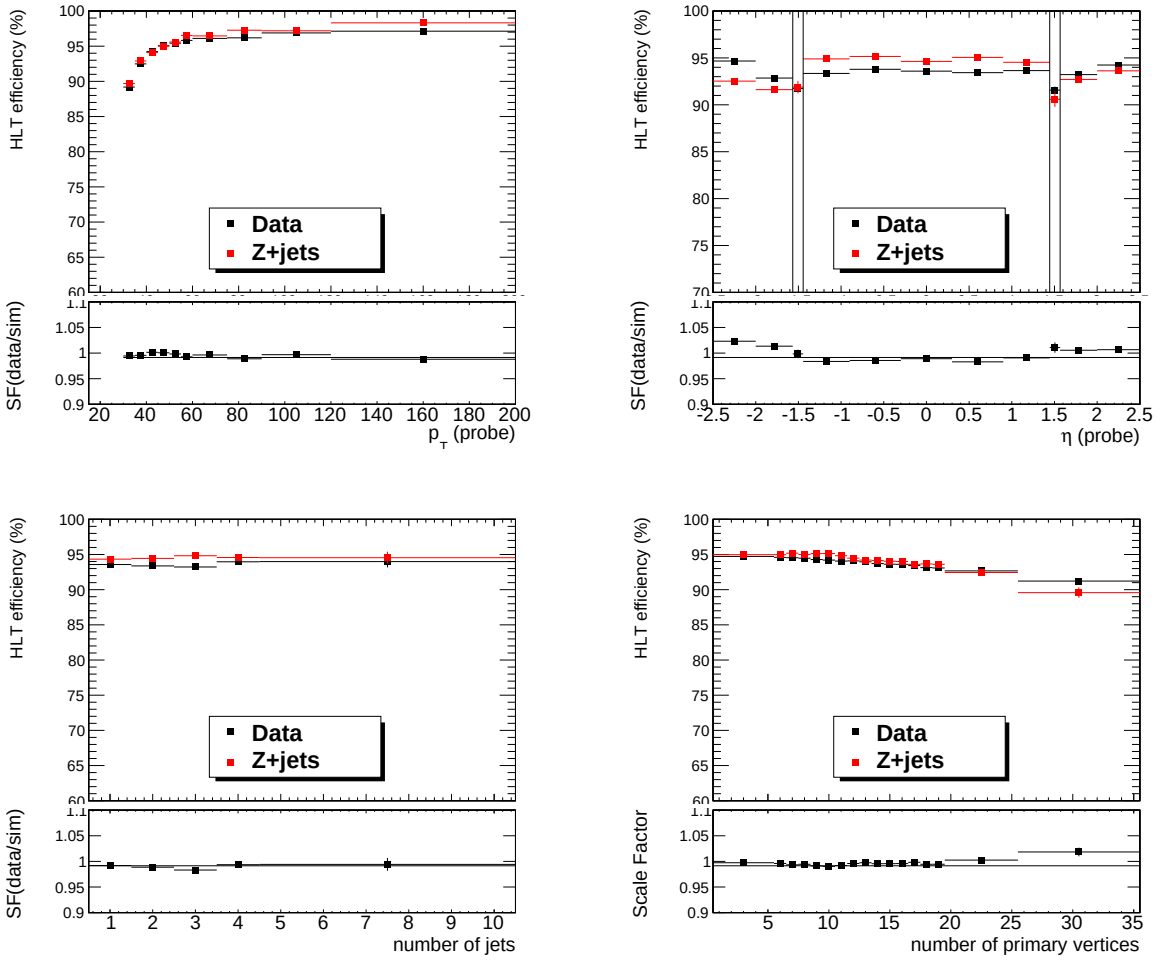

Figure 6.5: HLT efficiency for the electron leg of the top trigger path in the 2012D data run period as a function of the lepton transverse momentum, lepton pseudorapidity, jet multiplicity and vertex multiplicity. The scale factor (ratio of the data over simulation efficiency) is shown at the bottom where the horizontal line indicates the average scale factor for this data run period.

Muon channel

Similarly, for the muon trigger efficiency, the tag and probe pass the tight muon selection as described in chapter 5. A passing probe is matched to the trigger object of the muon leg of the triggers under study. The events are selected from the SingleMuon dataset and it is required that the tag muon is matched to one of the trigger objects of the IsoMu24_eta2p1 trigger, so that the probe is not biased towards the muon trigger. The efficiencies in the data and simulation as a function of the transverse momentum, pseudo-rapidity, jet and vertex multiplicity are shown in figures 6.6-6.9 for each run period separately. In the bottom of each plot the scale factor is shown. The scale factors are not constant. Again the horizontal line in the scale factor plots shows the average scale factor for this run period. From the plots, we can conclude that in the all run periods a parametrisation in at least the muon transverse momentum and vertex multiplicity is needed.

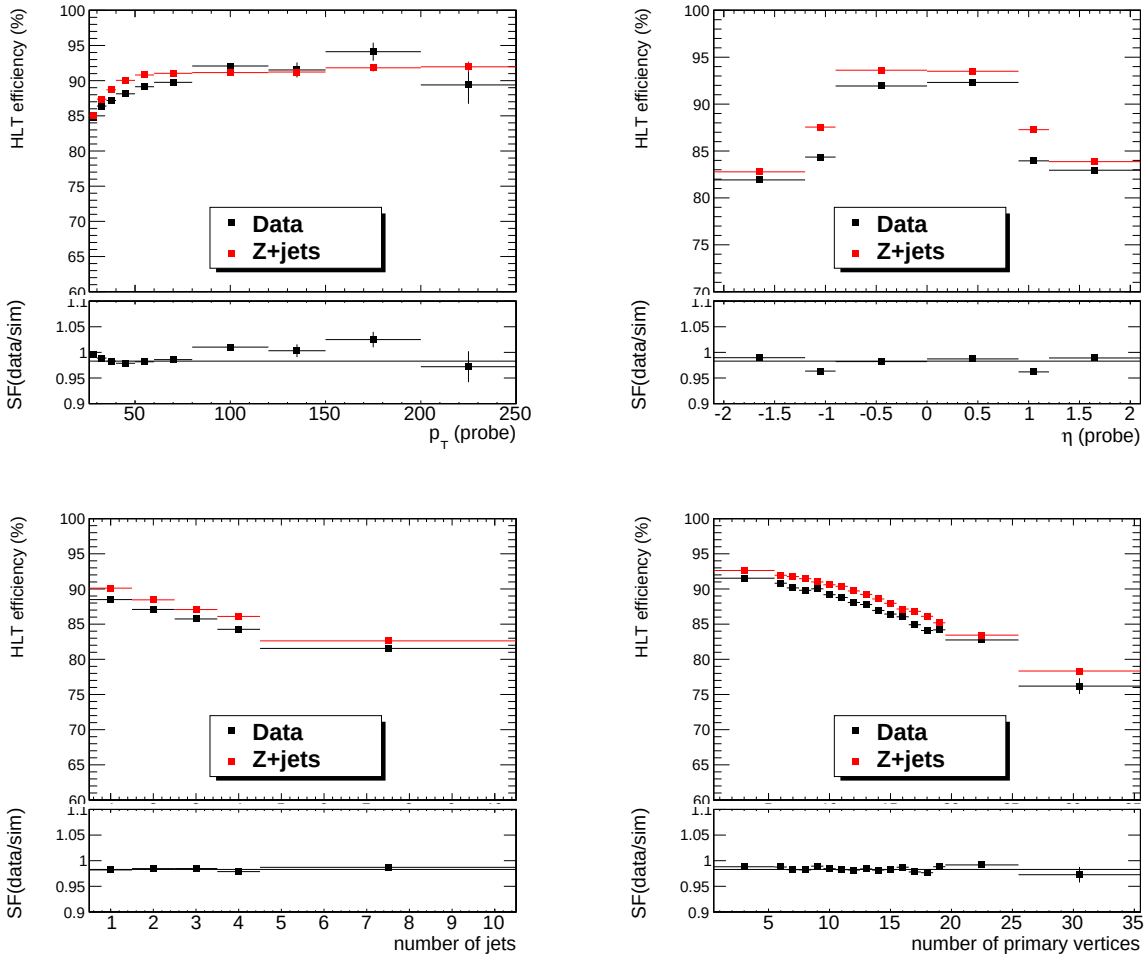

Figure 6.6: HLT efficiency for the muon leg of the top trigger path in the 2012A data run period as a function of the lepton transverse momentum, lepton pseudorapidity, jet multiplicity and vertex multiplicity. The scale factor (ratio of the data over simulation efficiency) is shown at the bottom where the horizontal line indicates the average scale factor for this data run period.

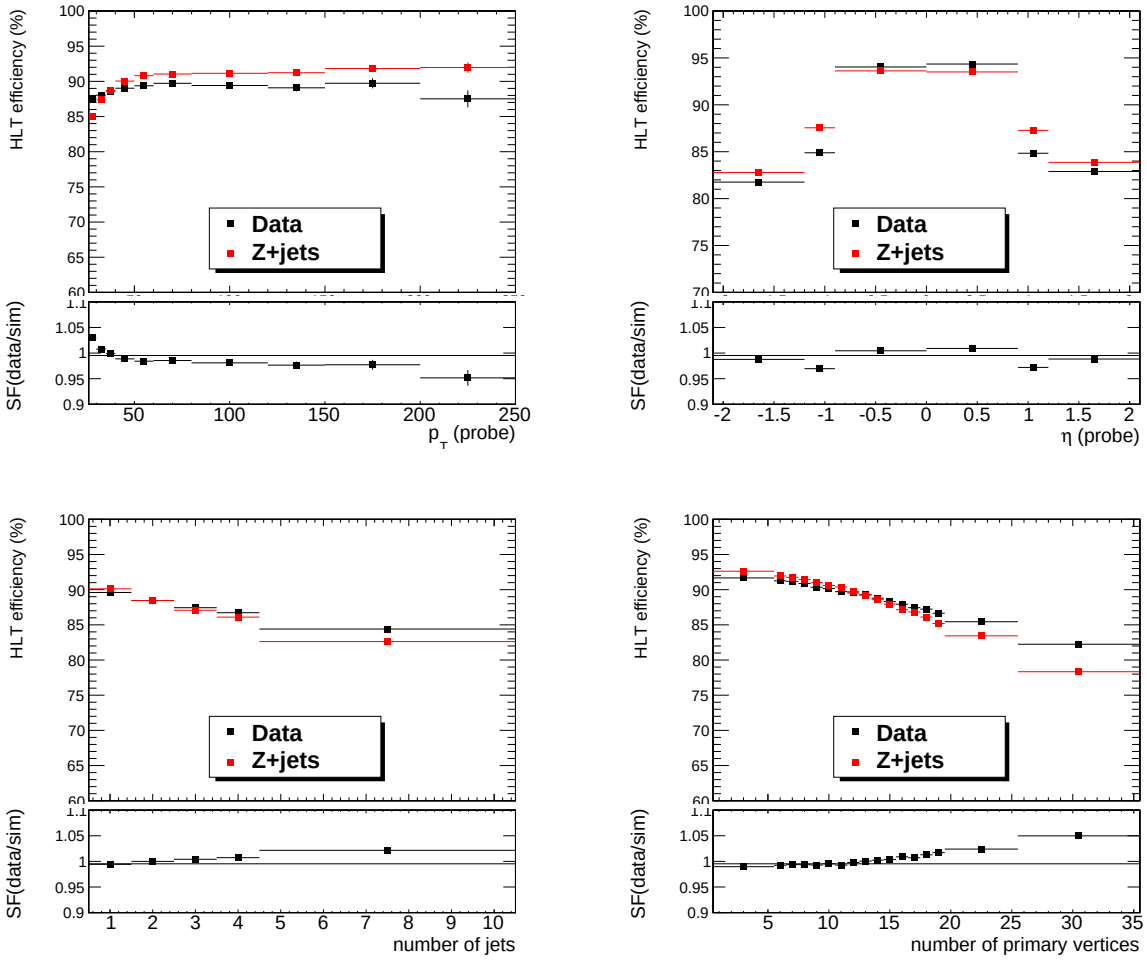

Figure 6.7: HLT efficiency for the muon leg of the top trigger path in the 2012B data run period as a function of the lepton transverse momentum, lepton pseudorapidity, jet multiplicity and vertex multiplicity. The scale factor (ratio of the data over simulation efficiency) is shown at the bottom where the horizontal line indicates the average scale factor for this data run period.

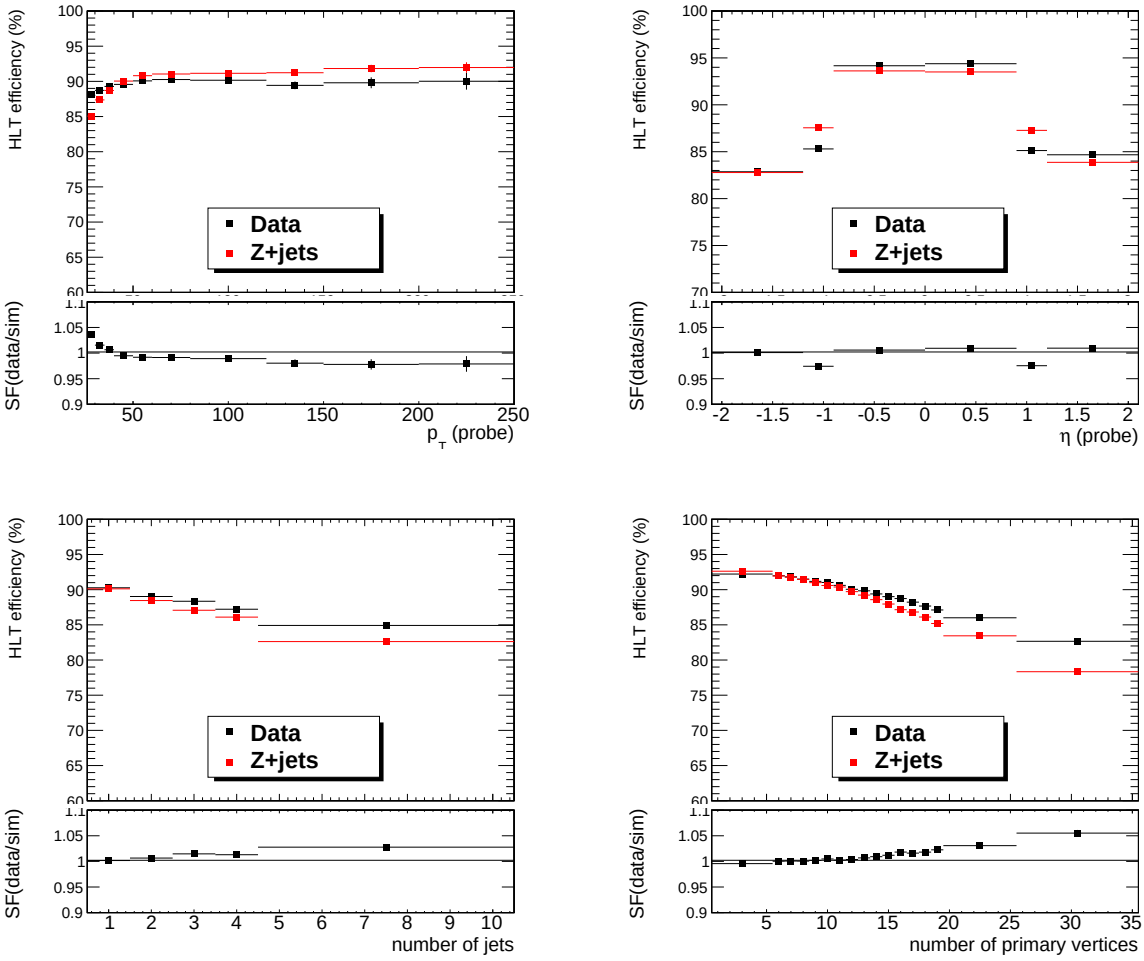

Figure 6.8: HLT efficiency for the muon leg of the top trigger path in the 2012C data run period as a function of the lepton transverse momentum, lepton pseudorapidity, jet multiplicity and vertex multiplicity. The scale factor (ratio of the data over simulation efficiency) is shown at the bottom where the horizontal line indicates the average scale factor for this data run period.

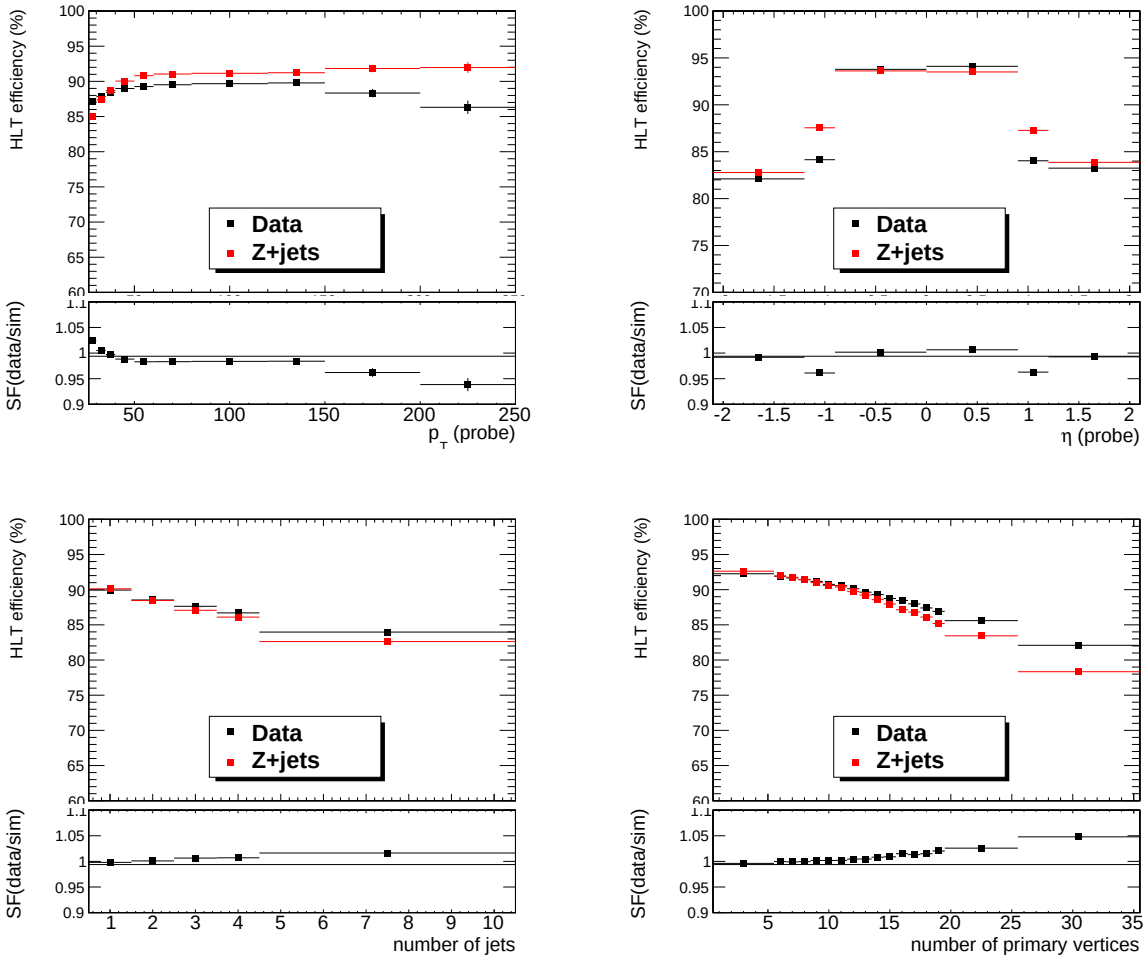

Figure 6.9: HLT efficiency for the muon leg of the top trigger path in the 2012D data run period as a function of the lepton transverse momentum, lepton pseudorapidity, jet multiplicity and vertex multiplicity. The scale factor (ratio of the data over simulation efficiency) is shown at the bottom where the horizontal line indicates the average scale factor for this data run period.

6.3 Cut and Count Method

A "Cut and Count" method has been developed for the hadronic leg of the top quark trigger paths. The "Tag and Probe" method is not capable of measuring the efficiency of multi-object selection criteria, as is the case with the hadronic part of the top quark triggers here. As in the "Tag and Probe" method, the first step is to find a pool of probe events, rather than probe leptons on which to test the efficiency of the selection criterium or in our case the efficiency of the hadronic leg of the trigger. The difficulty lies in finding a selection for the probe events which is unbiased with respect to the trigger under study.

In a first step in the probe event selection, the event needs to be recorded by a trigger without a hadronic leg as this would bias the trigger. Probe events are selected from the SingleElectron or SingleMuon datasets as this will ensure they are triggered only by the leptonic side of the event. In addition, we require that the leptonic leg of the top trigger path has triggered, ensuring that it is fully efficient. On this pool of events the recommended top quark pair selection is applied with one tight isolated lepton and four or more jets with staggered transverse momentum cuts of $55, 45, 35, 25$ GeV. On this pool of probe events, the efficiency of the trigger is the fraction of events which passes the full top trigger path.

The HLT efficiency of the hadronic leg is represented with respect to the fourth ranking jet in transverse momentum. There is a large mismatch between the online reconstruction in data and simulation as jet energy corrections are not applied in the trigger menu in the simulation. As a consequence the HLT efficiency has different dependencies in data and simulation. For this reason, we do not apply scale factors but the data efficiencies. In figures 6.10-6.13, we only show the data efficiencies in the different data run periods. The turn-on curve of the trigger as a function of the transverse momentum of the fourth offline jet is clearly visible. The trigger efficiency as a function of the jet pseudo-rapidity is quite stable. Unlike in the leptonic trigger efficiency, the trigger efficiency goes up with jet multiplicity as is expected. During the 2012 A period the hadronic trigger efficiency shows a dependence on the number of primary vertices, while in the other run periods pile-up subtraction has been performed online, resulting in a flatter dependence on the number of primary vertices.

6.4 Summary

Due to the number of changes that were applied to the top quark lepton+jets paths during the 2012 data-taking and the incomplete jet energy corrections in the simulation trigger menu, it was decided to not require a trigger selection in the simulation and apply a scale factor but rather apply the efficiencies measured in data. As a consequence no scale factors are provided but the absolute data efficiencies for the leptonic and hadronic leg separately which are multiplied to obtain the trigger efficiency of the full path $\epsilon_{\text{data}} = \epsilon_{\text{lepton, data}}\epsilon_{\text{jet, data}}$. As the absolute efficiencies have dependencies on several variables, a multidimensional parametrisation is provided on the jet and lepton transverse momentum and pseudo-rapidity, the jet and primary vertex multiplicity of the event. The efficiency of both the leptonic and hadronic leg is a weighted average of the efficiency during the different run periods. A systematic uncertainty of $1\,\%$ is considered on the total efficiency. As it was unexpectedly possible to keep the single lepton triggers unprescaled for the entire 2012 data-taking period, these triggers are usually preferred over the cross-triggers as these are more uniform. The SingleMuon trigger is used for this measurement as we want to keep the transverse momentum threshold on the jets in the event low. The scale factors for the single lepton triggers are determined very similarly with a "Tag and Probe" method.

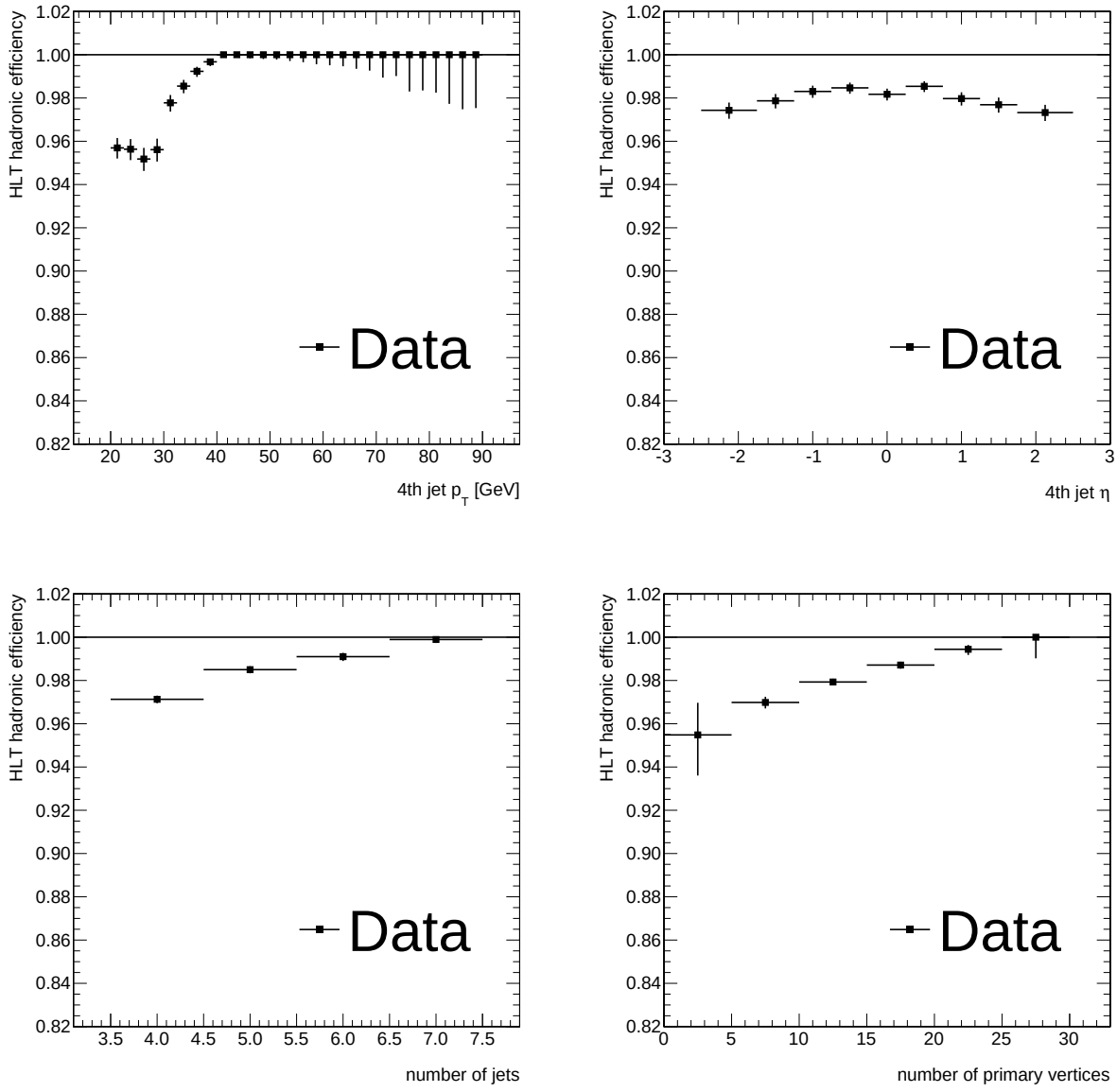

Figure 6.10: HLT efficiency for the hadronic leg of the top trigger path in the 2012A data run period as a function of the 4th leading jet transverse momentum, 4th leading jet pseudo-rapidity, jet multiplicity and vertex multiplicity.

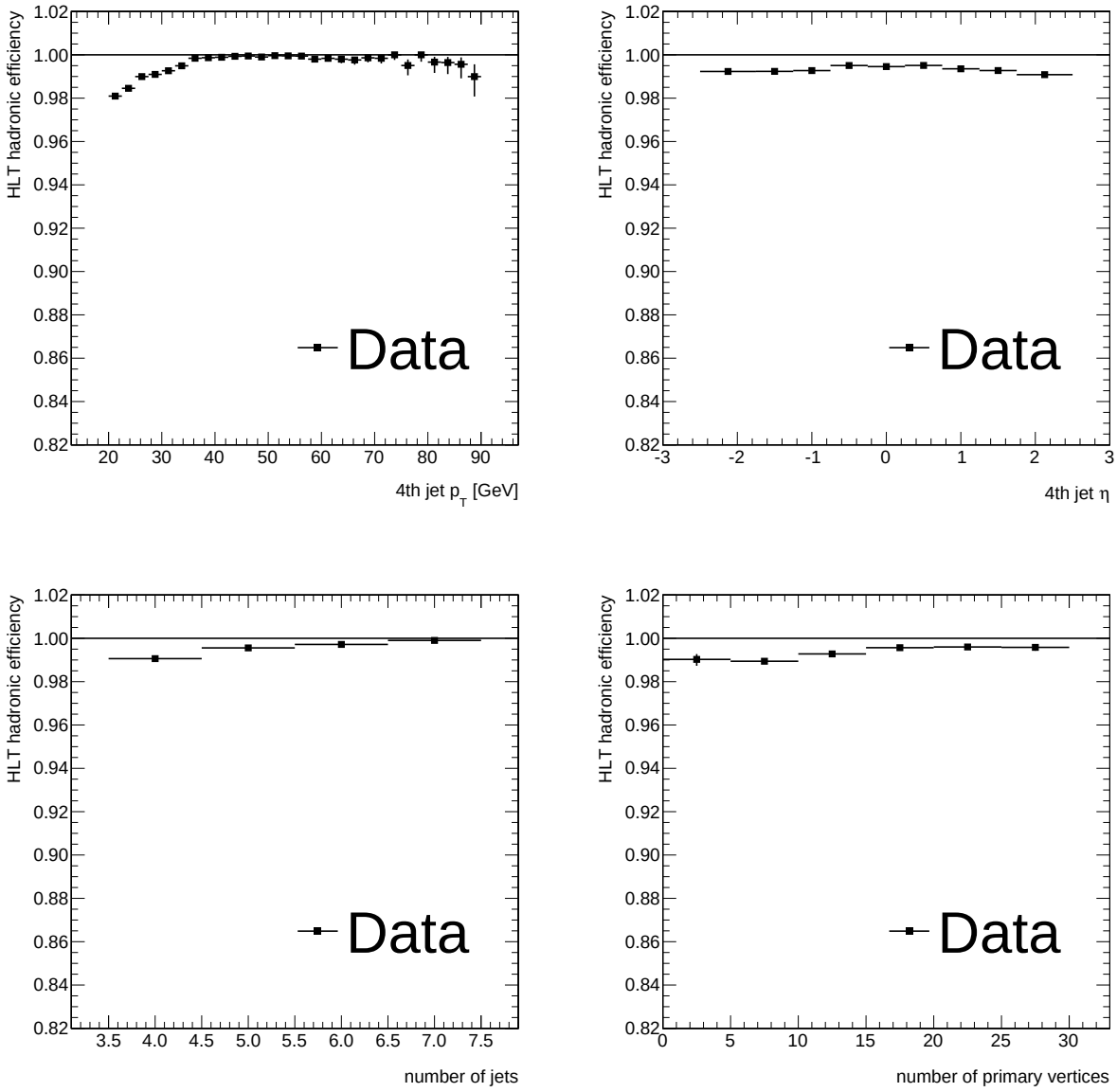

Figure 6.11: HLT efficiency for the hadronic leg of the top trigger path in the 2012B data run period as a function of the 4th leading jet transverse momentum, 4th leading jet pseudo-rapidity, jet multiplicity and vertex multiplicity.

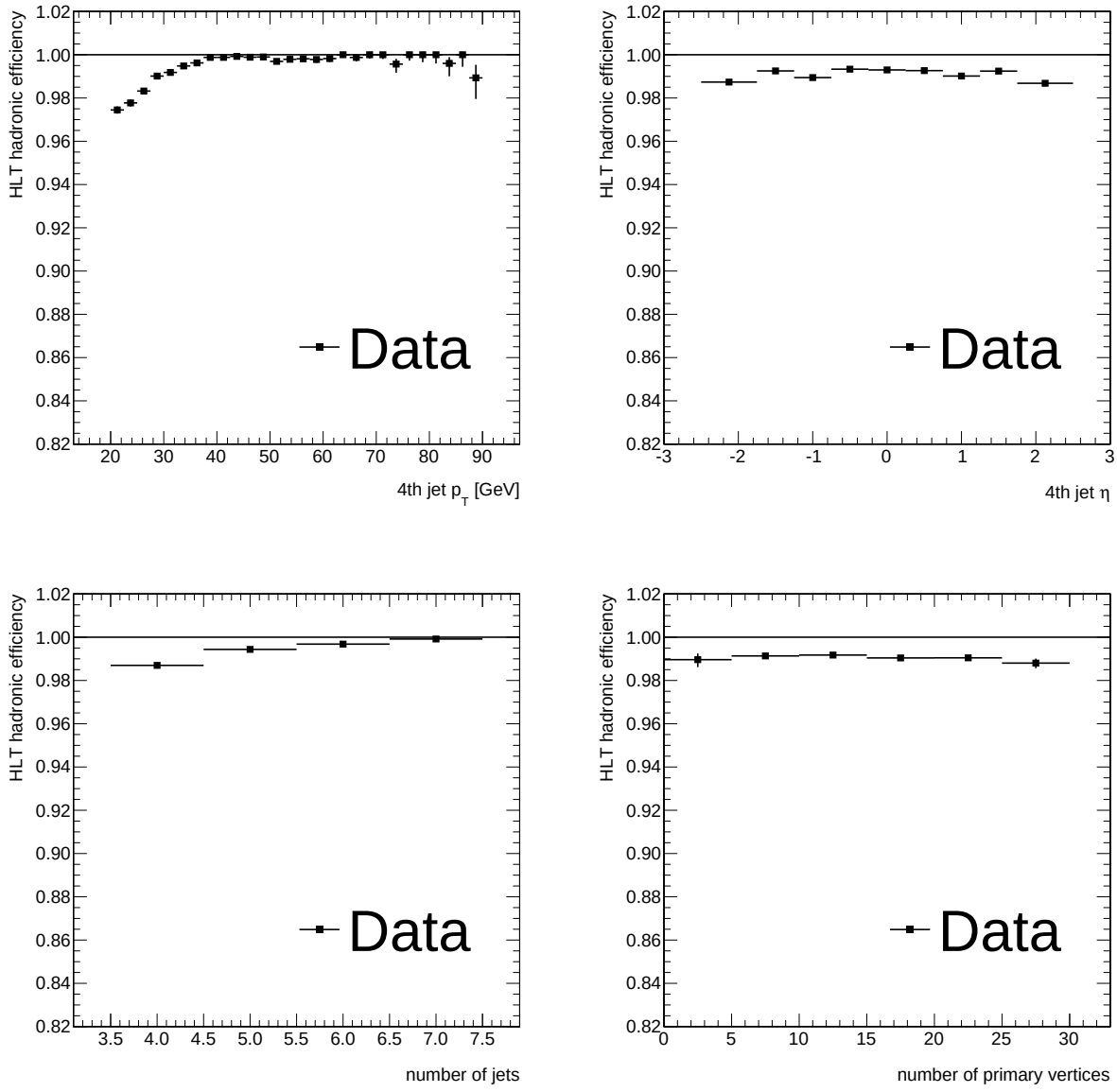

Figure 6.12: HLT efficiency for the hadronic leg of the top trigger path in the 2012C data run period as a function of the 4th leading jet transverse momentum, 4th leading jet pseudo-rapidity, jet multiplicity and vertex multiplicity.

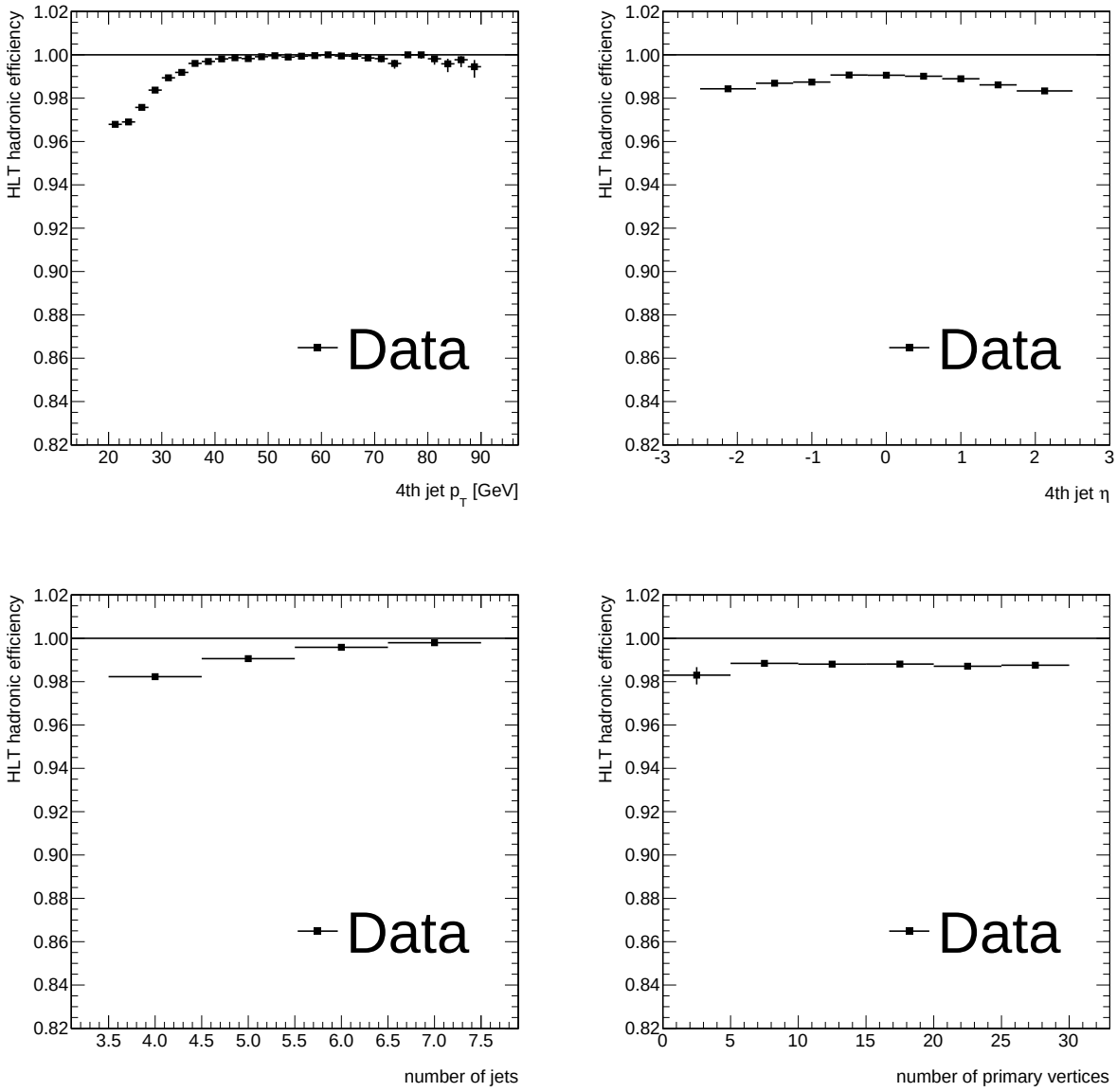

Figure 6.13: HLT efficiency for the hadronic leg of the top trigger path in the 2012D data run period as a function of the 4th leading jet transverse momentum, 4th leading jet pseudo-rapidity, jet multiplicity and vertex multiplicity.

Part IV

Top Quark Pair Spin Correlation Measurement

Chapter 7

Matrix Element Method

In this chapter, we give an introduction to the analysis method used in this work: the matrix element method (MEM). The MEM was first used at the DØ experiment at Fermilab to improve the statistical significance of the top quark mass measurement. In section 7.1, first a general introduction to the method will be given, to proceed with more details on the specific usage of the method in this analysis. Section 7.2 will focus on the calculation of a vital part of the MEM: the transfer functions.

7.1 Matrix Element Method

7.1.1 Method Description

The probability of observing an event, generated by a physical process, in a final state with certain kinematics is proportional to the differential cross section of that physical process. The total probability of observing the event is the sum of the probability of the event under each process which gives rise to this final state, weighed by the relative contributions of each process to this final state. The MEM explicitly calculates this probability for the event (called likelihood) under a specific physics process. The differential cross section of a hard-scattering interaction between two partons with four-vectors q_1 and q_2 decaying into a final state with n particles p, is given by

$$d\sigma = \frac{(2\pi)^4 |M|^2}{4\sqrt{(q_1 \cdot q_2)^2 - m_{q1}^2 m_{q2}^2}} d\Phi_n(q_1 + q_2; p_1, \ldots, p_n) \tag{7.1}$$

where M is the Lorentz-invariant matrix element of the process, m_{q1} and m_{q2} are the masses of the initial partons and $d\Phi_n$ is the n-body phase space element given by

$$d\Phi_n(P, p_1, \ldots, p_n) = \delta^4(P - \sum_{i=1}^{n} p_i) \prod_{i=1}^{n} \frac{d^3 p_i}{(2\pi)^3 2E_i} \tag{7.2}$$

In a realistic scenario, one needs to take into account that the collisions are done with composite particles (like protons at the LHC) and not partons. To obtain the differential cross section in pp collisions, the parton density functions (PDFs) $f(Q_1)$ and $f(Q_2)$ (where Q_1 and Q_2 are the fractions of longitudinal momentum of the proton carried by parton q_1 and q_2) need to be added, integrating over the initial parton kinematics and summing over all parton flavours. In addition, the resolution of the detector cannot be ignored and unobserved variables like the longitudinal component of a neutrino are integrated over. The resolution and bias of the observed kinematics is taken into account by the transfer function W(y,x). The transfer function is a probability density for measuring an object with kinematics x when an object with kinematics y was produced. The transfer function is 1 in the case of an unmeasured final state object. A Dirac δ-function is used to describe variables that are well measured. A Gaussian shape is used when the resolution or bias of a variable is not negligible. In order to be interpreted as a probability, the transfer function W(y,x) should follow $\int W(y,x)dx = 1$. The probability or

event likelihood $L_{event}(x, \alpha)$ for an event with observed kinematics x, under a physical process with parameters α is then given by

$$L_{event}(x;\alpha) = \frac{1}{\sigma}\int \frac{(2\pi)^4 |M(\alpha, y)|^2 f(Q_1) f(Q_2) W(y, x)}{4 Q_1 Q_2 s} d\Phi_n dQ_1 dQ_2 \tag{7.3}$$

where s is the square of the centre-of-mass energy of the collision and σ is the total cross-section in the full phase-space.

The likelihood of a sample with n events with measured kinematics $x_1, \cdots, x_n$ under a certain process is given by

$$L_{\text{sample}}(x_1, \cdots, x_n; \alpha) = \prod_{i=1}^{n} L_{\text{event}}(x_i; \alpha) \tag{7.4}$$

Traditionally, a MEM has been used to maximise the sample likelihood (or to minimise $-\ln L_{\text{sample}}$) with respect to a parameter α of the matrix element of the physical process. An example is the top quark mass which is a free parameter in the matrix element describing $t\bar{t}$ production and subsequent decay. The likelihood for the event or sample can also be used to discriminate between discrete hypotheses, for example $t\bar{t}$ production as signal hypothesis and W + jets as background hypothesis. In this analysis, we consider two discrete hypotheses: $t\bar{t}$ production and semi-leptonic decay with either SM spin correlation or zero spin correlation. Using discrete hypotheses a and b, a test statistic with maximum separating power can be set up, according to Neyman and Pearson [102], as:

$$\lambda = \frac{L(x, H = a)}{L(x, H = b)} \tag{7.5}$$

where $L(x, H = a)$ represents either the event or sample likelihood under hypothesis a and $L(x, H = b)$ the event or sample likelihood under hypothesis b and λ can therefore be calculated on an event-basis λ_{event} or on a sample basis λ_{sample}. In this analysis the variable $-2 \ln \lambda$ will be used as test statistic.

A big advantage of the MEM is that the full event information is used, rather than looking at only a few observables (in the leading order approximation). The method offers a direct comparison of theory (represented by the hypothesis under study) and experiment. In a statistically limited sample, the MEM will allow for the maximum statistical sensitivity obtainable. The main drawbacks of the MEM is that the likelihood calculations are computationally intensive and the MEM has not been extended to include NLO scenarios. As the analysis is calibrated with NLO simulation, this LO treatment does not lead to a bias, but at most to a suboptimal sensitivity.

7.1.2 Matrix Elements for $t\bar{t}$ Production and Semi-Leptonic Decay

In this analysis, we want to discriminate between two $t\bar{t}$ production and semi-leptonic decay hypotheses: one hypothesis with SM spin correlations and one hypothesis with no spin correlation. To evaluate both hypotheses, it is necessary to know the matrix elements (MEs) describing each hypothesis. For the SM, this ME is by default contained in the MadWeight 5 code which will be used to perform the event likelihood calculations (see section 3.3.1). However for the spin uncorrelated hypothesis, some modifications are in order. The spin uncorrelated hypothesis assumes a spin correlation strength $A = 0$ and is obtained by SM $t\bar{t}$ production but with the top and anti-top quark spins summed over, thus destroying the spin correlation. The resulting samples of spin uncorrelated top and anti-top quarks decay spherically and independent of each other. Due to the fact that in the MadGraph event generation and MadWeight likelihood calculation

both on-shell and off-shell top quarks are considered, the spin uncorrelated MEs should be valid for both on-shell and off-shell cases. The LO calculations available in the literature are valid only for on-shell quarks (e.g. [103, 104]). Therefore, for the spin uncorrelated hypothesis, MEs for the production and subsequent decay of the top quark pairs are calculated analytically by Werner Bernreuther [105] for the processes represented by the Feynman diagrams in Figures 7.1 and 7.2. These MEs are implemented in MadGraph for private event generation and also in MadWeight for likelihood calculation which required non-trivial modifications in these codes.

In order to test the implementation of the SM ME for $t\bar{t}$ production and subsequent decay, we first substituted the default ME in the MadGraph event generation code with the expression of the SM ME from Bernreuther. MadGraph and MadWeight are contained in the same framework and have the same matrix element code for event generation as for event likelihood calculation. For the $t\bar{t}$ semi-leptonic sample produced with this substituted SM ME, we plot the angular distributions sensitive to $t\bar{t}$ spin correlation. An example is shown in fig. 7.3 where the cosine of the opening angle between the decay lepton and the b-quark of the hadronically decaying top quark is plotted. A linear fit to this distribution is performed according to $\frac{1}{2}(1-Dcos\theta_{lb})$. The linear dependence of this distribution is valid since no kinematic cuts were applied in the generation of this private sample. Since the D-parameter depends on the decay products of which one plots the distribution, to compare with the value $D_{lj} = -0.111$ for lepton-jet where the jet is the least-energetic light jet for $\sqrt{s} = 14$ TeV calculated by Bernreuther in [21], we must divide our fitted $D_{lb} = 0.083 \pm 0.003$ with the spin analysing power for the b-quark and multiply with the spin analysing power of the least-energetic light jet (as obtained from [20]) to obtain $D_{lj} = -0.104 \pm 0.004$ at $\sqrt{s} = 7$ TeV, extracted from our simulation sample. The small difference between the value we obtain from our simulation sample and the value calculated by Bernreuther is due to a small dependence on the centre-of-mass energy. From this we can conclude that the substitution of the SM ME was successful. This conclusion becomes more apparent when we plot the ratio of the default MadWeight ME, ME(MW), and the analytic expression given to us by Bernreuther, ME(WBcor), calculated for the SM at LO. This ratio should be equal to unity when these MEs are evaluated in the same phase space point irrespective of whether the top quarks are on-shell or off-shell. This ratio is plotted in fig. 7.4 versus a quantity indicating how off-shell the two top quarks are (i.e. $|173 - \sqrt{t.t}| + |173 - \sqrt{\bar{t}.\bar{t}}|$). The ratio is indeed equal to one as expected. This gives us confidence that we can correctly substitute a ME in MadWeight.

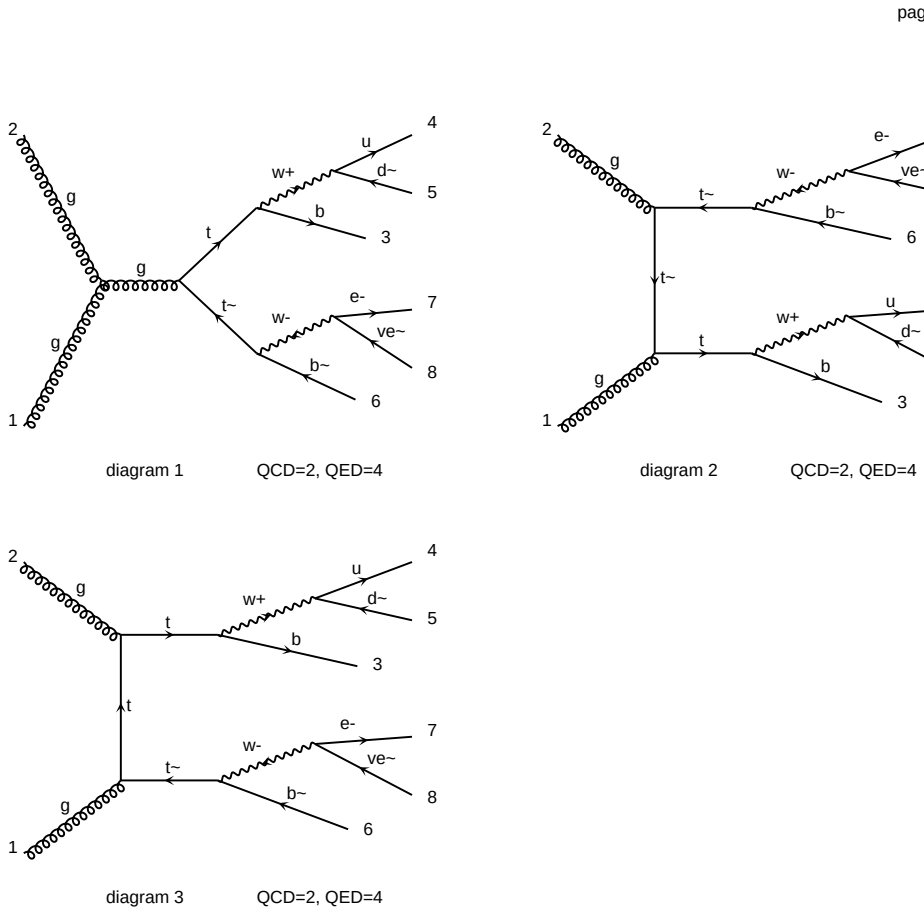

Figure 7.1: Diagrams contributing to the gg fusion channel in $t\bar{t}$ production and subsequent decay into electron+jets channel. Diagrams made with MadGraph5.

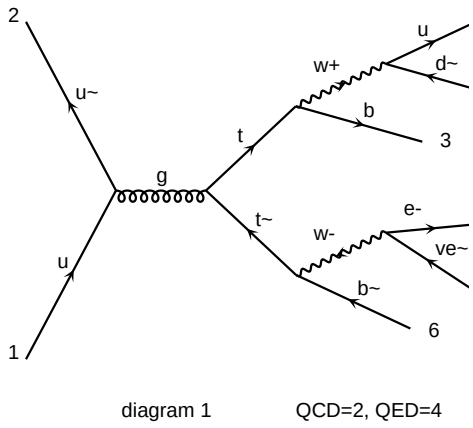

Figure 7.2: Diagram contributing to the qq channel in $t\bar{t}$ production and subsequent decay into electron+jets channel. Diagrams made with MadGraph5.

The correctness of the spin uncorrelated ME can only be tested by examining the angular distributions of the decay products and extracting the spin correlation strength from it. In fig. 7.5 the cosine of the angle between the decay lepton and the b-quark coming from the hadronically decaying top quark is shown. In the same plot, a linear fit to this distribution is plotted and a D-parameter of $D_{lb} = -0.002 \pm 0.003$ is extracted. From this we can conclude that our spin uncorrelated ME indeed describes a fully spin uncorrelated $t\bar{t}$ system compatible with $D_{lb} = 0$.

The expressions for the matrix elements in the MadWeight code, can be found in Appendix A.2. Please do not use these expressions without written permission by Werner Bernreuther.

7.1.3 Likelihood Calculation

The likelihood calculations are performed with MadWeight 5 using LO $t\bar{t}$ matrix elements. This gives us six particles in the final state to integrate over, plus the integration over the longitudinal momenta of the initial state partons. This gives us 20 variables to integrate over. Such a multi-dimensional integration is computationally very intensive. In addition, the correct jet-parton assignment is unknown, so all jet-parton permutations must be summed over. This gives us 4! possible permutations for a final state with four jets. The amount of permutations is reduced to 2 by using b-tagging information and taking into account that the light jets coming from the hadronic W-boson decay are interchangeable.

The transverse momentum of the initial partons is assumed to be zero. When the transverse momentum of the $t\bar{t}$ system is observed to be non-zero, the $t\bar{t}$ system is boosted back to the frame where the transverse momentum is zero. The resolution on all angular information and the energy of charged lepton is considered negligible, leading to a δ-function transfer function for these variables, reducing the dimension of the integral by 11. Conservation of energy and momentum adds another four δ-functions. The integration over the remaining variables is performed in MadWeight using VEGAS [106]. For more details on how the integration is performed and optimised, see [107].

The likelihood, as shown in eq. 7.3, is normalised by the cross section to be interpreted as

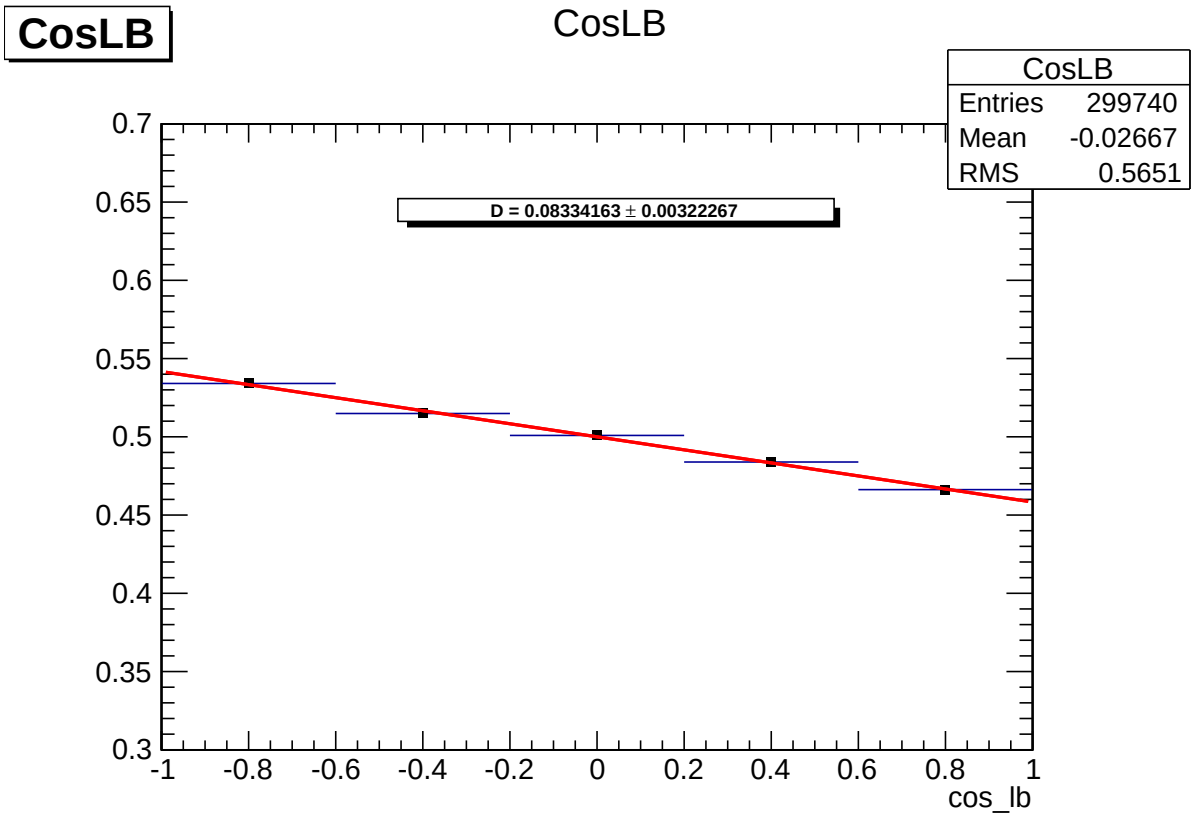

Figure 7.3: Cosine of the angle between the direction of the lepton and the b-quark coming from the hadronically decaying top quark both in their top quark parent rest frame in spin-correlated $t\bar{t}$ events from spin-correlated Bernreuther MEs and from MadGraph5 default MEs which are identical. A linear fit is performed to this distribution.

a probability. In addition the acceptance of the event selection needs to be taken into account. The event acceptance $Acc(x_i)$ is either 0 or 1 under the event selection. The average acceptance usually depends on the hypothesis under study (as is the case for a top quark mass measurement). In this analysis, the average acceptance is independent of the hypothesis: the cross sections for both correlated and uncorrelated $t\bar{t}$ production are identical. In addition, the event selection has been chosen not to bias towards any of the hypotheses, as will be shown in the next chapters, leading to identical selection efficiencies. Therefore, when considering the likelihood ratio, the normalisation and acceptance corrections cancel. This is considered in eq. 7.6 where the likelihood ratio is shown for one event taking the acceptance correction into account.

$$\overline{L}(x_i, \alpha) = \frac{Acc(x_i)L(x_i, \alpha)}{\int Acc(x)L(x, \alpha)dx} \tag{7.6}$$

In the ratio, this enters as

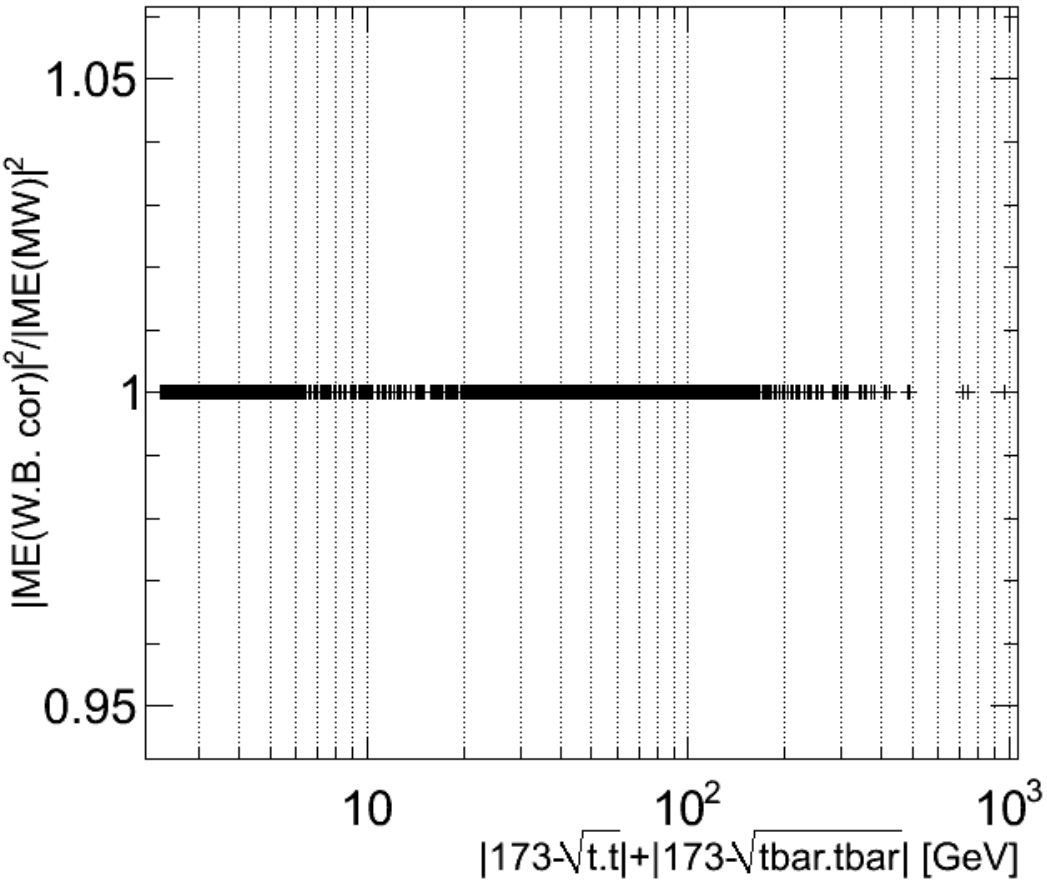

Figure 7.4: Ratio of the ME value for SM spin correlation provided by Bernreuther and the ME value in the default MadWeight evaluated in the same phase-space point.

$$
\begin{aligned}
-\ln\lambda &= -\ln\left(\frac{\overline{L}(x_i, H=Uncor)}{\overline{L}(x_i, H=Cor)}\right) \\
&= -\ln(\overline{L}(x_i, H=Uncor)) + \ln(\overline{L}(x_i, H=Cor)) \\
&= -\ln(L(x_i, H=Uncor)) + \ln(\int Acc(x)L(x, H=Uncor)dx) - \ln(Acc(x_i)) \\
&+ \ln(L(x_i, H=Cor)) - \ln(\int Acc(x)L(x, H=Cor)dx) + \ln(Acc(x_i)) \\
&= -\ln(L(x_i, H=Uncor)) + \ln(L(x_i, H=Cor))
\end{aligned}
$$

In the last line, we've taken into account that $\int Acc(x)L(x,\alpha)dx = \frac{N_{acc}}{N_{gen}}$ where the integration runs over the entire visible phase space, N_{acc} is the number of accepted events and N_{gen} is the number of generated events. In this analysis, since the cross section of $t\bar{t}$ production in both hypotheses is identical and since the event selection does not bias the acceptance towards one hypothesis, these terms are identical and therefore cancel. Similarly, the normalisation with the total cross section will cancel in the same manner.

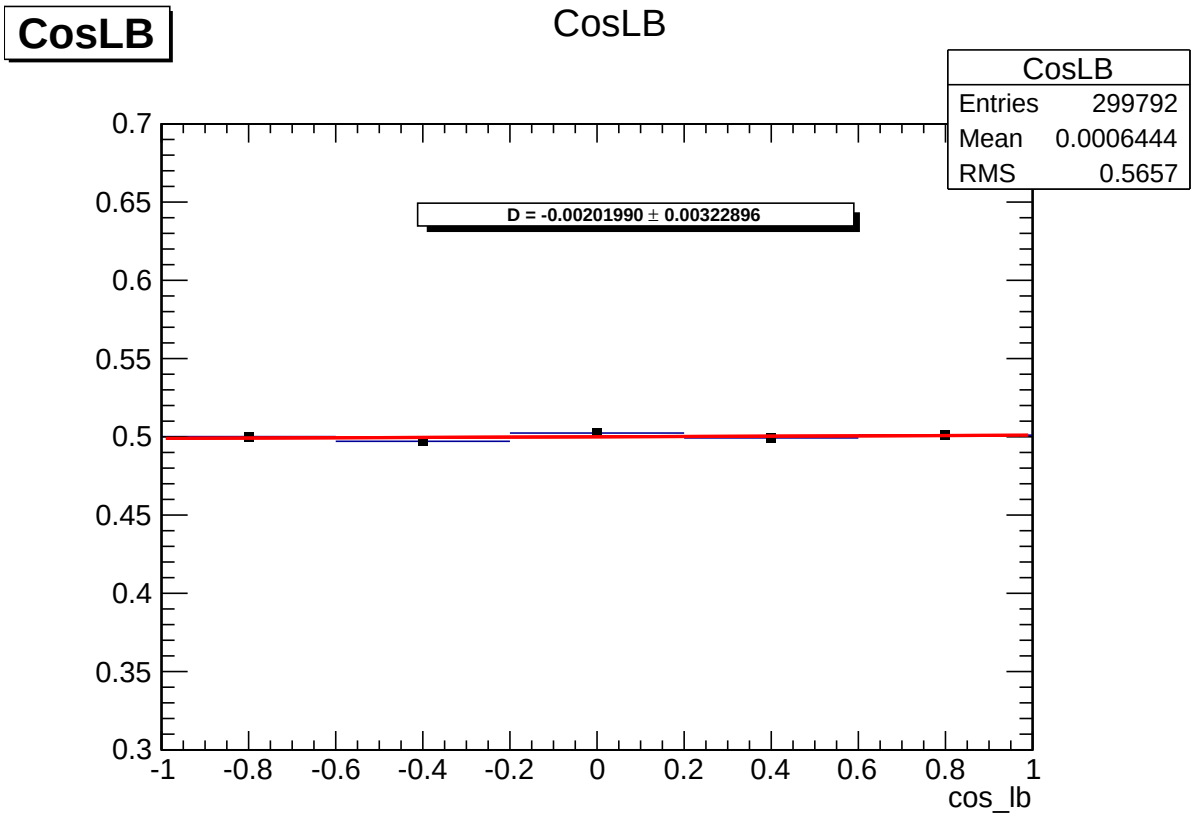

Figure 7.5: Cosine of the angle between the direction of the lepton and the b-quark coming from the hadronically decaying top quark both in their top quark parent rest frame in spin-uncorrelated $t\bar{t}$ events. A linear fit is performed to this distribution.

In appendix A.3, the MadWeight settings for the likelihood calculations are detailed. These settings differ a bit for the tests at generator level. During the calculations the top quark mass hypothesis is fixed to 172.5 GeV because this is the top quark mass used in the signal simulation. MadWeight runs over all jet-parton permutations which are compatible with the b-tagging information. The centre-of-mass energy of the proton beams is set to 8 TeV. The maximum amount of integration points is set to 12 000 which ensures that the integration errors are sufficiently small.

7.2 Transfer Functions

In the event likelihood calculations (discussed in 7.1), a transfer function (TF) is used to map the measured kinematics of the event to the parton level kinematics. This transfer function depends on the specifics of the detector and is different for different particle types which interact in various ways with the detector. We assume that the angular information we get from CMS is sufficiently accurate to describe the original direction of the particle. In addition, we assume that the energy of the muons does not need correcting as we will show in section 7.2.2. This approximation is valid as we are not considering dilepton resonances (such as a Z boson) in our hypothesis. As a result of these assumptions, we only use transfer functions to map the reconstructed jet energy (with jet energy corrections applied) to the parton level kinematics. Ideally, a transfer function for all variables would be used, but since each transfer function adds additional CPU time to the calculation, it is necessary to make the trade-off between accuracy

and computation time needed.

7.2.1 Jet Energy

We calculate the transfer functions on $t\bar{t}$ signal simulation only (SM correlated and uncorrelated added). Even though the transfer function is object and detector dependent and we assume that a factorised approach applies, there could be some sample dependence due to the proximity of other objects in the event, for example cross talk between light and b-jets. We determine the transfer function in the full kinematic phase space. For each jet in the event, unambiguously matched to a parton coming from the semi-leptonic $t\bar{t}$ decay using $\Delta R(\text{jet}, \text{parton}) < 0.3$, we store the E_{parton} and E_{jet} information. We consider true b-jets (meaning the jet is matched to a generator level b-quark) and light jets separately. We bin the E_{jet} distribution in narrow slices of parton energy and pseudo-rapidity. As can be seen in fig. 7.6 and 7.7, where some random example slices in E_{parton} are shown, the distribution has a Gaussian core, but shows a small tail on the positive side of the distribution. We have tried fits with both a single Gaussian and a double Gaussian transfer function, and we find that in both the b-jet and light jet case the single Gaussian transfer function gives more stable results. The transfer functions are determined in three slices of parton pseudo-rapidity: $0 < |\eta_{parton}| < 0.87$, $0.87 < |\eta_{parton}| < 1.479$ and $1.479 < |\eta_{parton}| < 2.5$. In each pseudo-rapidity slice, we divide the E_{jet} distribution in parton energy slices of 5 GeV and fit with a Gaussian function. The result of the fit parameters as a function of E_{parton} is shown in fig. 7.8 and 7.9. For the Gaussian mean μ of the E_{jet} distribution, a linear dependence as a function of E_{parton} is visible ($m_0 + m_1 * E_{parton}$). The dependence of the Gaussian width σ, showing the resolution of the jet energy, can be fitted with a functional form of $s_0 + s_1 E_{parton} + s_2\sqrt{E_{parton}}$ showing us the three terms that contribute to calorimeter resolution. The parametrised dependence has been fitted in the range $50\,\text{GeV} < E_{parton} < 200\,\text{GeV}$, to take into account only the slices where there are sufficient events to make a reliable fit.

Based on the fits of the parametrised dependence, we can then convert our single Gaussian expression to a transfer function in the difference between the parton and jet energy. In table 7.1 and 7.2 the fitted parameters for the following shape are shown

$$TF = \frac{\exp\left[-\frac{1}{2}\left(\frac{\Delta E + m_0 + m_1 E_{parton}}{s_0 + s_1 E_{parton} + s_2\sqrt{E_{parton}}}\right)^2\right]}{\sqrt{2\pi}(s_0 + s_1 E_{parton} + s_2\sqrt{E_{parton}})} \tag{7.7}$$

for b-jets and light jets respectively with $\Delta E = E_{parton} - E_{jet}$. In fig. 7.6 and 7.7, we can see the comparison between the fitted Gaussian and the parametrised transfer function in some random slices. The transfer function of this form is normalised to unity for each E_{parton} bin.

Table 7.1: Single Gaussian transfer function parameters for b-jets in three parton pseudo-rapidity slices.

parameter	$0 < \lvert\eta_{parton}\rvert < 0.87$	$0.87 < \lvert\eta_{parton}\rvert < 1.479$	$1.479 < \lvert\eta_{parton}\rvert < 2.5$
m_0	-2.4 ± 0.2	-2.7 ± 0.3	-3.3 ± 0.7
m_1	-0.006 ± 0.002	-0.013 ± 0.003	0.002 ± 0.005
s_0	0.010 ± 0.001	0.010 ± 0.001	0.010 ± 0.001
s_1	0.044 ± 0.003	0.065 ± 0.005	0.12 ± 0.01
s_2	1.24 ± 0.03	1.43 ± 0.05	1.27 ± 0.11

As another test of the validity of the transfer functions, we plot the ΔE-distribution for all η_{parton}-slices superimposed in various broader E_{parton} ranges in fig. 7.10 and 7.11. For each

Table 7.2: Single Gaussian transfer function parameters for light jets in three parton pseudo-rapidity slices.

parameter	$0 < \lvert\eta_{parton}\rvert < 0.87$	$0.87 < \lvert\eta_{parton}\rvert < 1.479$	$1.479 < \lvert\eta_{parton}\rvert < 2.5$
m_0	-2.6 ± 0.2	-1.1 ± 0.3	5.3 ± 0.6
m_1	0.038 ± 0.002	0.024 ± 0.003	0.018 ± 0.005
s_0	0.010 ± 0.001	0.010 ± 0.001	0.010 ± 0.001
s_1	0.02 ± 0.02	0.014 ± 0.005	0.052 ± 0.009
s_2	1.1 ± 0.4	1.87 ± 0.05	2.1 ± 0.1

entry in the transfer function histogram, we added the transfer function using expression 7.7 evaluated at the E_{parton} of that entry which is normalised to unity. The simulation histogram is filled by using the ΔE entry from the simulation. Even though we used a single Gaussian transfer function to describe the ΔE-distribution instead of the more complicated double Gaussian, we obtain fairly good agreement between the simulation and the transfer function. The mean and resolution of the distributions are adequately described. The usage of a suboptimal transfer function would only give rise to a decreased separation power between the hypotheses and not to a bias.

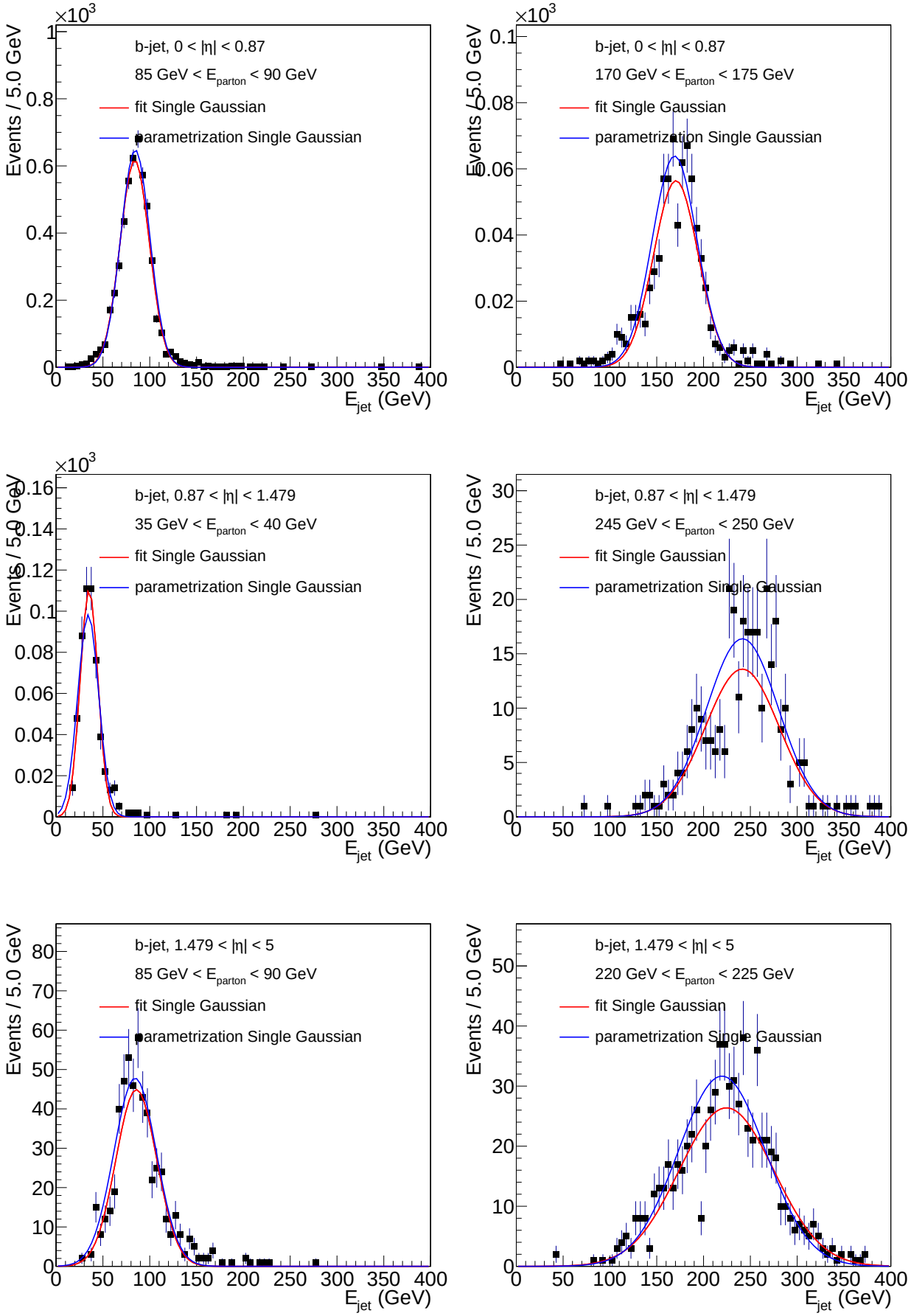

Figure 7.6: Comparison between fitting a single Gaussian and the parametrised results in several bins of E_{parton} and η_{parton} for b-jets.

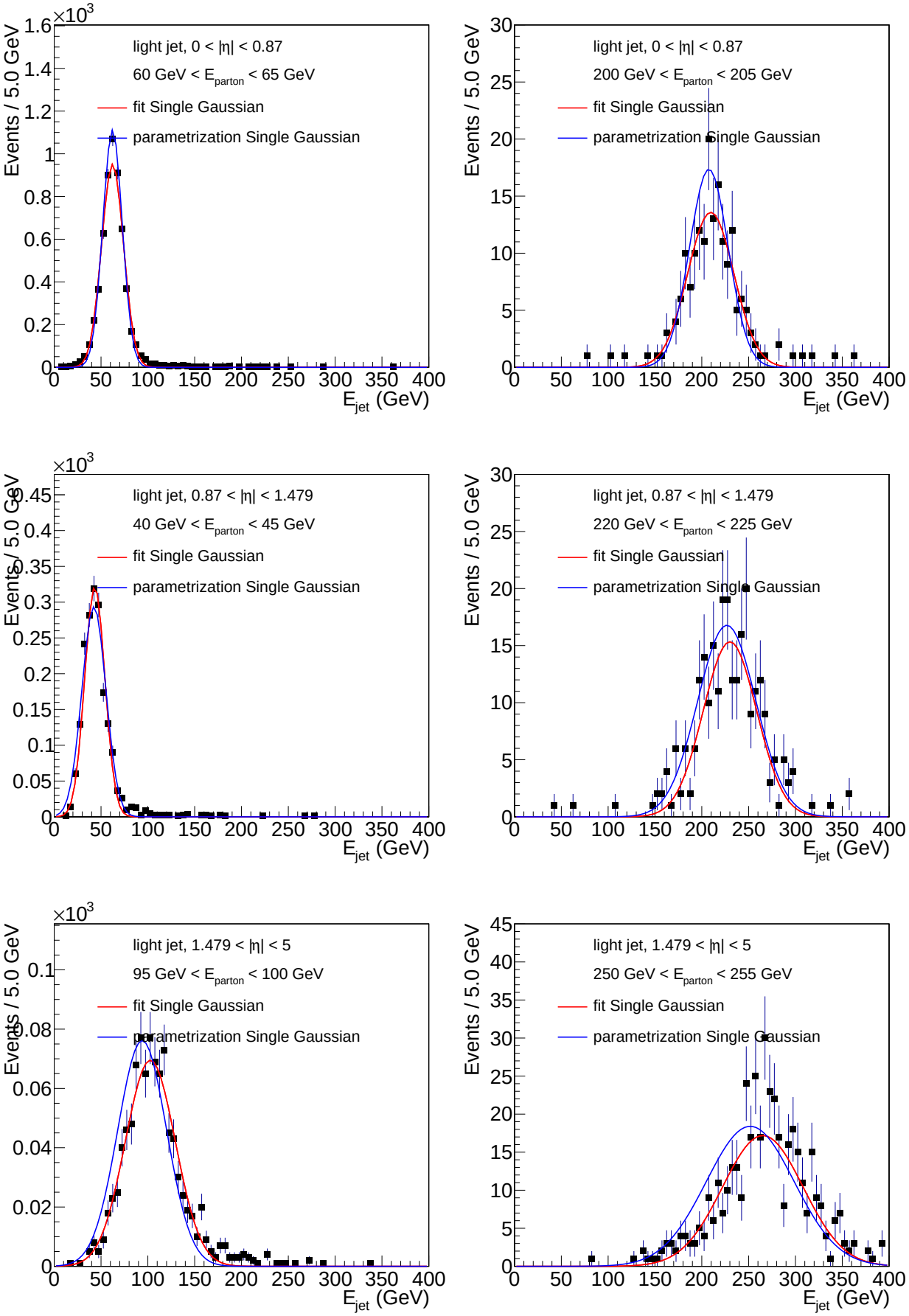

Figure 7.7: Comparison between fitting a single Gaussian and the parametrised results in several bins of E_{parton} and η_{parton} for light jets.

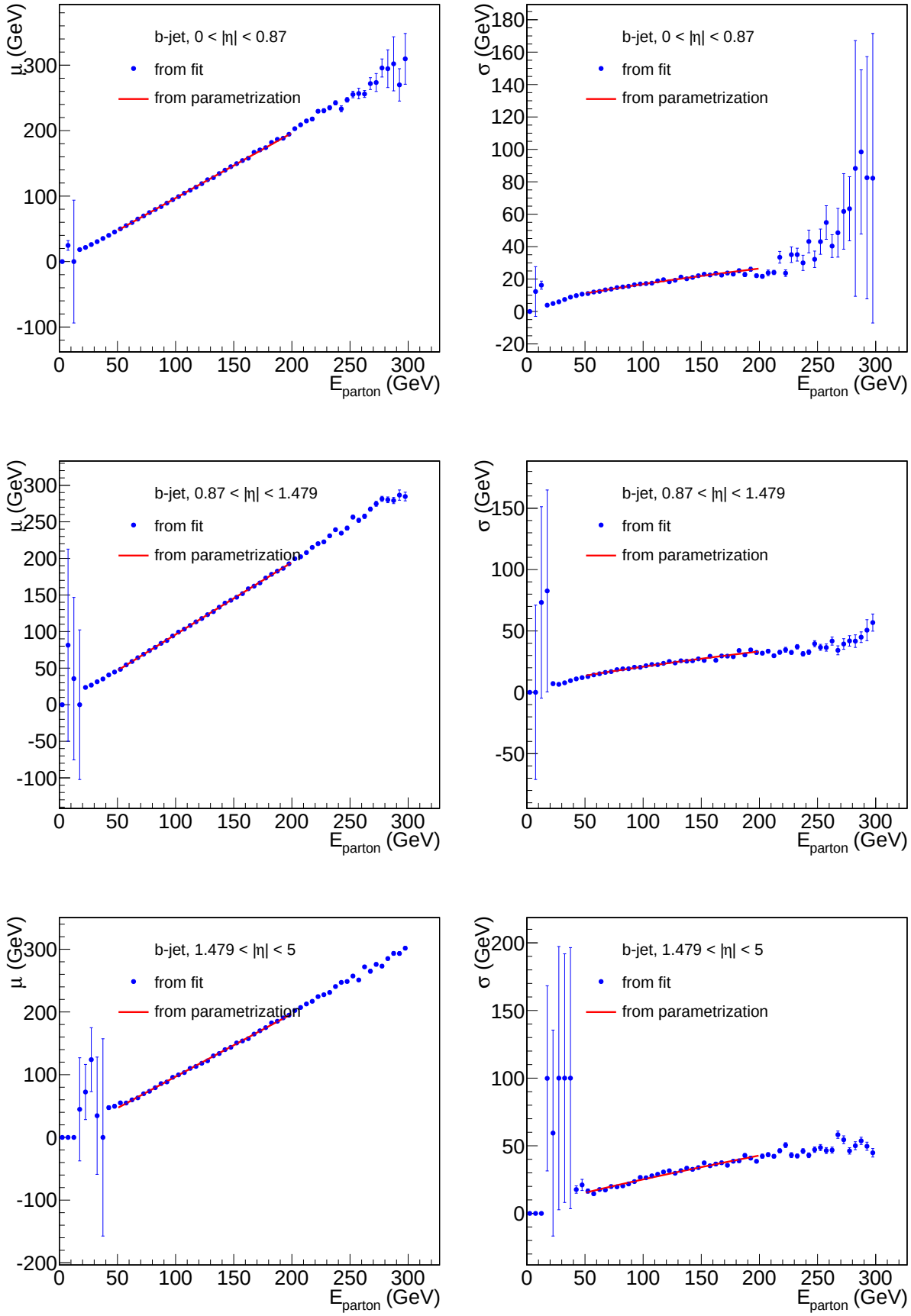

Figure 7.8: Results of the fit used to extract the transfer function parametrisation for b-jets in three slices of parton pseudo-rapidity. The fitted Gaussian mean is plotted on the left, whereas the fitted Gaussian width is plotted on the right.

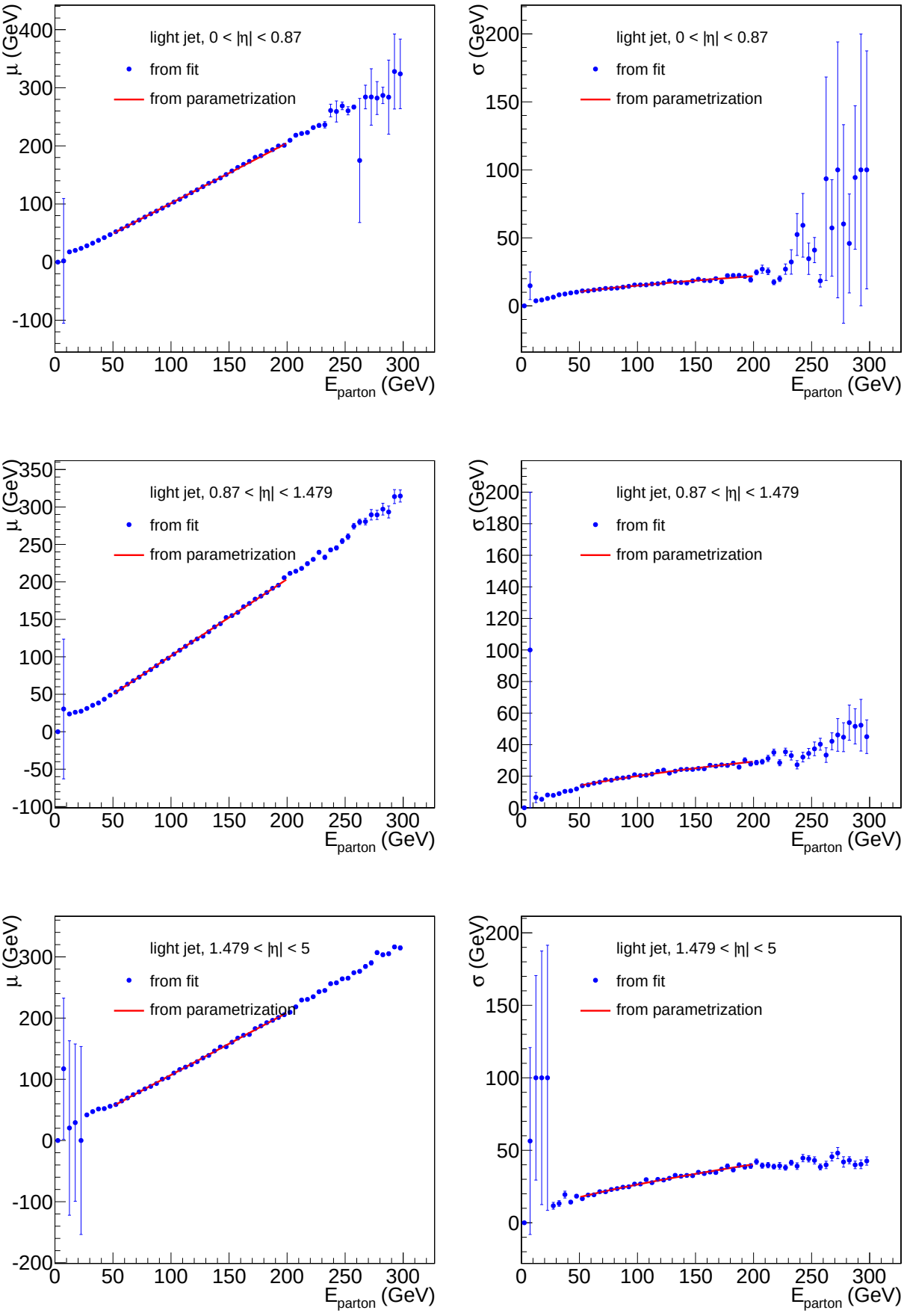

Figure 7.9: Results of the fit used to extract the transfer function parametrisation for light jets in three slices of parton pseudo-rapidity. The fitted Gaussian mean is plotted on the left, whereas the fitted Gaussian width is plotted on the right.

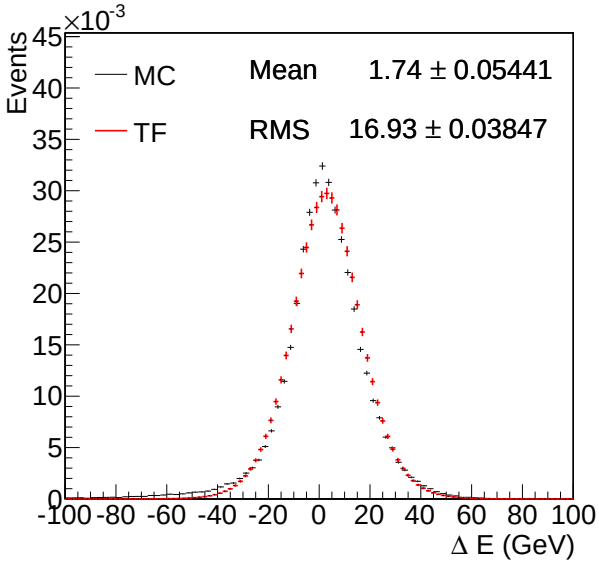

(a) 30GeV $< E_{parton} <$ 100GeV

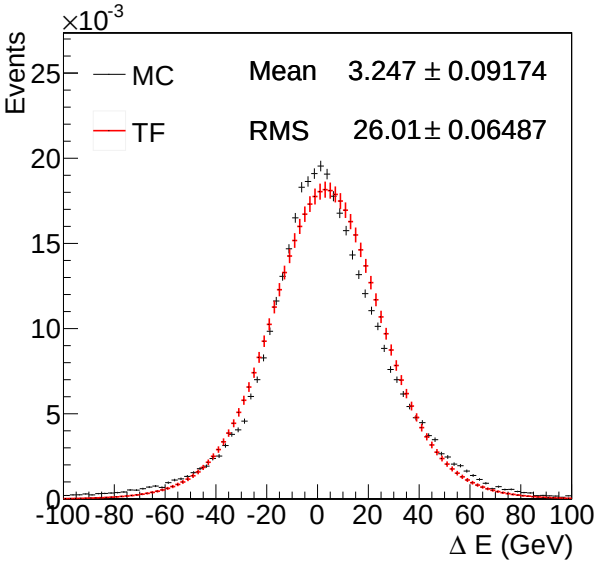

(b) 90GeV $< E_{parton} <$ 180GeV

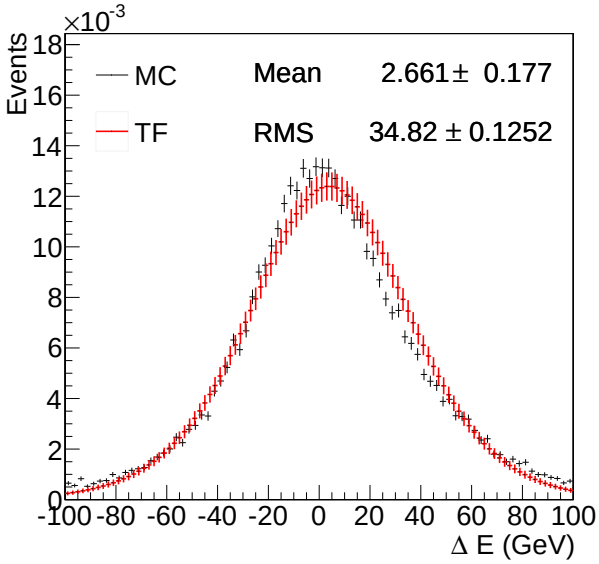

(c) 150GeV $< E_{parton} <$ 250GeV

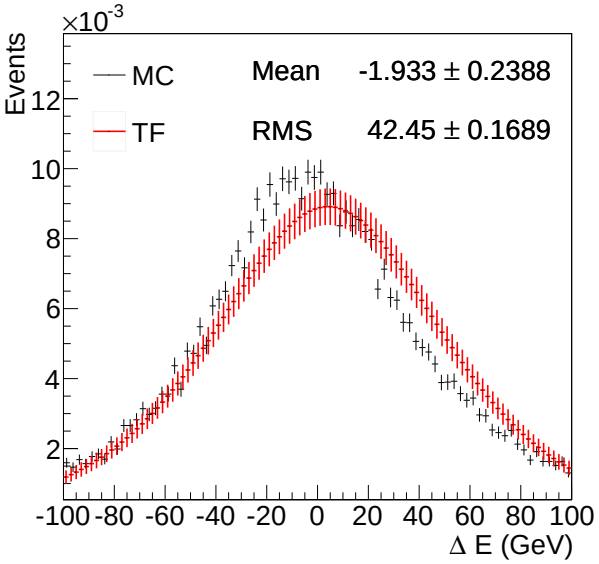

(d) 200GeV $< E_{parton}$

Figure 7.10: Comparison of ΔE-distribution ($E_{parton} - E_{jet}$) based on the simulation values (blue) and based on the determined transfer function (red) in all η_{parton}-slices combined, for b-jets.

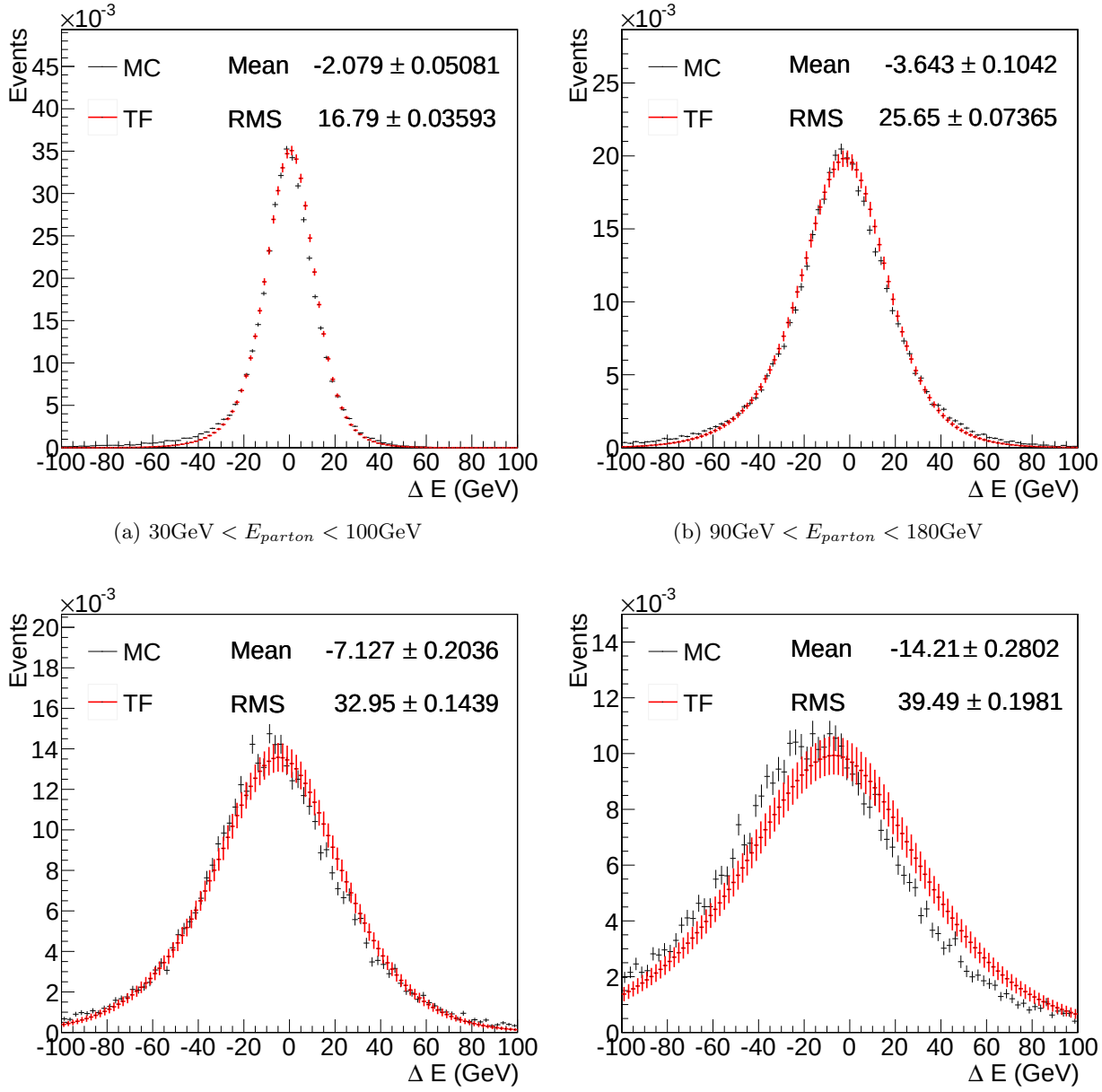

(a) 30GeV $< E_{parton} <$ 100GeV

(b) 90GeV $< E_{parton} <$ 180GeV

(c) 150GeV $< E_{parton} <$ 250GeV

(d) 200GeV $< E_{parton}$

Figure 7.11: Comparison of ΔE-distribution ($E_{parton} - E_{jet}$) based on the simulation values (blue) and based on the determined transfer function (red) in all η_{parton}-slices combined, for light jets.

7.2.2 Angular Variables and Muon Energy

In the CMS detector, angular information is determined precisely enough so that no transfer function needs to be taken into account. This was explicitly checked. In fig. 7.12, the $\Delta\eta = \eta_{parton} - \eta_{jet}$ and $\Delta\phi = \phi_{parton} - \phi_{jet}$ distributions are shown for the same unambiguously, tightly matched jets used in the previous sections, but for all jet types, all jet and parton energies combined. From the plots, we can see that there is no bias in the measured angles as the distribution peaks around 0 and the resolution is sufficiently narrow to be described by a Dirac δ-function.

Also for the reconstructed muon collection, the resolution and potential bias of the kinematic variables were checked. The reconstructed muon was matched to the generator level muon with $\Delta R = 0.3$ to construct the $\Delta\eta$, $\Delta\phi$ and ΔE distributions shown in fig. 7.13-7.14. Also here we see that the angular information is very precise and unbiased. The muon energy resolution is much better than is the case for jets with no bias observed, justifying the usage of a transfer function for the jet energy only.

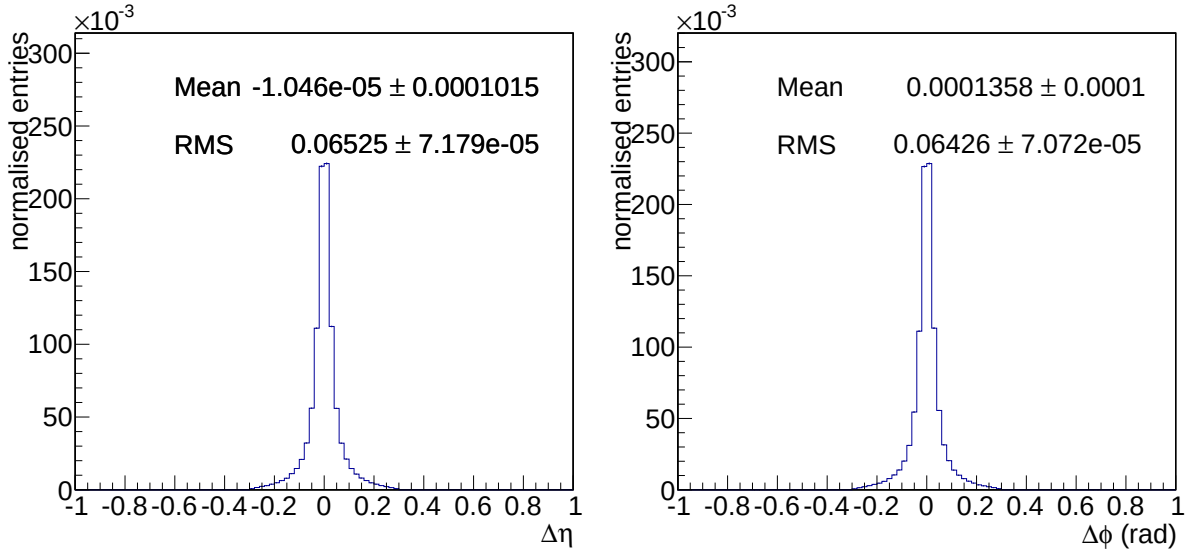

Figure 7.12: $\Delta\eta = \eta_{parton} - \eta_{jet}$ (left) and $\Delta\phi = \phi_{parton} - \phi_{jet}$ (right) distribution of unambiguously matched jets.

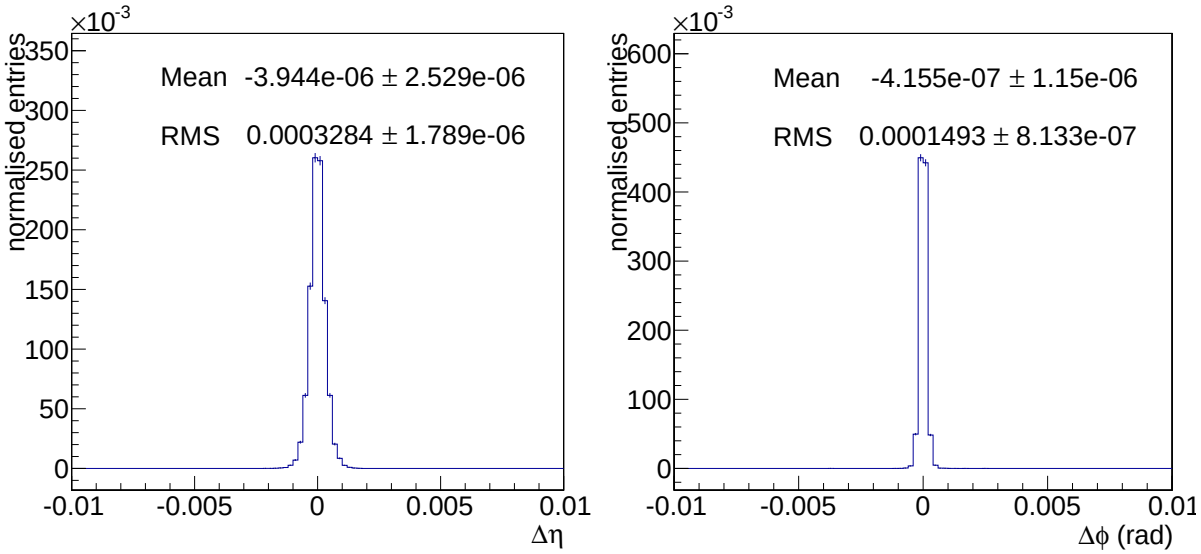

Figure 7.13: $\Delta\eta = \eta_{gen\mu} - \eta_{RECO\mu}$ (left) and $\Delta\phi = \phi_{gen\mu} - \phi_{RECO\mu}$ (right) distribution of unambiguously matched muons.

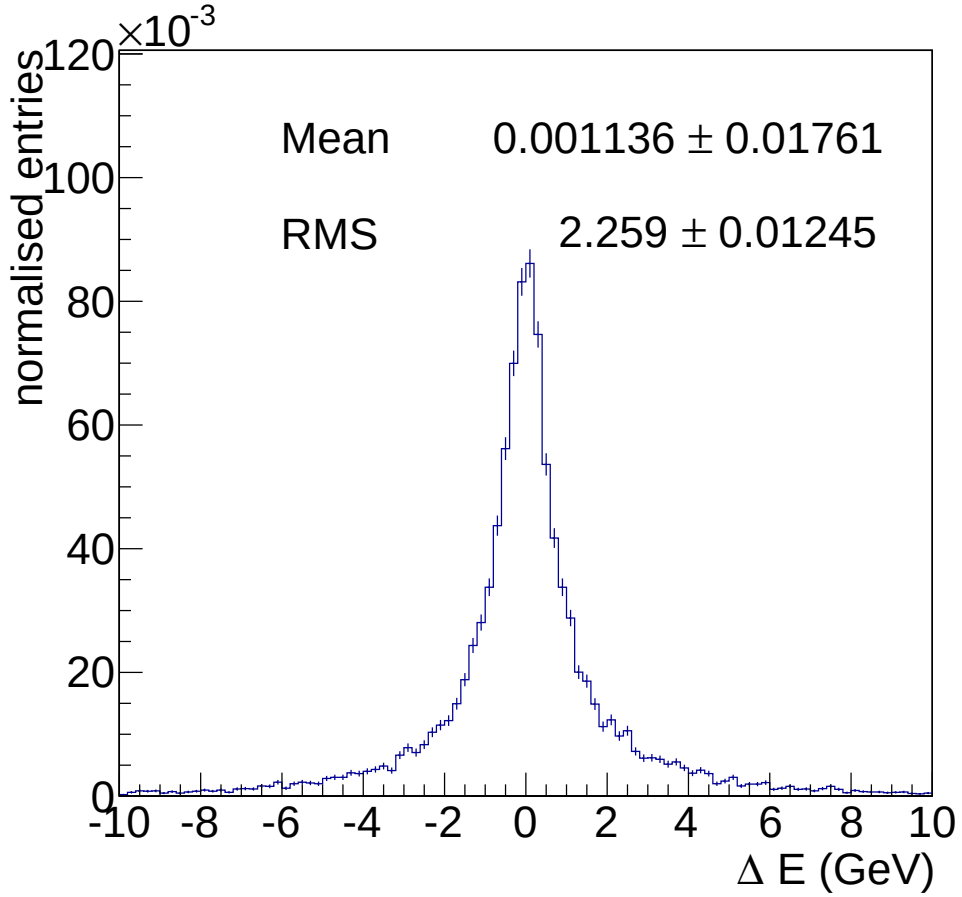

Figure 7.14: $\Delta E = E_{gen\mu} - E_{RECO\mu}$ distribution of unambiguously matched muons.

Chapter 8

Closure Tests

In this analysis, we present a measurement of spin correlation in $t\bar{t}$ systems by making use of a matrix element method. The MEM allows for a two-fold approach in this measurement. We can use the likelihood of the collected data to discriminate between the SM correlated and the uncorrelated hypothesis, which we refer to as: hypothesis testing. In addition, we measure the fraction of events f which exhibit SM spin correlations leading to a measurement of the spin correlation strength. The extraction of this fraction f is done with a template fit to a sensitive variable. In previous measurements, the sensitive variables used are angular dependencies between the $t\bar{t}$ decay products. In this analysis, the sensitive variable is $-2\ln\lambda$, as discussed in chapter 7 which makes use of the full event information.

As a spin correlations measurement using the MEM had not yet been performed at the LHC, extensive closure tests were performed with increasing levels of complexity. With these closure tests, we check the feasibility of this measurement and test whether the analysis methods give consistent results with the known input. At a first stage, the methodology was tested using privately generated samples at LO which offer full control with the production described in section 8.1.1. In a second stage, simulation centrally provided by the CMS collaboration was used, which included NLO calculations, expected background contributions, hadronisation and reconstruction effects.

8.1 Closure Tests at Parton Level

A measurement of the $t\bar{t}$ spin correlation using a MEM requires the reconstruction of the $t\bar{t}$ final state. At NLO, and taking into account hadronisation effects, this is not a trivial task. The feasibility of the analysis is tested at LO parton level which allows for full control. At the parton level, the performance of the HitFit kinematic fitter can be tested and optimised. There are various ways to combine the HitFit output with event likelihood calculations. Here we describe and test the various scenarios. For the tests discussed in this section, privately generated simulation was used. The event generation is described in section 8.1.1. A full description of the hypothesis testing part of this analysis with some sanity checks is shown in section 8.1.2. In section 8.1.3 the template fit part of this analysis has been tested with increasing levels of complication. Finally, in section 8.1.4, the reconstruction of the $t\bar{t}$ final state is taken into account.

8.1.1 Event Generation

For the validation of the analysis at LO, the samples have been produced with the MadGraph event generator, using the matrix elements described in section 7.1.2. The samples were produced at a centre-of-mass energy of 7 TeV, using the CTEQ6L1 PDFs. At the time of the parton level closure tests, the strategy was to perform the measurement on both 7 and 8 TeV CMS data. As the spin correlation strength only has a weak dependence on the center-of-mass energy and the tests are intended to validate the overall methodology, there is no need to perform a set of closure tests with a centre-of-mass energy of 8 TeV. Two $t\bar{t}$ samples were produced: one with the SM correlated matrix element and one with the uncorrelated matrix element. Both samples were generated in the $pp \to t\bar{t} \to bjj\bar{b}e^{-}\overline{\nu}_{e}$ final state. During the event generation, the cross-section

of the generated process is evaluated. The cross-section for the SM correlated and uncorrelated process are identically equal to 4.33 ± 0.02 pb. In addition a background sample was generated from the process $pp \to W^- b\bar{b}jj \to bjj\bar{b}e^-\overline{\nu}_e$ to mimic a background with the same final state as the signal. This background will be referred to as W+jets in the following. 700 000 events were generated for each signal sample and 400 000 events for the background sample. Table 8.1 lists the parameters used in the event generation.

Table 8.1: Parameters used for MadGraph signal generation and matrix element calculation.

Parameter	Value	Unit
$\sqrt{s}$	7	TeV
renormalisation scale	91.1880	GeV
factorisation scale	91.1880	GeV
Breit-Wigner cut-off	15	GeV
m_b	4.7	GeV
m_t	173	GeV
α_s	0.118	
Γ_t	1.491500	GeV
Γ_W	2.047600	GeV

8.1.2 Hypothesis Testing

Each generated event, whether it is a signal or a background event, is processed under the two hypotheses we consider: SM correlated or uncorrelated $t\bar{t}$ semi-leptonic decay. When calculating the event likelihoods, we give the correct jet-parton permutation to MadWeight. This is only possible at the parton level and drastically reduces the CPU requirements for the event likelihood calculation as only one jet-parton permutation needs to be taken into account. In a further stage, described in section 8.2, we will proceed with CMS simulation and data, and it is no longer possible to know the exact jet-parton permutation. However, by placing a b-tag requirement and using a kinematic fitter such as HitFit (see section 4.2), it is possible to make an estimate of the correct permutation. This aspect of the analysis will be discussed extensively in section 8.1.4 to investigate the best strategy to include kinematic fitting information in the analysis. The likelihoods obtained per event for each hypothesis are very close together. The test statistic with maximum separating power λ according to Neyman and Pearson [102] is given by

$$\lambda = \frac{L(H = Uncor)}{L(H = Cor)} \tag{8.1}$$

where $L(H = Cor)$ is the likelihood for the event or the complete sample under the SM correlated hypothesis and similarly $L(H = Uncor)$ for the fully uncorrelated hypothesis, so that λ can be evaluated on the event level or on the sample level. When plotting $-2\ln\lambda_{event}$ (hereafter referred to as the event likelihood ratio) for each event, one obtains a distribution (see fig. 8.1) which is slightly different in shape for $t\bar{t}$ SM correlated events and uncorrelated events. When taking the ratio of the correlated distribution over the uncorrelated distribution, as shown on the bottom plot of fig. 8.1, we can assess whether the difference between both templates is statistically significant. From this plot, we can conclude that (at least at LO parton level), the event likelihood ratio can be used to discriminate between a sample of $t\bar{t}$ semi-leptonic SM correlated or uncorrelated events. When considering the sample likelihood, which is the product of the event likelihoods, this difference becomes larger when more events are added to the sample. Therefore one can plot the distribution of the $-2\ln\lambda_{sample} = -\Sigma 2\ln\lambda_{event}$ (referred to as the sample likelihood ratio) for pseudo-experiments with a fixed sample size N. Due to

the central limit theorem, in case of a large number of pseudo-experiments and large enough sample sizes, this distribution will tend to a Gaussian for which the mean scales by N and the RMS by $\sqrt{N}$. As can be seen from fig. 8.2, where the sample likelihood ratio distribution for repeated pseudo-experiments at a few different sample sizes N are shown, these distributions for the SM correlated and uncorrelated events separate from each other with increasing N. From these distributions, it is possible to calculate the separation power one can obtain with a sample of a given size. The separation power σ is given by

$$\sigma = \frac{\mu_{Cor} - \mu_{Uncor}}{\sqrt{\sigma^2_{Cor} + \sigma^2_{Uncor}}} \tag{8.2}$$

with $\mu_{Cor,Uncor}$ being the means of the distribution and $\sigma_{Cor,Uncor}$ being the spreads of the distributions. The separation power is expressed in standard deviations. This procedure is discussed in [108].

Using pseudo-experiments with varying sample sizes, we can extract the separation power as a function of sample size as plotted in fig. 8.3. Fitting a power law to the distribution, we obtain an exponent of 0.505 ± 0.014, meaning the separation power scales with the square root of the sample size, which is expected from statistics theory [108] and provides a sanity check. This implies that we can calculate a priori what the necessary sample size is to obtain a certain separation power, at the generator level. This procedure could be repeated using the reconstructed simulation to evaluate what the obtainable separating power is at the observed dataset size in the collected 2012 data. However this treatment of the separating power only includes statistical effects. When systematic effects are taken into account, the sample likelihood ratio distributions are no longer expected to be Gaussian and as a consequence, it is no longer possible to use equation 8.2 to calculate the separation power.

On the data sample we will investigate later on, we calculate the sample likelihood once under the SM hypothesis and once under the uncorrelated hypothesis. This will give us one value of $-2\ln\lambda_{sample}$. By drawing pseudo-experiments at the observed dataset size from the reconstructed simulation, including background processes and all corrections to account for differences observed in simulation and data, the $-2\ln\lambda_{sample}$ distributions will be set up. By comparing the sample likelihood ratio observed in data to the distributions made by our two hypotheses, we can conclude whether the data is more compatible with either the SM hypothesis or the uncorrelated hypothesis. This compatibility can be quantised in terms of the separating power we've briefly discussed earlier and this will be further discussed in chapter 9.

8.1.3 Extraction of Spin Correlation Fraction

In section 8.1.2, we have discussed hypothesis testing which allows us to evaluate which hypothesis the data is more compatible with. In addition, we would like to extract the fraction of events which exhibit SM spin correlations, denoted by f, to have a more direct measurement of the spin correlation strength. As discussed in section 1.3, the SM fraction f is defined as $N^{SM}_{t\bar{t}}/(N^{SM}_{t\bar{t}} + N^{Uncor}_{t\bar{t}})$.

In a template fit, the goal is to extract a certain parameter (in our case f), by setting up templates of a distribution sensitive to this parameter, with varying values of this parameter. In a fit to this distribution in the data, a linear combination of the simulation templates is fitted to describe the data best, leading to a measurement of the admixture of the different templates in the data. Here we present closure tests at parton-level information, where we have full control, to test the methodology.

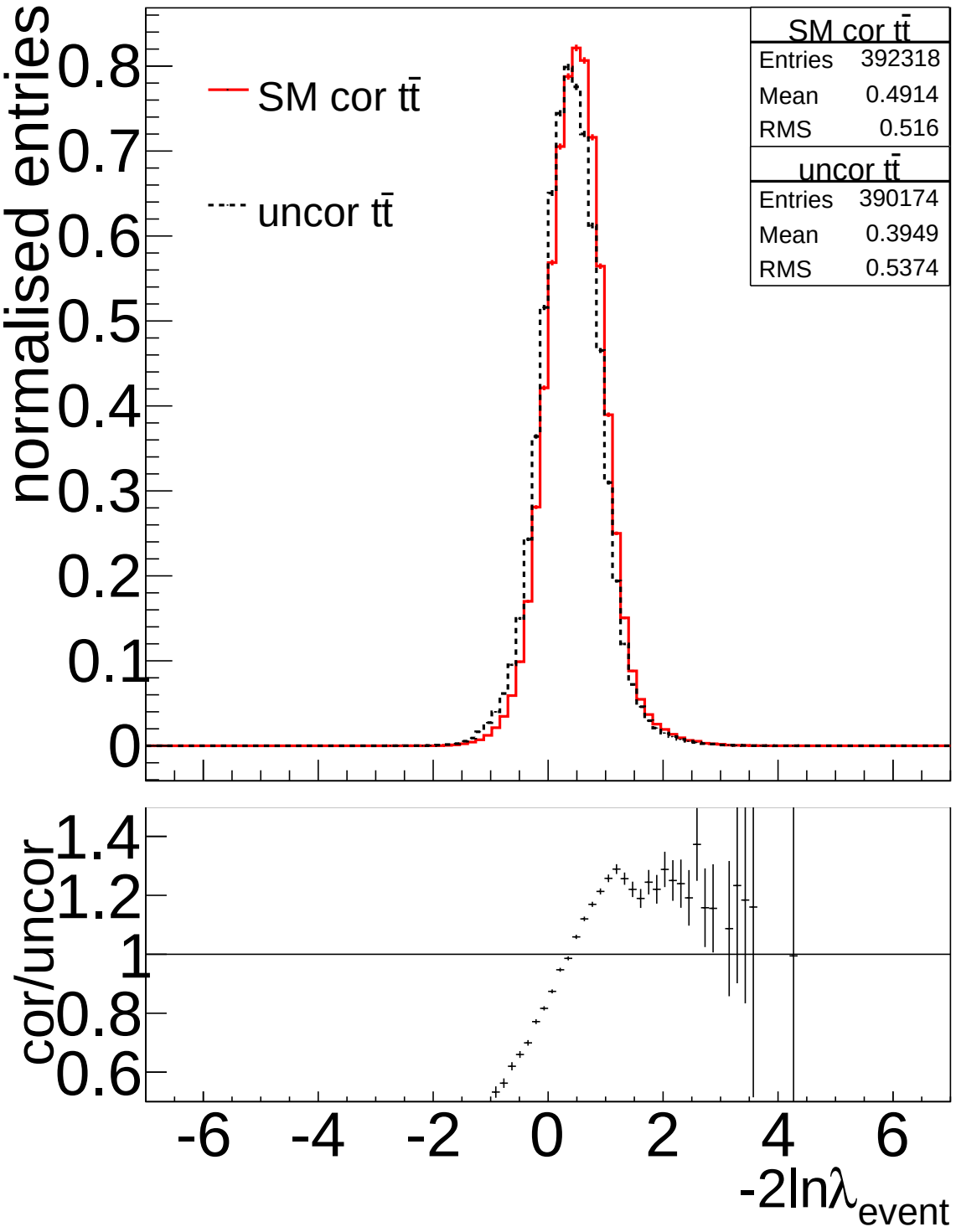

Figure 8.1: Histograms of $-2\ln\lambda_{event} = 2\ln L_{event}(H = Cor) - 2\ln L_{event}(H = Uncor)$ for individual events from generated samples according to $H = Cor$ (red solid histogram) and $H = Uncor$ (black dashed histogram). The plot shows a shape comparison. The ratio of the correlated likelihood ratio over the uncorrelated likelihood ratio is shown in the bottom plot.

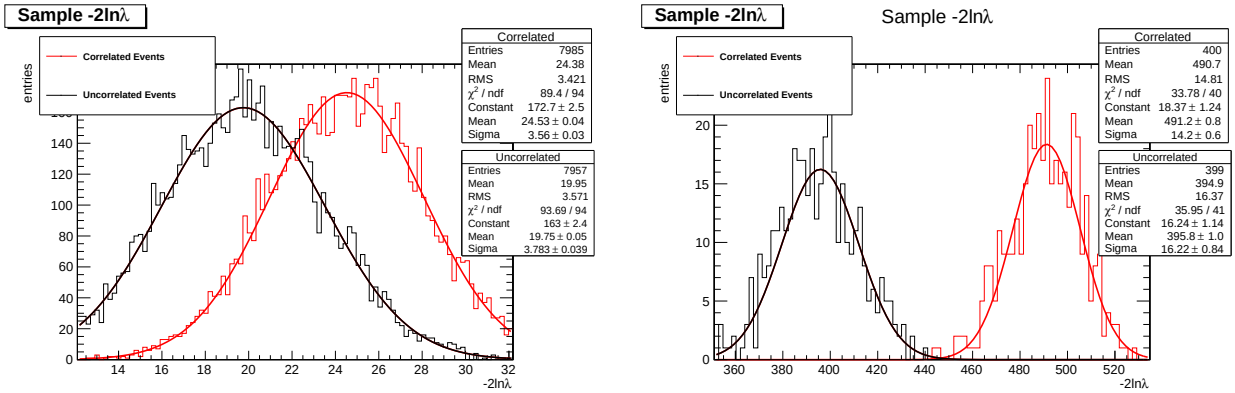

Figure 8.2: Histograms of $-2\ln\lambda_{sample}$ for 50 events (left) and 1000 events (right) per pseudo-experiment. In each plot the red curve (right) represents correlated data, while the black curve (left) represents uncorrelated data. The superimposed Gaussian fits have a mean and RMS which is compatible with the values expected from the scaling laws.

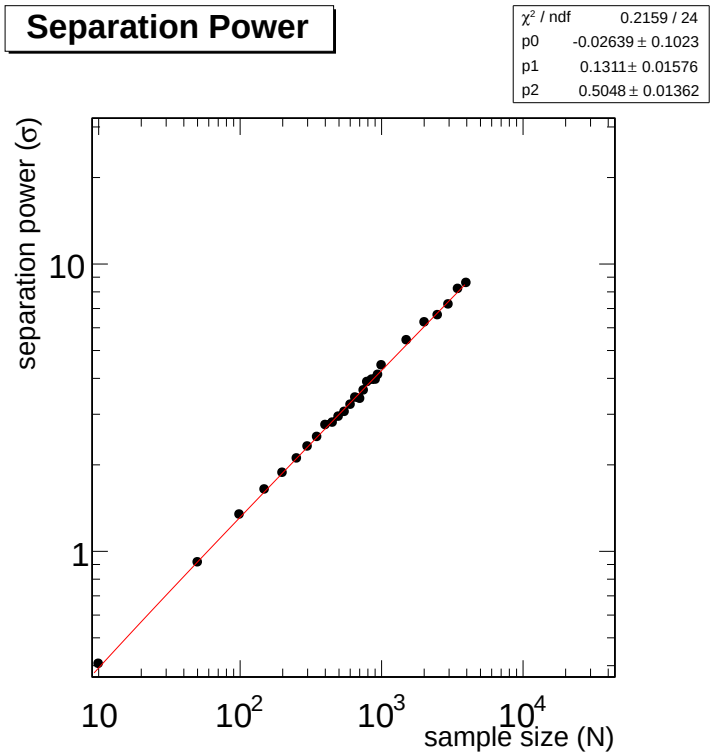

Figure 8.3: Separation power (expressed in number of standard deviations as defined in eq. 8.2) as a function of the sample size of the performed pseudo-experiments. The power law fit to the plot is also shown.

To extract the fraction of events with SM spin correlation f, we set up a template fit to the $-2\ln\lambda_{event}$ distribution of the event likelihoods. Any distribution that is able to discriminate between spin-correlated (i.e. SM) and spin-uncorrelated events can be used, but to have maximum sensitivity the $-2\ln\lambda_{event}$ distribution, normalised to unit integral, was chosen as template since the likelihood calculations take the full event information into account. We need three input templates: one of spin-correlated signal events (corresponding to $f = 1$), one of spin-uncorrelated signal events (corresponding to $f = 0$) and one describing the background.

The templates include the full statistics we have available, and the effect of the statistical precision of the templates will be estimated. The fit is based on a binned maximum likelihood fit in RooFit [70], using Minuit [109]. The fit model is implemented as follows:

$$model = N_{t\bar{t}}[fT_{cor} + (1-f)T_{uncor}] + N_{bkg}T_{bkg} \tag{8.3}$$

The templates are represented by T_{cor}, T_{uncor}, and T_{bkg} for the spin-correlated, spin-uncorrelated and the background templates respectively. Here, f (often referred to as f^{SM} in other analyses) is the fit parameter of interest. $N_{t\bar{t}}$ and N_{bkg} describe the yield of $t\bar{t}$ signal events and background events. In the generator level closure tests, the total event yield is left floating in the fit and the background term is dropped in the closure tests that do not take background into account. In the fit, all fit parameters f,$N_{t\bar{t}}$ and N_{bkg} are fully unconstrained. Example fits to spin-correlated pseudo-data which have $f_{input} = 1$ and no background contribution, can be found in fig. 8.4. Three different scenarios are shown in which the fitted f is compatible with the input within the uncertainty, in which the fitted f overestimates the input and in which the fitted f underestimates the input. The different contributions from the input templates are shown in the plot. The fit range used is [-7,7] in the parton level closure tests. The bin-width for each histogram is 0.14.
The fit is performed numerous times to independent pseudo-data samples. The pseudo-experiments are set up to be completely independent from each other i.e. no resampling is used. The number of pseudo-data events per pseudo-experiment is drawn from a Poisson distribution with a mean of 500. This allows us to study the statistical fluctuations on the fit results. A series of closure tests at the generator level with increasing complexity have been performed. For these tests, our LO simulation samples (described in 8.1.1) have been used, where we have kept the correct matching between the event kinematics and the role of the parton in the decay. As a first level of complication, acceptance cuts (described in table 8.2) were introduced. The selection efficiency of the correlated and uncorrelated events was compared. No bias towards correlated or uncorrelated events due to the kinematic acceptance cuts is observed. As a second level of complication, background was added to the pseudo-data. We chose a W+jets sample described in section 8.1.1. A third level of complication is the smearing of the parton kinematics with a semi-realistic double-Gaussian transfer function. The same transfer function was then used in the event likelihood calculation. A list of the various closure tests performed is shown in table 8.3.

Table 8.2: Cumulative selection efficiency table. Based on unsmeared parton level information.

Variable and Cut	$\epsilon\, N_{t\bar{t}}^{SM}$	$\epsilon\, N_{t\bar{t}}^{uncor}$
$p_T(j) > 30$ GeV,$\lvert\eta(j)\rvert < 2.4$	48 %	48 %
$p_T(e) > 30$ GeV,$\lvert\eta(e)\rvert < 2.5$ (excluding the gap in ECAL)	31 %	31 %

Closure Test Gen. Level 1: Signal Only, Unsmeared Kinematics, Full Phase Space
The first set of closure tests is performed with only $t\bar{t}$ semi-leptonic events at LO generator level with no cuts on the transverse momentum or the pseudo-rapidity applied. This allows us to keep full control and maintain the full separating power of the $-2\ln\lambda_{event}$ distribution, undiluted by NLO, showering or kinematic cut effects. The failure of this basic closure test would teach us that this measurement is not feasible with the $-2\ln\lambda_{event}$ distribution.

For this closure test, a simplified version of the fit model in eq. 8.3 is used, since no background

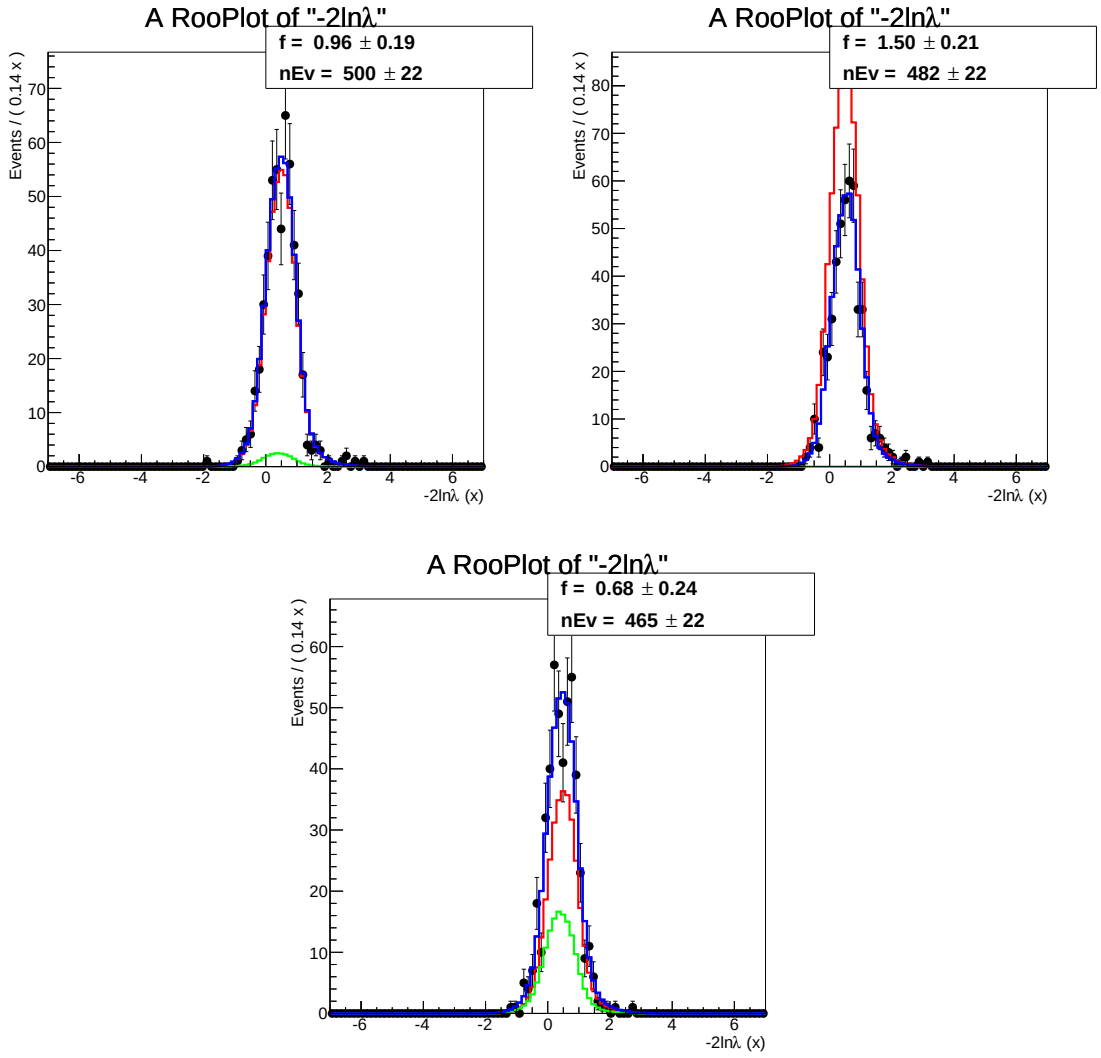

Figure 8.4: Example fits for three different pseudo-experiments performed using RooFit and Minuit, using spin-correlated pseudo-data with 500 events per pseudo-experiment. In the fit for the three pseudo-experiment, a value of $f = 1$ is expected. The fits show the fluctuations possible for $f \approx 1$ (top left), $f > 1$ (top right) and $f < 1$ (bottom). The blue curve shows the total fit, the red one shows the contribution of the spin-correlated template and the green one of the spin-uncorrelated template.

Table 8.3: Various scenarios and conditions of the closure tests

Closure test	Background contribution	smeared parton kinematics	acceptance cuts
Gen. level 1	-	-	-
Gen. level 2	-	-	yes
Gen. level 3	yes	-	yes
Gen. level 4	-	yes	yes
Gen. level 5	yes	yes	yes

is included in the tests.

$$model = N_{obs}[fT_{cor} + (1-f)T_{uncor}] \tag{8.4}$$

Here $N_{t\bar{t}}$ corresponds to the total number of observed events N_{obs}. The results of the pseudo-experiments on spin-correlated data ($f_{input} = 1$) are reported in fig. 8.5. On the left plot of that figure, f obtained from the fit for each pseudo-experiment is plotted. One can see a Gaussian distribution centred around 1, which is what one anticipates for spin-correlated data. The middle plot shows the distribution of the fit uncertainty δf. With these elements, one can generate the pull $\frac{f-f_{input}}{\delta f}$ for each pseudo-experiment. The Pull distribution of the fitted f's is shown in fig. 8.5 on the right. We obtain a Gaussian distribution centred around zero, meaning our fit results are not biased and we see a RMS of ≈ 1, ensuring our method estimates the uncertainties correctly. In plot 8.6, the left plot shows the fitted number of events N_{obs} for each pseudo-experiment, Gaussian distributed around a mean of 500, which is consistent with the way we set up our pseudo-experiments, as a Poisson distribution tends to a Gaussian at high means. The middle plot shows the uncertainty on the fitted number of events δN_{obs} and the right plot shows the pull distribution for N_{obs} calculated as $(N_{obs} - 500)/\delta N_{obs}$. The absolute correlation between the fit parameters f and N_{obs} is less than $\sim 10^{-6}$. From this low correlation and the unbiased pull distributions, we can conclude that we can simultaneously extract f and make a cross section estimate (in the form of the total number of observed events). In fig. 8.7-8.8 the same plots are shown for the spin-uncorrelated pseudo-data (where $f_{input} = 0$), where we see a mean f of zero. From the pull distributions, we can conclude that also for uncorrelated pseudo-data, we can extract both f and N_{obs} without a bias and with proper uncertainty estimation.
The uncertainties obtained from the fit are driven by the statistical uncertainties of the pseudo-data distribution. Therefore we checked whether the uncertainties scale appropriately with the sample size. We repeated the extraction of the mean fit uncertainty for varying sample sizes, the result of which is plotted in fig. 8.9. It is checked that the uncertainties on the spin-correlated and spin-uncorrelated pseudo-data are very similar. Applying a power law fit to the points, we obtain an exponent of -0.51, which is not completely in agreement with the expected value of -0.5, but with low sample sizes as in the first two points, the template fit error calculation has a small bias as we have noticed in our pseudo-experiments and which is also the reason we do not go below a sample size of 500 for the closure tests.

Now we have established that the method performs adequately on generator level in the extreme cases of spin-correlated or fully spin-uncorrelated pseudo-data. As a next step in the validation, we tested the performance on samples with varying fractions of SM spin correlation. Since it is not possible to vary this fraction at generation, we manually mixed the spin-correlated and spin-uncorrelated samples in the corresponding fractions of f_{input}. For each spin correlation fraction, we perform pseudo-experiments in which the total number of events ($N_{obs} = N_{t\bar{t}}$) is drawn from a Poisson distribution with a mean of 500. Of this total, we require exactly $f \times N_{obs}$ spin-correlated events and $(1-f) \times N_{obs}$ spin-uncorrelated events. The distribution of f and the pull are Gaussian. The Gaussian mean of the f distribution is presented in fig. 8.10 as a function of the input SM fraction f_{input} and the uncertainty bars represent the uncertainty on the Gaussian mean. In order to have an unbiased method, the mean f as a function of f_{input} should be compatible with the unit line. From fig. 8.10 we see that the linear fit is indeed compatible with the unit line. The bottom plot shows the difference of the mean f and f_{input} and shows the uncertainty bars and a potential bias more clearly. The mean and RMS of the pull distribution are shown in fig. 8.11, from which we conclude there is a negligible bias and correct uncertainty estimation.

Lastly, we wish to have an initial check of the effect of the template statistics. For this purpose, the fit was repeated for one given pseudo-experiment of about 500 events (of $f_{input} = 1$), but

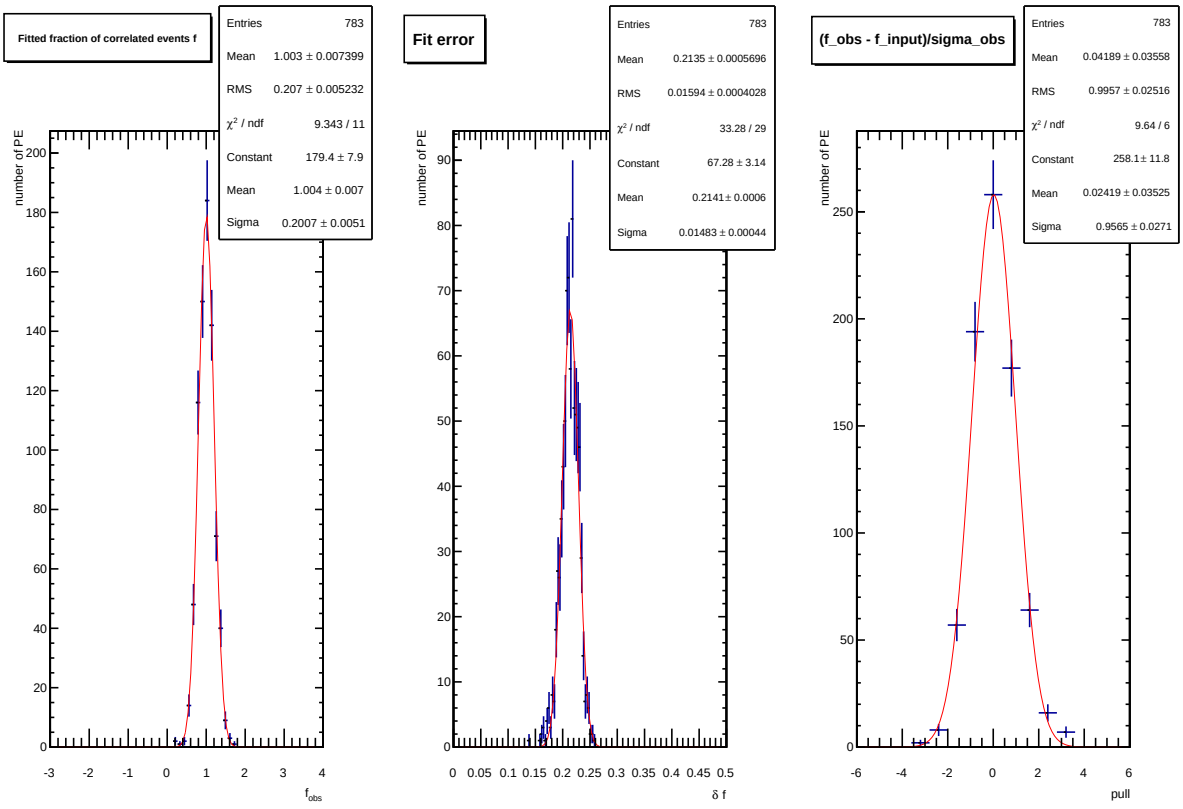

Figure 8.5: Pseudo-experiments performed using spin-correlated simulation events ($f_{input} = 1$) with Poisson distributed sample size with a mean of 500. The distributions of the spread of the fitted f (left), of the fit uncertainty δf (middle), pull distribution (right).

each bin in the template shape was varied within the statistical uncertainty bars. This fit was repeated on the same pseudo-experiment 500 times and the variation of the fitted f is shown in fig. 8.12. In this case the mean of the fitted f distribution is not important, we are interested however in the RMS which is now solely due to the statistical template shape variation. At the generator level, with about $4 \cdot 10^5$ events in the templates, we see the uncertainty on the fit result due to template statistics is of the order of a few percent. This shows that the effect of the template statistics will definitely have to be propagated to the final result of the measurement. In addition, this check gives a handle on the statistics needed in the full CMS simulation.

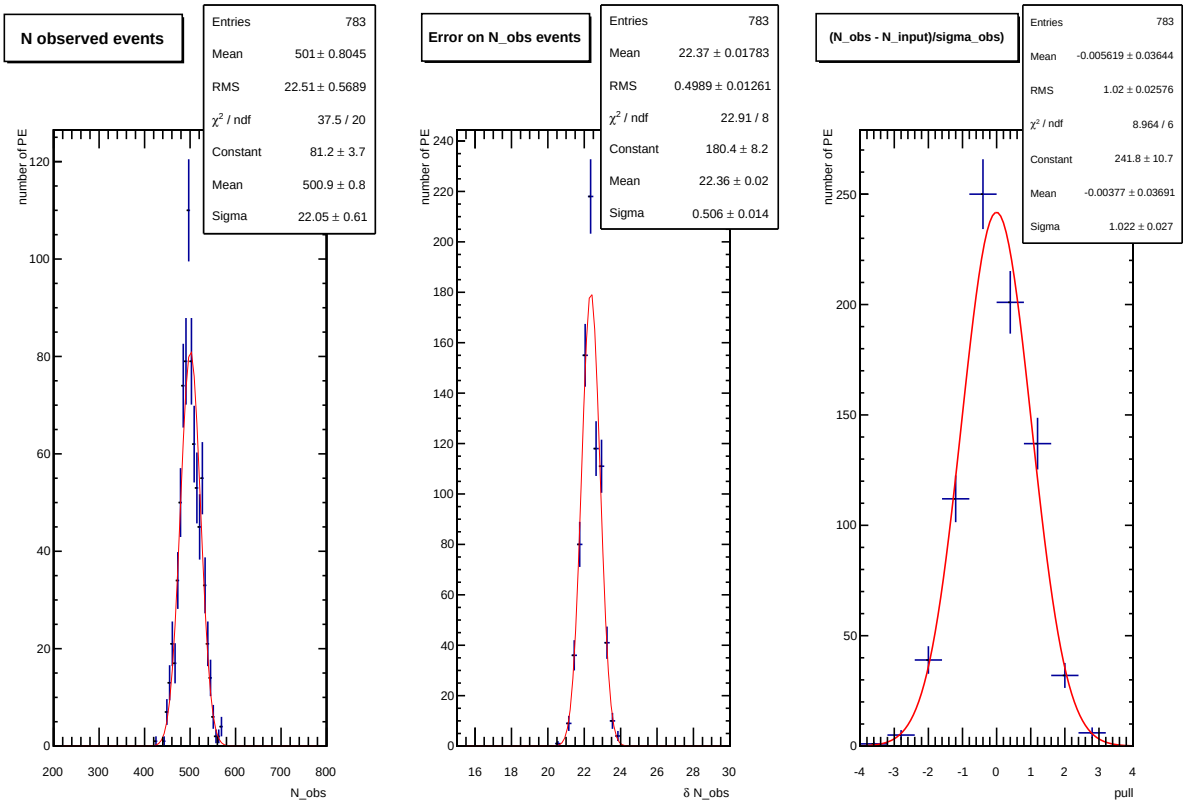

Figure 8.6: Pseudo-experiments performed using spin-correlated simulation events ($f_{input} = 1$) with Poisson distributed sample size with a mean of 500. The fitted number of observed events in the pseudo-experiment is shown N_{obs} (left), the fit uncertainty δN_{obs} (middle) and pull distribution (right).

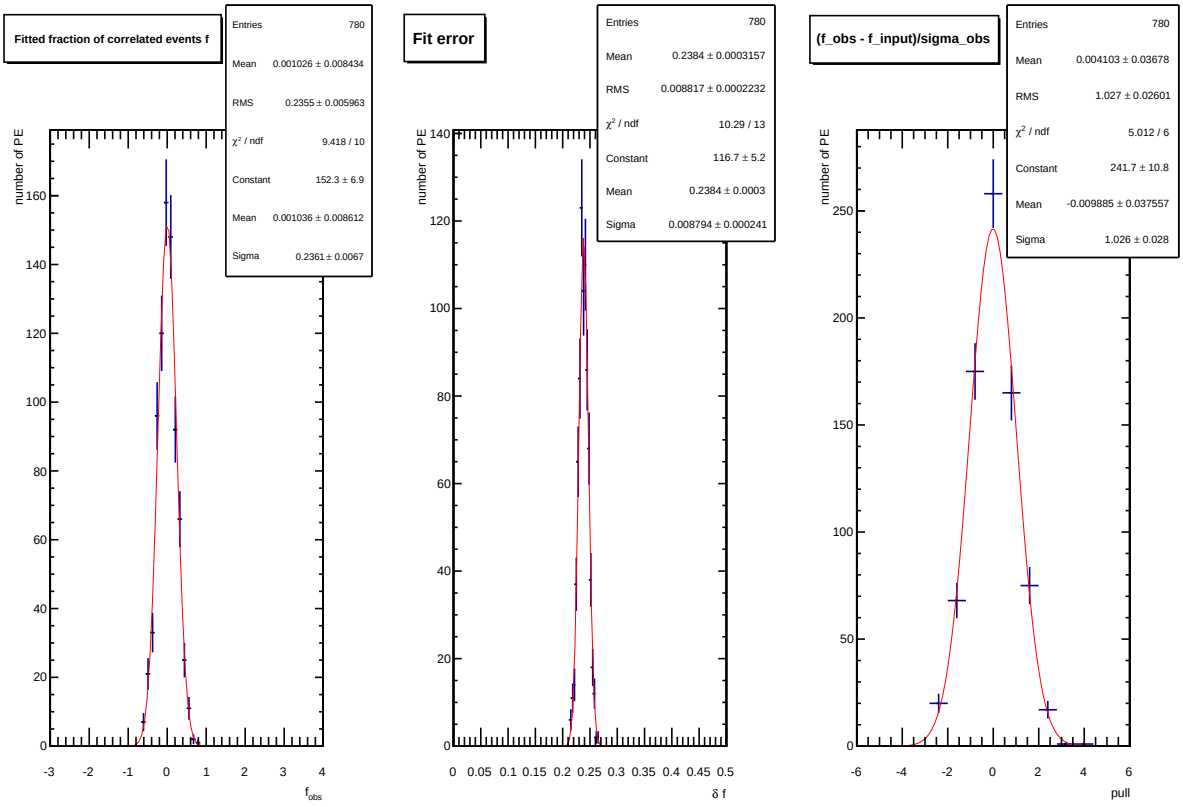

Figure 8.7: Pseudo-experiments performed using spin-uncorrelated simulation events ($f_{input} = 0$) with Poisson distributed sample size with a mean of 500. The distributions of the spread of the fitted f (left), of the fit uncertainty δf (middle), pull distribution (right).

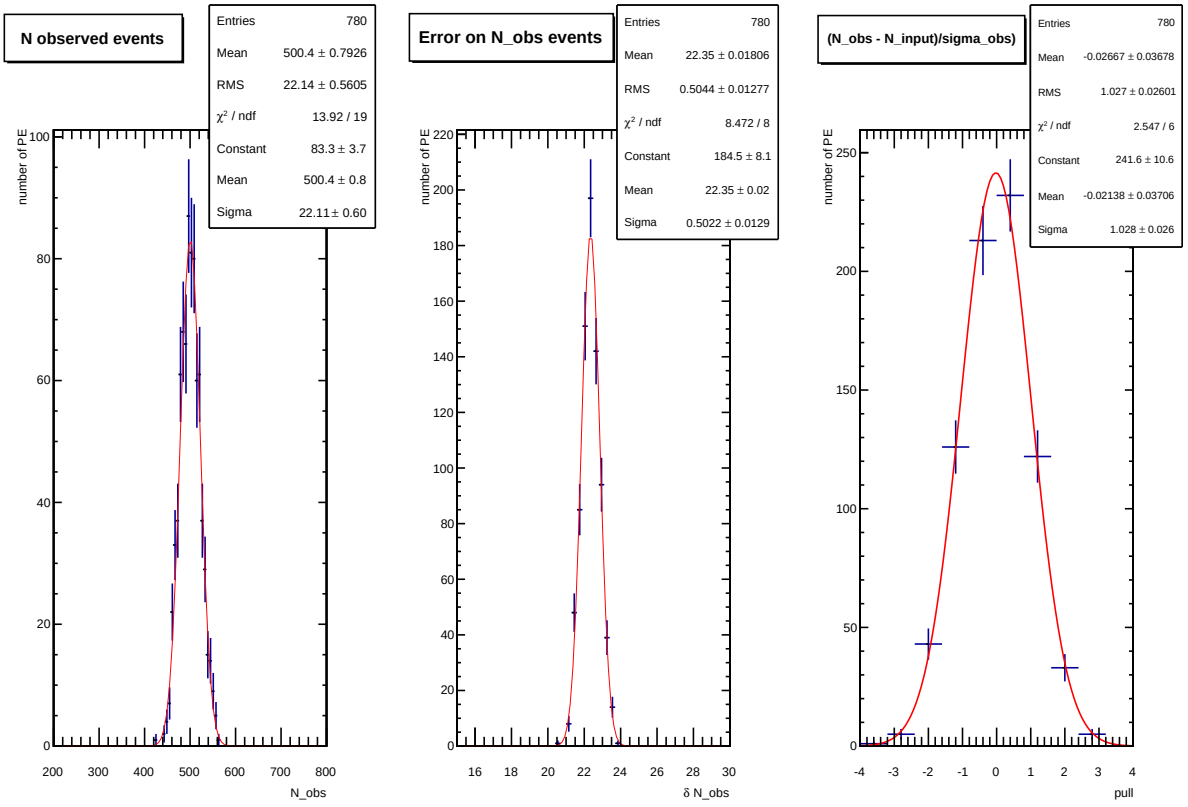

Figure 8.8: Pseudo-experiments performed using spin-uncorrelated simulation events ($f_{input} = 0$) with Poisson distributed sample size with a mean of 500. The fitted number of observed events in the pseudo-experiment is shown (left), the fit uncertainty (middle) and pull distribution (right).

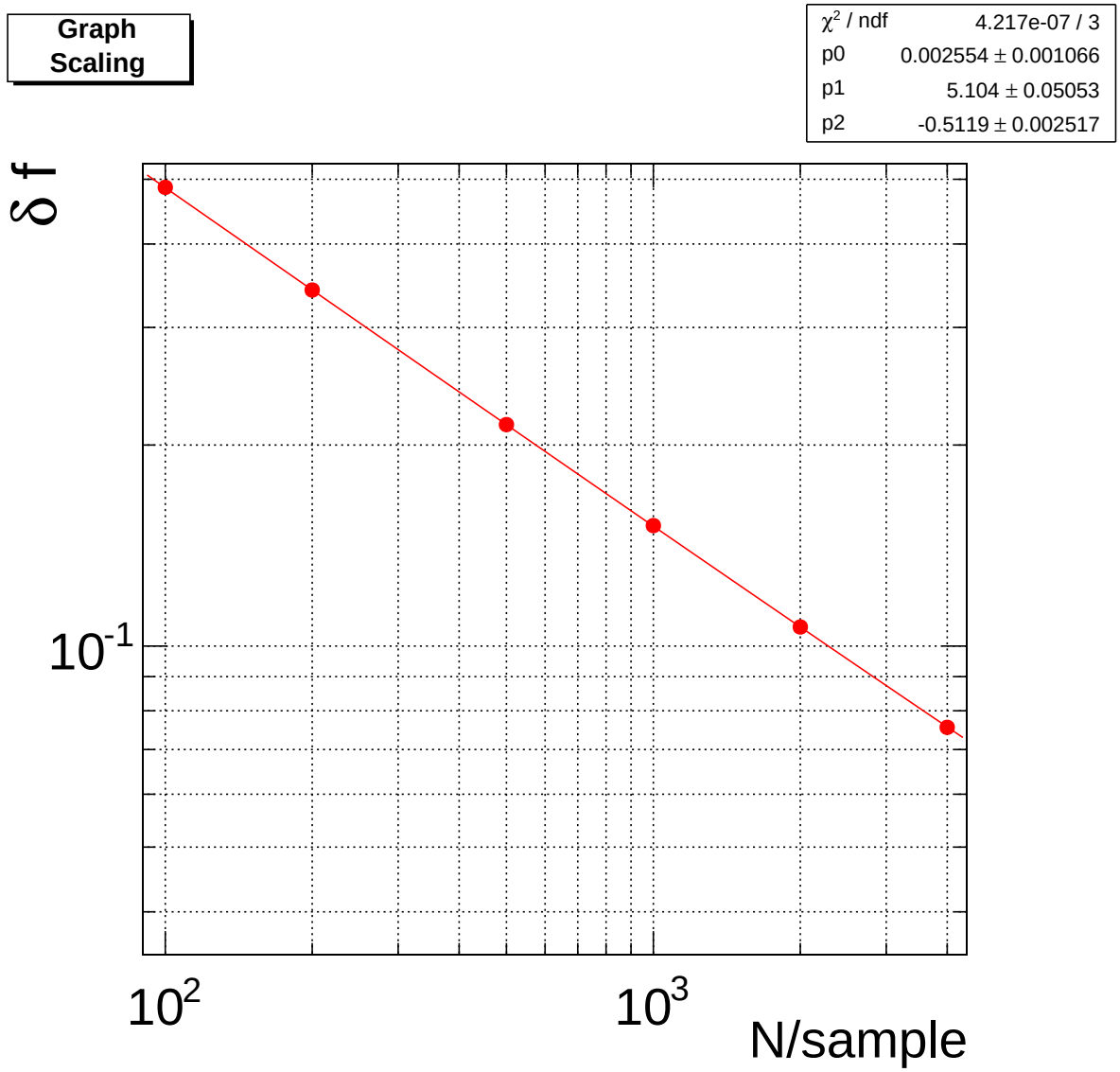

Figure 8.9: The mean fit uncertainty obtained from repeated pseudo-experiments as a function of the sample size of the pseudo-experiments. A power-law fit is also shown. This uncertainty represents the statistical uncertainty attainable with a certain sample size at the generator level assuming an ideal detector.

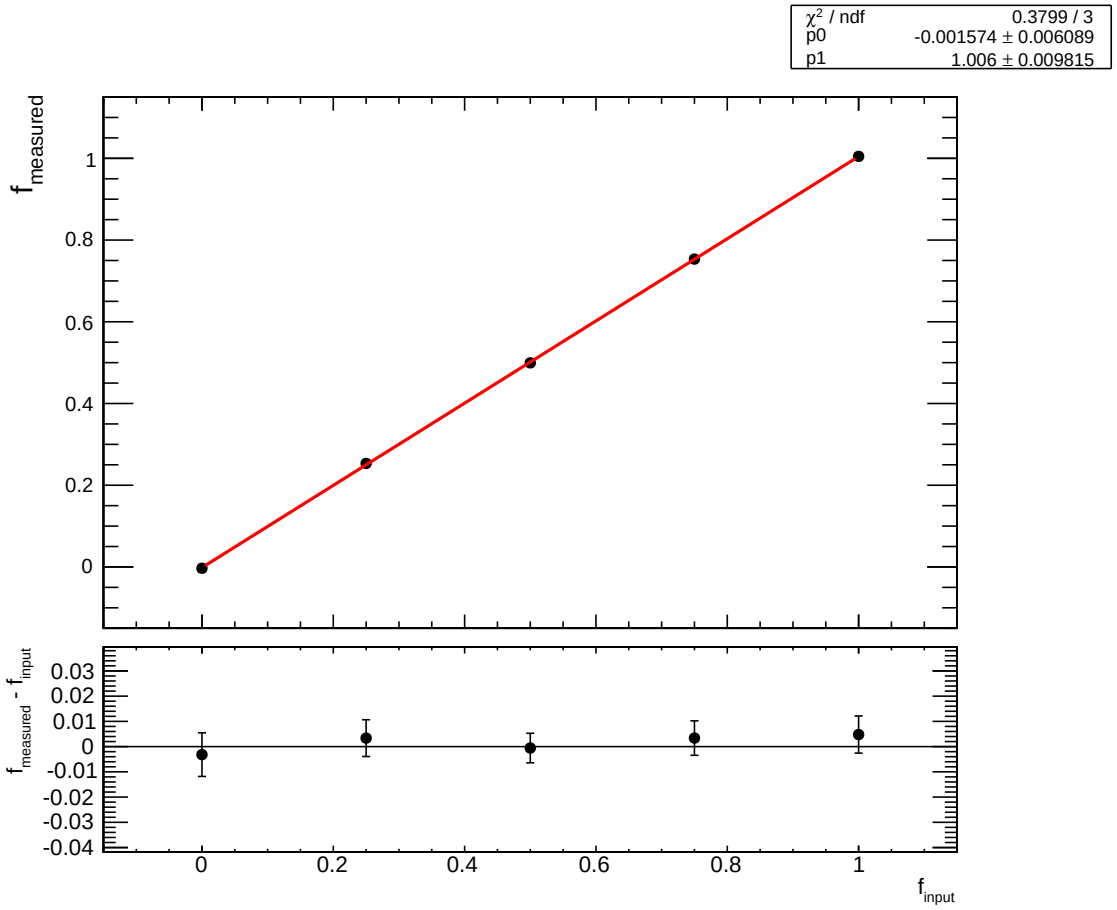

Figure 8.10: Mean of the Gaussian distribution fitted to the f as a function of f_{input}, which is obtained by mixing spin-correlated and spin-uncorrelated samples. The uncertainty bar is obtained from the uncertainty on the Gaussian fit parameter. The results are obtained from repeated pseudo-experiments with a sample size of 500 events each.

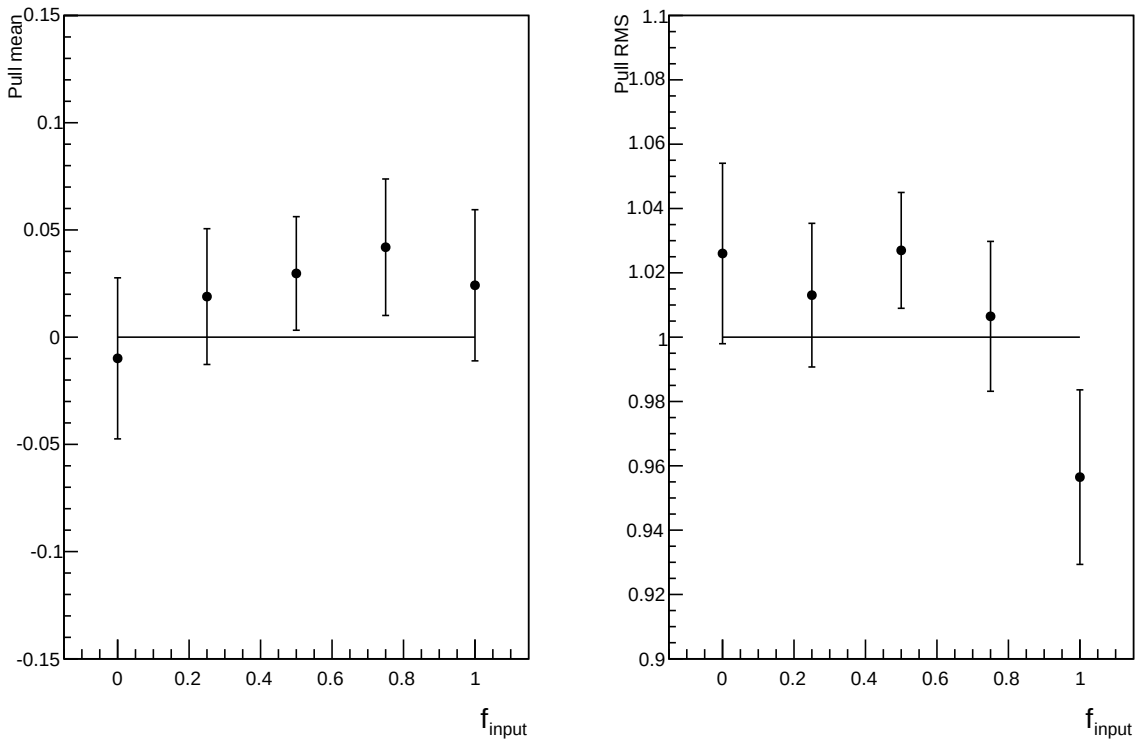

Figure 8.11: Mean of the Gaussian distribution fitted to the pulls (left) as a function of f_{input}, which is obtained by mixing spin-correlated and spin-uncorrelated samples and the pull RMS on the right. The uncertainty bars are obtained from the uncertainty on the Gaussian fit parameter. The results are obtained from repeated pseudo-experiments with a sample size of 500 events each.

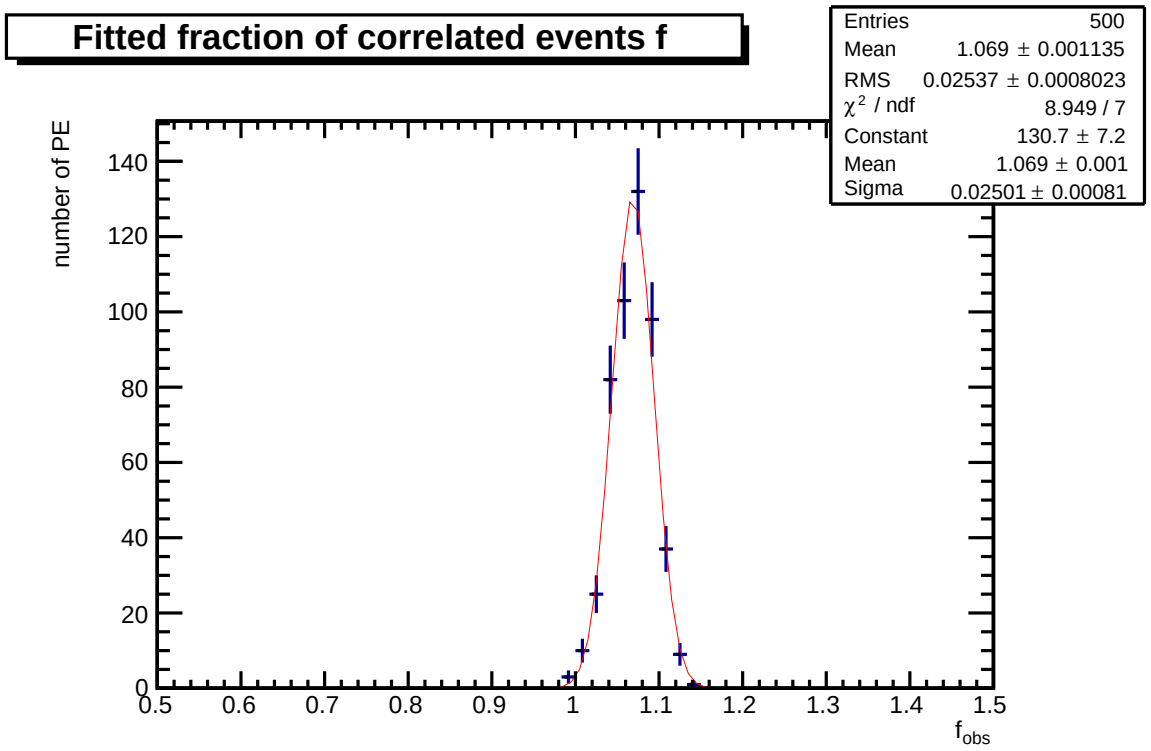

Figure 8.12: The variation of the fitted f due to the template fluctuations is shown. The fit is performed on a given pseudo-experiment of $f_{input} = 1$ and $f = 1.07$ with about 500 spin-correlated simulation events. The template shape is varied within the template statistics and the fit is repeated 500 times.

Closure Test Gen. Level 2: Signal Only, Unsmeared Kinematics, With Acceptance Cuts To assess the effect of the geometric and kinematic acceptance cuts listed in table 8.2, we filter out the events not passing the kinematic selection criteria and we repeat the studies. From table 8.2, we see that the selection efficiencies of the spin-correlated and spin-uncorrelated sample are the same. This is an important aspect, as it shows that the kinematic cuts do not bias the event selection towards one or the other hypothesis. The statistics in the templates are drastically reduced and as is shown in the previous paragraph, template statistics induces a non-negligible uncertainty.

We perform similar pseudo-experiments as before, where we again draw the number of events from a Poisson distribution with mean 500 after event selection. In fig. 8.13, the $-2\ln\lambda_{event}$ distribution for both hypotheses is shown and more importantly from the ratio of the spin-correlated over the spin-uncorrelated distribution at the bottom of the figure, we can conclude that also with acceptance cuts, we have sufficient discriminating power between the templates. From fig. 8.14 and 8.15, we can draw similar conclusions as before: the extracted fit parameters and their uncertainties are still Gaussian distributed leading to a Gaussian pull distribution of which again the mean and RMS are compatible with an unbiased fit with proper error estimation. In fig. 8.16, the mean of the f for a set of f_{input} values is shown together with the results of a linear fit. The linear fit is again compatible with the unit line within the uncertainties, indicating an unbiased fit. In fig. 8.17, the Pull mean and RMS of the f fit parameter as a function of f_{input} are shown, which are compatible with 0 and 1 respectively.

The conclusions are the same as in the previous set of closure tests: we can still make an unbiased fit of the fraction of spin-correlated events f and make a cross section estimate. The mean fit uncertainty δf is slightly smaller when using accepted events.

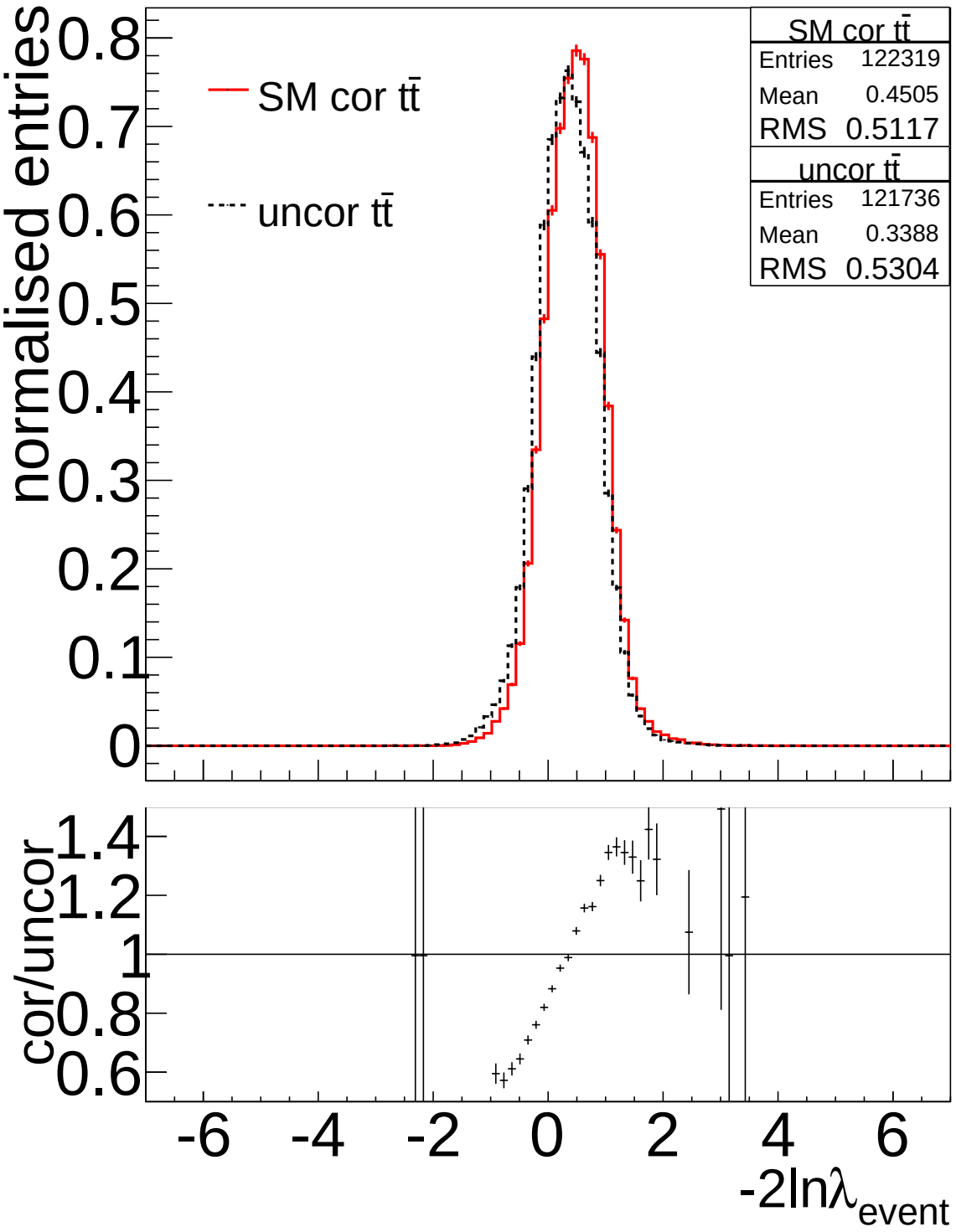

Figure 8.13: Histograms of $-2\ln\lambda_{event} = 2\ln L_{event}(H = Cor) - 2\ln L_{event}(H = Uncor)$ for individual events from generated samples according to $H = Cor$ (red solid histogram) and $H = Uncor$ (black dashed histogram) within acceptance. The ratio of the spin-correlated template over the spin-uncorrelated template is shown in the bottom plot.

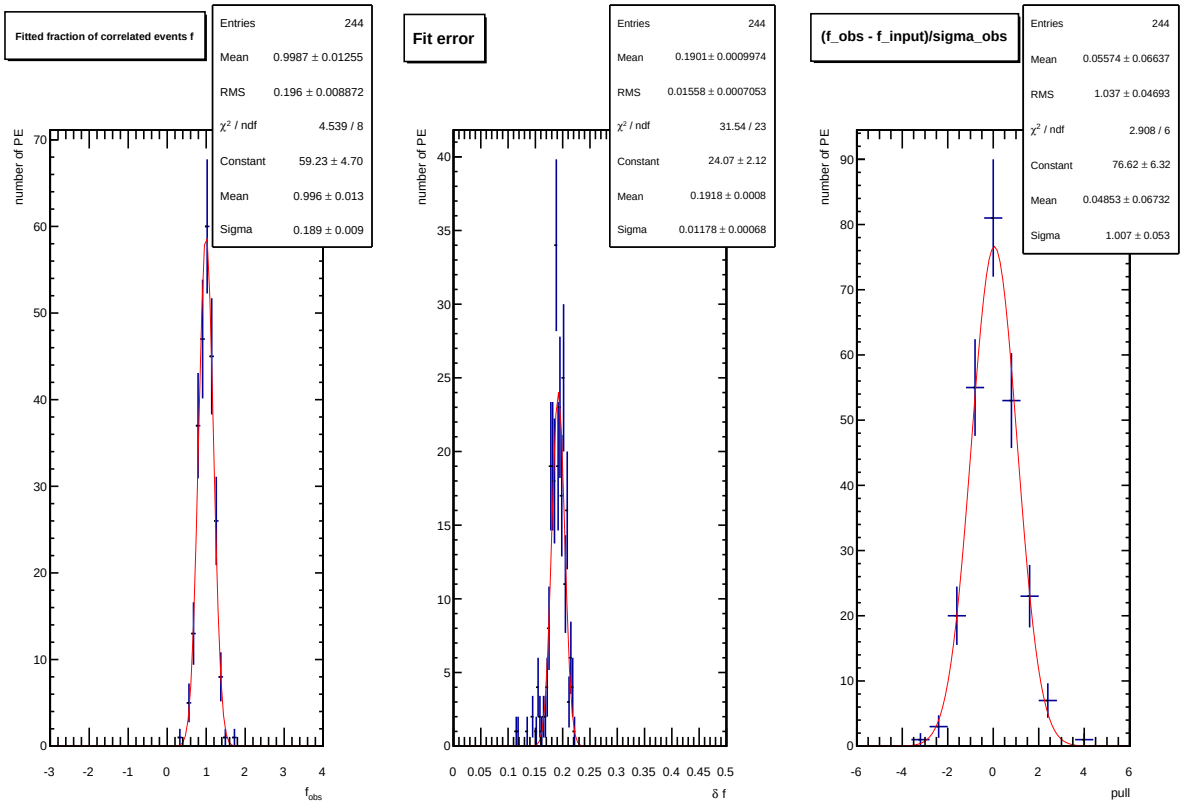

Figure 8.14: Pseudo-experiments performed to spin-correlated simulation events ($f_{input} = 1$) within acceptance with sample size Poisson distributed with mean of 500. The spread of the fitted f (left), of the fit uncertainty δf (middle), and the pull distribution (right).

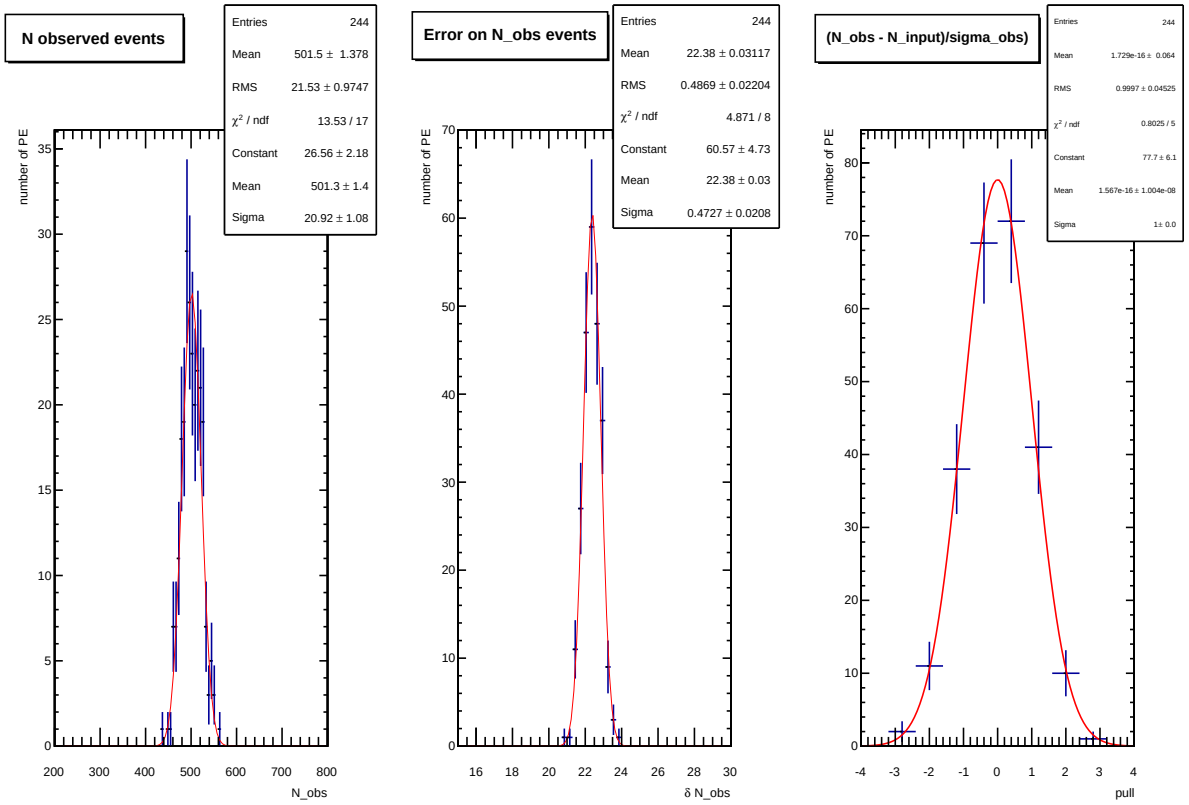

Figure 8.15: Pseudo-experiments performed using spin-correlated simulation events ($f_{input} = 1$) within acceptance with sample size 500. The fitted number of events N_{obs} in the pseudo-experiment is shown (left), the fit uncertainty δN_{obs} (middle) and the pull distribution (right).

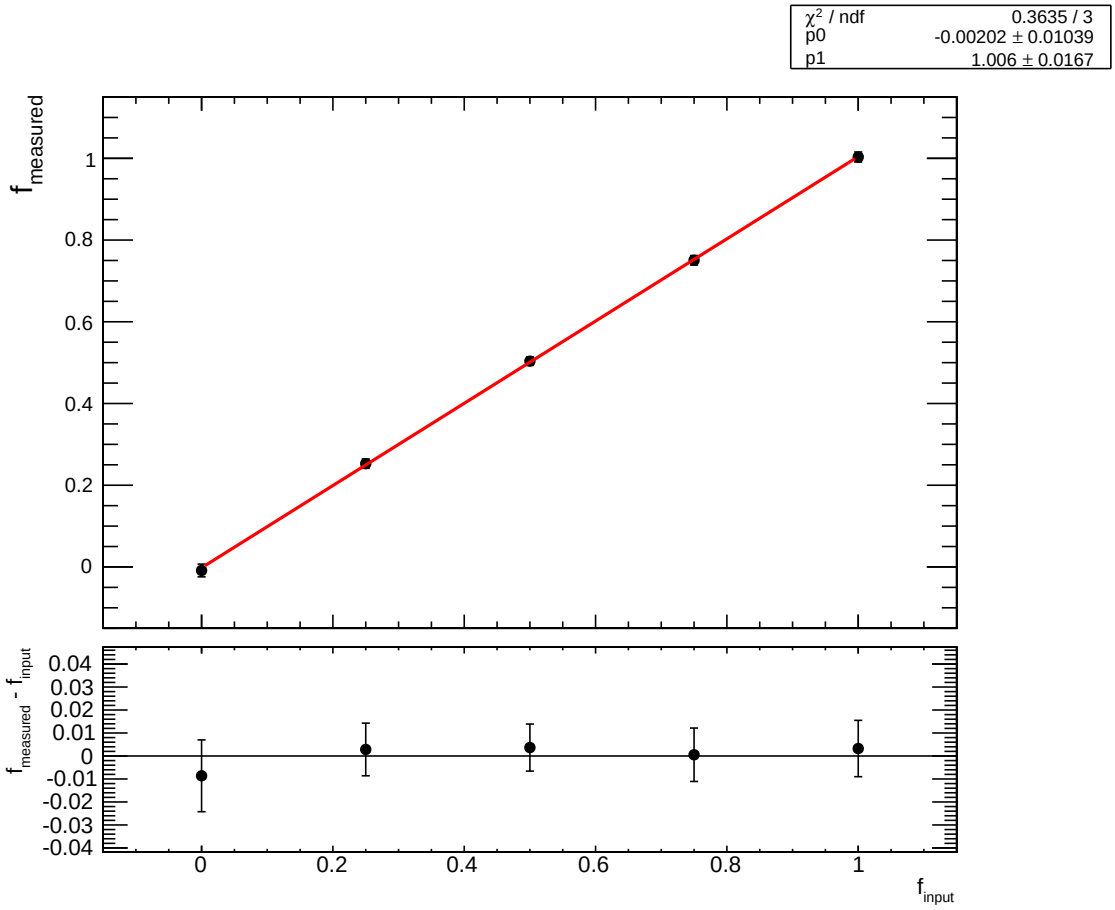

Figure 8.16: Mean of the Gaussian distribution fitted to the f vs. input f, which is obtained by mixing spin-correlated and spin-uncorrelated samples. The uncertainty bar is obtained from the uncertainty on the Gaussian fit parameter. The results are obtained from repeated pseudo-experiments with a sample size of 500 events each of events generated within acceptance.

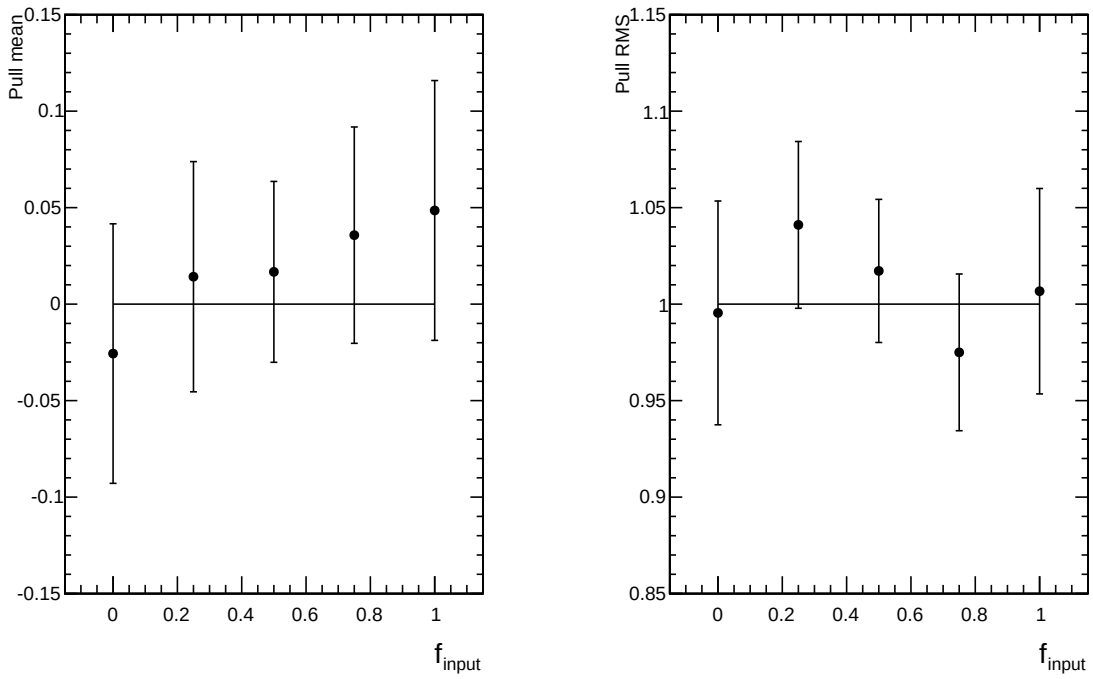

Figure 8.17: Mean of the Gaussian distribution fitted to the pulls (left) as a function of f_{input}, which is obtained by mixing spin-correlated and spin-uncorrelated samples and the pull RMS on the right. The uncertainty bar is obtained from the uncertainty on the Gaussian fit parameter. The results are obtained from repeated pseudo-experiments with a sample size of 500 events each of events generated within acceptance.

Closure Test Gen. Level 3: Signal + Background, Unsmeared Kinematics, With Acceptance Cuts Despite all efforts to design an event selection to obtain a pure $t\bar{t}$ semi-leptonic sample, there will always be background present. In a template fit, the background is taken into account in a separate template and added to the linear combination of templates. In this generator level closure test, we consider a background with an identical final state to the signal. We have chosen for a W+jets sample, where the additional jets consist of two light flavour quarks and a $b\bar{b}$ pair as described in section 8.1.1. The same kinematic acceptance cuts as were placed on the signal events, are applied to the W+jets background events. The selection efficiency for background events is much lower than for signal, leading to reduced statistics in the background template. These background events are processed in MadWeight under both the $t\bar{t}$ spin-correlated and $t\bar{t}$ spin-uncorrelated hypotheses, just as is done for signal events. The $-2\ln\lambda_{event}$ distribution of this background process is significantly different from both signal shapes, as can be seen in fig. 8.18. We can add this template to the fit model as in eq. 8.3, where we now leave in addition the number of background events floating and we have the total number of observed events as $N_{tot} = N_{t\bar{t}} + N_{bkg}$. As such we can extract the fraction of spin correlation f , background and $t\bar{t}$ cross section in the pseudo-data. Again the fit ranges from [-7,7] with bin-width of 0.14. All fit parameters are kept fully unconstrained.

As a closure test, about 250 pseudo-experiments were performed in which the relative W+jets background contribution β was varied from 10 to 30 %. We chose these two background contributions to show that the method works at any background contribution including background levels as high as 30 %. However in the data and the full simulation, we expect the background contributions to be about 15 % and the background is an admixture of various sources. As before the total number of events N_{tot} in the pseudo-experiment is drawn from a Poisson distribution with mean 500. Of this N_{tot}, $\beta = 10\,\%$ (or 30 % respectively) is required to be background events, so $N_{bkg}^{input} = \beta N_{tot}$ and $N_{t\bar{t}}^{input} = (1-\beta)N_{tot}$. Of this $N_{t\bar{t}}^{input}$ again exactly $f_{input}N_{t\bar{t}}$ correlated events are drawn and $(1-f_{input})N_{t\bar{t}}$ uncorrelated events. The results of the f, $N_{t\bar{t}}$ and N_{bkg} extraction are shown in fig. 8.19-8.22. As we can see from fig. 8.19 top and bottom, the correct correlation fraction can still be extracted, but the fit uncertainty on the fitted fractions increases with increasing background contribution. The number of observed $t\bar{t}$ events $N_{t\bar{t}}$ is again fitted and shown in fig. 8.20 top and bottom. The results of the background estimation extraction can be seen in figs. 8.21 top and bottom. Even though we see from the pull distribution that the uncertainties on the background determination are slightly overestimated, the main focus is on the fraction of spin-correlated events f, which remains unbiased. The correlation between the fit parameters is shown in fig. 8.22. The correlation between the fit parameters is no longer negligible but not yet extreme. We again tested the linearity of the f extraction, as shown in fig. 8.23. The pull mean and RMS as a function of the varying mixing fractions are shown in fig. 8.24 for a background contribution of 10 and 30 %. The conclusion is again that we obtain an unbiased extraction of f.

In treating this background explicitly, we see that we are still able to extract the correct fraction of spin-correlated events and (at least at the parton level) can extract both the signal and background cross sections. Moreover, the event likelihoods also give us an extra means to discriminate $t\bar{t}$ from W+jets events and a cut on the likelihood value could used to increase the purity of our data sample. The event likelihood distributions for the spin-correlated $-\ln L_{event}(H = Cor)$ and spin-uncorrelated $-\ln L_{event}(H = Uncor)$ hypothesis are shown for the various event samples in fig. 8.25. The distribution is very similar for both the spin-correlated and spin-uncorrelated $t\bar{t}$ sample, but significantly different for the W+jets sample, allowing us to cut away background while not biasing and retaining statistics in the signal samples. The distributions are very similar between the spin-correlated $-\ln L_{event}(H = Cor)$ and spin-uncorrelated $-\ln L_{event}(H = Uncor)$ hypothesis and the conclusions are interchangeable. For any studies,

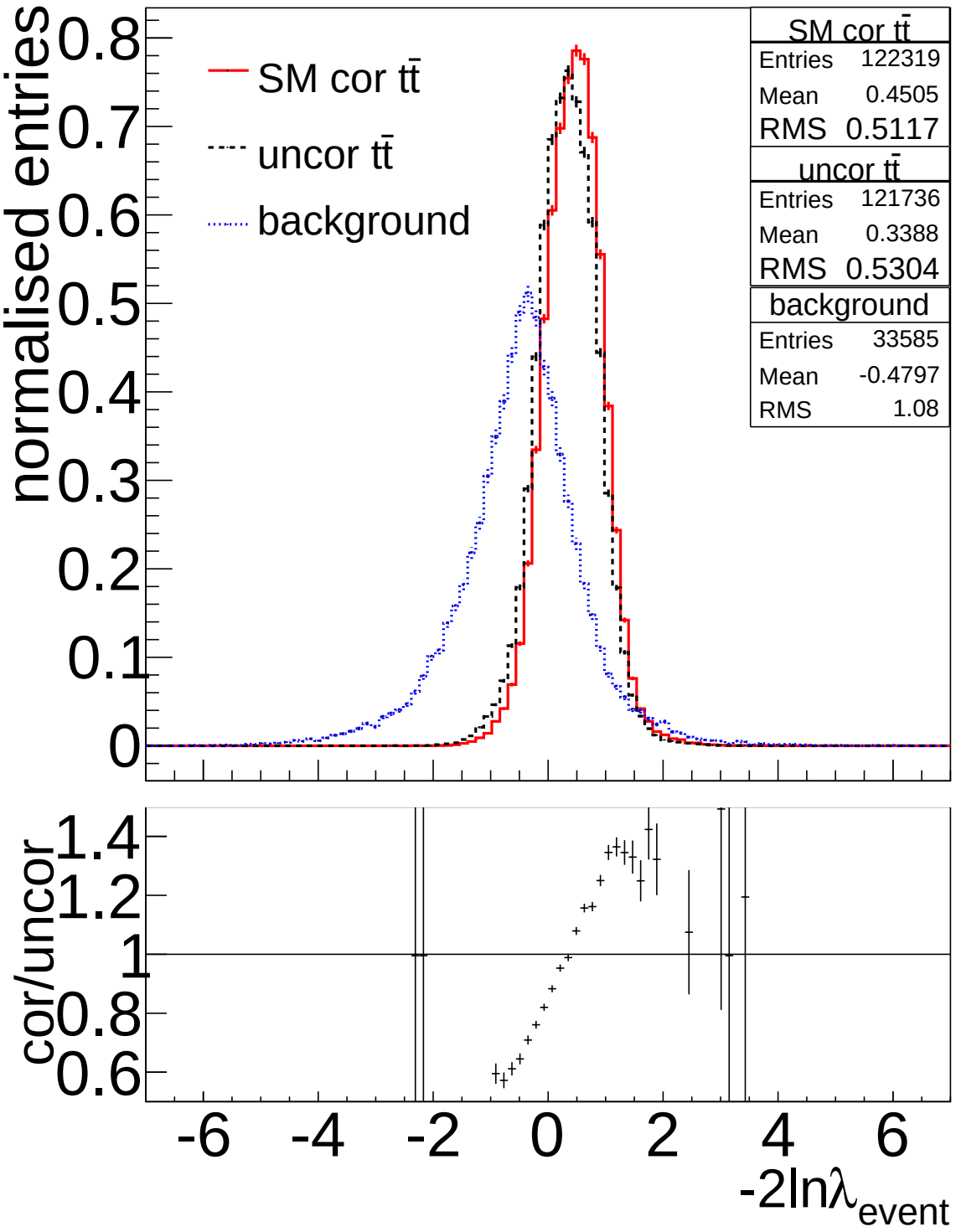

Figure 8.18: Input templates of the $-2\ln\lambda_{event}$ distribution for the fit to the pseudo-experiments. As before the spin-correlated template is shown with the full red line, the spin-uncorrelated one in the black dashed line and the WJets template in the blue dotted line. The ratio of the spin-correlated template over the spin-uncorrelated template is shown in the bottom plot.

we usually work with $-\ln L_{event}(H = Cor)$. Another way to make use of this information is by performing a 2-dimensional template fit, in the $(-2\ln\lambda_{event}, -\ln L_{event}(H = Cor))$-plane. Such a 2D fit is useful when the background template shape is closer to the signal shape, making it more difficult for the fit to converge on all three parameters resulting in high correlation between the fit parameters. For the analysis, we do not place a cut on the $-\ln L_{event}$ variable and use this 2D fit as a cross check.

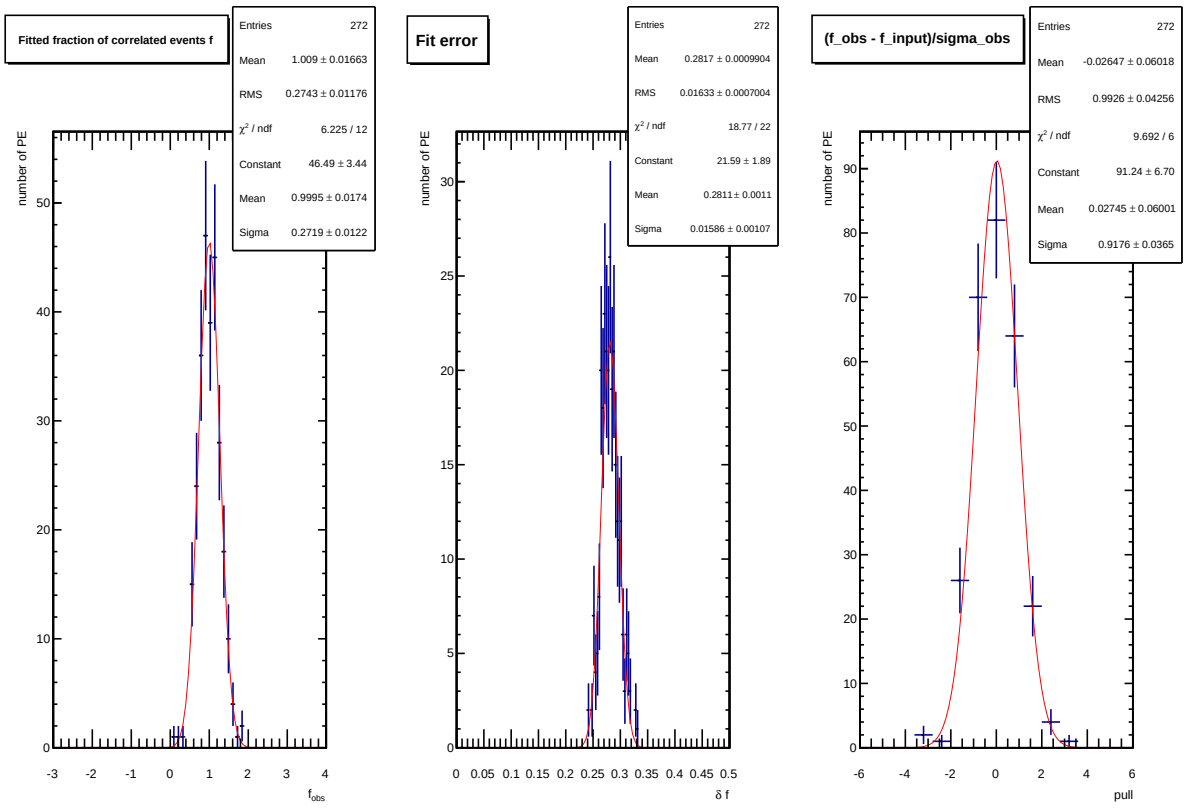

(a) $\beta = 10\,\%$

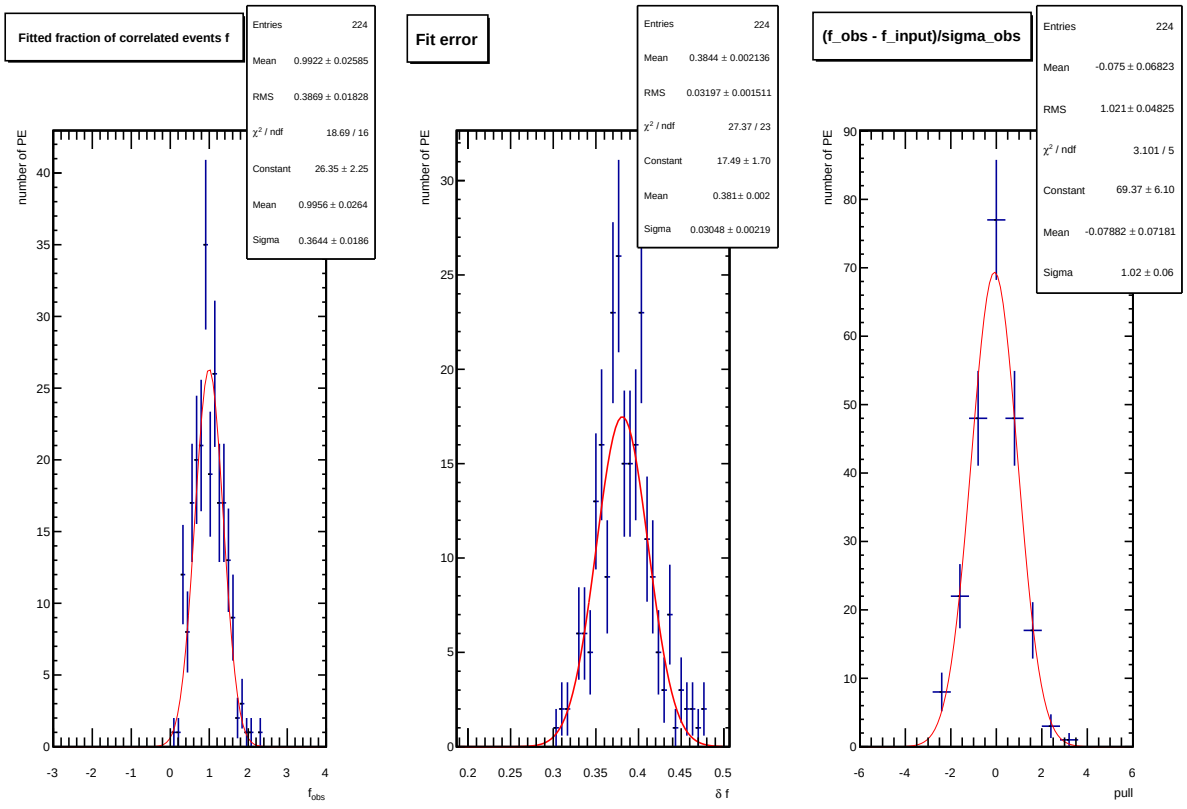

(b) $\beta = 30\,\%$

Figure 8.19: Pseudo-experiments performed using spin-correlated events ($f_{input} = 1$) with sample size 500 including β W+jets background. The spread of the fitted f (left), of the fit uncertainty δf(middle) and the pull distribution (right).

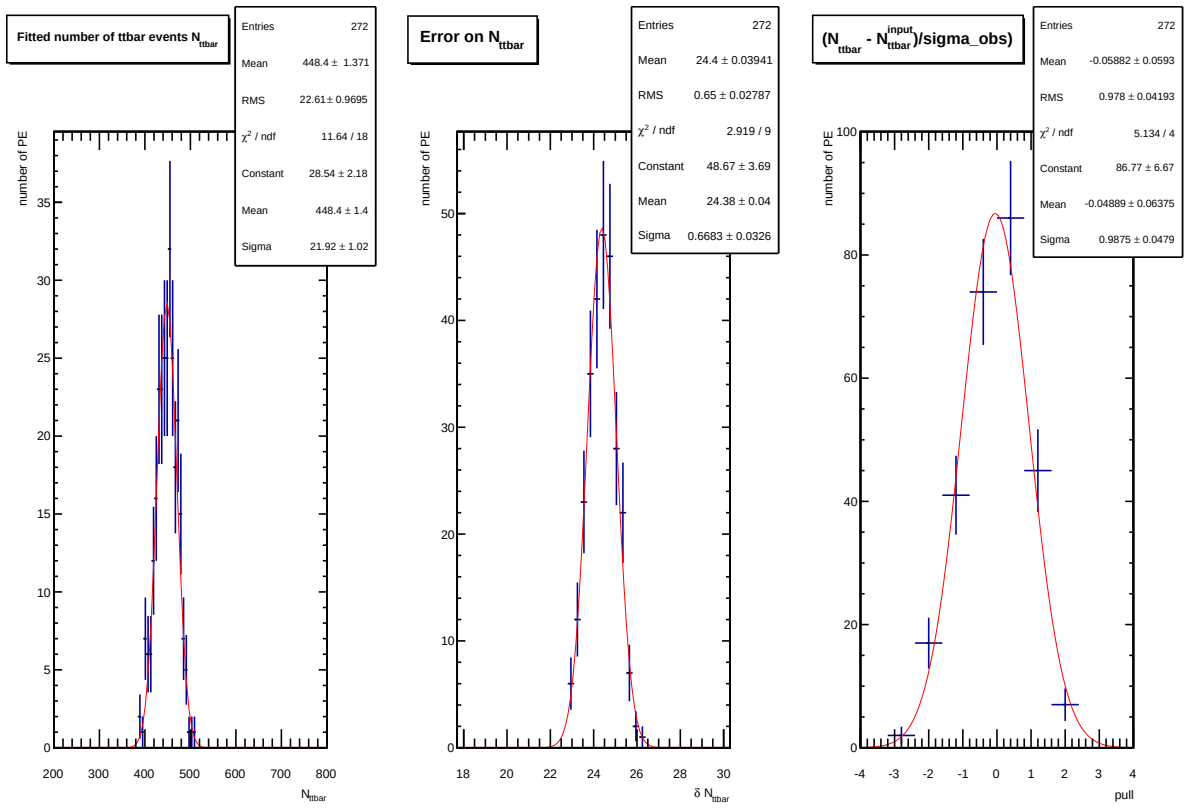

(a) $\beta = 10\,\%$

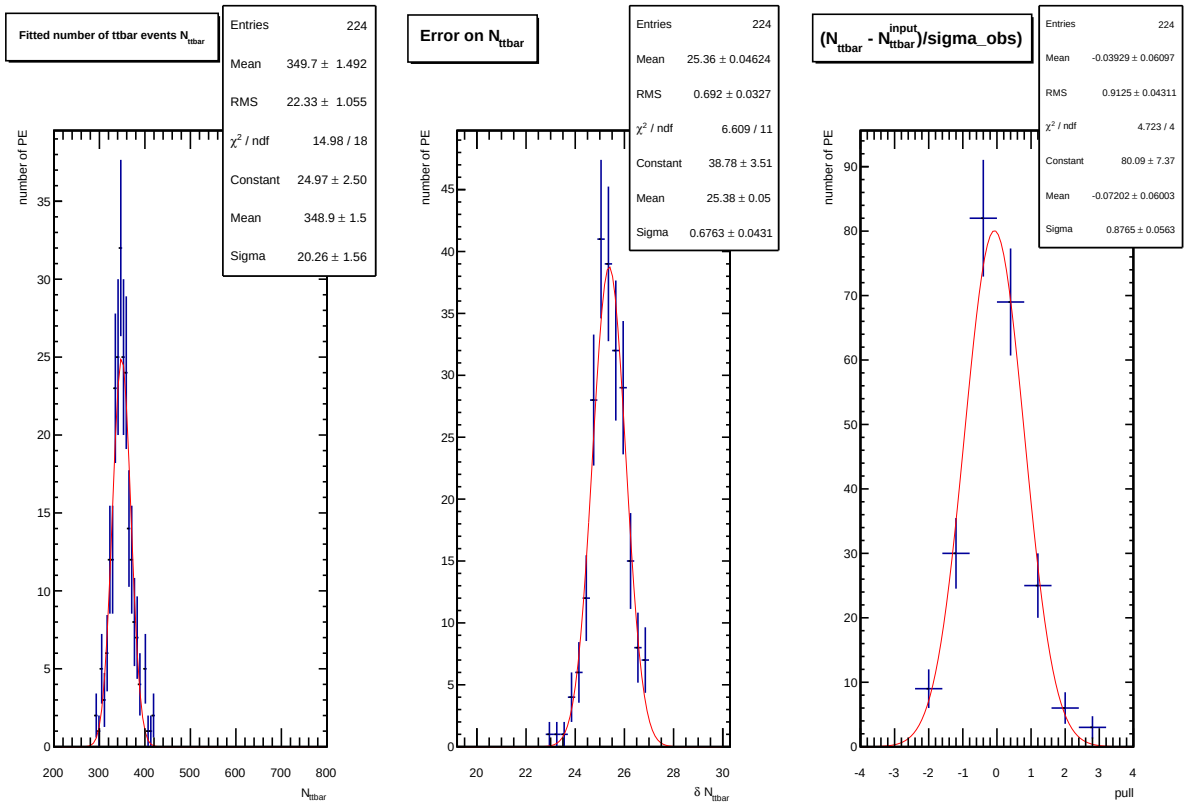

(b) $\beta = 30\,\%$

Figure 8.20: Pseudo-experiments performed using spin-correlated events ($f_{input} = 1$) with sample size 500 including a β W+jets background. The fitted number of $t\bar{t}$ events $N_{t\bar{t}}$ is shown (left), the fit uncertainty $\delta N_{t\bar{t}}$ (middle) and the pull distribution (right). A mean $N_{t\bar{t}}$ of 450, 350 is expected in the (top, bottom) plots respectively.

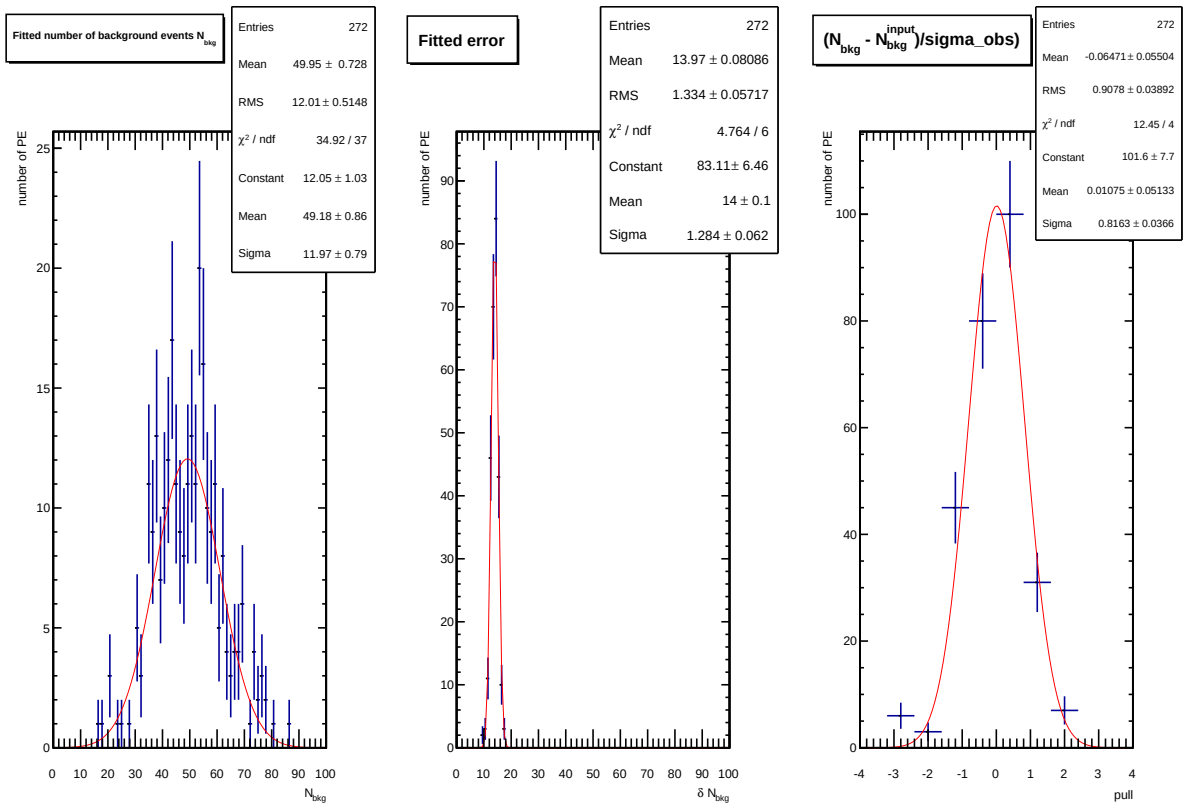

(a) $\beta = 10\,\%$

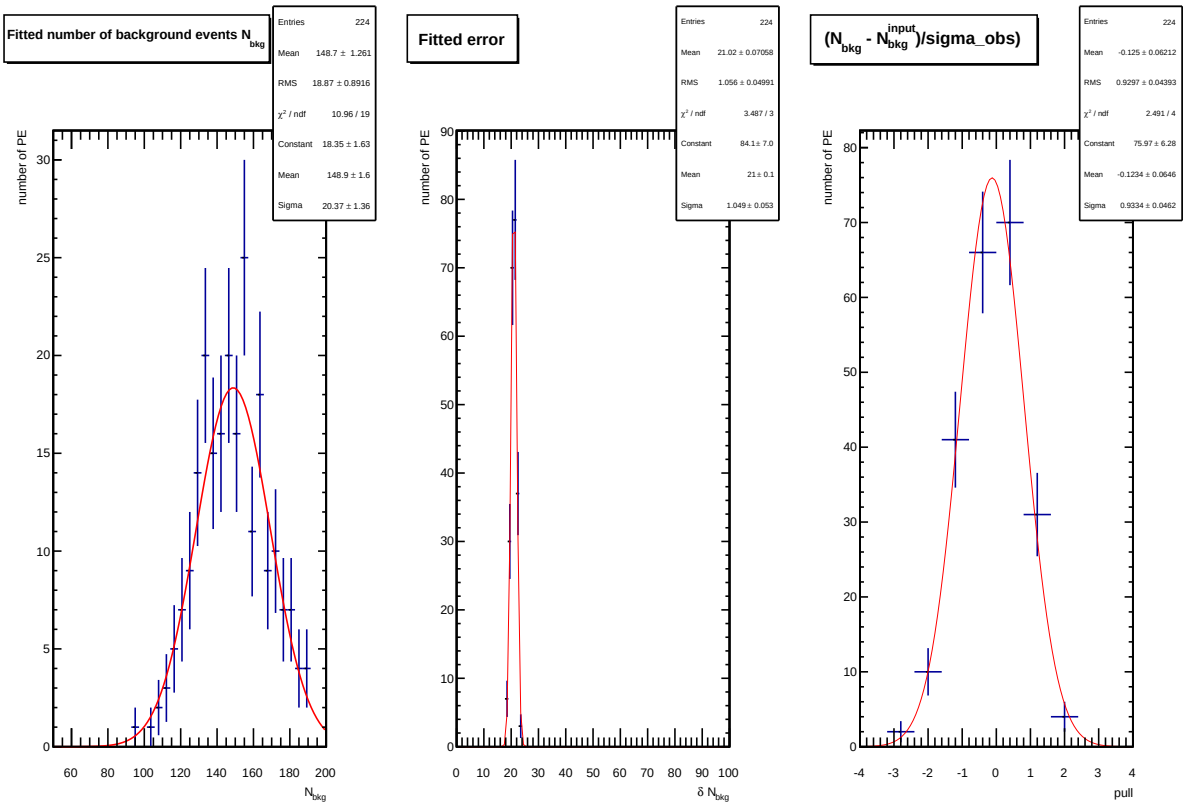

(b) $\beta = 30\,\%$

Figure 8.21: Pseudo-experiments performed using spin-correlated events ($f_{input} = 1$) with sample size 500 including a β W+jets background. The fitted number of background events N_{bkg} is shown (left), the fit uncertainty δN_{bkg} (middle) and the pull distribution (right). A mean N_{bkg} of 50, 150 is expected in the (top,bottom) plots respectively.

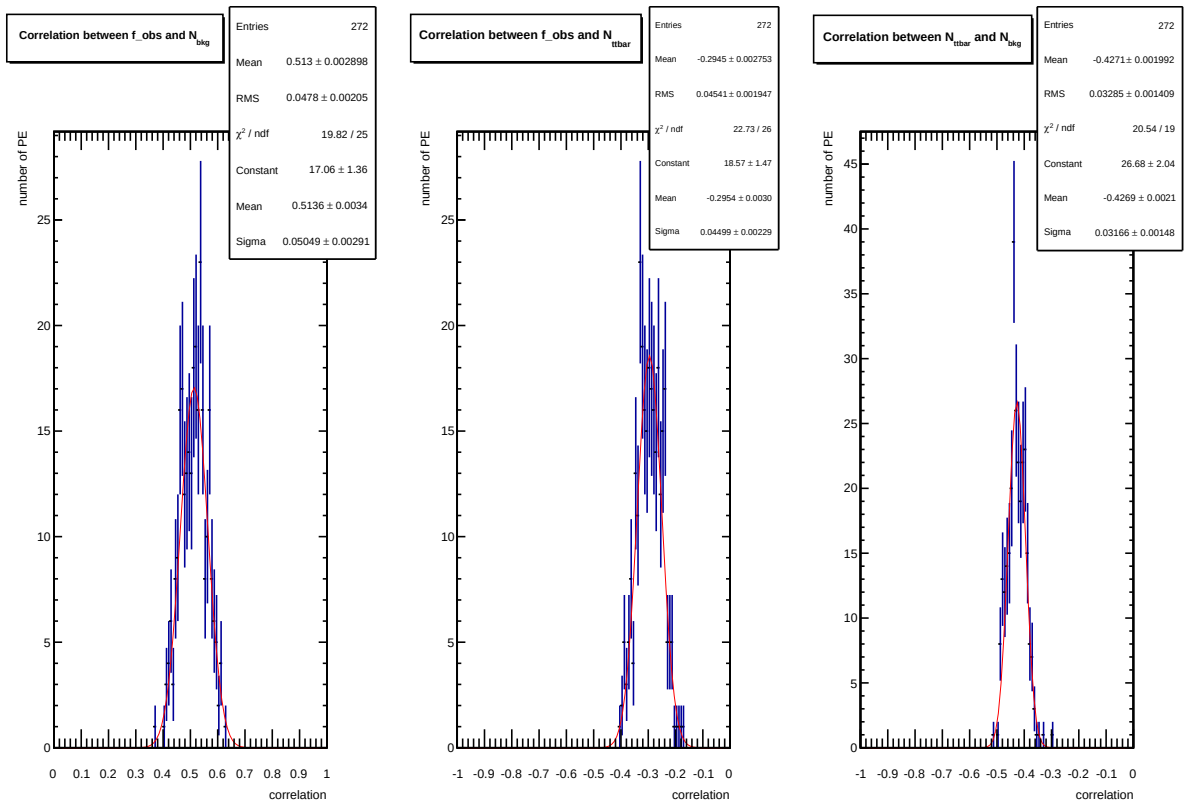

(a) $\beta = 10\,\%$

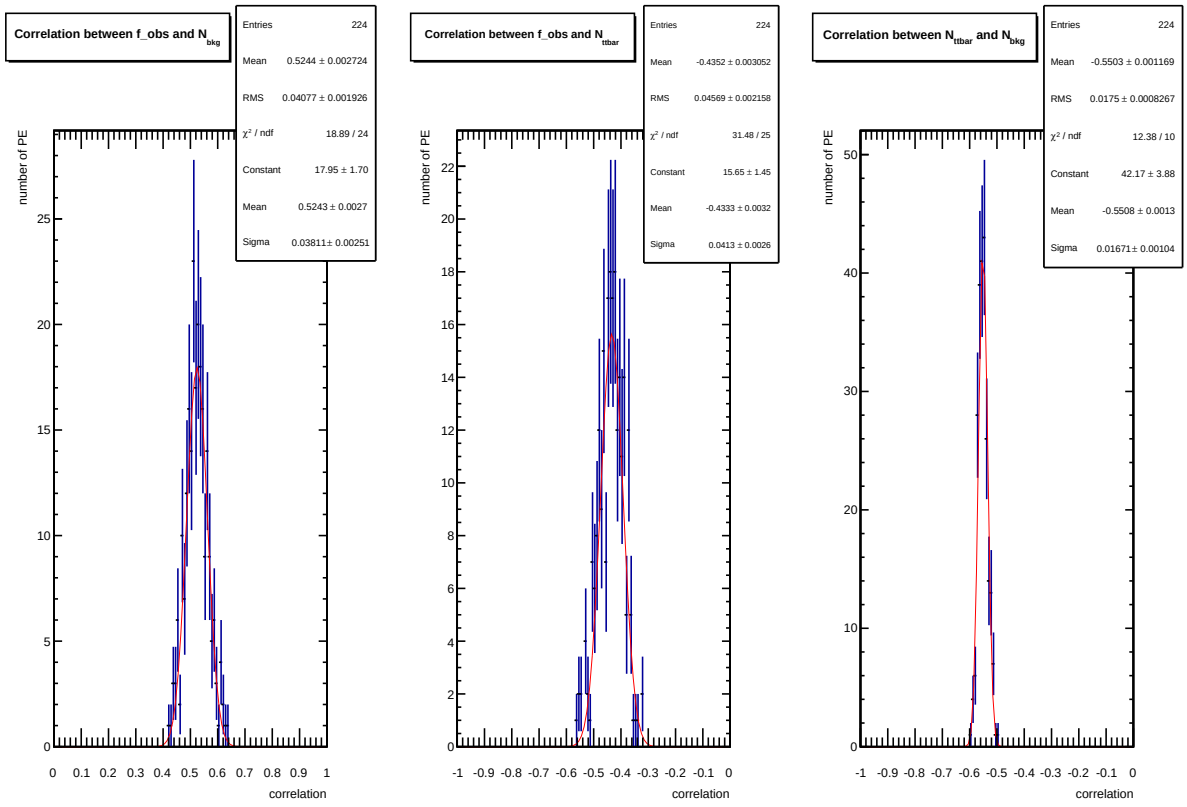

(b) $\beta = 30\,\%$

Figure 8.22: Pseudo-experiments performed using spin-correlated events ($f_{input} = 1$) with sample size 500 including a β W+jets background. The correlation between the fit parameters f, $N_{t\bar{t}}$ and N_{bkg} is shown.

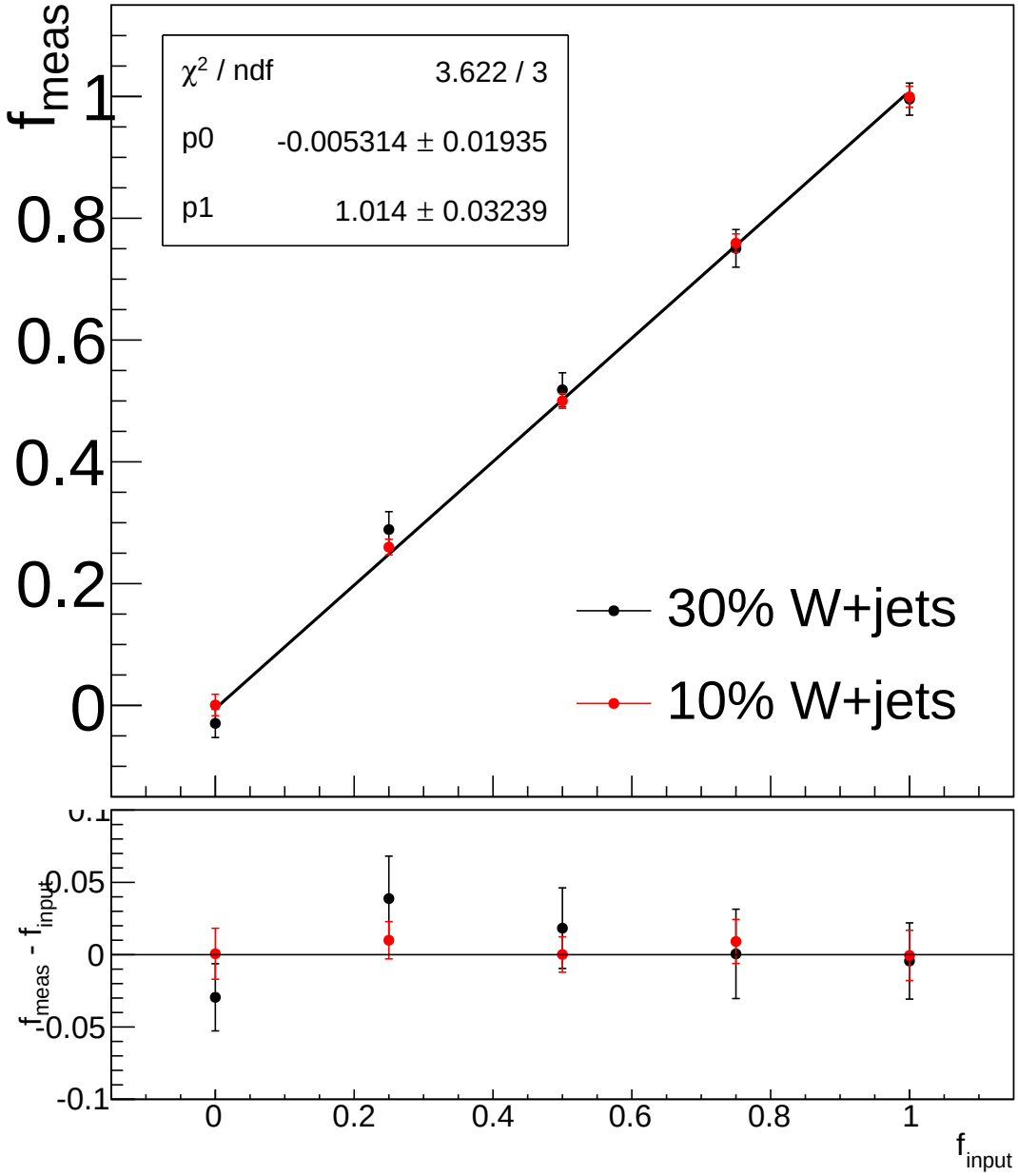

Figure 8.23: Mean fitted f as a function of f_{input}, which is obtained by mixing spin-correlated and spin-uncorrelated samples. The uncertainty bar is obtained from the uncertainty on the mean of the fitted f. The results are obtained from repeated pseudo-experiments with a sample size of 500 events each including a 30% (10%) WJets background in black (red).

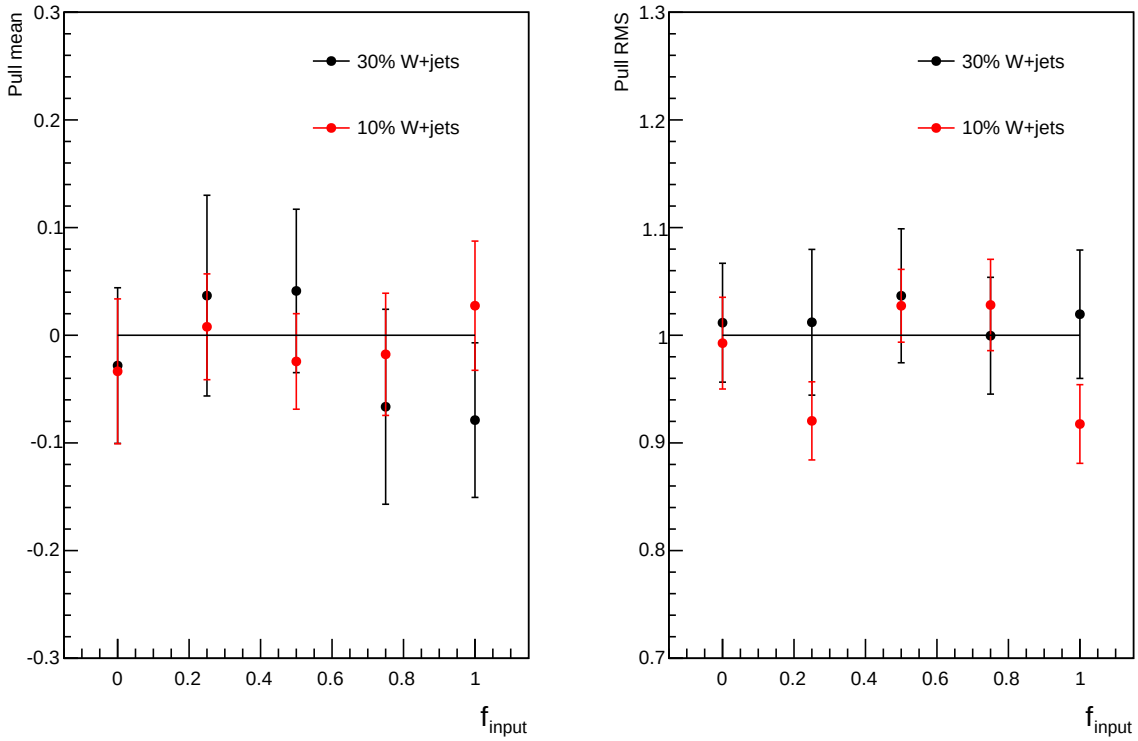

Figure 8.24: Mean of the Gaussian distribution fitted to the pulls (left) as a function of f_{input}, which is obtained by mixing spin-correlated and spin-uncorrelated samples and the pull RMSs on the right. The uncertainty bar is obtained from the uncertainty on the Gaussian fit parameter. The results are obtained from repeated pseudo-experiments with a sample size of 500 events each with a 30% WJets background contribution.

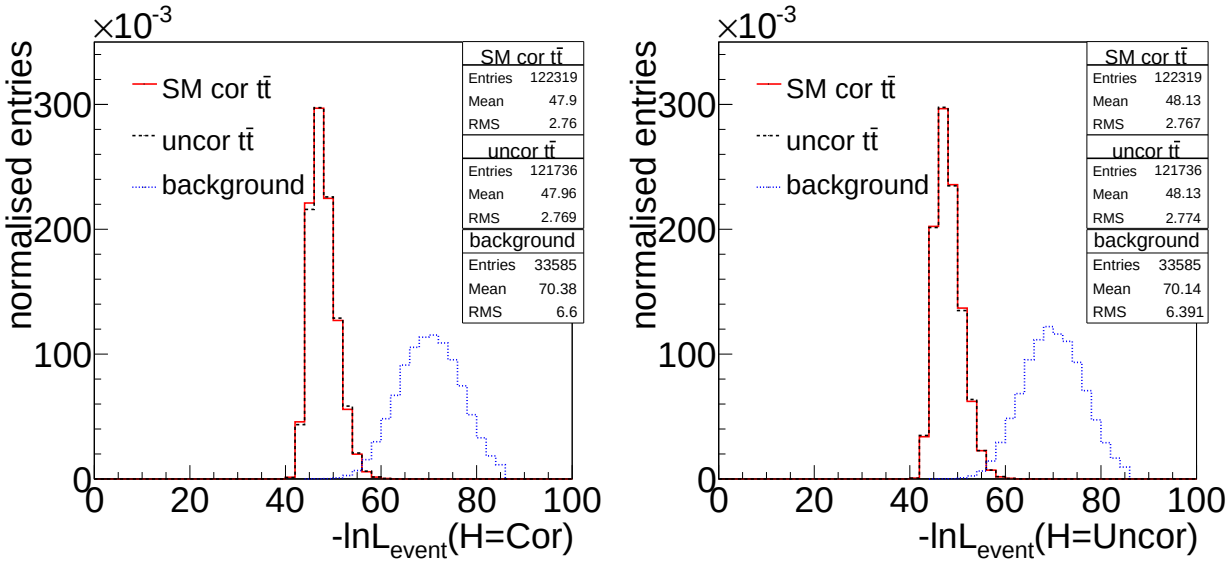

Figure 8.25: Event Likelihood distributions $-\ln L_{event}(H = Cor)$ (left) and $-\ln L_{event}(H = Uncor)$ (right) for the spin-correlated event sample in red solid line, the spin-uncorrelated sample in the black dashed line and the W+jets sample in the blue dotted line.

Closure Test Gen. Level 4: Signal Only, Smeared Parton Kinematics, With Acceptance Cuts Up to this point, the results have been presented with parton level information. To mimic the effect of reconstruction in the CMS detector, we smear the parton kinematics in our samples. A resolution function estimating the parton level kinematics based on the jet kinematics measured in the CMS detector, is set up from $t\bar{t}$ simulation. This semi-realistic resolution function is used to smear the p_T of the partons in our LO simulation samples and is also inserted as transfer function in MadWeight to process the smeared events. After smearing, the kinematic cuts described in table 8.2 are applied to restrict the measurement to the phase space accessible with the CMS reconstruction and to which the transfer functions are determined. The same closure tests as described earlier are performed, considering signal $t\bar{t}$ events only.

In fig. 8.26, again the $-2\ln\lambda_{event}$ templates are shown. The effect of smearing is seen more clearly when we overlay the unsmeared and smeared templates (both with acceptance cuts) in fig. 8.27. Smearing shifts the mean by ~ 0.03 in both cases in the same direction and broadens the distributions slightly. In fig. 8.28 the results of the extracted f are shown together with the fit uncertainty δf and the pull distribution. All distributions are Gaussian in shape. From the pull distribution, we conclude that the extraction of f is unbiased and that the uncertainties are properly estimated. In fig. 8.29, the observed number of events N_{obs} ($N_{obs} = N_{t\bar{t}}$), is shown, in addition to the uncertainty δN_{obs}. The pull distribution on the right is again calculated as $(N_{obs} - 500)/\delta N_{obs}$. Also here, we conclude that the extraction of N_{obs} is unbiased and with proper uncertainty estimation. When plotting mean f as a function of f_{input} in fig. 8.30, the fit is still consistent with the unit line. Also the pull means and RMSs are well behaved as shown in fig. 8.31.

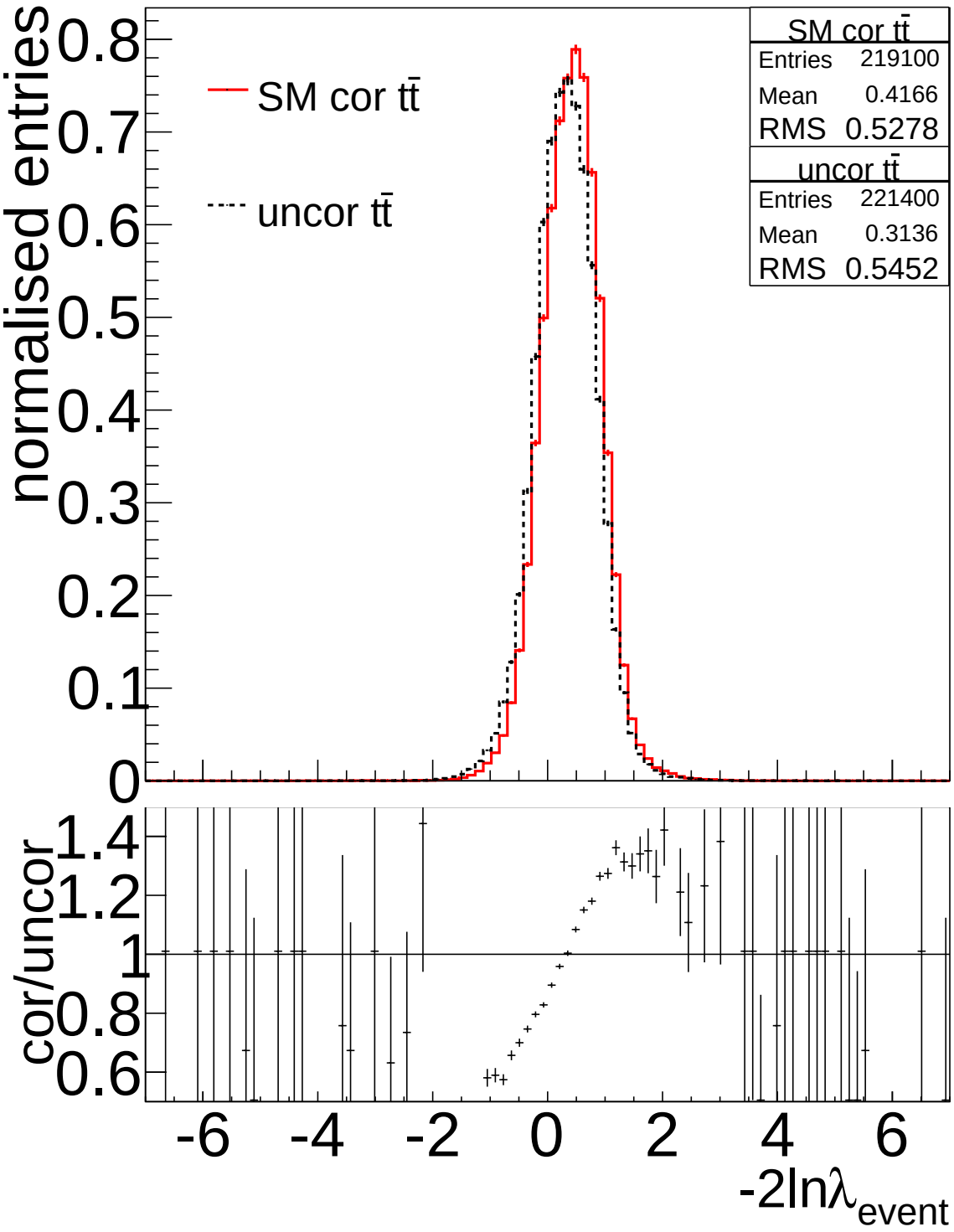

Figure 8.26: Input templates of the $-2\ln\lambda$ distribution for the fit to the pseudo-experiments on smeared simulation samples. As before the spin-correlated template is shown in the full red line and the spin-uncorrelated one in the black dashed line. The ratio of the spin-correlated template over the spin-uncorrelated template is shown in the bottom plot.

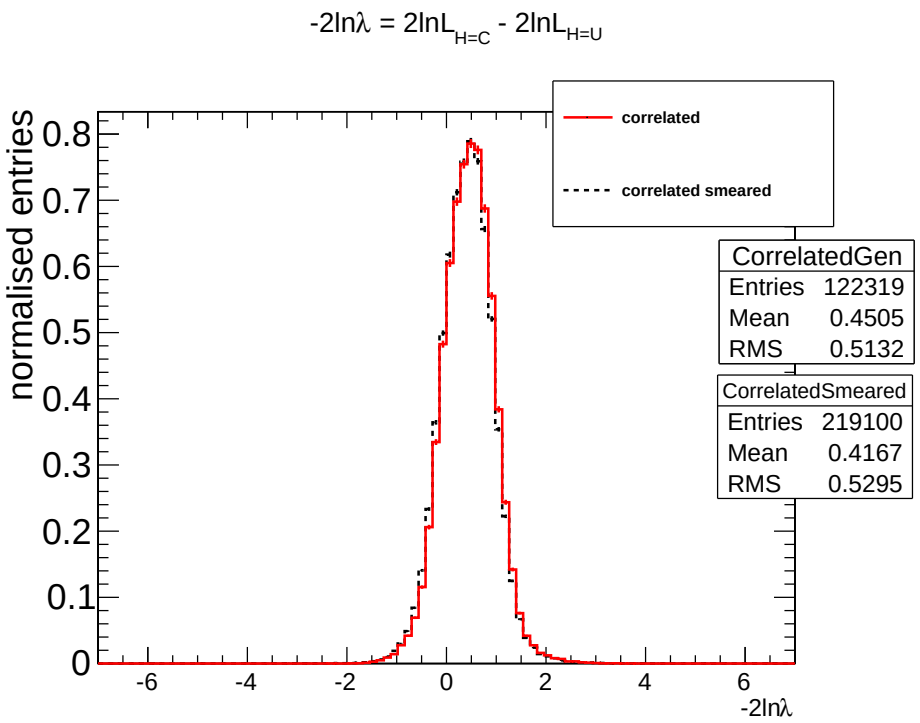

(a) spin-correlated sample

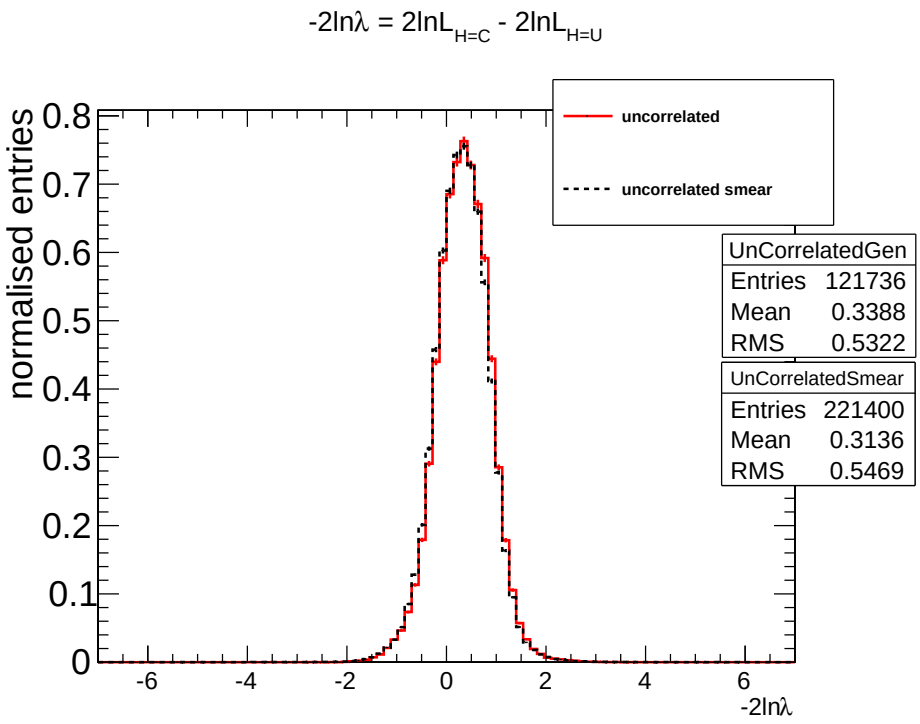

(b) spin-uncorrelated sample

Figure 8.27: Input templates of the $-2\ln\lambda$ distribution for the fit to the pseudo-experiments. The plots show the difference between the templates at generator level with acceptance cuts and smeared kinematics with acceptance cuts for the spin-correlated sample (top) and the spin-uncorrelated sample (bottom).

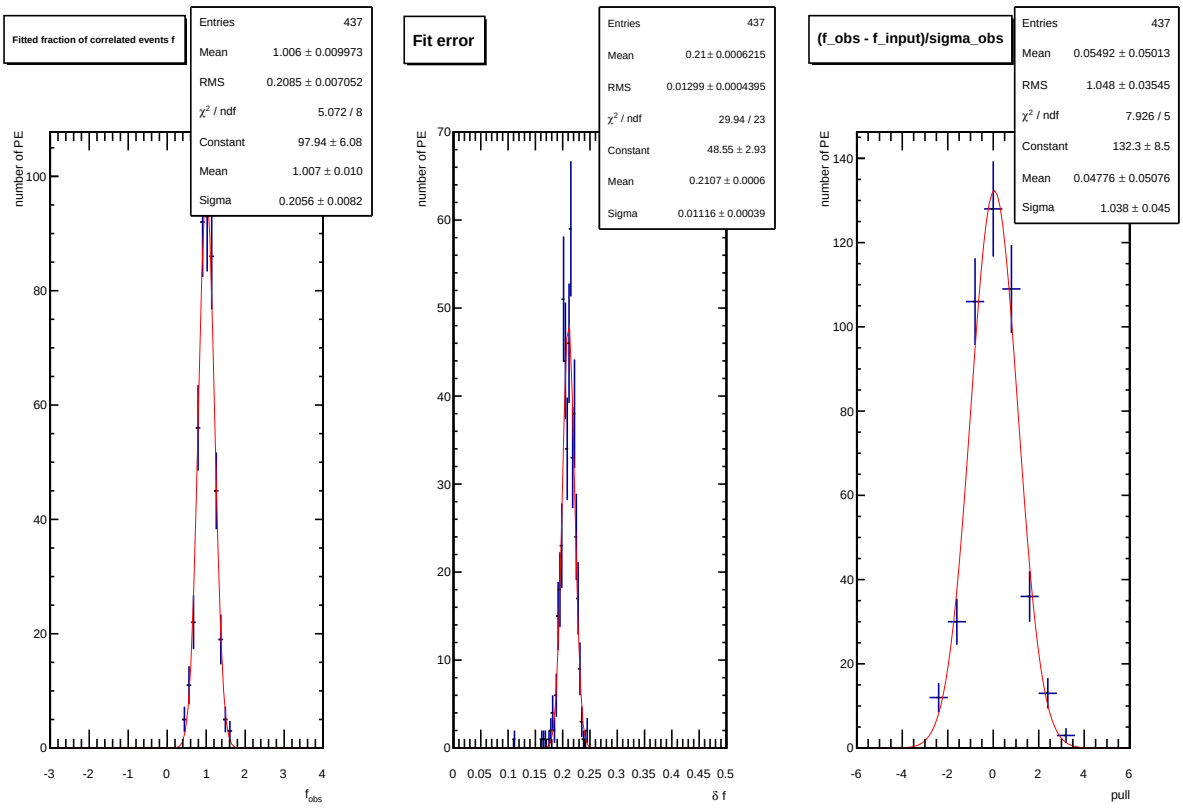

Figure 8.28: Pseudo-experiments performed to smeared spin-correlated simulation events ($f_{input} = 1$) within acceptance with sample size Poisson distributed with mean of 500. The spread of the fitted f (left), of the fit uncertainty δf (middle), and the pull distribution (right) is shown.

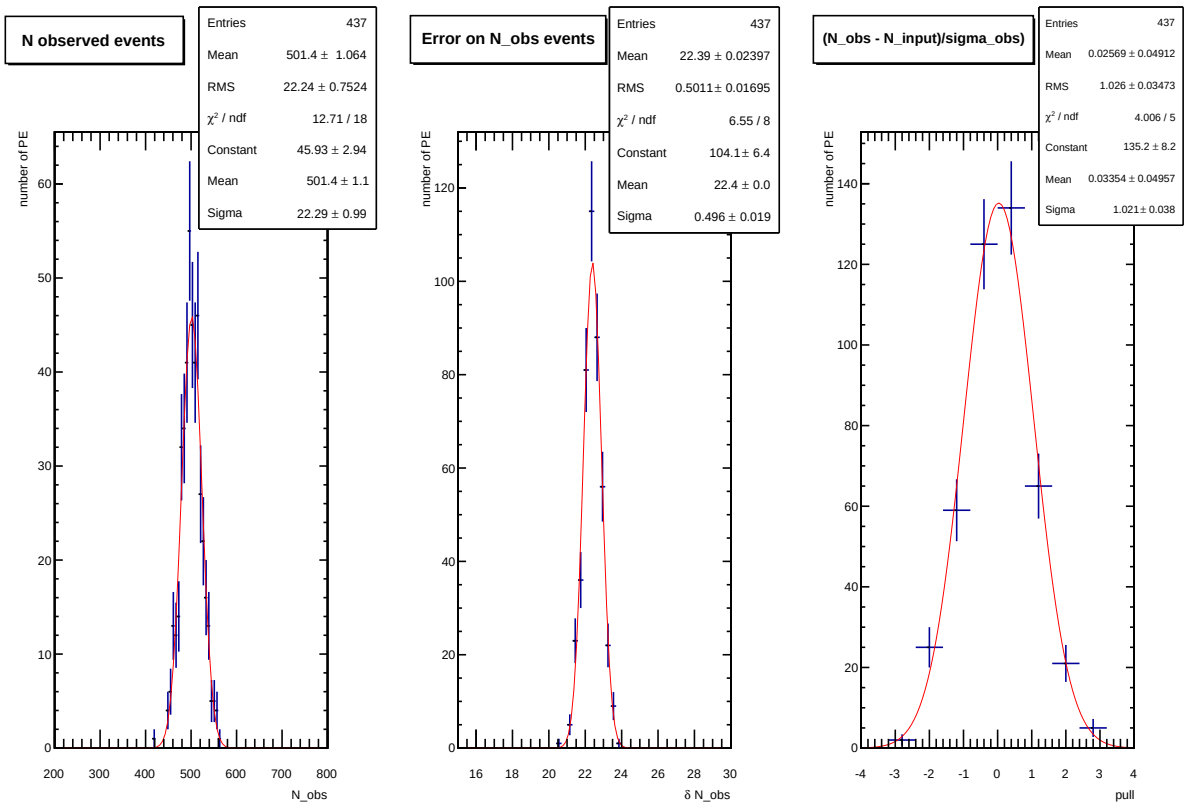

Figure 8.29: Pseudo-experiments performed to smeared spin-correlated simulation events ($f_{input} = 1$) within acceptance with sample size 500. The fitted number of $t\bar{t}$ events $N_{t\bar{t}}$ in the pseudo-experiment is shown (left), the fit uncertainty $\delta N_{t\bar{t}}$ (middle) and the pull distribution (right).

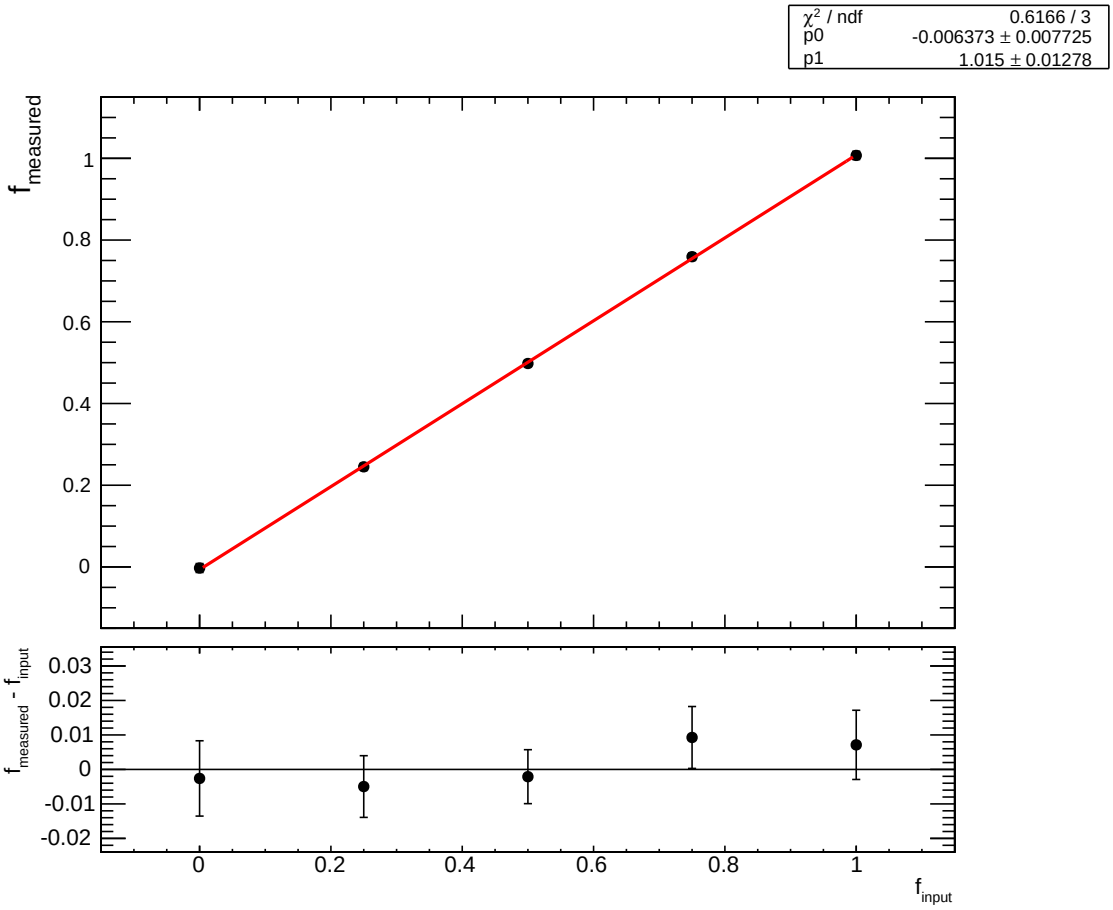

Figure 8.30: Mean fitted f as a function of f_{input}, which is obtained by mixing spin-correlated and spin-uncorrelated samples. The uncertainty bar is obtained from the uncertainty on the mean of the fitted f. The results are obtained from repeated pseudo-experiments on smeared simulation with a sample size of 500 events each.

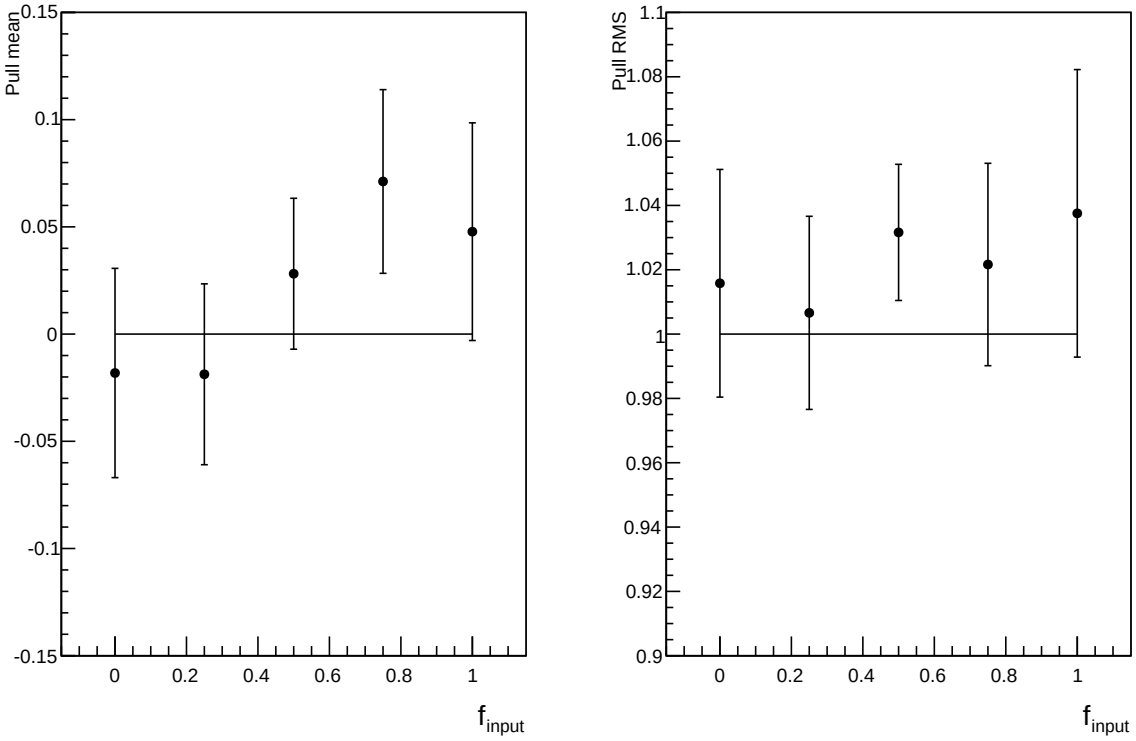

Figure 8.31: Mean of the Gaussian distribution fitted to the pulls (left) as a function of f_{input}, which is obtained by mixing spin-correlated and spin-uncorrelated samples and the pull RMSs on the right. The uncertainty bar is obtained from the uncertainty on the Gaussian fit parameter. The results are obtained from repeated pseudo-experiments on smeared simulation with a sample size of 500 events.

Closure Test Gen. Level 5: Signal + Background, Smeared Parton Kinematics, With Acceptance Cuts As a final, parton level closure test, we add in the background with smeared parton kinematics. In fig. 8.32, the input templates with smeared kinematics and kinematic cuts are shown, now including the W+jets background template. The pseudo-experiments with a sample size drawn from a Poisson distribution with mean 500, include a W+jets background contribution of 10 %. At the time the closure tests were performed, a 10 % background contribution was our rough estimate, the background contribution from reconstruction level simulation with all relevant background processes considered is 15 %. In fig. 8.33 the results on the spin-correlated $f_{input} = 1$ sample are shown. Again the pull distribution for f for the spin-correlated sample is consistent with a mean of 0 and a RMS of 1. The number of $t\bar{t}$ events $N_{t\bar{t}}$ and background events N_{bkg} can be fitted as seen in fig. 8.34 and 8.35. The correlation between the three fit parameters is shown in fig. 8.36, showing no exteme correlation between any of the fit parameters. From the linearity plot in fig. 8.37, we see that we can still extract an unbiased f for each f_{input} since the fit is compatible with the unit line within one sigma. Also the pull means and RMSs are well behaved (fig. 8.38). From this we can conclude that adding the background and smearing the simulation does not introduce a bias in our measurements at the generator level.

When including the background, it is interesting to also study the absolute event likelihood distributions $-\ln L_{event}(H = Cor)$ and $-\ln L_{event}(H = Uncor)$, shown in fig 8.39. The smearing degrades the discriminating power between signal and background, but the bulk of the background distribution could still be removed even though we decided not to use this option.

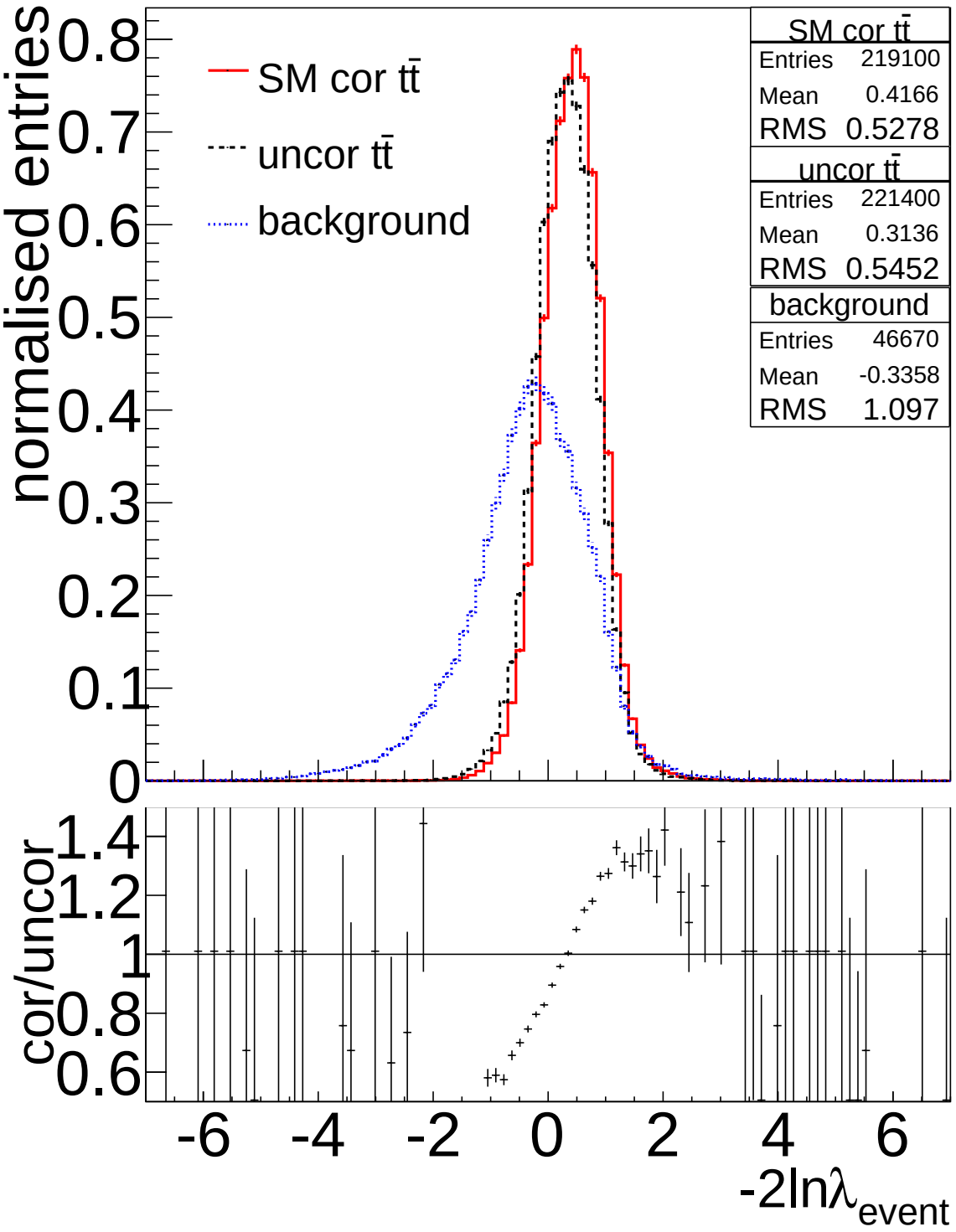

Figure 8.32: Input templates of the $-2\ln\lambda$ distribution for the fit to the pseudo-experiments. As before the spin-correlated template is shown in the red solid line, the spin-uncorrelated one in the black dashed line and the WJets template in the blue dotted line. The ratio of the spin-correlated template over the spin-uncorrelated template is shown in the bottom plot.

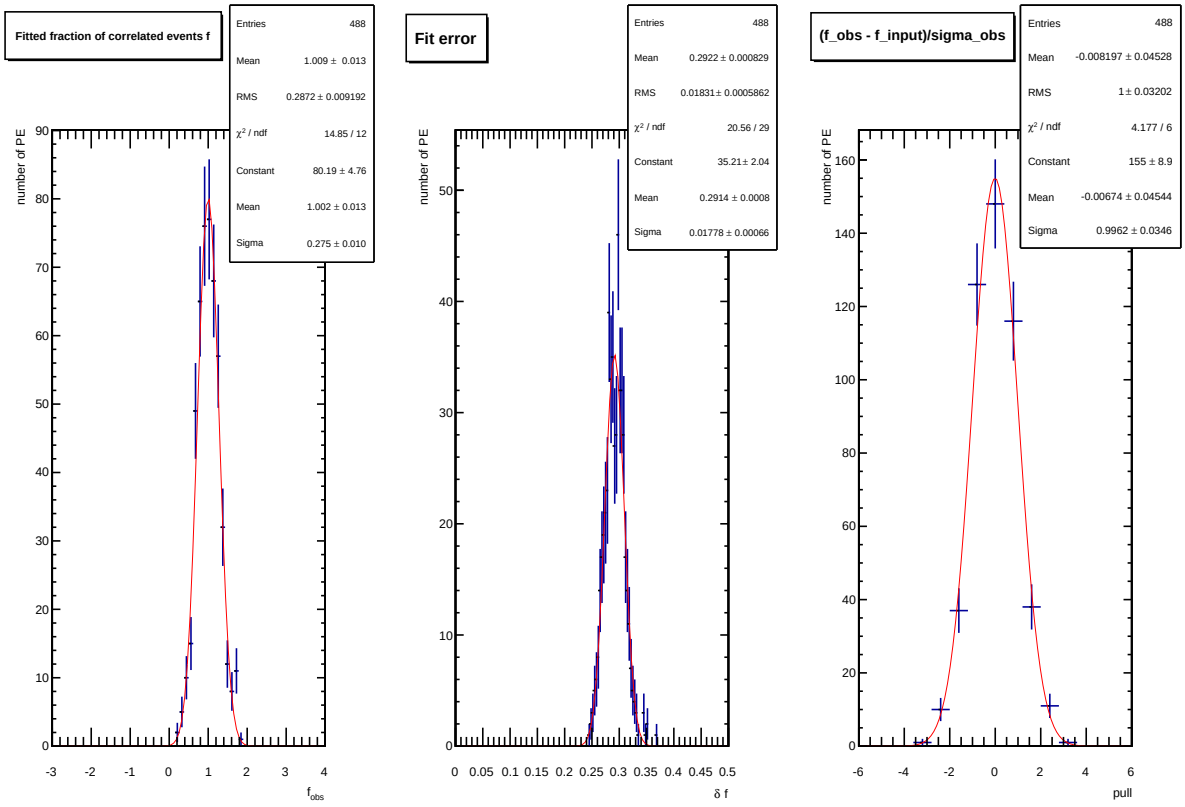

Figure 8.33: Pseudo-experiments performed on smeared spin-correlated events ($f_{input} = 1$) with sample size 500 including a 10% smeared W+jets background. The spread of the fitted f (left), of the fit uncertainty δf (middle) and the pull distribution (right) is shown.

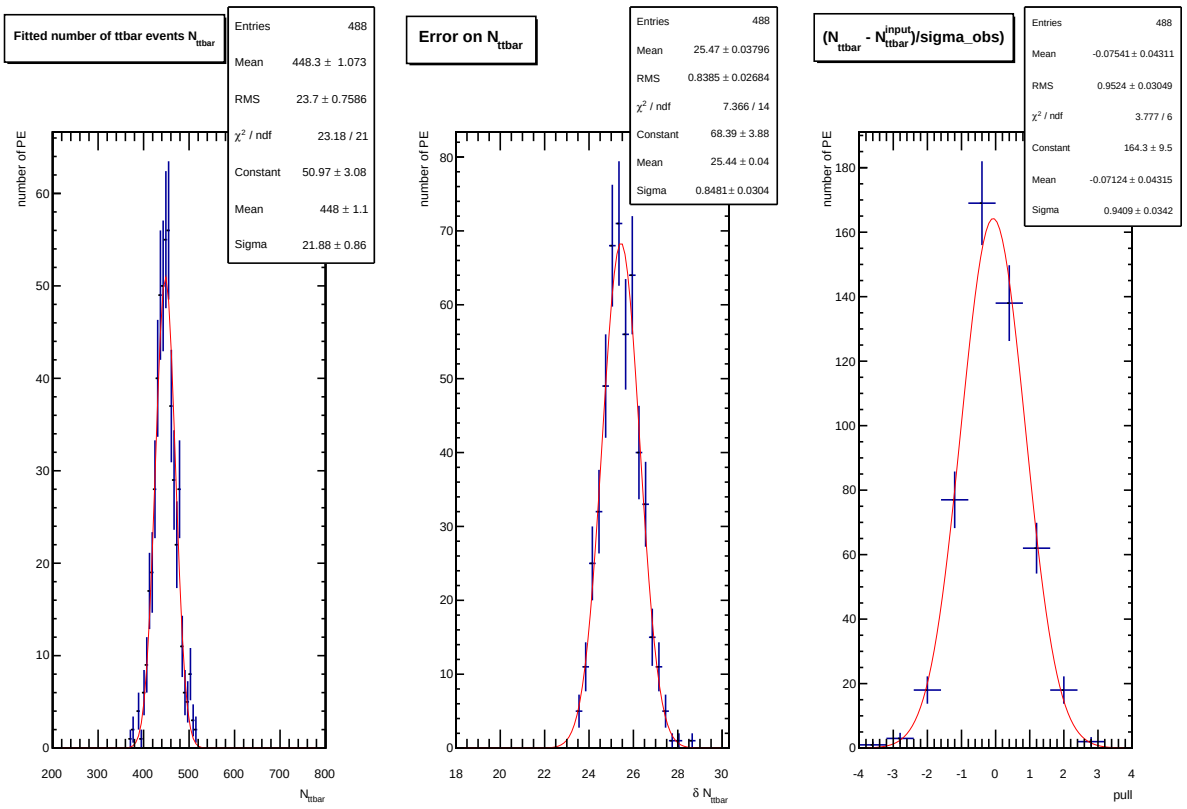

Figure 8.34: Pseudo-experiments performed to smeared spin-correlated events ($f_{input} = 1$) with sample size 500 including a 10% smeared W+jets background. The fitted number of $t\bar{t}$ events $N_{t\bar{t}}$ in the pseudo-experiment is shown (left), the fit uncertainty $\delta N_{t\bar{t}}$ (middle) and the pull distribution (right). A mean $N_{t\bar{t}}$ of 450 is expected.

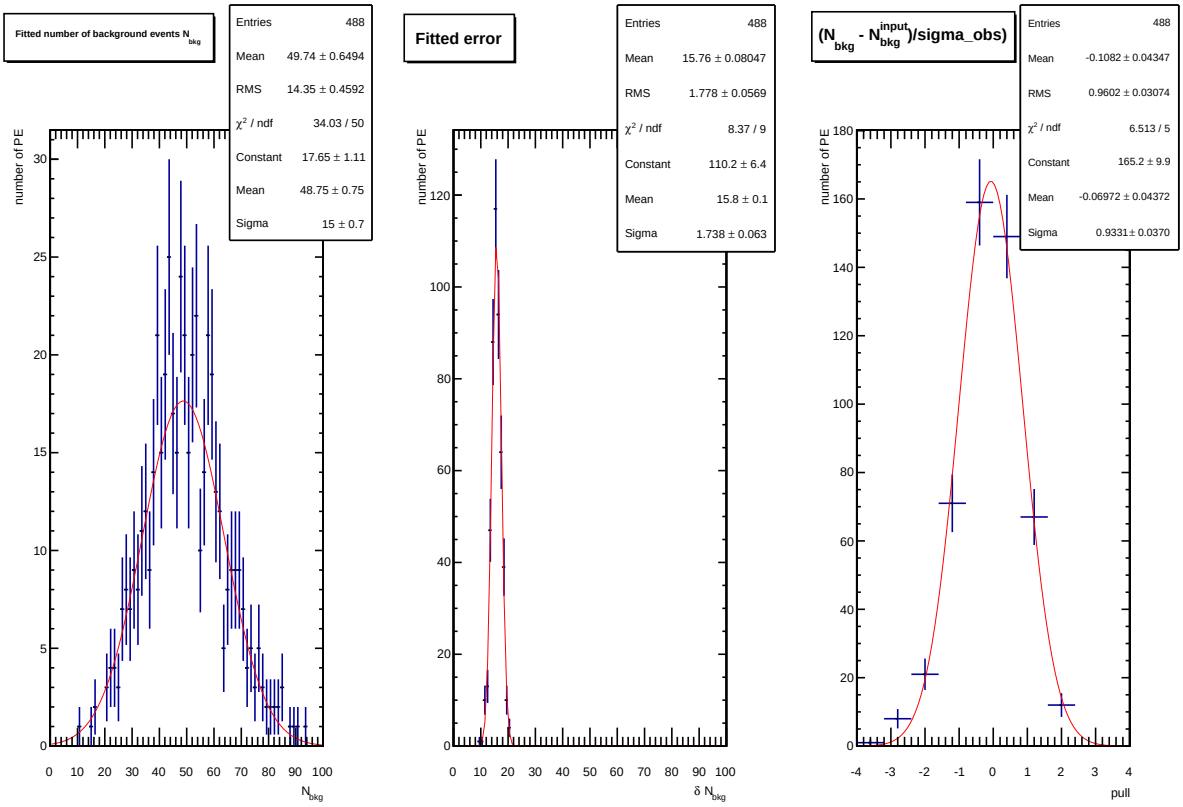

Figure 8.35: Pseudo-experiments performed to smeared spin-correlated events ($f_{input} = 1$) with sample size 500 including a 10% smeared W+jets background. The fitted number of background events N_{bkg} in the pseudo-experiment is shown (left), the fit uncertainty δN_{bkg} (middle) and the pull distribution (right). A mean N_{bkg} of 50 is expected.

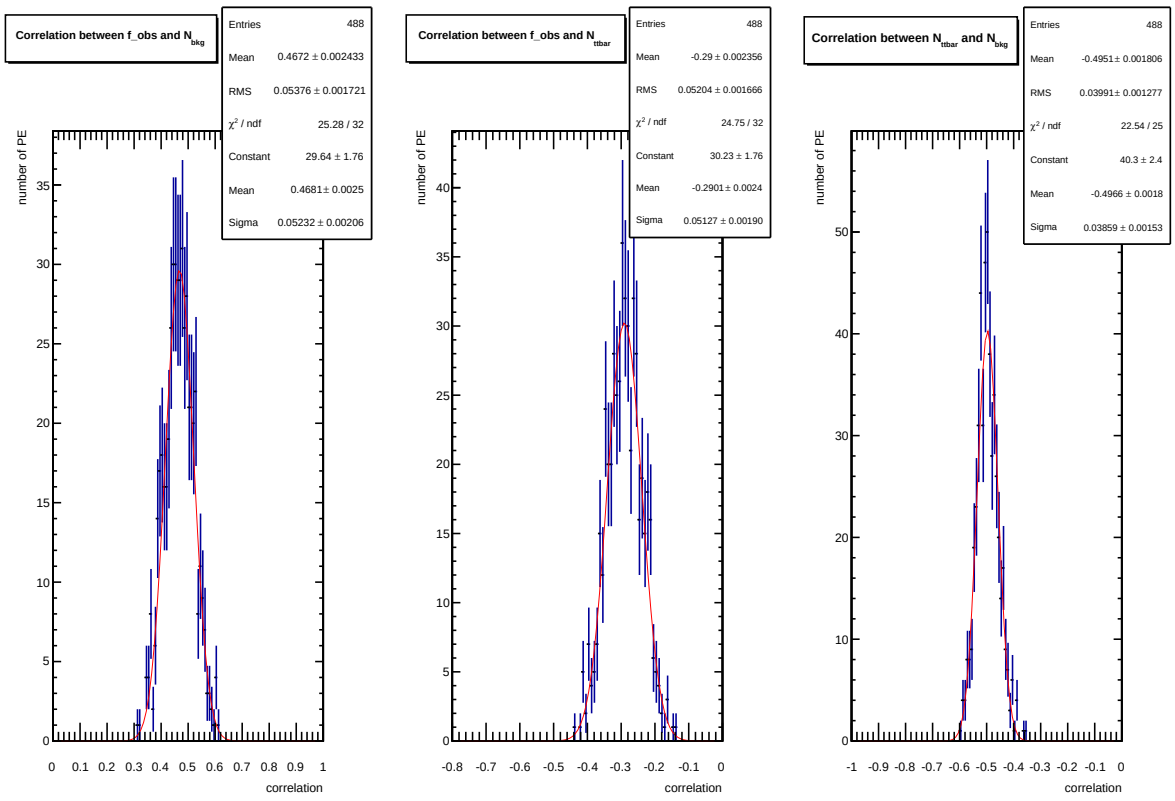

Figure 8.36: Pseudo-experiments performed using spin-correlated events ($f_{input} = 1$) with sample size 500 including a 10% W+jets background. The correlation between the fit parameters f, N_{ttbar} and N_{bkg} is shown.

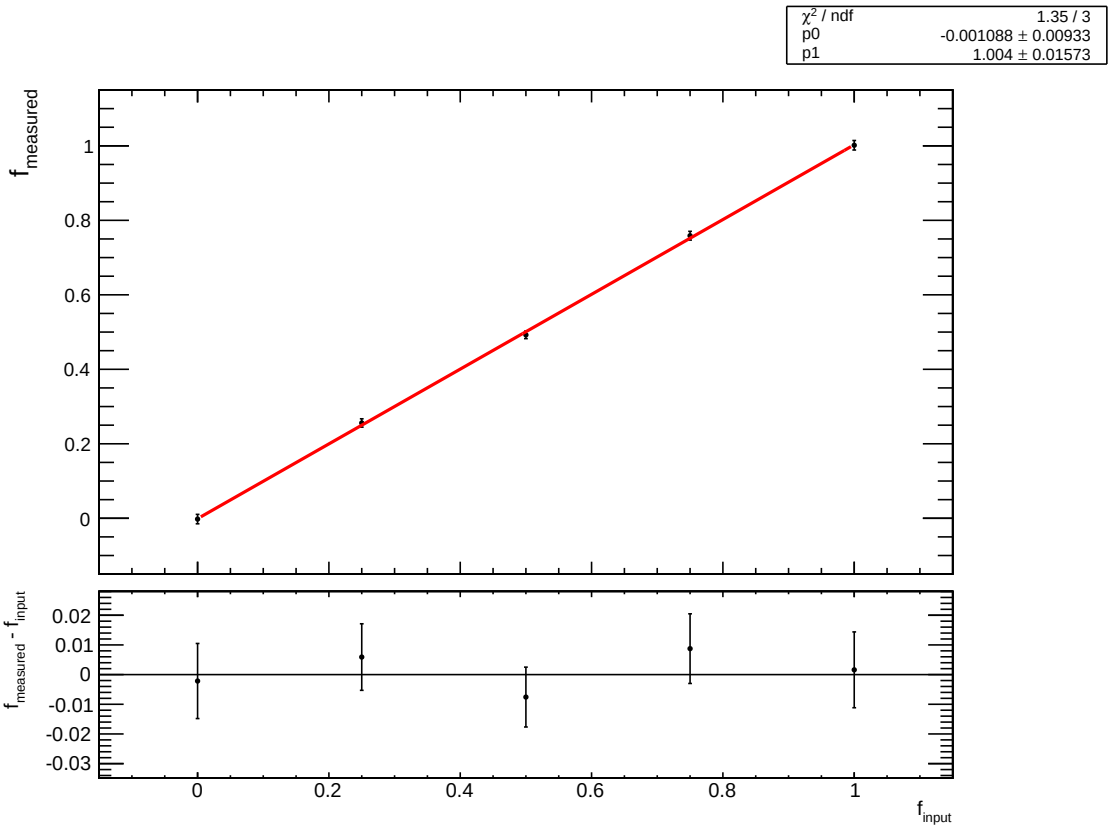

Figure 8.37: Mean fitted f as a function of f_{input}, which is obtained by mixing spin-correlated and spin-uncorrelated samples. The uncertainty bar is obtained from the uncertainty on the mean of the fitted f. The results are obtained from repeated pseudo-experiments on smeared simulation with a sample size of 500 events each including a 10% W+jets background.

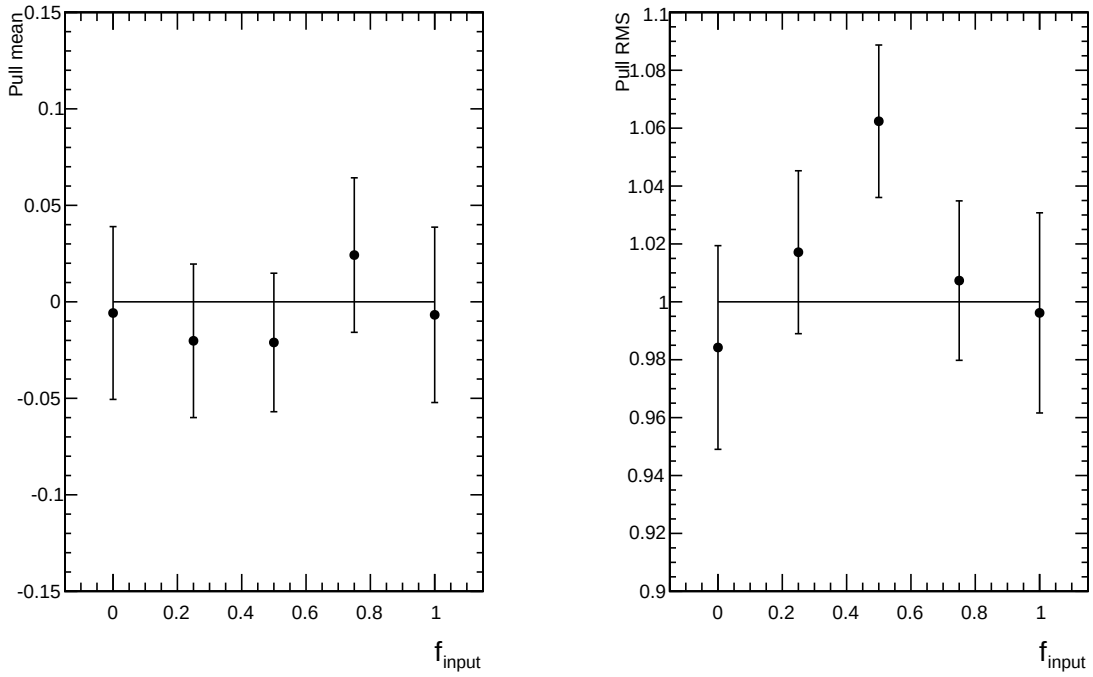

Figure 8.38: Mean of the Gaussian distribution fitted to the pulls (left) as a function of f_{input}, which is obtained by mixing spin-correlated and spin-uncorrelated samples and the pull RMSs on the right. The uncertainty bar is obtained from the uncertainty on the Gaussian fit parameter. The results are obtained from repeated pseudo-experiments with a sample size of 500 events each including a 10% W+jets background.

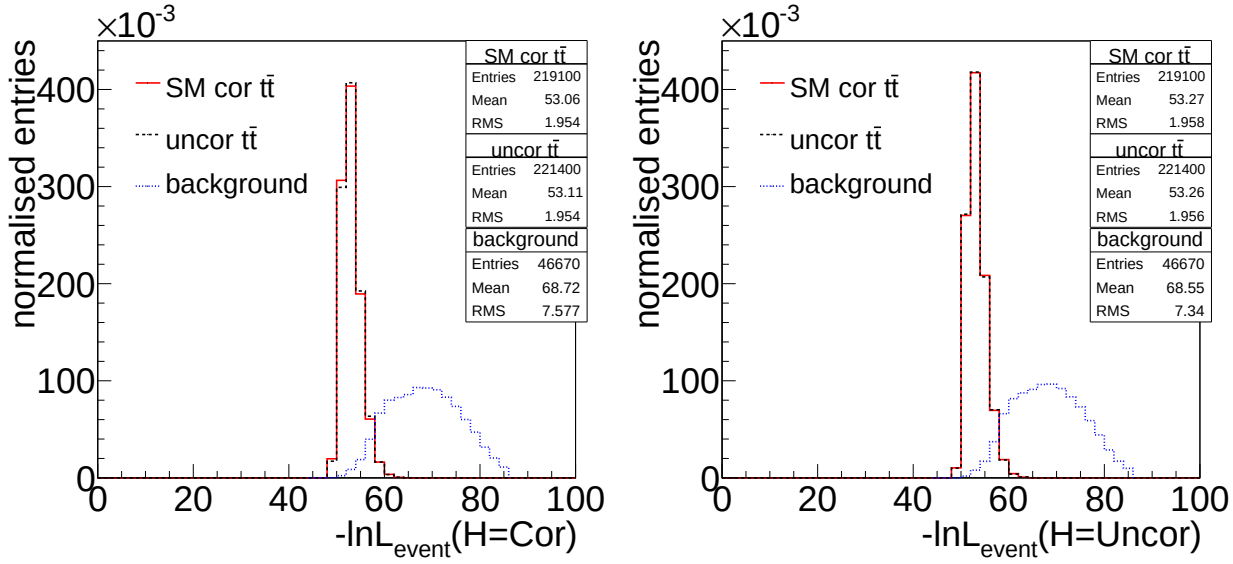

Figure 8.39: Event Likelihood distributions $-\ln L_{event}(H = Cor)$ and $-\ln L_{event}(H = Uncor)$ for the spin-correlated event sample in red solid line, the spin-uncorrelated sample in the black dashed line and the W+jets sample in the blue dotted line.

8.1.4 HitFit

Up to now, we have performed the basic closure tests, checking whether the method works in the ideal scenarios. We have always worked under the assumption that we knew the correct jet-parton permutation. Giving a wrong jet-parton permutation to MadWeight will have a significant influence on the likelihood distributions and therefore to a certain extent on the likelihood ratios. When moving to reconstruction level CMS simulation or to data, we do not know the true jet-parton combination, or even know which jets in the event are coming from the $t\bar{t}$ decay. To make an estimate of the correct jet-parton permutation, we will use a kinematic fitter, HitFit. HitFit is designed specifically to identify the role a reconstructed jet plays in the $t\bar{t}$ semi-leptonic decay. To do this, HitFit varies the measured object kinematics within the resolution (determined from simulation) and checks how well a certain combination matches a semi-leptonic $t\bar{t}$ decay. The χ^2 indicates the goodness of fit for a certain permutation. The jet-parton permutation which is the best estimate for the true jet-parton combination is given by the solution with the lowest χ^2. For more general information on HitFit, see section 4.2.

HitFit Settings and Performance HitFit imposes constraints on the semi-leptonic $t\bar{t}$ decay by using Lagrangian multipliers. These constraints are fully controlled by the user and typically include the mass of the hadronically decaying W-boson and equal mass of the top (m_t) and anti-top quark ($m_{\bar{t}}$). In addition it is possible to add a b-tag constraint, which consists of HitFit trying out all permutations and only keeping those which are consistent with the b-tagging information. The missing energy in the form of a neutrino is calculated based on four-momentum conservation. In our set-up HitFit has been used with the options listed in table. 8.4.
In table 8.5, some results concerning the HitFit performance are shown. We ran HitFit on our LO, smeared parton-level samples, in two different configurations. Once, we used the settings exactly as detailed in table 8.4 which are the default settings. A second time, we imposed an extra constraint. We always impose the $m_t = m_{\bar{t}}$ constraint, but sometimes we added the extra constraint that $m_t = 173$ GeV, which is the top quark mass we used during the generation of our LO samples. In table 8.5, we list in which closure test the constraint was turned on.

Two aspects define the HitFit performance:

- **Fit efficiency**
  The fit efficiency is defined as the fraction of events in which the HitFit calculations converged and at least one jet-parton permutation is returned. Since we are working with smeared parton level information, we expect the fit efficiency to be very high, as is the case for the $t\bar{t}$ samples. The fit efficiency is naturally lower for the W+jets background sample, offering some discrimination against background. For the $t\bar{t}$ samples, imposing the top quark mass constraint does not vary the fit efficiency by much, as is expected since this constraint is consistent with the $t\bar{t}$ event generation. We also note that the fit efficiency is almost identical for both signal samples, therefore leaving our signal samples unbiased.

- **Purity**
  Another aspect of the HitFit performance is the purity. The purity is defined as the fraction of events in which the best returned jet-parton permutation (we remind the reader that the best permutation is defined as the one with the lowest χ^2) is also the correct jet-parton permutation as given by the simulation truth information. This is decided based on ΔR matching of the jets with the simulation truth information where $\Delta R < 0.5$ is imposed. We strive for the highest purity possible and this is influenced by various settings. Without making use of the b-tagging information the purity is low. All HitFit results in which the chosen jet-parton permutation is not consistent with the b-tagging information, are regarded as being invalid solutions leading to a higher fraction of correct matches. The purity is highest ($\approx 86\,\%$) when imposing the top quark mass constraint and is similar in

Table 8.4: HitFit settings (note: the e_com variable will be changed to 8000 for 8 TeV simulation). Here putting mTop or mw equal to zero means that the constraint is not applied, while inserting a value larger than zero means the mass will be fitted to be equal to that value.

Parameter	Value	Description
use_e	true	Particle energy is kept constant during the fit, 3-momentum is scaled.
solve_nu_tmass	false	If false, use the W-boson mass constraint to extract the p_z^ν. If true, use the hadronic top quark mass to extract the p_z^ν
equal_side	true	Leptonic and hadronic top quark mass are set equal.
e_com	7000	Centre-of-mass energy of the colliding beams (GeV).
bmass	4.7	Mass of the b-quark (GeV).
mwhad_max_cut	10000	Maximum hadronic W mass before the fit (GeV).
mwhad_min_cut	0	Minimum hadronic W mass before the fit (GeV).
jet_mass_cut	10000	The maximum invariant mass of the jets (GeV).
mtdiff_max_cut	10000	The maximum m_t, $m_{\bar{t}}$ difference (GeV) before the fit.
maxit	10000	Maximum number of iterations in the fit for each permutation.
maxcut	20	Maximum number of times the stepsize may be cut.
cutsize	0.5	Fraction by which the stepsize is cut.
min_tot_cutsize	10^{-10}	Smallest fractional cut step allowed during the fit.
chisq_diff_eps	0.01	Convergence threshold for change in χ^2.
constraint_sum_eps	0.01	Convergence threshold for sum of constraints.
maxNJets	6	Maximum number of jets to be considered.
maxEtaMu	2.1	Maximum absolute η value for the muon.
maxEtaJet	2.5	Maximum absolute η value for the jets.
bTagAlgo	CSV	B-tagging algorithm.
minBDiscBJets	0.670	Discriminator value for b-jets.
maxBDiscLightJets	0.670	Discriminator value for light jets.
useBTagging	true	Flag to apply b-tagging.
mw	80.4	Mass of the W-boson (GeV).
mTop	0	Mass of the top quark (GeV). mTop = 0: no mass constraint.

both signal samples. The purity is not defined for the W+jets background sample, since there is no true jet-parton permutation.

In order to obtain the highest purity and largest background rejection, it is possible to place quality cuts on the HitFit output, which are listed and discussed below.

- **χ^2-cut**
  A cut on the χ^2 of the best combination (which is a measure for the goodness-of-fit) is very effective in discriminating signal against background. In fig. 8.40, the χ^2 distribution of the permutation with lowest χ^2 per event is shown. In the $t\bar{t}$ signal plots the colour-coding

Table 8.5: HitFit performance. The cut efficiencies are listed with respect to the events which have a HitFit solution. All efficiencies are listed in %.

	Sample	with $m_t = m_{\bar{t}} =$ 173 GeV constraint	with $m_t = m_{\bar{t}}$ constraint
Fit efficiency	$t\bar{t}$ cor	93.99 ± 0.05	94.45 ± 0.05
	$t\bar{t}$ uncor	94.06 ± 0.05	94.54 ± 0.05
	W+jets	80.12 ± 0.28	84.43 ± 0.18
Purity	$t\bar{t}$ cor	86.80 ± 0.08	75.78 ± 0.10
	$t\bar{t}$ uncor	86.52 ± 0.08	75.50 ± 0.10
$\chi^2 < 20$ cut efficiency	$t\bar{t}$ cor	78.23 ± 0.10	97.10 ± 0.04
	$t\bar{t}$ uncor	78.11 ± 0.10	97.05 ± 0.04
	W+jets	13.82 ± 0.19	32.91 ± 0.26
Purity post $\chi^2 < 20$ cut	$t\bar{t}$ cor	87.67 ± 0.09	76.07 ± 0.10
	$t\bar{t}$ uncor	87.45 ± 0.09	75.77 ± 0.10
$150\,\text{GeV} < m_t < 225\,\text{GeV}$ cut efficiency	$t\bar{t}$ cor	x	86.79 ± 0.08
	$t\bar{t}$ uncor	x	86.45 ± 0.08
	W+jets	x	40.75 ± 0.27
Purity post $150\,\text{GeV} < m_t < 225\,\text{GeV}$ cut	$t\bar{t}$ cor	x	85.86 ± 0.09
	$t\bar{t}$ uncor	x	85.80 ± 0.09
$\chi^2 < 20 + 150\,\text{GeV} < m_t < 225\,\text{GeV}$ cut efficiency	$t\bar{t}$ cor	x	84.81 ± 0.08
	$t\bar{t}$ uncor	x	84.44 ± 0.08
	W+jets	x	15.95 ± 0.20
Purity post $\chi^2 < 20$ and $150\,\text{GeV} < m_t < 225\,\text{GeV}$ cut	$t\bar{t}$ cor	x	85.90 ± 0.09
	$t\bar{t}$ uncor	x	85.86 ± 0.09
Cumulative efficiency	$t\bar{t}$ cor	73.53 ± 0.10	80.10 ± 0.09
	$t\bar{t}$ uncor	73.47 ± 0.10	79.83 ± 0.09
	W+jets	11.07 ± 0.15	13.47 ± 0.17

indicates which permutation has been selected, with the correct jet-parton permutation shown in red. As there is no correct permutation for the W+jets events, the colour-coding has been removed. In the left plots of fig. 8.40 the top quark mass constraint was turned on in the fit, leading to higher values of χ^2. From the plots, it is clearly visible that the background sample has a much broader χ^2 distribution. The corresponding distributions for the uncorrelated $t\bar{t}$ sample are shown in Appendix A.4. In table 8.5 we show the fraction of events which remain after cutting away events with $\chi^2 > 20$. Applying the χ^2-cut is very efficient in removing background, but does not significantly improve the purity. The selection efficiency after the χ^2 is very similar for correlated and uncorrelated $t\bar{t}$ events. Plots of the χ^2 fit probability are also shown in Appendix A.4.

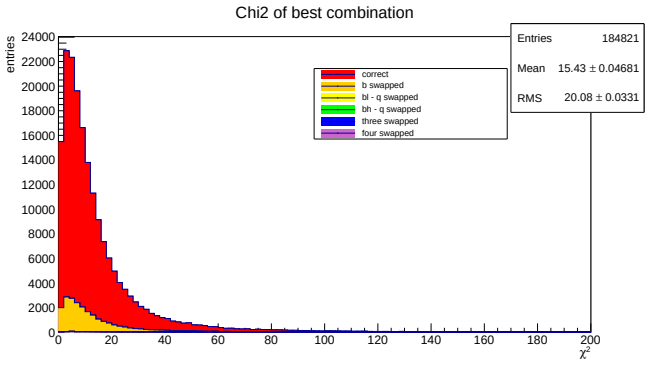

(a) $t\bar{t}$ spin-correlated events with $m_t = 173$ GeV constraint.

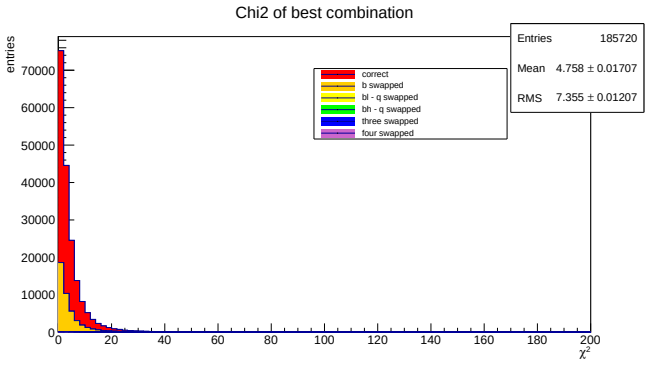

(b) $t\bar{t}$ spin-correlated events.

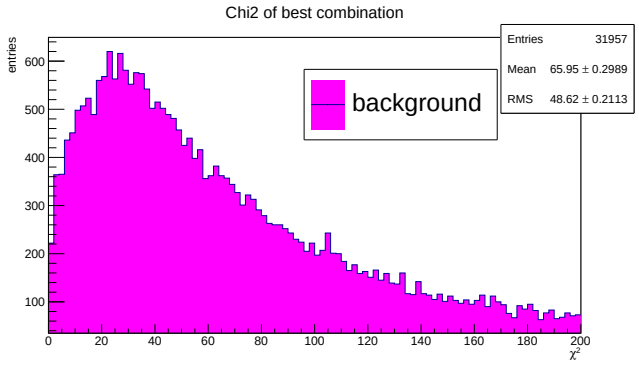

(c) W+jets events with $m_t = 173$ GeV constraint.

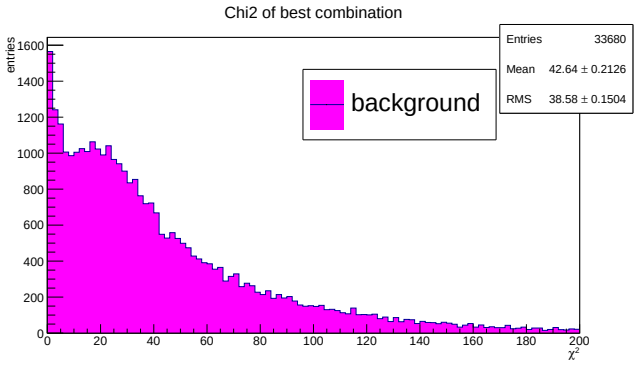

(d) W+jets events.

Figure 8.40: χ^2 distribution of the best permutation returned by HitFit. The colour coding indicates the jet-parton permutation.

- **top quark mass window**
  In the case where the top quark mass is not forced to be 173 GeV, the distribution of the fitted top quark mass of the best combination is a broad peak around the top quark mass value as is shown in fig. 8.41. The peak is caused by the correct jet-parton permutation, whereas the incorrect jet-parton permutations have a much flatter distribution of fitted top quark mass values, similarly for the background events. Applying a broad window around the known top quark mass, helps to increase the purity and reduce the background. Table 8.5 shows the fraction of events which is retained after applying the top quark mass window, and the purity after this selection. The table also shows the cumulative effect of χ^2-cut and the top quark mass window. Note that the overall cut efficiency for the background is similar with or without the top quark mass constraint, but that more signal is retained without the top quark mass constraint. The purity is drastically increased after adding this loose top quark mass window and is now similar as when applying the top quark mass constraint in the fit.

We want to note that the $t\bar{t}$ spin-correlated sample and the $t\bar{t}$ spin-uncorrelated sample behave very similar under HitFit, so the use of HitFit will not bias the data towards spin-correlated or spin-uncorrelated events. Based on these numbers at the parton level, we prefer the scenario in which the top quark mass is left floating in the fit, but extra quality cuts are applied afterwards. This is the conclusion when we consider only the HitFit performance.

Evaluation of HitFit Output Combined with MadWeight In the previous section we discussed the various options in which HitFit can be used and how this affects the performance.

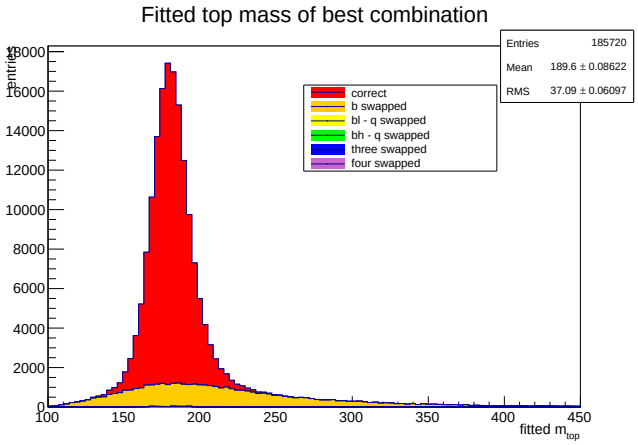

(a) $t\bar{t}$ spin-correlated events.

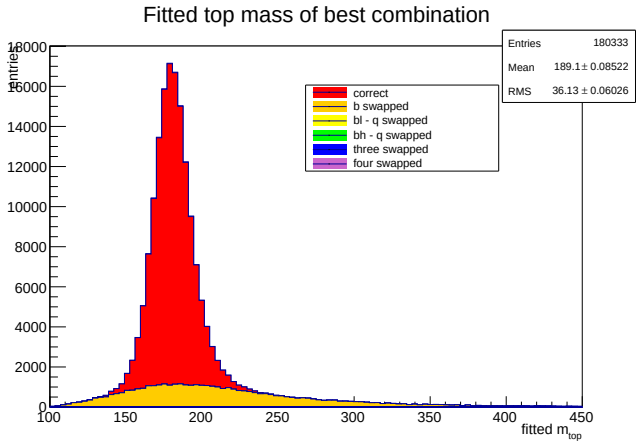

(b) $t\bar{t}$ spin-correlated events with χ^2 cut.

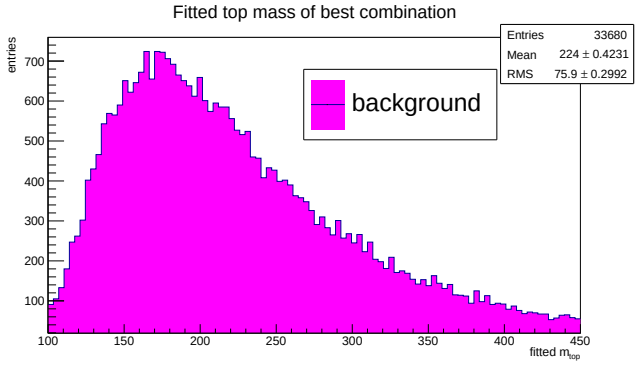

(c) W+jets events.

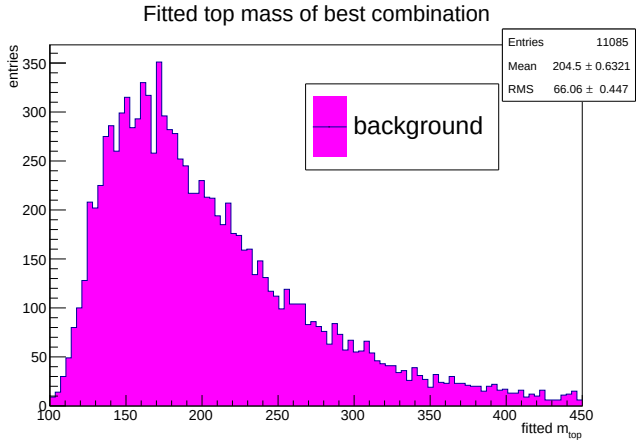

(d) W+jets events with χ^2 cut.

Figure 8.41: Fitted top quark mass distribution of the best permutation returned by HitFit. The colour coding indicates the jet-parton permutation.

There are various ways in which we can incorporate the HitFit output in the likelihood calculations performed by MadWeight. There is the option to use only the jet-parton permutation that HitFit returns, or to use the jet-parton permutation and the updated kinematics to which the kinematic fitter converges. As mentioned before, HitFit varies the kinematics of the decay products within the resolutions to try to correct for detector resolution effects. By using the HitFit updated kinematics, we have an estimate of the parton level kinematics of the event which are compatible with the imposed constraints. If the estimate of the kinematics is accurate enough, running MadWeight with these kinematics and a δ transfer function should give equally accurate results as using the original kinematics processed with the double Gaussian transfer function that was used for the smearing. If the HitFit estimate of the kinematics is accurate enough to be processed with a δ transfer function, this offers a CPU advantage as the integration over the phase space during the likelihood calculation is faster then. The second point to test is whether it is feasible to perform the likelihood calculation only over the HitFit returned permutation (and therefore having a fraction of events in which a wrong permutation is considered) or to have MadWeight iterate over all possible permutations leading to higher processing times, but the advantage that the correct permutation is always considered (in the parton level tests). As such, we end up with several scenarios in which the HitFit output can be combined with MadWeight.

The set-up of the various scenarios is listed in table 8.6 with for each scenario marked which option was used. These tests are performed on the LO simulation samples used in the previous section including smearing and acceptance cuts. There is a significant difference in CPU requirements for the various scenarios, but the goal is to find the scenario which gives the best precision. The result of the different scenarios is shown in table 8.7 (in pseudo-experiments with and without background contribution) and figs. 8.42-8.43. Here the results from HitFit are used ad hoc. The quality cuts described earlier for the case in which the top quark mass is left floating are not yet applied, leading to a lower purity in those scenarios. The pseudo-experiments are set up in exactly the same way as in the previous section: the number of events is drawn from a Poisson distribution with mean 500, a bin width of 0.14 is used, the fit range is [-7,7], the same fit parameters are chosen. From table 8.6, it is obvious that there are even more options available, however the presented tests should be enough to draw conclusions.

Table 8.6: List of studied combinations of HitFit output with MadWeight calculations. For each scenario, there is indicated whether the $m_t = 173$ GeV constraint is turned on, whether HitFit kinematics and permutation are used and which transfer function (TF) is used in the MadWeight calculation (either a double Gaussian DG or Dirac δ).

Scenario	$m_t = 173$ GeV constraint	HF kinematics	HF permutation	TF
a	x	x	x	δ
b	x	x	x	DG
c		x	x	δ
d		x	x	DG
e			x	DG
f				DG
g		x		δ

- *Scenario a: HitFit kinematics + permutation, $m_t = 173$ GeV constraint, δ-TF*
  In this option, the HitFit combination and updated kinematics are used. The fit is performed imposing the $m_t = 173$ GeV constraint. In MadWeight, the δ-TF is used for all particles.

  In fig. 8.42a, the $-2\ln\lambda_{event}$ distribution is shown for this scenario. What is most obvious at first sight is how similar the W+jets background template is to the signal templates. This is not surprising since HitFit forces the kinematics of the W+jets background events to converge to kinematics compatible with the imposed $t\bar{t}$ constraints. This indicates there is low discriminating power between signal and background. From the bottom plot, showing the ratio of the signal templates, we see that we still have some discriminating power between the signal hypotheses. In fig. 8.43a, the $-\ln L_{event}(H = Cor)$ distribution is shown. We also see that the W+jets distribution is very similar to the signal distributions. As a result the likelihood distribution can no longer be used to effectively discriminate against background. In table 8.7, the mean observed f and fit error is shown in the case of $f_{input} = 1$ and in addition the parameters of the linear fit to the mean f as a function of f_{input}. From the results, we conclude that the discriminating power in the signal is still high enough to correctly extract the spin correlation fraction f when there is no background contamination, but very biased results are obtained when background is included due to the low discrimination between signal and background.

- *Scenario b: HitFit kinematics + permutation, $m_t = 173$ GeV constraint, double Gaussian TF*

This scenario is the same as scenario a, apart from the fact that a double Gaussian TF was used instead of the δ-TF.

In fig. 8.42b, the $-2\ln\lambda_{event}$ distribution is narrower than in fig. 8.42a and the W+jets template is slightly different. The same effect is observed in fig. 8.43b: the likelihood distribution is much narrower and offers more discriminating power with respect to the background. From scenario's a and b, we conclude that even with the $m_t = 173$ GeV constraint, the estimate of the parton kinematics is not sufficient to remove the transfer function from the MadWeight calculation.

- *Scenario c: HitFit kinematics + permutation, δ-TF*
  In this scenario, the HitFit combination and updated kinematics are used. The fit is performed while leaving the top quark mass floating. In MadWeight, the δ-TF is used for all particles.

  In fig. 8.42c the input templates for this scenario are shown. Releasing the top quark mass constraint has a significant influence on the shape of the background template. It is now significantly different from the signal templates. From the ratio plot at the bottom we can see that we have little discriminating power between the signal hypotheses. In fig. 8.43c, also here we confirm the significantly different behaviour between signal and background. However here we see that the discriminating power between the spin-correlated and spin-uncorrelated signal is too small to give reasonable results. Not only is there a bias in the obtained f value (as seen in table 8.7), but the mean fit uncertainty is very large.

- *Scenario d: HitFit kinematics + permutation, double Gaussian TF*
  Same scenario as in scenario c, but with a double Gaussian TF.

  In fig. 8.42d the input templates for the signal now show a larger discriminating power and the background template is even further distorted from the signal. In fig. 8.43d, the $-\ln L_{event}(H = Cor)$ distribution is again very narrow. Here we clearly see a shoulder on the high tail of the signal distributions. This feature is due to the events having the wrong permutation and therefore show up at lower likelihood values (higher $-\ln L_{event}(H = Cor)$ values). I remind the reader here that the purity in this scenario is significantly lower than in the first two scenarios which included the $m_t = 173$ GeV constraint. With this sufficiently narrow distribution, the events with a wrong permutation can be resolved. From table 8.7, we see that in this scenario f can be extracted without bias.

- *Scenario e: HitFit permutation, double Gaussian TF*
  In this case, we choose to use the best combination provided by HitFit, but to use the original kinematics. In the fit, the top quark mass is left floating. In this case, there has been no correction to parton level kinematics, so a double Gaussian TF must always be used.

  As can be seen from fig. 8.42e, the input templates are very similar to the ones from the previous scenario, indicating that the difference between HitFit updated kinematics and original kinematics is not substantial when the m_t constraint is not applied. Also from fig. 8.43e we see that the situation is very similar to the previous case.

- *Scenario f: MadWeight permutations switched on, double Gaussian TF*
  Up to now, we have used the HitFit best permutation and letting MadWeight calculate the likelihood only for that combination, knowing that in a certain fraction of the events this permutation is wrong. We can also be conservative and let MadWeight sum over all possible jet-parton permutations, making a weighted average and therefore always in-

cluding the right permutation. This scenario does not use any HitFit information at all and MadWeight performs a fourfold permutation by swapping the b-jets and swapping the light jets. In RECO simulation and data, where we have initial state radiation (ISR) and final state radiation (FSR), we would always need HitFit to decide which jets (in case of an event with more than four jets) belong to the $t\bar{t}$ decay, even if we want to turn the MadWeight permutations on. Looping over the possible permutations with a double Gaussian TF is by far the slowest option.

In fig. 8.42f the input templates are shown. We clearly see that the signal templates are much narrower and offer a far greater discriminating power. The W+jets background template is significantly different. In fig. 8.43f the likelihood distribution is shown. It shows a very narrow distribution for the signal and a very broad distribution for the background. Notice how the shoulder at the high tail of the signal templates is no longer there, since there are no events in which only a wrong permutation is taken into account. In table 8.7, we see that there is no bias in extracting f, but more importantly: this scenario has the smallest average fit error. Based on the low fit error and larger discrimination against background, this scenario is clearly the preferred option.

- *Scenario g: HitFit kinematics, MadWeight permutations on, δ-TF*
  We revisit the scenario in which the HitFit updated kinematics are used. The top quark mass constraint is not imposed. MadWeight is run with a δ-TF, but with the permutations on. In scenario c, there are two limiting factors: limited resolution by using a δ-TF when this is not warranted and the effect of wrong permutations. This scenario eliminates the effect of the wrong permutations.

  In fig. 8.44 the input templates are shown, also with the permutations turned on there is not enough discriminating power in the $t\bar{t}$ signal templates. The likelihood distribution in 8.45 still shows a discrepancy between the spin-correlated and spin-uncorrelated sample. These plots are very similar to scenario c, indicating that the limiting factor in scenario c was the limited resolution.

In the previous, we discussed the various scenarios and showed in table 8.7 the precision that can be obtained with each scenario in the given set-up. An important point we have to make with this comparison is the following: in all these scenarios we used 500 events per pseudo-experiment, but in sec. 8.1.4, we saw that HitFit has a certain fit efficiency which is different depending on the constraints you apply. So we need to take into account that these pseudo-experiments are applied at different luminosity. Using HitFit will reduce our available statistics and the precision with which we can extract f will go down accordingly. The mean fit errors corrected for the fit efficiency will be shown in table 8.9. From the comparison between all the scenarios in table 8.7, scenario f is preferred as it offers the best average error on f and in addition no bias in the results is observed. Scenario f has the permutations turned on in MadWeight and a transfer function for the jet energy is used during the calculations.

Table 8.7: HitFit scenarios and results at $f_{input} = 1$ for columns 2 and 3

Scenario	mean f	mean δf	Linearity Curve Slope	Linearity Curve Offset
a: HitFit kin, $m_t = 173$ GeV constraint, δ-TF	1.031 ± 0.039	0.650 ± 0.002	0.992 ± 0.044	0.016 ± 0.02
a: HitFit kin, $m_t = 173$ GeV constraint, δ-TF, 10 % W+jets	0.813 ± 0.055	0.699 ± 0.034	0.824 ± 0.058	−0.020 ± 0.031
b: HitFit kin, $m_t = 173$ GeV constraint, double Gaussian TF	1.002 ± 0.029	0.586 ± 0.002	0.997 ± 0.039	0.001 ± 0.024
b: HitFit kin, $m_t = 173$ GeV constraint, double Gaussian TF, 10 % W+jets	0.865 ± 0.054	0.698 ± 0.022	0.863 ± 0.055	0.006 ± 0.030
c: HitFit kin, δ-TF	1.242 ± 0.082	1.318 ± 0.103	1.386 ± 0.086	−0.178 ± 0.047
c: HitFit kin, δ-TF, 10 % W+jets	1.025 ± 0.107	1.686 ± 0.103	1.044 ± 0.110	−0.765 ± 0.059
d: HitFit kin, double Gaussian TF	1.007 ± 0.036	0.642 ± 0.002	1.038 ± 0.044	−0.018 ± 0.026
d: HitFit kin, double Gaussian TF, 10 % W+jets	0.999 ± 0.043	0.770 ± 0.005	1.013 ± 0.049	−0.011 ± 0.028
e: HitFit combination only, double Gaussian TF	1.030 ± 0.040	0.643 ± 0.002	1.006 ± 0.046	−0.015 ± 0.027
e: HitFit combination only, double Gaussian TF, 10 % W+jets	1.016 ± 0.045	0.794 ± 0.005	0.981 ± 0.050	0.007 ± 0.029
f: MadWeight perm on, double Gaussian TF	1.002 ± 0.020	0.401 ± 0.001	1.005 ± 0.025	0.002 ± 0.015
f: MadWeight perm on, double Gaussian TF, 10 % W+jets	1.011 ± 0.022	0.466 ± 0.001	1.018 ± 0.027	0.002 ± 0.020
g: HitFit kin, perm on, δ-TF	1.493 ± 0.063	0.994 ± 0.066	1.666 ± 0.073	−0.209 ± 0.041
g: HitFit kin, perm on, δ-TF, 10 % W+jets	1.451 ± 0.071	1.202 ± 0.084	1.370 ± 0.081	−0.118 ± 0.045

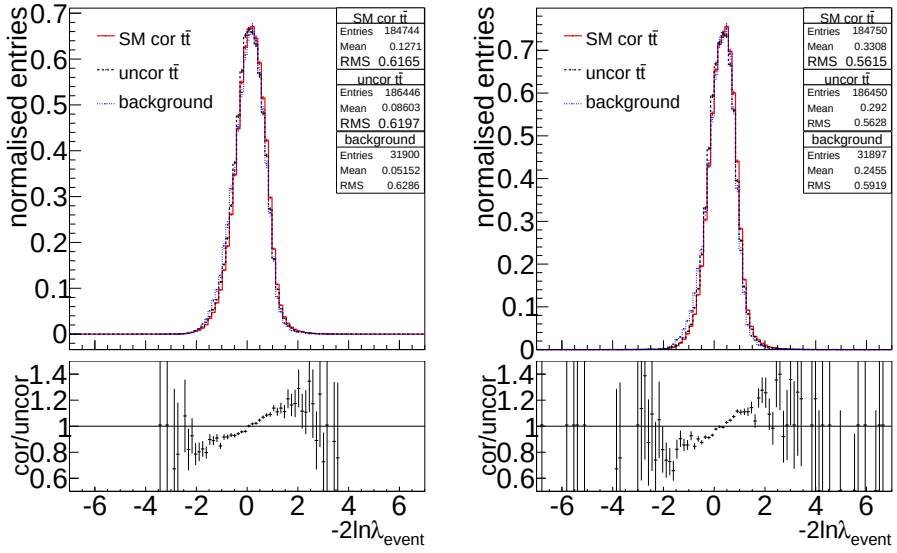

(a)

(b)

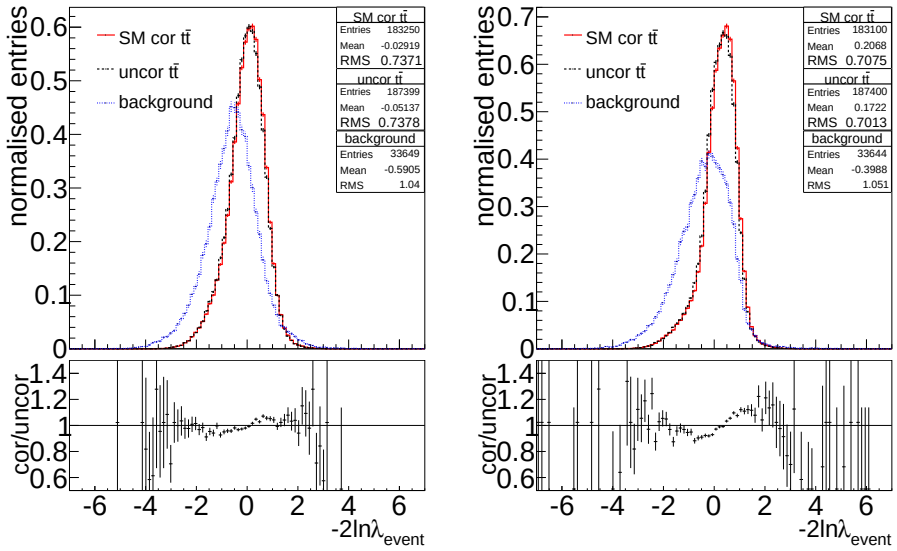

(c)

(d)

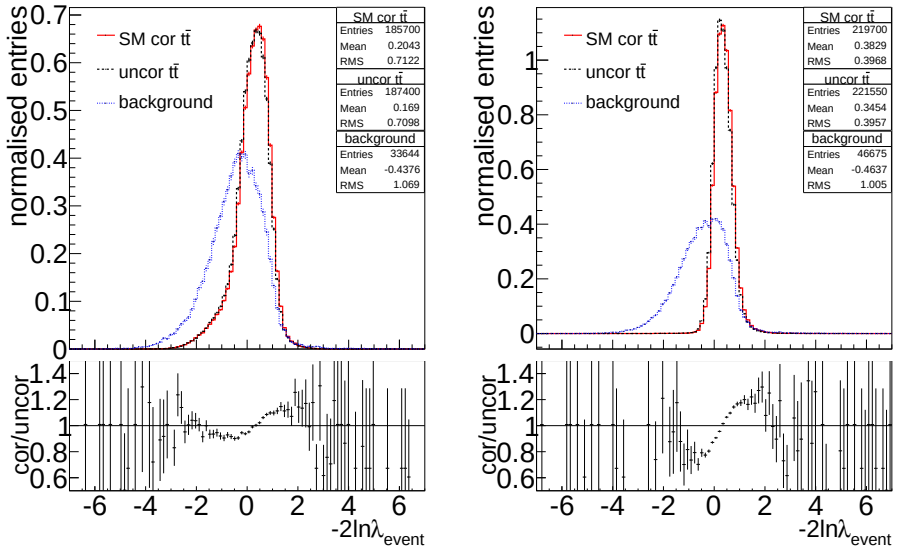

(e)

(f)

Figure 8.42: Histograms of $-2\ln\lambda_{event} = 2\ln L_{event}(H = Cor) - 2\ln L_{event}(H = Uncor)$ for individual events from SM correlated $t\bar{t}$ (red solid) and uncorrelated $t\bar{t}$ (black dashed) within acceptance. The ratio of cor/uncor is shown at the bottom of each plot.

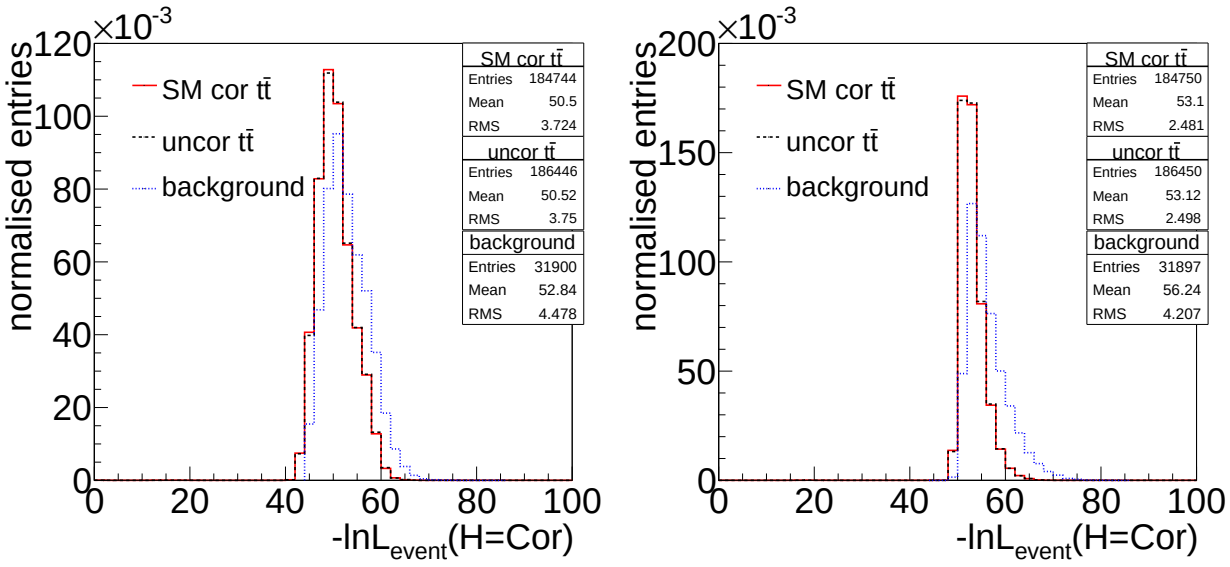

(a)

(b)

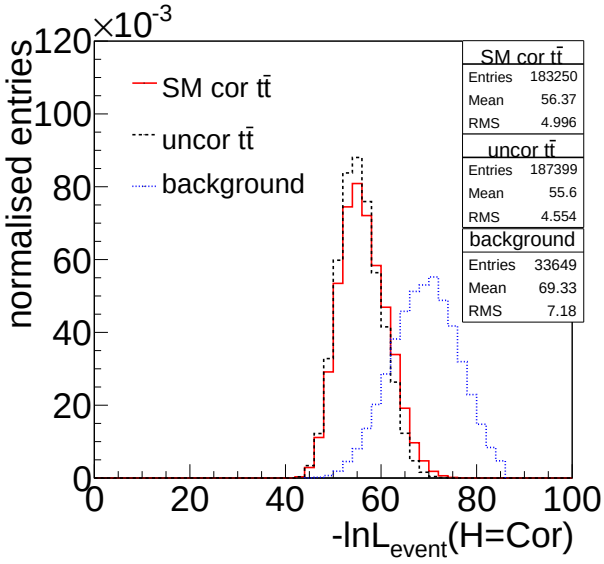

(c)

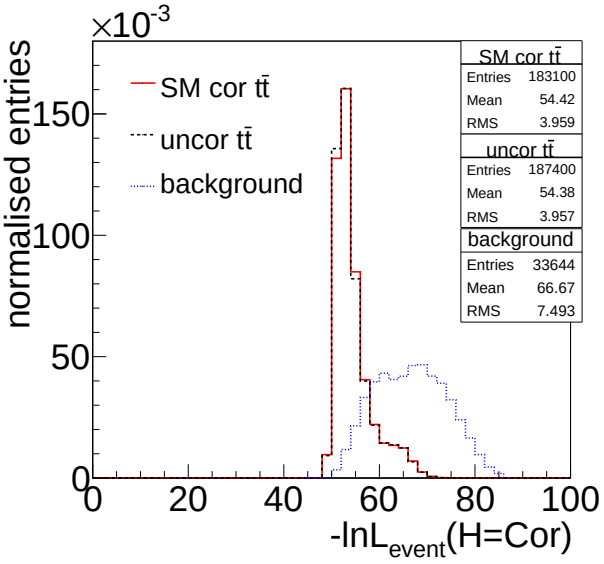

(d)

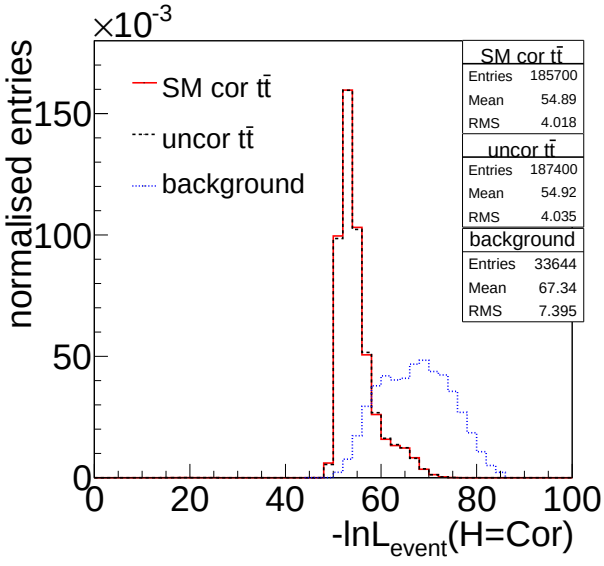

(e)

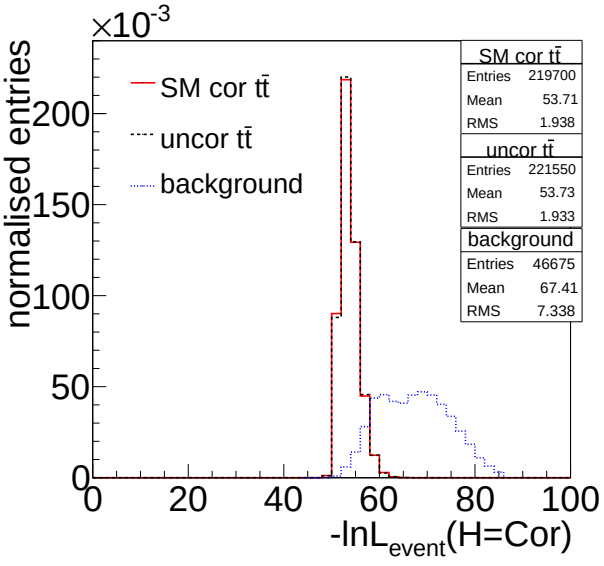

(f)

Figure 8.43: Event Likelihood distributions $-\ln L_{event}(H = Cor)$ for the spin-correlated event sample in red solid line, the spin-uncorrelated sample in the black dashed line and the W+jets sample in the blue dotted line.

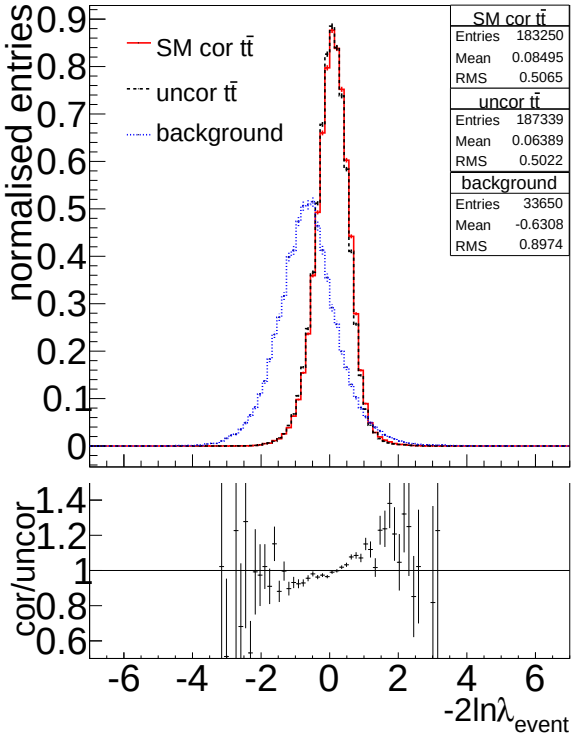

Figure 8.44: Scenario g: Histograms of $-2\ln\lambda_{event} = 2\ln L_{event}(H = Cor) - 2\ln L_{event}(H = Uncor)$ for individual events from generated samples according to $H = Cor$ (red solid histogram) and $H = Uncor$ (black dashed histogram) within acceptance. The ratio of the spin-correlated template over the spin-uncorrelated template is shown in the bottom plot.

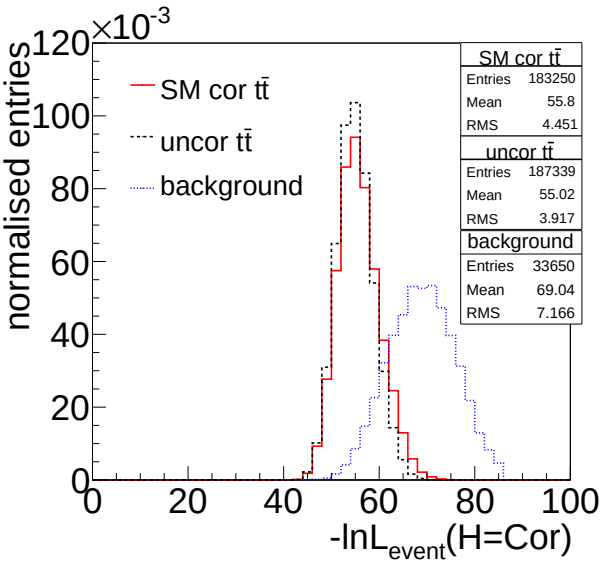

Figure 8.45: Scenario g: Event Likelihood distributions $-\ln L_{event}(H = Cor)$ for the spin-correlated event sample in red solid line, the spin-uncorrelated sample in the black dashed line and the W+jets sample in the blue dotted line.

Evaluation of HitFit Output with Quality Cuts Applied Combined with MadWeight
We consider in this paragraph the same scenarios (with a one-to-one correspondence in the naming) as in the previous paragraph with the addition of the previously discussed HitFit quality cuts: a cut of $\chi^2 < 20$ and in addition the top quark mass window $150\,\text{GeV} < m_t < 225\,\text{GeV}$ when m_t is not constrained in the fit.

- *Scenario a: HitFit kinematics + permutation, $m_t = 173$ GeV constraint, δ-TF, $\chi^2 < 20$*
  In fig. 8.46a, the effect of the χ^2-cut on the input templates is shown. When we compare with fig. 8.42a we see the signal template did not vary much, and also the W+jets background template is very similar to the one without the χ^2-cut when we take into account the uncertainty bars. The W+jets template contains very limited statistics as the selection efficiency for the background events is very low with the χ^2-cut. From table 8.8, we learn that we can extract results consistent with the input.

- *Scenario b: HitFit kinematics + permutation, $m_t = 173$ GeV constraint, double Gaussian TF, $\chi^2 < 20$*
  As before the double Gaussian TF is the better option with a larger discrepancy in the likelihood for W+jets and the $t\bar{t}$ signal, as can be seen in fig. 8.46b and fig. 8.47b. And again the discriminating power in the signal is slightly larger than in scenario a. From table 8.8, we learn that we can extract results consistent with the input.

- *Scenario c: HitFit kinematics + permutation, δ-TF, $\chi^2 < 20$, $150\,\text{GeV} < m_t < 225\,\text{GeV}$*
  Since from here on we do not fix the top quark mass in the fit, we can apply the top quark mass window. Without the quality cuts, this scenario of using δ-TFs gave inconsistent results. In fig. 8.46c, we still see little discriminating power between the spin-correlated and spin-correlated templates but larger discrimination between signal and background, very similar to the scenario without quality cuts. We obtained biased results with large uncertainties.

- *Scenario d: HitFit kinematics + permutation, double Gaussian TF, $\chi^2 < 20$, $150\,\text{GeV} < m_t < 225\,\text{GeV}$*
  Using the double Gaussian TF for this scenario gives us the separation we need between the spin-correlated template and spin-correlated template as seen in fig. 8.46d. The likelihood for the W+jets sample in fig. 8.47d is shifted from the $t\bar{t}$ likelihoods, but the shift and shape difference from the signal distribution is far less pronounced than in the scenario without quality cuts. The shoulder at the high tail of the $t\bar{t}$ likelihoods has disappeared, due to the higher purity of the sample. With the quality cuts applied, all scenarios have similar purities. Without including backgrounds the results are consistent with the input. The mean fitted error has significantly reduced with respect to the scenario without the quality cuts. When considering a background contribution, we obtain biased results with large uncertainties.

- *Scenario e: HitFit permutation, double Gaussian TF, $\chi^2 < 20$, $150\,\text{GeV} < m_t < 225\,\text{GeV}$*
  As before this scenario is very similar to the previous scenario. In fig. 8.46e and fig. 8.47e the input templates and the likelihood distribution are shown. Again the additional quality cuts significantly narrow the signal distribution and brings the background closer to the signal. When not considering background all results are compatible with the input within the error. The mean fit error has significantly gone down with respect to the case without the quality cuts. When including background the fits do not converge properly, again due to the W+jets background mimicking the signal and the limited statistics.

- *Scenario f: MadWeight permutations switched on, double Gaussian TF, $\chi^2 < 20$, $150\,\text{GeV} < m_t < 225\,\text{GeV}$*
  In the previous version of scenario f the only HitFit information that was used was whether

the fit converged for the event or not. Here, some more information is used by the application of the quality cuts, but again HitFit only acts as a selection criterium. In fig. 8.46f the input templates are shown. We clearly see that the signal templates are much narrower and offer a far greater discriminating power still than the other scenarios. The W+jets background template is significantly different, but also here the quality cuts push the background template closer to the signal templates. In fig. 8.47f the likelihood distribution is shown. It shows a very narrow distribution for the signal and a broader distribution for the background, but again the discriminating power against the background of this distribution is reduced by applying the HitFit quality cuts. Again we are able to extract consistent results. The mean fit error has only slightly improved by adding these quality cuts though.

- *Scenario g: HitFit kin, perm on, δ-TF, $\chi^2 < 20$, $150\,GeV < m_t < 225\,GeV$*
  Before this scenario gave inconsistent results and adding the quality cuts did not improve the situation. This is a scenario which can be eliminated for consideration.

The general conclusion to this discussion is that adding the quality cuts improves the fit error when only considering signal. When background is added, the quality cuts introduce large correlations between the fit parameters since the background sample is forced to resemble the signal more. However the statistics in the background template is so low, due to the efficiency of the quality cuts to reject the background, that the scenarios where background is added to the fit, cannot be properly assessed. The fluctuation of the background template should be taken into account and not enough pseudo-experiments can be set up from the pool of background events.

Just as in the previous section, we have to make the remark that these scenarios are evaluated at different luminosities since we have different selection efficiencies for the different scenarios. Comparing the average fit uncertainty at a fixed dataset size (as is done in table 8.7 and 8.8) gives a good overview of which scenario has the best intrinsic precision. However, to have an accurate comparison the effect of the lower dataset size due to the efficiency of the quality cuts needs to be taken into account. In table 8.9, the mean fit uncertainties are shown, corrected for the HitFit selection efficiency. For each scenario only the case with signal only is shown and it has been corrected with the efficiency of the correlated sample, since this shows the scenario $f_{input} = 1$. In the second column, the results are shown without quality cuts, so only the fit efficiency was taken into account ($\approx 94\%$). The third column shows the results with all the quality cuts applied, so the cumulative efficiency has been used. Notice how in the scenarios in which the top quark mass constraint has been applied (a and b), the cumulative efficiency of the quality cuts is quite low and results overall in a lower precision. The net effect of improved fit results but less statistics is positive in the scenarios where the top quark mass is kept floating in the fit (scenario c, d and e), so applying the quality cuts is beneficial in those scenarios. The entry for scenario f without quality cuts is the same as in table 8.7 as it does not make use of HitFit information and therefore does not need to be corrected. Here we see that the average fit uncertainty goes up a bit when considering quality cuts on scenario f (0.425 ± 0.004 versus 0.401 ± 0.001), but since this is the slowest scenario, the gain in CPU time by rejecting events prior to processing them through MadWeight would also be the largest. Also based on this table, we conclude that scenario f is the best option. Some of the efficiency loss caused by the HitFit quality cuts can be recovered by considering the jet-parton permutation with the second lowest χ^2 if the best permutation fails the cuts, but this procedure will not be considered here.

Considering the above scenarios, we can conclude that the HitFit updated kinematics are not close enough to parton level kinematics to justify the usage of a δ-TF. Therefore, the usage of the HitFit updated kinematics does not offer any advantages, since a transfer function based on the HitFit updated kinematics would have to be determined. We have seen that relying on

Table 8.8: HitFit scenarios and results with the quality cuts applied at $f_{input} = 1$ for columns 2 and 3

Scenario	mean f	mean δf	Linearity Curve Slope	Linearity Curve Offset
a: HitFit kin, $m_t = 173$ GeV constraint, δ-TF, $\chi^2 < 20$	1.007 ± 0.041	0.617 ± 0.002	0.973 ± 0.048	0.016 ± 0.028
a: HitFit kin, $m_t = 173$ GeV constraint, δ-TF, $\chi^2 < 20$, 10 % W+jets	1.012 ± 0.111	0.700 ± 0.029	0.961 ± 0.104	0.010 ± 0.052
b: HitFit kin, $m_t = 173$ GeV constraint, double Gaussian TF, $\chi^2 < 20$	1.012 ± 0.036	0.556 ± 0.002	1.049 ± 0.043	-0.021 ± 0.025
b: HitFit kin, $m_t = 173$ GeV constraint, double Gaussian TF, $\chi^2 < 20$, 10 % W+jets	1.041 ± 0.095	0.675 ± 0.025	1.098 ± 0.113	-0.027 ± 0.066
c: HitFit kin, δ-TF, $\chi^2 < 20$, 150 GeV $< m_t <$ 225 GeV	1.174 ± 0.074	0.817 ± 0.004	1.312 ± 0.073	-0.147 ± 0.041
c: HitFit kin, δ-TF, $\chi^2 < 20$, 150 GeV $< m_t <$ 225 GeV, 10 % W+jets	0.313 ± 0.244	1.012 ± 1.842	-0.147 ± 0.225	-0.325 ± 0.100
d: HitFit kin, double Gaussian TF, $\chi^2 < 20$, 150 GeV $< m_t <$ 225 GeV	1.032 ± 0.034	0.538 ± 0.002	1.020 ± 0.040	-0.005 ± 0.024
d: HitFit kin, double Gaussian TF, $\chi^2 < 20$, 150 GeV $< m_t <$ 225 GeV, 10 % W+jets	1.124 ± 0.081	0.702 ± 0.013	1.155 ± 0.087	-0.037 ± 0.047
e: HitFit combination only, double Gaussian TF, $\chi^2 < 20$, 150 GeV $< m_t <$ 225 GeV	0.990 ± 0.038	0.554 ± 0.002	1.022 ± 0.042	-0.013 ± 0.024
e: HitFit combination only, double Gaussian TF, $\chi^2 < 20$, 150 GeV $< m_t <$ 225 GeV, 10 % W+jets	1.189 ± 0.100	0.739 ± 0.023	1.321 ± 0.109	-0.130 ± 0.058
f: MadWeight perm on, double Gaussian TF, $\chi^2 < 20$, 150 GeV $< m_t <$ 225 GeV	1.015 ± 0.023	0.380 ± 0.002	1.015 ± 0.029	0.000 ± 0.018
f: MadWeight perm on, double Gaussian TF, $\chi^2 < 20$, 150 GeV $< m_t <$ 225 GeV, 10 % W+jets	1.060 ± 0.050	0.458 ± 0.005	1.023 ± 0.060	0.032 ± 0.031
g: HitFit kin, perm on, δ-TF, $\chi^2 < 20$, 150 GeV $< m_t <$ 225 GeV	1.586 ± 0.071	0.945 ± 0.010	1.663 ± 0.075	-0.172 ± 0.041
g: HitFit kin, perm on, δ-TF, $\chi^2 < 20$, 150 GeV $< m_t <$ 225 GeV, 10 % W+jets	-41.53 ± 30.20	5.71 ± 2.83	-1.516 ± 0.333	-0.229 ± 0.104

Table 8.9: Mean fit errors for each scenario (considering signal only) corrected for the luminosity loss due to the efficiency of the HitFit quality cuts.

Scenario	mean δf	mean δf with quality cuts
a	0.670 ± 0.003	0.720 ± 0.003
b	0.604 ± 0.003	0.648 ± 0.003
c	1.356 ± 0.092	0.913 ± 0.005
d	0.661 ± 0.003	0.601 ± 0.003
e	0.662 ± 0.003	0.619 ± 0.003
f	0.401 ± 0.001	0.425 ± 0.004
g	1.023 ± 0.068	1.056 ± 0.011

the HitFit returned permutation dilutes the measurement since there is a non-negligible fraction of events in which only the wrong permutation is considered. Applying the top quark mass constraint during the HitFit calculations reduces the discriminating power between the signal and background to the extent that the template fit can no longer distinguish between signal and background. The optimal scenario seems to be scenario f (based on LO parton level studies) which only uses HitFit as a selection criterium. This includes running over all permutations in the MadWeight calculation which are compatible with the b-tagging information. This means that a very CPU intensive scenario is selected. Although from these LO parton level studies, we have concluded that a slightly better precision in scenario f is obtained by not applying quality cuts, at reconstruction level the quality cuts offer rejection against mismodelled events. As we will see in section 8.2, a quality cut on the HitFit output of $\chi^2 < 5$ is optimal.

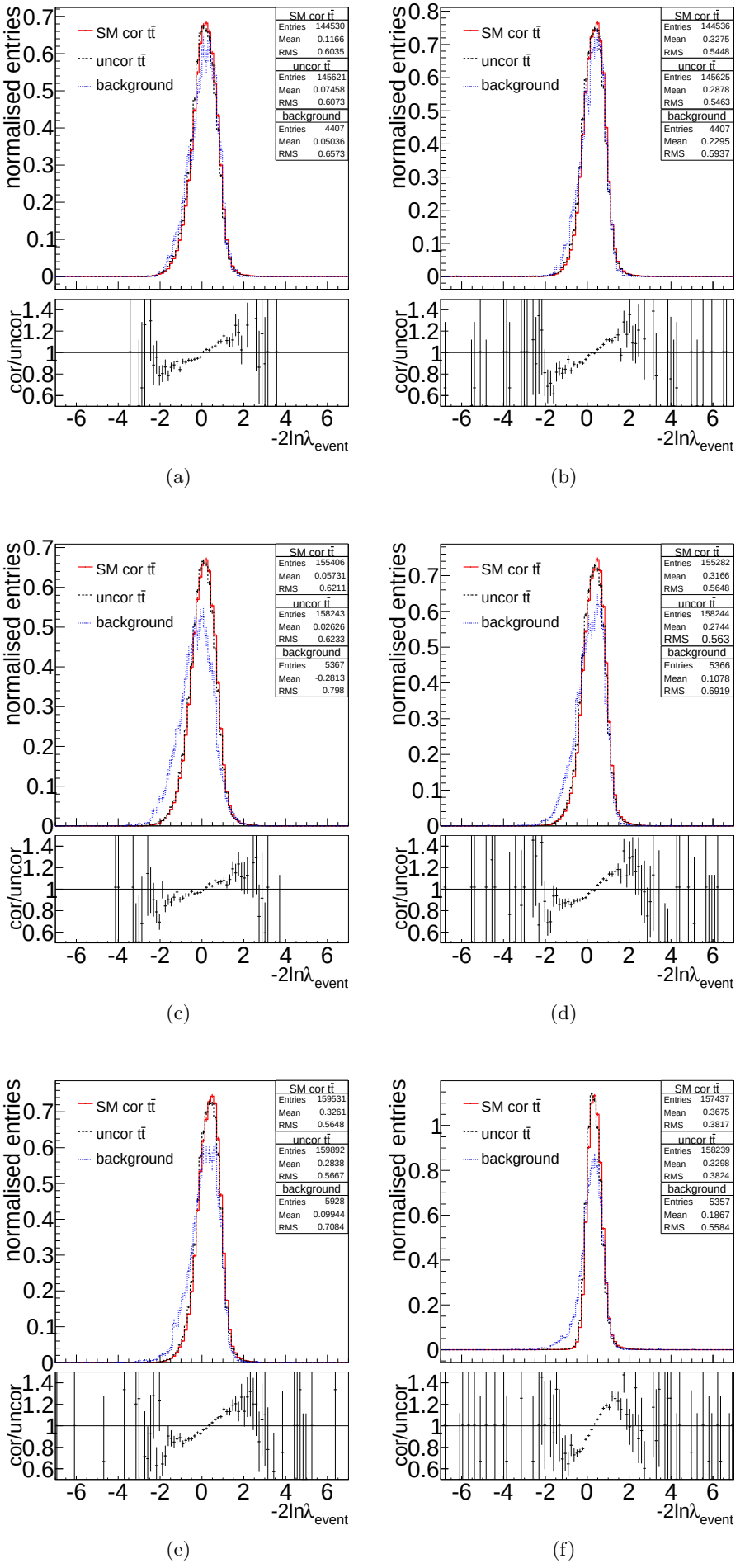

Figure 8.46: Histograms of $-2\ln\lambda_{event} = 2\ln L_{event}(H = Cor) - 2\ln L_{event}(H = Uncor)$ for individual events from SM correlated $t\bar{t}$ (red solid) and uncorrelated $t\bar{t}$ (black dashed) within acceptance. The ratio of cor/uncor is shown at the bottom of each plot.

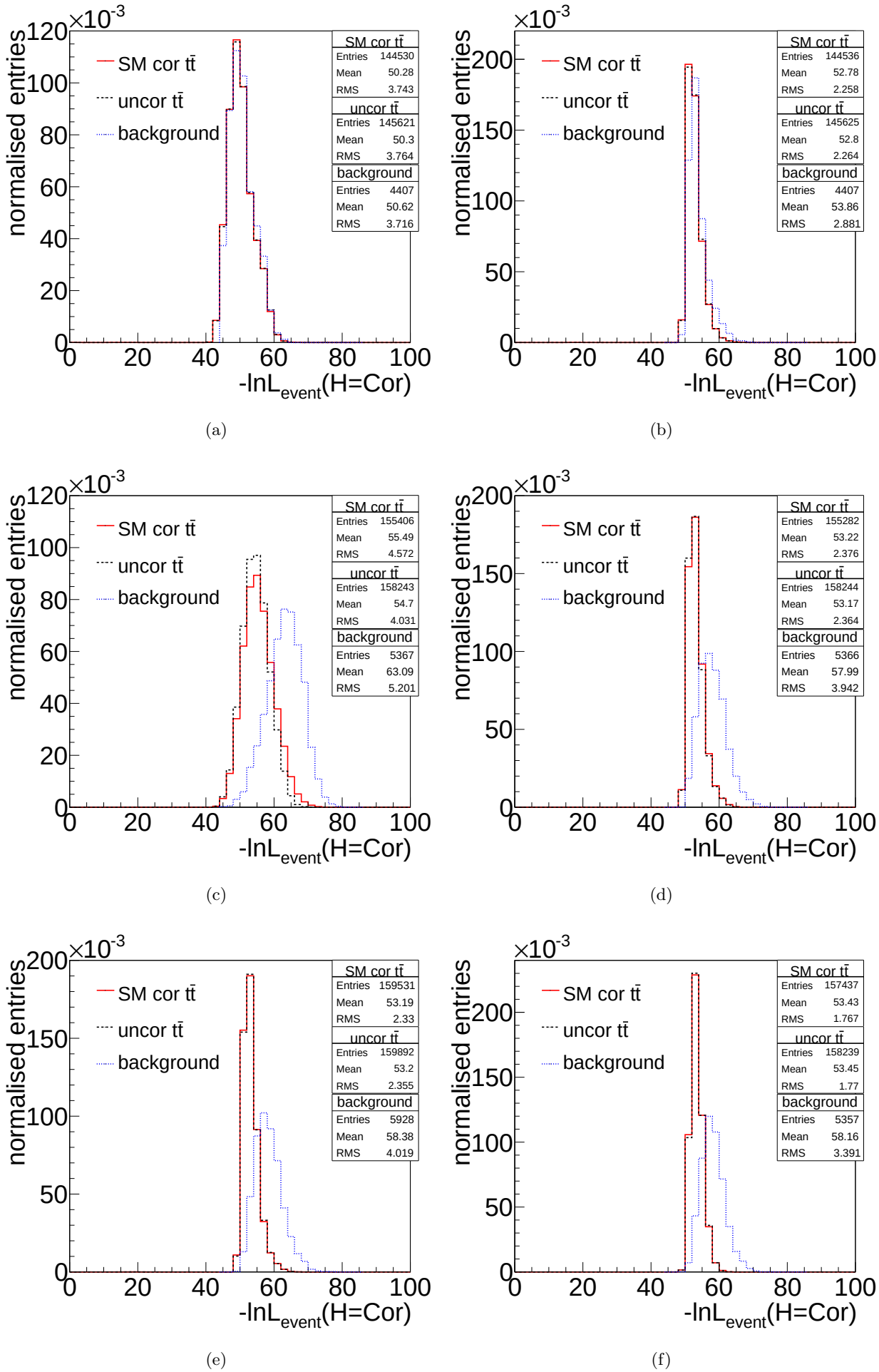

(a) (b) (c) (d) (e) (f)

Figure 8.47: Event Likelihood distributions $-\ln L_{event}(H = Cor)$ for the spin-correlated event sample in red solid line, the spin-uncorrelated sample in the black dashed line and the W+jets sample in the blue dotted line.

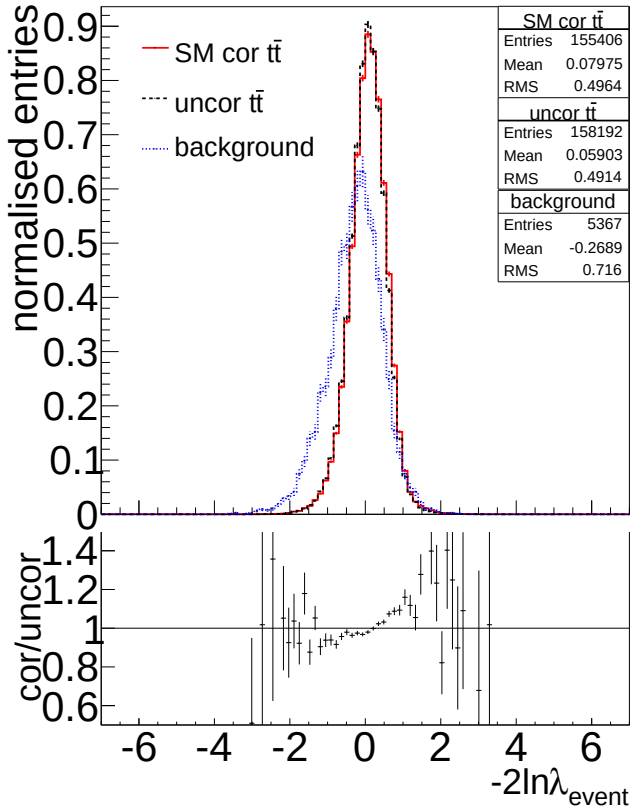

Figure 8.48: Scenario g: Histograms of $-2\ln\lambda_{event} = 2\ln L_{event}(H = Cor) - 2\ln L_{event}(H = Uncor)$ for individual events from generated samples according to $H = Cor$ (red solid histogram) and $H = Uncor$ (black dashed histogram) within acceptance. The ratio of the spin-correlated template over the spin-uncorrelated template is shown at the bottom of each plot.

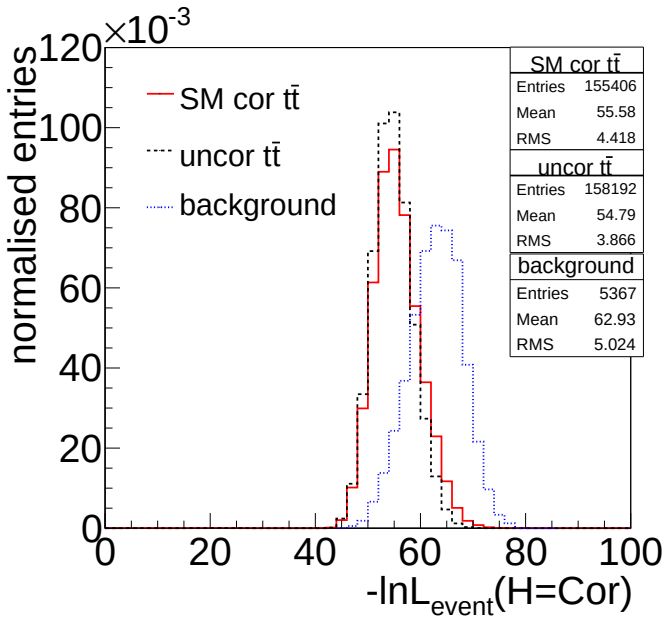

Figure 8.49: Scenario g: Event Likelihood distributions $-\ln L_{event}(H = Cor)$ for the spin-correlated event sample in red solid line, the spin-uncorrelated sample in the black dashed line and the W+jets sample in the blue dotted line.

8.2 Closure Tests at RECO Level

There are a number of effects which will dilute the measurement which cannot be tested at the parton level. Reconstructed simulation, as described in chapter 3, includes radiative contributions, hadronisation, next-to-leading order effects, detector resolution and inefficiencies. In addition, the background shape will be modelled with all relevant background contributions in the simulation, as given in table 5.2 in section 5. In section 8.2.1, some of the selection criteria listed in section 5.7 will be detailed. These additional quality cuts are designed to reject events which suffer from mismodelling. In section 8.2.2, some optimisations are discussed to increase the expected separating power of the $-2\ln\lambda_{event}$ distribution and the effect on the hypothesis testing. In section 8.2.3, the template fit will be tested at reconstruction level and a calibration curve will be set up to correct for any observed bias in the fit.

8.2.1 Additional Quality Cuts

χ^2/ndof cut Mismodelling of events and misreconstruction of jet kinematics will result in a worse χ^2 for the kinematic fit. The χ^2 distribution of the reconstructed simulation with relative contributions according to the theoretical cross sections and normalised to the data, is shown in fig. 8.50. There is good agreement between the simulation and the data. NLO effects, initial state and final state radiation, cause a large fraction of $t\bar{t}$ events to have more than four jets in the final state. To match the event to a LO $t\bar{t}$ matrix element, HitFit is used which selects the jet-parton combination which is most compatible with a LO $t\bar{t}$ semi-leptonic final state and consequently which subset of jets should be given to the MadWeight likelihood calculation. In accordance to what we found in the parton level studies in section 8.1, the MadWeight calculation will take into account the original reconstructed kinematics of all jet-parton permutations compatible with the b-tagging information using the subset of jets in the event selected with HitFit. Initially, no further HitFit information is used.

The $-\ln L_{event}(H = Cor)$ and $-\ln L_{event}(H = Uncor)$ likelihood distributions at reconstruction level are shown in fig. 8.51 separately for four jet and five jet events for $t\bar{t}$ signal events. Again the conclusions for the $-\ln L_{event}(H = Cor)$ and $-\ln L_{event}(H = Uncor)$ distributions are interchangeable. From the comparison with the distribution at smeared parton level in fig. 8.39, at reconstruction level the $-\ln L_{event}(H = Cor)$ distribution is much broader, meaning there are more events with low likelihood values. There is a significantly different behaviour between the four and five jet distribution. In the four jet distribution, a shoulder is visible, reminiscent of the shoulder at parton level due to the evaluation of an incorrect jet-parton permutation. During the likelihood calculations, all available jet-parton permutations compatible with the b-tagging information were evaluated eliminating this as the cause for the shoulder, but there are various effects which could lead to a similar behaviour. If a light jet is mistakenly b-tagged, the current set of permutations would not involve the correct one, but as the mistag rate of the CSVM algorithm is only of the order of a percent, this effect cannot be responsible for the shoulder. An effect similar to evaluating a wrong jet-parton permutation can be considered when in events which include radiation, the selected subset of jets does not contain the decay partons. Events reconstructed as four jet events can have undergone radiation where the gluon carries off most of the momentum, leaving the recoiling parton with insufficient momentum to be selected by the jet criteria, or the parton can be outside of the selected pseudorapidity range. These events, which we will refer to as events with a parton outside of acceptance, give a similar feature in the $-\ln L_{event}(H = Cor)$ distribution as the wrong permutation at parton level. This shoulder is much less pronounced in the five jet category as there the probability to select the correct jet subset is higher. The overall broadening of the $-\ln L_{event}(H = Cor)$ distribution can be attributed to events containing poorly reconstructed jet kinematics.

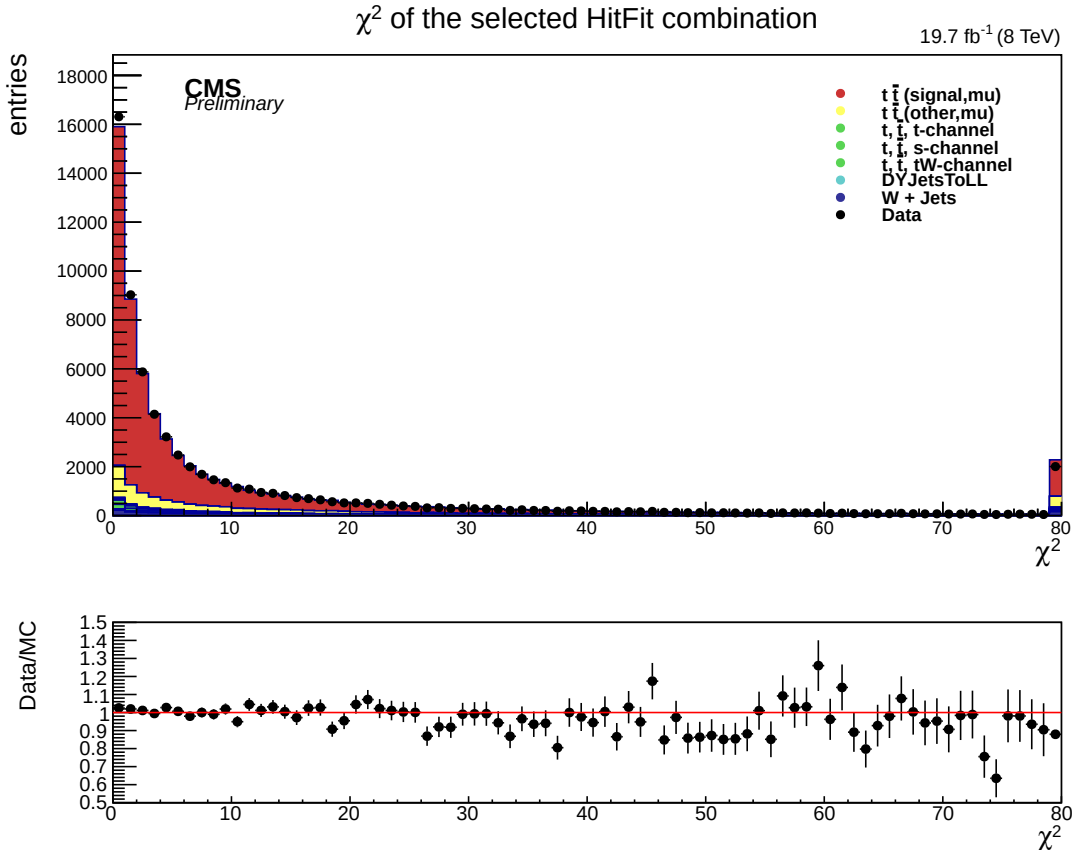

Figure 8.50: The χ^2-distribution of the selected HitFit solutions in the Muon channel, showing a comparison between data and Simulation. Both data and simulation are normalised to unity, while the relative contributions in simulation are calculated using the theoretical cross sections.

To bring the $-\ln L_{event}(H = Cor)$ distribution closer to parton level, a $\chi^2/ndof$ cut was applied to the selected events. To determine the optimal value of the χ^2 cut, the separation power as a function of the χ^2 cut was evaluated. In the separating power or expected significance there are two competing effects. On the one hand a strict χ^2 selects better events which will result in a higher separating power. On the other hand a χ^2-cut can also significantly reduce the dataset size, which, as we have studied at the parton level, leads to a smaller separating power. In fig. 8.52, the expected significance is shown as a function of the χ^2 value, evaluated at the same luminosity. As can be seen from the figure, the result of both competing effects shows a maximum at a cut value of $\chi^2 < 5$. Unless stated otherwise, all the following results and studies are performed with the $\chi^2 < 5$ cut applied.

The effect of the $\chi^2/ndof < 5.0$ selection cut on the $-\ln L_{event}(H = Cor)$ and $-\ln L_{event}(H = Uncor)$ distribution is shown in fig. 8.53, where we can see that the shoulder has disappeared in both the four and five jet category. The distributions are narrower and there is better agreement between the four and five jet category. Still the $-\ln L_{event}(H = Cor)$ distribution is broader in the five jet category. This is to be expected, as it is known that the likelihood calculations do not take the full event kinematics into account in this category.

Relative likelihood uncertainty The final quality cuts refer to the event likelihood values obtained by MadWeight. For a minimal fraction of events $O(0.1\%)$, the likelihood calculations do not converge. The majority of the non-converging events are background events. Increasing

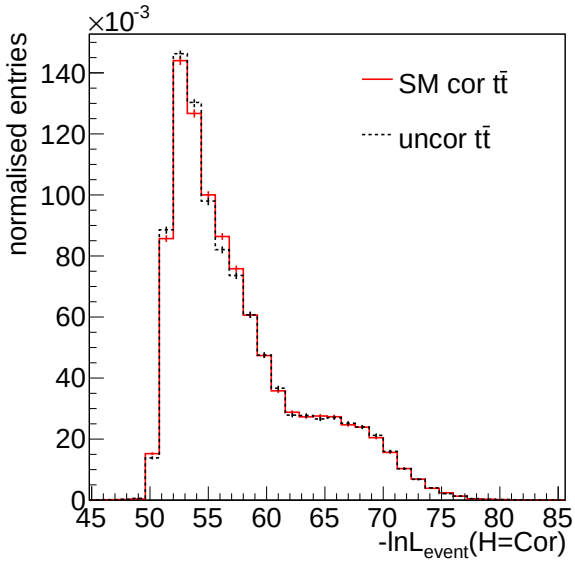

(a) $-\ln L_{event}(H = Cor)$, four jet events

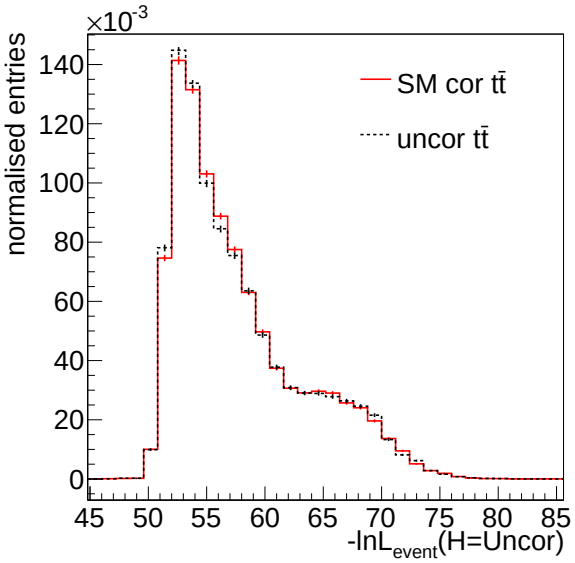

(b) $-\ln L_{event}(H = Uncor)$, four jet events

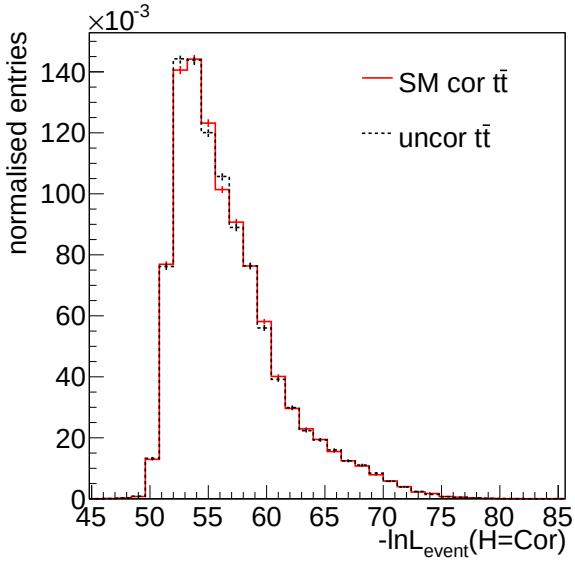

(c) $-\ln L_{event}(H = Cor)$, five jet events

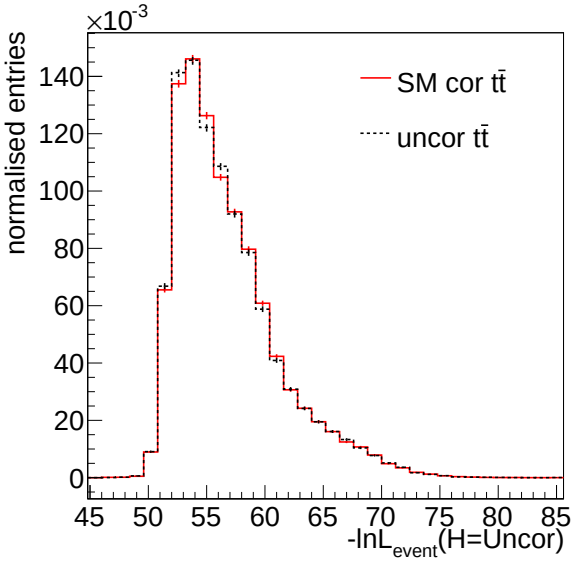

(d) $-\ln L_{event}(H = Uncor)$, five jet events

Figure 8.51: $-\ln L_{event}(H = Cor)$-distribution for signal $t\bar{t}$ events. The red curve corresponds to SM correlated events and the black dashed curve corresponds to the uncorrelated events.

the number of integration points would reduce the fraction of non-converging events (especially in the signal sample) but this fraction is already so low that this has not been done. Implicitly, we require that the event likelihood calculation should converge under both hypotheses as the event likelihood ratio cannot be calculated without them. For another minimal fraction of events $O(0.1\%)$, the calculations converge but result in an integration error larger than the obtained event likelihood as can be seen in fig. 8.54 where the relative uncertainty $\delta L/L$ is shown on the left while the $\ln \delta L/\ln L$ is shown on the right. Events with $\delta L/L > 1$ (or $\ln \delta L/\ln L < 1$ as the likelihood values have negative exponents) do not add any information to the measurement but cause large errors when considering sample likelihoods. Therefore events with $\ln \delta L/\ln L > 1$, with L being the event likelihood either in the SM hypothesis or uncorrelated hypothesis, are

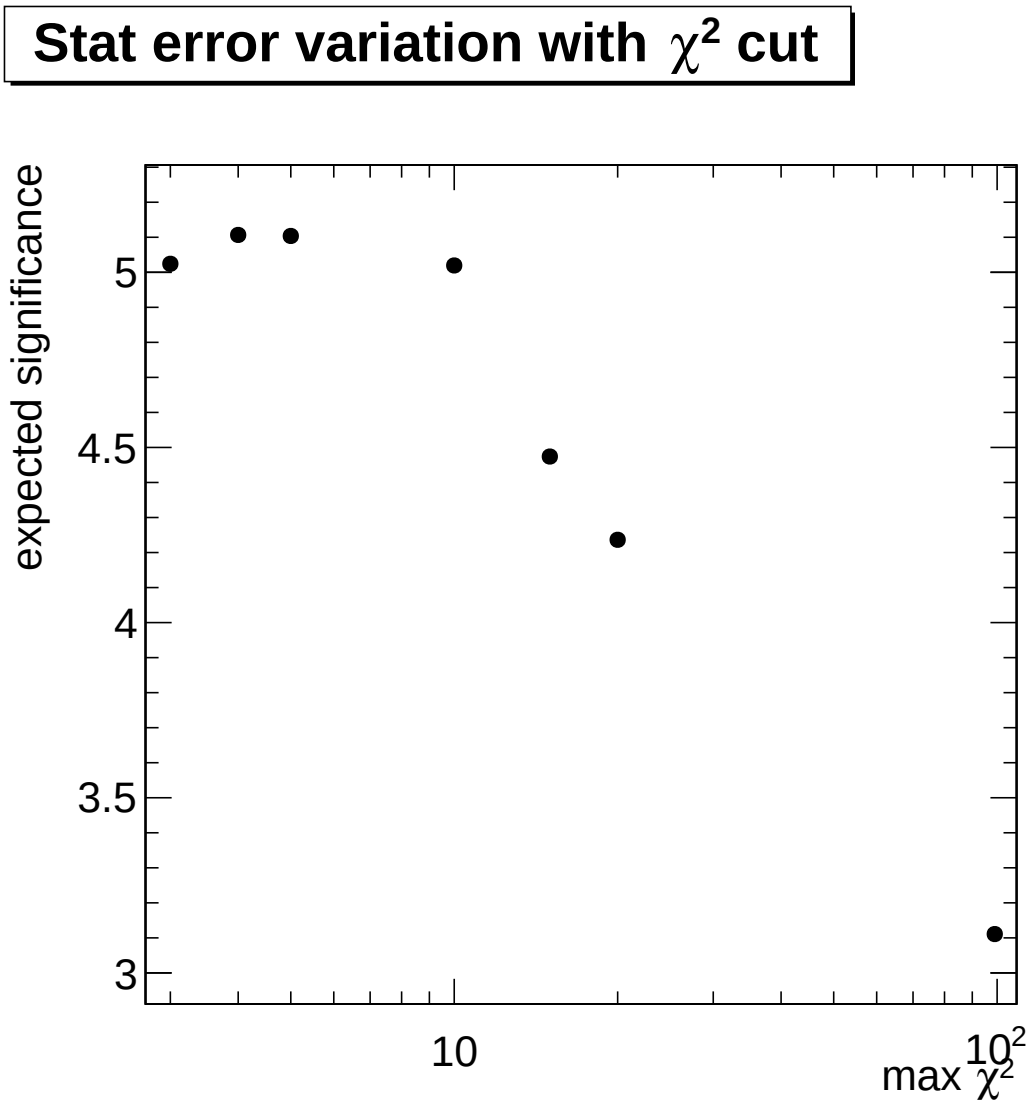

Figure 8.52: Separation power in the positive muon channel using signal only as a function of the χ^2 cut value. Events with a χ^2 value above the cut value are discarded.

rejected. The cut value is again chosen to maximise the expected significance, but unlike in the case of the χ^2/ndof cut, the improvement is minimal $O(0.1\sigma)$.

8.2.2 Hypothesis Testing

At reconstruction level, some optimisation studies have been performed in the hypothesis testing procedure. In fig. 8.55, the signal $-2\ln\lambda_{event}$-distribution is shown at reconstruction level, with at the bottom the ratio between the $t\bar{t}$ signal correlated and uncorrelated events. From this distribution, we conclude that at reconstruction level, there is still sufficient discriminating power. In addition, the $-2\ln\lambda_{event}$-distribution of the background is shown. The background distribution is normalised to unity, but has the correct relative contributions of the physics processes. As the majority of the background is due to $t\bar{t}$ events from the dileptonic or electron+jets channel, we can construct the background shape with both the correlated and uncorrelated $t\bar{t}$ background. As can be seen from fig. 8.55, the correlated and uncorrelated background shape

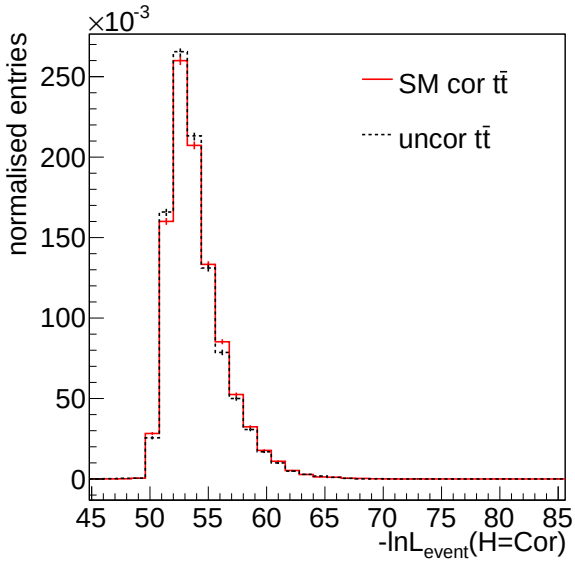

(a) $-\ln L_{event}(H = Cor)$, four jet events

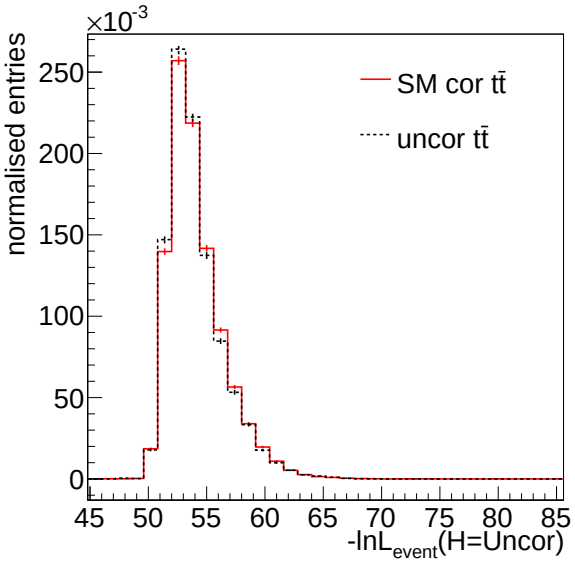

(b) $-\ln L_{event}(H = Uncor)$, four jet events

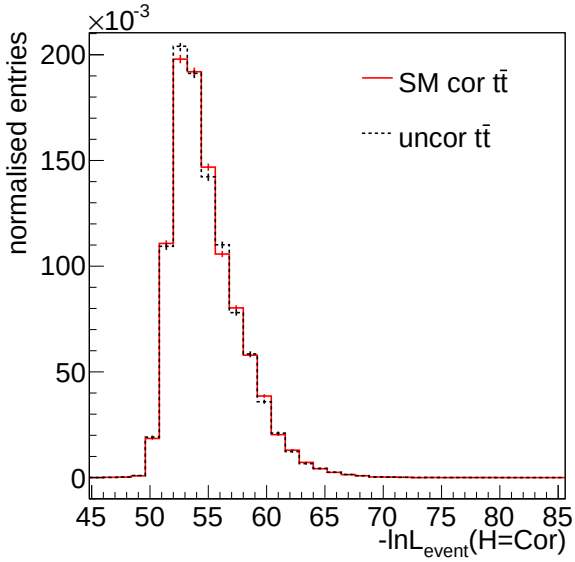

(c) $-\ln L_{event}(H = Cor)$, five jet events

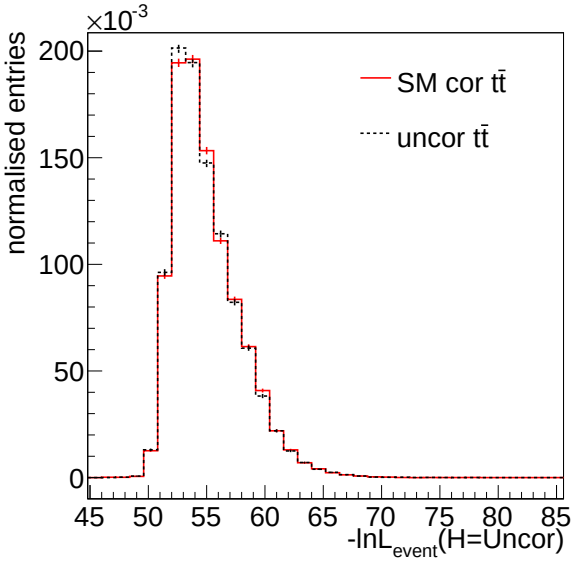

(d) $-\ln L_{event}(H = Uncor)$, five jet events

Figure 8.53: $-\ln L_{event}(H = Cor)$ and $-\ln L_{event}(H = Uncor)$ distribution for signal $t\bar{t}$ events with $\chi^2/ndof < 5.0$. The red curve corresponds to SM correlated events and the black dashed curve corresponds to the uncorrelated events.

are compatible within the statistical uncertainty bars. This has as a consequence that the $t\bar{t}$ background can be averaged over both the correlated and uncorrelated distribution, with the advantage of having double the amount of events to describe this background and therefore reduce the effect of the simulation statistical uncertainty.

As was discussed in the parton-level section, the $-2\ln\lambda_{event}$ distribution is used to draw pseudo-experiments, but here these are evaluated at the observed dataset size. From these pseudo-experiments the $-2\ln\lambda_{sample}$ distribution in the RECO-level simulation is set up. As the pseudo-experiments are drawn from a binned distribution, the effect of the binwidth needs

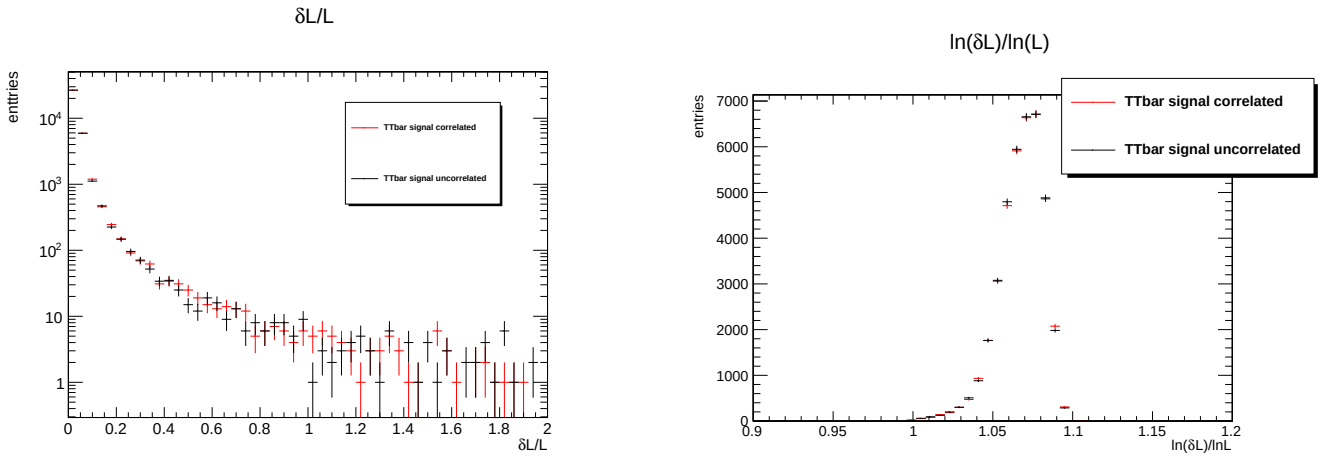

Figure 8.54: Relative uncertainty on the likelihood for events in the muon channel. With $\delta L/L$ on the left and $\ln \delta L / \ln L$ on the right.

to be studied and optimised. Too large of a binwidth will result in washing out the shape differences between the correlated and uncorrelated $t\bar{t}$ distributions. Too small of a binwidth will result in large statistical uncertainties in the bins. The effect of the binwidth on the expected significance is studied. The range of the $-2\ln\lambda_{event}$ distribution was kept fixed at [-7,7], while the number of bins was varied to generate pseudo-experiments with which to evaluate the expected significance. The result is shown in fig. 8.56. We see a clear plateau region, meaning that as long as the number of bins is varied within that region, the effect on this analysis is small. We have fixed the number of bins to 100 in the range [-7,7] in the $-2\ln\lambda_{event}$ distribution corresponding to a binwidth of 0.14 for the analysis.

In addition, the range used of the $-2\ln\lambda_{event}$ distribution has been optimised to maximize the expected significance in the case of statistical effects only. As we can see in fig. 8.55, the $-2\ln\lambda_{event}$ distribution only shows a statistically significant difference between the SM correlated and uncorrelated hypothesis in a narrow range. We have kept the binwidth fixed to 0.14 and reduced the range progressively to check the effect on the expected significance, as can be seen in table 8.10, which is a combination of the reduced dataset size and the increased separating power. We have chosen to proceed with the range [-0.7,1.26] as indicated by the vertical lines in 8.55, showing that the bins outside this range are statistically insignificant. Since these discarded bins do not offer any separating power between the correlated and uncorrelated $t\bar{t}$ samples, we are not introducing a bias by removing these. From this plot, we also conclude that we are still able to distinguish signal and background at reconstruction level and that the background set up with correlated $t\bar{t}$ other and uncorrelated $t\bar{t}$ other are not significantly different. Here, the optimisation is done only with respect to statistical effects, but as we will discuss in chapter 9, the selected range also helps in reducing the systematic uncertainties.

8.2.3 Extraction of Spin Correlation Fraction

For the extraction of the fraction of events with SM spin correlation f with the template fit, the calibration of the fit result needs to be calculated at reconstruction level. Similarly as described in the parton level closure tests in section 8.1.3, we draw pseudo-experiments with a certain f_{input} fraction and a certain background contamination. Here we draw the pseudo-experiments with total number of events fluctuated from a Poisson with mean at the observed dataset size. We start with the fit model eq. 8.3 as described in the parton level closure tests where three fit

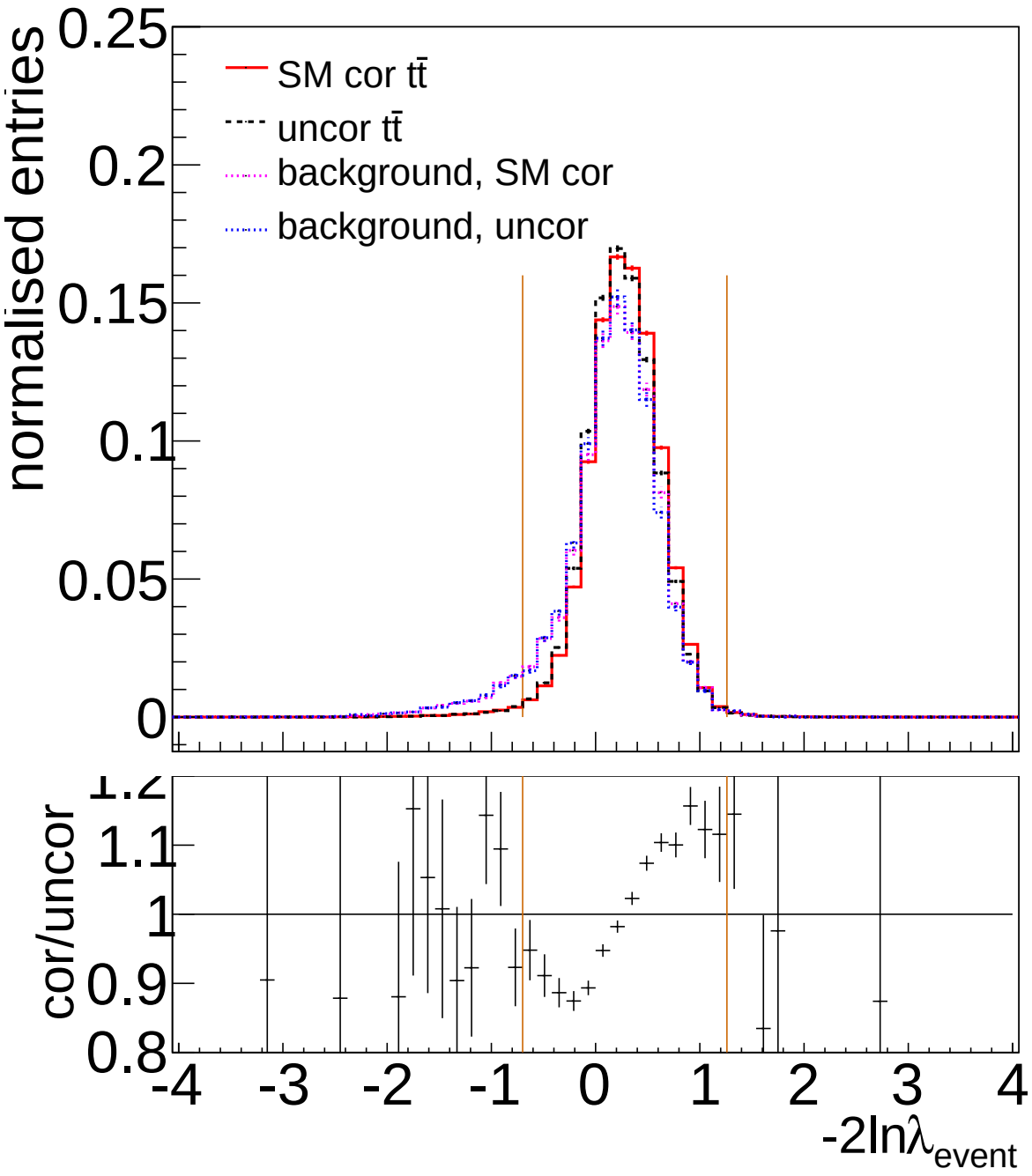

Figure 8.55: The $-2\ln\lambda_{event}$ distribution for signal correlated and uncorrelated and background correlated and uncorrelated. The vertical lines in the ratio plot indicate the chosen range for the analysis.

parameters are extracted (f, N_{bkg} and $N_{t\bar{t}}$), where the templates are now based on reconstruction level simulation. The background template is a combination of the various background processes with the relative contribution fixed using the theoretical cross sections. The total amount of background is left floating in the fit. In fig. 8.57, the correlation between the fit parameters using this fit model is displayed. There is a strong correlation between the fit parameters N_{bkg} and $N_{t\bar{t}}$, meaning we can no longer accurately extract the signal and background cross sections simultaneously.

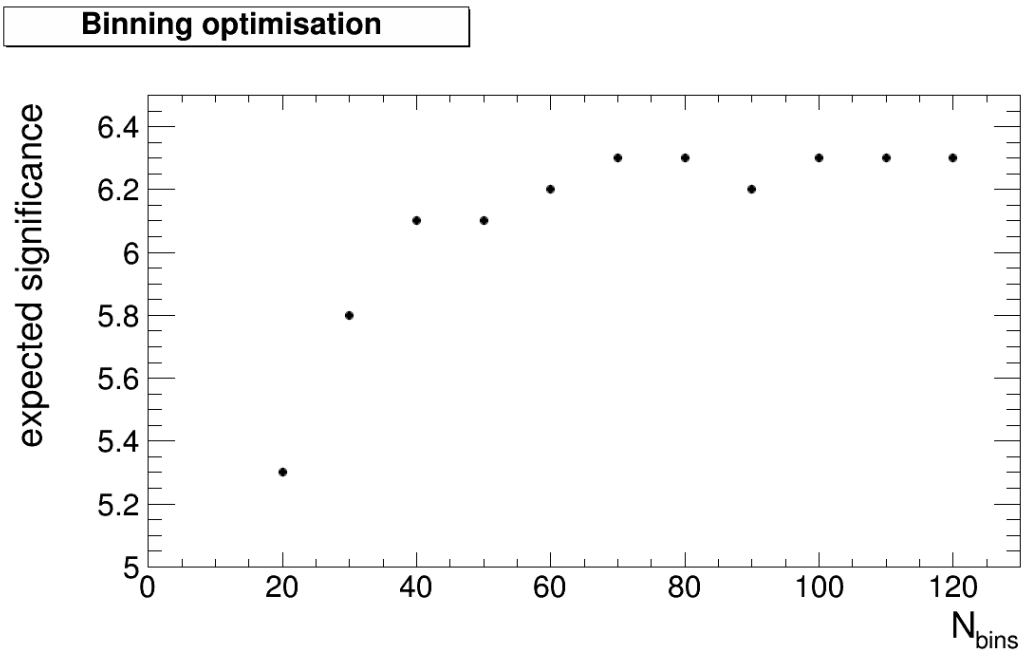

Figure 8.56: Expected significance as a function of the number of bins (for range [-7,7]) for the $-2\ln\lambda_{event}$ distribution.

Table 8.10: Data statistics and expected significance as a function of range used in $-2\ln\lambda_{event}$ distribution.

range	Data statistics	expected significance (σ)
$[-7, 7]$	38269	7.03
$[-2.1, 1.96]$	38154	7.21
$[-1.4, 1.96]$	38001	7.78
$[-0.7, 1.96]$	37254	8.46
$[-0.7, 1.26]$	36946	8.78
$[0, 0.98]$	28511	6.50

For this reason, we have moved to a modified fit model in which the total event yield is no longer kept floating, but is fixed to the observed dataset size (unextended likelihood fit). The relative background contribution β is still kept floating in the fit. The new fit model has the form:

$$model = (1-\beta)[f^{SM}T_{cor} + (1-f^{SM})T_{uncor}] + \beta T_{bkg} \tag{8.5}$$

where β is the background fraction and the total event yield is fixed in the fit. The correlation between the fit parameters f and β is shown in fig 8.58. The correlation is significant, but not extreme. The result of a high correlation is an increased statistical uncertainty on the fit parameters. In the template fit, the binwidth and the fit range of the $-2\ln\lambda_{event}$-distributions are kept fixed to 0.14 and [-0.7,1.26] respectively, consistent with what is used in the hypothesis testing. Tests with varying β_{input} input background fractions were performed. Here the result with $\beta_{input} = 15\,\%$ is shown, as this is the predicted background fraction from simulation. In fig. 8.59, the mean and RMS of the pull distribution for the fit parameter f is shown as a function of f_{input}. There is a bias in f, but a proper error estimation. The bias is due to the particular

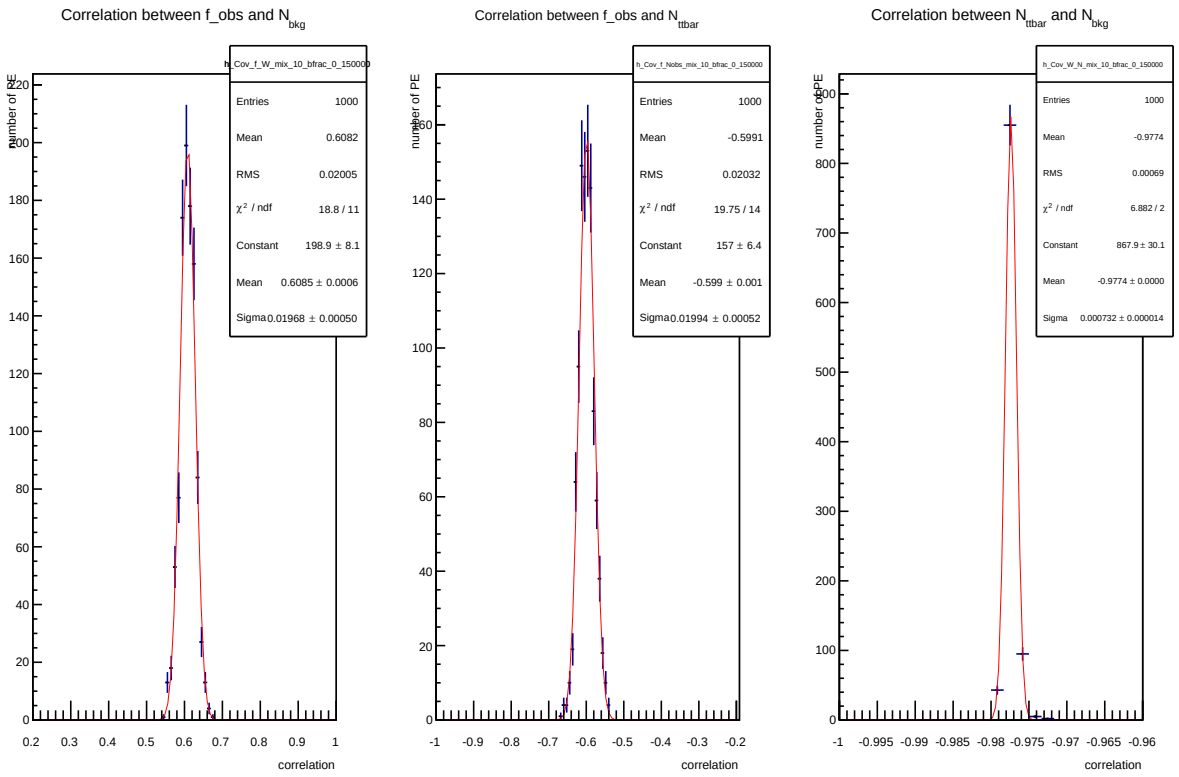

Figure 8.57: Correlation between fit parameters f, N_{bkg} and $N_{t\bar{t}}$.

background shape, which is not sufficiently different to allow for the simultaneous extraction of both fit parameters in the limited range. In fig. 8.60, the mean and RMS of the pull distribution for the β fit parameter is displayed as a function of f_{input}. Here there is also a small bias visible, but with again a proper error estimation. In fig. 8.61, the mean fitted f and mean δf is shown as a function of f_{input}. From this, we conclude that a calibration of the fit result for f is necessary.

A calibration curve is set up by generating pseudo-experiments at various $(f_{input}, \beta_{input})$ working points. There are 9 different f_{input} values evaluated, ranging from 0 to 1 with step sizes of 0.125 and 11 different β_{input} values ranging from 5 % to 25 % in step sizes of 2 %. At each working point 1000 pseudo-experiments are performed and the mean f and mean β are placed on the (x,y)-axis respectively, while f_{input} is placed on the z-axis. This curve allows to extract $f_{calibrated}$, being the estimate of the spin correlation fraction used to generate the pseudo-data, as a function of the f and β observed in the fit. We can fit a 2D curve to these working points, with functional form:

$$f_{calibrated} = p0 + p1 * (f') + p2 * (f') * (\beta') \tag{8.6}$$

where $f' = f - 0.502$ and $\beta' = \beta - 0.150$, allowing for an extrapolation between the evaluated working points. The f and β variables have been shifted by the weighted average of the working points on the x- and y-axis respectively to decorrelate the fit parameters. The fit parameters of the calibration function in eq. 8.6 are shown in table 8.11, in addition to the $\chi^2/ndof$ of the fit and the correlation between the fit parameters. As the correlation is low, we can ignore these. The calibration function is shown in fig. 8.62. This function will be used to calibrate the fit result obtained from data and the uncertainties on the fit parameters of the calibration curve will be treated as additional systematic uncertainty.

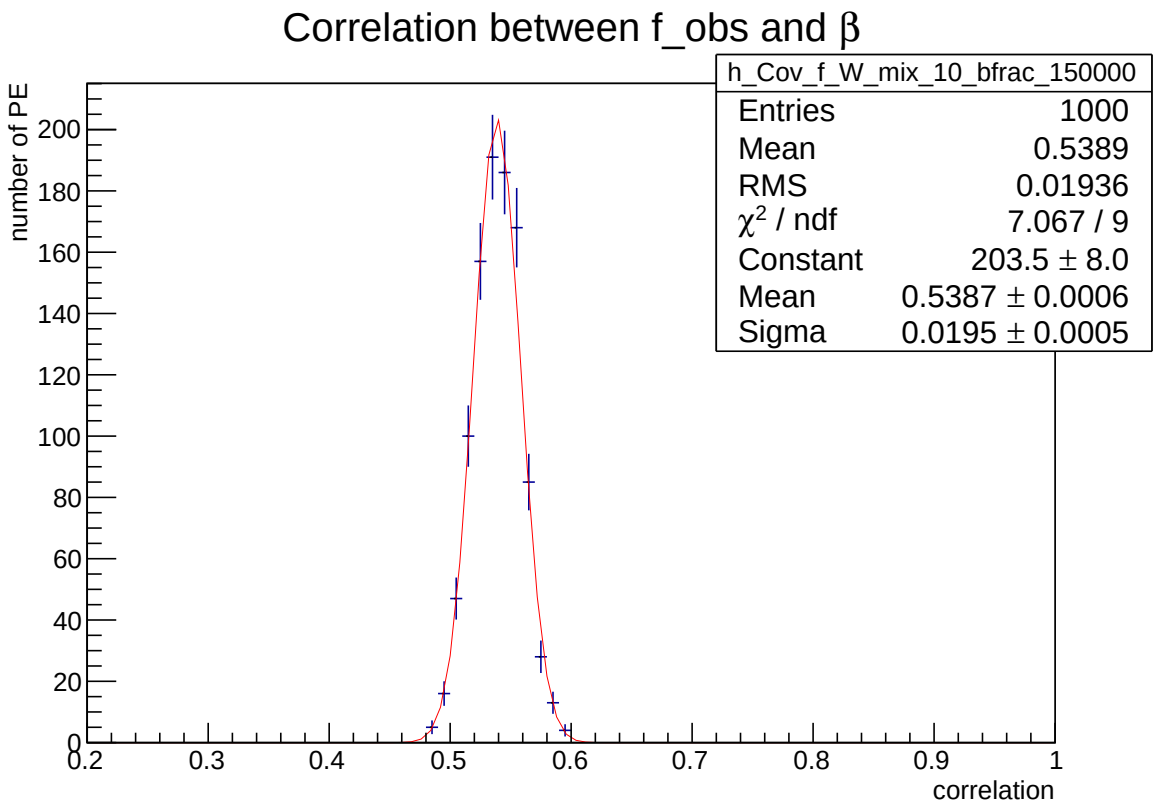

Figure 8.58: Correlation between fit parameters f and β.

Table 8.11: Fit parameters of the 2D calibration curve. The correlation between the fit parameters is low and will be ignored.

parameter	value
p0	0.5004 ± 0.0003
p1	0.9207 ± 0.0008
p2	-0.56 ± 0.01
$\chi^2/ndof$	79.9/95
correlation(p0,p1)	0.093
correlation(p0,p2)	0.072
correlation(p1,p2)	−0.021

The $\chi^2/ndof$ indicates the fit properly describes the working points. As an additional test of the quality of the fit, the difference between the f_{input} of the generated working points and the result obtained by evaluating $f_{calibrated}$ at the generated working points is shown in fig. 8.63. The difference is Gaussian distributed, centred around 0 with a resolution of 0.3 %. In addition, the difference between f_{input} and $f_{calibrated}$ for constant values of f and β is shown in fig. 8.64. The figures show that there is no systematic deviation in the fit of the calibration curve.

Extended Range 1D Fit As the correlation between the two extracted fit parameters f and β is rather high, we want to test the effect on the analysis. By extending the range in

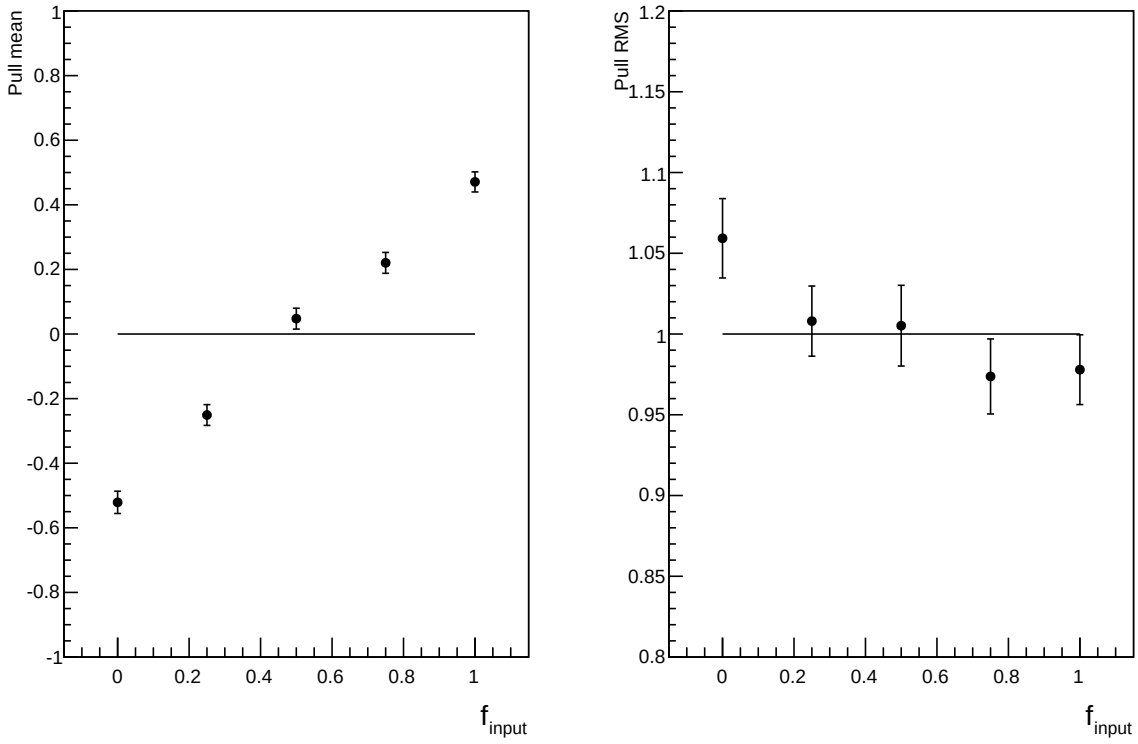

Figure 8.59: Pull means (left) and RMS (right) for f as a function of f_{input}. As β_{input} 15 % was used.

the fit to the $-2\ln\lambda_{event}$ distribution from $[-0.7, 1.26]$ to $[-2.1, 1.26]$, we are taking a region into account (as can be seen from fig. 8.55) where there is a larger discrimination between $t\bar{t}$ signal and background. As a consequence the correlation between the f and β fit parameter is decreased, as is visible from fig. 8.65. The calibration curve is redetermined for the fits in this range. As will be seen in the systematics section, this choice is not optimal as the systematic uncertainties are increased.

2D Fit The absolute event likelihood distributions $-\ln L_{event}(H = Cor)$ and $-\ln L_{event}(H = Uncor)$ are not very sensitive to the spin correlation fraction (as the likelihood ratio is the maximum discriminating variable), but offers larger discriminating power between $t\bar{t}$ signal events and background. By adding this distribution into the fit, we can decorrelate the parameters f and β. As a cross check, we have set up a two-dimensional fit with on the x-axis the $-2\ln\lambda_{event}$-distribution with a binwidth of 0.14 and range $[-0.7, 1.26]$ and on the y-axis the $-\ln L_{event}(H = Cor)$ variable with three bins ranging from $[45, 55]$, $[55, 65]$ and $[65, 80]$. Again, also the $-\ln L_{event}(H = Uncor)$ variable could be used. Due to time-constraints no explicit optimisation of the binning in the $-\ln L_{event}(H = Cor)$ variable was performed. The fit models are similar as before either $model = (1-\beta)(f^{SM}T_{cor} + (1-f^{SM})T_{uncor}) + \beta T_{bkg}$ or $model = N_{t\bar{t}}(f^{SM}T_{cor} + (1-f^{SM})T_{uncor}) + N_{bkg}T_{bkg}$ but where the templates are now two-dimensional.

In fig 8.66, the correlation between the fit parameters is shown in the case of a 2D, extended fit, where we extract the three fit parameters: f, N_{bkg} and $N_{t\bar{t}}$. These numbers can directly be compared to fig. 8.57. From the figure, we conclude that there is negligible correlation between

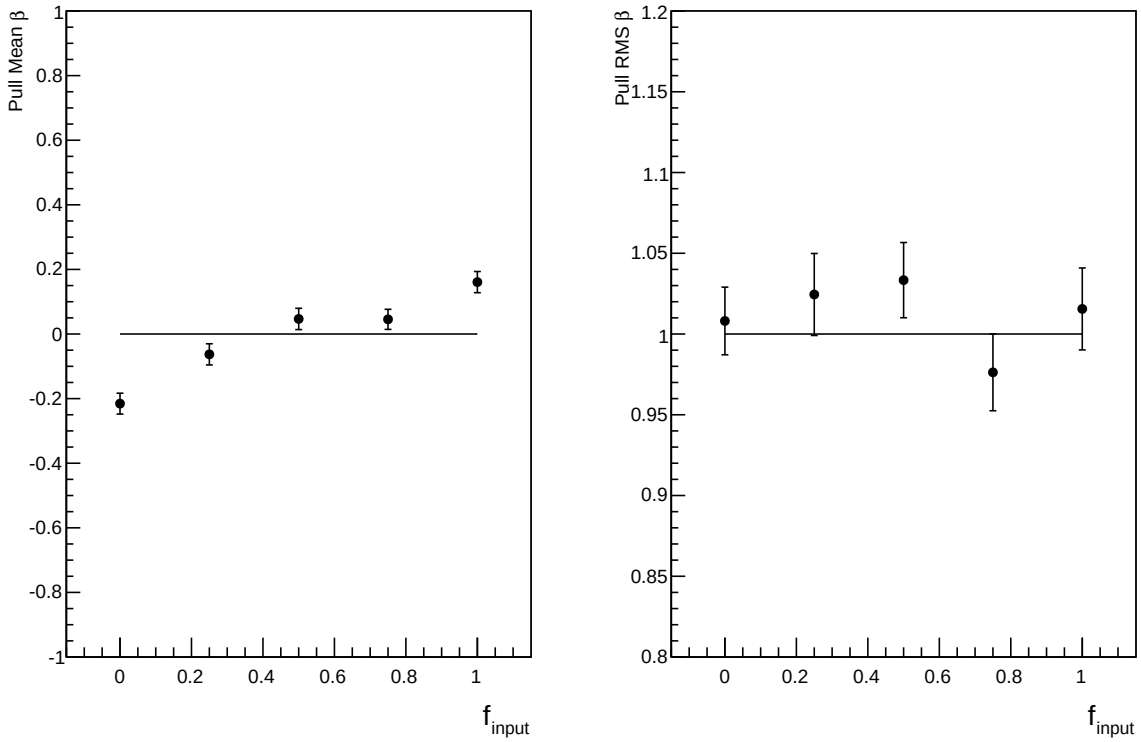

Figure 8.60: Pull means (left) and RMS (right) for β_{obs} as a function of f_{input}. As β_{input} 15 % was used.

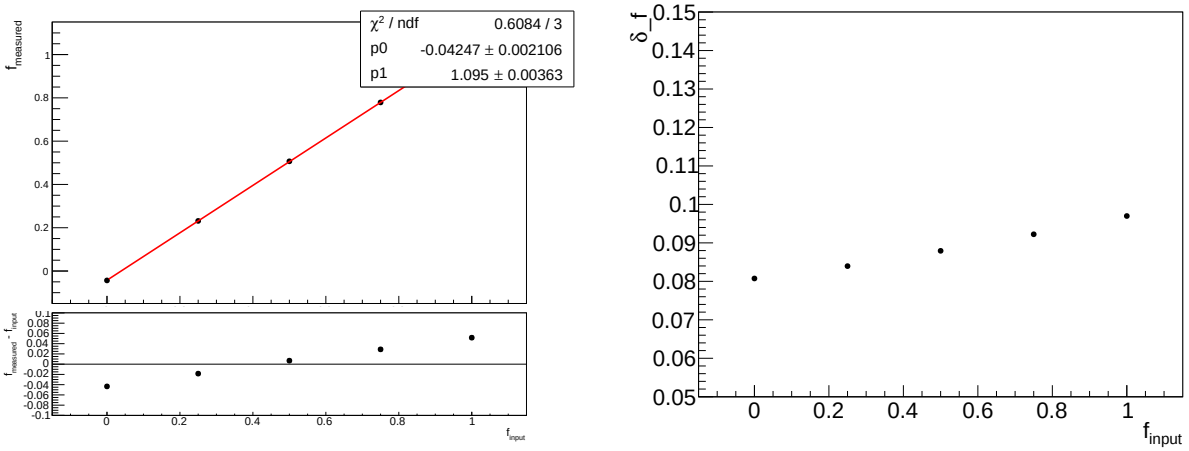

Figure 8.61: Mean fitted f (left) and δf (right) as a function of input f, which is obtained by mixing spin-correlated and spin-uncorrelated samples. The error bar is obtained from the error on the mean of the fitted f and δf respectively. The results are obtained from repeated pseudo-experiments on reconstruction level simulation at the observed dataset size with 15% background contamination.

the f-parameter and the background extraction, but the correlation is still too high to extract in addition the $N_{t\bar{t}}$ parameter which would give us a cross section determination.

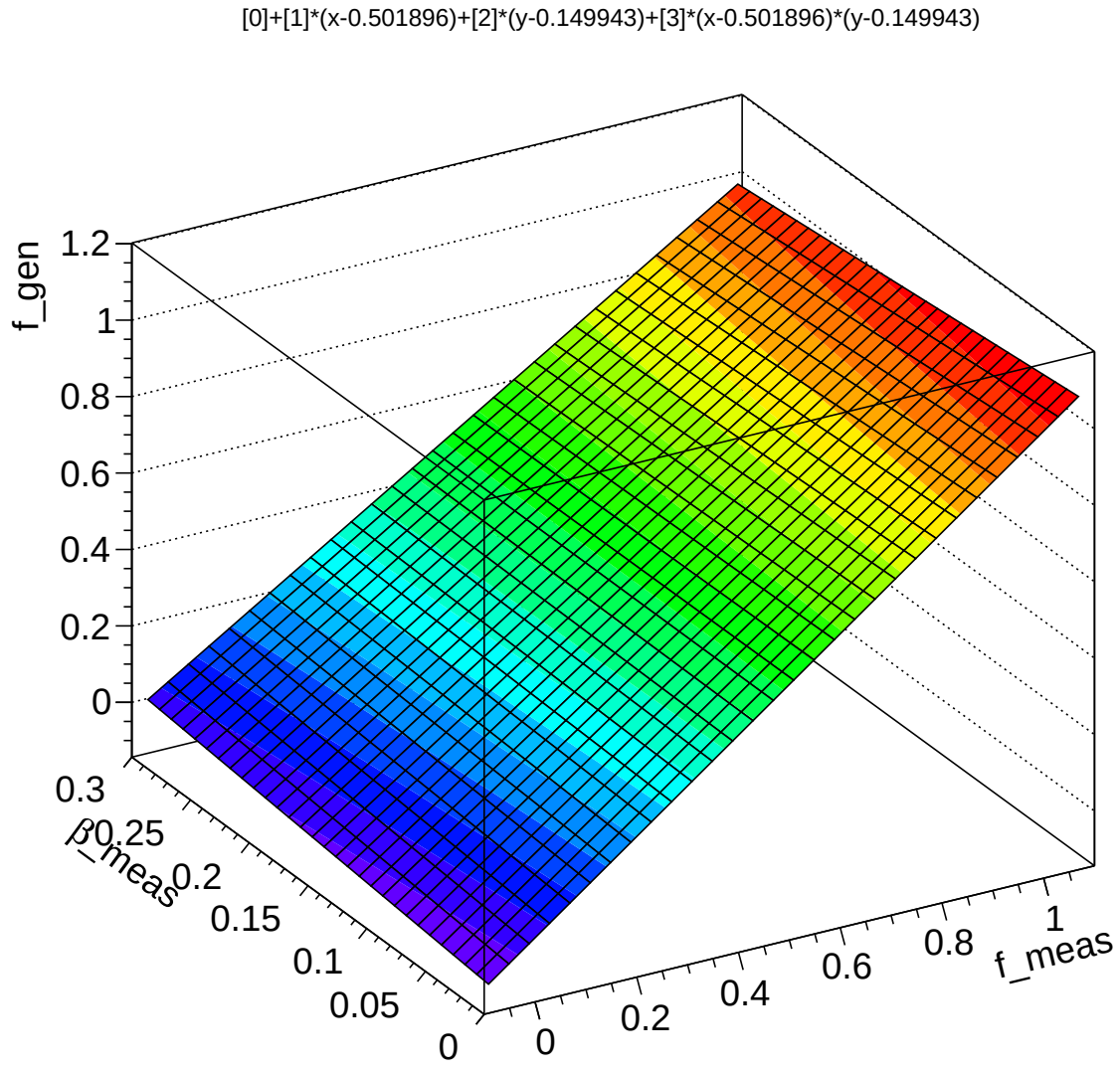

Figure 8.62: 2D calibration curve fitted to RECO simulation, to extract the f_{input} at a specific (f,β).

If we return to the fit model, where only f and β are extracted, the correlation is as shown in fig. 8.67 and negligible. For this particular fit model, the calibration curve was redetermined and the systematics were extracted, as will be shown in section 9.2.

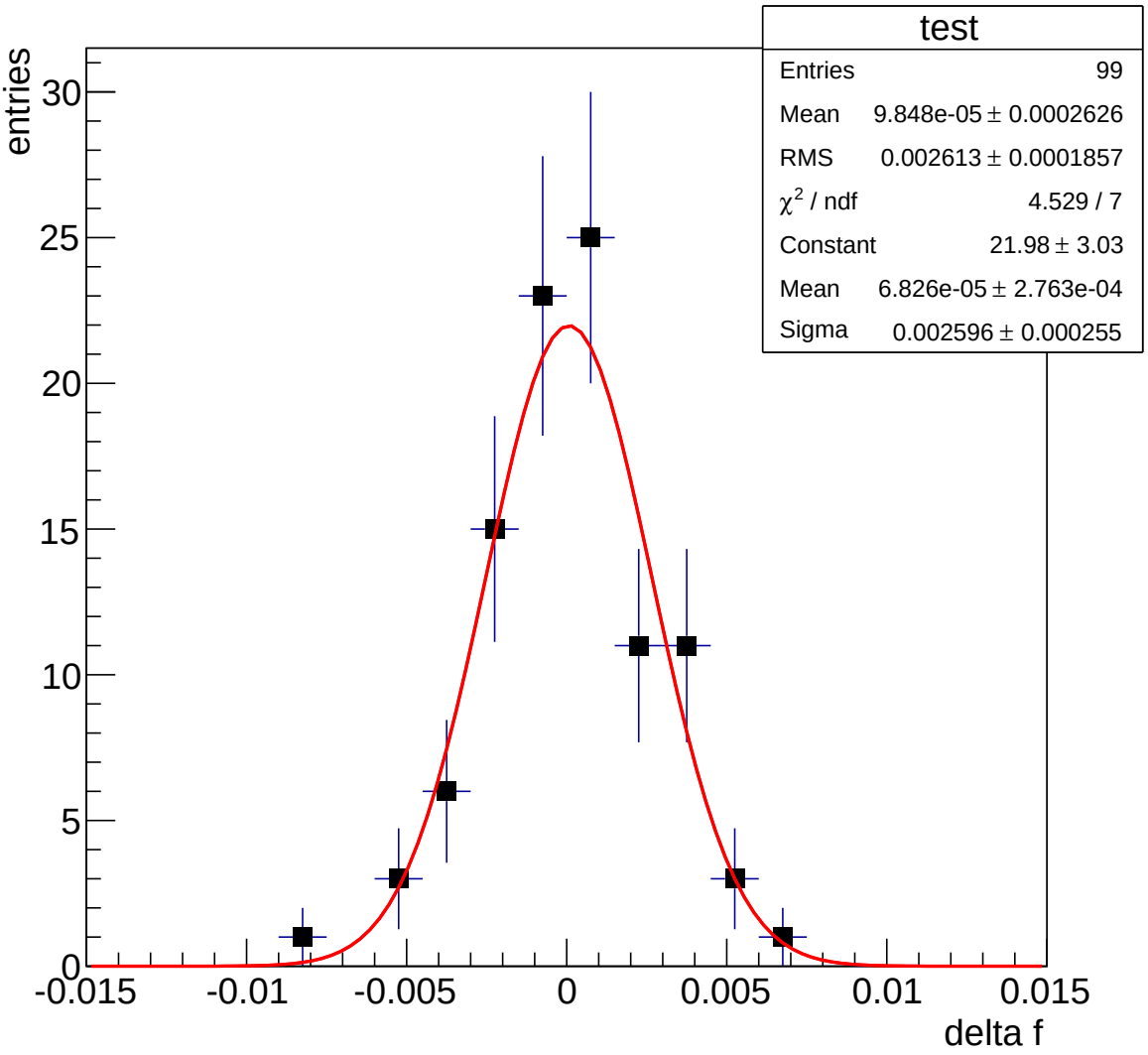

Figure 8.63: Difference between $f_{calibrated}(f, \beta)$ and $f_{input}(f, \beta)$ for all 99 evaluated working points $(f_{input}, \beta_{input})$. The difference is Gaussian distributed around 0.

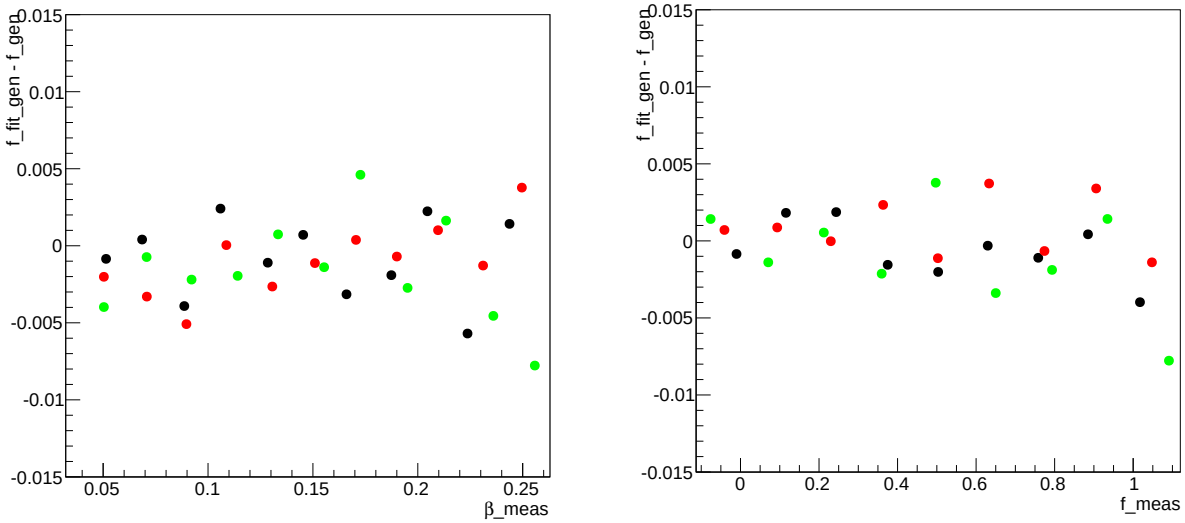

Figure 8.64: Difference between $f_{calibrated}(f, \beta)$ and $f_{input}(f, \beta)$ for fixed values of f_{input} (left) and β_{input} (right). The colours represent different values of f_{input} and β_{input} in the left and right plot respectively.

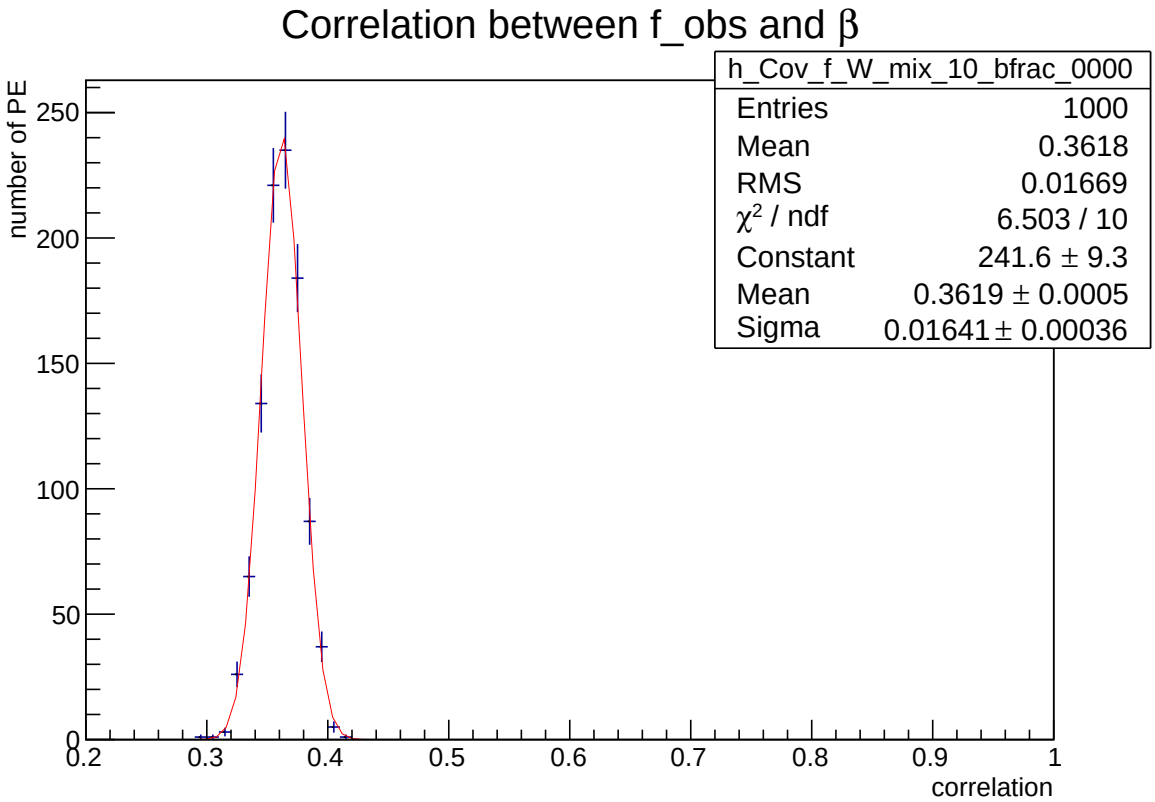

Figure 8.65: Correlation between fit parameters f and β fitted in the range $-2\ln\lambda_{event} = [-2.1, 1.26]$.

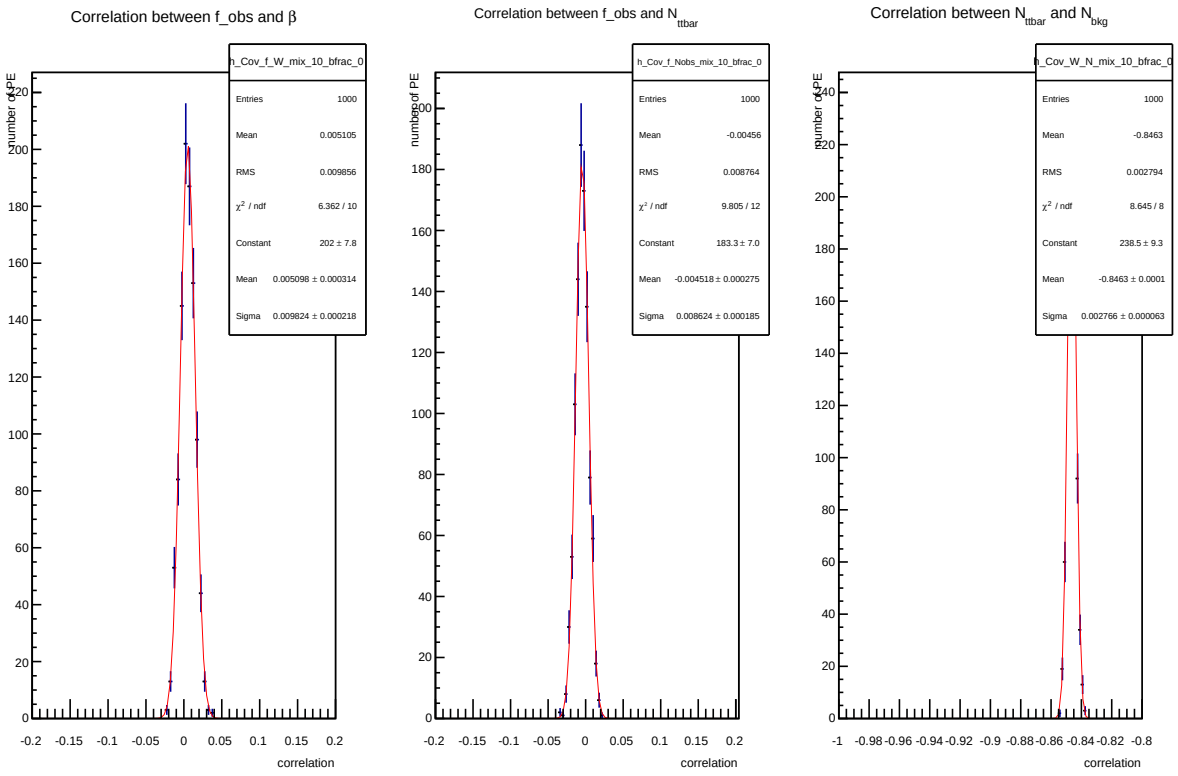

Figure 8.66: Correlation between fit parameters f, N_{bkg} and $N_{t\bar{t}}$ in the 2D, extended fit.

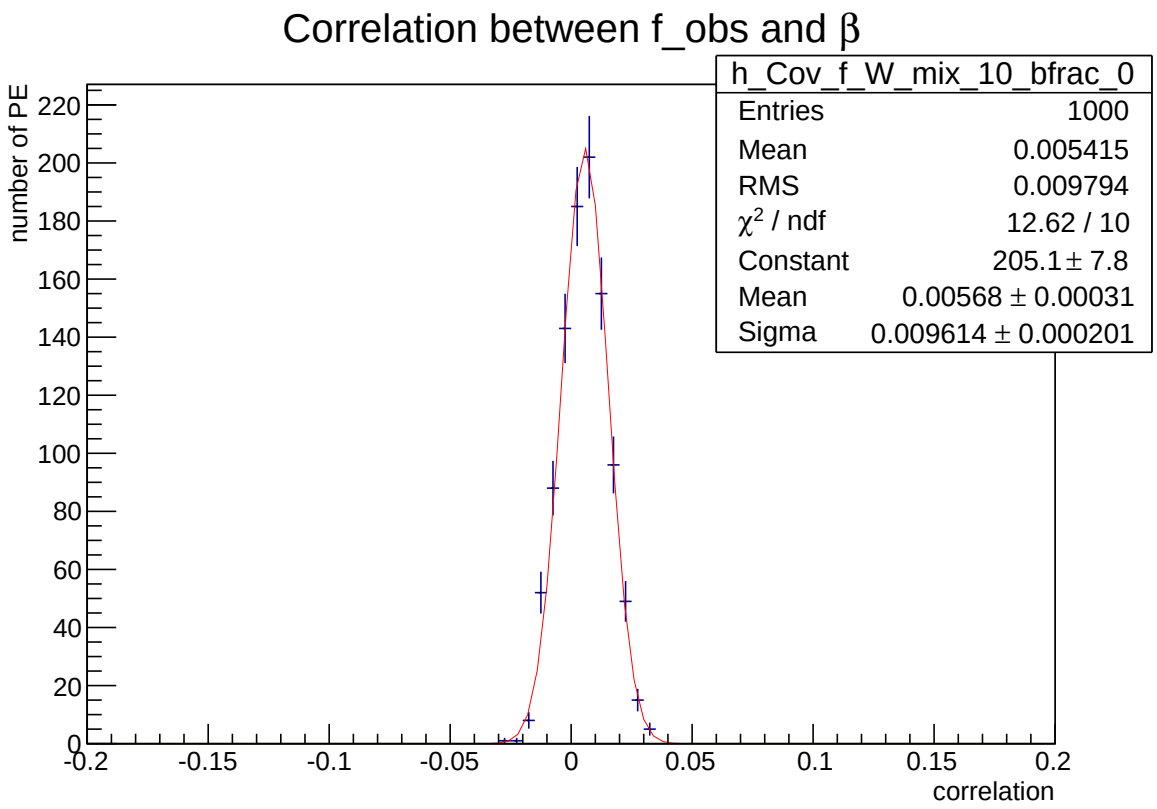

Figure 8.67: Correlation between fit parameters f and β in the 2D, unextended fit.

Chapter 9

Results and Systematic Uncertainties

In this chapter the results of the measurement of $t\bar{t}$ spin correlations with CMS data at a centre-of-mass energy of 8 TeV and an integrated luminosity of 19.7 fb^{-1} will be presented. In section 9.1, the results will be described both for the hypothesis testing part and for the extraction of the fraction of events with SM spin correlation f using a template fit. In section 9.2 the uncertainties on the results will be discussed and evaluated.

9.1 Results

The distribution of the likelihood under the SM hypothesis $-\ln L_{event}(H = Cor)$ is shown in fig. 9.1. The plots show a shape comparison between data and simulation, where both have been normalised to unity. The relative contribution of the different physics processes in the simulation are calculated based on the theoretical cross sections as used in table 5.12. There is good agreement between data and simulation.

The distributions of $-2\ln\lambda_{event}$ are shown in fig. 9.2. For the figure at the top, the SM correlated $t\bar{t}$ sample is used and for the figure at the bottom, the uncorrelated $t\bar{t}$ sample. Again the plots show a shape comparison between data and simulation. The binning shown in fig. 9.2 is the same binning used to generate pseudo-experiments from this distribution. At the bottom of these plots the ratio of the data over the simulation distribution is shown, including statistical and systematic uncertainties. From these distributions, we expect to find that the data is more compatible with the SM $t\bar{t}$ sample than with the uncorrelated $t\bar{t}$ sample.

9.1.1 Hypothesis Testing

In this section we report the results of the hypothesis testing procedure. The sample likelihood ratio, defined as $-2\ln\lambda_{sample} = -\Sigma 2\ln\lambda_{event}$, is evaluated by drawing pseudo-experiments with a fixed sample size N, in this case the observed dataset size of 36800 events. In total the dataset contains 37775 events but only 36800 in the $-2\ln\lambda_{event}$ range under study. In the pseudo-experiments, the relative signal and background ratios are respected based on the theoretical cross sections. These pseudo-experiments are performed once with the SM correlated signal sample and once with the uncorrelated signal sample. This evaluation of the sample likelihood ratio distribution in the simulation at the dataset size of 36800 events in the muon channel is shown in fig. 9.3. The blue curve shows the expected distribution of the sample likelihood ratios at this size using the SM correlated $t\bar{t}$ simulation as signal and the red curve using the uncorrelated $t\bar{t}$ simulation as signal. As is expected when only statistical effects are taken into account, these distributions are Gaussian. The value of the data sample likelihood ratio is indicated by the green arrow and has a value of 9882.07. As the simulated distributions are perfect Gaussians, the compatibility of the data with both hypotheses can be calculated as the amount of Gaussian widths the data value is away from the mean of the distribution. This gives us a compatibility of the data with the SM hypothesis of $3.7\,\sigma$ (expressed in standard deviations) and a compatibility with the uncorrelated hypothesis of $8.6\,\sigma$. The expected sep-

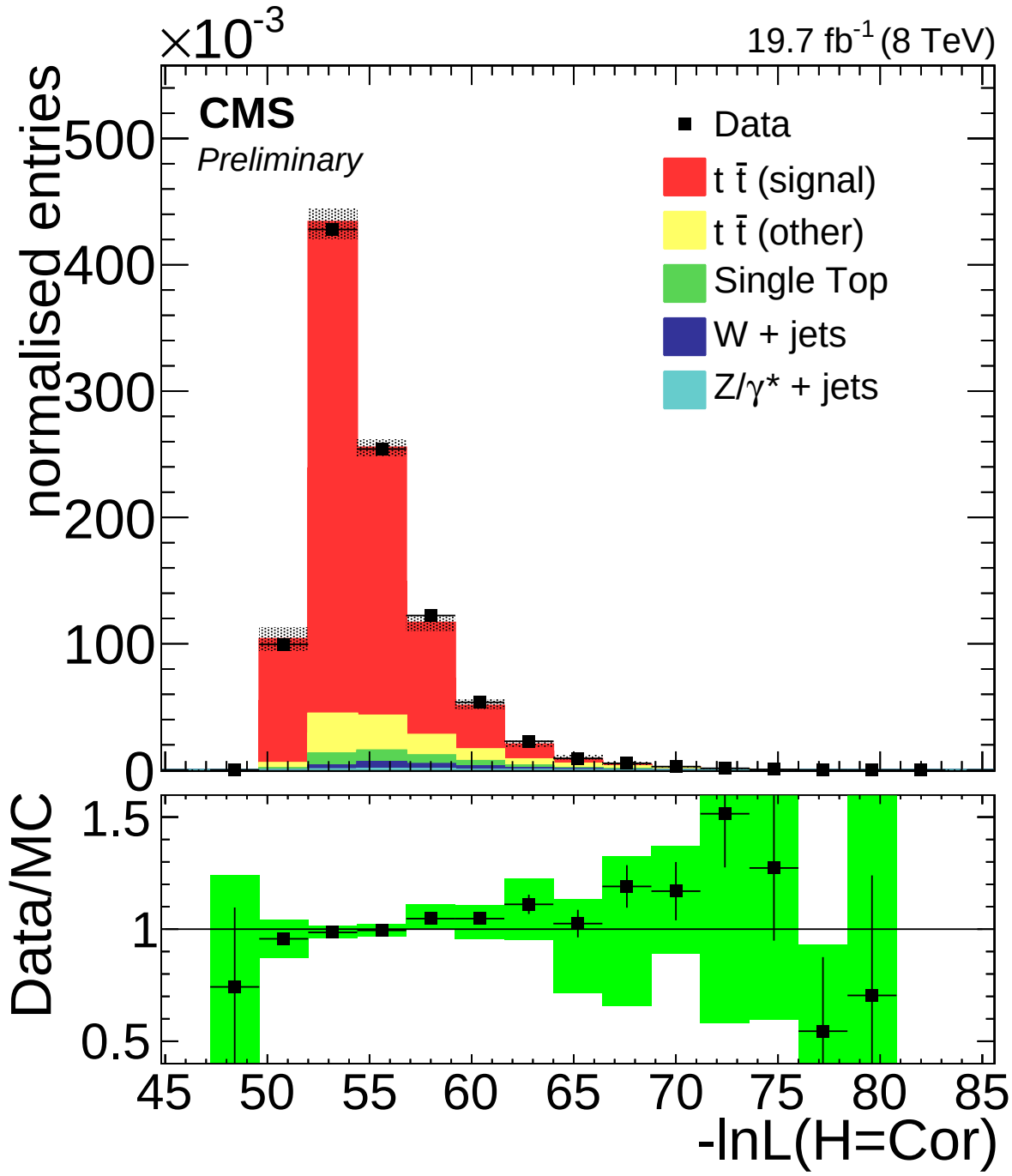

Figure 9.1: $-\ln L_{event}(H = Cor)$ distribution of the event likelihoods calculated under the SM hypothesis in the muon channel. The $t\bar{t}$ simulation is the MC@NLO correlated sample. Both data and simulation are normalised to unity. The hatched uncertainty band includes statistical and systematic uncertainties. The uncertainty bars in the ratio plot at the bottom only consider statistical uncertainties, while the hatched band includes both statistical and systematic uncertainties.

arating power, calculated using eq. 8.2, is $8.8\,\sigma$ without including systematic uncertainty sources.

Systematic uncertainty sources result in variations of the $-2\ln\lambda_{event}$ distributions used to draw pseudo-experiments to evaluate sample likelihood ratios. Each source of systematic uncertainty

will cause a broadening of the sample likelihood ratio distribution. As a result the distributions of both hypotheses show a decreased separation power.

9.1.2 Extraction of f

In this section we report on the results of the template fit method used to extract the fraction of events with SM spin correlations f. In the template fit, we use the $-2\ln\lambda_{event}$ distributions as templates. In total there are three templates based on simulation: $t\bar{t}$ signal SM correlated, $t\bar{t}$ signal uncorrelated and background. The shape of the templates is shown in section 8.2.2 in fig. 8.55. The bin width and range of the $-2\ln\lambda_{event}$ distribution is kept as described in section 8.2.2. In the fit the f and β fit parameters are kept completely floating and it has been checked that the initial values of the parameters have no influence on the fit result. The result of the fit on the data is shown in fig. 9.4 with $f_{fit,data} = 0.747 \pm 0.092$, $\beta_{fit,data} = 0.168 \pm 0.024$ and a $\chi^2/ndof = 1.552$. The correlation between $f_{fit,data}$ and $\beta_{fit,data}$ is 54 %. From simulation, a background fraction β of 15.5 % is expected in the fit range. In addition to the fit result, the statistical uncertainty is calibrated and scaled with a pull width of 1. After application of the calibration, described in table 8.11, the result including statistical uncertainty is

$$f_{calibrated} = 0.724 \pm 0.084\,(\text{stat}). \tag{9.1}$$

The fit results, after applying their respective calibrations including statistical uncertainty, for the two other fit models are: $f = 0.734 \pm 0.082\,(\text{stat})$ and $\beta = 0.183 \pm 0.014\,(\text{stat})$ in the 1D fit model in range $[-2.1, 1.26]$ is obtained, with a $\chi^2/ndof = 1.475$ and a correlation of 32 %. In the 2D fit model, we obtain $f = 0.784 \pm 0.070\,(\text{stat})$ and $\beta = 0.205 \pm 0.009\,(\text{stat})$ with a $\chi^2/ndof = 1.805$ in $-2\ln\lambda_{event}$, $\chi^2/ndof = 0.537$ in $-\ln L(H = Cor)$ and a correlation of -2 %.

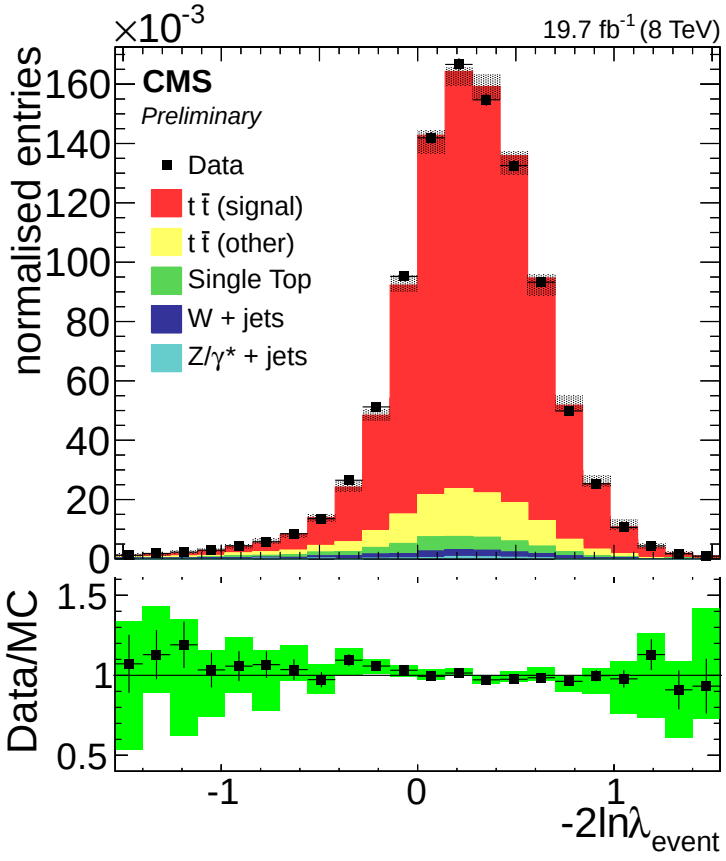

(a) $t\bar{t}$ SM correlated

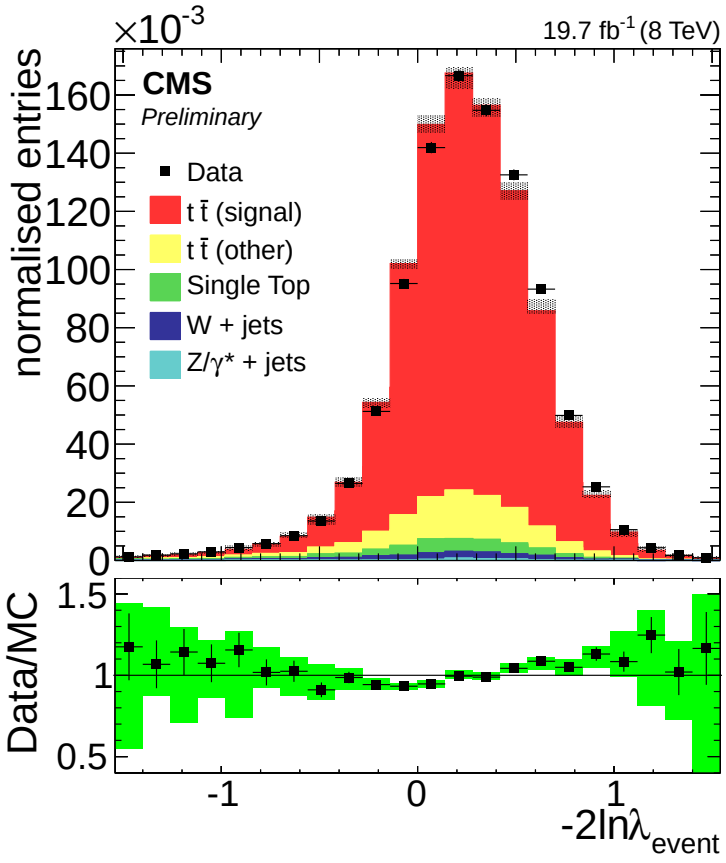

(b) $t\bar{t}$ uncorrelated

Figure 9.2: $-2\ln\lambda_{event}$ distribution of the event likelihoods in the muon channel. In 9.2a the SM correlated $t\bar{t}$ simulation was used and 9.2b the uncorrelated $t\bar{t}$ simulation. Both data and simulation are normalised to unity. The hatched uncertainty band includes statistical and systematic uncertainties. The uncertainty bars in the ratio plot at the bottom only consider statistical uncertainties while the hatched band includes both statistical and systematic uncertainties.

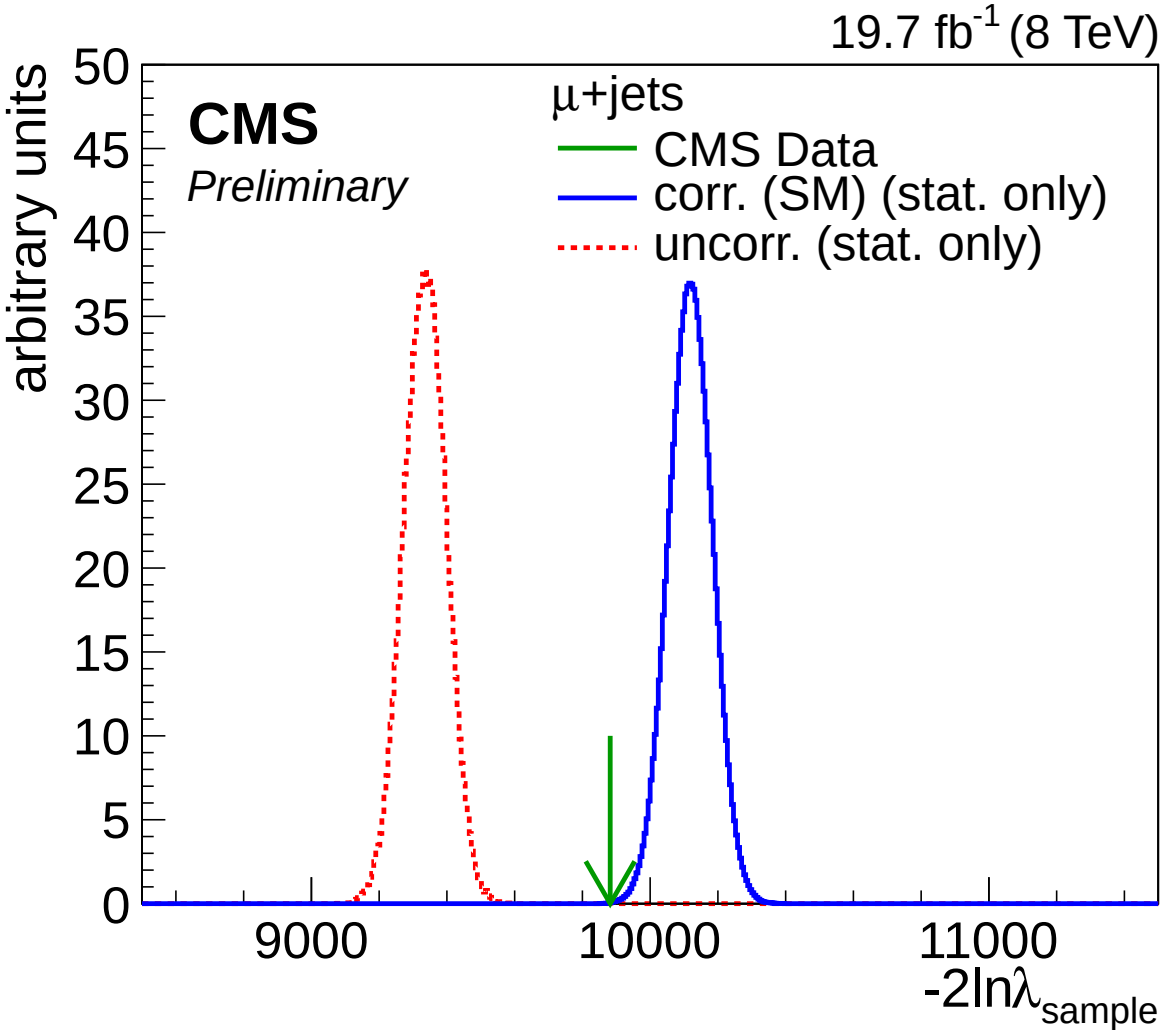

Figure 9.3: The $-2\ln\lambda_{sample}$ distribution is shown in simulation, extrapolated to the data sample size in the muon channel. The samples in simulation contain signal and background mixed according to the theoretical cross sections, with the blue Gaussian using SM correlated $t\bar{t}$ simulation and the red Gaussian using uncorrelated $t\bar{t}$ simulation. The green arrow indicates the $-2\ln\lambda_{sample}$ observed in data

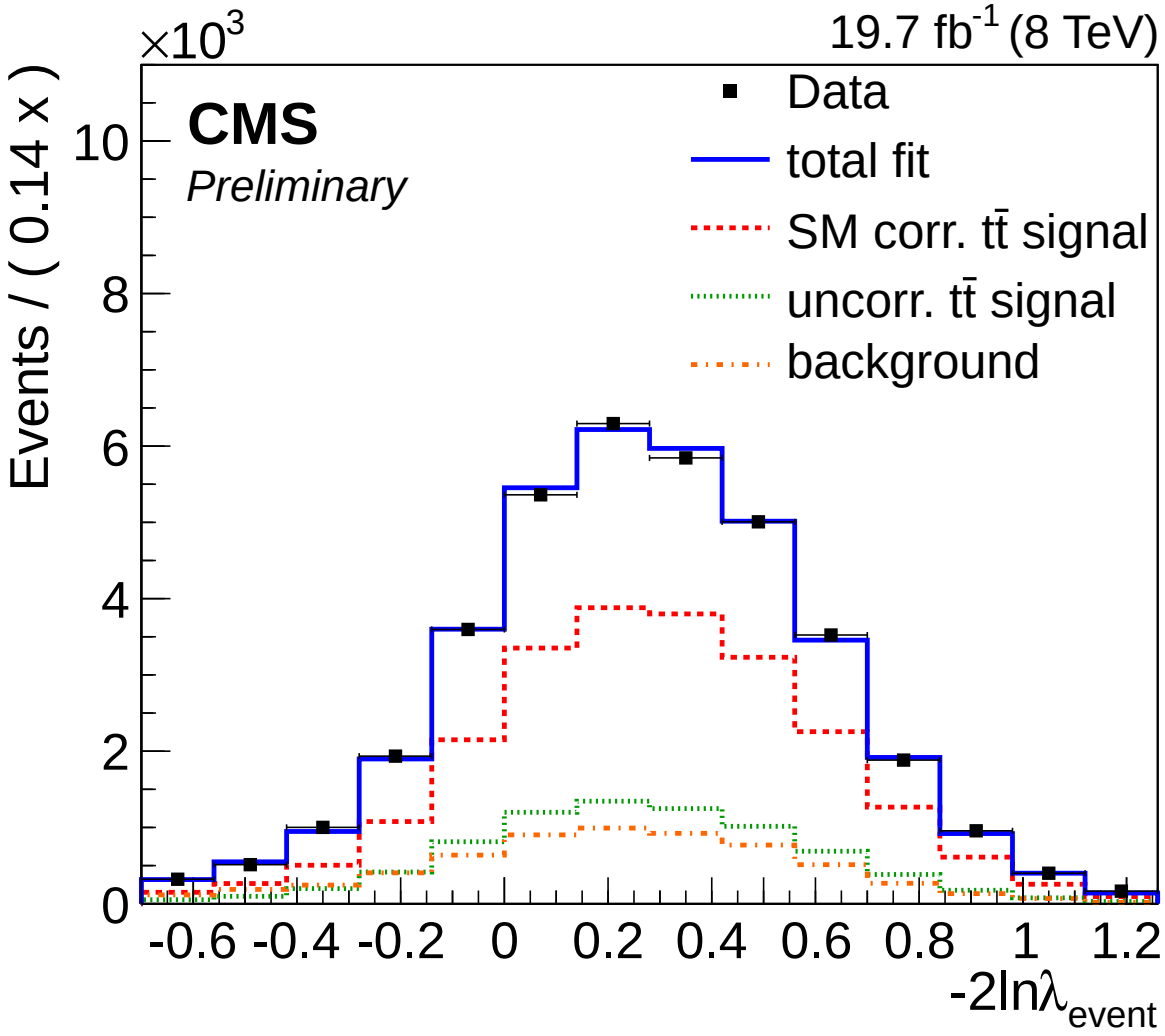

Figure 9.4: Result of the template fit to data. The black dots are the data, the blue curve is the overall result of the fit, the red curve is the contribution of the SM signal template to the fit, the green curve is the contribution of the uncorrelated signal, while the orange curve is the background contribution.

9.2 Systematic Uncertainties

In this measurement we rely on simulation which has been produced with specific physics models and parameter values. The variation of these assumptions gives rise to a systematic variation on the measurement. In this section, the effect of these assumptions is investigated and quantified. In the first section, the various sources of systematic uncertainty are discussed. In the following sections, the inclusion of these systematic uncertainties in both parts of the measurement is explained and the results of these evaluations are given.

9.2.1 Sources of Systematic Uncertainty

Systematic uncertainties affecting this analysis arise from various sources such as detector effects, theoretical uncertainties and mismodelling which affect the resolution and calibration. The simulation is corrected where necessary to account for efficiency differences in the data and simulation, e.g. muon identification, isolation efficiency, trigger efficiencies and others. The systematic uncertainties are determined, independently of each other, by varying the efficiency correction, resolution or scale correction factors within their uncertainties. For some uncertainties, this is equivalent by varying the event weights which gives rise to a variation of the template shapes from which pseudo-experiments are drawn. Other uncertainties require recalculating of the event likelihoods leading also to a modified template shape. Where possible, the varied $-2\ln\lambda_{event}$ and $-2\ln\lambda_{sample}$ distributions associated to the systematic uncertainty is shown. In section 9.2.2 more details will be given on the evaluation of the systematically varied $-2\ln\lambda_{sample}$ distribution.

We divide the systematic uncertainties in three categories depending on the treatment in the analysis:

- Type 0: Normalisation uncertainties.
- Type 1: Systematic effects that change the likelihood ratio shapes but can be estimated without re-running MadWeight.
- Type 2: Systematic effects that change the likelihood ratio shapes and need re-running MadWeight.

Type 0: Normalisation Uncertainties

- *Luminosity uncertainty* There is an uncertainty on the determination of the integrated luminosity during data-taking. The luminosity determination and the corresponding uncertainties are described in section 2.2.6. In this analysis, we normalise the distributions to the observed dataset size: the sample likelihood ratio distribution is evaluated at the dataset size and in the template fit the normalisation is kept fixed. This normalisation eliminates the uncertainty due to the determination of the integrated luminosity.
- *Background modelling and theoretical cross sections* The shape of the $-2\ln\lambda_{event}$ distribution is determined by combining the shapes of the individual physics processes in simulation. The relative contribution of the processes is determined using the theoretical cross sections and the selection efficiencies. Based on table 5.12, the relative weights are determined and fixed. In the template fit, only the relative background contributions are fixed while the signal-to-background ratio is left floating in the fit. For the hypothesis testing, the latter is also fixed. The theoretical cross sections have uncertainties associated to them due to factorisation and renormalisation scale uncertainties and uncertainties on the PDFs used. These uncertainties can be obtained from Monte Carlo event generators. For each physics process the theoretical uncertainty is varied within the uncertainties, leading

to a varied relative weight and therefore a varied template shape. This is done for each process independently. Most processes are properly modelled in the simulation, however in the case of W+jets an additional uncertainty is in order.

For the contribution of W+jets events, the yield is varied by 50% and the effects are propagated to the measurement, which is more than ample to cover the small uncertainties on the theoretical cross sections. The shape of the W+jets background template is also varied by excluding the W+jets contribution and only considering the $t\bar{t}$ other, Z+jets and single top background contributions. The total background fraction is kept fixed to the nominal value, which corresponds to a 100% uncertainty in the shape to cover the relatively less well-modelled W+heavy flavour jets.

Type 1: no re-evaluation of event likelihoods These uncertainties affect the template shapes by a variation of the event weights and can therefore be estimated without the recalculation of the likelihoods. The uncertainties listed below are expected to have very similar effects on T_{cor} and T_{uncor} as these are largely independent of the angular differences of the objects in the final state.

- *Lepton trigger, identification and isolation efficiencies:* p_T- and η-dependent scale factors are applied to the simulation to correct for efficiency differences in the data and simulation for the single lepton trigger, lepton identification and isolation. These scale factors are varied independently within their uncertainties and the effects are propagated to the measurement. The uncertainty on the scale factors is on the order of 0.5 %. The varied distributions are shown in fig. 9.5 and 9.6.

- *b-tagging efficiency and mistag rate:* The p_T- and η-dependent tagging and mistagging efficiencies for light-flavour as well as heavy-flavour jets are varied within their uncertainties and are propagated to the event weights in the simulation. The variation of the efficiencies is of the order of 0.5 - 1.0 %. The varied distributions are shown in fig. 9.7 and 9.8.

- *Pile-up:* A 5 % uncertainty on the inelastic pp cross section is taken into account and is propagated to the event weights used to correct the distribution of the number of pile-up interactions in simulation to the data as was shown in fig. 5.1. The varied distributions are shown in fig. 9.9.

- p_T^t *modelling:* The model of $t\bar{t}$ production in MadGraph as well as in MC@NLO simulation predicts a harder p_T^t spectrum than observed in the data [110–112]. There is a reweighting available for top quark pairs based on the spectrum of generator-level top quarks to obtain a better agreement to the measured differential cross section, but this reweighting is not applied in this analysis as was agreed for spin correlation analyses in the CMS Top quark group. However we assign an uncertainty by changing the event weights to take into account this reweighting and propagating the effect to the $-2\ln\lambda_{event}$ shape. The weights are derived as a function of the generated p_T of both top quarks in the $t\bar{t}$ pair, given by weight $= \sqrt{\mathrm{SF}(p_{T,t})\mathrm{SF}(p_{T,\bar{t}})}$ with $\mathrm{SF}(p_T) = exp(0.159 - 0.00141 p_T)$ where the p_T is expressed in GeV, for the lepton+jets channel [113]. The distribution of the weights after event selection on the $t\bar{t}$ signal sample is shown in fig. 9.10. As the event weights are designed to correct for shape differences in the top p_T distribution and the average weight is not one, the average weight is taken into account when considering the event yield in simulation.

  The varied $-2\ln\lambda_{event}$ and $-2\ln\lambda_{sample}$ distributions are shown in fig. 9.11.

- *Limited number of events in simulated samples:* The pseudo-experiments we draw at the dataset size are taken from simulation with limited statistics. The template shapes are subject to statistical fluctuations in each bin of the distribution. The signal samples have

been produced with sufficient statistics to keep this uncertainty small, but for several background samples, the number of events is rather limited. Each bin of the $-2\ln\lambda_{event}$ distribution is fluctuated within the statistical uncertainty of $\sigma_{Poisson} = \sqrt{N_{bin}}$ with N_{bin} representing the number of events in the corresponding bin. The contents of the bins are fluctuated independent of each other and of each simulation sample. Pseudo-experiments where this fluctuation is taken into account then show the spread of the $-2\ln\lambda_{sample}$ and fitted f distribution. An example of the statistical uncertainty on the $-2\ln\lambda_{event}$ distribution is shown in fig. 9.12 in the W+jets simulated sample.

- *PDF uncertainties:* Parton Distribution Functions (PDF) are used to model the hard scattering in proton-proton collisions in simulation as was discussed in Chapter 3. The theoretical uncertainties on the PDFs are propagated through this analysis by the Hessian Method [114]. In the determination of a parton distribution function, a χ^2 fit to collision data is performed with N free parameters. The fitted parameter values are used to describe the PDF set used in the production. In diagonalising the Hessian error matrix obtained in the fit, N eigenvectors are obtained. Due to the variation of the eigenvectors, 2N parameter sets are obtained. The PDF set used for the production of the $t\bar{t}$ signal sample is CTEQ6m. The procedure to calculate the uncertainty on an observable due to the PDF uncertainties is described in [115] and makes use of the so-called "Master equations".

$$\Delta X^{+}_{max} = \sqrt{\sum_{i=1}^{N}[max(X_i^{+} - X_0, X_i^{-} - X_0, 0)]^2} \tag{9.2}$$

$$\Delta X^{-}_{max} = \sqrt{\sum_{i=1}^{N}[max(X_0 - X_i^{+}, X_0 - X_i^{-}, 0)]^2} \tag{9.3}$$

In these equations X_0 is the central value of the observable, $X_i^{\pm}$ are the values obtained after the i^{th} eigenvector variation with the "+" and "-" sign representing the direction of the eigenvector variation. Here X_0 is the content of each bin in the $-2\ln\lambda_{event}$ distribution. The varied distributions are shown in fig. 9.13. In a matrix element method, the parton distribution function is used during the likelihood calculation. In principle it is possible to evaluate the PDF uncertainty during the likelihood calculation instead of using the Master equations which is a conservative approach. However due to the high computation time of the calculations, this is not preferred. The varied distributions are shown in fig. 9.13.

Type 2: re-evaluation of event likelihoods These are systematic effects that change the event kinematics and therefore need a re-evaluation of the event likelihoods.

- *Jet energy scale and resolution:* The jet energy resolution and scale corrections were described in section 5.6.4. The uncertainty on the jet energy resolution is estimated by varying the core resolution scale factor within its uncertainties (as listed in table 5.11) and redoing the analysis. The four-momenta of all jets reconstructed in simulated events (both signal and background) are scaled up or down by the uncertainties of the p_T- and η-dependent jet energy scale [88], [87] prior to event selection. The likelihood calculations are performed with the varied jet kinematics, using the nominal transfer functions. The JES/JER uncertainty enters the measurement in two aspects: acceptance effects modify the relative contributions of the backgrounds and the event likelihood values change, the latter being the dominant effect. It is important to note that an uncertainty due to the transfer functions used is indirectly included in jet energy scale and resolution uncertainties. Varying the jet energy scale induces a mismatch between the jet energies evaluated and the jet energies used to generate the transfer function, which could also be interpreted

as evaluating the event likelihoods with fixed jet energy scale but with varied transfer functions. The varied distributions are shown in fig. 9.14 and 9.15. As can be seen from fig. 9.14, the JES uncertainty is asymmetric in the $-2\ln\lambda_{event}$ and more distinctly in the $-2\ln\lambda_{sample}$ distribution. This asymmetric behaviour is as expected since the nominal transfer function corrects the kinematics in one direction. It has explicitly been tested that the JES uncertainty gives symmetric distributions when no transfer function is used in the likelihood calculation.

- *Top quark mass uncertainty:* SM correlated and uncorrelated $t\bar{t}$ samples with varied top quark mass values have been produced. All event likelihoods are evaluated at the $m_{top} = 172.5\,\text{GeV}$ hypothesis. The nominal samples are simulated with a top quark mass of 172.5 GeV, whereas the systematic samples are simulated with $m_{top} = 169.5\,\text{GeV}$ and $m_{top} = 175.5\,\text{GeV}$. For the variation of the template, we fluctuate within 1/3 of the deviation shown by the 175.5 GeV and 169.5 GeV samples to mimic the template variation that is caused by the 1 GeV uncertainty of the top quark mass world average [116]. This top quark mass variation is evaluated only in $t\bar{t}$ signal and background from other $t\bar{t}$ decay channels. The variation was not performed in single top samples as the total background contribution is quite low. As the matrix element method was originally designed to perform a measurement of the top quark mass, we expect a significant effect due to the top quark mass uncertainty. The varied distributions based on the ± 1 GeV variation are shown in fig. 9.16. This effect of this uncertainty is again twofold: the variation of the top quark mass leads to a change in the kinematics of the decay products and therefore to a varied observed cross section. In addition it causes a variation of the event likelihoods as there is a mismatch between the top quark mass hypothesis used to produce and evaluate the event.

- Q^2 *scale uncertainty:* The factorisation and renormalisation scale defines the amount of squared transverse momentum used in the evolution of the parton shower (see Section 1.2.1):

$$Q^2 = \sum m_T^2/2 \tag{9.4}$$

where the sum is over the transverse mass of the final state particles. Variation of the scale affects the amount of radiation in the event and therefore migrates events between bins of jet multiplicity. Since final state radiation is not explicitly treated in the analysis, the Q^2 scale variation has significant effects on the result. SM correlated and uncorrelated $t\bar{t}$ samples with the Q^2 scale varied to $Q^2/4$ or $4Q^2$ are used to estimate the uncertainty caused by the Q^2 scale uncertainty. The scale uncertainty is evaluated only on $t\bar{t}$ signal and background from other $t\bar{t}$ decay channels. The variation has not been performed on the other background samples as the total background contribution is low. The varied distributions are shown in fig. 9.17.

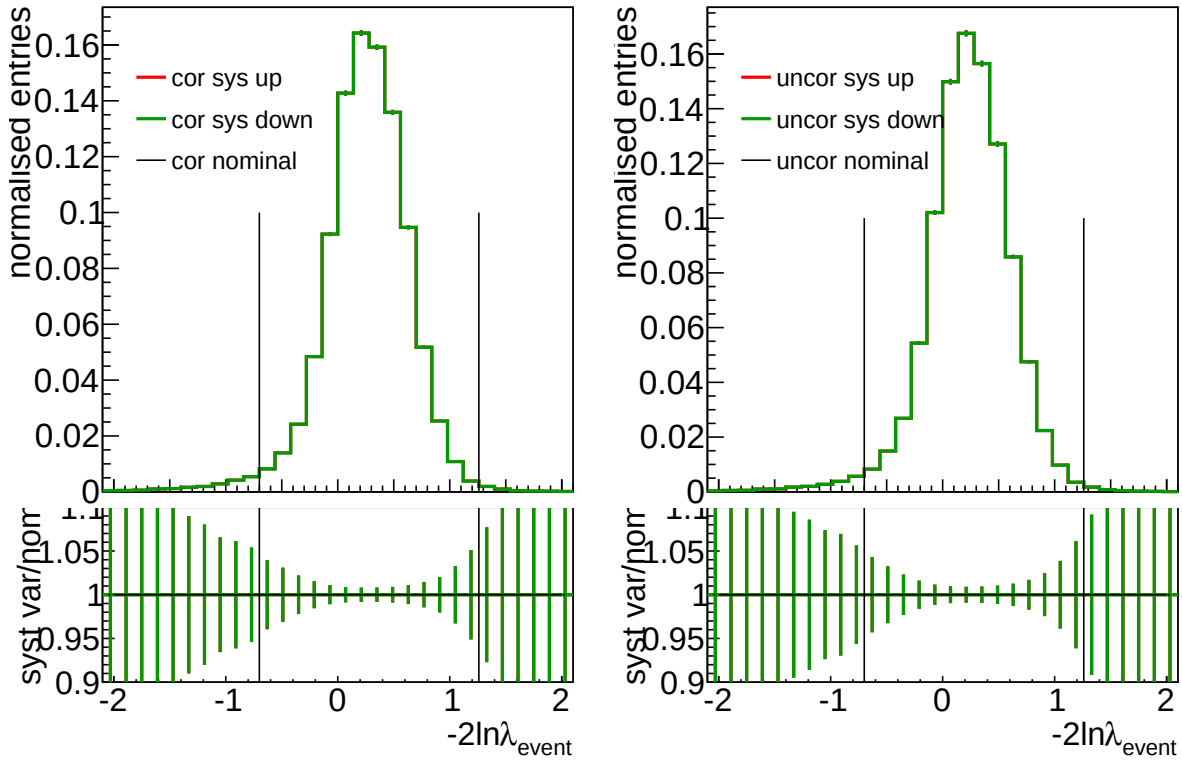

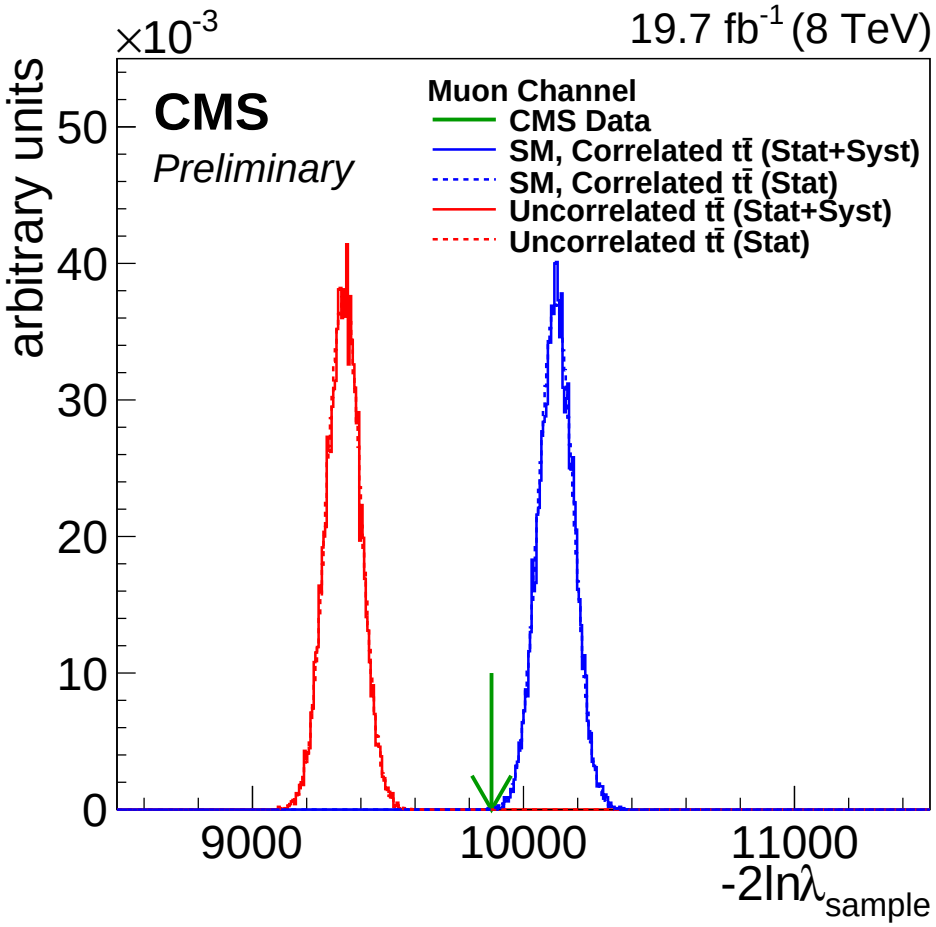

Figure 9.5: Systematically varied $-2\ln\lambda_{event}$ distribution and $-2\ln\lambda_{sample}$ distribution associated to the lepton trigger efficiency variation.

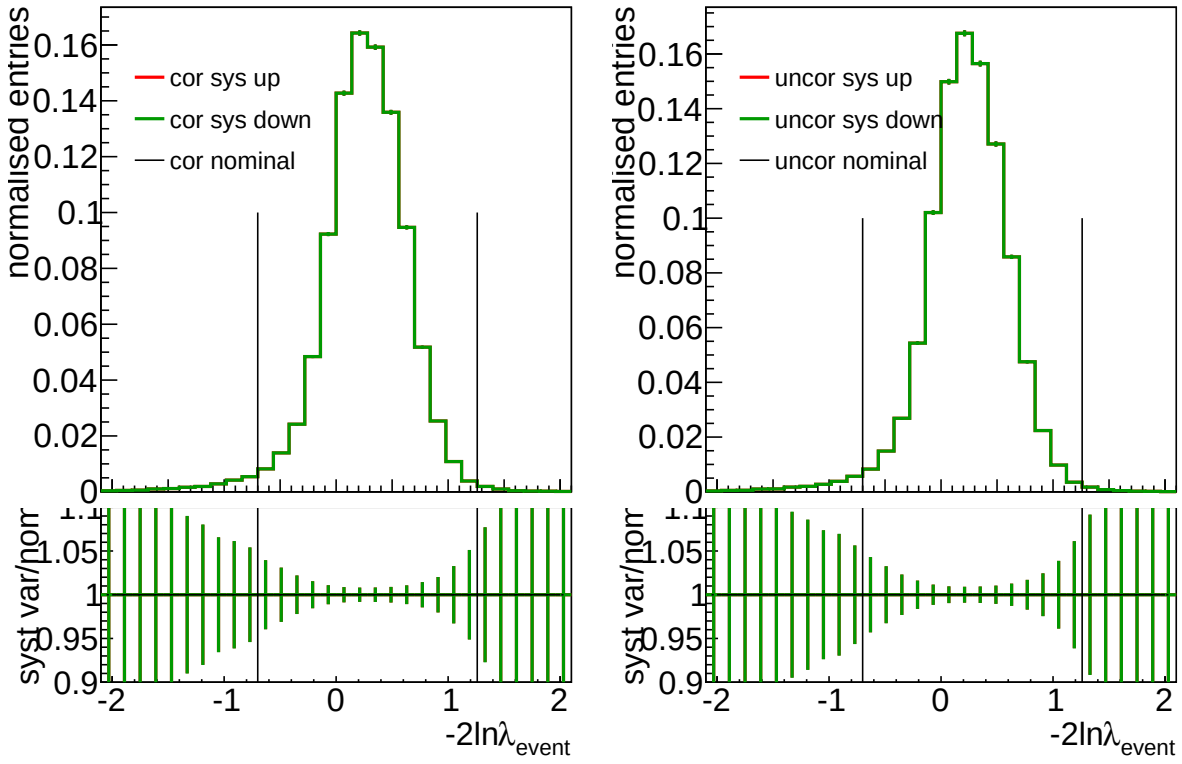

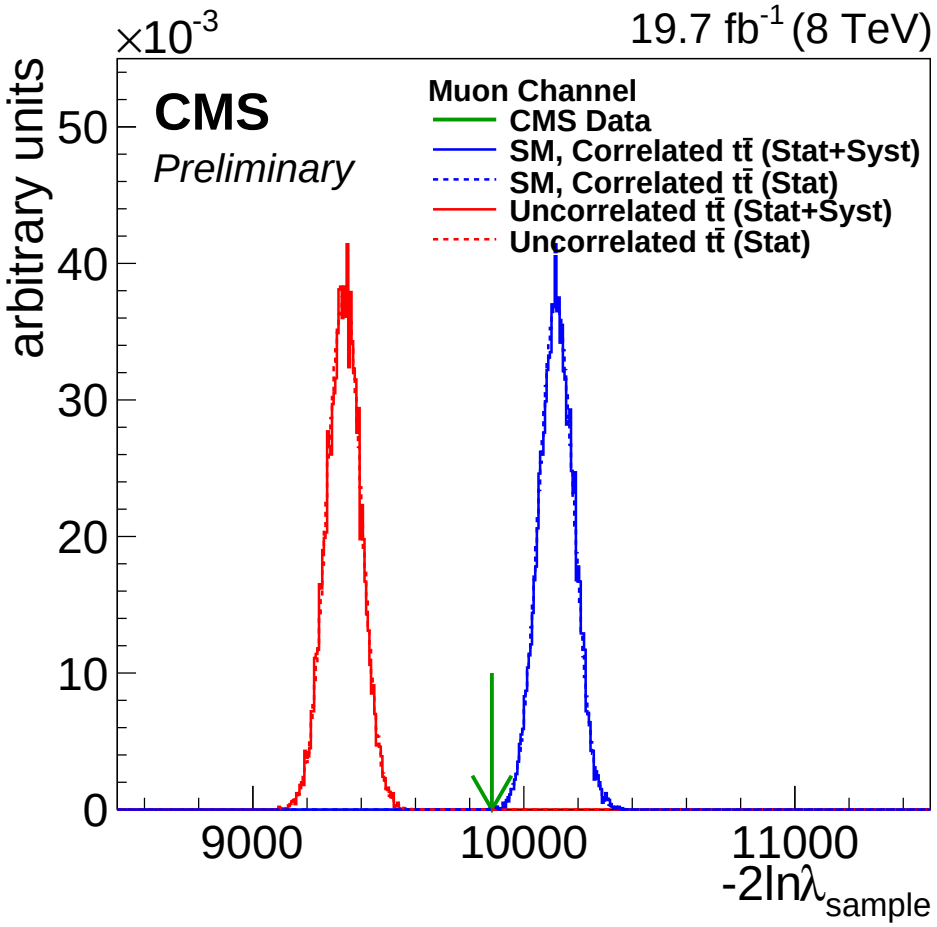

Figure 9.6: Systematically varied $-2\ln\lambda_{event}$ distribution and $-2\ln\lambda_{sample}$ distribution associated to the lepton identification and isolation efficiency variation.

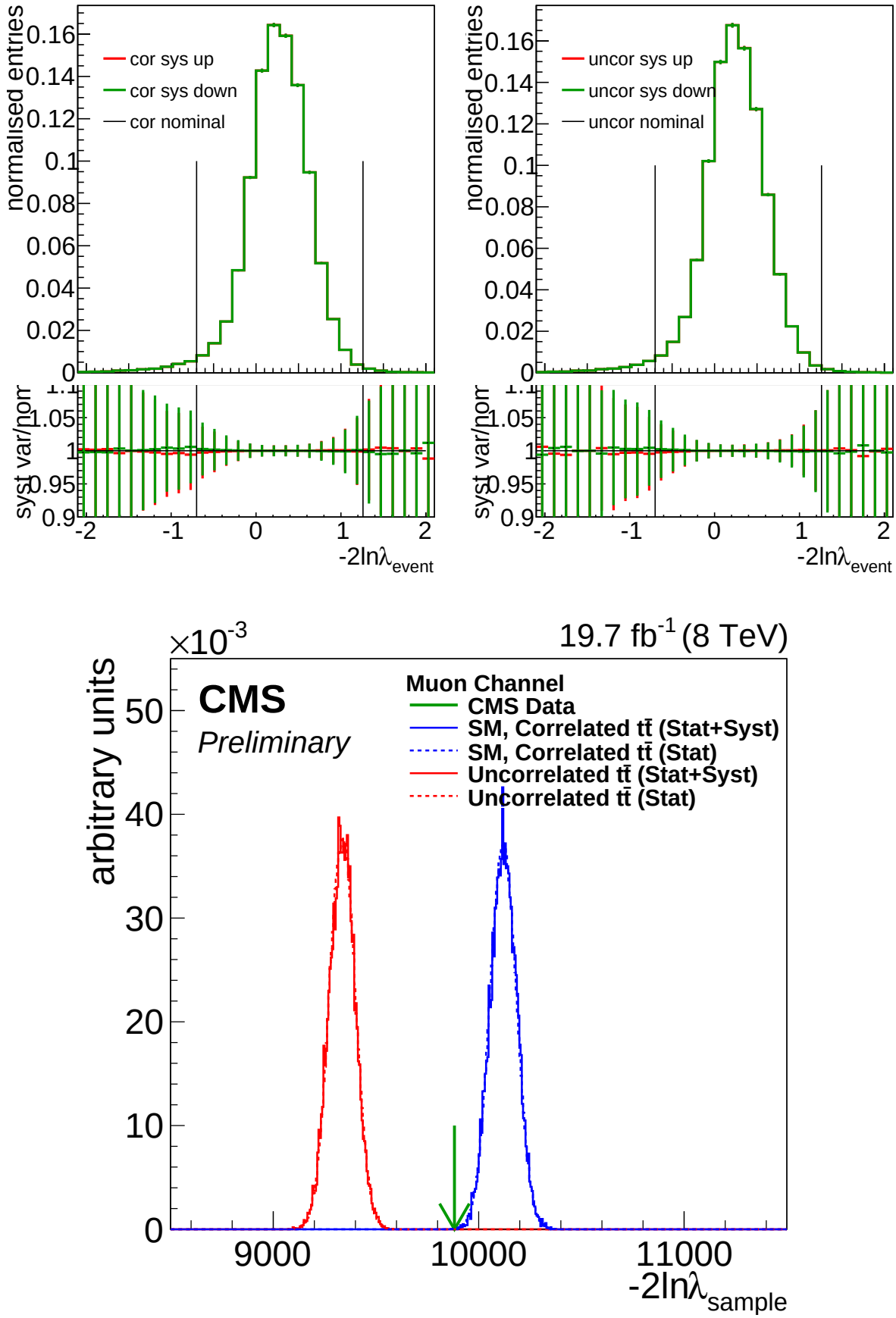

Figure 9.7: Systematically varied $-2\ln\lambda_{event}$ distribution and $-2\ln\lambda_{sample}$ distribution associated to the b-tagging efficiency variation.

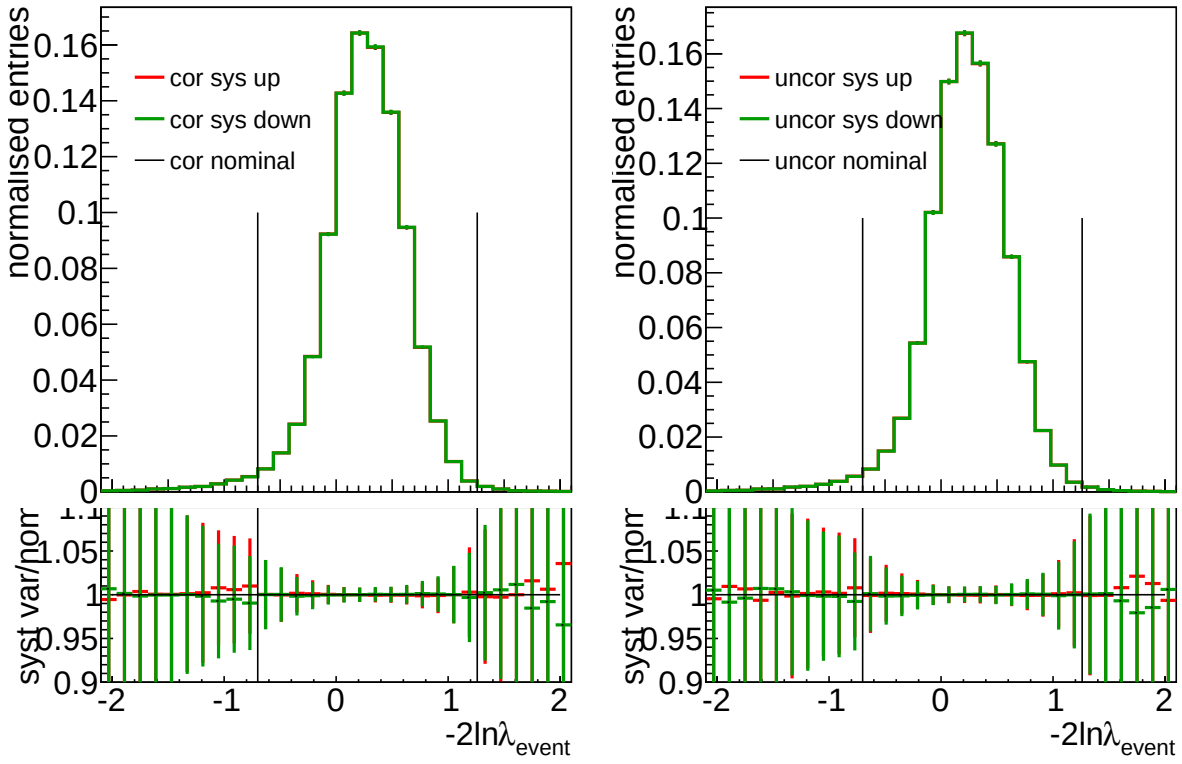

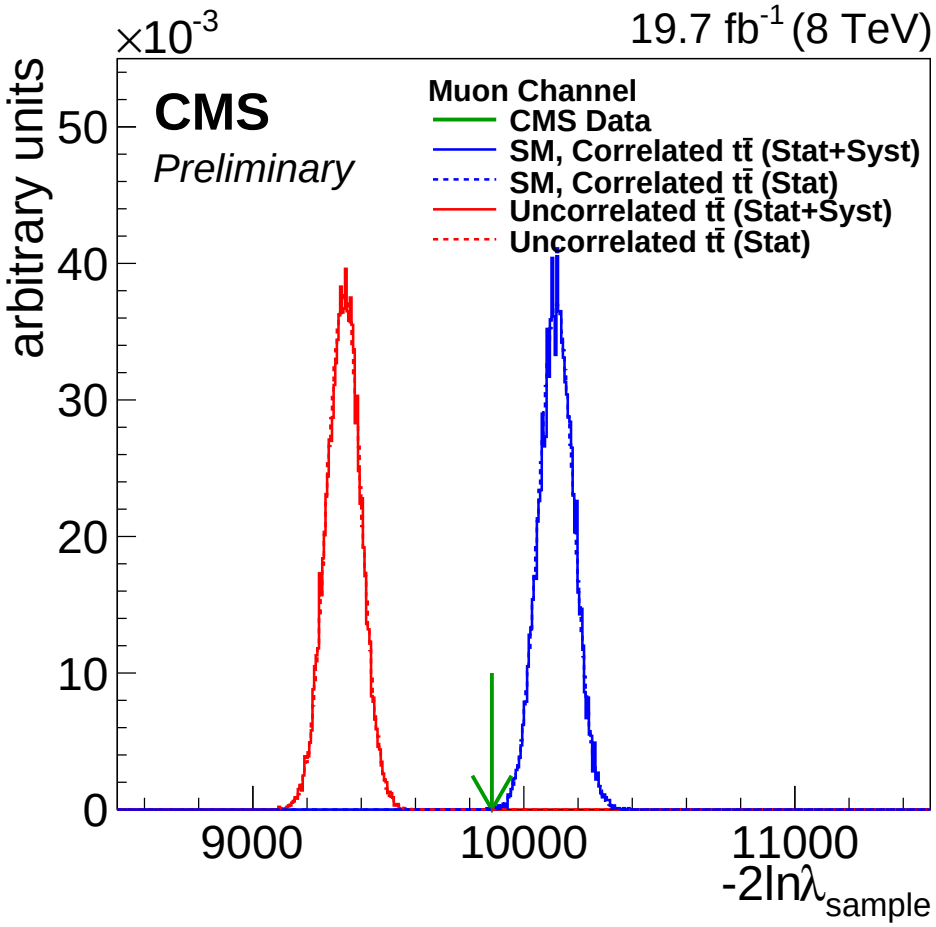

Figure 9.8: Systematically varied $-2\ln\lambda_{event}$ distribution and $-2\ln\lambda_{sample}$ distribution associated to the mistagging rate variation.

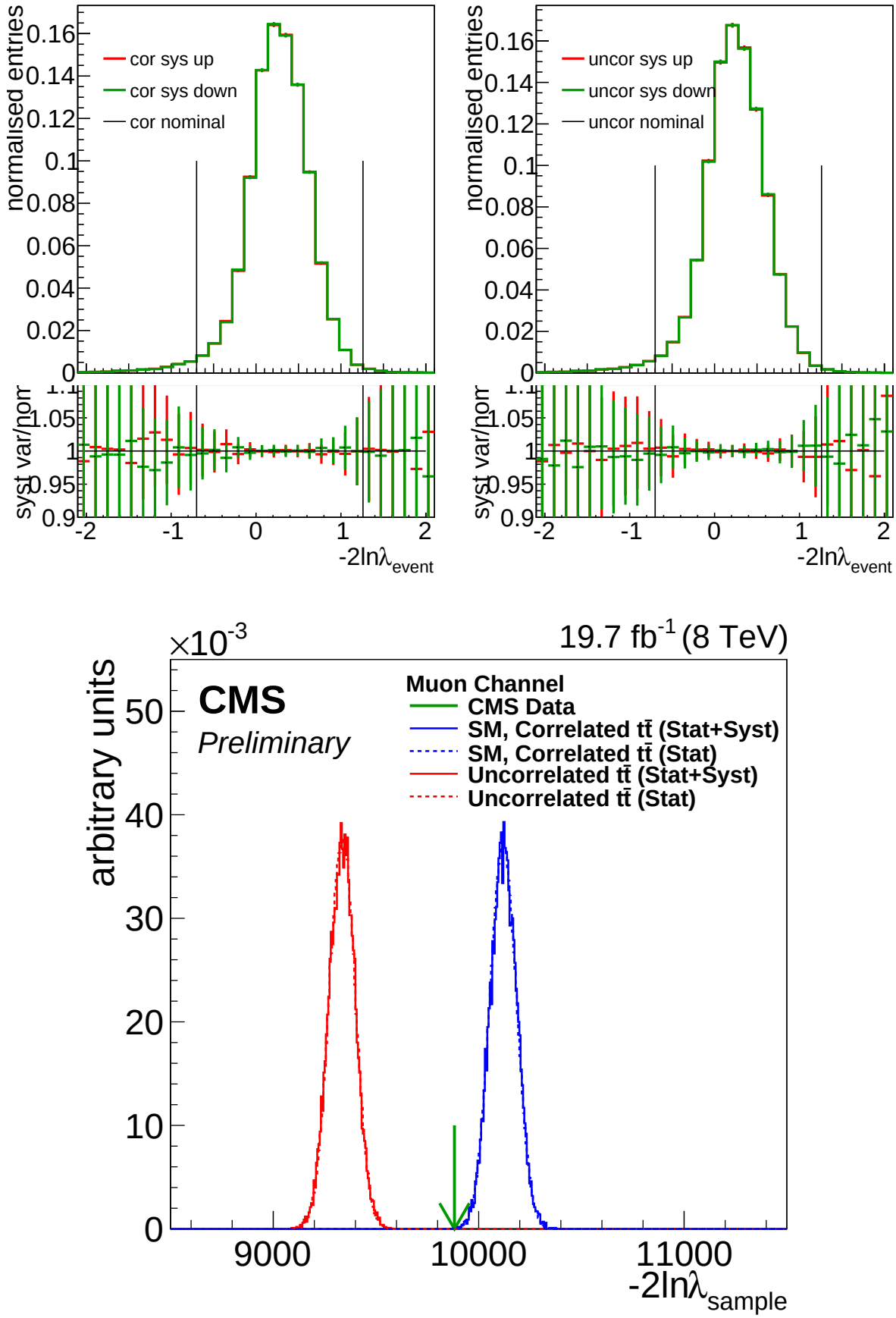

Figure 9.9: Systematically varied $-2\ln\lambda_{event}$ distribution and $-2\ln\lambda_{sample}$ distribution associated to the pile-up interaction uncertainty.

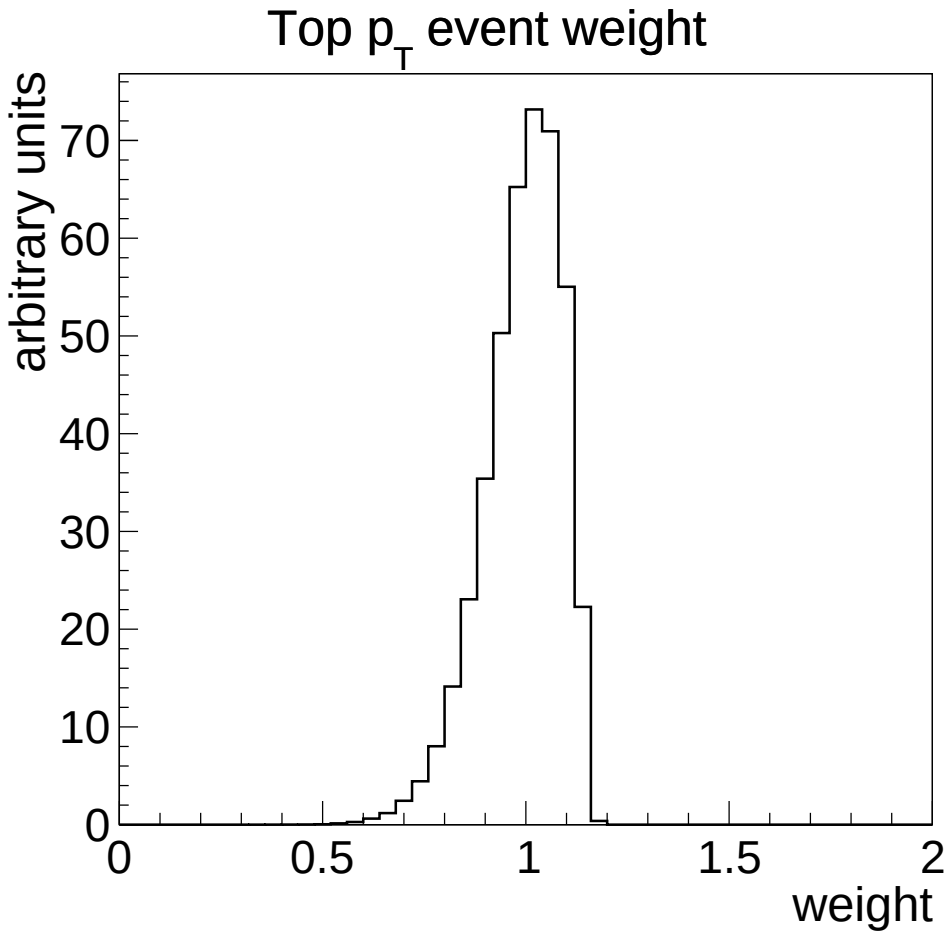

Figure 9.10: Distribution of the event weights correcting for the top p_T distribution in simulation. The weights correspond to the $t\bar{t}$ signal sample after event selection.

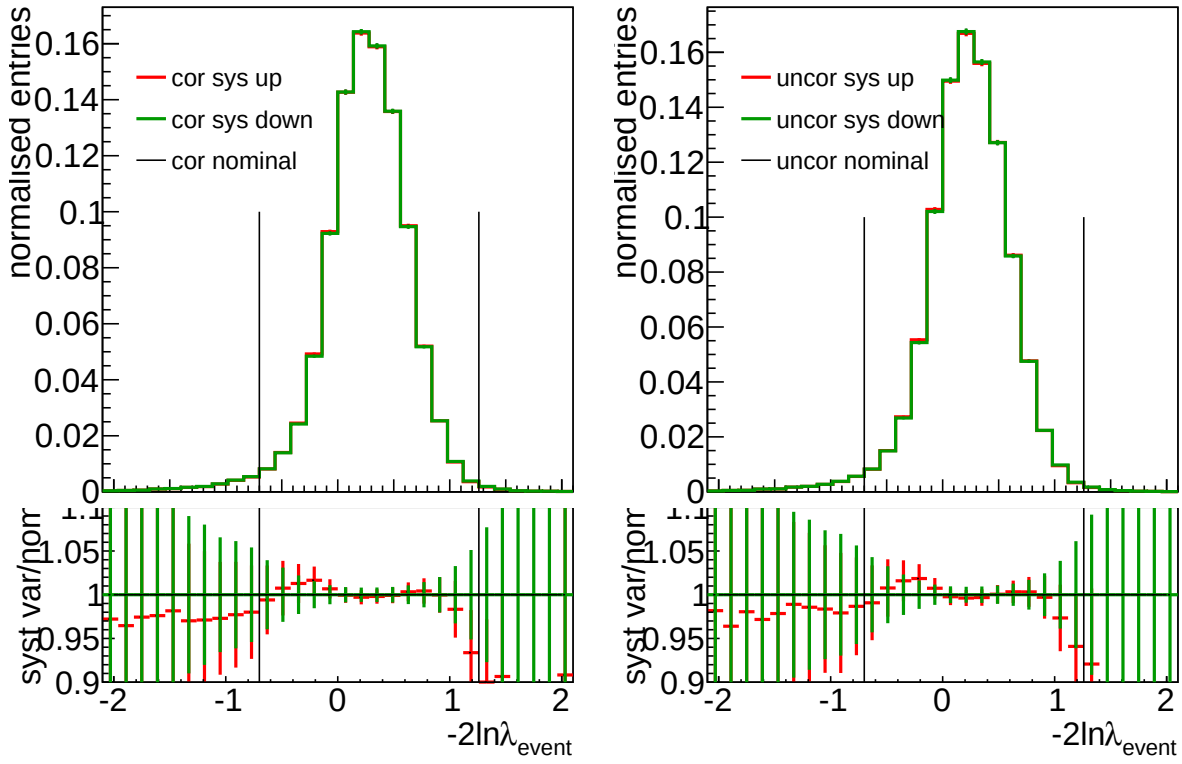

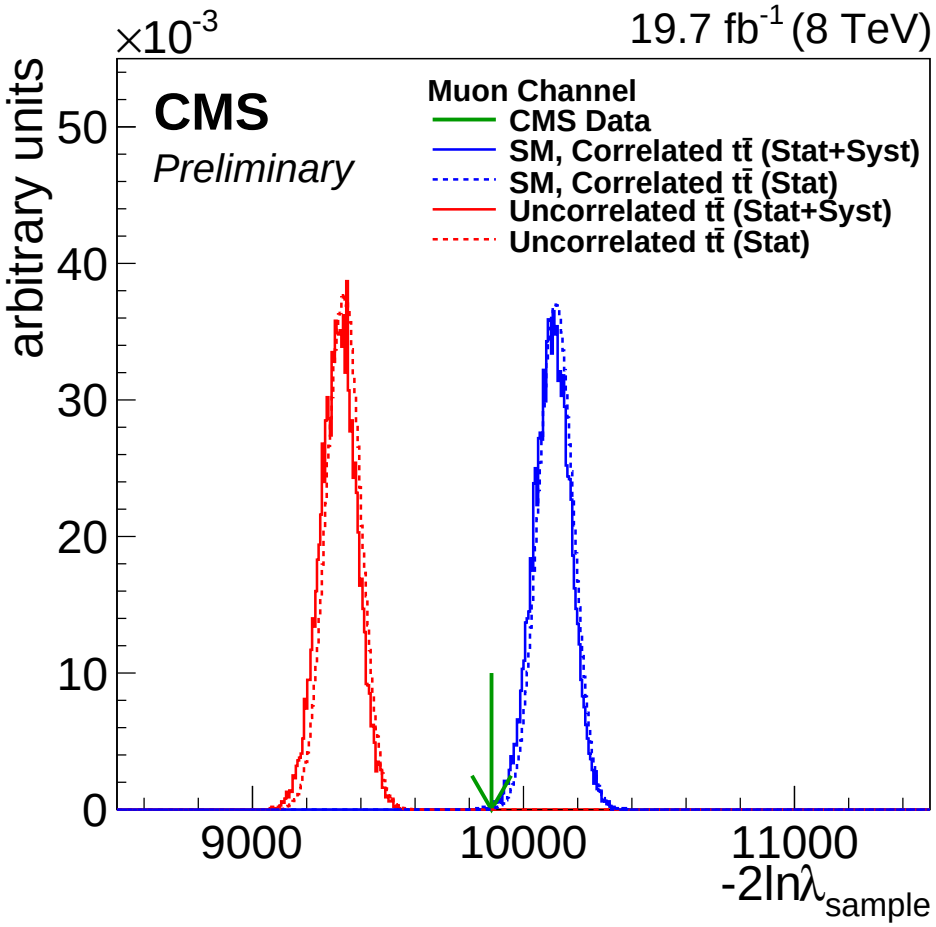

Figure 9.11: Systematically varied $-2\ln\lambda_{event}$ distribution and $-2\ln\lambda_{sample}$ distribution associated to the p_T^t modelling.

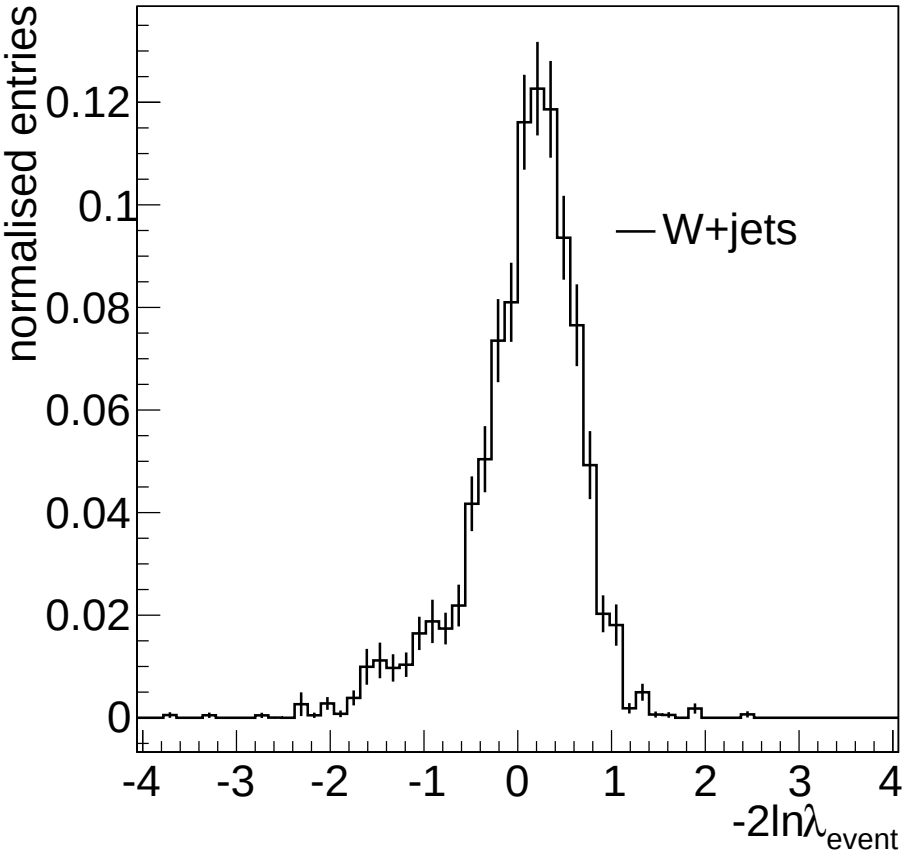

Figure 9.12: $-2\ln\lambda_{event}$ distribution for the W+jets simulated sample.

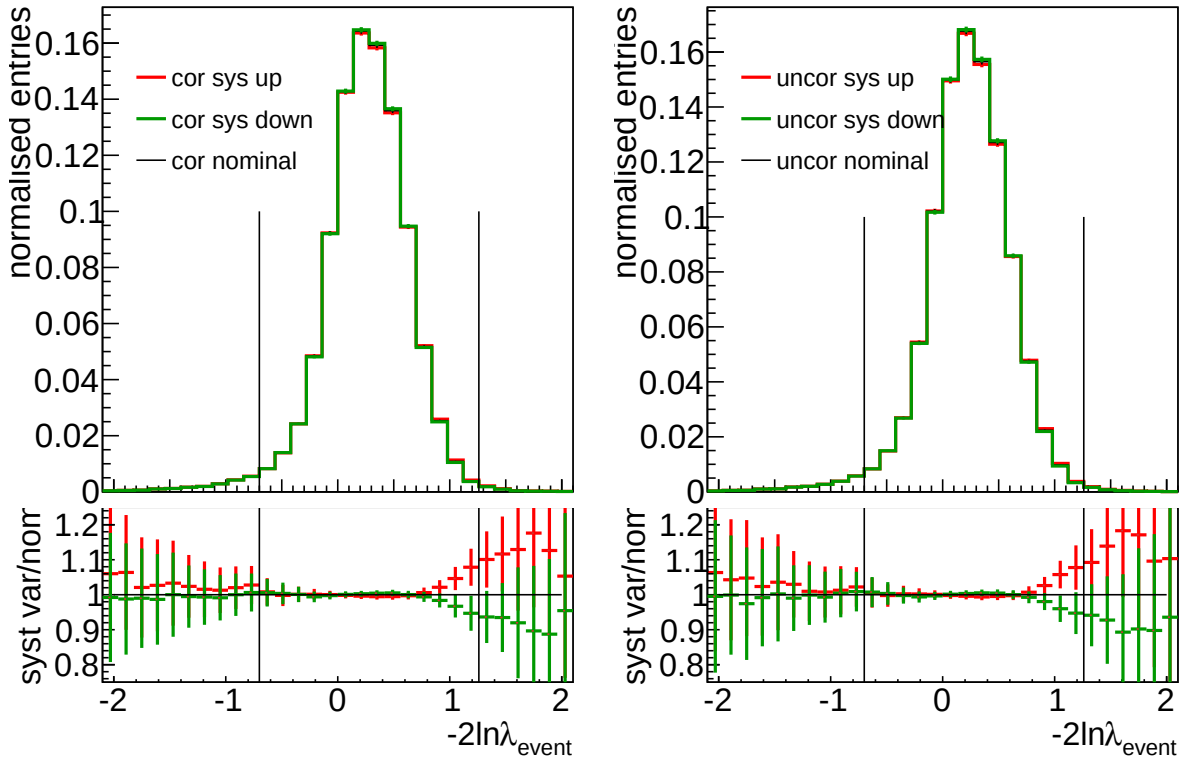

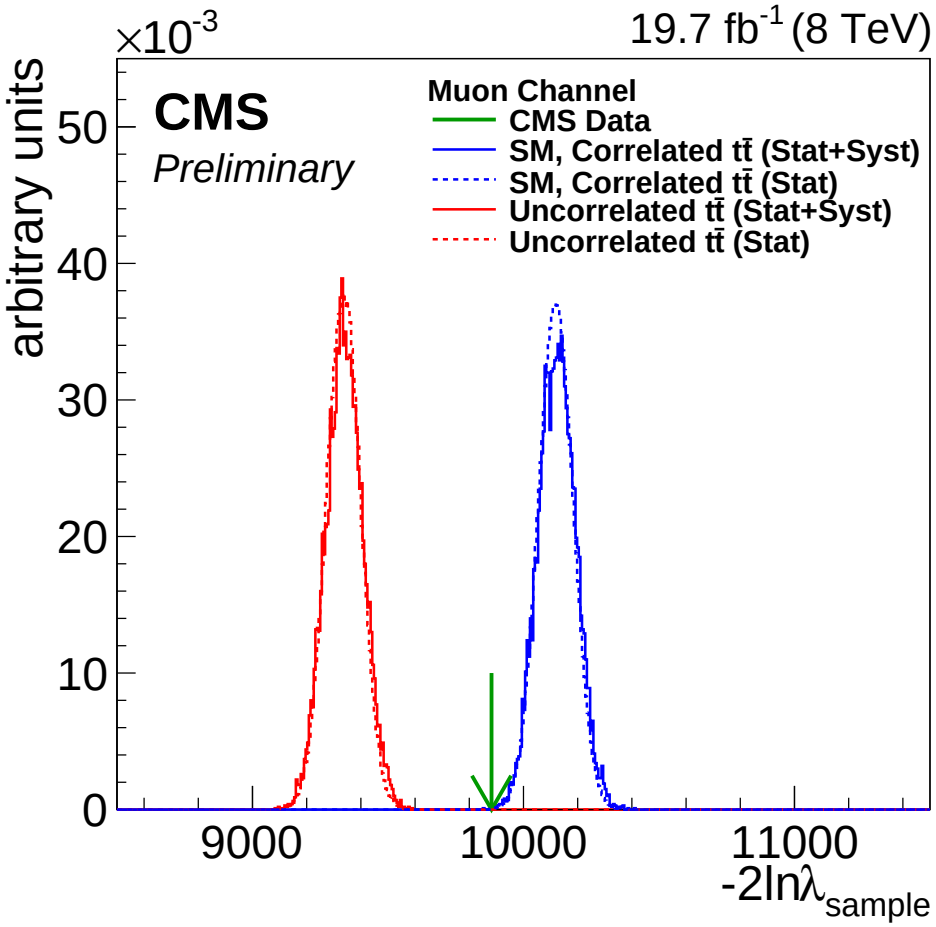

Figure 9.13: Systematically varied $-2\ln\lambda_{event}$ distribution and $-2\ln\lambda_{sample}$ distribution associated to the PDF uncertainty.

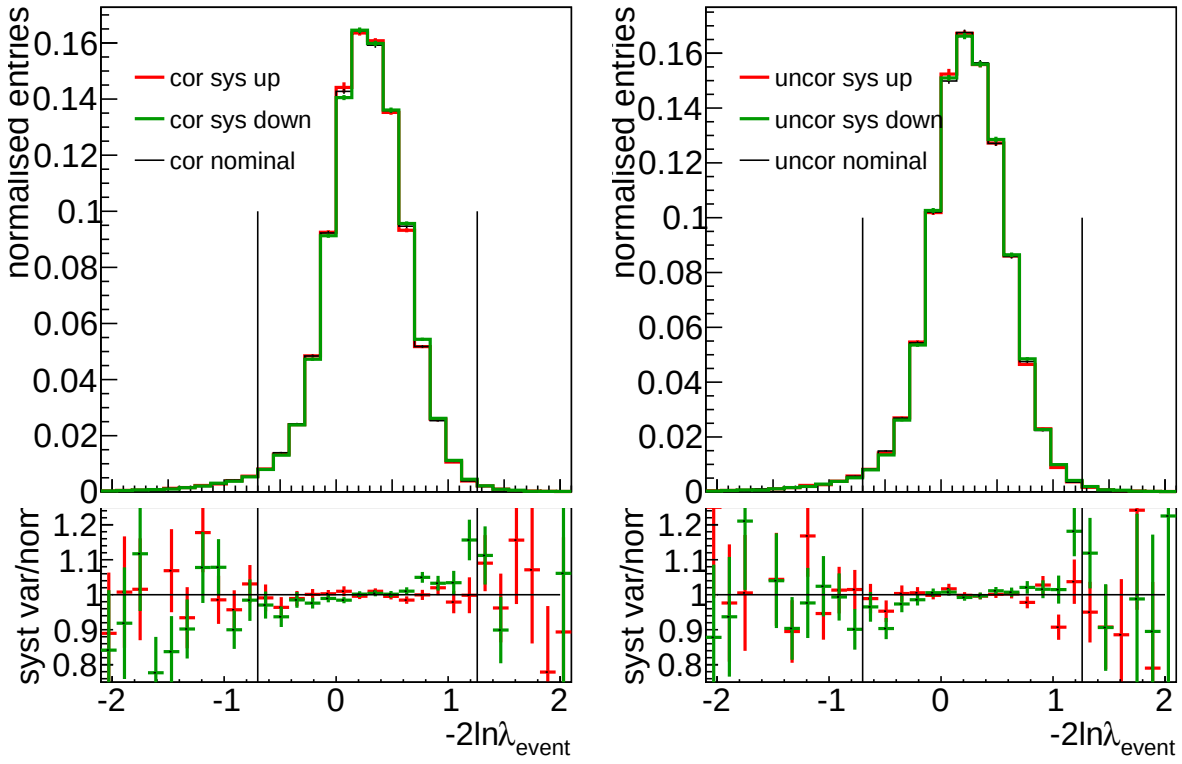

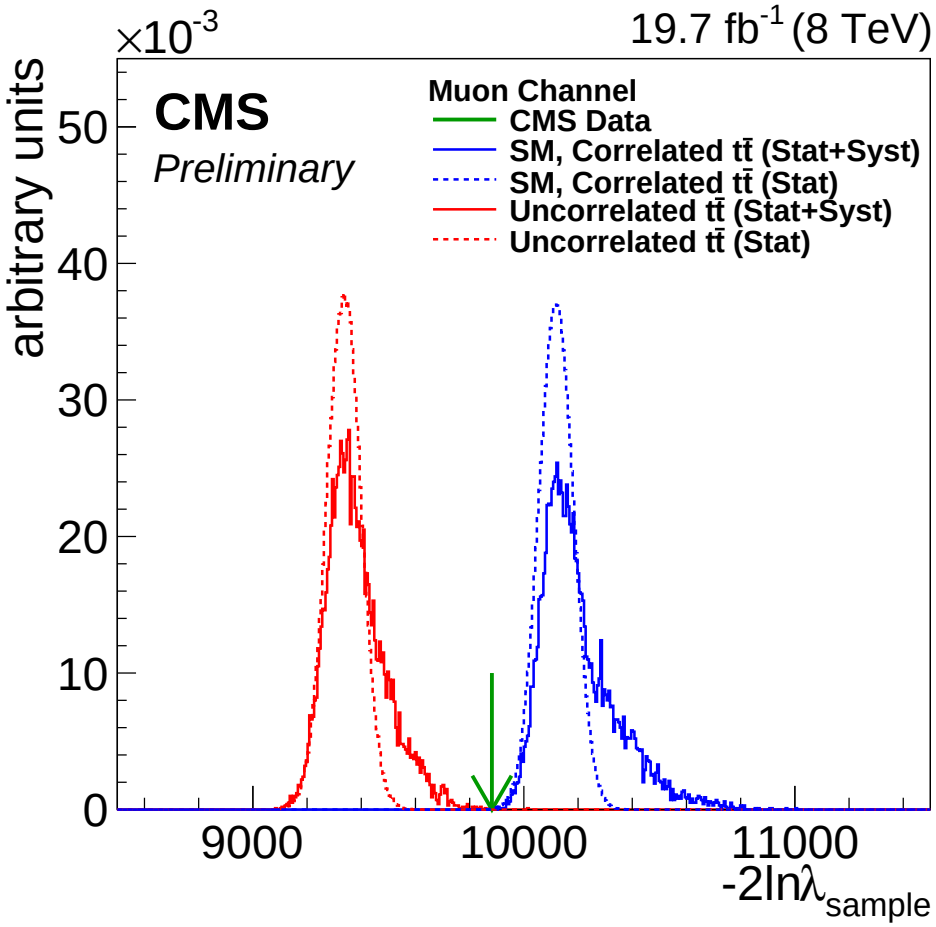

Figure 9.14: Systematically varied $-2\ln\lambda_{event}$ distribution and $-2\ln\lambda_{sample}$ distribution associated to the jet energy scale uncertainty.

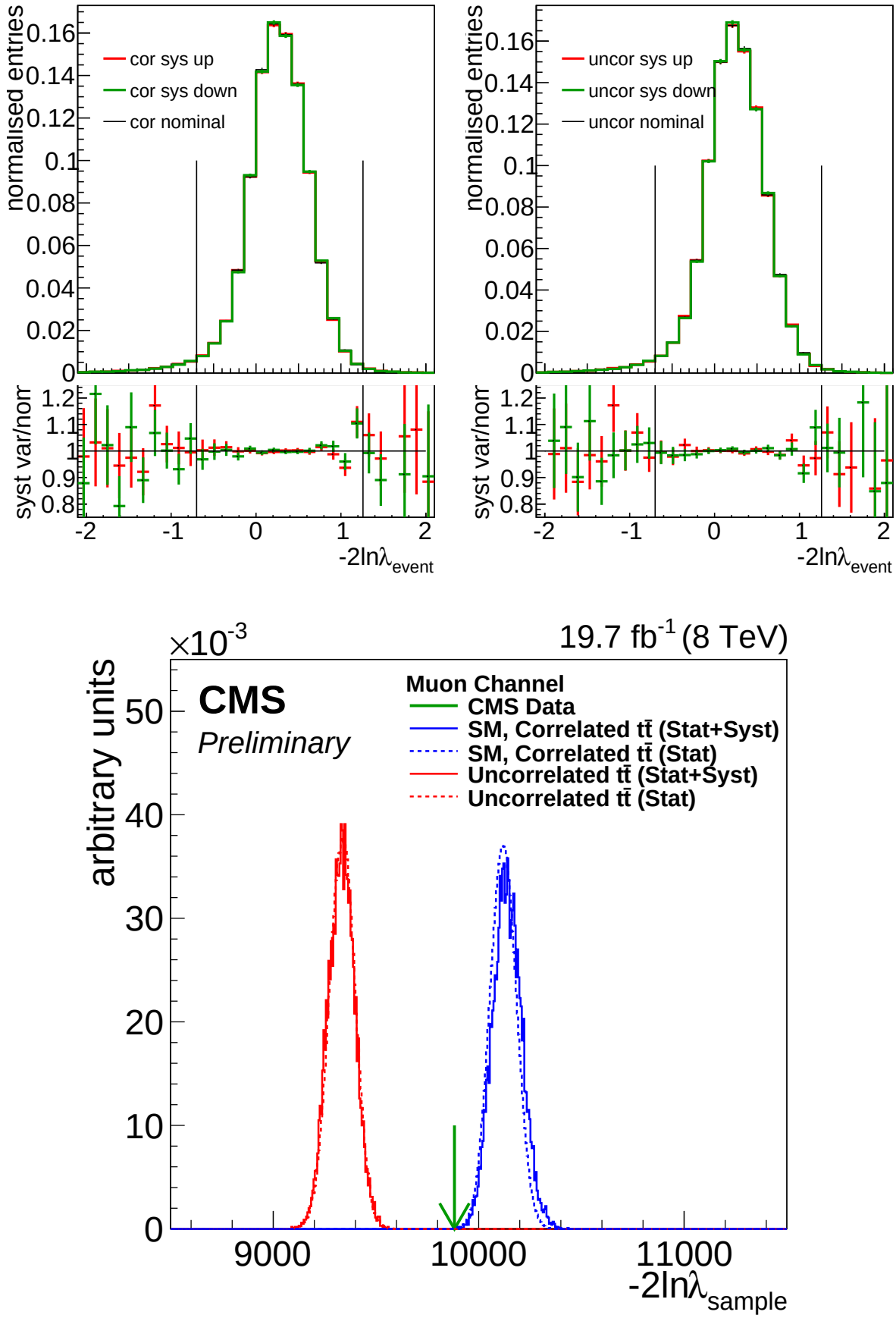

Figure 9.15: Systematically varied $-2\ln\lambda_{event}$ distribution and $-2\ln\lambda_{sample}$ distribution associated to the jet energy resolution uncertainty.

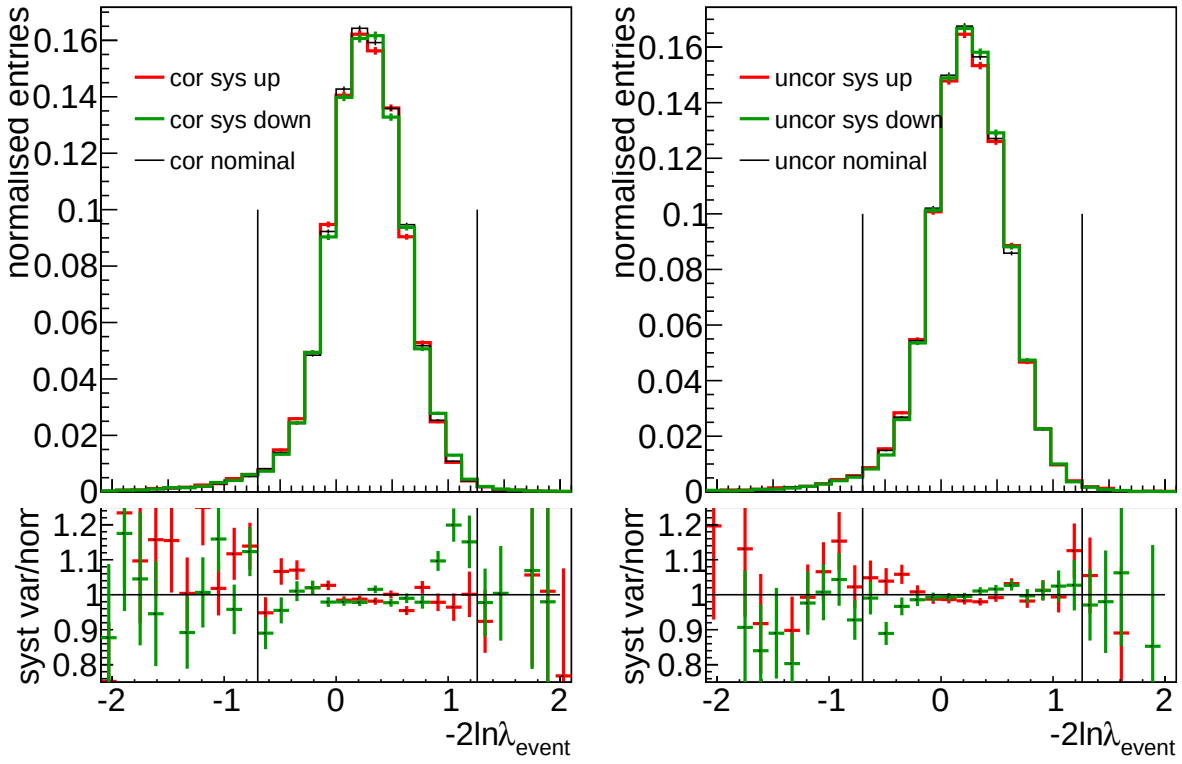

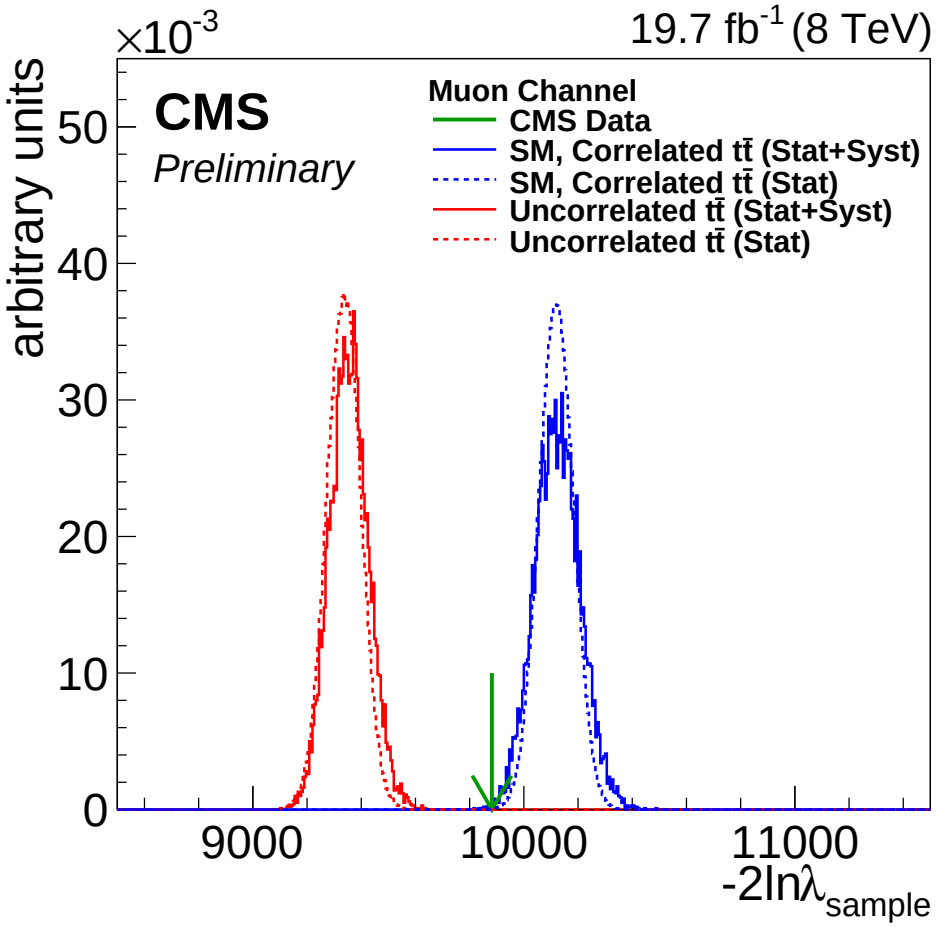

Figure 9.16: Systematically varied $-2\ln\lambda_{event}$ distribution and $-2\ln\lambda_{sample}$ distribution associated to the top quark mass uncertainty of ± 1 GeV variation.

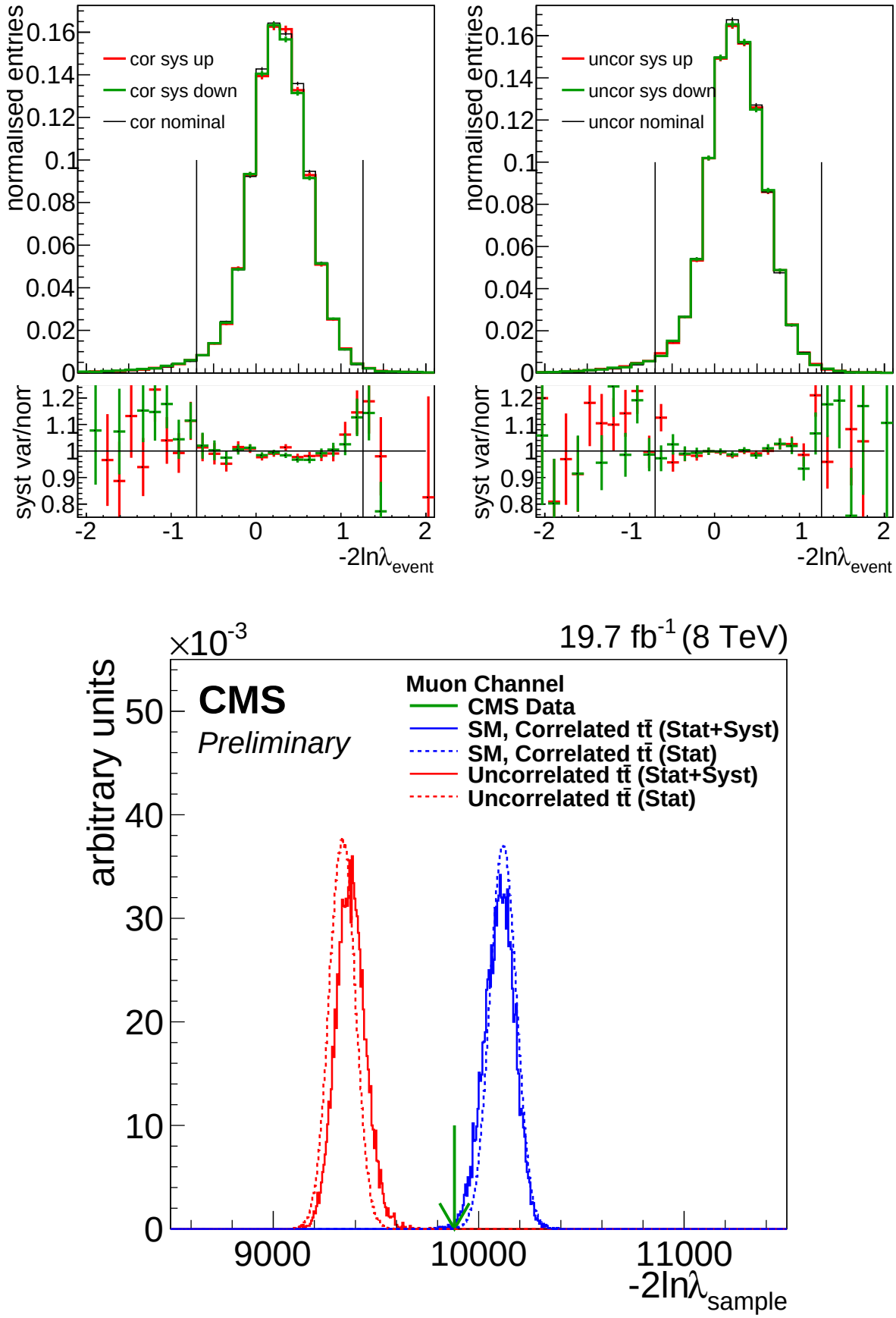

Figure 9.17: Systematically varied $-2\ln\lambda_{event}$ distribution and $-2\ln\lambda_{sample}$ distribution associated to the factorisation and renormalisation scale uncertainty.

9.2.2 Hypothesis Testing

To evaluate the compatibility of the data with both hypotheses, the systematic variation of the $-2\ln\lambda_{event}$ distribution needs to be propagated to the $-2\ln\lambda_{sample}$ distribution. We assess the effect of this event likelihood ratio template fluctuation by a template morphing technique in which all systematic uncertainties are evaluated simultaneously. Per morphed template iteration, we draw a pseudo-experiment at the dataset size and evaluate the sample likelihood ratio.

The event likelihood ratio distribution is morphed in the following way. We draw a vector of random numbers x_k from a Gaussian distribution with mean 0 and width 1. Per systematic uncertainty source k, we have an independent entry x_k in the vector. In each bin of the morphed template, the bin content N_i is calculated as shown in equation 9.5 with $H(x_k)$ a Heaviside step function with N_i^{nom} the original bin content.

$$N_i = N_i^{nom} + \Sigma_k |x_k| \left(H(x_k) \left[N_i^{k,up} - N_i^{nom} \right] + H(-x_k) \left[N_i^{k,down} - N_i^{nom} \right] \right) \tag{9.5}$$

In equation 9.5, the summation runs over all systematic uncertainty sources. The systematic upward fluctuation is chosen for a systematic when x_k is positive and the downward fluctuation when x_k is negative. This equation shows us that all systematic uncertainties are varied simultaneously while the bin-to-bin correlations of the systematic effect is preserved. If the systematic up and down effect is asymmetric or on the same side as the nominal bin content, this asymmetry is preserved. We perform this template morphing 10^7 times to obtain the systematically varied sample likelihood ratio distribution as seen in fig. 9.18. 10^7 pseudo-experiments is enough to populate the Gaussian tails in the multidimensional template morphing phase space, causing a negligible statistical uncertainty from the procedure compared to statistical precision on f itself. In fig. 9.18 the degradation of the separating power between the SM correlated distribution and the uncorrelated distribution due to the systematic uncertainties is shown. In addition, the result of the asymmetric behaviour of some systematic uncertainty sources is clearly visible. Due to the non-Gaussian shape of the $-2\ln\lambda_{sample}$ distribution, the compatibility with the data can no longer be calculated as the amount of Gaussian widths the data is away from the mean of the distribution. The compatibility is evaluated by the fractional area of the distribution that lies above the data position. The compatibility with the data is expressed in standard deviations by evaluating the cumulative distribution of a Gaussian at the observed fractional area. From the position of the data sample likelihood ratio value, we obtain that 98.7 % of the SM simulated area is above the data value, leading to an observed agreement for the SM hypothesis of 2.2 σ (expressed in standard deviations). 0.2 % of the uncorrelated simulated area is above the data value, leading to an observed agreement of the uncorrelated hypothesis of 2.9 σ. From this we can conclude that the data is more compatible with the SM hypothesis than with the uncorrelated hypothesis.

As a check of the compatibility of the result in the hypothesis testing and the extraction of f, the hypothesis testing has been performed where the $t\bar{t}$ sample was selected to consist of 72 % SM $t\bar{t}$ events and 28 % uncorrelated $t\bar{t}$ events. As a result we find a sample likelihood ratio distribution, shown in fig. 9.18, in between the SM and uncorrelated scenario, with a data compatibility of 0.6 σ (expressed in standard deviations). The data position, which is slightly below the mean of the distribution, is within the expected uncertainty due to statistical effects and considering that the world average measurement of the top quark mass is slightly above the value used in the simulation, which gives a shift in the same direction as the data deviation.

Now it is easier to understand how the systematically varied distributions for the individual systematic uncertainty sources in the previous section were obtained: the Gaussian template morphing technique was evaluated with only the relevant systematic uncertainty. The plots of

the $-2\ln\lambda_{sample}$ under only one systematic uncertainty are very useful for the qualitative evaluation of the size of the uncertainty, the asymmetry of the distribution and the evaluation if the effect is similar in both the correlated and uncorrelated distributions. However for a quantitative evaluation of the size of a systematic uncertainty to the $-2\ln\lambda_{sample}$ distribution, a different approach is used. An estimate of the importance of each systematic uncertainty can be obtained by turning one systematic effect off ($x_k = 0$) at a time in the template morphing technique. The value of the systematic uncertainty is then taken as the difference in fractional area ϵ above the data position in the case of (N) systematic uncertainties and the case of $(N-1)$ systematic uncertainties. The plots in the previous section correspond to taking the difference between the fractional area in the case where no systematic uncertainties are considered (0) and where only the relevant systematic is considered (1).

There are two reasons why the former scenario is preferred over the latter. First, the first scenario answers the question "What would the analysis look like without this systematic uncertainty?" which seems to us more natural than the question "How would the analysis look like with only this systematic uncertainty?" which is the question the second scenario answers. Note that both questions will only give the same answer when there is no correlation present between any of the systematic uncertainty sources. All evaluations of the contribution of individual systematic uncertainty sources to a hypothesis testing method are only qualitative and the only relevant statement on the systematic uncertainty is the change in compatibility with data before and after the inclusion of systematic effects. The second reason to prefer the estimate of the individual systematic uncertainties in the (N) - (N-1) form versus the (1) - (0) form is the CPU time required. As the width of the $-2\ln\lambda_{sample}$ distribution in the case of only one systematic uncertainty is too narrow to offer any overlap between the data position and the uncorrelated distribution with 10^7 pseudo-experiments, many orders of magnitude more pseudo-experiments would have to be performed for the evaluation of each systematic uncertainty. Computationally it is much more advantageous to assess the (N-1) $-2\ln\lambda_{sample}$ distribution for which 10^7 pseudo-experiments is ample. The estimate of the contribution of each systematic uncertainty is given in table 9.1 by the difference in fractional area ϵ of the (N) versus (N-1) distribution for both the SM hypothesis and uncorrelated hypothesis. Let's take as example the JES variation in the SM hypothesis. The fraction $\epsilon(N)$ for the SM hypothesis is given by 9872560/10000000, which gives us $\epsilon(N) = 0.98726 \pm 0.00004$ with the error being binomial. In the scenario where the JES uncertainty is removed, we obtain the fraction $\epsilon(N-1) = 9795056/10000000 = 0.97951 \pm 0.00004$ with again a binomial error. This gives us as a result for the systematic uncertainty $\epsilon(N) - \epsilon(N-1) = 0.7750 \pm 0.0057\,\%$. The uncertainties quoted here are statistical uncertainties due to the procedure of evaluating 10^7 pseudo-experiments and are not a consequence of the statistical uncertainties on the shape of the $-2\ln\lambda_{event}$ distributions (these are evaluated quantitatively with the template fit).

The results in table 9.1 can be interpreted as follows. Imagine that the systematically varied $-2\ln\lambda_{sample}$ distribution is a perfect Gaussian in shape. As we performed the Gaussian template fluctuations around the nominal value, the (N) and (N-1) $-2\ln\lambda_{sample}$ distributions will have the same mean but different width. The width of the systematically varied $-2\ln\lambda_{sample}$ distribution increases as more systematic effects are included, so the (N-1) distribution will always be narrower than the (N) distribution. As a consequence, and remembering that the data position is between the distributions of both hypotheses, the fraction of pseudo-experiments above the data position in the (N-1) case will increase for the SM hypothesis and decrease for the uncorrelated hypothesis, leading to $\epsilon(N) - \epsilon(N-1) < 0$ for the SM and > 0 for the uncorrelated hypothesis. In case of asymmetric systematic uncertainty sources, the (N-1) distribution will still have a narrower width overall, but in addition the mean and shape of the distribution will differ. As a consequence, this simple relation between the fractional area difference of the

SM and uncorrelated hypothesis no longer holds. Even though an asymmetric systematic uncertainty can have a similar shape change in both the SM and uncorrelated hypothesis, due to the fact that the data is located between both distributions, this can give rise to very different variations in fractional area in both hypotheses.

From table 9.1, we can see that the effects due to trigger, lepton ID/Isolation efficiency, b-tagging and mistagging rates are so small that these cannot be evaluated with 10^7 pseudo-experiments. As will be seen in section 9.2.3, these uncertainties are statistically irrelevant. The dominant uncertainties are due to the JES, Q^2 scale variation and top quark mass uncertainty as is expected.

Table 9.1: Difference of fractional area above the data position $\epsilon(N) - \epsilon(N-1)$ where $\epsilon(N) = 98.7\%$ in the SM hypothesis and $\epsilon(N) = 0.2\%$ in the uncorrelated hypothesis. The uncertainty is given by the statistical accuracy obtained with 10^7 pseudo-experiments.

systematic	variation SM (%)	variation Uncor (%)
simulation stat.	-0.200 ± 0.005	0.029 ± 0.002
JER	0.357 ± 0.005	-0.009 ± 0.002
JES	0.775 ± 0.006	0.212 ± 0.002
trigger	0.003 ± 0.005	-0.001 ± 0.002
lepton ID/Iso	0.003 ± 0.005	-0.003 ± 0.002
b tag efficiency	0.003 ± 0.005	-0.001 ± 0.002
mistag rate	-0.004 ± 0.005	-0.001 ± 0.002
Pile up	-0.010 ± 0.005	-0.002 ± 0.002
p_T^t modelling	-0.462 ± 0.005	-0.060 ± 0.002
Q^2	-0.799 ± 0.004	0.143 ± 0.002
m_t	-0.565 ± 0.004	0.098 ± 0.002
PDF	-0.074 ± 0.005	0.036 ± 0.002
background yield	-0.127 ± 0.005	0.016 ± 0.002

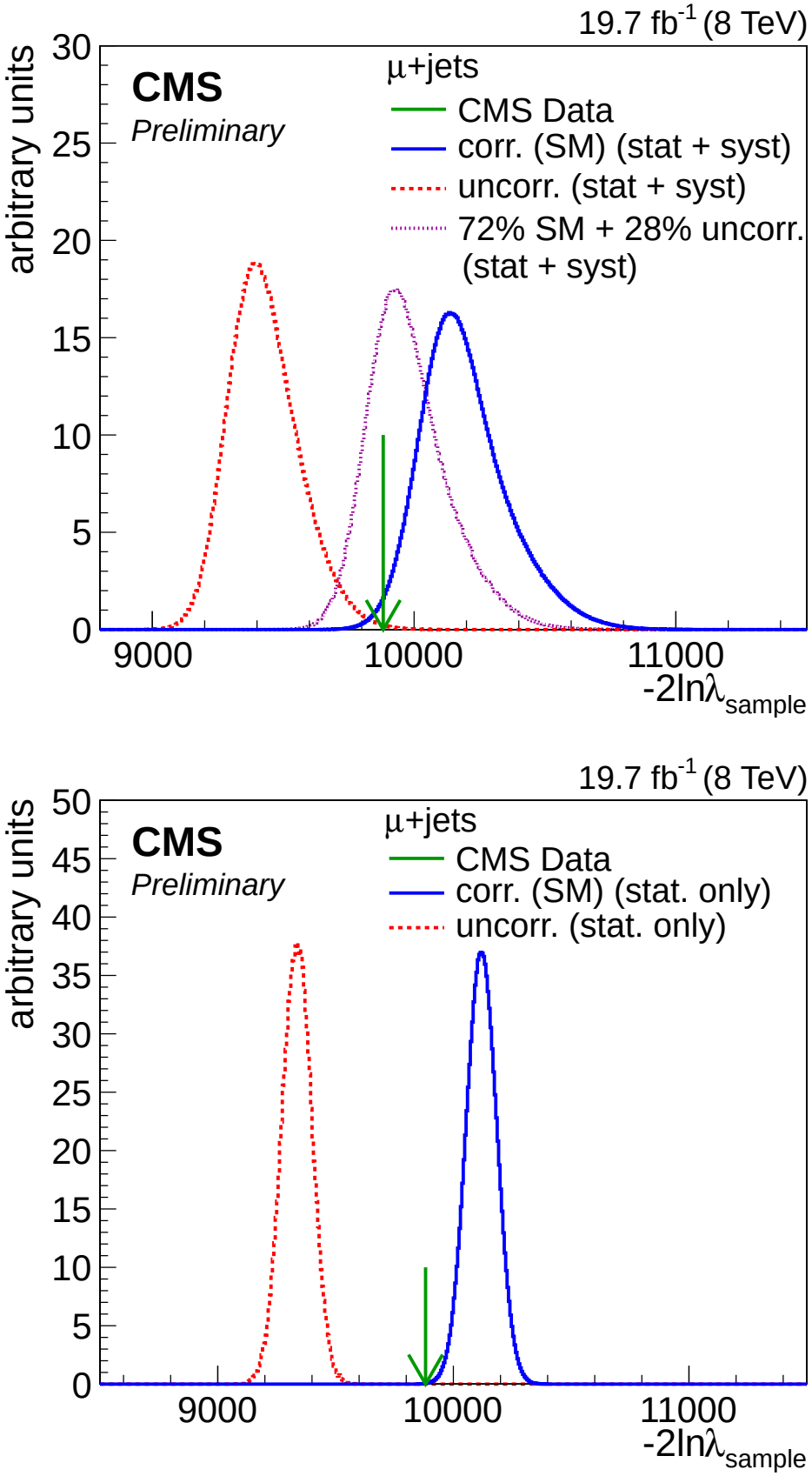

Figure 9.18: The $-2\ln\lambda_{sample}$ distribution is shown in simulation including statistical and systematic effects (top) and statistical effects only (bottom), evaluated at the data sample size in the muon channel. The samples in simulation contain signal and background mixed according to the theoretical cross sections, with the blue solid distribution obtained using SM correlated $t\bar{t}$ simulation and the red dashed distribution obtained using uncorrelated $t\bar{t}$ simulation including systematic uncertainties. The green arrow indicates the $-2\ln\lambda_{sample}$ observed in data. The magenta dotted curve shows a mixture of 72 % SM correlated $t\bar{t}$ events and 28 % uncorrelated $t\bar{t}$ events.

9.2.3 Extraction of f

In the extraction of the SM fraction f using a template fit to the variable $-2\ln\lambda_{event}$, we have the same list of systematic uncertainty sources as evaluated in the hypothesis testing procedure, but in addition a systematic uncertainty due to the calibration of the method is taken into account. The calibration uncertainty covers two aspects: the parameters of the calibration curve have uncertainties associated to them and in addition the observed parameter $\beta_{fit,data}$ used as input to the calibration curve has a fit uncertainty. Both uncertainties are propagated to the calibrated result and combined in quadrature to obtain the systematic uncertainty due to the calibration. The total uncertainty caused by the calibration is small.

In this section, we will distinguish between the observed and the expected systematic uncertainties. The observed systematic uncertainties are evaluated by fitting the data with systematically varied templates. The observed systematic uncertainty is then obtained by evaluating the calibration curve at the fit points shown in table 9.2 and obtaining $f_{calibrated,syst}$. The difference between $f_{calibrated,syst}$ and $f_{calibrated}$ is the value of the systematic uncertainty. The systematic contributions are shown in table 9.3 where the statistical error on the nominal result is also shown. The systematic uncertainty due to the available simulation statistics is evaluated by fitting one pseudo-dataset in the simulation by 1000 Poisson fluctuated templates. The Gaussian width of the fit result f_{fit} is taken as the value of this systematic uncertainty source.

Table 9.2: Results of the fit to data with systematically varied templates.

systematic	variation	$f_{fit,data} \pm \delta f$	$\beta_{fit,data} \pm \delta\beta$	$\chi^2/ndof$
nominal		0.747 ± 0.092	0.168 ± 0.024	1.552
JER	up	0.721 ± 0.083	0.160 ± 0.023	1.286
	down	0.744 ± 0.090	0.180 ± 0.024	1.067
JES	up	0.809 ± 0.098	0.198 ± 0.027	1.612
	down	0.653 ± 0.086	0.212 ± 0.025	1.103
trigger	up	0.747 ± 0.092	0.168 ± 0.024	1.552
	down	0.747 ± 0.092	0.168 ± 0.024	1.553
lepton ID/Iso	up	0.747 ± 0.092	0.168 ± 0.024	1.552
	down	0.747 ± 0.092	0.168 ± 0.024	1.553
btag efficiency	up	0.747 ± 0.092	0.169 ± 0.024	1.563
	down	0.747 ± 0.092	0.166 ± 0.024	1.543
mistag rate	up	0.753 ± 0.092	0.167 ± 0.024	1.510
	down	0.741 ± 0.091	0.168 ± 0.024	1.596
Pile up	up	0.761 ± 0.091	0.168 ± 0.024	1.479
	down	0.730 ± 0.091	0.166 ± 0.025	1.655
p_T^t modelling	up	0.771 ± 0.090	0.161 ± 0.024	1.708
Q^2	up	0.671 ± 0.103	0.163 ± 0.023	2.055
	down	0.885 ± 0.107	0.175 ± 0.022	1.343
m_t	up	0.746 ± 0.101	0.151 ± 0.024	1.304
	down	0.709 ± 0.092	0.169 ± 0.023	1.415
PDF	up	0.765 ± 0.091	0.163 ± 0.024	1.456
	down	0.798 ± 0.093	0.171 ± 0.024	2.037

Before we discuss the observed systematic uncertainties and the comparison between the different fit models, let us investigate the expected systematic uncertainties on the nominal result, being

the 1D fit in the range [-0.7,1.26]. The expected systematic uncertainties are evaluated using simulation only, by drawing 1000 pseudo-experiments at the dataset size from the nominal template distributions. These pseudo-experiments are fitted twice: once using the nominal templates and once using the systematically varied templates. The SM fraction f obtained from each fit is calibrated with the nominal calibration curve (as is the case for the observed systematic uncertainties) and per pseudo-experiment, the difference, Δf, between f_{syst} and $f_{nominal}$ is plotted. The mean of the Δf distribution obtained in this way is the estimate for the expected value of the systematic uncertainty, whereas the width of the Δf distribution gives us information on whether the systematic uncertainty is statistically relevant or not. The expected systematic uncertainties are shown in table 9.3 with a comparison to the observed systematic uncertainties. The trigger, lepton ID/Isolation and b-tagging systematic uncertainties are very small and not statistically relevant. Also the JER uncertainty, which has larger values is seen to be statistically irrelevant. We can also note that the Q^2 uncertainty, which is one of the dominant systematic uncertainties, has a significant statistical component. This is to be expected as this source of systematic uncertainty has been evaluated with dedicated systematic simulation samples with a smaller size than the nominal samples. Both the sign and size of the observed and expected systematic uncertainties are in good agreement. Similarly as in the hypothesis testing procedure, the JES and Q^2 scale variation systematic uncertainties are dominant. Note that there is not necessarily a one-to-one correspondence between the systematic uncertainties evaluated in the hypothesis testing procedure and the template fit as during the template fit the background fraction is left floating while in the hypothesis testing it is kept fixed.

Table 9.3: Breakdown of expected systematic uncertainty contributions in the 1D fit in the range $[-0.7, 1.26]$. The comparison with the observed systematic uncertainties is made. Statistical uncertainty is before calibration.

systematic	observed up	expected up	observed down	expected down
stat uncer.	0.092	0.091 ± 0.004	-0.092	0.091 ± 0.004
calibration	0.003	0.003	-0.003	-0.003
simulation stat	0.042	0.042	-0.042	-0.042
JER	-0.023	-0.027 ± 0.022	-0.004	-0.011 ± 0.014
JES	0.051	0.062 ± 0.015	-0.090	-0.107 ± 0.019
trigger	-0.0	$-2.2.10^{-5} \pm 1.9.10^{-6}$	0.0	$2.3.10^{-5} \pm 1.5.10^{-6}$
lepton ID/Iso	-0.0	$-3.7.10^{-5} \pm 1.6.10^{-6}$	0.0	$4.0.10^{-5} \pm 3.0.10^{-6}$
btag efficiency	-0.001	-0.00024 ± 0.00037	0.001	0.00039 ± 0.00037
mistag rate	0.005	0.0040 ± 0.0009	-0.006	-0.004 ± 0.001
Pile up	0.012	0.009 ± 0.005	-0.015	-0.011 ± 0.004
p_T^t modelling	0.023	0.028 ± 0.003	-	-
Q^2	-0.068	-0.026 ± 0.033	0.124	0.062 ± 0.040
m_t	0.001	0.023 ± 0.017	-0.034	-0.062 ± 0.016
PDF	0.018	0.020 ± 0.002	0.045	0.043 ± 0.001

In table 9.4, the observed systematic uncertainties for the 1D fit in the nominal range $[-0.7, 1.26]$, the range $[-2.1, 1.26]$ and for the 2D fit are shown. The total systematic uncertainty is obtained by adding the positive and negative contributions in table 9.4 in quadrature. In cases where both the systematic up and down variation gives an uncertainty in the same direction, only the largest value is taken into account in the given direction, and no uncertainty is assigned to the opposite direction. The statistical uncertainty in both cross-check fit models is lower as is expected due to the lower correlation between the fit parameters f and β in those models. As was mentioned earlier, the range optimisation in the hypothesis testing procedure took only the separating power with statistical uncertainties into account. However, as we can see from

Table 9.4: Breakdown of observed systematic uncertainty contributions. The comparison is made between the results in the 1D fit in the range [-0.7,1.26],[-2.1,1.26] and in the 2D fit. Statistical uncertainty is before calibration.

systematic	up [-0.7,1.26]	up [-2.1,1.26]	up 2D	down [-0.7,1.26]	down [-2.1,1.26]	down 2D
stat uncer.	0.092	0.082	0.070	0.092	−0.082	−0.070
calibration	0.003	0.002	0.008	−0.003	−0.002	−0.008
simulation stat	0.042	0.042	0.020	−0.042	−0.042	−0.020
JER	−0.023	−0.029	−0.017	−0.004	−0.014	0.031
JES	0.051	0.029	0.005	−0.090	−0.126	−0.071
trigger	−0.0	−0.0	−0.001	0.0	0.0	0.001
lepton ID/Iso	−0.0	−0.0	−0.001	0.0	0.0	0.001
btag efficiency	−0.001	−0.001	−0.001	0.001	0.001	0.001
mistag rate	0.005	0.003	0.003	−0.006	−0.004	−0.003
Pile up	0.012	0.010	−0.001	−0.015	−0.012	0.001
p_T^t modelling	0.023	0.042	0.063	-	-	-
Q^2	−0.068	−0.113	−0.078	0.124	−0.015	−0.014
m_t	0.001	0.002	−0.019	−0.034	−0.048	−0.003
PDF	0.018	0.015	−0.001	0.045	0.042	0.001
background yield	0.017	0.020	0.018	−0.016	−0.042	−0.006
	[-0.7,1.26]		[-2.1,1.26]		2D	
total syst. uncer.	+0.151 −0.129		+0.082 −0.205		+0.076 −0.111	
total uncer.	+0.177 −0.158		+0.116 −0.221		+0.103 −0.131	

the comparison in the table here, the range $[-0.7, 1.26]$ is also perferred over the broader range $[-2.1, 1.26]$ when systematic effects are evaluated. In the range $[-2.1, 1.26]$ the systematic uncertainties become more asymmetric. From this table, the 2D fit model is clearly preferred as it gives lower statistical and systematic uncertainties due to the better extraction of the background contribution. As this fit model has not been studied at the parton level and hasn't been optimised, it will therefore only be used as a cross check.

9.3 Conclusion on the Measurement of the Spin Correlation Strength

When systematic uncertainty effects are taken into account, the $-2\ln\lambda_{sample}$ distribution broadens to what is seen in fig. 9.18. From the data sample likelihood ratio value, we obtain that 98.73 % of the SM simulated area is above the data value, leading to an observed compatibility with the SM hypothesis of 2.2 σ expressed in standard deviations. 0.2 % of the uncorrelated simulated area is above the data value, leading to an observed compatibility with the uncorrelated hypothesis of 2.9 σ expressed in standard deviations.

The inclusion of the systematic uncertainties is described in section 9.2. We obtain a total observed systematic uncertainty of $+0.15$ and -0.13 on the template fit result. The total result of the template fit is then:

$$f_{calibrated} = 0.72 \pm 0.08\,(\text{stat.})\,^{+0.15}_{-0.13}\,(\text{syst.}). \tag{9.6}$$

It has been verified that the results of the template fit and the hypothesis testing procedure are in agreement. The hypothesis testing result is compatible within 0.6 σ with the obtained Standard Model fraction of 72 %.

Chapter 10

Outlook and Conclusions

We have presented a measurement of the spin correlation strength in top quark pair production in the muon + jets channel using a matrix element method. The data consist of 19.7 fb^{-1} collected in proton-proton collisions in 2012 at a centre-of-mass energy of 8 TeV by the CMS detector at the LHC. In a hypothesis testing procedure, the data was found to be compatible with the SM hypothesis of $t\bar{t}$ production and decay within 2.2 standard deviations, while being compatible with the uncorrelated hypothesis within 2.9 standard deviations. In a template fit to the $-2\ln\lambda_{event}$ distribution, the fraction of $t\bar{t}$ pairs with SM spin correlations was measured to be

$$f = 0.72 \pm 0.08\,(\text{stat.})\,^{+0.15}_{-0.13}\,(\text{syst.}).$$

In the assumption that there are only SM $t\bar{t}$ pairs or uncorrelated $t\bar{t}$ pairs, this results in an indirect extraction of A_{hel}. By making use of the relation $A_{hel}^{measured} = f^{SM} A_{hel}^{SM}$ where $A_{hel}^{SM} = 0.31$ [21], $A_{hel}^{measured} = 0.22 \pm 0.03\,(\text{stat})\,^{+0.05}_{-0.04}\,(\text{syst})$ is obtained. The data position in the hypothesis testing procedure is compatible with the SM fraction obtained from the template fit within 0.6 standard deviations.

At 8 TeV a measurement has been presented by the ATLAS collaboration in the dilepton channel, giving $f = 1.20 \pm 0.05\,(\text{stat.}) \pm 0.13\,(\text{syst.})$ [117]. In the CMS collaboration, at 7 TeV in the dilepton channel $f = 0.74 \pm 0.08\,(\text{stat.}) \pm 0.24\,(\text{syst.})$ is obtained [28]. ATLAS has also presented results at 7 TeV in several channels and variables in [118]. The result presented in this thesis is the most precise determination of the SM fraction f in the lepton+jets channel to date with a precision very close to the most accurate result in the dilepton channel. The results are in good agreement with the measurement of the SM fraction presented by CMS at 7 TeV.

Despite the fact that the analysis has obtained the most precise determination of the SM fraction f in the lepton+jets channel, there are still various improvements possible to the analysis presented here. Here, we have only evaluated the muon+jets channel. We could improve the statistical uncertainty by including the electron+jets channel, but more importantly an independent channel would allow for a cross-check of the result and the observed systematic uncertainties. Due to the heavy CPU constraints of the event likelihood calculations, the inclusion of the second channel is not in the time scale of this work. Another interesting study would be the differential measurement of the SM fraction f. At higher invariant mass of the top quark pair, the spin correlation strength decreases in the SM, making a differential measurement in this variable more sensitive to new physics [103]. More particularly for this analysis, the measurement could be performed as a function of the jet multiplicity as we expect different sensitivity to certain systematic uncertainties such as the Q^2 scale variation. We did compare the sensitivity of the four and five jet bin separately taking into account statistical effects only. As we know that at least a part of the event information is not used in the five jet events, we expect to have reduced sensitivity in this bin, which was consistent with our observations. In addition, we have touched upon moving to a 2D template fit which would allow for a better extraction of the background normalisation (reducing the effect of some systematic uncertainty sources) and a decorrelation of the f and β fit parameter leading to a lower statistical uncertainty. The result using the 2D fit has been quoted as a cross-check and does seem to offer reduced uncertainties. However, more parton level and optimisation studies would be needed to allow for this result

to be more than a cross-check. The event selection has been optimised to obtain maximum separating power between both hypotheses including statistical effects. An explicit optimisation to reduce systematic uncertainties has not been performed although visual inspection of the $-2\ln\lambda_{event}$ distributions shows that the currently chosen fitrange already offers some reduction. The cross-check using a 1D fit with an extended fit range, also supports this claim. The dominant systematic uncertainty source is the jet energy scale. In this analysis, we have worked with a fixed jet energy scale with a variation of one standard deviation to determine the uncertainty. It is however possible in the matrix element method to view the jet energy scale as an additional parameter in the hypothesis. The event likelihoods can then be maximised with respect to the jet energy scale. This would require evaluating the event likelihoods under various jet energy scale hypotheses, which is a very time-consuming task.

The matrix element method offers a direct comparison between theory and experiment and offers the largest statistical sensitivity at a given dataset size. The matrix element method was developed at DØ for the top quark mass measurement where the measurements were limited by statistical uncertainties. One needs to ask the question whether using a matrix element method at the LHC, which is a top quark factory, is still beneficial as most of the analyses in the top quark sector are no longer statistically limited. Due to the large statistical power of the method, we were able to put tight quality cuts on the event selection which allows to reduce the effect of certain systematic uncertainties, and still obtain a result which does not suffer from the strongly reduced dataset size. The matrix element method as it stands now is a leading order method, while at the LHC we have entered the NLO and even NNLO regime. Although the result we obtained is correct, as we have calibrated using NLO simulation, the sensitivity will be suboptimal. To remain competitive in the future, the matrix element method should be upgraded to take final state radiation into account, possibly convoluted into the transfer function expression. Still it is probably simpler to move to a simplification of the matrix element method without an integration over the parton phase space, but for example only using the expressions of the matrix elements itself, as was done by the ATLAS collaboration in one of their spin correlation analyses [118]. In addition the CPU time required to perform a full matrix element method is non-negligible. A reprocessing of all the event likelihoods (i.e. nominal and systematically varied event kinematics) in only one channel, takes about one month when on average 3000 cores are used in parallel. The amount of cores available in parallel to a single user at the lxbatch facilities at CERN is variable and was increased during the long shutdown LS1, as many cores which normally are used for triggering algorithms and reconstruction of the data were freed up. Technological advances will lead to more CPU available to CERN users and there could be advances in the matrix element method which decrease the calculation time for the multidimensional phase space integration. But equally, the LHC is preparing to increase the amount of integrated luminosity collected during one year of data-taking. The collisions will be at higher energies, meaning a higher $t\bar{t}$ production cross-section. It will be interesting to see whether the balance of both effects is in favour of a matrix element method or not. In conclusion, the matrix element method is still a very powerful tool, but significant effort should go into speeding up the calculations and bringing the method to NLO to remain competitive with other methods which are a bit less sensitive but which have a much shorter time scale.

In an extension of this analysis, the results could be interpreted in the framework of several BSM models. Top quark pair spin correlations can be used to access certain (R-parity conserving) Minimal Super-Symmetric Models (MSSM) [119–122]. In the specific model with light stop squarks where the stop squark decays 100 % of the time to a top quark and a neutralino, there are certain regions of the MSSM phase space where the stop squark mass is very close to the top quark mass and the neutralino mass is very light, which cannot easily be accessed by the traditional search methods. For more information on this procedure and an example of this extension

we refer to a spin correlation analysis performed by the ATLAS collaboration [117]. Another BSM model includes top chromo-magnetic couplings, which has been discussed in section 1.3.2. This extension has been studied in a CMS spin correlations analysis in [123]. The extension to these models in a matrix element method is not trivial. The data could be compared to a simulated sample of these BSM processes which has been evaluated under the two hypotheses presented in this work, but for optimal sensitivity the event likelihood calculations should be evaluated in addition under these BSM hypotheses. For this, the matrix elements of these BSM processes would need to be included in MadWeight which is not a straightforward task, as we have experienced with the inclusion of the uncorrelated matrix element. The time scale of this work would not allow for the processing of the samples under this new hypotheses and thorough closure testing of this extension.

Chapter 11

Nederlandstalige Samenvatting

De elementaire deeltjesfysica probeert de fundamentele bouwstenen van de natuur en hun onderlinge interacties te beschrijven. Het Standaard Model is het theoretische framework dat onze huidige kennis van de elementaire deeltjesfysica beschrijft. In het Standaard Model wordt alle materie beschreven door twaalf fundamentele deeltjes: zes leptonen en zes quarks. Er zijn vier krachten bekend die interacties tussen de materie overbrengen door middel van krachtdeeltjes: de bosonen. De elektromagnetische, zwakke en sterke kracht zijn beschreven in het Standaard Model. Tot nog toe kon de zwaartekracht niet geformuleerd worden in het Standaard Model. Het zwaarste deeltje tot nog toe ontdekt is het top quark. Doordat het top quark zo zwaar is, speelt het een belangrijker rol bij hogere orde correcties van het Standaard Model en bij voorspellingen van Nieuwe Fysica fenomenen. Dit maakt het top quark een erg interessant deeltje om met grote precisie te bestuderen.

In maart 2010, startte de Large Hadron Collider (LHC) aan het CERN met de productie van hoog-energetische proton-proton botsingen. De botsingen worden waargenomen door middel van de Compact Muon Solenoid (CMS) detector. Top quarks worden voornamelijk geproduceerd in paren aan de LHC. Alhoewel er geen restricties zijn op de richting van de top quark spin, is er wel een grote mate van correlatie tussen de spin van het top and anti-top quark in een paar. De sterkte van deze spin correlatie wordt voorspeld in het Standaard Model. Een afwijking van de waarde bepaald door het Standaard Model geeft aan dat er onbekende fysische processen een invloed hebben op deze grootheid. De meting van deze grootheid is het doel van deze thesis.

Doordat de top quarks zo zwaar zijn, vervallen deze deeltjes bijna onmiddelijk. Wat waargenomen wordt in the CMS detector zijn dan ook niet de top quarks zelf, maar eerder de dochterdeeltjes. Er zijn verscheidene vervalswijzen mogelijk voor een top quark en daardoor dus ook voor een top quark paar. In deze thesis verkiezen we het kanaal waar een van de top quarks vervalt met productie van een lepton (meer bepaald een muon) en het andere top quark vervalt in hadronische producten (jets). Op de data worden selectie criteria opgelegd om top quark paren in het lepton + jets kanaal te selecteren en de achtergrond komende van processen die geen aanleiding geven tot top quark paren te reduceren. In een volgende stap worden de vervalproducten die gemeten werden in de detector gebruikt om de oorspronkelijke top quark paren te reconstrueren.

Met het gereconstrueerde top quark paar kunnen we een matrix element methode uitvoeren. De matrix element methode brengt experimenteel gemeten grootheden in verband met de theoretische voorspellingen. In het Standaard Model, kunnen we het matrix element berekenen dat de productie en het verval van een top quark paar aan de LHC beschrijft. Door de gemeten kinematische variabelen van het top quark paar in the matrix element in te voegen en te integreren over de gehele parameter ruimte bekomt men de waarschijnlijkheid dat het experimenteel geobserveerde event effectief door dit process beschreven wordt. Door deze waarschijnlijkheid voor een collectie events te vergelijken onder verschillende hypothesen kan men besluiten welke hypothese meer waarschijnlijk is dan de andere. In deze thesis worden twee hypothesen voor de productie en verval van top quark paren bestudeerd: enerzijds het Standaard Model met een definitieve waarde voor de spin correlatie in het top quark paar en anderzijds een hypothese waarbij er geen correlatie is tussen de spins van een top quark paar. De verhouding van de waarschijnlijkheden voor een event onder beide hypothesen is een variabele die maximaal on-

derscheid maakt tussen twee hypothesen. De verdeling van deze variabele is beduidend anders voor een verzameling events geproduceerd onder de Standaard Model hypothese als onder de ongecorreleerde hypothese. Met behulp van de simulatie, kunnen we de vorm van de verdeling van de waarschijnlijkheidsverhouding bepalen om zo een fit aan de data uit te voeren. Tijdens deze fit wordt de verhouding van beide hypothesen in de data bepaald. Dit geeft ons een meting van de Standaard Model fractie f: de fractie aan top quark paren die spin correlatie volgens het Standaard Model vertonen.

We bekomen dat de data geobserveerd met de CMS detector tijdens de 2012 data-periode met een energie van 8 TeV in het muon+jets top quark paar kanaal compatibel is met de Standaard Model hypothese binnen 2.2 standaardafwijkingen en compatibel is met de hypothese van ongecorreleerde top quark paren binnen 2.9 standaardafwijkingen. In de meting van de Standaard Model fractie f, bekomen we dat $f = 0.72 \pm 0.08\,(\text{stat.})\,^{+0.15}_{-0.13}\,(\text{syst.})$. Deze meting voor f gepresenteerd in deze thesis is de meest nauwkeurige meting van deze variabele in het lepton+jets kanaal op heden.

Appendix A

Appendix

A.1 Datasets and Simulation

Table A.1: Summer12 8TeV Monte Carlo samples used for signal processes. A top quark mass of 172.5 GeV was used.

Data set	σ (pb)
/TT_8TeV-mcatnlo/Summer12_DR53X-PU_S10_START53_V7Av1/AODSIM	245.8
/TT_noCorr_8TeV-mcatnlo/Summer12_DR53X-PU_S10_START53_V7Cv1/AODSIM	245.8

Table A.2: Summer12 8 TeV Monte Carlo samples used for the estimation of the backgrounds along with their cross-sections. Cross sections taken from theory.

Data set (Summer12_DR53X-PU_S10_START53_V7A-v1/AOD)	Cross Section [pb]
/TTJets_MassiveBinDECAY_TuneZ2star_8TeV-madgraph-tauola/	245.8
/DYJetsToLL_M-50_TuneZ2Star_8TeV-madgraph-tarball/	3503.71
/WJetsToLNu_TuneZ2Star_8TeV-madgraph-tarball/	37509.0
/T_s-channel_TuneZ2star_8TeV-powheg-tauola/	3.79
/Tbar_s-channel_TuneZ2star_8TeV-powheg-tauola/	1.76
/T_t-channel_TuneZ2star_8TeV-powheg-tauola/	56.4
/Tbar_t-channel_TuneZ2star_8TeV-powheg-tauola/	30.7
/T_tW-channel-DR_TuneZ2star_8TeV-powheg-tauola/	11.1
/Tbar_tW-channel-DR_TuneZ2star_8TeV-powheg-tauola/	11.1

A.2 Matrix Element Code

The following pages include the matrix elements used in the likelihood calculations in MadWeight 5. The pages labelled with matrix1_cor.f contain the matrix element for gg fusion and the pages labelled with matrix2_cor.f contain the matrix element for $q\overline{q}$ annihilation. The code is set up so that one can switch between the SM ME and uncorrelated ME by setting the variable $kappa = 1$ or $kappa = 0$ respectively.

```
      Subroutine SMATRIX1(P,ANS)
C
C     Generated by MadGraph 5 v. 1.4.5, 2012-04-20
C     By the MadGraph Development Team
C     Please visit us at https://launchpad.net/madgraph5
C
C     MadGraph Version StandAlone
C
C     Returns amplitude squared summed/avg over colors
C     and helicities
C     for the point in phase space P(0:3,NEXTERNAL)
C
C     Process: g g > t t~ WEIGHTED=2
C     *   Decay: t > b u d~ WEIGHTED=4
C     *   Decay: t~ > b~ mu- vm~ WEIGHTED=4
C     Process: g g > t t~ WEIGHTED=2
C     *   Decay: t > b c s~ WEIGHTED=4
C     *   Decay: t~ > b~ mu- vm~ WEIGHTED=4
C
      IMPLICIT NONE
C
C     CONSTANTS
C
      Include "coupl.inc"

      INTEGER    NEXTERNAL
      PARAMETER (NEXTERNAL=8)
      INTEGER                 NCOMB
      PARAMETER (             NCOMB=256)
C
C     ARGUMENTS
C
      REAL*8 P(0:3,NEXTERNAL),ANS
C
C     LOCAL VARIABLES
C
CCCCCCCCCCCCCCCCCCCCCCCCCCCCCCCCCCCCCCCCCCCCCCCCCCCCCCCCCCCCCCCCCCCC
      double precision pt_wb(0:3),ptb_wb(0:3)
      double precision pb_wb(0:3),peb_wb(0:3),pne_wb(0:3)
      double precision pbb_wb(0:3),pm_wb(0:3),pnm_wb(0:3)
      DOUBLE PRECISION kappa
      double precision q0(0:3),q1(0:3),q2(0:3)

      DOUBLE PRECISION p1_wb(0:3),p2_wb(0:3),p3_wb(0:3)
      DOUBLE PRECISION p4_wb(0:3),p5_wb(0:3),p6_wb(0:3)
      DOUBLE PRECISION p7_wb(0:3),p8_wb(0:3),q_wb(0:3),qb_wb(0:3)
      DOUBLE PRECISION mw_wb, mt_wb,Gamma_wb,GamW_wb,pi_wb
      double precision alpha_wb,alphas_wb,sw2_wb,Kfak_wb

      double precision ms1_wb, ms2_wb, ebmin_wb, ebmax1_wb, ebmax2_wb
      double precision deleb1_wb, deleb2_wb, eb_wb, cthe1_wb, phi1_wb
      double precision cthe2_wb, phi2_wb
      double precision y_wb, beta1_wb
      double precision ebb_wb,cthe1b_wb,phi1b_wb,cthe2b_wb,phi2b_wb

      double precision Qs_wb(0:3)

      double precision pb1_wb(0:3),pnl1_wb(0:3),pl1_wb(0:3)
      double precision pb2_wb(0:3),pnl2_wb(0:3),pl2_wb(0:3)
      double precision sh_wb, rsh_wb
      double precision mprod_wb,qmod_wb,qbmod_wb

      double precision fgg_wb, mpgg
      double precision  mqqun_wb, qqoffun_wb
      double precision  mggun_wb, ggoffun_wb
```

```
      INTEGER i1_wb,i1
      INTEGER iflag_wb, i0, iii_wb, i_sp

      COMMON/par_wb/mw_wb,mt_wb,Gamma_wb,GamW_wb,pi_wb
      common/moment_wb/q_wb,qb_wb,p1_wb,p2_wb,p3_wb,p4_wb,
     #p5_wb,p6_wb,p7_wb,p8_wb
      common/faktors_wb/alpha_wb,alphas_wb,sw2_wb,Kfak_wb
      common/flagge_wb/iflag_wb

      external mprod_wb

C      parameter(pi=3.141592654d0)
C      parameter(a_s=0.1300)
C      parameter(g_f=1.16639d-5)


      parameter(kappa=1.0d0)


CCCCCCCCCCCCCCCCCCCCCCCCCCC

      INTEGER NHEL(NEXTERNAL,NCOMB),NTRY
      REAL*8 T
      REAL*8 MATRIX1
      INTEGER IHEL,IDEN, I
      INTEGER JC(NEXTERNAL)
      LOGICAL GOODHEL(NCOMB)
      DATA NTRY/0/
      DATA GOODHEL/NCOMB*.FALSE./
      DATA (NHEL(I,   1),I=1,8) /-1,-1,-1,-1,-1,-1,-1,-1/
      DATA (NHEL(I,   2),I=1,8) /-1,-1,-1,-1,-1,-1,-1, 1/
      DATA (NHEL(I,   3),I=1,8) /-1,-1,-1,-1,-1,-1, 1,-1/
      DATA (NHEL(I,   4),I=1,8) /-1,-1,-1,-1,-1,-1, 1, 1/
      DATA (NHEL(I,   5),I=1,8) /-1,-1,-1,-1,-1, 1,-1,-1/
      DATA (NHEL(I,   6),I=1,8) /-1,-1,-1,-1,-1, 1,-1, 1/
      DATA (NHEL(I,   7),I=1,8) /-1,-1,-1,-1,-1, 1, 1,-1/
      DATA (NHEL(I,   8),I=1,8) /-1,-1,-1,-1,-1, 1, 1, 1/
      DATA (NHEL(I,   9),I=1,8) /-1,-1,-1,-1, 1,-1,-1,-1/
      DATA (NHEL(I,  10),I=1,8) /-1,-1,-1,-1, 1,-1,-1, 1/
      DATA (NHEL(I,  11),I=1,8) /-1,-1,-1,-1, 1,-1, 1,-1/
      DATA (NHEL(I,  12),I=1,8) /-1,-1,-1,-1, 1,-1, 1, 1/
      DATA (NHEL(I,  13),I=1,8) /-1,-1,-1,-1, 1, 1,-1,-1/
      DATA (NHEL(I,  14),I=1,8) /-1,-1,-1,-1, 1, 1,-1, 1/
      DATA (NHEL(I,  15),I=1,8) /-1,-1,-1,-1, 1, 1, 1,-1/
      DATA (NHEL(I,  16),I=1,8) /-1,-1,-1,-1, 1, 1, 1, 1/
      DATA (NHEL(I,  17),I=1,8) /-1,-1,-1, 1,-1,-1,-1,-1/
      DATA (NHEL(I,  18),I=1,8) /-1,-1,-1, 1,-1,-1,-1, 1/
      DATA (NHEL(I,  19),I=1,8) /-1,-1,-1, 1,-1,-1, 1,-1/
      DATA (NHEL(I,  20),I=1,8) /-1,-1,-1, 1,-1,-1, 1, 1/
      DATA (NHEL(I,  21),I=1,8) /-1,-1,-1, 1,-1, 1,-1,-1/
      DATA (NHEL(I,  22),I=1,8) /-1,-1,-1, 1,-1, 1,-1, 1/
      DATA (NHEL(I,  23),I=1,8) /-1,-1,-1, 1,-1, 1, 1,-1/
      DATA (NHEL(I,  24),I=1,8) /-1,-1,-1, 1,-1, 1, 1, 1/
      DATA (NHEL(I,  25),I=1,8) /-1,-1,-1, 1, 1,-1,-1,-1/
      DATA (NHEL(I,  26),I=1,8) /-1,-1,-1, 1, 1,-1,-1, 1/
      DATA (NHEL(I,  27),I=1,8) /-1,-1,-1, 1, 1,-1, 1,-1/
      DATA (NHEL(I,  28),I=1,8) /-1,-1,-1, 1, 1,-1, 1, 1/
      DATA (NHEL(I,  29),I=1,8) /-1,-1,-1, 1, 1, 1,-1,-1/
      DATA (NHEL(I,  30),I=1,8) /-1,-1,-1, 1, 1, 1,-1, 1/
      DATA (NHEL(I,  31),I=1,8) /-1,-1,-1, 1, 1, 1, 1,-1/
      DATA (NHEL(I,  32),I=1,8) /-1,-1,-1, 1, 1, 1, 1, 1/
      DATA (NHEL(I,  33),I=1,8) /-1,-1, 1,-1,-1,-1,-1,-1/
      DATA (NHEL(I,  34),I=1,8) /-1,-1, 1,-1,-1,-1,-1, 1/
      DATA (NHEL(I,  35),I=1,8) /-1,-1, 1,-1,-1,-1, 1,-1/
      DATA (NHEL(I,  36),I=1,8) /-1,-1, 1,-1,-1,-1, 1, 1/
      DATA (NHEL(I,  37),I=1,8) /-1,-1, 1,-1,-1, 1,-1,-1/
      DATA (NHEL(I,  38),I=1,8) /-1,-1, 1,-1,-1, 1,-1, 1/
```

```
      DATA (NHEL(I,  39),I=1,8) /-1,-1, 1,-1,-1, 1, 1,-1/
      DATA (NHEL(I,  40),I=1,8) /-1,-1, 1,-1,-1, 1, 1, 1/
      DATA (NHEL(I,  41),I=1,8) /-1,-1, 1,-1, 1,-1,-1,-1/
      DATA (NHEL(I,  42),I=1,8) /-1,-1, 1,-1, 1,-1,-1, 1/
      DATA (NHEL(I,  43),I=1,8) /-1,-1, 1,-1, 1,-1, 1,-1/
      DATA (NHEL(I,  44),I=1,8) /-1,-1, 1,-1, 1,-1, 1, 1/
      DATA (NHEL(I,  45),I=1,8) /-1,-1, 1,-1, 1, 1,-1,-1/
      DATA (NHEL(I,  46),I=1,8) /-1,-1, 1,-1, 1, 1,-1, 1/
      DATA (NHEL(I,  47),I=1,8) /-1,-1, 1,-1, 1, 1, 1,-1/
      DATA (NHEL(I,  48),I=1,8) /-1,-1, 1,-1, 1, 1, 1, 1/
      DATA (NHEL(I,  49),I=1,8) /-1,-1, 1, 1,-1,-1,-1,-1/
      DATA (NHEL(I,  50),I=1,8) /-1,-1, 1, 1,-1,-1,-1, 1/
      DATA (NHEL(I,  51),I=1,8) /-1,-1, 1, 1,-1,-1, 1,-1/
      DATA (NHEL(I,  52),I=1,8) /-1,-1, 1, 1,-1,-1, 1, 1/
      DATA (NHEL(I,  53),I=1,8) /-1,-1, 1, 1,-1, 1,-1,-1/
      DATA (NHEL(I,  54),I=1,8) /-1,-1, 1, 1,-1, 1,-1, 1/
      DATA (NHEL(I,  55),I=1,8) /-1,-1, 1, 1,-1, 1, 1,-1/
      DATA (NHEL(I,  56),I=1,8) /-1,-1, 1, 1,-1, 1, 1, 1/
      DATA (NHEL(I,  57),I=1,8) /-1,-1, 1, 1, 1,-1,-1,-1/
      DATA (NHEL(I,  58),I=1,8) /-1,-1, 1, 1, 1,-1,-1, 1/
      DATA (NHEL(I,  59),I=1,8) /-1,-1, 1, 1, 1,-1, 1,-1/
      DATA (NHEL(I,  60),I=1,8) /-1,-1, 1, 1, 1,-1, 1, 1/
      DATA (NHEL(I,  61),I=1,8) /-1,-1, 1, 1, 1, 1,-1,-1/
      DATA (NHEL(I,  62),I=1,8) /-1,-1, 1, 1, 1, 1,-1, 1/
      DATA (NHEL(I,  63),I=1,8) /-1,-1, 1, 1, 1, 1, 1,-1/
      DATA (NHEL(I,  64),I=1,8) /-1,-1, 1, 1, 1, 1, 1, 1/
      DATA (NHEL(I,  65),I=1,8) /-1, 1,-1,-1,-1,-1,-1,-1/
      DATA (NHEL(I,  66),I=1,8) /-1, 1,-1,-1,-1,-1,-1, 1/
      DATA (NHEL(I,  67),I=1,8) /-1, 1,-1,-1,-1,-1, 1,-1/
      DATA (NHEL(I,  68),I=1,8) /-1, 1,-1,-1,-1,-1, 1, 1/
      DATA (NHEL(I,  69),I=1,8) /-1, 1,-1,-1,-1, 1,-1,-1/
      DATA (NHEL(I,  70),I=1,8) /-1, 1,-1,-1,-1, 1,-1, 1/
      DATA (NHEL(I,  71),I=1,8) /-1, 1,-1,-1,-1, 1, 1,-1/
      DATA (NHEL(I,  72),I=1,8) /-1, 1,-1,-1,-1, 1, 1, 1/
      DATA (NHEL(I,  73),I=1,8) /-1, 1,-1,-1, 1,-1,-1,-1/
      DATA (NHEL(I,  74),I=1,8) /-1, 1,-1,-1, 1,-1,-1, 1/
      DATA (NHEL(I,  75),I=1,8) /-1, 1,-1,-1, 1,-1, 1,-1/
      DATA (NHEL(I,  76),I=1,8) /-1, 1,-1,-1, 1,-1, 1, 1/
      DATA (NHEL(I,  77),I=1,8) /-1, 1,-1,-1, 1, 1,-1,-1/
      DATA (NHEL(I,  78),I=1,8) /-1, 1,-1,-1, 1, 1,-1, 1/
      DATA (NHEL(I,  79),I=1,8) /-1, 1,-1,-1, 1, 1, 1,-1/
      DATA (NHEL(I,  80),I=1,8) /-1, 1,-1,-1, 1, 1, 1, 1/
      DATA (NHEL(I,  81),I=1,8) /-1, 1,-1, 1,-1,-1,-1,-1/
      DATA (NHEL(I,  82),I=1,8) /-1, 1,-1, 1,-1,-1,-1, 1/
      DATA (NHEL(I,  83),I=1,8) /-1, 1,-1, 1,-1,-1, 1,-1/
      DATA (NHEL(I,  84),I=1,8) /-1, 1,-1, 1,-1,-1, 1, 1/
      DATA (NHEL(I,  85),I=1,8) /-1, 1,-1, 1,-1, 1,-1,-1/
      DATA (NHEL(I,  86),I=1,8) /-1, 1,-1, 1,-1, 1,-1, 1/
      DATA (NHEL(I,  87),I=1,8) /-1, 1,-1, 1,-1, 1, 1,-1/
      DATA (NHEL(I,  88),I=1,8) /-1, 1,-1, 1,-1, 1, 1, 1/
      DATA (NHEL(I,  89),I=1,8) /-1, 1,-1, 1, 1,-1,-1,-1/
      DATA (NHEL(I,  90),I=1,8) /-1, 1,-1, 1, 1,-1,-1, 1/
      DATA (NHEL(I,  91),I=1,8) /-1, 1,-1, 1, 1,-1, 1,-1/
      DATA (NHEL(I,  92),I=1,8) /-1, 1,-1, 1, 1,-1, 1, 1/
      DATA (NHEL(I,  93),I=1,8) /-1, 1,-1, 1, 1, 1,-1,-1/
      DATA (NHEL(I,  94),I=1,8) /-1, 1,-1, 1, 1, 1,-1, 1/
      DATA (NHEL(I,  95),I=1,8) /-1, 1,-1, 1, 1, 1, 1,-1/
      DATA (NHEL(I,  96),I=1,8) /-1, 1,-1, 1, 1, 1, 1, 1/
      DATA (NHEL(I,  97),I=1,8) /-1, 1, 1,-1,-1,-1,-1,-1/
      DATA (NHEL(I,  98),I=1,8) /-1, 1, 1,-1,-1,-1,-1, 1/
      DATA (NHEL(I,  99),I=1,8) /-1, 1, 1,-1,-1,-1, 1,-1/
      DATA (NHEL(I, 100),I=1,8) /-1, 1, 1,-1,-1,-1, 1, 1/
      DATA (NHEL(I, 101),I=1,8) /-1, 1, 1,-1,-1, 1,-1,-1/
      DATA (NHEL(I, 102),I=1,8) /-1, 1, 1,-1,-1, 1,-1, 1/
      DATA (NHEL(I, 103),I=1,8) /-1, 1, 1,-1,-1, 1, 1,-1/
      DATA (NHEL(I, 104),I=1,8) /-1, 1, 1,-1,-1, 1, 1, 1/
      DATA (NHEL(I, 105),I=1,8) /-1, 1, 1,-1, 1,-1,-1,-1/
```

```
      DATA (NHEL(I, 106),I=1,8) /-1, 1, 1,-1, 1,-1,-1, 1/
      DATA (NHEL(I, 107),I=1,8) /-1, 1, 1,-1, 1,-1, 1,-1/
      DATA (NHEL(I, 108),I=1,8) /-1, 1, 1,-1, 1,-1, 1, 1/
      DATA (NHEL(I, 109),I=1,8) /-1, 1, 1,-1, 1, 1,-1,-1/
      DATA (NHEL(I, 110),I=1,8) /-1, 1, 1,-1, 1, 1,-1, 1/
      DATA (NHEL(I, 111),I=1,8) /-1, 1, 1,-1, 1, 1, 1,-1/
      DATA (NHEL(I, 112),I=1,8) /-1, 1, 1,-1, 1, 1, 1, 1/
      DATA (NHEL(I, 113),I=1,8) /-1, 1, 1, 1,-1,-1,-1,-1/
      DATA (NHEL(I, 114),I=1,8) /-1, 1, 1, 1,-1,-1,-1, 1/
      DATA (NHEL(I, 115),I=1,8) /-1, 1, 1, 1,-1,-1, 1,-1/
      DATA (NHEL(I, 116),I=1,8) /-1, 1, 1, 1,-1,-1, 1, 1/
      DATA (NHEL(I, 117),I=1,8) /-1, 1, 1, 1,-1, 1,-1,-1/
      DATA (NHEL(I, 118),I=1,8) /-1, 1, 1, 1,-1, 1,-1, 1/
      DATA (NHEL(I, 119),I=1,8) /-1, 1, 1, 1,-1, 1, 1,-1/
      DATA (NHEL(I, 120),I=1,8) /-1, 1, 1, 1,-1, 1, 1, 1/
      DATA (NHEL(I, 121),I=1,8) /-1, 1, 1, 1, 1,-1,-1,-1/
      DATA (NHEL(I, 122),I=1,8) /-1, 1, 1, 1, 1,-1,-1, 1/
      DATA (NHEL(I, 123),I=1,8) /-1, 1, 1, 1, 1,-1, 1,-1/
      DATA (NHEL(I, 124),I=1,8) /-1, 1, 1, 1, 1,-1, 1, 1/
      DATA (NHEL(I, 125),I=1,8) /-1, 1, 1, 1, 1, 1,-1,-1/
      DATA (NHEL(I, 126),I=1,8) /-1, 1, 1, 1, 1, 1,-1, 1/
      DATA (NHEL(I, 127),I=1,8) /-1, 1, 1, 1, 1, 1, 1,-1/
      DATA (NHEL(I, 128),I=1,8) /-1, 1, 1, 1, 1, 1, 1, 1/
      DATA (NHEL(I, 129),I=1,8) / 1,-1,-1,-1,-1,-1,-1,-1/
      DATA (NHEL(I, 130),I=1,8) / 1,-1,-1,-1,-1,-1,-1, 1/
      DATA (NHEL(I, 131),I=1,8) / 1,-1,-1,-1,-1,-1, 1,-1/
      DATA (NHEL(I, 132),I=1,8) / 1,-1,-1,-1,-1,-1, 1, 1/
      DATA (NHEL(I, 133),I=1,8) / 1,-1,-1,-1,-1, 1,-1,-1/
      DATA (NHEL(I, 134),I=1,8) / 1,-1,-1,-1,-1, 1,-1, 1/
      DATA (NHEL(I, 135),I=1,8) / 1,-1,-1,-1,-1, 1, 1,-1/
      DATA (NHEL(I, 136),I=1,8) / 1,-1,-1,-1,-1, 1, 1, 1/
      DATA (NHEL(I, 137),I=1,8) / 1,-1,-1,-1, 1,-1,-1,-1/
      DATA (NHEL(I, 138),I=1,8) / 1,-1,-1,-1, 1,-1,-1, 1/
      DATA (NHEL(I, 139),I=1,8) / 1,-1,-1,-1, 1,-1, 1,-1/
      DATA (NHEL(I, 140),I=1,8) / 1,-1,-1,-1, 1,-1, 1, 1/
      DATA (NHEL(I, 141),I=1,8) / 1,-1,-1,-1, 1, 1,-1,-1/
      DATA (NHEL(I, 142),I=1,8) / 1,-1,-1,-1, 1, 1,-1, 1/
      DATA (NHEL(I, 143),I=1,8) / 1,-1,-1,-1, 1, 1, 1,-1/
      DATA (NHEL(I, 144),I=1,8) / 1,-1,-1,-1, 1, 1, 1, 1/
      DATA (NHEL(I, 145),I=1,8) / 1,-1,-1, 1,-1,-1,-1,-1/
      DATA (NHEL(I, 146),I=1,8) / 1,-1,-1, 1,-1,-1,-1, 1/
      DATA (NHEL(I, 147),I=1,8) / 1,-1,-1, 1,-1,-1, 1,-1/
      DATA (NHEL(I, 148),I=1,8) / 1,-1,-1, 1,-1,-1, 1, 1/
      DATA (NHEL(I, 149),I=1,8) / 1,-1,-1, 1,-1, 1,-1,-1/
      DATA (NHEL(I, 150),I=1,8) / 1,-1,-1, 1,-1, 1,-1, 1/
      DATA (NHEL(I, 151),I=1,8) / 1,-1,-1, 1,-1, 1, 1,-1/
      DATA (NHEL(I, 152),I=1,8) / 1,-1,-1, 1,-1, 1, 1, 1/
      DATA (NHEL(I, 153),I=1,8) / 1,-1,-1, 1, 1,-1,-1,-1/
      DATA (NHEL(I, 154),I=1,8) / 1,-1,-1, 1, 1,-1,-1, 1/
      DATA (NHEL(I, 155),I=1,8) / 1,-1,-1, 1, 1,-1, 1,-1/
      DATA (NHEL(I, 156),I=1,8) / 1,-1,-1, 1, 1,-1, 1, 1/
      DATA (NHEL(I, 157),I=1,8) / 1,-1,-1, 1, 1, 1,-1,-1/
      DATA (NHEL(I, 158),I=1,8) / 1,-1,-1, 1, 1, 1,-1, 1/
      DATA (NHEL(I, 159),I=1,8) / 1,-1,-1, 1, 1, 1, 1,-1/
      DATA (NHEL(I, 160),I=1,8) / 1,-1,-1, 1, 1, 1, 1, 1/
      DATA (NHEL(I, 161),I=1,8) / 1,-1, 1,-1,-1,-1,-1,-1/
      DATA (NHEL(I, 162),I=1,8) / 1,-1, 1,-1,-1,-1,-1, 1/
      DATA (NHEL(I, 163),I=1,8) / 1,-1, 1,-1,-1,-1, 1,-1/
      DATA (NHEL(I, 164),I=1,8) / 1,-1, 1,-1,-1,-1, 1, 1/
      DATA (NHEL(I, 165),I=1,8) / 1,-1, 1,-1,-1, 1,-1,-1/
      DATA (NHEL(I, 166),I=1,8) / 1,-1, 1,-1,-1, 1,-1, 1/
      DATA (NHEL(I, 167),I=1,8) / 1,-1, 1,-1,-1, 1, 1,-1/
      DATA (NHEL(I, 168),I=1,8) / 1,-1, 1,-1,-1, 1, 1, 1/
      DATA (NHEL(I, 169),I=1,8) / 1,-1, 1,-1, 1,-1,-1,-1/
      DATA (NHEL(I, 170),I=1,8) / 1,-1, 1,-1, 1,-1,-1, 1/
      DATA (NHEL(I, 171),I=1,8) / 1,-1, 1,-1, 1,-1, 1,-1/
      DATA (NHEL(I, 172),I=1,8) / 1,-1, 1,-1, 1,-1, 1, 1/
```

```
      DATA (NHEL(I, 173),I=1,8) / 1,-1, 1,-1, 1, 1,-1,-1/
      DATA (NHEL(I, 174),I=1,8) / 1,-1, 1,-1, 1, 1,-1, 1/
      DATA (NHEL(I, 175),I=1,8) / 1,-1, 1,-1, 1, 1, 1,-1/
      DATA (NHEL(I, 176),I=1,8) / 1,-1, 1,-1, 1, 1, 1, 1/
      DATA (NHEL(I, 177),I=1,8) / 1,-1, 1, 1,-1,-1,-1,-1/
      DATA (NHEL(I, 178),I=1,8) / 1,-1, 1, 1,-1,-1,-1, 1/
      DATA (NHEL(I, 179),I=1,8) / 1,-1, 1, 1,-1,-1, 1,-1/
      DATA (NHEL(I, 180),I=1,8) / 1,-1, 1, 1,-1,-1, 1, 1/
      DATA (NHEL(I, 181),I=1,8) / 1,-1, 1, 1,-1, 1,-1,-1/
      DATA (NHEL(I, 182),I=1,8) / 1,-1, 1, 1,-1, 1,-1, 1/
      DATA (NHEL(I, 183),I=1,8) / 1,-1, 1, 1,-1, 1, 1,-1/
      DATA (NHEL(I, 184),I=1,8) / 1,-1, 1, 1,-1, 1, 1, 1/
      DATA (NHEL(I, 185),I=1,8) / 1,-1, 1, 1, 1,-1,-1,-1/
      DATA (NHEL(I, 186),I=1,8) / 1,-1, 1, 1, 1,-1,-1, 1/
      DATA (NHEL(I, 187),I=1,8) / 1,-1, 1, 1, 1,-1, 1,-1/
      DATA (NHEL(I, 188),I=1,8) / 1,-1, 1, 1, 1,-1, 1, 1/
      DATA (NHEL(I, 189),I=1,8) / 1,-1, 1, 1, 1, 1,-1,-1/
      DATA (NHEL(I, 190),I=1,8) / 1,-1, 1, 1, 1, 1,-1, 1/
      DATA (NHEL(I, 191),I=1,8) / 1,-1, 1, 1, 1, 1, 1,-1/
      DATA (NHEL(I, 192),I=1,8) / 1,-1, 1, 1, 1, 1, 1, 1/
      DATA (NHEL(I, 193),I=1,8) / 1, 1,-1,-1,-1,-1,-1,-1/
      DATA (NHEL(I, 194),I=1,8) / 1, 1,-1,-1,-1,-1,-1, 1/
      DATA (NHEL(I, 195),I=1,8) / 1, 1,-1,-1,-1,-1, 1,-1/
      DATA (NHEL(I, 196),I=1,8) / 1, 1,-1,-1,-1,-1, 1, 1/
      DATA (NHEL(I, 197),I=1,8) / 1, 1,-1,-1,-1, 1,-1,-1/
      DATA (NHEL(I, 198),I=1,8) / 1, 1,-1,-1,-1, 1,-1, 1/
      DATA (NHEL(I, 199),I=1,8) / 1, 1,-1,-1,-1, 1, 1,-1/
      DATA (NHEL(I, 200),I=1,8) / 1, 1,-1,-1,-1, 1, 1, 1/
      DATA (NHEL(I, 201),I=1,8) / 1, 1,-1,-1, 1,-1,-1,-1/
      DATA (NHEL(I, 202),I=1,8) / 1, 1,-1,-1, 1,-1,-1, 1/
      DATA (NHEL(I, 203),I=1,8) / 1, 1,-1,-1, 1,-1, 1,-1/
      DATA (NHEL(I, 204),I=1,8) / 1, 1,-1,-1, 1,-1, 1, 1/
      DATA (NHEL(I, 205),I=1,8) / 1, 1,-1,-1, 1, 1,-1,-1/
      DATA (NHEL(I, 206),I=1,8) / 1, 1,-1,-1, 1, 1,-1, 1/
      DATA (NHEL(I, 207),I=1,8) / 1, 1,-1,-1, 1, 1, 1,-1/
      DATA (NHEL(I, 208),I=1,8) / 1, 1,-1,-1, 1, 1, 1, 1/
      DATA (NHEL(I, 209),I=1,8) / 1, 1,-1, 1,-1,-1,-1,-1/
      DATA (NHEL(I, 210),I=1,8) / 1, 1,-1, 1,-1,-1,-1, 1/
      DATA (NHEL(I, 211),I=1,8) / 1, 1,-1, 1,-1,-1, 1,-1/
      DATA (NHEL(I, 212),I=1,8) / 1, 1,-1, 1,-1,-1, 1, 1/
      DATA (NHEL(I, 213),I=1,8) / 1, 1,-1, 1,-1, 1,-1,-1/
      DATA (NHEL(I, 214),I=1,8) / 1, 1,-1, 1,-1, 1,-1, 1/
      DATA (NHEL(I, 215),I=1,8) / 1, 1,-1, 1,-1, 1, 1,-1/
      DATA (NHEL(I, 216),I=1,8) / 1, 1,-1, 1,-1, 1, 1, 1/
      DATA (NHEL(I, 217),I=1,8) / 1, 1,-1, 1, 1,-1,-1,-1/
      DATA (NHEL(I, 218),I=1,8) / 1, 1,-1, 1, 1,-1,-1, 1/
      DATA (NHEL(I, 219),I=1,8) / 1, 1,-1, 1, 1,-1, 1,-1/
      DATA (NHEL(I, 220),I=1,8) / 1, 1,-1, 1, 1,-1, 1, 1/
      DATA (NHEL(I, 221),I=1,8) / 1, 1,-1, 1, 1, 1,-1,-1/
      DATA (NHEL(I, 222),I=1,8) / 1, 1,-1, 1, 1, 1,-1, 1/
      DATA (NHEL(I, 223),I=1,8) / 1, 1,-1, 1, 1, 1, 1,-1/
      DATA (NHEL(I, 224),I=1,8) / 1, 1,-1, 1, 1, 1, 1, 1/
      DATA (NHEL(I, 225),I=1,8) / 1, 1, 1,-1,-1,-1,-1,-1/
      DATA (NHEL(I, 226),I=1,8) / 1, 1, 1,-1,-1,-1,-1, 1/
      DATA (NHEL(I, 227),I=1,8) / 1, 1, 1,-1,-1,-1, 1,-1/
      DATA (NHEL(I, 228),I=1,8) / 1, 1, 1,-1,-1,-1, 1, 1/
      DATA (NHEL(I, 229),I=1,8) / 1, 1, 1,-1,-1, 1,-1,-1/
      DATA (NHEL(I, 230),I=1,8) / 1, 1, 1,-1,-1, 1,-1, 1/
      DATA (NHEL(I, 231),I=1,8) / 1, 1, 1,-1,-1, 1, 1,-1/
      DATA (NHEL(I, 232),I=1,8) / 1, 1, 1,-1,-1, 1, 1, 1/
      DATA (NHEL(I, 233),I=1,8) / 1, 1, 1,-1, 1,-1,-1,-1/
      DATA (NHEL(I, 234),I=1,8) / 1, 1, 1,-1, 1,-1,-1, 1/
      DATA (NHEL(I, 235),I=1,8) / 1, 1, 1,-1, 1,-1, 1,-1/
      DATA (NHEL(I, 236),I=1,8) / 1, 1, 1,-1, 1,-1, 1, 1/
      DATA (NHEL(I, 237),I=1,8) / 1, 1, 1,-1, 1, 1,-1,-1/
      DATA (NHEL(I, 238),I=1,8) / 1, 1, 1,-1, 1, 1,-1, 1/
      DATA (NHEL(I, 239),I=1,8) / 1, 1, 1,-1, 1, 1, 1,-1/
```

```
      DATA (NHEL(I, 240),I=1,8) / 1, 1, 1,-1, 1, 1, 1, 1/
      DATA (NHEL(I, 241),I=1,8) / 1, 1, 1, 1,-1,-1,-1,-1/
      DATA (NHEL(I, 242),I=1,8) / 1, 1, 1, 1,-1,-1,-1, 1/
      DATA (NHEL(I, 243),I=1,8) / 1, 1, 1, 1,-1,-1, 1,-1/
      DATA (NHEL(I, 244),I=1,8) / 1, 1, 1, 1,-1,-1, 1, 1/
      DATA (NHEL(I, 245),I=1,8) / 1, 1, 1, 1,-1, 1,-1,-1/
      DATA (NHEL(I, 246),I=1,8) / 1, 1, 1, 1,-1, 1,-1, 1/
      DATA (NHEL(I, 247),I=1,8) / 1, 1, 1, 1,-1, 1, 1,-1/
      DATA (NHEL(I, 248),I=1,8) / 1, 1, 1, 1,-1, 1, 1, 1/
      DATA (NHEL(I, 249),I=1,8) / 1, 1, 1, 1, 1,-1,-1,-1/
      DATA (NHEL(I, 250),I=1,8) / 1, 1, 1, 1, 1,-1,-1, 1/
      DATA (NHEL(I, 251),I=1,8) / 1, 1, 1, 1, 1,-1, 1,-1/
      DATA (NHEL(I, 252),I=1,8) / 1, 1, 1, 1, 1,-1, 1, 1/
      DATA (NHEL(I, 253),I=1,8) / 1, 1, 1, 1, 1, 1,-1,-1/
      DATA (NHEL(I, 254),I=1,8) / 1, 1, 1, 1, 1, 1,-1, 1/
      DATA (NHEL(I, 255),I=1,8) / 1, 1, 1, 1, 1, 1, 1,-1/
      DATA (NHEL(I, 256),I=1,8) / 1, 1, 1, 1, 1, 1, 1, 1/
      DATA IDEN/256/


CCCCC CONSTANTS TO BE USED WITH MG
      pi_wb=dacos(-1.d0)
      alpha_wb = 1.d0/1.325070D+02
      alphas_wb = G**2/(4.d0*pi_wb)
      mt_wb = mt
      mw_wb = mw
      Gamma_wb = WT
      GamW_wb = WW
      sw2_wb = 1.000000D+00-MW**2/MZ**2
      iflag_wb=1


      Kfak_wb=(4*pi_wb*alphas_wb)**2*(4*pi_wb*alpha_wb)**4/sw2_wb**4

      do 10 i0=0,3
         q1(i0)=P(i0,1)
         q2(i0)=P(i0,2)
         pb_wb(i0)=P(i0,3)
         peb_wb(i0)=P(i0,5)
         pne_wb(i0)=P(i0,4)
         pbb_wb(i0)=P(i0,6)
         pm_wb(i0)=P(i0,7)
         pnm_wb(i0)=P(i0,8)

         pt_wb(i0)=pb_wb(i0)+peb_wb(i0)+pne_wb(i0)
         ptb_wb(i0)=pbb_wb(i0)+pm_wb(i0)+pnm_wb(i0)

         p3_wb(i0)=pbb_wb(i0)
         p4_wb(i0)=pm_wb(i0)
         p5_wb(i0)=pnm_wb(i0)
         p6_wb(i0)=pb_wb(i0)
         p7_wb(i0)=pne_wb(i0)
         p8_wb(i0)=peb_wb(i0)
         q_wb(i0)=pt_wb(i0)
         qb_wb(i0)=ptb_wb(i0)

 10   enddo

      do i_sp=0,3
         q0(i_sp)=q1(i_sp)+q2(i_sp)
      enddo

      call boosta(q0,q1,p1_wb)
      call boosta(q0,q2,p2_wb)
      call boosta(q0,pb_wb,p6_wb)
      call boosta(q0,pne_wb,p7_wb)
      call boosta(q0,peb_wb,p8_wb)
```

```fortran
      call boosta(q0,pbb_wb,p3_wb)
      call boosta(q0,pm_wb,p4_wb)
      call boosta(q0,pnm_wb,p5_wb)

      do i_sp=0,3
         q_wb(i_sp)= p6_wb(i_sp) + p8_wb(i_sp) + p7_wb(i_sp)
         qb_wb(i_sp) = p3_wb(i_sp) + p4_wb(i_sp) + p5_wb(i_sp)

      enddo

      ms1_wb = sqrt(mprod_wb(q_wb,q_wb))
      ms2_wb = sqrt(mprod_wb(qb_wb,qb_wb))


CCCCCCCCCCCCCCCCCCCCCCCCCCCCCCCCCCCCCCCCCCCCCCCCCCCCCCCCCCCCCCCCCCCCCCCCCCCCCCCCC
C      This is the correct definition of sh --> sh = (p1+p2)**2=2p1.p2 because for both qq~ and gg
initial states, p1.p1 = p2.p2 = 0
      sh_wb = 2*mprod_wb(p1_wb,p2_wb)
CCCCCCCCCCCCCCCCCCCCCCCCCCCCCCCCCCCCCCCCCCCCCCCCCCCCCCCCCCCCCCCCCCCCCCCC
      ggoffun_wb = 0.d0


c      if(kappa.eq.1.0d0)call ggttmat_wb(fgg_wb,sh_wb)
      if(kappa.eq.0.0d0)call goffunc_wb(ggoffun_wb)

C     ----------
C     BEGIN CODE
C     ----------
      NTRY=NTRY+1
      DO IHEL=1,NEXTERNAL
        JC(IHEL) = +1
      ENDDO
      ANS = 0D0
      DO IHEL=1,NCOMB
        IF (GOODHEL(IHEL) .OR. NTRY .LT. 2) THEN
          T=MATRIX1(P ,NHEL(1,IHEL),JC(1))
          ANS=ANS+T
          IF (T .NE. 0D0 .AND. .NOT.    GOODHEL(IHEL)) THEN
            GOODHEL(IHEL)=.TRUE.
          ENDIF
        ENDIF
      ENDDO
      ANS=ANS/DBLE(IDEN)
      fgg_wb = ANS

      ANS=(1.d0-kappa)*ggoffun_wb+kappa*fgg_wb

      END


      REAL*8 FUNCTION MATRIX1(P,NHEL,IC)
C
C     Generated by MadGraph 5 v. 1.4.5, 2012-04-20
C     By the MadGraph Development Team
C     Please visit us at https://launchpad.net/madgraph5
C
C     Returns amplitude squared summed/avg over colors
C     for the point with external lines W(0:6,NEXTERNAL)
C
C     Process: g g > t t~ WEIGHTED=2
C     *   Decay: t > b u d~ WEIGHTED=4
C     *   Decay: t~ > b~ mu- vm~ WEIGHTED=4
C     Process: g g > t t~ WEIGHTED=2
C     *   Decay: t > b c s~ WEIGHTED=4
C     *   Decay: t~ > b~ mu- vm~ WEIGHTED=4
C
      IMPLICIT NONE
```

```
C
C     CONSTANTS
C
      INTEGER    NGRAPHS
      PARAMETER (NGRAPHS=3)
      INTEGER    NEXTERNAL
      PARAMETER (NEXTERNAL=8)
      INTEGER    NWAVEFUNCS, NCOLOR
      PARAMETER (NWAVEFUNCS=15, NCOLOR=2)
      REAL*8     ZERO
      PARAMETER (ZERO=0D0)
      COMPLEX*16 IMAG1
      PARAMETER (IMAG1=(0D0,1D0))
C
C     ARGUMENTS
C
      REAL*8 P(0:3,NEXTERNAL)
      INTEGER NHEL(NEXTERNAL), IC(NEXTERNAL)
C
C     LOCAL VARIABLES
C
      INTEGER I,J
      COMPLEX*16 ZTEMP
      REAL*8 DENOM(NCOLOR), CF(NCOLOR,NCOLOR)
      COMPLEX*16 AMP(NGRAPHS), JAMP(NCOLOR)
      COMPLEX*16 W(18,NWAVEFUNCS)
      COMPLEX*16 DUM0,DUM1
      DATA DUM0, DUM1/(0D0, 0D0), (1D0, 0D0)/
C
C     GLOBAL VARIABLES
C
      INCLUDE 'coupl.inc'
C
C     COLOR DATA
C
      DATA DENOM(1)/1/
      DATA (CF(I,  1),I=  1,  2) /   16,   -2/
C     1 T(1,2,3,6) T(4,5)
      DATA DENOM(2)/1/
      DATA (CF(I,  2),I=  1,  2) /   -2,   16/
C     1 T(2,1,3,6) T(4,5)
C     ----------
C     BEGIN CODE
C     ----------
      CALL VXXXXX(P(0,1),ZERO,NHEL(1),-1*IC(1),W(1,1))
      CALL VXXXXX(P(0,2),ZERO,NHEL(2),-1*IC(2),W(1,2))
      CALL OXXXXX(P(0,3),MB,NHEL(3),+1*IC(3),W(1,3))
      CALL OXXXXX(P(0,4),ZERO,NHEL(4),+1*IC(4),W(1,4))
      CALL IXXXXX(P(0,5),ZERO,NHEL(5),-1*IC(5),W(1,5))
      CALL FFV2_3(W(1,5),W(1,4),GC_100,MW, WW, W(1,6))
      CALL FFV2_1(W(1,3),W(1,6),GC_100,MT, WT, W(1,7))
      CALL IXXXXX(P(0,6),MB,NHEL(6),-1*IC(6),W(1,8))
      CALL OXXXXX(P(0,7),ZERO,NHEL(7),+1*IC(7),W(1,9))
      CALL IXXXXX(P(0,8),ZERO,NHEL(8),-1*IC(8),W(1,10))
      CALL FFV2_3(W(1,10),W(1,9),GC_100,MW, WW, W(1,11))
      CALL FFV2_2(W(1,8),W(1,11),GC_100,MT, WT, W(1,12))
      CALL VVV1_1(W(1,1),W(1,2),GC_10,ZERO, ZERO, W(1,13))
C     Amplitude(s) for diagram number 1
      CALL FFV1_0(W(1,12),W(1,7),W(1,13),GC_11,AMP(1))
      CALL FFV1_1(W(1,7),W(1,1),GC_11,MT, WT, W(1,14))
C     Amplitude(s) for diagram number 2
      CALL FFV1_0(W(1,12),W(1,14),W(1,2),GC_11,AMP(2))
      CALL FFV1_2(W(1,12),W(1,1),GC_11,MT, WT, W(1,15))
C     Amplitude(s) for diagram number 3
      CALL FFV1_0(W(1,15),W(1,7),W(1,2),GC_11,AMP(3))
      JAMP(1)=+IMAG1*AMP(1)-AMP(2)
      JAMP(2)=-IMAG1*AMP(1)-AMP(3)
```

```
      MATRIX1 = 0.D0
      DO I = 1, NCOLOR
        ZTEMP = (0.D0,0.D0)
        DO J = 1, NCOLOR
          ZTEMP = ZTEMP + CF(J,I)*JAMP(J)
        ENDDO
        MATRIX1 = MATRIX1+ZTEMP*DCONJG(JAMP(I))/DENOM(I)
      ENDDO
      END


      DOUBLE COMPLEX FUNCTION sp_wb(v1_wb,v2_wb)
C     ***** computes spinor product s+ (Bernreuther)


      IMPLICIT NONE

      DOUBLE PRECISION v1_wb(0:3),v2_wb(0:3)
      double precision v201_wb,v101_wb,r1_wb,r2_wb,re12_wb,im12_wb

      if((v1_wb(0).eq.v1_wb(1)).or.(v2_wb(0).eq.v2_wb(1))) then
c        write(*,*) 'Mist'
      else
        v201_wb=v2_wb(0)-v2_wb(1)
        v101_wb=v1_wb(0)-v1_wb(1)
        r1_wb=dsqrt(v201_wb/v101_wb)
        r2_wb=dsqrt(v101_wb/v201_wb)
        re12_wb=v1_wb(2)*r1_wb-v2_wb(2)*r2_wb
        im12_wb=v1_wb(3)*r1_wb-v2_wb(3)*r2_wb
        sp_wb=dcmplx(re12_wb,im12_wb)
      end if

      RETURN
      END

c-----------------------------------------------------
      DOUBLE COMPLEX FUNCTION ptop_wb(vec_wb,iflag_wb)
C     *****  computes denominator of top
propagator
      IMPLICIT NONE

      include "coupl.inc"

      DOUBLE PRECISION vec_wb(0:3),mprod_wb, Gammat_wb, GamW_wb, Gamma_wb
      DOUBLE PRECISION  mw_wb,mt_wb,pi_wb

      integer iflag_wb

      COMMON/par_wb/mw_wb,mt_wb,Gamma_wb,GamW_wb,pi_wb

      external mprod_wb

      if(iflag_wb.eq.1) then
C      Gammat=WT
      Gammat_wb=Gamma_wb
      else
      Gammat_wb=0.d0
      endif

C      write(*,*) "TOP MASS = ", mt_wb

      ptop_wb=dcmplx(mprod_wb(vec_wb,vec_wb)-mt_wb**2,mt_wb*Gammat_wb)
C      write(*,*) 'vec, mt, Gammat, ptop= ',
C     #vec_wb, mt_wb, iflag_wb, Gammat_wb, ptop_wb

      RETURN
```

```
      END
c*****************************************************

      DOUBLE COMPLEX FUNCTION pw_wb(vec_wb)
C     *****  computes denominator of W propagator
      IMPLICIT NONE

      include "coupl.inc"

      DOUBLE PRECISION vec_wb(0:3), mprod_wb
      DOUBLE PRECISION  mw_wb,mt_wb,Gamma_wb,GamW_wb,pi_wb

      COMMON/par_wb/mw_wb,mt_wb,Gamma_wb,GamW_wb,pi_wb


      external mprod_wb

      pw_wb=dcmplx(mprod_wb(vec_wb,vec_wb)-mw_wb**2,mw_wb*GamW_wb)

      RETURN
      END
c*****************************************************

c*************************************************
c****    gg-> (ttbar)_off -> 6 fermions

      subroutine ggttmat_wb(fgg_wb,sh_wb)



      implicit none

      DOUBLE PRECISION p1_wb(0:3),p2_wb(0:3),p3_wb(0:3),p4_wb(0:3)
      DOUBLE PRECISION p5_wb(0:3),p6_wb(0:3)
      DOUBLE PRECISION p7_wb(0:3),p8_wb(0:3),q_wb(0:3),qb_wb(0:3)

      DOUBLE PRECISION p45_wb(0:3),p78_wb(0:3),p9_wb(0:3),p10_wb(0:3)
      DOUBLE PRECISION qp1_wb(0:3),qp2_wb(0:3),p11_wb(0:3),p12_wb(0:3)


      DOUBLE PRECISION  mw_wb,mt_wb,Gamma_wb,GamW_wb,pi_wb
      double precision alpha_wb,alphas_wb,sw2_wb,Kfak_wb
      DOUBLE PRECISION mprod_wb, mt2_wb

      DOUBLE PRECISION sh_wb,rsh_wb,etop_wb,qmod_wb

      DOUBLE PRECISION wfak_wb, beta_wb,sheta_wb,betab_wb
      DOUBLE PRECISION shetab_wb,cgg_wb,fgg_wb
      DOUBLE PRECISION prod1_wb,prod2_wb,prod3_wb,prod4_wb,prod5_wb
      DOUBLE PRECISION quot1_wb,quot2_wb,quot3_wb
      DOUBLE PRECISION prod6_wb,quot4_wb

      double complex sp_wb,pw_wb,ptop_wb,ch_wb, prop_wb
      double complex sp810_wb,sp19_wb,sp81_wb,sp29_wb,sp82_wb,sp12_wb
      double complex sp11k1_wb,sp21_wb,sp11k2_wb
      double complex sp1k11_wb,sp2k11_wb,sp2k12_wb,sp12k2_wb
      double complex sm102_wb,sm94_wb,sm24_wb,sm101_wb,sm14_wb,sm21_wb
      double complex sm11k2_wb,sm2k11_wb
      double complex sm12_wb,sm11k1_wb,sm1k11_wb,sm12k1_wb,sm1k12_wb
      double complex npp_wb,c12_wb,c21_wb,npm_wb,nmp_wb,nmm_wb,pw45_wb
      double complex pw78_wb,ptq_wb,ptqb_wb
      double complex pwwqq_wb,dq_wb,d1g_wb,d2g_wb
      double complex d3g_wb,t3g11_wb,t3g22_wb
      double complex t1g11_wb,t1g12_wb,t1g21_wb,t1g22_wb,t2g11_wb
      double complex t2g12_wb,t2g21_wb,t2g22_wb
      double complex m1g11_wb,m1g12_wb,m1g21_wb,m1g22_wb,m2g11_wb
      double complex m2g12_wb,m2g21_wb,m2g22_wb,m3g11_wb,m3g22_wb
```

```
      integer i1_wb,iflag_wb

      COMMON/par_wb/mw_wb,mt_wb,Gamma_wb,GamW_wb,pi_wb
      common/moment_wb/q_wb,qb_wb,p1_wb,p2_wb,p3_wb,p4_wb,
     #p5_wb,p6_wb,p7_wb,p8_wb
      common/faktors_wb/alpha_wb,alphas_wb,sw2_wb,Kfak_wb
      common/flagge_wb/iflag_wb

      EXTERNAL sp_wb,mprod_wb,pw_wb,ptop_wb

c      double precision fggo,fggs
c      double precision cggo,cggs,cggt

      mt2_wb=mt_wb**2


      prod1_wb=mprod_wb(q_wb,q_wb)
      prod2_wb=mprod_wb(q_wb,p8_wb)
      prod3_wb=mprod_wb(qb_wb,qb_wb)
      prod4_wb=mprod_wb(qb_wb,p4_wb)

      prod5_wb=mprod_wb(q_wb,p1_wb)
      prod6_wb=mprod_wb(q_wb,p2_wb)
      quot1_wb=prod1_wb/(2*prod2_wb)
      quot2_wb=prod3_wb/(2*prod4_wb)
      quot3_wb=prod1_wb/(2*prod5_wb)
      quot4_wb=prod1_wb/(2*prod6_wb)

c     auxiliary vectors

      do i1_wb=0,3

         p10_wb(i1_wb) = q_wb(i1_wb) - p8_wb(i1_wb)*quot1_wb
         p9_wb(i1_wb) = qb_wb(i1_wb) - p4_wb(i1_wb)*quot2_wb
         p11_wb(i1_wb) = q_wb(i1_wb) - p1_wb(i1_wb)*quot3_wb

         p12_wb(i1_wb )= q_wb(i1_wb) - p2_wb(i1_wb)*quot4_wb

         qp1_wb(i1_wb)=q_wb(i1_wb)-p1_wb(i1_wb)
         qp2_wb(i1_wb)=q_wb(i1_wb)-p2_wb(i1_wb)

         p45_wb(i1_wb) = p4_wb(i1_wb) + p5_wb(i1_wb)
         p78_wb(i1_wb) = p7_wb(i1_wb) + p8_wb(i1_wb)

      enddo

      sp810_wb=sp_wb(p8_wb,p10_wb)
      sp19_wb=sp_wb(p1_wb,p9_wb)
      sp81_wb=sp_wb(p8_wb,p1_wb)
      sp29_wb=sp_wb(p2_wb,p9_wb)
      sp82_wb=sp_wb(p8_wb,p2_wb)
      sp12_wb=sp_wb(p1_wb,p2_wb)
      sp21_wb=-sp12_wb
      sp11k1_wb=sp_wb(p11_wb,p1_wb)
      sp11k2_wb=sp_wb(p11_wb,p2_wb)
      sp1k11_wb=-sp11k1_wb
      sp2k11_wb=-sp11k2_wb
      sp2k12_wb=sp_wb(p2_wb,p12_wb)
      sp12k2_wb=-sp2k12_wb

      sm102_wb=-dconjg(sp_wb(p10_wb,p2_wb))
      sm94_wb=-dconjg(sp_wb(p9_wb,p4_wb))
      sm24_wb=-dconjg(sp_wb(p2_wb,p4_wb))
      sm101_wb=-dconjg(sp_wb(p10_wb,p1_wb))
      sm14_wb=-dconjg(sp_wb(p1_wb,p4_wb))
      sm21_wb=-dconjg(sp21_wb)
```

```
       sm11k2_wb=-dconjg(sp11k2_wb)
       sm2k11_wb=-sm11k2_wb
       sm12_wb=-sm21_wb
       sm11k1_wb=-dconjg(sp11k1_wb)
       sm1k11_wb=-sm11k1_wb
       sm12k1_wb=-dconjg(sp_wb(p12_wb,p1_wb))
       sm1k12_wb=-sm12k1_wb

       npp_wb=2*sm12_wb*sm21_wb
       c12_wb=dconjg(sm12_wb)
       c21_wb=dconjg(sm21_wb)
       npm_wb=2*sm12_wb*c21_wb
       nmp_wb=2*c12_wb*sm21_wb
       nmm_wb=2*c12_wb*c21_wb


       wfak_wb= mprod_wb(p3_wb,p5_wb)*mprod_wb(p6_wb,p7_wb)

C      in prop iflag = 1 in WB code even for MP cpmparison case
       prop_wb=ptop_wb(q_wb,1)*ptop_wb(qb_wb,1)
      #*pw_wb(p45_wb)*pw_wb(p78_wb)


c *** for comparison with on-shell ttbar,
c ***  iflag=0 in ptop of d1g and d2g
c *** for comparison with Madgraph, iflag=1
c


       d1g_wb=ptop_wb(qp1_wb,iflag_wb)*prop_wb
       d2g_wb=ptop_wb(qp2_wb,iflag_wb)*prop_wb
       d3g_wb=sh_wb*prop_wb


c
c      helicity amps.: g g -> .....
c

       t1g11_wb= -2*prod5_wb*sp810_wb*sm102_wb*sp29_wb*sm94_wb+
      #mt2_wb*sp810_wb*sm102_wb*sp12_wb*sm14_wb -
      #mt2_wb*sp81_wb*sm21_wb*sp29_wb*sm94_wb+
      #2*mt2_wb*mprod_wb(qp1_wb,p2_wb)*sp81_wb*sm14_wb

       t1g12_wb= -sp810_wb*sm102_wb*sp1k11_wb*sm11k2_wb*sp19_wb*sm94_wb+
      #mt2_wb*sp81_wb*sm2k11_wb*sp11k1_wb*sm24_wb

       t1g21_wb= -sp810_wb*sm101_wb*sp2k12_wb*sm12k1_wb*sp29_wb*sm94_wb+
      #mt2_wb*sp82_wb*sm1k12_wb*sp12k2_wb*sm14_wb

       t1g22_wb= -2*mprod_wb(qp1_wb,p2_wb)*
      #sp810_wb*sm101_wb*sp19_wb*sm94_wb+
      #mt2_wb*sp810_wb*sm101_wb*sp21_wb*sm24_wb -
      #mt2_wb*sp82_wb*sm12_wb*sp19_wb*sm94_wb+
      #2*prod5_wb*sp82_wb*sm24_wb*mt_wb**2

       t2g11_wb= -2*prod6_wb*sp810_wb*sm101_wb*sp19_wb*sm94_wb+
      #mt2_wb*sp810_wb*sm101_wb*sp21_wb*sm24_wb -
      #mt2_wb*sp82_wb*sm12_wb*sp19_wb*sm94_wb+
      #2*mt2_wb*mprod_wb(qp2_wb,p1_wb)*sp82_wb*sm24_wb

       t2g12_wb=t1g12_wb
       t2g21_wb=t1g21_wb

       t2g22_wb= -2*mprod_wb(qp2_wb,p1_wb)*sp810_wb*
      #sm102_wb*sp29_wb*sm94_wb+
      #mt2_wb*sp810_wb*sm102_wb*sp12_wb*sm14_wb -
      #mt2_wb*sp81_wb*sm21_wb*sp29_wb*sm94_wb+
```

```
     #2*prod6_wb*sp81_wb*sm14_wb*mt_wb**2

      t3g11_wb= mprod_wb(p1_wb,p2_wb)*(sp810_wb*sm101_wb*
     #sp19_wb*sm94_wb-
     #sp810_wb*sm102_wb*sp29_wb*sm94_wb - mt2_wb*(sp81_wb*sm14_wb -
     #sp82_wb*sm24_wb))

      t3g22_wb=t3g11_wb

      m1g11_wb=t1g11_wb/(d1g_wb*npp_wb)
      m1g12_wb=t1g12_wb/(d1g_wb*npm_wb)
      m1g21_wb=t1g21_wb/(d1g_wb*nmp_wb)
      m1g22_wb=t1g22_wb/(d1g_wb*nmm_wb)

      m2g11_wb=t2g11_wb/(d2g_wb*npp_wb)
      m2g12_wb=t2g12_wb/(d2g_wb*npm_wb)
      m2g21_wb=t2g21_wb/(d2g_wb*nmp_wb)
      m2g22_wb=t2g22_wb/(d2g_wb*nmm_wb)

      m3g11_wb=t3g11_wb/(d3g_wb*npp_wb)
      m3g22_wb=t3g22_wb/(d3g_wb*nmm_wb)


      cgg_wb = (7.d0/3.d0)*((cdabs(m1g11_wb+m2g11_wb))**2+
     & (cdabs(m1g12_wb+m2g12_wb))**2+
     & (cdabs(m1g21_wb+m2g21_wb))**2+
     & (cdabs(m1g22_wb+m2g22_wb))**2)+
     & 3*((cdabs(m1g12_wb -m2g12_wb))**2+
     &    (cdabs(m1g21_wb -m2g21_wb))**2+
     &    (cdabs(m1g11_wb-m2g11_wb+ 2*m3g11_wb))**2+
     &    (cdabs(m1g22_wb-m2g22_wb+ 2*m3g22_wb))**2)



       fgg_wb = wfak_wb*cgg_wb/4.d0

c**    multiply overall coupling constant factor
c***        (4pi)**2 * alpha_s**2 * e**8/sw2**4

C     multiply by 3 becuase of the transformation from dilepton to lepton+jets channel

      fgg_wb =3*Kfak_wb*fgg_wb


      RETURN
      END

C************************************
      DOUBLE PRECISION FUNCTION mprod_wb(v1_wb,v2_wb)
C *****  computes Minkowski scalar product of two 4-vectors

      IMPLICIT NONE
      DOUBLE PRECISION v1_wb,v2_wb
      DIMENSION v1_wb(0:3),v2_wb(0:3)
      mprod_wb=v1_wb(0)*v2_wb(0)-v1_wb(1)*v2_wb(1)-
     #v1_wb(2)*v2_wb(2)-v1_wb(3)*v2_wb(3)

      RETURN
      END
c************************************************************
C ************************************************************

      subroutine tdec3(ms_wb,eb_wb,el_wb,cthe1_wb,phi1_wb,cthe2_wb,
     +phi2_wb,pb_wb,pnl_wb,pl_wb)


c*** this subroutine computes the b, l, nu_l momenta
```

```
c*** in top or tbar decay, according to 4-momentum conservation
c**  the b, l, nu_l momenta are on-shell

      implicit none

      double precision pb_wb(0:3),pnl_wb(0:3),pl_wb(0:3)
      double precision pb0_wb(1:3)
      double precision ms_wb,cthe1_wb,phi1_wb,sthe1_wb
      double precision el_wb,eb_wb,cthe2_wb,sthe2_wb,phi2_wb,pbb_wb

      double precision  pnmink_wb, mprod_wb
      DOUBLE PRECISION  mw_wb,mb_wb,mt_wb,Gamma_wb,GamW_wb,pi_wb
      double precision r11_wb, r21_wb, r31_wb, r13_wb, r23_wb, r33_wb
       integer i1_t

      COMMON/par/mw_wb,mb_wb,mt_wb,Gamma_wb,GamW_wb,pi_wb

      external mprod_wb


c** l 4-momentum

      pl_wb(0)=el_wb

      sthe2_wb =dsqrt(1.d0-cthe2_wb**2)

      pl_wb(1)=el_wb*sthe2_wb*dsin(phi2_wb)
      pl_wb(2)=el_wb*sthe2_wb*dcos(phi2_wb)
      pl_wb(3)=el_wb*cthe2_wb

c*** b 4-momentum

      pbb_wb =dsqrt(eb_wb**2-mb_wb**2)
      sthe1_wb =dsqrt(1.d0-cthe1_wb**2)

      pb_wb(0)= eb_wb

      pb0_wb(1)=pbb_wb*sthe1_wb
      pb0_wb(2)=0.d0
      pb0_wb(3)=pbb_wb*cthe1_wb

      r11_wb=dcos(phi2_wb)*dcos(phi1_wb)-
     +cthe2_wb*dsin(phi1_wb)*dsin(phi2_wb)
      r21_wb=-dsin(phi2_wb)*dcos(phi1_wb)-
     +cthe2_wb*dsin(phi1_wb)*dcos(phi2_wb)
      r31_wb=sthe2_wb*dsin(phi1_wb)
      r13_wb=dsin(phi2_wb)*sthe2_wb
      r23_wb=dcos(phi2_wb)*sthe2_wb
      r33_wb=cthe2_wb

      pb_wb(1)=r11_wb*pb0_wb(1)+r13_wb*pb0_wb(3)
      pb_wb(2)=r21_wb*pb0_wb(1)+r23_wb*pb0_wb(3)
      pb_wb(3)=r31_wb*pb0_wb(1)+r33_wb*pb0_wb(3)

c**  nu_l 4-momentum

      pnl_wb(0)= ms_wb - eb_wb - el_wb

      do 33 i1_t = 1,3
      pnl_wb(i1_t)=-pb_wb(i1_t)-pl_wb(i1_t)
 33   continue

c      pnmink=mprod(pnl,pnl)
c      write(6,*) 'pnmink', pnmink
```

```
      return
      end


C _____________________________________________________________
C *************************************************************
      SUBROUTINE boosta(P12,k1ecm,k1)

      implicit none
      DOUBLE PRECISION P12(0:3),k1(0:3),Batt(3),BaP
      DOUBLE PRECISION k1ecm(0:3),m12,gamma
      INTEGER i

      m12=dsqrt(p12(0)**2-p12(1)**2-p12(2)**2-p12(3)**2)
      gamma = p12(0)/m12


      batt(1)=-p12(1)/p12(0)
      batt(2)=-p12(2)/p12(0)
      batt(3)=-p12(3)/p12(0)


      bap=batt(1)*k1ecm(1)+batt(2)*k1ecm(2)+batt(3)*k1ecm(3)

      k1(0)=gamma*(k1ecm(0)-bap)

      do 2 i=1,3
      K1(i)=k1ecm(i)-gamma*k1ecm(0)*batt(i)+
     &  gamma**2*bap*batt(i)/(1.d0+gamma)
 2    continue

      RETURN
      END
c**************************************
      subroutine zmf(p0_yp,p_in_yp,p_out_yp)
c     take momenta p_in in frame in which particle 0 has momentum p0
c     and convert to frame in which particle 0 is at rest
c     p-out is the resulting vector

      implicit none
      real*8 p0_yp(0:3),p_in_yp(0:3),p_out_yp(0:3)
      real*8 mass_yp,gam_yp,beta_yp(1:3),bdotp_yp
      integer j_yp,k_yp
      mass_yp=dsqrt(dabs(p0_yp(0)**2-p0_yp(1)**2-p0_yp(2)**2-
     +p0_yp(3)**2))
      gam_yp=p0_yp(0)/mass_yp

      bdotp_yp=0.d0
      do j_yp=1,3
         beta_yp(j_yp)=+p0_yp(j_yp)/p0_yp(0)
         bdotp_yp=bdotp_yp+p_in_yp(j_yp)*beta_yp(j_yp)
      enddo

      do k_yp=1,3
         p_out_yp(k_yp)=p_in_yp(k_yp)+gam_yp*beta_yp(k_yp)*
     +        (gam_yp/(gam_yp+1.d0)*bdotp_yp-p_in_yp(0))
      enddo
      p_out_yp(0)=gam_yp*(p_in_yp(0)-bdotp_yp)

      return
      end

c**********************************************

c     ################################################################
c     ##### Mahlon, Parke gg -> (ttbar)_on, correlated  -> 6 fermions
c            PRD81 (2010) 074024, Gl. (47) - (49)
```

```
c
c     4-momenta of the final partons:
c
c                 4-vectors in parton c.m. frame
c             p1 <-> initial antiquark (gluon)
c             p2 <-> initial quark (gluon)
c             q  <-> top quark
c             qb <-> antitop quark
c             p3 <-> b-bar
c             p4 <-> lepton-        (or d-type quark)
c             p5 <-> antineutrino   (or u-bar type quark)
c             p6 <-> b
c             p8 <-> lepton+        (or d-bar type quark)
c             p7 <-> neutrino       (or u-type quark)
c
c*********************************************************************

      subroutine ggmpmat(mpgg,sh_wb)

      implicit none

      double complex pw_wb, ptop_wb

      DOUBLE PRECISION p1_wb(0:3),p2_wb(0:3),p3_wb(0:3)
      DOUBLE PRECISION p4_wb(0:3),p5_wb(0:3),p6_wb(0:3)
      DOUBLE PRECISION p7_wb(0:3),p8_wb(0:3),q_wb(0:3),qb_wb(0:3)
      DOUBLE PRECISION  mw_wb,mb_wb,mt_wb,Gamma_wb,GamW_wb,pi_wb
      double precision alpha_wb,alphas_wb,sw2_wb,Kfak_wb

      DOUBLE PRECISION p45_wb(0:3), p78_wb(0:3)


      double precision mt2_wb, mprod_wb, sh_wb, prop_wb
      double precision mpgg1, mpgg2, mpgg, Kgg_mp

      INTEGER i1_wb

      COMMON/par_wb/mw_wb,mt_wb,Gamma_wb,GamW_wb,pi_wb

      common/moment_wb/q_wb,qb_wb,p1_wb,p2_wb,p3_wb,p4_wb,
     #p5_wb,p6_wb,p7_wb,p8_wb

      common/faktors_wb/alpha_wb,alphas_wb,sw2_wb,Kfak_wb

      mt2_wb=mt_wb**2

      mpgg1=
     &(2*mprod_wb(p1_wb,q_wb)*mprod_wb(p2_wb,q_wb)-mt2_wb
     &*mprod_wb(p1_wb,p2_wb))/(mprod_wb(p1_wb,p2_wb))**2
     &*(2*mprod_wb(q_wb,p8_wb)*mprod_wb(qb_wb,p4_wb)
     &*((mprod_wb(p1_wb,q_wb))**2+(mprod_wb(p2_wb,q_wb))**2)
     &-mt2_wb*(mprod_wb(p1_wb,p2_wb)*(mprod_wb(q_wb,p8_wb)
     &*mprod_wb(q_wb,p4_wb)+mprod_wb(qb_wb,p8_wb)*mprod_wb(qb_wb,p4_wb)
     &-mt2_wb*mprod_wb(p8_wb,p4_wb))-2*(mprod_wb(p1_wb,q_wb)
     &*mprod_wb(p1_wb,p4_wb)*mprod_wb(p2_wb,p8_wb)
     &+mprod_wb(p2_wb,q_wb)*mprod_wb(p1_wb,p8_wb)*mprod_wb(p2_wb,p4_wb)
     &-mprod_wb(p1_wb,q_wb)*mprod_wb(p2_wb,q_wb)
     &*mprod_wb(p8_wb,p4_wb))))

      mpgg2=
     &mt2_wb**2*(mprod_wb(q_wb,p8_wb)*mprod_wb(q_wb,p4_wb)
     &+mprod_wb(qb_wb,p8_wb)*mprod_wb(qb_wb,p4_wb)
     &-mt2_wb*mprod_wb(p8_wb,p4_wb))

      do i1_wb=0,3

      p45_wb(i1_wb) = p4_wb(i1_wb) + p5_wb(i1_wb)
```

```
      p78_wb(i1_wb) = p7_wb(i1_wb) + p8_wb(i1_wb)

      enddo

C-- overall factor, in addition multiplied by 1/2*2*8*8 (spin color av.)

      Kgg_mp=(1.d0/12.d0)*(Kfak_wb/mt2_wb**2/Gamma_wb**4)
     &*(4*(mprod_wb(p1_wb,q_wb))**2+4*(mprod_wb(p2_wb,q_wb))**2
     &-mprod_wb(p1_wb,q_wb)*mprod_wb(p2_wb,q_wb))
     &/((mprod_wb(p1_wb,q_wb))**2*(mprod_wb(p2_wb,q_wb))**2)
     &*mprod_wb(p6_wb,p7_wb)*mprod_wb(p3_wb,p5_wb)
     &/((cdabs(pw_wb(p78_wb)))**2*(cdabs(pw_wb(p45_wb)))**2)

      mpgg=Kgg_mp*(mpgg1 + mpgg2)


      RETURN
      END
c*************************************************
c*********************************************************************
      subroutine goffunc_wb(ggoffun_wb)

      implicit none

      double complex pw_wb, ptop_wb

      DOUBLE PRECISION p1_wb(0:3),p2_wb(0:3),p3_wb(0:3)
      DOUBLE PRECISION p4_wb(0:3),p5_wb(0:3),p6_wb(0:3)
      DOUBLE PRECISION p7_wb(0:3),p8_wb(0:3),q_wb(0:3),qb_wb(0:3)
      DOUBLE PRECISION  mw_wb,mt_wb,Gamma_wb,GamW_wb,pi_wb
      double precision alpha_wb,alphas_wb,sw2_wb,Kfak_wb

      DOUBLE PRECISION p45_wb(0:3), p78_wb(0:3)


      double precision mt2_wb, mprod_wb, sh_wb, prop_un_wb

      double precision p12_wb,q11_wb,q22_wb,p1q_wb,p2qb_wb
      double precision p1qb_wb, p2q_wb, s_wb, t_wb, u_wb
      double precision ungg_wb, ggoffun_wb

      INTEGER i1_wb

      COMMON/par_wb/mw_wb,mt_wb,Gamma_wb,GamW_wb,pi_wb
      common/moment_wb/q_wb,qb_wb,p1_wb,p2_wb,p3_wb,p4_wb,
     #p5_wb,p6_wb,p7_wb,p8_wb

      common/faktors_wb/alpha_wb,alphas_wb,sw2_wb,Kfak_wb


      EXTERNAL sp_wb,mprod_wb,pw_wb,ptop_wb

      mt2_wb=mt_wb**2

      p12_wb=mprod_wb(p1_wb,p2_wb)
      q11_wb=mprod_wb(q_wb,q_wb)
      q22_wb=mprod_wb(qb_wb,qb_wb)
      p1q_wb=mprod_wb(p1_wb,q_wb)
      p2qb_wb=mprod_wb(p2_wb,qb_wb)

      p1qb_wb=p12_wb-p1q_wb
      p2q_wb =p12_wb-p2qb_wb

      s_wb=2*p12_wb
      t_wb=q11_wb-2*p1q_wb
      u_wb=q22_wb-2*p1qb_wb
```

```
       ungg_wb=
     & (6*(-4*p1qb_wb*p2q_wb + 4*p1q_wb*(p1qb_wb - p2qb_wb) +
     & 4*p2q_wb*p2qb_wb +
     & 2*mt2_wb*s_wb - q11_wb*s_wb - q22_wb*s_wb + s_wb**2) +
     & (32*((-((2*p1q_wb*p2qb_wb + mt2_wb*s_wb)*
     & (-8*p1q_wb*p2q_wb + (mt2_wb + q11_wb)*s_wb)) +
     & 2*p1qb_wb*(s_wb*(-(p2q_wb*(mt2_wb + q11_wb)) + mt2_wb*s_wb) +
     & p1q_wb*(8*p2q_wb**2 - 4*p2q_wb*s_wb + s_wb**2)))/
     & (mt2_wb - t_wb)**2 +
     & (16*p1q_wb**2*p2q_wb*p2qb_wb +
     & 2*p1q_wb*(8*p1qb_wb*p2q_wb**2 +
     & 4*p2q_wb*(mt2_wb - p2qb_wb)*s_wb -
     & p2qb_wb*(mt2_wb + q11_wb)*s_wb)
     & - s_wb*(2*p1qb_wb*p2q_wb*(mt2_wb + q11_wb) +
     & (-2*(mt2_wb + p2q_wb)*p2qb_wb + mt2_wb*(mt2_wb + q11_wb))*s_wb))/
     & (mt2_wb - u_wb)**2))/3. +
     & (2*(8*p1q_wb**2*p2qb_wb*(-8*p2q_wb + s_wb) +
     & q11_wb*s_wb*((6*mt2_wb - s_wb)*s_wb + 2*p2q_wb*(4*p1qb_wb+s_wb)+
     & 2*p1q_wb*(-4*p2q_wb + 4*p2qb_wb + s_wb)) +
     & s_wb*(-2*mt2_wb - 2*p2q_wb + s_wb)*
     & (-4*p1qb_wb*p2q_wb + s_wb*(-q22_wb + s_wb)) -
     & 2*p1q_wb*(32*p1qb_wb*p2q_wb**2 -
     & 4*p2q_wb*s_wb*(-2*mt2_wb + p1qb_wb + p2qb_wb - q22_wb + s_wb) +
     & s_wb*(s_wb*(-q22_wb + s_wb) + p2qb_wb*(-4*mt2_wb + 2*s_wb)))))/
     & (3.*(mt2_wb - t_wb)*(mt2_wb - u_wb)) -
     & (3*(8*p1q_wb**2*p2qb_wb*(-t_wb + u_wb) +
     & s_wb*(-2*p2q_wb*(-4*p2qb_wb*(mt2_wb - t_wb) +
     & (-q11_wb - q22_wb + s_wb)*(t_wb - u_wb)) +
     & s_wb*(2*mt2_wb - q11_wb - q22_wb + s_wb)*(2*mt2_wb-t_wb-u_wb)+
     & 4*mt2_wb*p2qb_wb*(-t_wb + u_wb)) +
     & 4*p1qb_wb*(2*p2q_wb**2*(t_wb - u_wb) + mt2_wb*s_wb*(t_wb - u_wb)+
     & p2q_wb*s_wb*(-2*mt2_wb + t_wb + u_wb)) +
     & 2*p1q_wb*(4*p1qb_wb*(s_wb*(mt2_wb - u_wb)-3*p2q_wb*(t_wb-u_wb)) +
     & s_wb*(-q11_wb - q22_wb + s_wb)*(t_wb - u_wb) +
     & 2*p2qb_wb*(6*p2q_wb*(t_wb - u_wb)+s_wb*(-2*mt2_wb+t_wb+u_wb)))))/
     & ((mt2_wb - t_wb)*(mt2_wb - u_wb)))/s_wb**2


       do i1_wb=0,3

       p45_wb(i1_wb) = p4_wb(i1_wb) + p5_wb(i1_wb)
       p78_wb(i1_wb) = p7_wb(i1_wb) + p8_wb(i1_wb)

       enddo

C*** in the following functions 'ptop', iflag=1 always!

       prop_un_wb= cdabs(ptop_wb(q_wb,1)*ptop_wb(qb_wb,1)
     #*pw_wb(p45_wb)*pw_wb(p78_wb))

       ggoffun_wb=(1.d0/8.d0)*ungg_wb*mprod_wb(q_wb,p8_wb)
     & *mprod_wb(p6_wb,p7_wb)
     & *mprod_wb(qb_wb,p4_wb)*mprod_wb(p3_wb,p5_wb)/prop_un_wb**2


c** no  factor 4

       ggoffun_wb= 3*Kfak_wb*ggoffun_wb

       RETURN
       END
```

```
      SUBROUTINE SMATRIX2(P,ANS)
C
C     Generated by MadGraph 5 v. 1.4.5, 2012-04-20
C     By the MadGraph Development Team
C     Please visit us at https://launchpad.net/madgraph5
C
C     MadGraph StandAlone Version
C
C     Returns amplitude squared summed/avg over colors
C     and helicities
C     for the point in phase space P(0:3,NEXTERNAL)
C
C     Process: u u~ > t t~ WEIGHTED=2
C     *   Decay: t > b u d~ WEIGHTED=4
C     *   Decay: t~ > b~ mu- vm~ WEIGHTED=4
C     Process: c c~ > t t~ WEIGHTED=2
C     *   Decay: t > b u d~ WEIGHTED=4
C     *   Decay: t~ > b~ mu- vm~ WEIGHTED=4
C     Process: d d~ > t t~ WEIGHTED=2
C     *   Decay: t > b u d~ WEIGHTED=4
C     *   Decay: t~ > b~ mu- vm~ WEIGHTED=4
C     Process: s s~ > t t~ WEIGHTED=2
C     *   Decay: t > b u d~ WEIGHTED=4
C     *   Decay: t~ > b~ mu- vm~ WEIGHTED=4
C     Process: u u~ > t t~ WEIGHTED=2
C     *   Decay: t > b c s~ WEIGHTED=4
C     *   Decay: t~ > b~ mu- vm~ WEIGHTED=4
C     Process: c c~ > t t~ WEIGHTED=2
C     *   Decay: t > b c s~ WEIGHTED=4
C     *   Decay: t~ > b~ mu- vm~ WEIGHTED=4
C     Process: d d~ > t t~ WEIGHTED=2
C     *   Decay: t > b c s~ WEIGHTED=4
C     *   Decay: t~ > b~ mu- vm~ WEIGHTED=4
C     Process: s s~ > t t~ WEIGHTED=2
C     *   Decay: t > b c s~ WEIGHTED=4
C     *   Decay: t~ > b~ mu- vm~ WEIGHTED=4
C
      IMPLICIT NONE
C
C     CONSTANTS
C


      Include "../../Source/MODEL/coupl.inc"


      INTEGER    NEXTERNAL
      PARAMETER (NEXTERNAL=8)
      INTEGER                 NCOMB
      PARAMETER (             NCOMB=256)
C
C     ARGUMENTS
C
      REAL*8 P(0:3,NEXTERNAL),ANS
C
C     LOCAL VARIABLES
C

CCCCCCCCCCCCCCCCCCCCCCCCCCCCCCCCCCCCCCCCCCCCCCCCCCCCCCCCCCCCCCCCCCCCCCC
      integer i_s,init, ki
      real*8 qqb,qqb_corr,qqb_uncorr,Kqqb
      real*8 qqb_corrp
      real*8 kappa,gamma,nume
      real*8 a_s,g_s,pi
      real*8 g_f,gwsq

      real*8 p1_s(0:3),p2_s(0:3),pt(0:3),ptb(0:3)
      real*8 pb(0:3),peb(0:3),pne(0:3)
```

```
      real*8 pbb(0:3),pm(0:3),pnm(0:3)
      real*8 p0(0:3),pwp(0:3),pwm(0:3)

      real*8 dbpnp,dbana,dtpla,dtplp,dtala,dtalp,dp1p2,dlpla
      real*8 dp1tp,dp2tp,dtpta,dp1lp,dp1la,dp2lp,dp2la

      real*8 dotp
      real*8 tsq,tbsq,wpsq,wmsq
      real*8 m_b,m_w,gam_w,m_z,gam_z,m_t,gam_t,m_h,gam_h
      real*8 m_wc, wmass, tmass, wwidth, twidth

CCCCCCCC Bernreuther
      DOUBLE PRECISION prod1,prod2,prod3,prod4,quot1,quot2
      DOUBLE PRECISION p45(0:3), p78(0:3),p9(0:3),p10(0:3)
      INTEGER i1
      DOUBLE PRECISION wfak,fqq

      double complex sp810,sp19,sp81,sp29,sp82
      double complex sm102,sm94,sm24,sm101,sm14

      double complex sp,sm,tq1,tq2

      DOUBLE PRECISION mt2, Kfak, alpha, sw2

CCCCCCCCCCCCCCCCCCCCC


      parameter(pi=3.141592654d0)
C      parameter(a_s=0.1300)
      parameter(g_f=1.16639d-5)

      parameter(kappa=1.0d0)




c------- kappa=1 is the full for correct matrix element sq(UD+DU in off-diagonal
c                basis including interference.
c        kappa=0 is the no spin correlation matrix element sq (UD+DU+UU+DD)
c        kappa=-1 is (2*kappa=0 minus kappa=1) that is an approx to UU+DD valid for Parke matrix
elements.
C-----------------------------------------------------------------------

      data init/0/
CCCCCCCCCCCCCCCCCCCCCCCCCC


      INTEGER NHEL(NEXTERNAL,NCOMB),NTRY
      REAL*8 T
      REAL*8 MATRIX2
      INTEGER IHEL,IDEN, I
      INTEGER JC(NEXTERNAL)
      LOGICAL GOODHEL(NCOMB)
      DATA NTRY/0/
      DATA GOODHEL/NCOMB*.FALSE./
      DATA (NHEL(I,   1),I=1,8) /-1,-1,-1,-1,-1,-1,-1,-1/
      DATA (NHEL(I,   2),I=1,8) /-1,-1,-1,-1,-1,-1,-1, 1/
      DATA (NHEL(I,   3),I=1,8) /-1,-1,-1,-1,-1,-1, 1,-1/
      DATA (NHEL(I,   4),I=1,8) /-1,-1,-1,-1,-1,-1, 1, 1/
      DATA (NHEL(I,   5),I=1,8) /-1,-1,-1,-1,-1, 1,-1,-1/
      DATA (NHEL(I,   6),I=1,8) /-1,-1,-1,-1,-1, 1,-1, 1/
      DATA (NHEL(I,   7),I=1,8) /-1,-1,-1,-1,-1, 1, 1,-1/
      DATA (NHEL(I,   8),I=1,8) /-1,-1,-1,-1,-1, 1, 1, 1/
      DATA (NHEL(I,   9),I=1,8) /-1,-1,-1,-1, 1,-1,-1,-1/
      DATA (NHEL(I,  10),I=1,8) /-1,-1,-1,-1, 1,-1,-1, 1/
      DATA (NHEL(I,  11),I=1,8) /-1,-1,-1,-1, 1,-1, 1,-1/
      DATA (NHEL(I,  12),I=1,8) /-1,-1,-1,-1, 1,-1, 1, 1/
```

```
      DATA (NHEL(I,  13),I=1,8) /-1,-1,-1,-1, 1, 1,-1,-1/
      DATA (NHEL(I,  14),I=1,8) /-1,-1,-1,-1, 1, 1,-1, 1/
      DATA (NHEL(I,  15),I=1,8) /-1,-1,-1,-1, 1, 1, 1,-1/
      DATA (NHEL(I,  16),I=1,8) /-1,-1,-1,-1, 1, 1, 1, 1/
      DATA (NHEL(I,  17),I=1,8) /-1,-1,-1, 1,-1,-1,-1,-1/
      DATA (NHEL(I,  18),I=1,8) /-1,-1,-1, 1,-1,-1,-1, 1/
      DATA (NHEL(I,  19),I=1,8) /-1,-1,-1, 1,-1,-1, 1,-1/
      DATA (NHEL(I,  20),I=1,8) /-1,-1,-1, 1,-1,-1, 1, 1/
      DATA (NHEL(I,  21),I=1,8) /-1,-1,-1, 1,-1, 1,-1,-1/
      DATA (NHEL(I,  22),I=1,8) /-1,-1,-1, 1,-1, 1,-1, 1/
      DATA (NHEL(I,  23),I=1,8) /-1,-1,-1, 1,-1, 1, 1,-1/
      DATA (NHEL(I,  24),I=1,8) /-1,-1,-1, 1,-1, 1, 1, 1/
      DATA (NHEL(I,  25),I=1,8) /-1,-1,-1, 1, 1,-1,-1,-1/
      DATA (NHEL(I,  26),I=1,8) /-1,-1,-1, 1, 1,-1,-1, 1/
      DATA (NHEL(I,  27),I=1,8) /-1,-1,-1, 1, 1,-1, 1,-1/
      DATA (NHEL(I,  28),I=1,8) /-1,-1,-1, 1, 1,-1, 1, 1/
      DATA (NHEL(I,  29),I=1,8) /-1,-1,-1, 1, 1, 1,-1,-1/
      DATA (NHEL(I,  30),I=1,8) /-1,-1,-1, 1, 1, 1,-1, 1/
      DATA (NHEL(I,  31),I=1,8) /-1,-1,-1, 1, 1, 1, 1,-1/
      DATA (NHEL(I,  32),I=1,8) /-1,-1,-1, 1, 1, 1, 1, 1/
      DATA (NHEL(I,  33),I=1,8) /-1,-1, 1,-1,-1,-1,-1,-1/
      DATA (NHEL(I,  34),I=1,8) /-1,-1, 1,-1,-1,-1,-1, 1/
      DATA (NHEL(I,  35),I=1,8) /-1,-1, 1,-1,-1,-1, 1,-1/
      DATA (NHEL(I,  36),I=1,8) /-1,-1, 1,-1,-1,-1, 1, 1/
      DATA (NHEL(I,  37),I=1,8) /-1,-1, 1,-1,-1, 1,-1,-1/
      DATA (NHEL(I,  38),I=1,8) /-1,-1, 1,-1,-1, 1,-1, 1/
      DATA (NHEL(I,  39),I=1,8) /-1,-1, 1,-1,-1, 1, 1,-1/
      DATA (NHEL(I,  40),I=1,8) /-1,-1, 1,-1,-1, 1, 1, 1/
      DATA (NHEL(I,  41),I=1,8) /-1,-1, 1,-1, 1,-1,-1,-1/
      DATA (NHEL(I,  42),I=1,8) /-1,-1, 1,-1, 1,-1,-1, 1/
      DATA (NHEL(I,  43),I=1,8) /-1,-1, 1,-1, 1,-1, 1,-1/
      DATA (NHEL(I,  44),I=1,8) /-1,-1, 1,-1, 1,-1, 1, 1/
      DATA (NHEL(I,  45),I=1,8) /-1,-1, 1,-1, 1, 1,-1,-1/
      DATA (NHEL(I,  46),I=1,8) /-1,-1, 1,-1, 1, 1,-1, 1/
      DATA (NHEL(I,  47),I=1,8) /-1,-1, 1,-1, 1, 1, 1,-1/
      DATA (NHEL(I,  48),I=1,8) /-1,-1, 1,-1, 1, 1, 1, 1/
      DATA (NHEL(I,  49),I=1,8) /-1,-1, 1, 1,-1,-1,-1,-1/
      DATA (NHEL(I,  50),I=1,8) /-1,-1, 1, 1,-1,-1,-1, 1/
      DATA (NHEL(I,  51),I=1,8) /-1,-1, 1, 1,-1,-1, 1,-1/
      DATA (NHEL(I,  52),I=1,8) /-1,-1, 1, 1,-1,-1, 1, 1/
      DATA (NHEL(I,  53),I=1,8) /-1,-1, 1, 1,-1, 1,-1,-1/
      DATA (NHEL(I,  54),I=1,8) /-1,-1, 1, 1,-1, 1,-1, 1/
      DATA (NHEL(I,  55),I=1,8) /-1,-1, 1, 1,-1, 1, 1,-1/
      DATA (NHEL(I,  56),I=1,8) /-1,-1, 1, 1,-1, 1, 1, 1/
      DATA (NHEL(I,  57),I=1,8) /-1,-1, 1, 1, 1,-1,-1,-1/
      DATA (NHEL(I,  58),I=1,8) /-1,-1, 1, 1, 1,-1,-1, 1/
      DATA (NHEL(I,  59),I=1,8) /-1,-1, 1, 1, 1,-1, 1,-1/
      DATA (NHEL(I,  60),I=1,8) /-1,-1, 1, 1, 1,-1, 1, 1/
      DATA (NHEL(I,  61),I=1,8) /-1,-1, 1, 1, 1, 1,-1,-1/
      DATA (NHEL(I,  62),I=1,8) /-1,-1, 1, 1, 1, 1,-1, 1/
      DATA (NHEL(I,  63),I=1,8) /-1,-1, 1, 1, 1, 1, 1,-1/
      DATA (NHEL(I,  64),I=1,8) /-1,-1, 1, 1, 1, 1, 1, 1/
      DATA (NHEL(I,  65),I=1,8) /-1, 1,-1,-1,-1,-1,-1,-1/
      DATA (NHEL(I,  66),I=1,8) /-1, 1,-1,-1,-1,-1,-1, 1/
      DATA (NHEL(I,  67),I=1,8) /-1, 1,-1,-1,-1,-1, 1,-1/
      DATA (NHEL(I,  68),I=1,8) /-1, 1,-1,-1,-1,-1, 1, 1/
      DATA (NHEL(I,  69),I=1,8) /-1, 1,-1,-1,-1, 1,-1,-1/
      DATA (NHEL(I,  70),I=1,8) /-1, 1,-1,-1,-1, 1,-1, 1/
      DATA (NHEL(I,  71),I=1,8) /-1, 1,-1,-1,-1, 1, 1,-1/
      DATA (NHEL(I,  72),I=1,8) /-1, 1,-1,-1,-1, 1, 1, 1/
      DATA (NHEL(I,  73),I=1,8) /-1, 1,-1,-1, 1,-1,-1,-1/
      DATA (NHEL(I,  74),I=1,8) /-1, 1,-1,-1, 1,-1,-1, 1/
      DATA (NHEL(I,  75),I=1,8) /-1, 1,-1,-1, 1,-1, 1,-1/
      DATA (NHEL(I,  76),I=1,8) /-1, 1,-1,-1, 1,-1, 1, 1/
      DATA (NHEL(I,  77),I=1,8) /-1, 1,-1,-1, 1, 1,-1,-1/
      DATA (NHEL(I,  78),I=1,8) /-1, 1,-1,-1, 1, 1,-1, 1/
      DATA (NHEL(I,  79),I=1,8) /-1, 1,-1,-1, 1, 1, 1,-1/
```

```
      DATA (NHEL(I,  80),I=1,8) /-1, 1,-1,-1, 1, 1, 1, 1/
      DATA (NHEL(I,  81),I=1,8) /-1, 1,-1, 1,-1,-1,-1,-1/
      DATA (NHEL(I,  82),I=1,8) /-1, 1,-1, 1,-1,-1,-1, 1/
      DATA (NHEL(I,  83),I=1,8) /-1, 1,-1, 1,-1,-1, 1,-1/
      DATA (NHEL(I,  84),I=1,8) /-1, 1,-1, 1,-1,-1, 1, 1/
      DATA (NHEL(I,  85),I=1,8) /-1, 1,-1, 1,-1, 1,-1,-1/
      DATA (NHEL(I,  86),I=1,8) /-1, 1,-1, 1,-1, 1,-1, 1/
      DATA (NHEL(I,  87),I=1,8) /-1, 1,-1, 1,-1, 1, 1,-1/
      DATA (NHEL(I,  88),I=1,8) /-1, 1,-1, 1,-1, 1, 1, 1/
      DATA (NHEL(I,  89),I=1,8) /-1, 1,-1, 1, 1,-1,-1,-1/
      DATA (NHEL(I,  90),I=1,8) /-1, 1,-1, 1, 1,-1,-1, 1/
      DATA (NHEL(I,  91),I=1,8) /-1, 1,-1, 1, 1,-1, 1,-1/
      DATA (NHEL(I,  92),I=1,8) /-1, 1,-1, 1, 1,-1, 1, 1/
      DATA (NHEL(I,  93),I=1,8) /-1, 1,-1, 1, 1, 1,-1,-1/
      DATA (NHEL(I,  94),I=1,8) /-1, 1,-1, 1, 1, 1,-1, 1/
      DATA (NHEL(I,  95),I=1,8) /-1, 1,-1, 1, 1, 1, 1,-1/
      DATA (NHEL(I,  96),I=1,8) /-1, 1,-1, 1, 1, 1, 1, 1/
      DATA (NHEL(I,  97),I=1,8) /-1, 1, 1,-1,-1,-1,-1,-1/
      DATA (NHEL(I,  98),I=1,8) /-1, 1, 1,-1,-1,-1,-1, 1/
      DATA (NHEL(I,  99),I=1,8) /-1, 1, 1,-1,-1,-1, 1,-1/
      DATA (NHEL(I, 100),I=1,8) /-1, 1, 1,-1,-1,-1, 1, 1/
      DATA (NHEL(I, 101),I=1,8) /-1, 1, 1,-1,-1, 1,-1,-1/
      DATA (NHEL(I, 102),I=1,8) /-1, 1, 1,-1,-1, 1,-1, 1/
      DATA (NHEL(I, 103),I=1,8) /-1, 1, 1,-1,-1, 1, 1,-1/
      DATA (NHEL(I, 104),I=1,8) /-1, 1, 1,-1,-1, 1, 1, 1/
      DATA (NHEL(I, 105),I=1,8) /-1, 1, 1,-1, 1,-1,-1,-1/
      DATA (NHEL(I, 106),I=1,8) /-1, 1, 1,-1, 1,-1,-1, 1/
      DATA (NHEL(I, 107),I=1,8) /-1, 1, 1,-1, 1,-1, 1,-1/
      DATA (NHEL(I, 108),I=1,8) /-1, 1, 1,-1, 1,-1, 1, 1/
      DATA (NHEL(I, 109),I=1,8) /-1, 1, 1,-1, 1, 1,-1,-1/
      DATA (NHEL(I, 110),I=1,8) /-1, 1, 1,-1, 1, 1,-1, 1/
      DATA (NHEL(I, 111),I=1,8) /-1, 1, 1,-1, 1, 1, 1,-1/
      DATA (NHEL(I, 112),I=1,8) /-1, 1, 1,-1, 1, 1, 1, 1/
      DATA (NHEL(I, 113),I=1,8) /-1, 1, 1, 1,-1,-1,-1,-1/
      DATA (NHEL(I, 114),I=1,8) /-1, 1, 1, 1,-1,-1,-1, 1/
      DATA (NHEL(I, 115),I=1,8) /-1, 1, 1, 1,-1,-1, 1,-1/
      DATA (NHEL(I, 116),I=1,8) /-1, 1, 1, 1,-1,-1, 1, 1/
      DATA (NHEL(I, 117),I=1,8) /-1, 1, 1, 1,-1, 1,-1,-1/
      DATA (NHEL(I, 118),I=1,8) /-1, 1, 1, 1,-1, 1,-1, 1/
      DATA (NHEL(I, 119),I=1,8) /-1, 1, 1, 1,-1, 1, 1,-1/
      DATA (NHEL(I, 120),I=1,8) /-1, 1, 1, 1,-1, 1, 1, 1/
      DATA (NHEL(I, 121),I=1,8) /-1, 1, 1, 1, 1,-1,-1,-1/
      DATA (NHEL(I, 122),I=1,8) /-1, 1, 1, 1, 1,-1,-1, 1/
      DATA (NHEL(I, 123),I=1,8) /-1, 1, 1, 1, 1,-1, 1,-1/
      DATA (NHEL(I, 124),I=1,8) /-1, 1, 1, 1, 1,-1, 1, 1/
      DATA (NHEL(I, 125),I=1,8) /-1, 1, 1, 1, 1, 1,-1,-1/
      DATA (NHEL(I, 126),I=1,8) /-1, 1, 1, 1, 1, 1,-1, 1/
      DATA (NHEL(I, 127),I=1,8) /-1, 1, 1, 1, 1, 1, 1,-1/
      DATA (NHEL(I, 128),I=1,8) /-1, 1, 1, 1, 1, 1, 1, 1/
      DATA (NHEL(I, 129),I=1,8) / 1,-1,-1,-1,-1,-1,-1,-1/
      DATA (NHEL(I, 130),I=1,8) / 1,-1,-1,-1,-1,-1,-1, 1/
      DATA (NHEL(I, 131),I=1,8) / 1,-1,-1,-1,-1,-1, 1,-1/
      DATA (NHEL(I, 132),I=1,8) / 1,-1,-1,-1,-1,-1, 1, 1/
      DATA (NHEL(I, 133),I=1,8) / 1,-1,-1,-1,-1, 1,-1,-1/
      DATA (NHEL(I, 134),I=1,8) / 1,-1,-1,-1,-1, 1,-1, 1/
      DATA (NHEL(I, 135),I=1,8) / 1,-1,-1,-1,-1, 1, 1,-1/
      DATA (NHEL(I, 136),I=1,8) / 1,-1,-1,-1,-1, 1, 1, 1/
      DATA (NHEL(I, 137),I=1,8) / 1,-1,-1,-1, 1,-1,-1,-1/
      DATA (NHEL(I, 138),I=1,8) / 1,-1,-1,-1, 1,-1,-1, 1/
      DATA (NHEL(I, 139),I=1,8) / 1,-1,-1,-1, 1,-1, 1,-1/
      DATA (NHEL(I, 140),I=1,8) / 1,-1,-1,-1, 1,-1, 1, 1/
      DATA (NHEL(I, 141),I=1,8) / 1,-1,-1,-1, 1, 1,-1,-1/
      DATA (NHEL(I, 142),I=1,8) / 1,-1,-1,-1, 1, 1,-1, 1/
      DATA (NHEL(I, 143),I=1,8) / 1,-1,-1,-1, 1, 1, 1,-1/
      DATA (NHEL(I, 144),I=1,8) / 1,-1,-1,-1, 1, 1, 1, 1/
      DATA (NHEL(I, 145),I=1,8) / 1,-1,-1, 1,-1,-1,-1,-1/
      DATA (NHEL(I, 146),I=1,8) / 1,-1,-1, 1,-1,-1,-1, 1/
```

```
      DATA (NHEL(I, 147),I=1,8) / 1,-1,-1, 1,-1,-1, 1,-1/
      DATA (NHEL(I, 148),I=1,8) / 1,-1,-1, 1,-1,-1, 1, 1/
      DATA (NHEL(I, 149),I=1,8) / 1,-1,-1, 1,-1, 1,-1,-1/
      DATA (NHEL(I, 150),I=1,8) / 1,-1,-1, 1,-1, 1,-1, 1/
      DATA (NHEL(I, 151),I=1,8) / 1,-1,-1, 1,-1, 1, 1,-1/
      DATA (NHEL(I, 152),I=1,8) / 1,-1,-1, 1,-1, 1, 1, 1/
      DATA (NHEL(I, 153),I=1,8) / 1,-1,-1, 1, 1,-1,-1,-1/
      DATA (NHEL(I, 154),I=1,8) / 1,-1,-1, 1, 1,-1,-1, 1/
      DATA (NHEL(I, 155),I=1,8) / 1,-1,-1, 1, 1,-1, 1,-1/
      DATA (NHEL(I, 156),I=1,8) / 1,-1,-1, 1, 1,-1, 1, 1/
      DATA (NHEL(I, 157),I=1,8) / 1,-1,-1, 1, 1, 1,-1,-1/
      DATA (NHEL(I, 158),I=1,8) / 1,-1,-1, 1, 1, 1,-1, 1/
      DATA (NHEL(I, 159),I=1,8) / 1,-1,-1, 1, 1, 1, 1,-1/
      DATA (NHEL(I, 160),I=1,8) / 1,-1,-1, 1, 1, 1, 1, 1/
      DATA (NHEL(I, 161),I=1,8) / 1,-1, 1,-1,-1,-1,-1,-1/
      DATA (NHEL(I, 162),I=1,8) / 1,-1, 1,-1,-1,-1,-1, 1/
      DATA (NHEL(I, 163),I=1,8) / 1,-1, 1,-1,-1,-1, 1,-1/
      DATA (NHEL(I, 164),I=1,8) / 1,-1, 1,-1,-1,-1, 1, 1/
      DATA (NHEL(I, 165),I=1,8) / 1,-1, 1,-1,-1, 1,-1,-1/
      DATA (NHEL(I, 166),I=1,8) / 1,-1, 1,-1,-1, 1,-1, 1/
      DATA (NHEL(I, 167),I=1,8) / 1,-1, 1,-1,-1, 1, 1,-1/
      DATA (NHEL(I, 168),I=1,8) / 1,-1, 1,-1,-1, 1, 1, 1/
      DATA (NHEL(I, 169),I=1,8) / 1,-1, 1,-1, 1,-1,-1,-1/
      DATA (NHEL(I, 170),I=1,8) / 1,-1, 1,-1, 1,-1,-1, 1/
      DATA (NHEL(I, 171),I=1,8) / 1,-1, 1,-1, 1,-1, 1,-1/
      DATA (NHEL(I, 172),I=1,8) / 1,-1, 1,-1, 1,-1, 1, 1/
      DATA (NHEL(I, 173),I=1,8) / 1,-1, 1,-1, 1, 1,-1,-1/
      DATA (NHEL(I, 174),I=1,8) / 1,-1, 1,-1, 1, 1,-1, 1/
      DATA (NHEL(I, 175),I=1,8) / 1,-1, 1,-1, 1, 1, 1,-1/
      DATA (NHEL(I, 176),I=1,8) / 1,-1, 1,-1, 1, 1, 1, 1/
      DATA (NHEL(I, 177),I=1,8) / 1,-1, 1, 1,-1,-1,-1,-1/
      DATA (NHEL(I, 178),I=1,8) / 1,-1, 1, 1,-1,-1,-1, 1/
      DATA (NHEL(I, 179),I=1,8) / 1,-1, 1, 1,-1,-1, 1,-1/
      DATA (NHEL(I, 180),I=1,8) / 1,-1, 1, 1,-1,-1, 1, 1/
      DATA (NHEL(I, 181),I=1,8) / 1,-1, 1, 1,-1, 1,-1,-1/
      DATA (NHEL(I, 182),I=1,8) / 1,-1, 1, 1,-1, 1,-1, 1/
      DATA (NHEL(I, 183),I=1,8) / 1,-1, 1, 1,-1, 1, 1,-1/
      DATA (NHEL(I, 184),I=1,8) / 1,-1, 1, 1,-1, 1, 1, 1/
      DATA (NHEL(I, 185),I=1,8) / 1,-1, 1, 1, 1,-1,-1,-1/
      DATA (NHEL(I, 186),I=1,8) / 1,-1, 1, 1, 1,-1,-1, 1/
      DATA (NHEL(I, 187),I=1,8) / 1,-1, 1, 1, 1,-1, 1,-1/
      DATA (NHEL(I, 188),I=1,8) / 1,-1, 1, 1, 1,-1, 1, 1/
      DATA (NHEL(I, 189),I=1,8) / 1,-1, 1, 1, 1, 1,-1,-1/
      DATA (NHEL(I, 190),I=1,8) / 1,-1, 1, 1, 1, 1,-1, 1/
      DATA (NHEL(I, 191),I=1,8) / 1,-1, 1, 1, 1, 1, 1,-1/
      DATA (NHEL(I, 192),I=1,8) / 1,-1, 1, 1, 1, 1, 1, 1/
      DATA (NHEL(I, 193),I=1,8) / 1, 1,-1,-1,-1,-1,-1,-1/
      DATA (NHEL(I, 194),I=1,8) / 1, 1,-1,-1,-1,-1,-1, 1/
      DATA (NHEL(I, 195),I=1,8) / 1, 1,-1,-1,-1,-1, 1,-1/
      DATA (NHEL(I, 196),I=1,8) / 1, 1,-1,-1,-1,-1, 1, 1/
      DATA (NHEL(I, 197),I=1,8) / 1, 1,-1,-1,-1, 1,-1,-1/
      DATA (NHEL(I, 198),I=1,8) / 1, 1,-1,-1,-1, 1,-1, 1/
      DATA (NHEL(I, 199),I=1,8) / 1, 1,-1,-1,-1, 1, 1,-1/
      DATA (NHEL(I, 200),I=1,8) / 1, 1,-1,-1,-1, 1, 1, 1/
      DATA (NHEL(I, 201),I=1,8) / 1, 1,-1,-1, 1,-1,-1,-1/
      DATA (NHEL(I, 202),I=1,8) / 1, 1,-1,-1, 1,-1,-1, 1/
      DATA (NHEL(I, 203),I=1,8) / 1, 1,-1,-1, 1,-1, 1,-1/
      DATA (NHEL(I, 204),I=1,8) / 1, 1,-1,-1, 1,-1, 1, 1/
      DATA (NHEL(I, 205),I=1,8) / 1, 1,-1,-1, 1, 1,-1,-1/
      DATA (NHEL(I, 206),I=1,8) / 1, 1,-1,-1, 1, 1,-1, 1/
      DATA (NHEL(I, 207),I=1,8) / 1, 1,-1,-1, 1, 1, 1,-1/
      DATA (NHEL(I, 208),I=1,8) / 1, 1,-1,-1, 1, 1, 1, 1/
      DATA (NHEL(I, 209),I=1,8) / 1, 1,-1, 1,-1,-1,-1,-1/
      DATA (NHEL(I, 210),I=1,8) / 1, 1,-1, 1,-1,-1,-1, 1/
      DATA (NHEL(I, 211),I=1,8) / 1, 1,-1, 1,-1,-1, 1,-1/
      DATA (NHEL(I, 212),I=1,8) / 1, 1,-1, 1,-1,-1, 1, 1/
      DATA (NHEL(I, 213),I=1,8) / 1, 1,-1, 1,-1, 1,-1,-1/
```

```
      DATA (NHEL(I, 214),I=1,8) / 1, 1,-1, 1,-1, 1,-1, 1/
      DATA (NHEL(I, 215),I=1,8) / 1, 1,-1, 1,-1, 1, 1,-1/
      DATA (NHEL(I, 216),I=1,8) / 1, 1,-1, 1,-1, 1, 1, 1/
      DATA (NHEL(I, 217),I=1,8) / 1, 1,-1, 1, 1,-1,-1,-1/
      DATA (NHEL(I, 218),I=1,8) / 1, 1,-1, 1, 1,-1,-1, 1/
      DATA (NHEL(I, 219),I=1,8) / 1, 1,-1, 1, 1,-1, 1,-1/
      DATA (NHEL(I, 220),I=1,8) / 1, 1,-1, 1, 1,-1, 1, 1/
      DATA (NHEL(I, 221),I=1,8) / 1, 1,-1, 1, 1, 1,-1,-1/
      DATA (NHEL(I, 222),I=1,8) / 1, 1,-1, 1, 1, 1,-1, 1/
      DATA (NHEL(I, 223),I=1,8) / 1, 1,-1, 1, 1, 1, 1,-1/
      DATA (NHEL(I, 224),I=1,8) / 1, 1,-1, 1, 1, 1, 1, 1/
      DATA (NHEL(I, 225),I=1,8) / 1, 1, 1,-1,-1,-1,-1,-1/
      DATA (NHEL(I, 226),I=1,8) / 1, 1, 1,-1,-1,-1,-1, 1/
      DATA (NHEL(I, 227),I=1,8) / 1, 1, 1,-1,-1,-1, 1,-1/
      DATA (NHEL(I, 228),I=1,8) / 1, 1, 1,-1,-1,-1, 1, 1/
      DATA (NHEL(I, 229),I=1,8) / 1, 1, 1,-1,-1, 1,-1,-1/
      DATA (NHEL(I, 230),I=1,8) / 1, 1, 1,-1,-1, 1,-1, 1/
      DATA (NHEL(I, 231),I=1,8) / 1, 1, 1,-1,-1, 1, 1,-1/
      DATA (NHEL(I, 232),I=1,8) / 1, 1, 1,-1,-1, 1, 1, 1/
      DATA (NHEL(I, 233),I=1,8) / 1, 1, 1,-1, 1,-1,-1,-1/
      DATA (NHEL(I, 234),I=1,8) / 1, 1, 1,-1, 1,-1,-1, 1/
      DATA (NHEL(I, 235),I=1,8) / 1, 1, 1,-1, 1,-1, 1,-1/
      DATA (NHEL(I, 236),I=1,8) / 1, 1, 1,-1, 1,-1, 1, 1/
      DATA (NHEL(I, 237),I=1,8) / 1, 1, 1,-1, 1, 1,-1,-1/
      DATA (NHEL(I, 238),I=1,8) / 1, 1, 1,-1, 1, 1,-1, 1/
      DATA (NHEL(I, 239),I=1,8) / 1, 1, 1,-1, 1, 1, 1,-1/
      DATA (NHEL(I, 240),I=1,8) / 1, 1, 1,-1, 1, 1, 1, 1/
      DATA (NHEL(I, 241),I=1,8) / 1, 1, 1, 1,-1,-1,-1,-1/
      DATA (NHEL(I, 242),I=1,8) / 1, 1, 1, 1,-1,-1,-1, 1/
      DATA (NHEL(I, 243),I=1,8) / 1, 1, 1, 1,-1,-1, 1,-1/
      DATA (NHEL(I, 244),I=1,8) / 1, 1, 1, 1,-1,-1, 1, 1/
      DATA (NHEL(I, 245),I=1,8) / 1, 1, 1, 1,-1, 1,-1,-1/
      DATA (NHEL(I, 246),I=1,8) / 1, 1, 1, 1,-1, 1,-1, 1/
      DATA (NHEL(I, 247),I=1,8) / 1, 1, 1, 1,-1, 1, 1,-1/
      DATA (NHEL(I, 248),I=1,8) / 1, 1, 1, 1,-1, 1, 1, 1/
      DATA (NHEL(I, 249),I=1,8) / 1, 1, 1, 1, 1,-1,-1,-1/
      DATA (NHEL(I, 250),I=1,8) / 1, 1, 1, 1, 1,-1,-1, 1/
      DATA (NHEL(I, 251),I=1,8) / 1, 1, 1, 1, 1,-1, 1,-1/
      DATA (NHEL(I, 252),I=1,8) / 1, 1, 1, 1, 1,-1, 1, 1/
      DATA (NHEL(I, 253),I=1,8) / 1, 1, 1, 1, 1, 1,-1,-1/
      DATA (NHEL(I, 254),I=1,8) / 1, 1, 1, 1, 1, 1,-1, 1/
      DATA (NHEL(I, 255),I=1,8) / 1, 1, 1, 1, 1, 1, 1,-1/
      DATA (NHEL(I, 256),I=1,8) / 1, 1, 1, 1, 1, 1, 1, 1/
      DATA IDEN/36/
C     ----------
C     BEGIN CODE
C     ----------
      NTRY=NTRY+1
      DO IHEL=1,NEXTERNAL
        JC(IHEL) = +1
      ENDDO
      ANS = 0D0
      DO IHEL=1,NCOMB
        IF (GOODHEL(IHEL) .OR. NTRY .LT. 2) THEN
          T=MATRIX2(P ,NHEL(1,IHEL),JC(1))
          ANS=ANS+T
          IF (T .NE. 0D0 .AND. .NOT.    GOODHEL(IHEL)) THEN
            GOODHEL(IHEL)=.TRUE.
          ENDIF
        ENDIF
      ENDDO
      ANS=ANS/DBLE(IDEN)

      qqb_corr = ANS
CC      END

cccc new MEs
```

```
      a_s=G**2/(4.d0*pi)
      sw2=1.000000D+00-MW**2/MZ**2
      alpha=1.d0/1.325070D+02

      wmass = MW
      g_s=dsqrt(4.d0*pi*a_s)
      gwsq=4.d0*dsqrt(2.d0)*wmass**2*g_f

      Kfak = (4*pi*a_s)**2*(4*pi*alpha)**4/sw2**4


      if(init.eq.0)then
         init=1
      endif

      do i_s=0,3
         p1_s(i_s)=P(i_s,1)
         p2_s(i_s)=P(i_s,2)

         pb(i_s)=P(i_s,3)
         peb(i_s)=P(i_s,5)
         pne(i_s)=P(i_s,4)
         pbb(i_s)=P(i_s,6)
         pm(i_s)=P(i_s,7)
         pnm(i_s)=P(i_s,8)


         pwp(i_s)=peb(i_s)+pne(i_s)
         pwm(i_s)=pm(i_s)+pnm(i_s)
         pt(i_s)=pb(i_s)+peb(i_s)+pne(i_s)
         ptb(i_s)=pbb(i_s)+pm(i_s)+pnm(i_s)
      enddo

      dbpnp=dotp(pb,pne)
      dbana=dotp(pbb,pnm)
      dtpla=dotp(pt,peb)
      dtplp=dotp(pt,pm)
      dtala=dotp(ptb,peb)
      dtalp=dotp(ptb,pm)
      dp1p2=dotp(p1_s,p2_s)
      dlpla=dotp(peb,pm)
      dp1tp=dotp(p1_s,pt)
      dp2tp=dotp(p2_s,pt)
      dtpta=dotp(pt,ptb)
      dp1lp=dotp(p1_s,pm)
      dp1la=dotp(p1_s,peb)
      dp2lp=dotp(p2_s,pm)
      dp2la=dotp(p2_s,peb)
      wpsq=2.d0*dotp(peb,pne)
      wmsq=2.d0*dotp(pm,pnm)

      m_wc = sqrt((wpsq+wmsq)/2.0)

      tsq=dotp(pt,pt)
      tbsq=dotp(ptb,ptb)

      m_t = sqrt((dotp(pt,pt)+dotp(ptb,ptb))/2.0)

      wwidth = WW
      twidth = WT

      tmass = MT
      mt2 = MT**2

CCCCC Bernreuther CCCCCCCCCCCCCCCCCCCCCCCCCCCCCCCCCCCCCCCCC
      prod1=tsq
```

```
      prod2=dotp(pt,peb)
      prod3=tbsq
      prod4=dotp(ptb,pm)

      quot1=prod1/(2*prod2)
      quot2=prod3/(2*prod4)

      do i1=0,3

         p10(i1) = pt(i1) - peb(i1)*quot1
         p9(i1) = ptb(i1) - pm(i1)*quot2

         p45(i1) = pm(i1) + pnm(i1)
         p78(i1) = pne(i1) + peb(i1)

      enddo

      sp19=sp(p1_s,p9)
      sp810=sp(peb,p10)
      sp81=sp(peb,p1_s)
      sp29=sp(p2_s,p9)
      sp82=sp(peb,p2_s)

      sm102=-dconjg(sp(p10,p2_s))
      sm94=-dconjg(sp(p9,pm))
      sm24=-dconjg(sp(p2_s,pm))
      sm101=-dconjg(sp(p10,p1_s))
      sm14=-dconjg(sp(p1_s,pm))


      wfak= dotp(pbb,pnm)*dotp(pb,pne)

c     helicity amps.: q q-bar -> .....


c      if(kappa.eq.1.0d0)tq1= (-sp810*sm102*sp19*sm94+mt2*sp81*sm24)
c      if(kappa.eq.1.0d0)tq2= (-sp810*sm101*sp29*sm94+mt2*sp82*sm14)

c      qqb_corr = 0.0d0
c      if(kappa.eq.1.0d0)fqq = (3*8/9.d0)
c     > *((cdabs(tq1)**2 + cdabs(tq2)**2))/(2.*dp1p2)**2
c      if(kappa.eq.1.0d0)qqb_corr = fqq
CCCCCCCCCCCCCCCCCCCCCCCCCCCCCCCCCCCCCCCCCCCCCCCCCCCCCCCCCCCCCCCCCCCC
      qqb_uncorr = 0.0d0
CCCCCCCCCCCCCCCC Bernreuther CCCCCCCCCCCCCCCCCCCCCCCCCCCCCCCCCCCCCCCC
       if(kappa.eq.0.0d0) qqb_uncorr=dotp(pt,peb)*dotp(ptb,pm)
     >    *(dotp(p1_s,pt)*dotp(ptb,p2_s)+dotp(pt,p2_s)*dotp(ptb,p1_s)
     >    +mt2*dotp(p1_s,p2_s))/dp1p2**2
CCCCCCCCCCCCCCCCCCCCCCCCCCCCCCCCCCCCCCCCCCCCCCCCCCCCCCCCCCCCCCCCCCCC

c          qqb=(1.d0-kappa)*qqb_uncorr+kappa*qqb_corr

           Kqqb = 0D0
           qqb_uncorr = qqb_uncorr*Kfak*dbpnp*dbana
     >  /((tsq-tmass**2)**2+(tmass*twidth)**2)
     >  /((tbsq-tmass**2)**2+(tmass*twidth)**2)
     >  /((wpsq-wmass**2)**2+(wmass*wwidth)**2)
     >  /((wmsq-wmass**2)**2+(wmass*wwidth)**2)

        ANS=(1.d0-kappa)*qqb_uncorr+kappa*qqb_corr

      END


      REAL*8 FUNCTION MATRIX2(P,NHEL,IC)
C
C     Generated by MadGraph 5 v. 1.4.5, 2012-04-20
```

```
C     By the MadGraph Development Team
C     Please visit us at https://launchpad.net/madgraph5
C
C     Returns amplitude squared summed/avg over colors
C     for the point with external lines W(0:6,NEXTERNAL)
C
C     Process: u u~ > t t~ WEIGHTED=2
C     *   Decay: t > b u d~ WEIGHTED=4
C     *   Decay: t~ > b~ mu- vm~ WEIGHTED=4
C     Process: c c~ > t t~ WEIGHTED=2
C     *   Decay: t > b u d~ WEIGHTED=4
C     *   Decay: t~ > b~ mu- vm~ WEIGHTED=4
C     Process: d d~ > t t~ WEIGHTED=2
C     *   Decay: t > b u d~ WEIGHTED=4
C     *   Decay: t~ > b~ mu- vm~ WEIGHTED=4
C     Process: s s~ > t t~ WEIGHTED=2
C     *   Decay: t > b u d~ WEIGHTED=4
C     *   Decay: t~ > b~ mu- vm~ WEIGHTED=4
C     Process: u u~ > t t~ WEIGHTED=2
C     *   Decay: t > b c s~ WEIGHTED=4
C     *   Decay: t~ > b~ mu- vm~ WEIGHTED=4
C     Process: c c~ > t t~ WEIGHTED=2
C     *   Decay: t > b c s~ WEIGHTED=4
C     *   Decay: t~ > b~ mu- vm~ WEIGHTED=4
C     Process: d d~ > t t~ WEIGHTED=2
C     *   Decay: t > b c s~ WEIGHTED=4
C     *   Decay: t~ > b~ mu- vm~ WEIGHTED=4
C     Process: s s~ > t t~ WEIGHTED=2
C     *   Decay: t > b c s~ WEIGHTED=4
C     *   Decay: t~ > b~ mu- vm~ WEIGHTED=4
C
      IMPLICIT NONE
C
C     CONSTANTS
C
      INTEGER    NGRAPHS
      PARAMETER (NGRAPHS=1)
      INTEGER    NEXTERNAL
      PARAMETER (NEXTERNAL=8)
      INTEGER    NWAVEFUNCS, NCOLOR
      PARAMETER (NWAVEFUNCS=13, NCOLOR=2)
      REAL*8     ZERO
      PARAMETER (ZERO=0D0)
      COMPLEX*16 IMAG1
      PARAMETER (IMAG1=(0D0,1D0))
C
C     ARGUMENTS
C
      REAL*8 P(0:3,NEXTERNAL)
      INTEGER NHEL(NEXTERNAL), IC(NEXTERNAL)
C
C     LOCAL VARIABLES
C
      INTEGER I,J
      COMPLEX*16 ZTEMP
      REAL*8 DENOM(NCOLOR), CF(NCOLOR,NCOLOR)
      COMPLEX*16 AMP(NGRAPHS), JAMP(NCOLOR)
      COMPLEX*16 W(18,NWAVEFUNCS)
      COMPLEX*16 DUM0,DUM1
      DATA DUM0, DUM1/(0D0, 0D0), (1D0, 0D0)/
C
C     GLOBAL VARIABLES
C
      INCLUDE 'coupl.inc'
C
C     COLOR DATA
C
```

```
      DATA DENOM(1)/1/
      DATA (CF(I,  1),I=  1,  2) /   27,    9/
C     1 T(2,1) T(3,6) T(4,5)
      DATA DENOM(2)/1/
      DATA (CF(I,  2),I=  1,  2) /    9,   27/
C     1 T(2,6) T(3,1) T(4,5)
C     ----------
C     BEGIN CODE
C     ----------
      CALL IXXXXX(P(0,1),ZERO,NHEL(1),+1*IC(1),W(1,1))
      CALL OXXXXX(P(0,2),ZERO,NHEL(2),-1*IC(2),W(1,2))
      CALL OXXXXX(P(0,3),MB,NHEL(3),+1*IC(3),W(1,3))
      CALL OXXXXX(P(0,4),ZERO,NHEL(4),+1*IC(4),W(1,4))
      CALL IXXXXX(P(0,5),ZERO,NHEL(5),-1*IC(5),W(1,5))
      CALL FFV2_3(W(1,5),W(1,4),GC_100,MW, WW, W(1,6))
      CALL FFV2_1(W(1,3),W(1,6),GC_100,MT, WT, W(1,7))
      CALL IXXXXX(P(0,6),MB,NHEL(6),-1*IC(6),W(1,8))
      CALL OXXXXX(P(0,7),ZERO,NHEL(7),+1*IC(7),W(1,9))
      CALL IXXXXX(P(0,8),ZERO,NHEL(8),-1*IC(8),W(1,10))
      CALL FFV2_3(W(1,10),W(1,9),GC_100,MW, WW, W(1,11))
      CALL FFV2_2(W(1,8),W(1,11),GC_100,MT, WT, W(1,12))
      CALL FFV1_3(W(1,1),W(1,2),GC_11,ZERO, ZERO, W(1,13))
C     Amplitude(s) for diagram number 1
      CALL FFV1_0(W(1,12),W(1,7),W(1,13),GC_11,AMP(1))
      JAMP(1)=+1./2.*(+1./3.*AMP(1))
      JAMP(2)=+1./2.*(-AMP(1))

      MATRIX2 = 0.D0
      DO I = 1, NCOLOR
        ZTEMP = (0.D0,0.D0)
        DO J = 1, NCOLOR
          ZTEMP = ZTEMP + CF(J,I)*JAMP(J)
        ENDDO
        MATRIX2 = MATRIX2+ZTEMP*DCONJG(JAMP(I))/DENOM(I)
      ENDDO
      END



CCCC THESE FUNCTIONS ARE ALREADY DEFINED MATRIX2.f CCCCCCCCC
C      real*8 function dotp(firstp,secondp)
Cc----------  dot product of two momenta
C      implicit none
C      real*8 firstp(0:3),secondp(0:3)
C      dotp=firstp(0)*secondp(0)-firstp(1)*secondp(1)
C     > -firstp(2)*secondp(2)-firstp(3)*secondp(3)
C      return
C      end




      DOUBLE COMPLEX FUNCTION sp(v1,v2)
CC     ***** computes spinor product s+ (Bernreuther)

      IMPLICIT NONE

      DOUBLE PRECISION v1(0:3),v2(0:3)
      double precision v201,v101,r1,r2,re12,im12

      if((v1(0).eq.v1(1)).or.(v2(0).eq.v2(1))) then
      else
        v201=v2(0)-v2(1)
        v101=v1(0)-v1(1)
        r1=dsqrt(v201/v101)
```

```
        r2=dsqrt(v101/v201)
        re12=v1(2)*r1-v2(2)*r2
        im12=v1(3)*r1-v2(3)*r2
        sp=dcmplx(re12,im12)
      end if

      RETURN
      END
CCCCCCCCCCCCCCCCCCCCCCCCCCCCCCCCCCCCCCCCCCCCCCCCCCCCCCCCCCCCCCCCCCCCC

      double precision function dotp(firstp,secondp)
c----------  dot product of two
momenta
      implicit none
      double precision firstp(0:3),secondp(0:3)
      dotp=firstp(0)*secondp(0)-firstp(1)*secondp(1)
     > -firstp(2)*secondp(2)-firstp(3)*secondp(3)
      return
      end
```

A.3 MadWeight Settings

In the likelihood calculations, the MadWeight directories have been produced with the following process:

```
set group_subprocesses Auto
set ignore_six_quark_processes False
set loop_optimized_output True
set gauge unitary
set complex_mass_scheme False
import model sm
define p = g u c d s u~ c~ d~ s~
define j = g u c d s u~ c~ d~ s~
define l+ = e+ mu+
define l- = e- mu-
define vl = ve vm vt
define vl~ = ve~ vm~ vt~

generate p p > t t~ , t > b j j, t~ > b~ mu- vm~
generate p p > t~ t, t > b mu+ vm, t~ > b~ j j
```

After production of the MadWeight directories, the ME have been modified to distinguish between the SM and uncorrelated hypothesis.

The likelihood calculation is configured in the MadWeight.dat card. The settings used in the analysis are listed below in fig. A.1.

```
Block MW_Run
#   TAG                 VALUE                   UTILITY
     name                 fermi    # name for the run
     cluster              0       # 0:single machine, 1: condor, 2: SGE
                                  # 3: Bash cluster, 4: multiprocessor, 5: qsub
                                  # For more info, see the wiki
     queue       'madgraph==True' # queue condition (usage depend of the cluster)
     nb_exp_events        50       # number of experimental events to consider
     write_log            T       # avoid writting of a lot of log files
     normalize            T       # normalizes weight  (1/sigma prefactor)
     ME_int_points        1       # number of points in MadEvent integration
     MW_int_points        12000       #number of points in MadWeight integration
     use_cut              F       # use the cut defined in run_card.dat
     bw_cut               F       # use the BW cut
     nwa                  F       # T= use narrow width approximation
     isr                  1       # isr=0 : ignore ISR effect (except if all FS particles are visible)
                                  # isr=1 : correct kinematic based on reconstructed Pt(isr)
                                  # isr=2 : correct kinematic based on reconstructed Pt(isr)
                                  #         + boost the weight to the CMS frame
     weight_format        %(lhco_event)s\t%(value)s\t%(error)s\n
#*********************************************************************
##                  define the different param_card's                ##
#*********************************************************************
Block MW_parameter
#   TAG      VALUE                    UTILITY
    mode         0           #    type of input
                             #    0 : inputs are read from the cards: param_card_1.dat, param_card_2.dat,...
                             #    1 : redefines some values from param_card.dat according to the form below
                             #    2 : same but the value for different parameters are modified simultaneously
#*********************************************************************
##                            Permutations                           ##
#*********************************************************************
Block MW_perm
#   TAG           VALUE                   UTILITY
     permutation  T         # make permutation
     bjet_is_jet  F         # consider permutation between b-jets and light jets
```

Figure A.1: MadWeight.dat card

File: /home/kelly/Matrix_Elements/param_card.dat Page 1 of 1

```
Block mass
    5 4.700000e+00 # MB
    6 1.725000e+02 # MT
   15 1.777000e+00 # MTA
   23 9.118800e+01 # MZ
   25 1.200000e+02 # MH
  1 0.000000 # d : 0.0
  2 0.000000 # u : 0.0
  3 0.000000 # s : 0.0
  4 0.000000 # c : 0.0
  11 0.000000 # e- : 0.0
  12 0.000000 # ve : 0.0
  13 0.000000 # mu- : 0.0
  14 0.000000 # vm : 0.0
  16 0.000000 # vt : 0.0
  21 0.000000 # g : 0.0
  22 0.000000 # a : 0.0
  24 80.419002 # w+ : cmath.sqrt(MZ__exp__2/2. + cmath.sqrt(MZ__exp__4/4. - (aEW*cmath.pi*MZ__exp__2)/
(Gf*sqrt__2)))

Block sminputs
    1 1.325070e+02 # aEWM1
    2 1.166390e-05 # Gf
    3 1.180000e-01 # aS

Block yukawa
    5 4.200000e+00 # ymb
    6 1.645000e+02 # ymt
   15 1.777000e+00 # ymtau

DECAY   6 1.491500e+00 # WT
DECAY  23 2.441404e+00 # WZ
DECAY  24 2.047600e+00 # WW
DECAY  25 5.753088e-03 # WH
DECAY  1 0.000000 # d : 0.0
DECAY  2 0.000000 # u : 0.0
DECAY  3 0.000000 # s : 0.0
DECAY  4 0.000000 # c : 0.0
DECAY  5 0.000000 # b : 0.0
DECAY  11 0.000000 # e- : 0.0
DECAY  12 0.000000 # ve : 0.0
DECAY  13 0.000000 # mu- : 0.0
DECAY  14 0.000000 # vm : 0.0
DECAY  15 0.000000 # ta- : 0.0
DECAY  16 0.000000 # vt : 0.0
DECAY  21 0.000000 # g : 0.0
DECAY  22 0.000000 # a : 0.0
```

Figure A.2: param_card.dat card

The parameters used in the calculations are listed the param_card.dat shown in fig. A.2.

There are no cuts placed on the phase space integration. Other relevan settings are listed in the run_card.dat shown in fig. A.3.

```
#*********************************************************************
# Collider type and energy                                           *
# lpp: 0=No PDF, 1=proton, -1=antiproton, 2=photon from proton,      *
#                                         3=photon from electron     *
#*********************************************************************
        1     = lpp1    ! beam 1 type
        1     = lpp2    ! beam 2 type
     4000     = ebeam1  ! beam 1 total energy in GeV
     4000     = ebeam2  ! beam 2 total energy in GeV
#*********************************************************************
# Beam polarization from -100 (left-handed) to 100 (right-handed)    *
#*********************************************************************
        0     = polbeam1 ! beam polarization for beam 1
        0     = polbeam2 ! beam polarization for beam 2
#*********************************************************************
# PDF CHOICE: this automatically fixes also alpha_s and its evol.    *
#*********************************************************************
 'cteq6l1'    = pdlabel     ! PDF set
#*********************************************************************
# Renormalization and factorization scales                           *
#*********************************************************************
 T        = fixed_ren_scale  ! if .true. use fixed ren scale
 T        = fixed_fac_scale  ! if .true. use fixed fac scale
 91.1880  = scale            ! fixed ren scale
 91.1880  = dsqrt_q2fact1    ! fixed fact scale for pdf1
 91.1880  = dsqrt_q2fact2    ! fixed fact scale for pdf2
 1        = scalefact        ! scale factor for event-by-event scales
```

Figure A.3: run_card.dat card

A.4 Additional HitFit Performance Plots

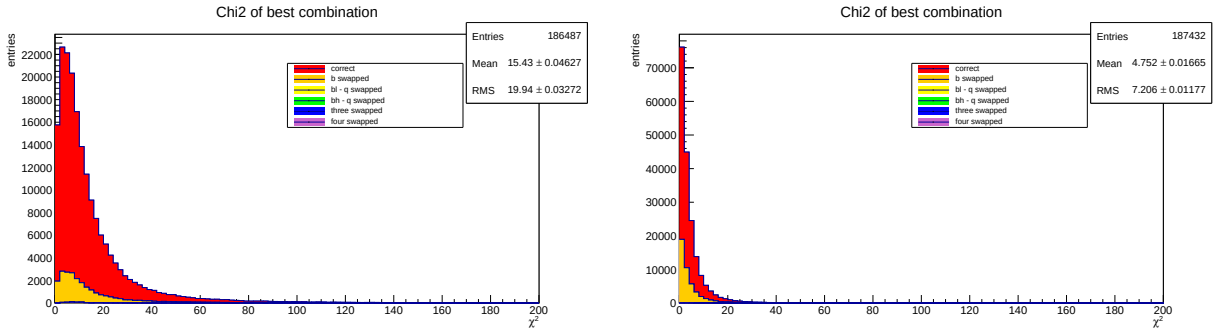

(a) $t\bar{t}$ spin-uncorrelated events with $m_t = 173$ GeV constraint.

(b) $t\bar{t}$ spin-uncorrelated events.

Figure A.4: χ^2 distribution of the best permutation returned by HitFit, showing the comparison between using the $m_t = 173$ GeV constraint (left) and without it (right). The colour coding indicates how the best permutation relates to the true jet-parton permutation with the red histogram indicating HitFit returned the correct jet-parton permutation. The number of entries, mean and RMS values of the complete sample (summed up over all permutation categories) is shown in each histogram.

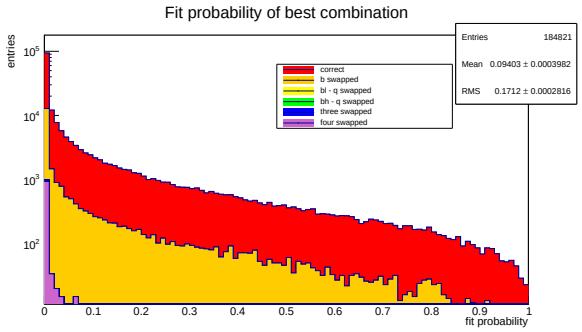

(a) $t\bar{t}$ spin-correlated events.

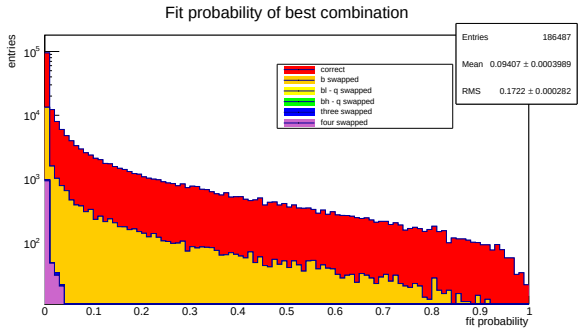

(b) $t\bar{t}$ spin-uncorrelated events.

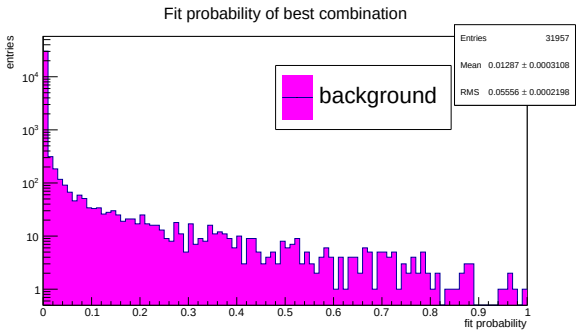

(c) W+jets events.

Figure A.5: Probability distribution of the best permutation returned by HitFit, keeping the $m_t = 173$ GeV constraint during the fit. The colour coding indicates how the best permutation relates to the true jet-parton permutation with the red histogram indicating HitFit returned the correct jet-parton permutation. In A.5c, the W+jets background sample is considered and the permutation cannot be related to a $t\bar{t}$ semi-leptonic jet-parton permutation. The number of entries, mean and RMS values of the complete sample (summed up over all permutation categories) is shown in each histogram.

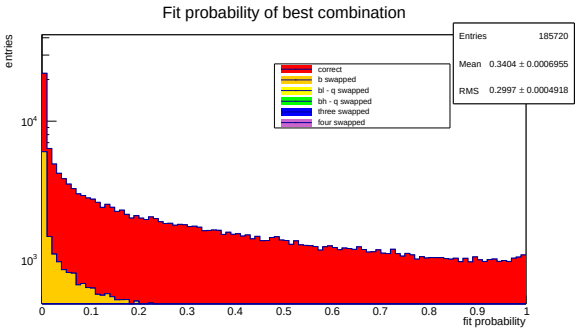

(a) $t\bar{t}$ spin-correlated events.

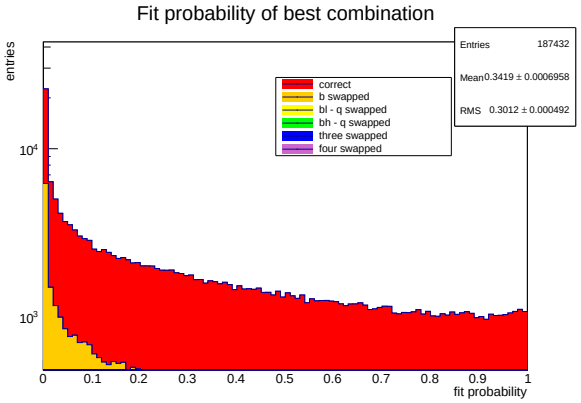

(b) $t\bar{t}$ spin-uncorrelated events.

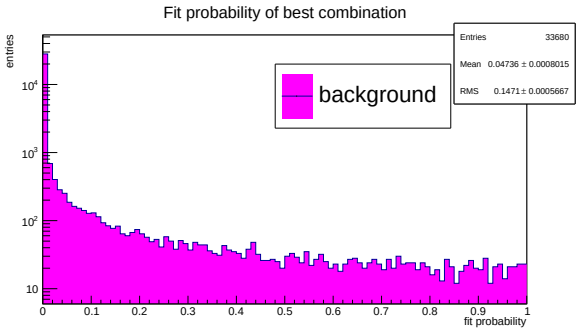

(c) W+jets events.

Figure A.6: Probability distribution of the best combination returned by HitFit, without the $m_t = 173$ GeV constraint during the fit. The colour coding indicates how the best permutation relates to the true jet-parton permutation with the red histogram indicating HitFit returned the correct jet-parton permutation. In A.6c, the W+jets background sample is considered and the permutation cannot be related to a $t\bar{t}$ semi-leptonic jet-parton permutation. The number of entries, mean and RMS values of the complete sample (summed up over all permutation categories) is shown in each histogram.

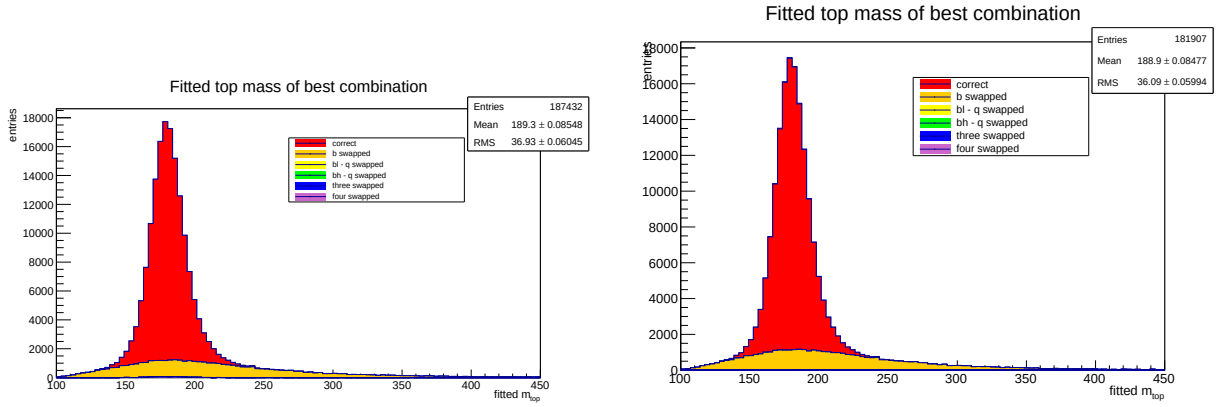

(a) $t\bar{t}$ spin-uncorrelated events.

(b) $t\bar{t}$ spin-uncorrelated events with χ^2.

Figure A.7: Top quark mass distribution of the best combination returned by HitFit, when the top quark mass is left unconstrained during the fit. The comparison between the distribution without (left) and with (right) the $\chi < 5$-cut is shown. The colour coding indicates how the best permutation relates to the true jet-parton permutation with the red histogram indicating HitFit returned the correct jet-parton permutation. The number of entries, mean and RMS values of the complete sample (summed up over all permutation categories) is shown in each histogram.

Bibliography

[1] P. Pullman, *His Dark Materials*. Scholastic, 1995.

[2] **Particle Data Group** Collaboration, "Review of Particle Physics," *Chin.Phys.* **C38** (2014) 090001.

[3] B. Pohv, K. Rith, C. Scholz, and F. Zetsche, *Particles and Nuclei. An Introduction to the Physical Concepts*. Springer, 2008.

[4] S. Weinberg, "Conceptual foundations of the unified theory of weak and electromagnetic interactions," *Reviews of Modern Physics* **52** no. 3, (1980) 515–523.

[5] S. L. Glashow, "Towards a unified theory: Threads in a tapestry," *Rev. Mod. Phys.* **52** (Jul, 1980) 539–543. http://link.aps.org/doi/10.1103/RevModPhys.52.539.

[6] A. Salam, "Gauge unification of fundamental forces," *Rev. Mod. Phys.* **52** no. 3, (July, 1980) 525–538.

[7] P. W. Higgs, "Broken symmetries and the masses of gauge bosons," *Phys. Rev. Lett.* **13** (Oct, 1964) 508–509. http://link.aps.org/doi/10.1103/PhysRevLett.13.508.

[8] F. Englert and R. Brout, "Broken symmetry and the mass of gauge vector mesons," *Phys. Rev. Lett.* **13** (Aug, 1964) 321–323. http://link.aps.org/doi/10.1103/PhysRevLett.13.321.

[9] **CMS** Collaboration, "Observation of a new boson at a mass of 125 GeV with the CMS experiment at the LHC," *Phys.Lett.* **B716** (2012) 30–61, arXiv:1207.7235 [hep-ex].

[10] **ATLAS** Collaboration, "Observation of a new particle in the search for the Standard Model Higgs boson with the ATLAS detector at the LHC," *Phys.Lett.* **B716** (2012) 1–29, arXiv:1207.7214 [hep-ex].

[11] S. Herb, D. Hom, L. Lederman, J. Sens, H. Snyder, *et al.*, "Observation of a Dimuon Resonance at 9.5-GeV in 400-GeV Proton-Nucleus Collisions," *Phys.Rev.Lett.* **39** (1977) 252–255.

[12] **CDF** Collaboration, "Observation of top quark production in $\bar{p}p$ collisions," *Phys.Rev.Lett.* **74** (1995) 2626–2631, arXiv:hep-ex/9503002 [hep-ex].

[13] **D0** Collaboration, "Observation of the top quark," *Phys.Rev.Lett.* **74** (1995) 2632–2637, arXiv:hep-ex/9503003 [hep-ex].

[14] **CDF, D0** Collaboration, "Combination of measurements of the top-quark pair production cross section from the Tevatron Collider," *Phys.Rev.* **D89** no. 7, (2014) 072001, arXiv:1309.7570 [hep-ex].

[15] **ATLAS** Collaboration, "Combination of ATLAS and CMS top-quark pair cross-section measurements using proton-proton collisions at $\sqrt{s} = 8$ TeV," *Conference Report* **ATLAS-CONF-2014-054, ATLAS-COM-CONF-2014-063** (2014) .

[16] W. J. Stirling, "private communication." http://mstwpdf.hepforge.org/plots/plots.html.

[17] F. Maltoni, T. McElmurry, R. Putman, and S. Willenbrock, "Choosing the Factorization Scale in Perturbative QCD," arXiv:hep-ph/0703156 [HEP-PH].

[18] S. J. Brodsky and L. Di Giustino, "Setting the Renormalization Scale in QCD: The Principle of Maximum Conformality," *Phys.Rev.* **D86** (2012) 085026, arXiv:1107.0338 [hep-ph].

[19] S. Moch, S. Weinzierl, S. Alekhin, J. Blumlein, L. de la Cruz, *et al.*, "High precision fundamental constants at the TeV scale," arXiv:1405.4781 [hep-ph].

[20] A. Brandenburg, Z. Si, and P. Uwer, "Qcd-corrected spin analysing power of jets in decays of polarized top quarks," *Physics Letters B* **539** (2002) 235–241.

[21] W. Bernreuther, A. Brandenburg, Z. Si, and P. Uwer, "Top quark pair production and decay at hadron colliders," *Nuclear Physics B* **690** (2004) 81–137.

[22] **CDF** Collaboration, "Measurement of ttbar Spin Correlation in ppbar Collisions Using the CDF II Detector at the Tevatron," *Phys. Rev. D.* **83** (2011) 031104, arXiv:1012.3093v2 [hep-ex].

[23] B. Abbott *et al.*, "Spin correlation in $t\bar{t}$ production from $p\overline{p}$ collisions at $\sqrt{s} = 1.8$TeV," *Phys. Rev. Lett.* **85** (Jul, 2000) 256–261. http://link.aps.org/doi/10.1103/PhysRevLett.85.256.

[24] **D0** Collaboration, "Measurement of spin correlation in ttbar production using dilepton final states," *Phys. Lett. B* **702** (2011) 16, arXiv:1103.1871v1 [hep-ex].

[25] **D0** Collaboration, "Measurement of spin correlation in $t\bar{t}$ production using a matrix element approach," *Phys.Rev.Lett.* **107** (2011) 032001, arXiv:1104.5194 [hep-ex].

[26] **D0** Collaboration, "Evidence for spin correlation in ttbar production," *Phys. Rev. Lett.* **108** (2012) 032004, arXiv:1110.4194v1 [hep-ex].

[27] **ATLAS** Collaboration, "Observation of spin correlation in ttbar events from pp collisions at sqrts = 7 TeV using the ATLAS detector," arXiv:1203.4081v1 [hep-ex].

[28] **CMS** Collaboration, "Measurement of Spin Correlation in ttbar production," *CMS-PAS-TOP-12-004* (2012) . http://cds.cern.ch/record/141788.

[29] **ATLAS** Collaboration, "Measurements of spin correlation in top-antitop quark events from proton-proton collisions at $\sqrt{s} = 7$ TeV using the atlas detector," arXiv:hep-ph/1407.4314.

[30] **CMS** Collaboration, "Measurement of spin correlations in top pair events in the muon + jets channel with the matrix element method at 8TeV," *CMS-PAS-TOP-13-015* (2015) . http://cds.cern.ch/record/2023918.

[31] E. Eichten and K. Lane *Phys. Lett. B* **327** (1994) .

[32] G. Mahlon and S. J. Parke, "Angular correlations in top quark pair production and decay at hadron colliders," *Phys.Rev.* **D53** (1996) 4886–4896, arXiv:hep-ph/9512264 [hep-ph].

[33] W. Bernreuther and Z.-G. Si, "Top quark spin correlations and polarization at the LHC: standard model predictions and effects of anomalous top chromo moments," *Phys.Lett.* **B725** (2013) 115–122, arXiv:1305.2066 [hep-ph].

[34] Z. Hioki and K. Ohkuma, "Optimal-observable Analysis of Possible Non-standard Top-quark Couplings in $pp- > t\bar{t}X- > l^+X'$," *Phys.Lett.* **B716** (2012) 310–315, arXiv:1206.2413 [hep-ph].

[35] S. P. Martin, "A Supersymmetry primer," *Adv.Ser.Direct.High Energy Phys.* **21** (2010) 1–153, arXiv:hep-ph/9709356 [hep-ph].

[36] Z. Han, A. Katz, D. Krohn, and M. Reece, "(Light) Stop Signs," *JHEP* **1208** (2012) 083, arXiv:1205.5808 [hep-ph].

[37] L. Evans and P. Bryant, "LHC Machine," *JINST* **3** (2008) S08001.

[38] S. Dailler, "Cross section of LHC dipole. Dipole LHC: coupe transversale.." AC Collection. Legacy of AC. Pictures from 1992 to 2002., Apr, 1999.

[39] O. S. Brüning, P. Collier, P. Lebrun, S. Myers, R. Ostojic, J. Poole, and P. Proudlock, *LHC Design Report*. CERN, Geneva, 2004.

[40] **CMS** Collaboration, "Cms luminosity - public results,". https://twiki.cern.ch/twiki/bin/view/CMSPublic/LumiPublicResults.

[41] C. Bulletin, "The particle suppliers. Les fournisseurs de particules,". https://cds.cern.ch/record/1255151.

[42] **CMS** Collaboration, "The cms experiment at the cern lhc," *Journal of Instrumentation* **3** no. 08, (2008) S08004. http://stacks.iop.org/1748-0221/3/i=08/a=S08004.

[43] **CMS** Collaboration, "Design, performance, and calibration of cms forward calorimeter wedges," *The European Physical Journal C* **53** no. 1, (2008) 139–166. http://dx.doi.org/10.1140/epjc/s10052-007-0459-4.

[44] **CMS** Collaboration, "Slice of cms detector,". https://cms-docdb.cern.ch/cgi-bin/PublicEPPOGDocDB/RetrieveFile?docid=97&version=1&filename=Slice.gif.

[45] **CMS** Collaboration, "The cms tracker system project: Technical design report," 1997. http://cdsweb.cern.ch/record/368412.

[46] D. Sprenger, M. Weber, R. Adolphi, R. Brauer, L. Feld, *et al.*, "Validation of Kalman Filter alignment algorithm with cosmic-ray data using a CMS silicon strip tracker endcap," *JINST* **5** (2010) P06007, arXiv:1003.5460 [physics.ins-det].

[47] **CMS** Collaboration, *The CMS electromagnetic calorimeter project: Technical Design Report*. Technical Design Report CMS. CERN, Geneva, 1997. http://cdsweb.cern.ch/record/349375.

[48] **CMS** Collaboration, *CMS Physics : Technical Design Report Volume 1: Detector Performance and Software*. Technical Design Report CMS. CERN, Geneva, 2006. http://cdsweb.cern.ch/record/922757.

[49] **CMS** Collaboration, *The CMS hadron calorimeter project: Technical Design Report*. Technical Design Report CMS. CERN, Geneva, 1997. http://cdsweb.cern.ch/record/357153.

[50] **CMS** Collaboration, "The cms barrel calorimeter response to particle beams from 2 to 350 gev/c," *The European Physical Journal C* **60** no. 3, (2009) 359–373. http://dx.doi.org/10.1140/epjc/s10052-009-0959-5.

[51] **CMS** Collaboration, *The CMS muon project: Technical Design Report*. Technical Design Report CMS. CERN, Geneva, 1997. http://cdsweb.cern.ch/record/343814.

[52] M. S. Kim, "Cms reconstruction improvement for the muon tracking by the rpc chambers," *Journal of Instrumentation* **8** no. 03, (2013) T03001. http://stacks.iop.org/1748-0221/8/i=03/a=T03001.

[53] **CMS** Collaboration, "CMS Luminosity Based on Pixel Cluster Counting - Summer 2013 Update," *CMS-PAS-LUM-13-001* (2013) .

[54] **CMS** Collaboration, S. Cittolin, A. Rácz, and P. Sphicas, *CMS The TriDAS Project: Technical Design Report, Volume 2: Data Acquisition and High-Level Trigger. CMS trigger and data-acquisition project.* Technical Design Report CMS. CERN, Geneva, 2002. http://cdsweb.cern.ch/record/578006.

[55] **CMS** Collaboration, *CMS TriDAS project: Technical Design Report, Volume 1: The Trigger Systems.* Technical Design Report CMS. CERN, Geneva, 200. http://cdsweb.cern.ch/record/706847.

[56] W. Badgett, S. Dasu, W. H. Smith, M. Jaworski, and J. Lackey, "CMS Calorimeter Level 1 Regional Trigger Electron Identification," Tech. Rep. CMS-NOTE-1999-026, CERN-CMS-NOTE-1999-026, 1999.

[57] **CMS** Collaboration, "Electron reconstruction and identification at sqrt(s) = 7 TeV," *CMS-PAS-EGM-10-004* (2010) . https://cds.cern.ch/record/1299116.

[58] M. Cacciari, G. P. Salam, and G. Soyez, "The anti- k t jet clustering algorithm," *Journal of High Energy Physics* **2008** no. 04, (2008) 063. http://stacks.iop.org/1126-6708/2008/i=04/a=063.

[59] J. Alwall, M. Herquet, F. Maltoni, O. Mattelaer, and T. Stelzer, "MadGraph 5 : Going Beyond," *JHEP* **1106** (2011) 128, arXiv:1106.0522 [hep-ph].

[60] S. Frixione and B. R. Webber, "Matching nlo qcd computations and parton shower simulations," *Journal of High Energy Physics* **2002** no. 06, (2002) 029. http://stacks.iop.org/1126-6708/2002/i=06/a=029.

[61] T. Sjöstrand, S. Mrenna, and P. Skands, "Pythia 6.4 physics and manual," *Journal of High Energy Physics* **2006** no. 05, (2006) 026. http://stacks.iop.org/1126-6708/2006/i=05/a=026.

[62] G. Corcella, I. G. Knowles, G. Marchesini, S. Moretti, K. Odagiri, P. Richardson, M. H. Seymour, and B. R. Webber, "Herwig 6: an event generator for hadron emission reactions with interfering gluons (including supersymmetric processes)," *Journal of High Energy Physics* **2001** no. 01, (2001) 010. http://stacks.iop.org/1126-6708/2001/i=01/a=010.

[63] P. Nason and B. Webber, "Next-to-Leading-Order Event Generators," *Ann.Rev.Nucl.Part.Sci.* **62** (2012) 187–213, arXiv:1202.1251 [hep-ph].

[64] T. Sjostrand, "High-energy physics event generation with PYTHIA 5.7 and JETSET 7.4," *Comput.Phys.Commun.* **82** (1994) 74–90.

[65] B. Andersson, G. Gustafson, G. Ingelman, and T. Sjostrand, "Parton Fragmentation and String Dynamics," *Phys.Rept.* **97** (1983) 31–145.

[66] **GEANT4** Collaboration, "GEANT4: A Simulation toolkit," *Nucl.Instrum.Meth.* **A506** (2003) 250–303.

[67] S. Abdoulline *et al.*, "The cms object-oriented simulation," in *Nuclear Science Symposium Conference Record, 2005 IEEE*, vol. 2, pp. 995–999. Oct, 2005.

[68] "Lhco event format." `http://www.jthaler.net/olympicswiki/doku.php`.

[69] R. Brun and F. Rademakers, "Root - an object oriented data analysis framework,". `http://root.cern.ch/`.

[70] W. Verkerke and D. Kirkby, "Roofit." `http://roofit.sourceforge.net`.

[71] **CMS** Collaboration, "Cmssw." `https://cmsdoc.cern.ch/cms/cpt/Software/html/General/`.

[72] E. Chabanat and N. Estre, "Deterministic Annealing for Vertex Finding at CMS,". `http://cds.cern.ch/record/865587`.

[73] R. Frühwirth, W. Waltenberger, and P. Vanlaer, "Adaptive Vertex Fitting," Tech. Rep. CMS-NOTE-2007-008, CERN, Geneva, Mar, 2007.

[74] **CMS** Collaboration, "Particle-Flow Event Reconstruction in CMS and Performance for Jets, Taus, and MET," *CMS-PAS-PFT-09-001* (2009) . `https://cds.cern.ch/record/1194487`.

[75] **CMS** Collaboration, "Cms tracking performance results from early lhc operation," *The European Physical Journal C* **70** no. 4, (2010) 1165–1192. `http://dx.doi.org/10.1140/epjc/s10052-010-1491-3`.

[76] **CMS** Collaboration, "Track reconstruction in the cms tracker," *CMS-PAS-TRK-09-001* (2009) .

[77] R. E. Kalman, "A New Approach to Linear Filtering and Prediction Problems," *Transactions of the ASME – Journal of Basic Engineering* no. 82 (Series D), (1960) 35–45. `http://www.cs.unc.edu/~{}welch/kalman/media/pdf/Kalman1960.pdf`.

[78] **CMS** Collaboration, "Particle-flow commissioning with muons and electrons from J/Psi and W events at 7 TeV," *CMS-PAS-PFT-10-003* (2010) . `https://cds.cern.ch/record/1279347`.

[79] **CMS** Collaboration, "Performance of CMS muon reconstruction in pp collision events at $\sqrt{s} = 7$ TeV," *JINST* **7** (2012) P10002, `arXiv:1206.4071 [physics.ins-det]`.

[80] W. Adam, R. Frühwirth, A. Strandlie, and T. Todorov, "Reconstruction of electrons with the gaussian-sum filter in the cms tracker at the lhc," *Journal of Physics G: Nuclear and Particle Physics* **31** no. 9, (2005) N9. `http://stacks.iop.org/0954-3899/31/i=9/a=N01`.

[81] **CMS** Collaboration, "Performance of electron reconstruction and selection with the CMS detector in proton-proton collisions at $\sqrt{s} = 8$ TeV." Submitted to *JINST*, 2015.

[82] M. Cacciari, G. P. Salam, and G. Soyez, "The Anti-k(t) jet clustering algorithm," *JHEP* **0804** (2008) 063, `arXiv:0802.1189 [hep-ph]`.

[83] Y. L. Dokshitzer, G. Leder, S. Moretti, and B. Webber, "Better jet clustering algorithms," *JHEP* **9708** (1997) 001, `arXiv:hep-ph/9707323 [hep-ph]`.

[84] S. D. Ellis and D. E. Soper, "Successive combination jet algorithm for hadron collisions," *Phys.Rev.* **D48** (1993) 3160–3166, `arXiv:hep-ph/9305266 [hep-ph]`.

[85] G. P. Salam and G. Soyez, "A Practical Seedless Infrared-Safe Cone jet algorithm," *JHEP* **0705** (2007) 086, arXiv:0704.0292 [hep-ph].

[86] **CMS** Collaboration, "Determination of jet energy calibration and transverse momentum resolution in cms," *Journal of Instrumentation* **6** no. 11, (2011) P11002. http://stacks.iop.org/1748-0221/6/i=11/a=P11002.

[87] **CMS** Collaboration, "8 TeV Jet Energy Corrections and Uncertainties based on 19.8 fb^{-1} of data in CMS,". https://cds.cern.ch/record/1627305.

[88] **CMS** Collaboration, "Determination of jet energy calibration and transverse momentum resolution in CMS," *JINST* **6** (2011) P11002, arXiv:1107.4277 [physics.ins-det].

[89] **CMS** Collaboration, "MET performance in 8 TeV data," *CMS-PAS-JME-12-002* (2013) . http://cds.cern.ch/record/1543527.

[90] **CMS** Collaboration, "Identification of b-quark jets with the CMS experiment," *J. Instrum.* **8** no. arXiv:1211.4462. CMS-BTV-12-001. CERN-PH-EP-2012-262, (Nov, 2012) P04013. 67 p. Comments: Submitted to the Journal of Instrumentation.

[91] **CMS** Collaboration, "Csv b-tagging algorithm efficiency curves." https://twiki.cern.ch/twiki/bin/view/CMSPublic/SWGuideBTagPerformance.

[92] J. D'Hondt, S. Lowette, O. L. Buchmüller, S. Cucciarelli, F.-P. Schilling, M. Spiropulu, S. Paktinat-Mehdiabadi, D. Benedetti, and L. Pape, "Fitting of Event Topologies with External Kinematic Constraints in CMS," Tech. Rep. CMS-NOTE-2006-023, CERN, Geneva, Jan, 2006.

[93] S. S. Snyder, "Measurement of the top quark mass at D0," 1995.

[94] O. Dahl, D. T.B., S. F.T., *et al.*, *SQUAW Kinematic Fitting Program.* No. Programming Note P-126. Berkely, July, 1968.

[95] **CMS** Collaboration, "Programming documentation of HitFit: A Kinematic Fitter for top quark-antiquark pair lepton+jets event," *CMS Analysis Note* **CMS-AN-2011/171** (2011) .

[96] **CMS** Collaboration, "Commissioning of the Particle-Flow Reconstruction in Minimum-Bias and Jet Events from pp Collisions at 7 TeV," *CMS-PAS-PFT-10-002* (2010) .

[97] **CMS** Collaboration, "Performance of electron reconstruction and selection with the CMS detector in proton-proton collisions at $\sqrt{s} = 8$ TeV," arXiv:1502.02701 [physics.ins-det].

[98] **CMS** Collaboration, "muon object efficiencies." https://twiki.cern.ch/twiki/bin/viewauth/CMS/MuonReferenceEffs.

[99] **CMS** Collaboration, "Pile-up reweighting." https://twiki.cern.ch/twiki/bin/view/CMS/PileupMCReweightingUtilities.

[100] **CMS** Collaboration, "Jet Transverse Momentum Resolution Measurement using Dijet Events at $\sqrt{s}$= 8 TeV," *CMS Analysis Note* **CMS-AN-2013/416** (2013) .

[101] **CMS** Collaboration, "Jet energy resolution." https://twiki.cern.ch/twiki/bin/viewauth/CMS/JetResolution.

[102] J. Neyman and E. Pearson, "On the problem of the most efficient tests of statistical hypotheses," *Phil. Trans. R. Soc. Series A* **231** (1933) 289.

[103] G. Mahlon and S. Parke, "Angular correlations in top quark pair production and decay at hadron colliders," *Phys. Rev. D* **53** (1996) 4886, arXiv:9512264v1 [hep-ph].

[104] G. Mahlon and S. Parke, "Spin correlation effects in top quark pair production at the lhc," *Phys. Rev. D* **81** (2010) 074024, arXiv:1001.3422 [hep-ph].

[105] W. Bernreuther, "private communication.".

[106] G. Lepage, *Vegas: An Adaptive Multi-dimensional Integration Program*, vol. preprint CLNS. Cornell, 1980.

[107] P. Artoisenet, V. Lemaitre, F. Maltoni, and O. Mattelaer, "Automation of the matrix element reweighting method," *JHEP* **1012** (2010) 068, arXiv:1007.3300 [hep-ph].

[108] R. Cousins, J. Mumford, J. Tucker, and V. Valuev, "Spin discrimination of new heavy resonances at the lhc," *JHEP* **11** (2005) 46.

[109] F. James and M. Roos, "Minuit: A System for Function Minimization and Analysis of the Parameter Errors and Correlations," *Comput.Phys.Commun.* **10** (1975) 343–367.

[110] **CMS** Collaboration, "Measurement of differential top-quark pair production cross sections in pp collisions at $\sqrt{s} = 7\,\text{TeV}$," *Eur.Phys.J.* **C73** (2013) 2339, arXiv:hep-ph/1211.2220.

[111] **CMS** Collaboration, "Measurement of differential top-quark pair production cross sections in the lepton+jets channel in pp collisions at 8 tev," *CMS-PAS-TOP-12-027* (2013) . http://cds.cern.ch/record/1523611.

[112] **CMS** Collaboration, "Measurement of the differential ttbar cross section in the dilepton channel at 8 tev," *CMS-PAS-TOP-12-028* (2013) . http://cds.cern.ch/record/1523664.

[113] **CMS** Collaboration, "Top p_T scale factors." https://twiki.cern.ch/twiki/bin/viewauth/CMS/TopPtReweighting.

[114] J. Pumplin, D. Stump, R. Brock, D. Casey, J. Huston, *et al.*, "Uncertainties of predictions from parton distribution functions. 2. The Hessian method," *Phys.Rev.* **D65** (2001) 014013, arXiv:hep-ph/0101032 [hep-ph].

[115] M. Botje, J. Butterworth, A. Cooper-Sarkar, A. de Roeck, J. Feltesse, *et al.*, "The PDF4LHC Working Group Interim Recommendations," arXiv:1101.0538 [hep-ph].

[116] **ATLAS, CDF, CMS, D0** Collaboration, "First combination of Tevatron and LHC measurements of the top-quark mass," arXiv:1403.4427 [hep-ex].

[117] **ATLAS** Collaboration, "Measurement of spin correlation in top-antitop quark events and search for top squark pair production in pp collisions at $\sqrt{s} = 8$ TeV using the atlas detector," *Phys. Rev. Lett.* **114** (Apr, 2015) 142001. http://link.aps.org/doi/10.1103/PhysRevLett.114.142001.

[118] **ATLAS** Collaboration, "Measurements of spin correlation in top-antitop quark events from proton-proton collisions at $\sqrt{s} = 7$ TeV using the atlas detector," *Phys. Rev. D* **90** (Dec, 2014) 112016. http://link.aps.org/doi/10.1103/PhysRevD.90.112016.

[119] P. Fayet, "Supersymmetry and weak, electromagnetic and strong interactions," *Phys. Lett. B* **64** (1976) 159.

[120] P. Fayet, "Spontaneously broken supersymmetric theories of weak, electromagnetic and strong interactions," *Phys. Lett. B* **69** (1977) 489.

[121] G. R. Farrar and P. Fayet, "Phenomenology of the Production, Decay, and Detection of New Hadronic States Associated with Supersymmetry," *Phys.Lett.* **B76** (1978) 575–579.

[122] S. Dimopoulos and H. Georgi, "Softly broken supersummetry and su(5)," *Nucl. Phys. B* **193** (1981) 150.

[123] **CMS** Collaboration, " Search for Anomalous Top Chromomagnetic Dipole Moments from angular distributions in $t\bar{t}$ Dileptonic events at $\sqrt{s} = 7$ TeV with the CMS detector.," *CMS-PAS-TOP-14-005* (2014) . `http://cds.cern.ch/record/1745175`.